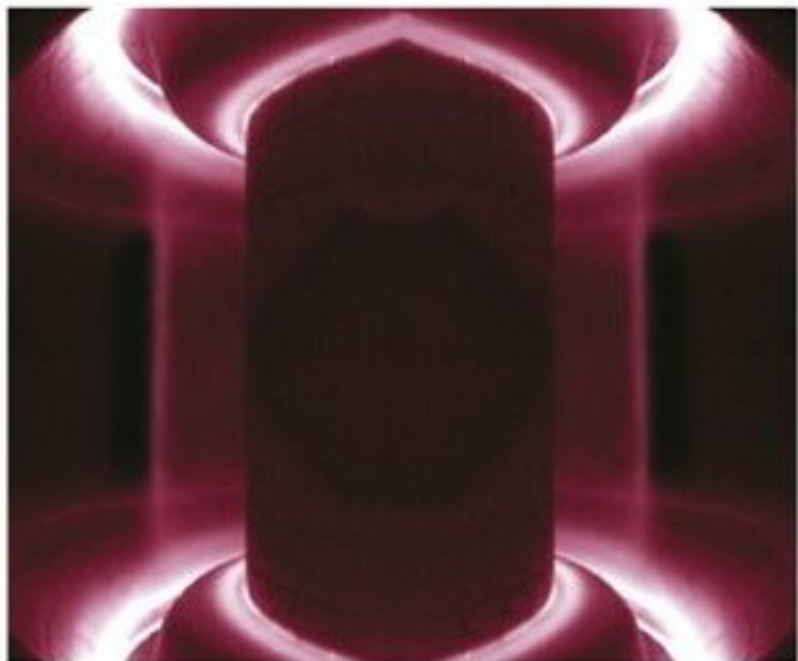


Weston M. Stacey

WILEY-VCH

Fusion Plasma Physics



Weston M. Stacey
Fusion Plasma Physics

Weston M. Stacey

Fusion Plasma Physics



WILEY-VCH Verlag GmbH & Co. KGaA

Dr. Weston M. Stacey
Georgia Institute of Technology
Nuclear & Radiological Engineering
and Medical Physics
900 Atlantic Drive, NW
Atlanta, GA 30332-0425
USA

All books published by Wiley-VCH are carefully produced. Nevertheless, authors, editors, and publisher do not warrant the information contained in these books, including this book, to be free of errors. Readers are advised to keep in mind that statements, data, illustrations, procedural details or other items may inadvertently be inaccurate.

Cover Picture
DIII-D Tokamak, General Atomics, San Diego

Library of Congress Card No.: applied for

British Library Cataloguing-in-Publication Data
A catalogue record for this book is available from the British Library

**Bibliographic information published by
Die Deutsche Bibliothek**

Die Deutsche Bibliothek lists this publication in the Deutsche Nationalbibliografie; detailed bibliographic data is available in the Internet at
<http://dnb.ddb.de>.

© 2005 WILEY-VCH Verlag GmbH & Co. KGaA,
Weinheim

All rights reserved (including those of translation into other languages). No part of this book may be reproduced in any form – by photopyting, microfilm, or any other means – nor transmitted or translated into a machine language without written permission from the publishers. Registered names, trademarks, etc. used in this book, even when not specifically marked as such, are not to be considered unprotected by law.

Printed in the Federal Republic of Germany
Printed on acid-free paper

Composition Da-TeX Gerd Blumenstein, Leipzig
Printing betz-druck GmbH, Darmstadt
Bookbinding Litges & Dopf Buchbinderei GmbH,
Heppenheim

ISBN-13: 978-3-527-40586-2
ISBN-10: 3-527-40586-0

Preface

The development of mankind's ultimate energy source, thermonuclear fusion, is a compelling intellectual challenge for those involved and a matter of enormous importance for all. Progress to date has been hard won, but substantial. We have come a long way from the beginning of this quest in the middle of the past century and now stand on the threshold of significant power production. The temperatures of laboratory plasmas (the working gas of fusion) have been increased from the tens of thousands of degrees of the early fusion experiments to above solar temperatures and then to the hundreds of millions of degrees required for terrestrial fusion. The proximity to the conditions at which this temperature could be maintained indefinitely by the self-heating of the fusion event has been reduced from the factor of hundreds of thousands that characterized the early experiments to within less than a factor of ten. Tens of kilowatts of fusion power have been produced. The engineering design and R & D for the International Thermonuclear Experimental Reactor (ITER), which will produce hundreds of millions of watts, has been completed. The construction of ITER in France will begin in the near future.

This progress in fusion energy development has been based on an ever-expanding understanding of the physics of magnetically confined plasmas and on improvements in the technology used for their heating and confinement. Most of the advances cited above have been realized in a toroidal confinement concept known as the "tokamak," and there are "advanced" variants of the tokamak which promise certain advantages relative to the "conventional" tokamak. Moreover, there are a number of other, less developed magnetic confinement concepts that may also lead to improved performance. The next quarter century will surely witness steps on the path to fusion power equally as exciting as those of the past.

I have worked on the development of fusion power for about 30 years and have taught graduate and advanced undergraduate courses in fusion plasma physics at Georgia Tech for almost that long. Over this period, both the details and the scope of the material that I felt was appropriate to include in a course on fusion plasma physics has changed significantly, so that the available textbooks (including one of my own) gradually became if not out of date at least somewhat dated, as more complete developments of the "conventional" topics of plasma physics (e.g. individual particle motion in electromagnetic fields, kinetic and fluid theory, MHD equilibrium, plasma instabilities, classical transport, neutral beam and wave heating) became available and as the portfolio of plasma physics was broadened to include new topics (e.g. non-inductive current-drive, fluctuation-driven transport, rotation, plasma-materials interactions, H-mode edge transport barriers, thermal instabilities, neutral atom transport, divertors, operational density and pressure limits, future fusion reactor and neutron source concepts). As my lecture notes evolved over the years, the new material came to dominate the conventional material found in the available textbooks on plasma physics; hence my decision to publish a new book based on these lecture notes.

This book is intended as a textbook for students with little or no knowledge of plasma physics but with the background in math and physics that would be expected of the graduate of a good undergraduate physics or nuclear engineering department. Essentially all of the material can be covered in a two-semester course. The sections that are *not* marked with an asterisk contain material that can be covered in a one-semester course for students at the senior or first year graduate level. The sections marked with an asterisk contain material that I would omit from a one-semester course either because it is of lower priority or at a more advanced level. The book should also serve as a self-study guide for advanced students and professionals on the newer material not found in other textbooks. Since the book provides many practical computational formulas, it should further serve as a useful reference for practicing professionals, and it has a detailed index for that purpose.

It is always necessary to be selective in choosing what to include and what to omit in a textbook. Most importantly, I have chosen to describe fusion plasma physics from a theoretical viewpoint, although the field is predominantly experimental, because this seems the best way to convey an understanding of the basic principles. I have attempted to be comprehensive in the treatment of plasma physics topics that are important to the development of fusion power, but have omitted other plasma physics topics. I have usually chosen a tokamak application to illustrate these topics because the tokamak applications are the most highly developed. I have tried both to develop the basic principles and to provide formulas that can be used in analyzing experimental results or designing future reactors, but I have stopped short of describing the calculational procedures used in the big codes of the field. I have included some discussion of experimental results, in particular for areas of current research, but have omitted any discussion of plasma diagnostics.

The person who masters the material in this book should be able to understand the work that is going on in fusion research laboratories and should be able to understand the research reported in the major fusion plasma physics research journals. He or she should have the background necessary to acquire the detailed expertise required for original research in any area of current interest in fusion plasma physics.

The author of a textbook such as this is always indebted to the many people who developed the subject matter and to the many other people who produced the lecture notes and finally the book. The subject matter of this book is based on material from many sources – the archival literature of the field, specialized monographs and reference books, earlier textbooks, laboratory reports, etc., only a fraction of which are cited in the section on further reading. John Mandrekas and Edward Thomas were involved in the assembling of material on plasma edge physics and plasma-materials interactions for an early version of the lecture notes. Several versions of the lecture notes and the final manuscript were prepared by Shauna Bennett-Boyd and Candace Salim. A generation of students called my attention to typos and worse in the lecture notes, and Zach Friis, Dingkang Zhang and Rob Johnson helped with the proofreading final. Finally, the team at Wiley-VCH – Cornelia Wanka, Claudia Grössl, Plamen Tanovski and others – expertly handled the conversion of the lecture notes into a book. To all of these people I am grateful.

Atlanta, Georgia
August 2005

Weston M. Stacey

Contents

1 Basic Physics	1
1.1 Fusion	1
1.2 Plasma	6
1.3 Coulomb Collisions	9
1.4 Electromagnetic Theory	15
2 Motion of Charged Particles	21
2.1 Gyromotion and Drifts	21
2.1.1 Gyromotion	21
2.1.2 $E \times B$ Drift	24
2.1.3 Grad- B Drift	25
2.1.4 Polarization Drift	27
2.1.5 Curvature Drift	28
2.2 Constants of the Motion	31
2.2.1 Magnetic Moment	31
2.2.2 Second Adiabatic Invariant	32
2.2.3 Canonical Angular Momentum	34
2.3 Diamagnetism*	36
3 Magnetic Confinement	41
3.1 Confinement in Mirror Fields	41
3.1.1 Simple Mirror	41
3.1.2 Tandem Mirrors*	46
3.2 Closed Toroidal Confinement Systems	49
3.2.1 Confinement	49
3.2.2 Flux Surfaces	53
3.2.3 Trapped Particles	55
3.2.4 Transport Losses	59
4 Kinetic Theory	65
4.1 Boltzmann and Vlasov Equations	66
4.2 Drift Kinetic Approximation	66
4.3 Fokker–Planck Theory of Collisions	69
4.4 Plasma Resistivity	76
4.5 Coulomb Collisional Energy Transfer	78
4.6 Krook Collision Operators	82

5 Fluid Theory	85
5.1 Moments Equations	85
5.2 One-Fluid Model	89
5.3 Magnetohydrodynamic Model	93
5.4 Anisotropic Pressure Tensor Model*	96
5.5 Strong Field, Transport Time Scale Ordering	98
6 Plasma Equilibria	103
6.1 General Properties	103
6.2 Axisymmetric Toroidal Equilibria	105
6.3 Large Aspect Ratio Tokamak Equilibria	111
6.4 Safety Factor	116
6.5 Shafranov Shift*	120
6.6 Beta	123
6.7 Magnetic Field Diffusion and Flux Surface Evolution*	125
6.8 Anisotropic Pressure Equilibria*	128
7 Waves	131
7.1 Waves in an Unmagnetized Plasma	131
7.1.1 Electromagnetic Waves	131
7.1.2 Ion Sound Waves	133
7.2 Waves in a Uniformly Magnetized Plasma	134
7.2.1 Electromagnetic Waves	134
7.2.2 Shear Alfvén Wave	137
7.3 Langmuir Waves and Landau Damping	139
7.4 Vlasov Theory of Plasma Waves*	142
7.5 Electrostatic Waves*	148
8 Instabilities	155
8.1 Hydromagnetic Instabilities	158
8.1.1 MHD Theory	159
8.1.2 Chew–Goldberger–Low Theory	160
8.1.3 Guiding Center Theory	162
8.2 Energy Principle	165
8.3 Pinch and Kink Instabilities	169
8.4 Interchange (Flute) Instabilities	173
8.5 Ballooning Instabilities	179
8.6 Drift Wave Instabilities	183
8.7 Resistive Tearing Instabilities*	186
8.7.1 Slab Model	186
8.7.2 MHD Regions	187
8.7.3 Resistive Layer	189
8.7.4 Magnetic Islands	190

8.8	Kinetic Instabilities*	192
8.8.1	Electrostatic Instabilities	192
8.8.2	Collisionless Drift Waves	193
8.8.3	Electron Temperature Gradient Instabilities	195
8.8.4	Ion Temperature Gradient Instabilities	196
8.8.5	Loss–Cone and Drift–Cone Instabilities	197
8.9	Sawtooth Oscillations*	201
9	Neoclassical Transport	205
9.1	Collisional Transport Mechanisms	205
9.1.1	Particle Fluxes	205
9.1.2	Heat Fluxes	207
9.1.3	Momentum Fluxes	208
9.1.4	Friction Force	210
9.1.5	Thermal Force	210
9.2	Classical Transport	212
9.3	Neoclassical Transport – Toroidal Effects in Fluid Theory	215
9.4	Multifluid Transport Formalism*	221
9.5	Closure of Fluid Transport Equations*	224
9.5.1	Kinetic Equations for Ion–Electron Plasma	224
9.5.2	Transport Parameters	228
9.6	Neoclassical Transport – Trapped Particles	231
9.7	Chang–Hinton Ion Thermal Conductivity*	237
9.8	Extended Neoclassical Transport – Fluid Theory*	238
9.8.1	Radial Electric Field	239
9.8.2	Toroidal Rotation	240
9.8.3	Transport Fluxes	240
9.9	Electrical Currents*	242
9.9.1	Bootstrap Current	242
9.9.2	Total Current	243
9.10	Orbit Distortion	244
9.10.1	Toroidal Electric Field – Ware Pinch	244
9.10.2	Potato Orbits	245
9.10.3	Orbit Squeezing	246
9.11	Transport in a Partially Ionized Gas*	247
10	Plasma Rotation*	251
10.1	Neoclassical Viscosity	251
10.1.1	Rate-of-Strain Tensor in Toroidal Geometry	251
10.1.2	Viscous Stress Tensor	252
10.1.3	Toroidal Viscous Force	253
10.1.4	Parallel Viscous Force	257
10.1.5	Neoclassical Viscosity Coefficients	258

10.2	Rotation Calculations	260
10.2.1	Poloidal Rotation and Density Asymmetries	260
10.2.2	Radial Electric Field and Toroidal Rotation Velocities	262
10.3	Momentum Confinement Times	264
10.3.1	Theoretical	264
10.3.2	Experimental	265
11	Turbulent Transport	267
11.1	Electrostatic Drift Waves	267
11.1.1	General	267
11.1.2	Ion Temperature Gradient Drift Waves	270
11.1.3	Quasilinear Transport Analysis	270
11.1.4	Saturated Fluctuation Levels	272
11.2	Magnetic Fluctuations	273
11.3	Candidate Microinstabilities	275
11.3.1	Drift Waves and ITG Modes	276
11.3.2	Trapped Ion Modes	276
11.3.3	Electron Temperature Gradient Modes	277
11.3.4	Resistive Ballooning Modes	277
11.3.5	Chaotic Magnetic Island Overlap	277
11.4	Wave–Wave Interactions*	278
11.4.1	Mode Coupling	278
11.4.2	Direct Interaction Approximation	279
11.5	Drift Wave Eigenmodes*	280
11.6	Gyrokinetic and Gyrofluid Simulations	282
12	Heating and Current Drive	285
12.1	Inductive	285
12.2	Adiabatic Compression*	288
12.3	Fast Ions	291
12.3.1	Neutral Beam Injection	291
12.3.2	Fast Ion Energy Loss	293
12.3.3	Fast Ion Distribution	296
12.3.4	Neutral Beam Current Drive	298
12.3.5	Toroidal Alfvén Instabilities	299
12.4	Electromagnetic Waves	301
12.4.1	Wave Propagation	301
12.4.2	Wave Heating Physics	304
12.4.3	Ion Cyclotron Resonance Heating	308
12.4.4	Lower Hybrid Resonance Heating	309
12.4.5	Electron Cyclotron Resonance Heating	310
12.4.6	Current Drive	311

13 Plasma–Material Interaction	315
13.1 Sheath	315
13.2 Recycling	318
13.3 Atomic and Molecular Processes	319
13.4 Sputtering	324
13.5 Impurity Radiation	326
14 Divertors	331
14.1 Configuration, Nomenclature and Physical Processes	331
14.2 Simple Divertor Model	334
14.2.1 Strip Geometry	334
14.2.2 Radial Transport and Widths	334
14.2.3 Parallel Transport	336
14.2.4 Solution of Plasma Equations	337
14.2.5 Two-Point Model	338
14.3 Divertor Operating Regimes	340
14.3.1 Sheath-Limited Regime	340
14.3.2 Detached Regime	341
14.3.3 High Recycling Regime	341
14.3.4 Parameter Scaling	342
14.3.5 Experimental Results	343
14.4 Impurity Retention	343
14.5 Thermal Instability*	346
14.6 2D Fluid Plasma Calculation*	349
14.7 Drifts*	351
14.7.1 Basic Drifts in the SOL and Divertor	351
14.7.2 Poloidal and Radial $E \times B$ Drifts	352
14.8 Thermoelectric Currents*	354
14.8.1 Simple Current Model	354
14.8.2 Relaxation of Simplifying Assumptions	356
14.9 Detachment	358
15 Plasma Edge	361
15.1 H-Mode Edge Transport Barrier	361
15.1.1 Relation of Edge Transport and Gradients	362
15.1.2 MHD Stability Constraints on Pedestal Gradients	364
15.1.3 Representation of MHD Pressure Gradient Constraint	368
15.1.4 Pedestal Widths	369
15.2 $E \times B$ Shear Stabilization of Turbulence	371
15.2.1 $E \times B$ Shear Stabilization Physics	372
15.2.2 Comparison with Experiment	374
15.2.3 Possible “Trigger” Mechanism for the L–H Transition	374

15.3 Thermal Instabilities	376
15.3.1 Temperature Perturbations in the Plasma Edge	376
15.3.2 Coupled Two-Dimensional Density–Velocity–Temperature Perturbations	379
15.3.3 Spontaneous Edge Transport Barrier Formation	384
15.3.4 Consistency with Observed L–H Phenomena	389
15.4 MARFEs	392
15.5 Radiative Mantle	397
15.6 Edge Operation Boundaries	398
15.7 Ion Particle Transport in the Edge*	398
15.7.1 Generalized “Pinch-Diffusion” Particle Flux Relations	399
15.7.2 Density Gradient Scale Length	402
15.7.3 Edge Density, Temperature, Electric Field and Rotation Profiles .	403
16 Neutral Particle Transport*	413
16.1 Fundamentals	413
16.1.1 1D Boltzmann Transport Equation	413
16.1.2 Legendre Polynomials	414
16.1.3 Charge Exchange Model	415
16.1.4 Elastic Scattering Model	416
16.1.5 Recombination Model	419
16.1.6 First Collision Source	419
16.2 P_N Transport and Diffusion Theory	421
16.2.1 P_N Equations	421
16.2.2 Extended Diffusion Theories	424
16.3 Multidimensional Neutral Transport	428
16.3.1 Formulation of Transport Equation	428
16.3.2 Boundary Conditions	430
16.3.3 Scalar Flux and Current	430
16.3.4 Partial Currents	432
16.4 Integral Transport Theory	432
16.4.1 Isotropic Point Source	433
16.4.2 Isotropic Plane Source	434
16.4.3 Anisotropic Plane Source	435
16.4.4 Transmission and Probabilities	437
16.4.5 Escape Probability	437
16.4.6 Inclusion of Isotropic Scattering and Charge Exchange	438
16.4.7 Distributed Volumetric Sources in Arbitrary Geometry	439
16.4.8 Flux from a Line Isotropic Source	439
16.4.9 Bickley Functions	440
16.4.10 Probability of Traveling a Distance t from a Line, Isotropic Source without a Collision	441

16.5	Collision Probability Methods	442
16.5.1	Reciprocity among Transmission and Collision Probabilities	442
16.5.2	Collision Probabilities for Slab Geometry	443
16.5.3	Collision Probabilities in Two-Dimensional Geometry	443
16.6	Interface Current Balance Methods	445
16.6.1	Formulation	445
16.6.2	Transmission and Escape Probabilities	445
16.6.3	2D Transmission/Escape Probabilities (TEP) Method	447
16.6.4	1D Slab Method	452
16.7	Discrete Ordinates Methods	453
16.7.1	\mathbf{P}_L and $\mathbf{D}-\mathbf{P}_L$ Ordinates	454
16.8	Monte Carlo Methods	456
16.8.1	Probability Distribution Functions	456
16.8.2	Analog Simulation of Neutral Particle Transport	457
16.8.3	Statistical Estimation	459
16.9	Navier–Stokes Fluid Model	460
17	Power Balance	463
17.1	Energy Confinement Time	463
17.1.1	Definition	463
17.1.2	Experimental Energy Confinement Times	464
17.1.3	Empirical Correlations	465
17.2	Radiation	468
17.2.1	Radiation Fields	468
17.2.2	Bremsstrahlung	470
17.2.3	Cyclotron Radiation	471
17.3	Impurities	473
17.4	Burning Plasma Dynamics	475
18	Operational Limits	479
18.1	Disruptions	479
18.1.1	Physics of Disruptions	479
18.1.2	Causes of Disruptions	481
18.2	Disruption Density Limit	481
18.2.1	Radial Temperature Instabilities	483
18.2.2	Spatial Averaging	485
18.2.3	Coupled Radial Temperature–Density Instabilities	487
18.3	Nondisruptive Density Limits	490
18.3.1	MARFEs	490
18.3.2	Confinement Degradation	491
18.3.3	Thermal Collapse of Divertor Plasma	494
18.4	Empirical Density Limit	495

18.5 MHD Instability Limits	495
18.5.1 β -Limits	495
18.5.2 Kink Mode Limits on $q(a)/q(0)$	498
19 Fusion Reactors and Neutron Sources	501
19.1 Plasma Physics and Engineering Constraints	501
19.1.1 Confinement	501
19.1.2 Density Limit	502
19.1.3 Beta Limit	503
19.1.4 Kink Stability Limit	504
19.1.5 Start-Up Inductive Volt-Seconds	504
19.1.6 Noninductive Current Drive	505
19.1.7 Bootstrap Current	506
19.1.8 Toroidal Field Magnets	506
19.1.9 Blanket and Shield	507
19.1.10 Plasma Facing Component Heat Fluxes	507
19.1.11 Radiation Damage to Plasma Facing Components	510
19.2 International Tokamak Program	511
19.2.1 Advanced Tokamak	514
19.3 Neutron Sources	515
Appendices	
A Frequently Used Physical Constants	521
B Dimensions and Units	523
C Vector Calculus	527
D Curvilinear Coordinates	529
E Plasma Formulas	537
F Further Reading	539
G Attributions	543
Subject Index	549

1 Basic Physics

We will begin our study of fusion plasmas by considering the basic physics that ultimately determines the properties of a thermonuclear plasma. The fusion process will be considered in the first section, and the conditions necessary for the achievement of fusion reactions will be established. In the second section, we will examine some fundamental properties of a plasma and will establish the criterion that determines when a collection of charged particles may be treated as a plasma. The consequences of charged-particle (Coulomb) collisions upon the particles that make up a plasma will be examined in the third section. Finally, the basic equations of electromagnetic theory will be reviewed in the fourth section.

1.1 Fusion

The actual mass of an atomic nucleus is not the sum of the masses (m_p) of the Z -protons and the masses (m_n) of the $A-Z$ neutrons of which it is composed. The stable nuclides have a mass defect

$$\Delta = [Zm_p + (A-Z)m_n] - Am_z \quad (1.1)$$

This mass defect is conceptually thought of as having been converted to energy ($E = \Delta c^2$) at the time that the nucleus was formed, putting the nucleus into a negative energy state. The amount of externally supplied energy that would have to be converted to mass in disassembling a nucleus into its separate nucleons is known as the “binding energy” of the nucleus, $BE = \Delta c^2$. The binding energy per nucleon (BE/A) is shown in Fig. 1.1.

Any process which results in nuclides being converted to other nuclides with more binding energy per nucleon will result in the conversion of mass into energy. The combination of low A -nuclides to form higher A -nuclides with a larger BE/A is the basis for the fusion process for the release of nuclear energy. The splitting of very high A -nuclides to form intermediate A -nuclides with a larger BE/A is the basis of the fission process for the release of nuclear energy.

The fusion of two light nuclei to form a compound nucleus in an excited state that then decays into reaction products, with an attendant conversion of mass into kinetic energy, is represented schematically by



The mass difference

$$\Delta m = (m_a + m_b) - (m_c + m_d) > 0 \quad (1.3)$$

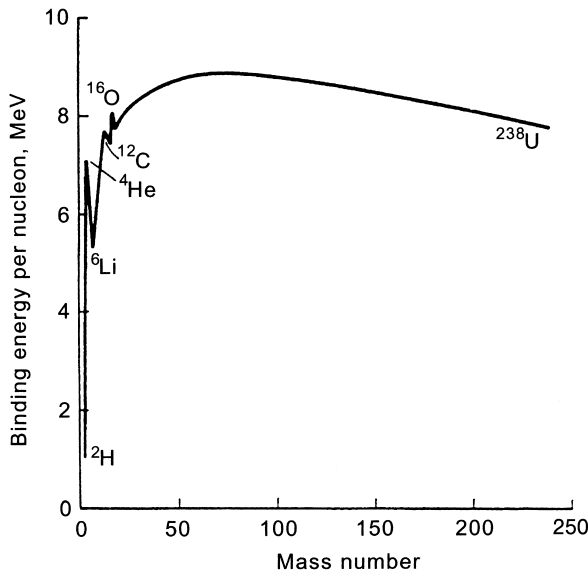


Figure 1.1. Binding energy per nucleon

is converted into kinetic energy according to Einstein's celebrated formula

$$\Delta E = (\Delta m)c^2 \quad (1.4)$$

In order for the fusion reaction to take place, the two nuclei must overcome the long-range Coulomb repulsion force and approach sufficiently close that the short-range nuclear attraction forces can lead to the formation of a compound nucleus. From the observation that hydrogen, deuterium, helium, and so on, do not fuse spontaneously under normal conditions, we conclude that the electrostatic repulsion between positively charged nuclei prevents nuclei approaching each other sufficiently close for the short-range attractive nuclear forces to become dominant. For fusion to occur as a result of random encounters between atomic nuclei, the nuclei must be made sufficiently energetic to overcome the Coulomb repulsive force. We will see that energies of the order of 10 keV to 100 keV are required, which corresponds to temperatures of 10^8 K to 10^9 K. At these thermonuclear temperatures, which are comparable to those of the sun's interior, light atoms are completely stripped of their orbital electrons. This macroscopically neutral gas of positively charged light atomic nuclei and electrons is a thermonuclear plasma.

The rate at which fusion reactions take place between atomic nuclei of species 1 and 2 in a thermonuclear plasma is

$$n_1 n_2 \langle \sigma v \rangle_f \equiv n_1 n_2 \int_{v_1 v_2} f_1(v_1) f_2(v_2) |v_1 - v_2| \sigma_f(|v_1 - v_2|) d^3 v_1 d^3 v_2 \quad (1.5)$$

where n_1 is the density, v_1 is the velocity, and f_1 is the velocity distribution function, respectively, of species 1, and σ_f is the fusion cross section. The velocity distributions of

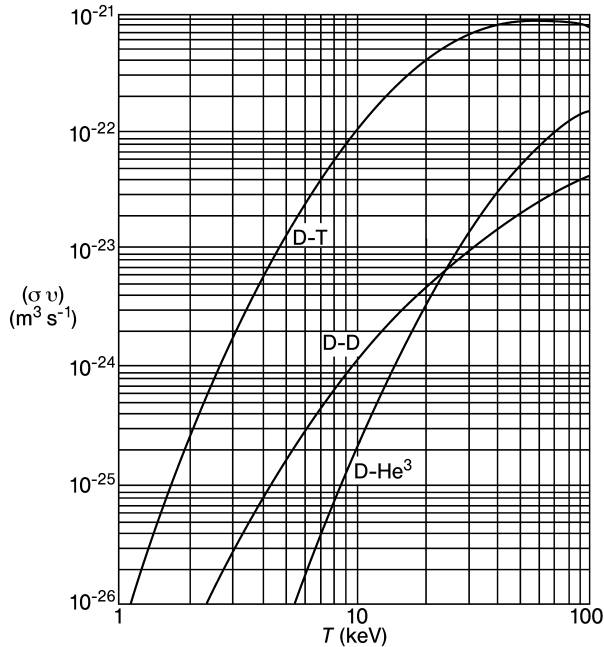


Figure 1.2. Fusion reaction rates

ions in a plasma can be represented in many cases by a Maxwellian distribution

$$f_{\max} = \left(\frac{m_i}{2\pi T_i} \right)^{\frac{3}{2}} e^{-(m_i v^2)/2T_i} \quad (1.6)$$

where T_i and m_i are the temperature and mass, respectively, and k is the Boltzmann constant. We will see that Coulomb collisions will cause all light ion species in a plasma to have about the same velocity distribution, so that the parameter $\langle \sigma v \rangle_f$ in Eq. (1.5) can be evaluated as a function of a single temperature $T = T_1 = T_2$.

Fusion reaction rates for the three reactions of primary interest for thermonuclear plasmas are shown in Fig. 1.2. At temperatures below the threshold value shown in Fig. 1.2 the reaction rates are negligible. As is apparent from this figure, and from Table 1.1, the reaction rate which becomes significant at the lowest temperature is for deuterium (D)–tritium (T) fusion. Table 1.1 also gives the amount of thermonuclear energy produced by a fusion event and indicates the part of that energy that is the kinetic energy of a neutron. The two branches shown for the D–D reaction occur with about equal probability. There are many other possible fusion reactions, but they generally have even higher threshold energies.

We can identify the principal challenges of fusion research from these data. The plasma must be heated to thermonuclear temperature (10^8 K to 10^9 K) and confined sufficiently long that the thermonuclear energy produced significantly exceeds the energy required to

Table 1.1. Fusion reactions of primary interest

Reaction	Thermonuclear energy release MeV	Threshold energy K	keV
$D + T \rightarrow {}^4\text{He} + n$ (14.1 MeV)	17.6	4.5×10^7	4
$D + D \rightarrow \begin{cases} T + p \\ {}^4\text{He} + n \end{cases}$ (14.1 MeV)	4.0 3.25	4.0×10^8	35
$D + {}^3\text{He} \rightarrow {}^4\text{He} + p$	18.2	3.5×10^8	30

heat the plasma. A simple energy balance (which ignores many important effects),

$$\left(\frac{1}{4}n^2 \langle \sigma v \rangle_f E_f \right) \tau_E > 3nT \quad (1.7)$$

which states that the product of the fusion energy production rate and the energy confinement time, τ_E , must exceed the amount of energy required to heat n ions per unit volume ($n_1 = n_2 = \frac{1}{2}n$) and n electrons to temperature T , may be used to derive a break-even criterion for the scientific feasibility of fusion power. Using physical constants typical of a D-T plasma, Eq. (1.7) can be rearranged to write the criterion

$$nT\tau_E > \frac{12k}{\langle \sigma v \rangle_f} E_f \simeq 3 \times 10^{21} \text{ keV} \cdot \text{s}^{-1} \text{m}^{-3} \quad (1.8)$$

The quantity $\frac{\langle \sigma v \rangle_f}{T^2}$ is approximately constant around 10 keV for the D-T reaction.

No conceivable material could confine a plasma at thermonuclear temperatures. Plasmas at these temperatures coming into direct contact with a material wall would produce wall vaporization, which would quickly destroy the wall and quench plasma due to the radiation produced by the ions of the wall material in the plasma. Thus, means other than wall confinement are necessary.

Two basically different approaches to achieving energy break-even are being pursued. In the first approach, use is made of the fact that charged particles spiral about magnetic field lines to create magnetic field configurations which confine plasmas in a magnetic trap. The goals of magnetic confinement research are to achieve plasma densities of $\sim 10^{20} \text{ m}^{-3}$ to 10^{22} m^{-3} and energy confinement times of $\sim 10^{-1} \text{ s}$ to 10^1 s . Magnetically confined plasmas are to be heated to thermonuclear temperatures by a number of different possible means.

In the second approach, known as inertial confinement, a 1 mm to 10 mm D-T pellet is compressed to densities of 10^{27} m^{-3} to 10^{28} m^{-3} and heated to thermonuclear temperatures by lasers or fast ion beams. In the 10 ns to 100 ns required for explosive disassembly, fusion takes place at a prodigious rate.

The fusion criterion is plotted against the central temperature for a number of magnetic and inertial confinement concepts in Fig. 1.3, with the years in which different values of the fusion criterion were achieved indicated. The Q-contours indicate the value of the ratio of the fusion power produced in the plasma to the supplemental input power to the plasma

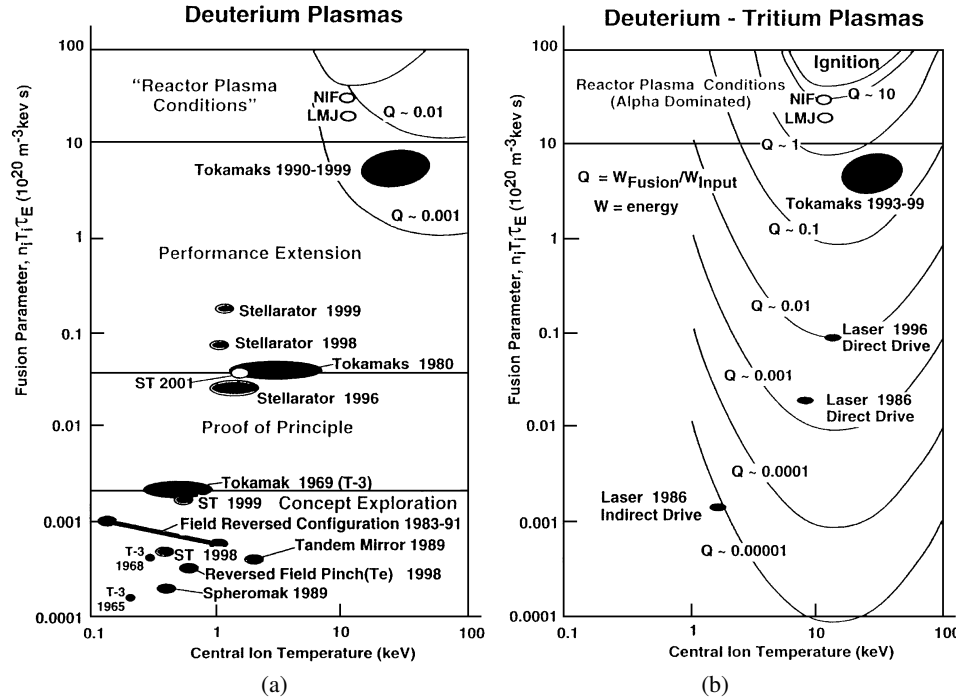


Figure 1.3. Progress in plasma confinement

necessary to maintain the temperature against radiative and transport losses. Fig. 1.3(a) is for deuterium plasmas in which the fusion power was produced by the D–D reaction, and Fig. 1.3(b) is for deuterium plasmas with a small admixture of tritium in which the fusion power was produced by the D–T reaction. The solid ovals indicate values achieved and the open ovals indicate anticipated values for existing experiments. As can be seen, the leading tokamak confinement concept has achieved values of the fusion criterion very close to what is needed for a reactor.

One D–T fusion yields 17.6 MeV, or 7.83×10^{-19} kWh, of thermonuclear energy. (The ultimate heat energy may be 20 % greater because of exothermic neutron reactions in the surrounding material.) The estimated worldwide lithium resources contain of the order of 6×10^{16} kWh of thermal energy based upon the D–T reaction, or roughly one third this amount of electrical energy. This number is comparable to the energy content of the estimated worldwide fossil fuel resources and to the accessible energy content of the estimated worldwide uranium resources, based on the fission reaction. (The accessible energy content of uranium resources can be increased substantially by breeding-neutron capture and subsequent radioactive decay of fissionable isotopes from the otherwise nonfissionable isotope of uranium.)

1.2 Plasma

A plasma is a collection of charged particles which is macroscopically neutral over a volume that is small compared to its dimensions. In principle, the motion of each particle can be determined from Newton's second Law and the electrostatic force that each particle exerts on all other particles. This is impractical in practice, because there might be some 10^{20} particles in a cubic meter of magnetically confined plasma, so other means of describing the plasma must be found. The fact that the electrostatic potential $\phi = e/(4\pi\epsilon_0 r)$ that a particle of charge e produces at a distance r is shielded by the presence of nearby charged particles can be exploited to develop a computationally tractable approximation.

Although a plasma is macroscopically neutral, it is locally nonneutral on some sufficiently small microscopic scale. Consider a macroscopically neutral plasma with a uniform ion distribution of density n_0 and a locally nonuniform electron distribution which varies according to the Maxwell–Boltzmann distribution

$$n_e = n_0 \exp\left(\frac{e\phi}{T_e}\right) \approx n_0 \left(1 + \frac{e\phi}{T_e}\right) \quad (1.9)$$

where $|e\phi| \ll |T_e|$. The local electrostatic potential, ϕ , arises from local nonuniformities in the electron distribution which lead to a local charge density $e(n_1 - n_e) = e(n_0 - n_e)$. The potential satisfies Poisson's equation

$$\nabla^2 \phi = \frac{e(n_e - n_0)}{\epsilon_0} = \frac{1}{\lambda_e^2} \phi \quad (1.10)$$

where we have used Eq. (1.9) in the last step and defined the electron Debye length

$$\lambda_e \equiv \left(\frac{\epsilon_0 T_e}{n_0 e^2}\right)^{\frac{1}{2}} \quad (1.11)$$

We know that the solution of Poisson's equation for an isolated point charge is $e/(4\pi\epsilon_0 r)$. Accordingly, we search for a solution to Eq. (1.10) which approaches this form as $r \rightarrow 0$ and which vanishes as $r \rightarrow \infty$. The appropriate solution, satisfying these boundary conditions, is

$$\phi(r) = \frac{e}{4\pi\epsilon_0 r} \exp\left(-\frac{r}{\lambda_e}\right) \quad (1.12)$$

Equation (1.12) describes a Coulomb potential at small r , ($r \ll \lambda_e$) but decreases much more rapidly than a Coulomb potential for $r \gtrsim \lambda_e$. Thus, the electrostatic potential arising from a microscopic nonuniformity in density – for example, the location of a charged particle – is shielded by a cloud of other charged particles within a distance λ_e . In order for this argument to be valid, the number of particles inside a sphere of radius λ_e must be large

$$n_\lambda \equiv \frac{4}{3}\pi \lambda_e^3 n_0 = \frac{4}{3}\pi \left(\frac{\epsilon_0 T_e}{n_0 e^2}\right)^{\frac{3}{2}} n_0 \gg 1 \quad (1.13)$$

(Note that the Debye length is the same for singly charged ions and electrons at the same temperature.) Equation (1.13) defines the criterion that must be satisfied in order for the

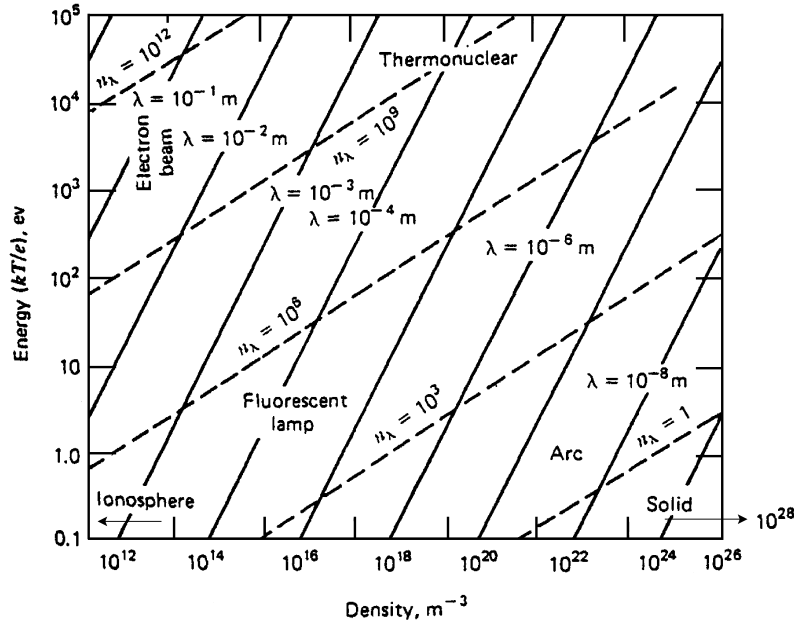


Figure 1.4. Debye length and number of particles in a Debye sphere

collection of charged particles to be a plasma. As can be seen from Fig. 1.4, plasmas exist over a wide range of densities (including solids) and temperatures.

In plasmas for which condition (1.13) is satisfied, the forces acting on a charged particle may be separated into two types for the purpose of developing a tractable computation approximation. The interaction of a given charged test particle with all other charged particles separated from it by λ_e or more may be treated by calculating the electric and magnetic fields produced by these other particles at the position of the test particle and the associated forces. The interactions of the test particle with all charged particles within less than λ_e of the test particle may be treated as two-body scattering interactions governed by the Coulomb electrostatic force acting between the two particles. The unshielded Coulomb potential $\phi = e/4\pi\epsilon_0 r$ is used in the latter calculation. Thus, the equation of motion of the test particle may be written

$$m \left(\frac{d\mathbf{v}}{dt} \right) = e(\mathbf{E} + \mathbf{v} \times \mathbf{B}) + \mathbf{F}_{sc} \quad (1.14)$$

where \mathbf{E} and \mathbf{B} are the electric and magnetic fields caused by other charges and currents due to the plasma particles and to external sources, and \mathbf{F}_{sc} is the force on the test particle due to the two-body scattering interactions with the other particles within λ_e of it.

The Debye length prescribes a lower limit on the macroscopic dimensions (L) of a plasma, by definition. For $L \leq \lambda_e$, the medium would behave as a collection of free charges dominated by mutual two-body interactions. For plasmas of thermonuclear interest, $\lambda_e \approx 10^{-5}$ m to 10^{-3} m, $N_\lambda \gg 1$, and $L \sim 1$ m.

A considerable amount can be learned about plasmas and their confinement by investigating the consequences of Eq. (1.14). First, it is necessary to calculate \mathbf{E} , \mathbf{B} and \mathbf{F}_{sc} , which is the purpose of the next two sections.

As an example of the collective treatment of a plasma, which also introduces the important concept of plasma frequency, consider a uniform plasma slab. Assume that at $t = 0$ all the electrons in the interval $x_1 < x < x_0$ are displaced to the left of x_1 , as shown in Fig. 1.5. Further assume that the ions are fixed. The excess charge to the left of x_1 , is $-n_0 e(x_0 - x_1)$. From Gauss' law, this produces a field at x_1 , in the $-x$ -direction of magnitude

$$E(x_1) = \frac{n_0 e}{\epsilon_0} (x_0 - x_1)$$

This field exerts a force on the electrons at x_1 , the equation of motion for which is

$$m_e \ddot{x}_1 = e E(x_1) = \frac{e^2 n_0}{\epsilon_0} (x_0 - x_1) \quad (1.15)$$

In terms of the relative displacement,

$$\xi \equiv x_0 - x_1 \quad (1.16)$$

this equation may be written

$$\frac{d^2 \xi}{dt^2} + \left(\frac{e^2 n_0}{m_e \epsilon_0} \right) \xi = 0 \quad (1.17)$$

This is the harmonic oscillator equation, with solution

$$\xi(t) = A e^{i \omega_{\text{pe}} t} + B e^{-i \omega_{\text{pe}} t} \quad (1.18)$$

where

$$\omega_{\text{pe}} \equiv \left(\frac{e^2 n_0}{m_e \epsilon_0} \right)^{\frac{1}{2}} \quad (1.19)$$

is the electron *plasma frequency*. A similar definition for the ion plasma frequency is

$$\omega_{\text{pi}} \equiv \left(\frac{z^2 e^2 n_0}{m_i \epsilon_0} \right)^{\frac{1}{2}} \quad (1.20)$$

where z is the ion charge.

Thus we see that the plasma frequency is a natural frequency of oscillation for each species in the plasma. As is well known from the theory of harmonic oscillators, the oscillations can be excited in response to an external stimulus with frequency less than or equal to the natural frequency. Thus each plasma species can respond to an internal perturbation with frequency $\omega < \omega_p$. Because

$$\omega_{\text{pi}} = z \sqrt{\frac{m_e}{m_i}} \omega_{\text{pe}} \quad (1.21)$$

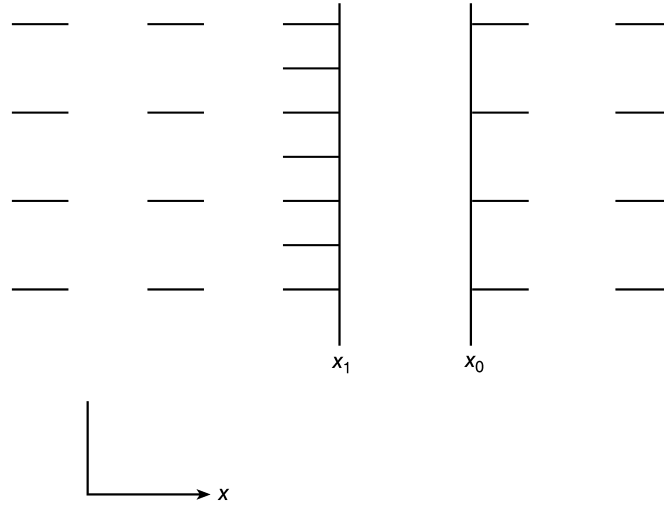


Figure 1.5. Plasma slab at $t = 0$

electrons are able to respond to much higher frequency perturbations than are ions. In MKS units, Eq. (1.19) is

$$\omega_{pe} = 56.4\sqrt{n_0} \text{ rad/s} \quad (1.22)$$

so that for a typical thermonuclear plasma density of $n_0 \approx 10^{20} \text{ m}^{-3}$, $\omega_{pe} \approx 5 \times 10^{11} \text{ rad/s}$.

1.3 Coulomb Collisions

Although most electrostatic interactions among particles in a plasma take place over distances that are large compared to a Debye length and can be treated collectively by fields, a smaller number of interactions take place over distances comparable to or less than a Debye length. These interactions, although relatively few in number, have important effects upon the properties of a plasma. These close encounters are treated separately, as scattering events, and take place on a time scale that is very short compared to most other plasma phenomena so that they may be considered to take place instantaneously.

The geometry of the scattering process is illustrated in Fig. 1.6. A particle of mass m_1 and initial velocity v_1 , approaches a stationary particle of mass m_2 . Assuming a repulsive electrostatic force (the final results are independent of the sign, although the trajectories are not) and defining the relative position vector

$$\mathbf{r} \equiv \mathbf{r}_1 - \mathbf{r}_2$$

and relative velocity vector

$$\mathbf{v} \equiv \mathbf{v}_1 - \mathbf{v}_2$$

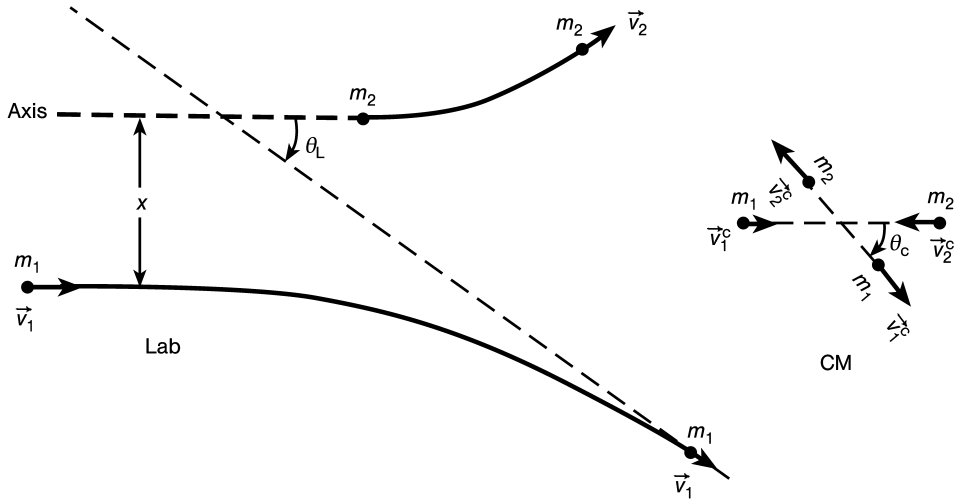


Figure 1.6. Particle trajectories in the laboratory and center-of-mass (prime indicates after collision)

the equations of motion can be combined to obtain

$$\frac{d^2\mathbf{r}}{dt^2} = \frac{m_1 + m_2}{m_1 m_2} \frac{e_1 e_2 \mathbf{r}}{4\pi\epsilon_0 |\mathbf{r}|^3} \equiv \frac{m_r^{-1} e_1 e_2 \mathbf{r}}{4\pi\epsilon_0 |\mathbf{r}|^3} \quad (1.23)$$

The solution of Eq. (1.23) is

$$\frac{1}{r} = \sqrt{1 + \frac{e_1^2 e_2^2}{x^2 v^4} \cos(\theta_c + \alpha)} - \frac{e_1 e_2}{m_r v^2 x^2} \quad (1.24)$$

where θ_c is the scattering angle in the center-of-mass (CM) system, α is a constant, and x is the impact parameter defined in Fig. 1.6.

Working out the kinematics of an elastic collision (conservation of energy and momentum) yields an expression for the scattering angle in the CM system.

$$\tan\left(\frac{\theta_c}{2}\right) = \frac{|e_1 e_2|}{m_r v^2 x 4\pi\epsilon_0} \quad (1.25)$$

and the relationship between the scattering angle in the lab and CM systems

$$\cot\theta_L = \left(\frac{m_1}{m_2}\right) \csc\theta_c + \cot\theta_c \quad (1.26)$$

Some special cases of Eq. (1.26) are of interest.

$$\begin{cases} m_1 \ll m_2, & \theta_L \approx \theta_c \\ m_1 = m_2, & \theta_L = \frac{1}{2}\theta_c \\ m_1 \gg m_2, & \theta_L \approx \frac{m_2}{m_1} \sin\theta_c \end{cases} \quad (1.27)$$

We have seen in Fig. 1.6 that the scattering event takes place in a plane. Actually, all particles of type 1 incident in the annular ring between x and $x + dx$ from the axis will

scatter into angles between θ_c and $\theta_c + d\theta_c$ or, equivalently, between θ_L and $\theta_L + d\theta_L$. For unit incident particle flux, the particle flux, $d\sigma$, scattered into the differential solid angle $d\Omega = 2\pi \sin \theta_c d\theta_c$ is equal to the cross sectional area of the annulus between x and $x + dx$

$$d\sigma = \sigma(\theta_c) d\Omega = \sigma(\theta_c) 2\pi \sin \theta_c d\theta_c = 2\pi x dx \quad (1.28)$$

where $\sigma(\theta_c)$ is the Rutherford scattering cross section

$$\sigma(\theta_c) \equiv \frac{2\pi x dx}{2\pi \sin \theta_c d\theta_c} = \frac{(e_1 e_2)^2}{\left(8\pi \epsilon_0 m_r v^2 \sin^2 \frac{\theta_c}{2}\right)^2} \quad (1.29)$$

Now, we will use these results to investigate the deflection of particles by Coulomb collisions. In particular, it will be shown that deflection through large angles (e.g., 90°) is much more probable as the result of multiple small-angle deflections than as the result of a single large-angle collision. This result has important consequences for our subsequent treatment of collision phenomena in plasmas.

First, consider the probability that a single interaction will scatter a particle through an angle $\gtrsim 90^\circ$ in the CM system. Since the angle of scatter increases as the impact parameter, x , decreases, this probability is just equal to the area of the cylinder surrounding the axis with radius corresponding to the impact parameter which results in $\theta_c = 90^\circ$

$$\sigma(\theta_c \geq 90^\circ) = \pi x_{90}^2$$

The $\theta_c = 90^\circ$ impact parameter can be determined from Eq. (1.25), so that

$$\sigma(\theta_c \geq 90^\circ) = \frac{(e_1 e_2)^2}{\pi (4\epsilon_0 m_r v^2)^2} \quad (1.30)$$

Now, consider a series of small-angle collisions. In the limit $\theta_c \rightarrow 0$, Eq. (1.25) yields an expression for the small-angle deflection in the CM system due to a single interaction

$$\Delta\theta_c = \frac{2|e_1 e_2|}{4\pi \epsilon_0 m_r v^2 x} \quad (1.31)$$

The mean square deflection of a “test” particle that travels a distance L in a plasma with scattering center density n_2 is

$$\begin{aligned} \overline{(\Delta\theta_c)^2} &= n_2 L \int_{\Delta\theta_{\min}}^{\Delta\theta_{\max}} (\Delta\theta_c)^2 \sigma(\Delta) (\Delta\theta_c) 2\pi \sin(\Delta\theta_c) d(\Delta\theta_c) \\ &= n_2 L \int_{x_{\min}}^{x_{\max}} (\Delta\theta_c)^2 2\pi x dx \\ &= \frac{n_2 L}{2\pi} \left(\frac{e_1 e_2}{\epsilon_0 m_r v^2} \right)^2 \int_{x_{\min}}^{x_{\max}} (\Delta\theta_c) \frac{dx}{x} \\ &= \frac{n_2 L}{2\pi} \left(\frac{e_1 e_2}{\epsilon_0 m_r v^2} \right)^2 \ln \left(\frac{x_{\max}}{x_{\min}} \right) \end{aligned} \quad (1.32)$$

The limits ($\Delta\theta_{\max} \rightarrow x_{\min}$, $\Delta\theta_{\min} \rightarrow x_{\max}$) are related by Eq. (1.31). Since only encounters at distances of the order of the Debye length are treated as collisions because of the screened Coulomb potential, we can choose

$$x_{\max} = \lambda_2 = \left(\frac{\epsilon_0 T_2}{n_2 e_2^2} \right)^{\frac{1}{2}} \quad (1.33)$$

For the minimum impact parameter, we take x_{90} , the value leading to 90° collisions, which is certainly an upper limit on scattering angles for “small” deflections:

$$x_{\min} = \frac{|e_1 e_2|}{4\pi\epsilon_0 m_r v^2} \quad (1.34)$$

With these limits, Eq. (1.32) becomes

$$\overline{(\Delta\theta_c)^2} = n_2 L \left(\frac{e_1 e_2}{\epsilon_0 m_r v^2} \right)^2 \ln \Lambda \quad (1.35)$$

where the *Coulomb logarithm* is defined by

$$\ln \Lambda \equiv \ln \left(\frac{x_{\max}}{x_{\min}} \right) = \ln \left[12\pi \left(\frac{(\epsilon_0 T)^3}{n_2 e_2^4 e_1^2} \right)^{\frac{1}{2}} \right] \quad (1.36)$$

and the assumption $m_r v^2 \approx 3T$ has been used.

The mean free path for 90° deflection by small-angle scattering ($L = \lambda_{90}$) can be estimated from Eq. (1.35) by setting $(\Delta\theta_c)^2 = 1$. The corresponding cross section, σ_{90} , can then be constructed

$$\sigma_{90} \equiv \frac{1}{n_2 \lambda_{90}} = \frac{(e_1 e_2)^2 \ln \Lambda}{2\pi(\epsilon_0 m_r v^2)^2} \quad (1.37)$$

Finally, the relative probabilities for a particle undergoing a 90° deflection due to multiple small-angle collisions and due to a single large-angle collision can be found from Eqs. (1.37) and (1.30):

$$\frac{\sigma_{90}}{\sigma(\theta_c > 90)} = 8 \ln \Lambda \quad (1.38)$$

The Coulomb logarithm is ~ 15 to 20 for thermonuclear plasmas. Thus, deflection through large angles via multiple small-angle collisions is about two orders of magnitude more probable than deflection via a single large-angle collision.

The characteristic time required for a 90° deflection in the CM system by multiple small-angle collisions is

$$\tau_{90} \equiv \frac{\lambda_{90}}{v} = \frac{2\pi\epsilon_0^2 m_r^2 v^3}{n_2(e_1 e_2)^2 \ln \Lambda} = \frac{2\pi\sqrt{m_r}\epsilon_0^2 (3T)^{\frac{3}{2}}}{n_2(e_1 e_2)^2 \ln \Lambda} \quad (1.39)$$

For like-particle scattering (e.g., ions on ions or electrons on electrons), $m_r = m_2$ and

$$\left. \begin{aligned} \tau_{90}^{ii} \\ \tau_{90}^{ee} \end{aligned} \right\} = \frac{6\pi\sqrt{3}\sqrt{m_r}\epsilon_0^2(T)^{\frac{3}{2}}}{ne^4 \ln \Lambda} \quad (1.40)$$

where $m = \frac{m_i}{m_e}$ and $e^4 \rightarrow z^4 e^4$ for τ_{90}^{ii} .

For electrons on ions

$$\tau_{90}^{ei} = \frac{6\sqrt{6\pi}\sqrt{m_e}\epsilon_0^2(T)^{\frac{3}{2}}}{n_i(ze^2)^2 \ln \Lambda} \quad (1.41)$$

and for ions on electrons the result is the same but with $n_i \rightarrow n_e$.

It follows from Eq. (1.27) that the deflection in the lab system is comparable to the deflection in the CM system when $m_1 \leq m_2$. Thus for like-particle scattering and for the scattering of electrons on ions the above expressions are also good estimates of the characteristic time for 90° deflection in the lab system.

However, for ions on electrons, $\Delta\theta_L \sim m_e/m_i \Delta\theta_c$. Thus the test particle must travel approximately $m_i/m_e \approx 2 \times 10^3$ times the distance (λ_{90}) required for a 90° deflection in the CM system before a 90° deflection occurs in the lab system. Consequently, the characteristic time for a 90° deflection in the lab is about m_i/m_e times the characteristic time for a 90° deflection in the CM system. Thus

$$\tau_{90}^{ie} \approx \left(\frac{m_i}{m_e} \right) \tau_{90}^{ei} \quad (1.42)$$

From Eq. (1.39) we discover the ordering

$$\tau_{90}^{ee} \sim \tau_{90}^{ei} \sim \left(\frac{m_e}{m_i} \right)^{\frac{1}{2}} \tau_{90}^{ii} \sim \left(\frac{m_e}{m_i} \right) \tau_{90}^{ie} \quad (1.43)$$

In a typical thermonuclear plasma ($n \sim 10^{20} \text{ m}^{-3}$, $T = 10 \text{ keV}$), $\tau_{90}^{ee} \sim \tau_{90}^{ei} \sim 10^{-4} \text{ s}$, $\tau_{90}^{ii} \sim 10^{-2} \text{ s}$, and $\tau_{90}^{ie} \sim 1 \text{ s}$.

The energy transferred from particle 1 to particle 2 in a collision can be found from the collision kinematics (conservation of energy and momentum). For an initial energy of E_0 , for particle 1, the energy transferred, ΔE , is

$$\frac{\Delta E}{E_0} = \frac{4m_1m_2}{(m_1 + m_2)^2} \sin^2 \frac{\theta_c}{2} \quad (1.44)$$

Multiple small-angle collisions that produce a 90° deflection in the CM system would cause an energy loss that can be estimated from Eq. (1.44) with $\theta_c = 90^\circ$:

$$\frac{\Delta E}{E_0} \approx \frac{2m_1m_2}{(m_1 + m_2)^2} \quad (1.45)$$

Thus like-particle collisions result in the transfer of about half of the initial energy in a 90° deflection time. For electrons scattering on ions or ions scattering on electrons, the

fractional energy transfer in a 90° deflection is only about m_e/m_i . Hence the characteristic time for energy transfer, τ_e , is related to the 90° deflection time as

$$\begin{aligned}\tau_e^{ee} &\sim \tau_{90}^{ee} \sim \tau_{90}^{ei} \\ \tau_e^{ii} &\sim \tau_{90}^{ii} \sim \left(\frac{m_i}{m_e}\right)^{\frac{1}{2}} \tau_{90}^{ei} \\ \tau_e^{ei} &\sim \frac{m_i}{m_e} \tau_e^{ei} \\ \tau_e^{ie} &\sim \frac{m_i}{m_e} \tau_{90}^{ei}\end{aligned}\tag{1.46}$$

A number of important conclusions follow immediately from Eq. (1.46). The electrons in a thermonuclear plasma exchange energy with each other and reach an equilibrium distribution – equilibrate – on a very short time scale, about 10^{-4} s. The ions equilibrate with themselves on a time scale that is longer by a factor of ~ 40 . The electrons transfer energy to ions, or vice versa, on a time scale that is $m_i/m_e \approx 2 \times 10^3$ times longer than the time scale required for the electrons to equilibrate with themselves.

Collisions have a randomizing effect on particle motion in a plasma. Consider the case of electrons drifting under the influence of an external electric field. Collisions tend to disorder the directed drift motion, which otherwise would be in the field direction. The equation of motion is

$$m_e \frac{dv_e}{dt} = -eE - \frac{m_e v_e}{\tau_{90}^{ei}} = -eE - \frac{e^4 n_e \ln \Lambda}{2\pi \epsilon_0^2 m_e v_e^2}\tag{1.47}$$

where the last term describes the rate of dissipation of ordered momentum due to collisions.

The first term on the right accelerates electrons (in the minus-direction for a positive E) and the second term acts to oppose the acceleration. Since the second term decreases with increasing v_e , electrons with velocity greater than the *Dreicer velocity*

$$v_{eD} = \left(\frac{e^3 n_e \ln \Lambda}{2\pi m_e \epsilon_0^2 E} \right)^{\frac{1}{2}}\tag{1.48}$$

are accelerated indefinitely and become *runaway electrons*. When $n \approx 10^{20} \text{ m}^{-3}$ and $E = 10 \text{ V} \cdot \text{m}^{-1}$, electrons with energy greater than 5 keV are runaway electrons.

Defining the current density

$$j \equiv -en_e v_e\tag{1.49}$$

and assuming that the drift velocity, v_e , is much less than the random thermal velocity, u_{th} , Eq. (1.47) becomes

$$\frac{m_e}{e^2 n_e} \frac{dj}{dt} = E - \eta j\tag{1.50}$$

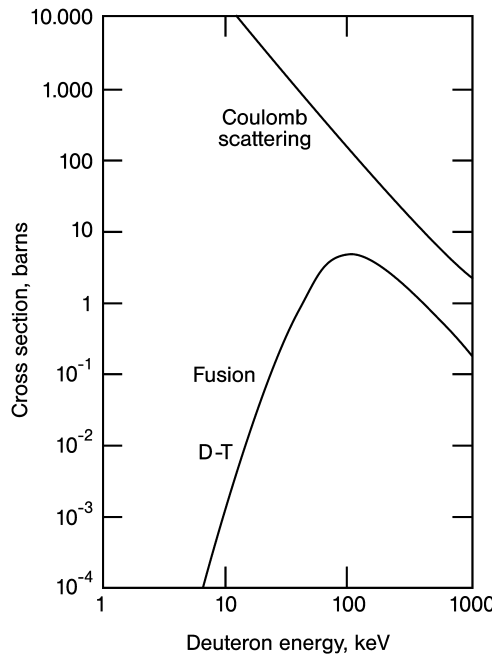


Figure 1.7. Fusion and Coulomb scattering cross sections (1 barn = 10^{-24} cm 2)

where

$$\eta \equiv \frac{\sqrt{m_e}ze^2 \ln \Lambda}{12\sqrt{3}\pi\epsilon_0^2(T)^{\frac{3}{2}}} \quad (1.51)$$

is the plasma resistivity. Note that Eq. (1.50) is of the form of an Ohm's law for the plasma.

The cross sections for ion–ion Coulomb collisions and for fusion are plotted in Fig. 1.7. From this figure, we conclude that an ion will suffer a large number of collisions, on average, before it undergoes fusion. Thus, the effects of collisions on the plasma are quite important.

1.4 Electromagnetic Theory

Much of the theory of plasmas is concerned with electric and magnetic fields. Such fields arise from external sources and from net charge and current distributions in the plasma. Recall that the long-range interactions among the charged particles that constitute a plasma are treated collectively in terms of fields. In this section, we review the basic laws of electromagnetism and discuss some useful properties of fields.

Gauss' law states that the normal outward component of the electric displacement, \mathbf{D} , integrated over the surface bounding any volume is equal to the net charge contained within

that volume

$$\int_s \mathbf{D} \cdot d\mathbf{s} = \int_v \rho d^3r \quad (1.52)$$

where ρ is the charge density. Using the divergence theorem on the LHS of Eq. (1.52) and requiring that the resulting equation be valid for arbitrary volumes leads to

$$\nabla \cdot \mathbf{D} = \rho \quad (1.53)$$

The magnetic field is divergence free – there is no magnetic equivalent of p . The normal outward component of the magnetic field, \mathbf{B} , integrated over any closed surface is zero:

$$\int_s \mathbf{B} \cdot d\mathbf{s} = 0 \quad (1.54)$$

Using the divergence theorem and the arbitrary volume argument leads to

$$\nabla \cdot \mathbf{B} = 0 \quad (1.55)$$

Since \mathbf{B} is solenoidal (i.e., satisfies Eq. (1.55)), it follows that it can be derived from a vector potential function, \mathbf{A} :

$$\mathbf{B} = \nabla \times \mathbf{A} \quad (1.56)$$

Faraday's law states that a changing magnetic flux, Φ , produces an electromotive force around a closed loop

$$\oint \mathbf{E} \cdot d\mathbf{l} = -\frac{d}{dt} \int_s \mathbf{B} \cdot d\mathbf{s} \equiv -\frac{d}{dt} \Phi \quad (1.57)$$

where s is any arbitrary surface bounded by the loop of arbitrary shape. If we assume that the loop and surface are fixed in time and make use of Stokes's theorem and the arbitrariness of the surface, Eq. (1.57) becomes

$$\nabla \times \mathbf{E} = -\frac{\partial \mathbf{B}}{\partial t} \quad (1.58)$$

Using Eq. (1.56) in Eq. (1.58) leads to

$$\nabla \times \left(\mathbf{E} + \frac{\partial \mathbf{A}}{\partial t} \right) = 0 \quad (1.59)$$

from which we conclude that the quantity in brackets can be represented by the gradient of a scalar potential. Thus the electric field can be written

$$\mathbf{E} = -\nabla \phi - \frac{\partial \mathbf{A}}{\partial t} \equiv \mathbf{E}_\phi + \mathbf{E}_A \quad (1.60)$$

When the electric field is linearly related to the electric displacement by the permittivity $\epsilon_0 = 8.854 \times 10^{-12} \text{ F} \cdot \text{m}^{-1}$,

$$\mathbf{D} = \epsilon_0 \mathbf{E}_\phi \quad (1.61)$$

Eqs. (1.53) and (1.61) can be combined to obtain Poisson's equation for the electrostatic potential,

$$\nabla^2 \phi = -\frac{\rho}{\epsilon_0} \quad (1.62)$$

The solution of Eq. (1.62) is

$$\phi(\mathbf{r}) = \frac{1}{4\pi\epsilon_0} \int \frac{\rho(\mathbf{r}')}{|\mathbf{r}' - \mathbf{r}|} d^3 r' \quad (1.63)$$

Thus the electrostatic contribution to the electric field can be determined from Eqs. (1.63) and (1.60), for a given charge distribution.

Ampere's law states that the normal component of the current plus the normal component of the time-rate-of-change of the electric displacement integrated over an arbitrary open surface produces a magnetomotive force around the closed loop bounding that surface:

$$\oint \mathbf{H} \cdot d\mathbf{l} = \int_s \mathbf{j} \cdot ds + \frac{d}{dt} \int_s \mathbf{D} \cdot ds \quad (1.64)$$

where \mathbf{H} is the magnetic intensity and \mathbf{j} is the current density. Using Stoke's theorem and the arbitrariness of the surface leads to

$$\nabla \times \mathbf{H} = \mathbf{j} + \frac{\partial \mathbf{D}}{\partial t} \quad (1.65)$$

for a fixed surface.

Equations (1.52), (1.54), (1.57) and (1.64) are based on experimental observation and are sometimes referred to as the integral form of Maxwell's equations. Equations (1.53), (1.55), (1.58) and (1.65) are the familiar, differential forms of Maxwell's equations for a stationary medium. (We will be interested later in the counterparts of Eqs. (1.58) and (1.65) in a moving medium.)

Now, reconsider the vector potential, \mathbf{A} . Assume that the magnetic field and the magnetic intensity are linearly related through the permeability, $\mu_0 = 1.257 \times 10^{-6} \text{ H} \cdot \text{m}^{-1}$,

$$\mathbf{B} = \mu_0 \mathbf{H} \quad (1.66)$$

Substitute Eq. (1.66) into Eq. (1.65) and use Eq. (1.60) to obtain

$$\nabla \times (\nabla \times \mathbf{A}) = \nabla(\nabla \cdot \mathbf{A}) - \nabla^2 \mathbf{A} = \mu_0 \mathbf{j} - \mu_0 \epsilon_0 \nabla \frac{\partial \phi}{\partial t} + \mu_0 \epsilon_0 \frac{\partial^2 \mathbf{A}}{\partial t^2} \quad (1.67)$$

Substitute Eq. (1.60) into Eq. (1.53) to obtain

$$\nabla^2 \phi + \nabla \cdot \frac{\partial \mathbf{A}}{\partial t} = -\frac{\rho}{\epsilon_0} \quad (1.68)$$

Note that \mathbf{A} is determined by Eq. (1.56) only within an arbitrary additive gradient of a scalar function, $R(\nabla \times \nabla R \equiv 0)$. It is convenient to choose the scalar function, R , so that

$$\nabla \cdot \mathbf{A} + \epsilon_0 \mu_0 \frac{\partial \phi}{\partial t} = 0 \quad (1.69)$$

Equation (1.69) is known as the *gauge condition* on the vector potential. This choice of gauge condition reduces Eq. (1.68) to

$$\nabla^2 \phi - \epsilon_0 \mu_0 \frac{\partial^2 \phi}{\partial t^2} = -\frac{\rho}{\epsilon_0} \quad (1.70)$$

and reduces Eq. (1.67) to

$$\nabla^2 \mathbf{A} - \epsilon_0 \mu_0 \frac{\partial^2 \mathbf{A}}{\partial t^2} = -\mu_0 \mathbf{j} \quad (1.71)$$

The solution to the time-independent version of Eq. (1.71) is

$$\mathbf{A}(\mathbf{r}) = \frac{\mu_0}{4\pi} \int \frac{\mathbf{j}(\mathbf{r}')}{|\mathbf{r} - \mathbf{r}'|} d^3 r' \quad (1.72)$$

The vector potential can be computed from the current distribution, in direct analogy with a computation of the scalar potential from the charge distribution according to Eq. (1.63). Knowing the scalar and vector potentials, one can compute the electrostatic and magnetic fields from Eq. (1.60) and Eq. (1.56), respectively. Thus electromagnetic theory provides the means for representing the collective, long-range interactions among the particles in a plasma in terms of fields.

The linear relationships of Eqs. (1.61) and (1.66) are only valid for an isotropic medium. More general constitutive relationships are frequently needed for plasmas, in which the magnetic field defines a unique set of directions in terms of which many phenomena are not isotropic. In general,

$$D_\alpha = \sum_\beta \epsilon_{\alpha\beta} E_\beta \quad \text{and} \quad B_\alpha = \sum_\beta \mu_{\alpha\beta} H_\beta \quad (1.73)$$

where α and β refer to the cartesian coordinates.

The concepts of electromagnetic energy density and electromagnetic stress associated with the fields follow directly from the manipulation of Eq. (1.73). Dotting \mathbf{H} into Eq. (1.58) and \mathbf{E} into Eq. (1.65), subtracting, and using the vector identity

$$\mathbf{H} \cdot \nabla \times \mathbf{E} - \mathbf{E} \cdot \nabla \times \mathbf{H} = \nabla \cdot (\mathbf{E} \times \mathbf{H})$$

leads to

$$\nabla \cdot (\mathbf{E} \times \mathbf{H}) + \frac{\partial}{\partial t} \left(\frac{\mathbf{E} \cdot \mathbf{D}}{2} + \frac{\mathbf{H} \cdot \mathbf{B}}{2} \right) + \mathbf{E} \cdot \mathbf{j} = 0 \quad (1.74)$$

Integrating Eq. (1.74) over an arbitrary volume and using the divergence theorem to convert the first term into a surface integral of the normal outward component of $\mathbf{S} = \mathbf{E} \times \mathbf{H}$

(the *Poynting vector*) over the closed surface bounding the volume leads to

$$\int_s (\mathbf{E} \times \mathbf{H}) \cdot d\mathbf{s} + \frac{\partial}{\partial t} \int \left(\frac{\mathbf{E} \cdot \mathbf{D}}{2} + \frac{\mathbf{H} \cdot \mathbf{B}}{2} \right) d^3r + \int \mathbf{E} \cdot \mathbf{j} d^3r = 0 \quad (1.75)$$

The first term represents the rate at which electromagnetic energy escapes across the surface. The first part of the integrand of the second term is the electrostatic energy density, which is equal to the work done to arrange the charges to create the electrostatic field. The second part of the integrand is the magnetic energy density, which is equal to the work done to establish the currents that create the magnetic field. The final term is the resistive work done by the electrostatic field on the charges within the volume.

Taking the cross product of Eq. (1.65) $\times \mathbf{D}$ and Eq. (1.58) $\times \mathbf{B}$, subtracting, and using Eqs. (1.53) and (1.55) yields

$$\rho \mathbf{E} + \mathbf{j} \times \mathbf{B} = \sum_{\alpha} \hat{\mathbf{n}}_{\alpha} \sum_{\beta} \frac{\partial T_{\alpha\beta}}{\partial x_{\beta}} - \epsilon_0 \mu_0 \frac{\partial \mathbf{S}}{\partial t} \quad (1.76)$$

The quantities $T_{\alpha\beta}$ are the components of the electromagnetic stress tensor, and $\hat{\mathbf{n}}_{\alpha}$ is the unit vector. In xyz coordinates

$$\begin{aligned} T_{xx} &= E_x D_x + B_x H_x - \frac{1}{2}(\mathbf{E} \cdot \mathbf{D} + \mathbf{B} \cdot \mathbf{H}) \\ T_{xy} &= E_x D_y + B_x H_y \\ T_{xz} &= E_x D_z + B_x H_z \\ T_{yx} &= E_y D_x + B_y H_x \\ T_{yy} &= E_y D_y + B_y H_y - \frac{1}{2}(\mathbf{E} \cdot \mathbf{D} + \mathbf{B} \cdot \mathbf{H}) \\ T_{yz} &= E_y D_z + B_y H_z \\ T_{zx} &= E_z D_x + B_z H_x \\ T_{zy} &= E_z D_y + B_z H_y \\ T_{zz} &= E_z D_z + B_z H_z - \frac{1}{2}(\mathbf{E} \cdot \mathbf{D} + \mathbf{B} \cdot \mathbf{H}) \end{aligned} \quad (1.77)$$

Integrating Eq. (1.76) over an arbitrary volume and using the divergence theorem on the stress tensor term leads to

$$\int (\rho \mathbf{E} + \mathbf{j} \times \mathbf{B}) d^3r = \sum_{\alpha} \hat{\mathbf{n}}_{\alpha} \sum_{\beta} \int T_{\alpha\beta} ds_{\beta} - \int \epsilon_0 \mu_0 \frac{\partial \mathbf{S}}{\partial t} d^3r \quad (1.78)$$

The first term in Eq. (1.78) represents the force exerted on the charge and currents within the volume by the electrostatic and magnetic fields, respectively. The second term represents the stresses integrated over the surface bounding the volume. The final term represents the change in momentum density within the volume.

As a special example, consider the case in which $\mathbf{E} = 0$ and \mathbf{B} is aligned along the z -axis. Then all the “off-diagonal” elements of the stress tensor vanish and

$$T_{xx} = T_{yy} = -T_{zz} = -\frac{B^2}{2\mu_0} \quad (1.79)$$

Thus $B^2/(2\mu_0)$ is the magnetic pressure in this case. We will make use of this subsequently when we consider the balancing of magnetic and kinetic pressures to establish a plasma equilibrium.

Problems for Chapter 1

1. Calculate the energy release in the fusion of 1 g of deuterium.
2. Calculate the deuterium and electron Debye lengths in a plasma with $T = 10 \text{ keV}$ and $n_D = n_e = 5 \times 10^{19} \text{ m}^{-3}$.
3. Calculate the number of plasma ions and electrons within a sphere of radius the Debye length for problem 2.
4. Calculate and plot the electrostatic potential due to a single deuteron located at $r = 0$ for the plasma of problems 2 and 3.
5. Calculate the Coulomb repulsive force between two deuterons that are separated by two nuclear radii.
6. Calculate the deuteron and electron plasma frequencies for the plasma of problem 2.
7. Calculate the Rutherford scattering cross section between deuterons and electrons for scattering events of 1° , 10° and 90° in the CM system for the plasma of problem 2.
8. Calculate the 90° multiple collision deflection times for ions and electrons scattering with ions and electrons for the plasma of problem 2.
9. Calculate the characteristic energy transfer times for a deuterium ion to other deuterium ions and to electrons for the plasma of problem 2.
10. Calculate the Dreicer runaway electron velocity for the plasma of problem 2 in electric fields of $1 \text{ V} \cdot \text{m}^{-1}$, $5 \text{ V} \cdot \text{m}^{-1}$ and $10 \text{ V} \cdot \text{m}^{-1}$.
11. Calculate the plasma resistivity for the plasma of problem 2.
12. Calculate the kinetic pressure of the plasma of problem 2.
13. Calculate the magnetic pressure of fields of $B = 1 \text{ T}$ and 10 T .

2 Motion of Charged Particles

Many useful insights into the properties of plasmas and the conditions requisite for their confinement can be obtained from a study of the motion of individual, noninteracting particles in electric and magnetic fields. (Recall that the long-range particle interactions can be represented by fields, so that it is only the short-range, collisional effects that are neglected in such a study.) The equation of motion for a charged particle in the presence of electric and magnetic fields,

$$m\ddot{\mathbf{r}} = \mathbf{F} = e(\mathbf{E} + \dot{\mathbf{r}} \times \mathbf{B}) \quad (2.1)$$

is the starting point for our study.

2.1 Gyromotion and Drifts

The resultant motion of charged particles in general electric and magnetic field configurations is quite complex. To gain insight, we assume that the equation of motion is linear (i.e., that \mathbf{B} does not depend on the particle motion). This assumption allows the net particle motion to be represented as the superposition of particle motions that correspond to the simpler field configurations. Thus we can achieve our ends by studying the motion of particles in a number of relatively simple field configurations.

2.1.1 Gyromotion

Consider the case when there is a uniform, constant \mathbf{B} directed along the z -axis ($\mathbf{B} = B_z \hat{\mathbf{n}}_z$) in an xyz coordinate system and $\mathbf{E} = 0$. Taking the scalar product of $\dot{\mathbf{r}}$ with Eq. (2.1) leads to

$$\frac{1}{2}m\dot{\mathbf{r}} \cdot \dot{\mathbf{r}} = \text{const} = W \quad (2.2)$$

where we identify W with the total kinetic energy. Equation (2.1) also yields, for the z -component of motion,

$$\ddot{z} = 0 \quad (2.3)$$

The solution of Eq. (2.3) is $\dot{z} \equiv v_{||} = \text{const}$, so that $W_{||} \equiv \frac{1}{2}mv_{||}^2 = \text{const}$. Taken together with Eq. (2.2), this result implies $W_{\perp} \equiv W - W_{||} = \text{const}$, so that $v_{\perp} \equiv (2W_{\perp}/m)^{\frac{1}{2}} = \text{const}$. In other words, the kinetic energy and speeds perpendicular to and parallel to the field are separately constants of the motion. The x - and y -components of Eq. (2.2) can be

written

$$\begin{aligned}\ddot{x} &= \Omega \dot{y} \\ \ddot{y} &= -\Omega \dot{x}\end{aligned}\tag{2.4}$$

where

$$\Omega \equiv \frac{eB}{m}\tag{2.5}$$

is the gyrofrequency. Equations (2.4) may be differentiated

$$\begin{aligned}\ddot{x} &= \Omega \ddot{y} = -\Omega^2 \dot{x} \\ \ddot{y} &= -\Omega \ddot{x} = -\Omega^2 \dot{y}\end{aligned}\tag{2.6}$$

Now Eqs. (2.3) and (2.6) can be solved for the particle speeds

$$\begin{aligned}\dot{z} &= v_{\parallel} \\ \dot{x} &= v_{\perp} \cos(\Omega t + \alpha) \\ \dot{y} &= -v_{\perp} \sin(\Omega t + \alpha)\end{aligned}\tag{2.7}$$

where α is a constant phase angle, and Eqs. (2.7) can be integrated to obtain

$$\begin{aligned}x &= \frac{v_{\perp}}{\Omega} \sin(\Omega t + \alpha) + x_0 \\ y &= \frac{v_{\perp}}{\Omega} \cos(\Omega t + \alpha) + y_0 \\ z &= v_{\parallel} t + z_0\end{aligned}\tag{2.8}$$

Equations (2.8) describe motion along a field line of a “guiding center” with instantaneous coordinates

$$r_{gc} = (x_0, y_0, z_0 + v_{\parallel} t)\tag{2.9}$$

and gyromotion about the field line with angular frequency Ω and gyroradius

$$r_L = \frac{v_{\perp}}{\Omega}\tag{2.10}$$

This gyromotion is oppositely directed for positive and negative charges, as shown in Fig. 2.1. In MKS units,

$$\begin{aligned}\frac{\Omega}{2\pi} (\text{Hz}) &\approx 1.5 \times 10^7 B && \text{(protons)} \\ &\approx 2.7 \times 10^{10} B && \text{(electrons)}\end{aligned}$$

and

$$\begin{aligned}r_L (\text{m}) &\approx 1.5 \times 10^{-4} \frac{\sqrt{W_{\perp}}}{B} && \text{(protons)} \\ &\approx 3.0 \times 10^{-6} \frac{\sqrt{W_{\perp}}}{B} && \text{(electrons)}\end{aligned}$$

when W_{\perp} is in units of eV. The quantity r_L is the gyroradius, or Larmor radius.

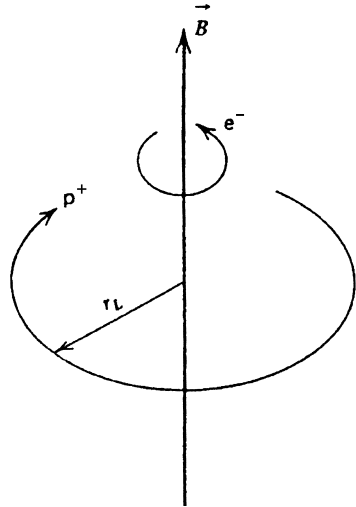


Figure 2.1. Gyromotion

2.1.1.1 Magnetic Moment

A circulating electric current, $I = -e(\Omega/2\pi)$, is produced by the gyromotion of each particle. This current produces a magnetic dipole moment equal to the product of the circulating current and the enclosed area, $A = \pi r_L^2$,

$$\mu = IA = \left(-e \frac{\Omega}{2\pi}\right) (\pi r_L^2) = -\frac{W_\perp}{B} \quad (2.11)$$

We will use the symbol $\bar{\mu}$ to denote $-\mu \equiv |\mu|$.

This magnetic moment is actually a vector quantity

$$\mu = -\frac{W_\perp}{B} \hat{\mathbf{n}}_{\parallel} \equiv -\frac{W_\perp}{B} \left(\frac{\mathbf{B}}{B} \right) \quad (2.12)$$

directed antiparallel to the field. The magnetic moments of ions and electrons are in the same direction and, when both have the same value of W_\perp , equal in magnitude.

The relative change in magnetic field produced in a plasma of particle (electrons plus ions) density $2n$ by the particle magnetic moments is

$$\frac{\delta B}{B} = \frac{\mu_0 2n \mu}{B} = -\frac{n W_\perp}{B^2 / 2\mu_0} \equiv -\beta \quad (2.13)$$

where the ratio of kinetic to magnetic pressures, β , has been introduced. Thus the gyromotion of the particles in a plasma produces a diamagnetic effect of magnitude on the order of β (μ_0 is the permeability).

2.1.2 $\mathbf{E} \times \mathbf{B}$ Drift

Now we consider how the particle motion just discussed is modified when there is a uniform and constant \mathbf{E} in addition to a uniform and constant $\mathbf{B} = B_z \hat{\mathbf{n}}_z$. Without any loss of generality, we can choose \mathbf{E} to have a parallel component, $E_{\parallel} \equiv E_z$, and a perpendicular component $E_{\perp} = E_y$. The equations of motion, in component form, are

$$\begin{aligned}\ddot{x} &= \Omega \dot{y} \\ \ddot{y} &= \frac{eE_{\perp}}{m} - \Omega \dot{x} \\ \ddot{z} &= \frac{eE_{\parallel}}{m}\end{aligned}\tag{2.14}$$

Solving these, as in section 2.1.1, we obtain

$$\begin{aligned}\dot{x} &= v_{\perp} \cos(\Omega t + \alpha) + \frac{E_{\perp}}{B} \\ \dot{y} &= -v_{\perp} \sin(\Omega t + \alpha) \\ \dot{z} &= v_{\parallel} + \frac{eE_{\parallel}}{m}t\end{aligned}\tag{2.15}$$

Comparing Eqs. (2.15) with Eqs. (2.7), we see that the parallel component of the electric field produces an acceleration along the z -axis, and the perpendicular component of the electric field produces a drift velocity that is perpendicular to both the magnetic field and the electric field, the E_{\perp}/B term in the first of Eqs. (2.15). This $\mathbf{E} \times \mathbf{B}$ drift motion

$$\mathbf{v}_E = \frac{\mathbf{E} \times \mathbf{B}}{B^2}\tag{2.16}$$

is superimposed upon the gyromotion to produce the net motion in the plane perpendicular to \mathbf{B} (in this case along the x -axis) that is illustrated in Fig. 2.2 for positively charged ions.

In the absence of an electric field, the motion perpendicular to \mathbf{B} shown in Fig. 2.2 would reduce to the gyromotion of the previous section. The perpendicular electric field accelerates a particle over half of the gyration and decelerates it over the other half, increasing W_{\perp} as the particle is moving in the $+E_{\perp}$ direction and decreasing it as the particle

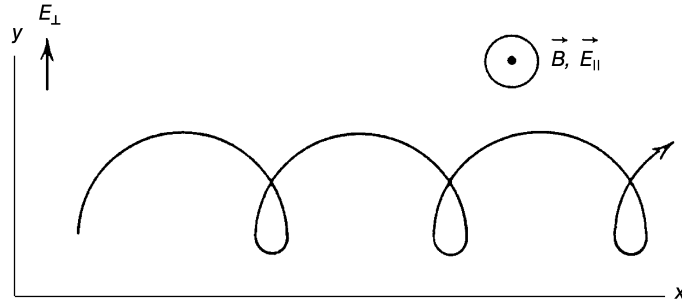


Figure 2.2. $\mathbf{E} \times \mathbf{B}$ drift motion for a positive charge (\mathbf{B} and \mathbf{E} out of page)

moves in the $-E_\perp$ direction (for a positive charge, and conversely for a negative charge). Thus from Eq. (2.10), the gyroradius is larger in the higher energy portion of the orbit. (For electrons, the larger part of the loop would be at the bottom in Fig. 2.2, but the net motion is still in the $+x$ -direction.)

The $\mathbf{E} \times \mathbf{B}$ drift is independent of the particle charge or mass. Thus there is a net plasma motion, but no net current.

The magnetic moment is no longer an exact constant of the motion, because W_\perp is not constant. However,

$$W_\perp = \frac{1}{2}m(\dot{x}^2 + \dot{y}^2)$$

averaged over a gyroperiod, $0 \leq t \leq 2\pi\Omega^{-1}$, is a constant, as may be verified by examination of Eqs. (2.15). Thus

$$\langle \mu \rangle = -\frac{\langle W_\perp \rangle}{B} \quad (2.17)$$

is a constant of the motion, where $\langle \rangle$ indicates the gyroperiod average.

Another way to arrive at the $\mathbf{E} \times \mathbf{B}$ drift is to note that the particle motion will be such that the net force on the particle (averaged over a gyroperiod) in the plane perpendicular to \mathbf{B} must vanish. In other words, the $e(\mathbf{v}_E \times \mathbf{B})$ Lorentz force will just balance the applied force $e\mathbf{E}$, or

$$-\mathbf{F} = -e\mathbf{E} = e(\mathbf{v}_E \times \mathbf{B}) \quad (2.18)$$

Simple vector manipulations lead immediately from Eqs. (2.18) to (2.16). More generally, the drift motion in response to any applied force, \mathbf{F} , can be obtained from Eq. (2.18), replacing \mathbf{v}_E by \mathbf{v}_F , and simple vector manipulation

$$\mathbf{v}_F = \frac{1}{e} \frac{\mathbf{F} \times \mathbf{B}}{B^2} \quad (2.19)$$

We see that, in general, the drift velocity depends upon the sign of the particle charge. (Note that we use the symbol e to represent the charge of the particle under consideration.)

2.1.3 Grad- B Drift

Next we consider how the particle motion that was discussed in section 2.1.1 is modified when the magnetic field is nonuniform in space. Consider, without loss of generality, that the field nonuniformity is in the y -direction, as shown in Fig. 2.3. Then $\mathbf{B} = B_Z(y)\hat{n}_z$. We will consider the case $\mathbf{E} = 0$ in order to isolate the ∇B drift. We will require that the spatial scale of the field nonuniformity is large compared to the gyroradius:

$$\left| \frac{\nabla B}{B} \right| \ll \frac{1}{r_L} \quad (2.20)$$

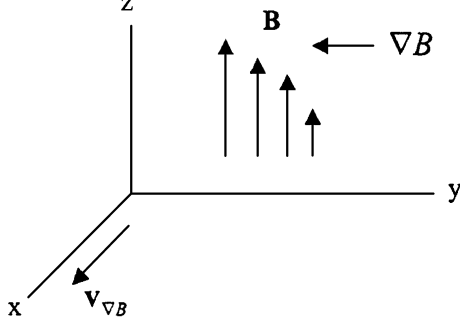


Figure 2.3. Grad- B drift

In this case, differentiating the equations of motion leads to

$$\begin{aligned}\ddot{x} &= -\Omega^2 \dot{x} + (\dot{y})^2 \frac{d\Omega}{dy} \\ \ddot{y} &= -\Omega^2 \dot{y} - \dot{x} \dot{y} \frac{d\Omega}{dy} \\ \ddot{z} &= 0\end{aligned}\tag{2.21}$$

instead of Eqs. (2.6).

We seek solutions to Eqs. (2.21) by making use of Eq. (2.20) to expand $\Omega(y)$ about its value at the position of the guiding center, $\Omega(y_0) \equiv \Omega_0$,

$$\Omega(y) = \Omega_0 + (y - y_0)\Omega'_0 \tag{2.22}$$

where

$$\Omega'_0 \equiv \left. \frac{d\Omega}{dy} \right|_{y=y_0}$$

Furthermore, we assume that we can use the uniform-field solutions for \dot{x} , \dot{y} , and y on the right side of Eqs. (2.21) and then solve the latter for

$$\begin{aligned}\dot{y} &= -v_\perp \sin(\Omega_0 t + \alpha) - \frac{1}{2} \frac{v_\perp^2 \Omega'_0}{\Omega_0^2} \sin 2(\Omega_0 t + \alpha) \\ \dot{x} &= v_\perp \cos(\Omega_0 t + \alpha) + \frac{1}{2} \frac{v_\perp^2 \Omega'_0}{\Omega_0^2} \cos 2(\Omega_0 t + \alpha) - \frac{v_\perp^2 \Omega'_0}{2\Omega_0^2} \\ \dot{z} &= v_\parallel\end{aligned}\tag{2.23}$$

The last term in the second of Eqs. (2.23) is a drift perpendicular to both the direction of the field and the direction of the field gradient,

$$v_{\nabla B} = -\frac{1}{2} m v_\perp^2 \frac{dB/dy}{e B^2} \tag{2.24}$$

directed along the x -axis, as shown in Fig. 2.3. More generally,

$$\mathbf{v}_{\nabla B} = \frac{1}{e} W_{\perp} \left(\frac{\mathbf{B} \times \nabla B}{B^3} \right) \quad (2.25)$$

Since $\mathbf{v}_{\nabla B} \cdot \nabla B = 0$, $B = \text{const}$ along the guiding center orbit in a nonuniform field. (This result is not true in general.) In the absence of an electric field, W_{\parallel} and W are constant, and therefore $W_{\perp} = W - W_{\parallel}$ is constant. This ∇B drift is oppositely directed for ions and electrons, resulting in a net current density

$$\mathbf{j}_{\nabla B} = n(e_i \mathbf{v}_{\nabla B,i} + e_e \mathbf{v}_{\nabla B,e}) = n(W_{\perp i} + W_{\perp e}) \left(\frac{\mathbf{B} \times \nabla B}{B^3} \right) \quad (2.26)$$

By analogy with Eq. (2.19), the force that produces the ∇B drift is

$$\mathbf{F}_{\nabla B} = -\frac{W_{\perp} \nabla B}{B} = -\bar{\mu} \nabla B \quad (2.27)$$

2.1.4 Polarization Drift

Next we consider the effect of a time-variable electric field on the particle motion that was described in section 2.1.2. A time-dependent electric field along the magnetic field would simply produce a corresponding time dependence in the z -component of motion. Of more interest is the effect of a time-dependent electric field component in a direction perpendicular to the magnetic field, which we will take as the y -direction as shown in Fig. 2.4. The equations of motion are given by Eqs. (2.14), except that E_{\perp} is now time dependent. Differentiation now leads to a set of equations that can be solved to obtain

$$\begin{aligned} \dot{x} &= v_{\perp} \cos(\Omega t + \alpha) + \frac{E_{\perp}}{B} \\ \dot{y} &= -v_{\perp} \sin(\Omega t + \alpha) + \frac{m}{eB^2} \dot{E}_{\perp} \\ \dot{z} &= v_{\parallel} + \int_0^t \frac{eE_{\parallel}(t')}{m} dt \end{aligned} \quad (2.28)$$

The second term in the first equation is the $\mathbf{E} \times \mathbf{B}$ drift, and the second term in the second equation is the polarization drift in the direction of the time-dependent electric field, as shown in Fig. 2.4.

$$v_p = \frac{m \dot{E}_{\perp}}{eB^2} \quad (2.29)$$

A more general form for the polarization drift, also valid for time-dependent B , can be derived from gyroperiod-average momentum conservation in the plane perpendicular to \mathbf{B} .

$$\frac{d}{dt}(mv_E) = ev_p B$$

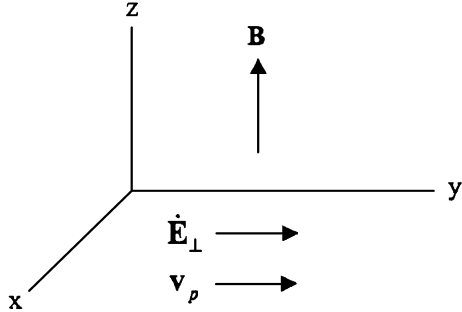


Figure 2.4. Polarization drift

which leads to

$$\mathbf{v}_p = \frac{m}{eB} \frac{d}{dt} \left(\frac{\mathbf{E}}{B} \right) \quad (2.30)$$

The polarization drift is oppositely directed for ions and electrons, leading to a net polarization current density

$$\mathbf{j}_p = n(e_i \mathbf{v}_{pi} + e_e \mathbf{v}_{pe}) = n \frac{(m_i + m_e)}{B} \frac{d}{dt} \left(\frac{\mathbf{E}}{B} \right) \quad (2.31)$$

2.1.5 Curvature Drift

Finally, we consider a curved magnetic field which is in the z -direction at $z = z_0$, but has a small y -component for $z \leq z_0$, as shown in Fig. 2.5. Limiting consideration to fields with small curvature, the field at any nearby point can be approximated as

$$\begin{aligned} B_z &\approx B_{z0} \equiv B_z(z = z_0) \\ B_y &\approx \left(\frac{\partial B_y}{\partial z} \right)_0 z \end{aligned} \quad (2.32)$$

Small curvature implies

$$|B_y| \ll |B_z|$$

The field line equation is

$$\frac{dy}{dz} \equiv \frac{B_y}{B_z} \simeq \frac{(\partial B_y / \partial z)_0 z}{B_{z0}} \quad (2.33)$$

which may be integrated to obtain

$$y - y_0 = \frac{1}{2} z^2 \frac{(\partial B_y / \partial z)_0}{B_{z0}} \quad (2.34)$$

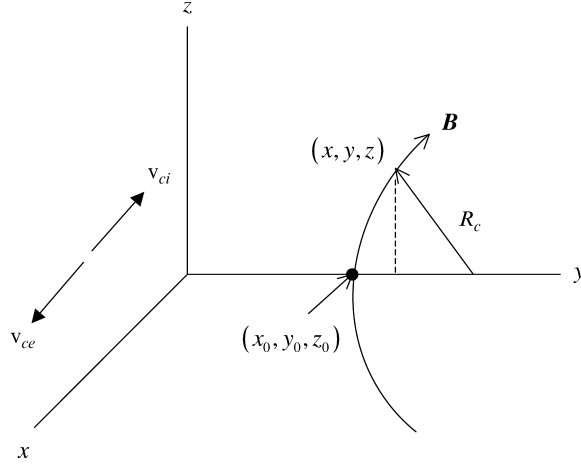


Figure 2.5. Curved magnetic field

From Fig. 2.3, the radius of curvature of the field line satisfies

$$R_c^2 = z^2 + [R_c - (y - y_0)]^2$$

from which we obtain

$$y - y_0 \simeq \frac{z^2}{2R_c} \quad (2.35)$$

for small curvature ($|y - y_0| \ll R_c$). Thus the radius of curvature may be related to the field and field gradient by Eqs. (2.34) and (2.35) to obtain

$$\left| \frac{1}{R_c} \right| = \left| \frac{(\partial B_y / \partial z)_0}{B_{z0}} \right| \quad (2.36)$$

This relation may be generalized to

$$\frac{\mathbf{R}_c}{R_c^2} = -(\hat{\mathbf{n}}_\parallel \cdot \nabla) \hat{\mathbf{n}}_\parallel \equiv -\left(\frac{\mathbf{B}}{B} \cdot \nabla \right) \frac{\mathbf{B}}{B} \quad (2.37)$$

The equations of motion are

$$\begin{aligned} \ddot{x} &= \Omega \dot{y} - \Omega_y \dot{z} \\ \ddot{y} &= -\Omega \dot{x} \\ \ddot{z} &= \Omega_y \dot{x} \end{aligned} \quad (2.38)$$

where Ω is defined in terms of B_z at $z = z_0$ and Ω_y is defined in terms of B_y by Eq. (2.5). Since Ω_y is small, $\dot{z} \simeq \text{const} = v_\parallel$, and the time dependence of the last term in the

first equation is due mainly to the change in Ω_y with motion along the field line. Thus differentiation of the first two of Eqs. (2.38) leads to

$$\begin{aligned}\ddot{x} + \Omega^2 \dot{x} &= -\frac{\partial \Omega_y}{\partial z} v_{\parallel}^2 \\ \ddot{y} + \Omega^2 \dot{y} &= \Omega_y \Omega v_{\parallel}\end{aligned}\quad (2.39)$$

These equations have the usual oscillatory solution describing the gyromotion plus non-oscillatory velocity components in both the x - and y -directions. The gyroperiod averages are

$$\begin{aligned}\langle \dot{y} \rangle &= \frac{\Omega_y}{\Omega_0} v_{\parallel} = \frac{B_y}{B_z} v_{\parallel} \\ \langle \dot{x} \rangle &= -\frac{(\partial \Omega_y / \partial z)}{\Omega_0^2} v_{\parallel}^2 = -2W_{\parallel} \frac{(\partial B_y / \partial z)_0}{B_{z0}^2} = \frac{2W_{\parallel}}{eR_c B_{z0}}\end{aligned}\quad (2.40)$$

The first of Eqs. (2.40) describes the motion of the guiding center along the curving field line. The second of Eqs. (2.40) describes the drift velocity of the guiding center in the direction perpendicular to the plane in which the field and the curvature vectors lie, as shown in Fig. 2.5. This result can be generalized to

$$\mathbf{v}_c = 2W_{\parallel} \frac{[\mathbf{B} \times (\mathbf{B} \cdot \nabla) \mathbf{B}]}{eB^4} = \frac{2W_{\parallel} [\mathbf{B} \times (\hat{\mathbf{n}}_{\parallel} \cdot \nabla) \hat{\mathbf{n}}_{\parallel}]}{eB^2} = -\frac{2W_{\parallel} \mathbf{B} \times \mathbf{R}_c}{eB^2 R_c^2} \quad (2.41)$$

The curvature drift is oppositely directed for ions and electrons, producing a net current density

$$\mathbf{j}_c = n(e_i \mathbf{v}_{ci} + e_e \mathbf{v}_{ce}) = 2n(W_{\parallel i} + W_{\parallel e}) \frac{\mathbf{B} \times (\mathbf{B} \cdot \nabla) \mathbf{B}}{B^4} \quad (2.42)$$

By analogy with Eq. (2.19), the centrifugal force that drives the curvature drift is

$$\mathbf{F}_c = -\frac{2W_{\parallel} (\mathbf{B} \cdot \nabla) \mathbf{B}}{B^2} = \frac{2W_{\parallel} \mathbf{R}_c}{R_c^2} \quad (2.43)$$

This force arises from the v_{\parallel} motion along the curved field line.

In a time-independent situation in a medium in which no current flows (e.g., a vacuum) Eq. (1.65) of chapter 1 reduces to $\nabla \times \mathbf{B} = 0$. In this case, Eqs. (2.41) to (2.43) reduce to a form similar to the results obtained for the grad- B drift.

$$\mathbf{v}_c = \frac{2W_{\parallel}}{e} \frac{\mathbf{B} \times \nabla B}{B^3} \quad (2.44)$$

$$\mathbf{j}_c = 2n(W_{\parallel i} + W_{\parallel e}) \frac{\mathbf{B} \times \nabla B}{B^3} \quad (2.45)$$

and

$$\mathbf{F}_c = -\frac{2W_{\parallel} \nabla B}{B} \quad (2.46)$$

2.2 Constants of the Motion

Particle motion in electric and magnetic fields in many instances is constrained by the equations of motion so that certain quantities are constants of the motion, either in an absolute sense or averaged over some “natural” period of motion. The magnetic moment is one example that we have already discussed.

Symmetry introduces a constant of the motion. When a system has symmetry in a given coordinate direction, that coordinate is said to be an “ignorable” coordinate, in that the solution cannot depend on it. We know from classical mechanics that the component of momentum along an ignorable coordinate is a constant of the motion.

We also know from classical mechanics that the action integral, $\oint p \, dl$, over a closed cycle of periodic motion is a constant of the motion, known as an adiabatic invariant. The action integral is the momentum along the orbit path integrated over the periodic orbit. The constancy of the action integral depends only upon the motion being periodic. There are three general types of periodic motion for magnetically confined particles. The gyromotion is periodic, and the associated adiabatic invariant is the magnetic moment. The guiding centers of particles that are trapped in a magnetic well execute a periodic motion between reflection points. Finally, there is a periodic motion of particle guiding centers due to drift motion in some confinement fields.

2.2.1 Magnetic Moment

The adiabatic invariant of the highest frequency periodic motion – the gyromotion – is the magnetic moment:

$$\begin{aligned} \oint_{\text{gyro-orbit}} p \, dl &= \oint mv_\perp \, dl = \oint mv_\perp^2 \frac{dl}{v_\perp} = -2 \oint W_\perp \frac{d\theta}{\Omega} \\ &= -\frac{2m}{e} \oint \frac{W_\perp}{B} \, d\theta = -\frac{4\pi m}{e} \left(\frac{W_\perp}{B} \right) \propto \langle \mu \rangle \end{aligned} \quad (2.47)$$

The gyroperiod-averaged magnetic moment, $\langle \mu \rangle$, is conserved even when there are perturbations in the gyro-orbit due to time-dependent field variations, provided the field variations take place over a time that is long compared to the time required for the particle to traverse a gyro-orbit, $\sim |\Omega|^{-1}$; that is,

$$\left| \frac{1}{B} \frac{\partial B}{\partial t} \right| \ll |\Omega| \quad (2.48)$$

During one gyroperiod, the perpendicular energy changes by

$$\begin{aligned} \Delta W_\perp &= -e \oint \mathbf{E} \cdot d\mathbf{l} = -e \int_s \nabla \times \mathbf{E} \cdot ds = e \int_s \frac{\partial \mathbf{B}}{\partial t} \cdot ds \\ &\simeq e \left\langle \frac{\partial B}{\partial t} \pi r_L^2 \right\rangle = \left\langle W_\perp \frac{2\pi}{|\Omega|} \frac{\partial B}{\partial t} / B \right\rangle \\ &\simeq \langle W_\perp \rangle \Delta B / \langle B \rangle \end{aligned} \quad (2.49)$$

Note that $d\mathbf{l}$ is the incremental path length vector along a gyro-orbit taken in the counter-clockwise direction in Fig. 2.1, and ds is the incremental area vector for the cross section enclosed by the orbit and is upward in Fig. 2.1. However,

$$\frac{\langle \Delta\mu \rangle}{\langle \mu \rangle} = -\frac{\Delta W_\perp}{\langle W_\perp \rangle} + \frac{\Delta B}{\langle B \rangle} \simeq 0 \quad (2.50)$$

when Eq. (2.49) is used to evaluate ΔW_\perp .

The gyroperiod-averaged magnetic moment is also a constant of the motion in a non-uniform magnetic field, as we discussed in connection with the grad- B drift, provided that Eq. (2.20) is satisfied.

2.2.2 Second Adiabatic Invariant

There is a second adiabatic invariant, associated with the action integral of the periodic motion, if any exists, of the particle guiding center along the field line,

$$J \equiv \oint v_\parallel dl \quad (2.51)$$

We will prove that J is a constant of the motion in a nonuniform, curved, time-independent magnetic field. The rate of change of field seen by a particle moving along the field line and drifting across the field is

$$\frac{d\mathbf{B}}{dt} = \mathbf{v}_d \cdot \nabla B \quad (2.52)$$

where we have assumed $\mathbf{B} \cdot \nabla B = 0$. The drift velocity is a superposition of grad- B and curvature drifts

$$\mathbf{v}_d = \mathbf{v}_{\nabla B} + \mathbf{v}_c = \frac{W_\perp(\mathbf{B} \times \nabla B)}{eB^3} + \frac{2W_\parallel(\mathbf{R}_c \times \mathbf{B})}{eB^2 R_c^2} \quad (2.53)$$

In evaluating Eq. (2.51), we must take into account that the drift motion carries the particle across field lines even as it moves along them.

The parallel velocity can be expressed

$$v_\parallel = \sqrt{\frac{2}{m}(W - W_\perp)} = \sqrt{\frac{2}{m}(W - \bar{\mu}B)} \quad (2.54)$$

so that the incremental change in v_\parallel due to the drift motion is

$$\Delta v_\parallel = \frac{\frac{1}{2}(2/m)^{\frac{1}{2}}(-\bar{\mu}\Delta B)}{(W - \bar{\mu}B)^{\frac{1}{2}}} = -\frac{1}{2}\left(\frac{2}{m}\right)^{\frac{1}{2}}\bar{\mu}\frac{(\mathbf{v}_{\nabla B} + \mathbf{v}_c) \cdot \nabla B}{(W - \bar{\mu}B)^{\frac{1}{2}}}\Delta t \quad (2.55)$$

where Eq. (2.52) has been used. From Eq. (2.25) we know that $\mathbf{v}_{\nabla B} \cdot \nabla B = 0$, so only the curvature drift contributes to Eq. (2.55). Using Eq. (2.53), (2.55) becomes

$$\Delta v_\parallel = \frac{-(2/m)^{\frac{1}{2}}W_\parallel\bar{\mu}\Delta t}{eB^2(W - \bar{\mu}B)^{\frac{1}{2}}}\frac{\mathbf{R}_c \times \mathbf{B}}{R_c^2} \cdot \nabla B = -\frac{v_\parallel W_\perp\Delta t}{eB^3 R_c^2}(\mathbf{R}_c \times \mathbf{B}) \cdot \nabla B \quad (2.56)$$

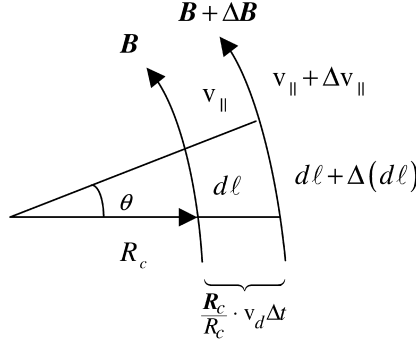


Figure 2.6. Effect of drift motion

As a particle drifts from one field line to the next, the incremental arc length along the new field line differs from the incremental arc length along the original field line, dl , by

$$\Delta(dl) = dl(\mathbf{v}_{\nabla B} + \mathbf{v}_c) \cdot \frac{\mathbf{R}_c}{R_c^2} \Delta t = \frac{dl W_{\perp}}{eB^3} (\mathbf{B} \times \nabla B) \cdot \frac{\mathbf{R}_c}{R_c^2} \Delta t \quad (2.57)$$

as illustrated in Fig. 2.6, where we have noted from Eq. (2.40) that $\mathbf{v}_c \cdot \mathbf{R}_c = 0$, so that only the grad- B drift contributes to Eq. (2.57), and have used Eq. (2.53) in the last step.

Now we are in a position to use Eq. (2.56) and Eq. (2.57) to demonstrate that

$$\Delta(v_{\parallel} dl) = (\Delta v_{\parallel})(dl) + v_{\parallel} \Delta(dl) = 0 \quad (2.58)$$

as a particle drifts in a curved, nonuniform magnetic field. The condition of Eq. (2.58) is stronger than the statement that J is constant but is certainly sufficient to prove the latter. This proof assumed the constancy of $\langle \mu \rangle$, thus is valid when Eq. (2.20) is satisfied.

Next, we will prove the constancy of J in a nonuniform time-variable magnetic field, provided that the field variation occurs on a time scale long compared to the time, τ_b , required for a particle to complete a cycle of periodic motion, i.e.,

$$\left| \frac{1}{B} \frac{\partial B}{\partial t} \right| \ll \tau_b^{-1} = \omega_b \quad (2.59)$$

where

$$\omega_b^{-1} \equiv \tau_b \equiv \oint \frac{dl}{v_{\parallel}} = \left(\frac{m}{2} \right)^{\frac{1}{2}} \oint \frac{dl}{[W - \bar{\mu} B(l)]^{\frac{1}{2}}} \quad (2.60)$$

The variation of J can be written

$$\Delta J = \left(\frac{2}{m} \right)^{\frac{1}{2}} \oint \frac{\Delta W - \bar{\mu} \Delta B}{(W - \bar{\mu} B)^{\frac{1}{2}}} dl \quad (2.61)$$

in terms of the variation of the field along the orbit over a cycle,

$$\Delta B(l) = \frac{\partial B(l)}{\partial t} \tau_b = \frac{\partial B(l)}{\partial t} \left(\frac{m}{2} \right)^{\frac{1}{2}} \oint \frac{dl}{[W - \bar{\mu} B(l)]^{\frac{1}{2}}} \quad (2.62)$$

and the variation in particle energy over a cycle

$$\Delta W = \int_0^{\tau_b} \frac{dW}{dt} dt = \int_0^{\tau_b} \left(m\ddot{l} + \bar{\mu} \frac{\partial B}{\partial t} + \bar{\mu} \frac{\partial B}{\partial l} \dot{l} \right) dt \quad (2.63)$$

The force $\mathbf{F} = -\bar{\mu} \nabla B$ acting on a particle as it moves along a field line in a nonuniform field is given by Eq. (2.27), so that the component of the particle equation of motion along the field line is

$$m\ddot{l} = -\bar{\mu} \frac{\partial B(l)}{\partial l} \quad (2.64)$$

With Eq. (2.64), Eq. (2.63) reduces to

$$\begin{aligned} \Delta W &= \int_0^{\tau_b} \bar{\mu} \frac{\partial B(l)}{\partial t} dt = \bar{\mu} \oint \frac{\partial B}{\partial t} \frac{dl}{v_{\parallel}} \\ &= \bar{\mu} \left(\frac{m}{2} \right)^{\frac{1}{2}} \frac{\partial B}{\partial t} \oint \frac{dl}{[W - \bar{\mu} B(l)]^{\frac{1}{2}}} \end{aligned} \quad (2.65)$$

where we have made use of the relation in Eq. (2.59).

Using Eqs. (2.62) and (2.65) in Eq. (2.61) demonstrates that $\Delta J = 0$ when the conditions in Eqs. (2.20), (2.48) and (2.59) are satisfied. The latter two conditions are required for $\langle \mu \rangle = \text{const}$, which was assumed here.

2.2.3 Canonical Angular Momentum

The component of momentum along an ignorable coordinate is a constant of the motion. In order to illustrate this point and to introduce several important consequences, we consider particle motion in a cylindrically symmetric configuration with an axial field; that is, a cylinder that is symmetric in the poloidal angle, θ . The θ -component of the momentum – the angular momentum – is a constant of the motion. We will prove this.

The currents that generate the axial field flow only in the poloidal direction, in a cylindrically symmetric system. This follows directly from the vector potential representation of the field $\mathbf{B} = \nabla \times \mathbf{A}$ that was discussed in section 1.4. From (1.72), it follows that the only nonzero component of the vector potential is A_{θ} ; that is, $\mathbf{A} = A_{\theta} \hat{\mathbf{n}}_{\theta}$. Thus we can make use of Eq. (1.52) to write the θ -component of Eq. (2.1) as

$$m(r\ddot{\theta} + 2\dot{r}\dot{\theta}) = -\frac{e}{r} \left(r\dot{A}_{\theta} + \dot{r}A_{\theta} + r\dot{r}\frac{\partial A_{\theta}}{\partial r} + r\dot{z}\frac{\partial A_{\theta}}{\partial z} \right) \quad (2.66)$$

in cylindrical coordinates. Only the E^A component of the electric field was retained in Eq. (2.1) in deriving Eq. (2.66). The right side of Eq. (2.66) is the substantive derivative of rA_{θ} , allowing Eq. (2.66) to be written

$$m(r\ddot{\theta} + 2\dot{r}\dot{\theta}) = -\frac{e}{r} \left(\frac{\partial}{\partial t} + \dot{\mathbf{r}} \cdot \nabla \right) (rA_{\theta}) \equiv -\frac{e}{r} \frac{d}{dt} (rA_{\theta}) \quad (2.67)$$

Multiplying Eq. (2.67) by r and rearranging leads to

$$\frac{d}{dt}(mr^2\dot{\theta} + erA_\theta) \equiv \frac{d}{dt}[r(mv_\theta + eA_\theta)] \equiv \frac{dP_\theta}{dt} = 0 \quad (2.68)$$

where the canonical angular momentum,

$$P_\theta = r(mv_\theta + eA_\theta) \quad (2.69)$$

has been proven to be a constant of the motion.

The axial field is given by

$$B_z = (\nabla \times \mathbf{A}) \cdot \hat{\mathbf{n}}_z = \frac{1}{r} \frac{\partial}{\partial r}(rA_\theta) \quad (2.70)$$

which provides, upon integration, an expression for

$$A_\theta(r) = \frac{1}{r} \int_0^r r' B_z(r') dr' \quad (2.71)$$

When we say that P_θ is a constant of the motion, what we mean is that a particle is constrained to move so that the terms on the right of Eq. (2.69) always sum to the same value. Consider the relative magnitudes of the first and second terms in Eq. (2.69).

$$\frac{|mv_\theta|}{|eA_\theta|} \approx \frac{|mv_\perp|}{|erB_z|} \approx \frac{r_L}{r} \ll 1 \quad (2.72)$$

where the last inequality arises from the fact that the dimensions of a confined plasma are normally large compared to a gyroradius. Thus particles move on surfaces defined by

$$\psi \equiv rA_\theta = \text{const} \quad (2.73)$$

except for excursions of the order of $r_L \ll r$.

The surfaces defined by Eq. (2.73) have a very special character – the magnetic field lines lie within them. To prove this, we must demonstrate that the normal to the surface is orthogonal to the field; that is, $\mathbf{B} \cdot \nabla\psi = 0$. Writing

$$\begin{aligned} \mathbf{B} \cdot \nabla\psi &= \mathbf{B} \cdot \nabla(rA_\theta) = \mathbf{B} \cdot \left[\frac{\partial(rA_\theta)}{\partial r} \hat{\mathbf{n}}_r + \frac{\partial(rA_\theta)}{\partial z} \hat{\mathbf{n}}_z \right] \\ &= B_r \frac{\partial(rA_\theta)}{\partial r} + B_z \frac{\partial(rA_\theta)}{\partial z} \end{aligned}$$

and noting that

$$\begin{aligned} B_r &\equiv \hat{\mathbf{n}}_r \cdot (\nabla \times \mathbf{A}) = -\frac{\partial A_\theta}{\partial z} \\ B_z &\equiv \hat{\mathbf{n}}_z \cdot (\nabla \times \mathbf{A}) = \frac{1}{r} \frac{\partial}{\partial r}(rA_\theta) \end{aligned}$$

leads immediately to

$$\mathbf{B} \cdot \nabla\psi \equiv \mathbf{B} \cdot \nabla(rA_\theta) = 0 \quad (2.74)$$

The surfaces $\psi = rA_\theta = \text{const}$ that satisfy Eq. (2.74) are known as flux surfaces of the magnetic field.

Thus, particles are constrained by conservation of angular momentum to move on flux surfaces of the magnetic field, except for excursions of the order of r_L associated with the gyromotion. Although we have used a relatively simple geometrical configuration to establish this result, it has wider applicability.

This result of particle motion confined to a flux surface, except for excursions of the order of a gyroradius, is consistent with the solution for particle motion in a uniform, constant magnetic field obtained in section 2.1.1, where we found that particles execute a gyration about a guiding center that moves along the field line. In subsequent parts of section 2.1, we found that field gradients and curvature drove particle drifts across field lines, hence across flux surfaces. In more general geometries than the one considered here, we will find that our results are modified by the presence of drifts and that particles move on “drift” surfaces instead of on flux surfaces.

2.3 Diamagnetism*

There is a magnetization current in nonuniform magnetized plasmas. This magnetization current arises from the gyromotion of particles about field lines. If the density, n , perpendicular energy, W_\perp , or magnetic field is nonuniform, then a net current can be produced by the gyromotion, even in the absence of any net motion of the guiding centers.

Plasmas in magnetic fields are diamagnetic, the gyro-orbits of the charged particles being such as to reduce the field. Consider the orbits of particles with a given velocity perpendicular to the magnetic field with the centers of their gyro-orbits on a particular field line. The particles gyrate about the field line on a cylinder and each contributes a current $\Omega_j/2\pi$. If there are δn particles per unit length, their orbits produce a cylindrical current per unit length

$$\delta i = -\frac{e_j \Omega_j}{2\pi} \delta n \quad (2.75)$$

and using $\Omega_j = e_j B / m_j$,

$$\delta i = -\frac{e_j^2}{2\pi m_j} \delta n B \quad (2.76)$$

The minus sign indicates that the current is in the opposite direction to that producing the main field B . From Ampère’s law the magnetic field resulting from this current is $\delta B = \mu_0 \delta i$, so that

$$\delta B = -\frac{\mu_0 e_j^2}{2\pi m_j} \delta n B \quad (2.77)$$

and δB is independent of the sign of the charge. Electrons gyrate in an opposite direction to ions, but carry a negative charge, so the current (hence the field) produced is the same.

Consider now the more general case with a distribution of particle velocities. Let the magnetic field be in the z -direction and consider those particles with velocity v_\perp perpendicular to the magnetic field. These particles contribute to the magnetic field at a given

point if their orbit center lies within a gyroradius, v_{\perp}/Ω_j , of that point. The sum of the currents of such particles in a velocity space element d^3v gives a current per unit length

$$di = -\pi \left(\frac{v_{\perp}}{\Omega_j} \right)^2 e_j \frac{\Omega_j}{2\pi} f_j d^3v = -\frac{e_j}{2\Omega_j} v_{\perp}^2 f_j d^3v \quad (2.78)$$

where f_j is the distribution function. The resulting magnetic field due to particles with a given v_{\perp} is

$$dB_{sj} = -\frac{\mu_0 m_j}{2B} v_{\perp}^2 f_j d^3v \quad (2.79)$$

Integrating over the velocity distribution yields

$$B_{sj} = -\frac{\mu_0}{B} \int \frac{1}{2} m_j v_{\perp}^2 f_j d^3v = -\frac{\mu_0 p_j}{B} \quad (2.80)$$

where p_j is the particle pressure.

It is seen that the circular orbits of particles of species j produce a field B_{sj} in the opposite direction to the applied field, and the full field B_s is obtained by summing over the species j to obtain the diamagnetic field

$$B_s = -\frac{\mu_0 p}{B} \quad (2.81)$$

where p is the plasma pressure. This result is a low β -approximation.

If the applied magnetic field is B_0 and the exact diamagnetic field is B_d , the pressure balance equation

$$\frac{(B_0 + B_d)^2}{2\mu_0} + p = \frac{B_0^2}{2\mu_0} \quad (2.82)$$

gives the full equation for B_d

$$B_d \left(1 - \frac{1}{2} \frac{B_d}{B_0} \right) = -\frac{\mu_0 p}{B_0} \quad (2.83)$$

The total pressure balance is obtained by recognizing that the gradient in the magnetic field leads to a drift of the particle orbits and the resulting current produces a further magnetic field. The current associated with the magnetic field B_s arising from the stationary orbits is obtained by applying Ampère's law to the gyrating particles

$$\mathbf{j}_s = \hat{\mathbf{n}}_{\parallel} \times \nabla \left(\frac{p}{B} \right) \quad (2.84)$$

where $\hat{\mathbf{n}}_{\parallel}$ is the unit vector along \mathbf{B} . From the force balance equation $\mathbf{j} \times \mathbf{B} = \nabla p$ and the total current is

$$\mathbf{j}_s = \hat{\mathbf{n}}_{\parallel} \times \frac{\nabla p}{B} \quad (2.85)$$

and so the residual current is

$$\mathbf{j} - \mathbf{j}_s = \hat{\mathbf{n}}_{\parallel} \times \frac{p}{B^2} \nabla \mathbf{B} \quad (2.86)$$

The current, \mathbf{j}_d , caused by the magnetic field gradient drift is

$$\mathbf{j}_d = \sum_j n_j e_j \langle \mathbf{v}_{dj} \rangle \quad (2.87)$$

where \mathbf{v}_{dj} is the grad- B drift velocity given by Eq. (2.25), which we write as

$$\langle \mathbf{v}_{dj} \rangle = \frac{m_j v_{thj}^2}{e_j B^2} \hat{\mathbf{n}}_{\parallel} \times \nabla \mathbf{B} \quad (2.88)$$

and, since $n_j m_j v_{thj}^2 = p_j$, the drift current given by Eq. (2.87)

$$\mathbf{j}_d = \hat{\mathbf{n}}_{\parallel} \times \frac{p}{B^2} \nabla \mathbf{B} \quad (2.89)$$

By comparison with Eq. (2.86) we see that

$$\mathbf{j} = \mathbf{j}_s + \mathbf{j}_d$$

showing that the total diamagnetic current is the sum of the current due to the circular orbits and that due to their drift. The primary diamagnetic effect arising from the magnetic field of circular orbits is perhaps surprising since the orbit is stationary and the averaged current is zero. For a uniform plasma the diamagnetically induced magnetic field given by Eq. (2.80) is constant and the diamagnetic current inside the plasma is indeed zero. However, there is always a pressure gradient, as well as a magnetic field gradient, in a magnetically confined plasma.

Consider the flux of ions through an element of area parallel to the field, as shown in Fig. 2.7. The upward (in our picture) flux of ions consists of all ions to the right whose guiding centers lie within r_L of the surface element, and the downward flux consists of all ions to the left whose guiding centers lie within r_L of the surface element. If there are more particles to the right than the left (∇n as shown in Fig. 2.7), then there will be a net upward flux across the surface elements. If the particle density is uniform, but the gyroradius is larger for particles located to the left than to the right of the surface element, then there will be a net downward ion flux through the surface element. Magnetic field and energy gradients as shown in Fig. 2.7 would produce this type of variation in r_L .

The magnetization current can be represented in terms of the magnetic (dipole) moment associated with each particle. The net magnetization per unit volume is

$$\mathbf{M} = n\mu = -n \frac{W_{\perp}}{B} \hat{\mathbf{n}}_{\parallel} \quad (2.90)$$

The net current density produced by this magnetization is

$$\begin{aligned} \mathbf{j}_m &= -\nabla \times \mathbf{M} = \nabla \times \left(n \frac{W_{\perp}}{B} \hat{\mathbf{n}}_{\parallel} \right) \\ &= \frac{nW_{\perp}}{B^2} (\hat{\mathbf{n}}_{\parallel} \times \nabla B) - \frac{1}{B} [\hat{\mathbf{n}}_{\parallel} \times \nabla (nW_{\perp})] + \frac{nW_{\perp}}{B} \nabla \times \hat{\mathbf{n}}_{\parallel} \end{aligned} \quad (2.91)$$

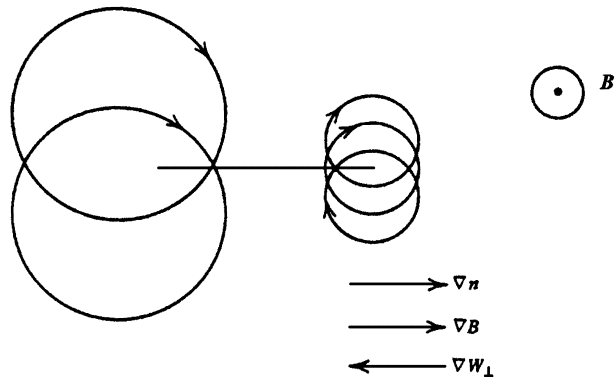


Figure 2.7. Gyro-orbits in nonuniform plasma

Problems for Chapter 2

1. Calculate the deuterium and electron gyrofrequencies and gyroradii in a plasma with $T = 10 \text{ keV}$, $n_D = n_e = 5 \times 10^{19} \text{ m}^{-3}$ and $B = 5 \text{ T}$ directed along the z -axis.
2. Calculate the $E \times B$ drift velocity for ions and electrons in a plasma with $E = 10 \text{ V} \cdot \text{m}^{-1}$ directed along the positive x -axis and $B = 5 \text{ T}$ directed along the positive y -axis.
3. Calculate the grad- B drift for deuterons and electrons in the plasma of problem 1 when there is a field gradient $dB/dy = 1 \text{ T m}^{-1}$ directed along the positive y -axis. Calculate the net current density produced by this drift.
4. Calculate the polarization drift for deuterons and electrons in the plasma of problem 1 where there is a changing electric field $dE_y/dt = 1 \text{ V} \cdot \text{m}^{-1} \cdot \text{s}^{-1}$ directed along the positive y -axis.
5. Calculate the curvature drift for deuterons and electrons for the plasma of problem 1 if the magnetic field has a radius of curvature of $R_c = 3 \text{ m}$ instead of being straight.
6. Derive an expression for the gravitational drift. Calculate the gravitational drift for the plasma of problem 1 for the B -field parallel to the earth's surface.

3 Magnetic Confinement

Now that a description of charged particle motion in electric and magnetic fields and an understanding of how collisions affect that motion has been developed, it is possible to develop an understanding of the principles of the magnetic confinement of a plasma, which is the purpose of this chapter. In considering magnetic confinement concepts there is a hierarchy of questions that must be asked. First, does the magnetic field configuration confine particles whose principal motion is gyration along the magnetic field lines? If not, the confinement is only for the few microseconds required for a particle moving along fields at the thermal speed ($\sim 10^7 \text{ m} \cdot \text{s}^{-1}$ for electrons) to traverse the dimensions (\sim meters) of the system. If so, then the next question is about the drift motion – do drifts carry the charged particles out of the intended confinement volume? If not, then the third question that must be examined regards the macroscopic stability of the electromagnetic confinement configuration and the confined plasma. If the electromagnetic configuration plus the confined plasma are macroscopically stable, then the final question regards the transport loss rates due to collisions and to microscopic instabilities.

3.1 Confinement in Mirror Fields

The idea of using field lines which enter and leave the confinement region, thus connecting with the external world, to confine charged particles whose lowest order motion is along a field line (with a superimposed gyromotion) may at first seem paradoxical. However, it is possible to confine particles in “magnetic well” field configurations because of the constraints on the particle motion imposed by the conservation of magnetic moment and of energy.

3.1.1 Simple Mirror

Consider the “simple mirror” field configuration illustrated in Fig. 3.1, in which a strong field is created by solenoidal coils at $s = \pm s_{\max}$. The field is weaker for $s_0 < |s| < s_{\max}$ and is a minimum for $s = s_0$.

Conservation of kinetic energy requires

$$\frac{1}{2}m \left[v_{11}^2(s) + v_{\perp}^2(s) \right] = \text{KE} = \text{const} \quad (3.1)$$

since the stationary magnetic field does no work on a charged particle. Conservation of angular momentum requires

$$p_{\theta} \equiv mr_L v_{\perp} = \frac{mv_{\perp}^2(s)}{B(s)} = \text{const} \quad (3.2)$$

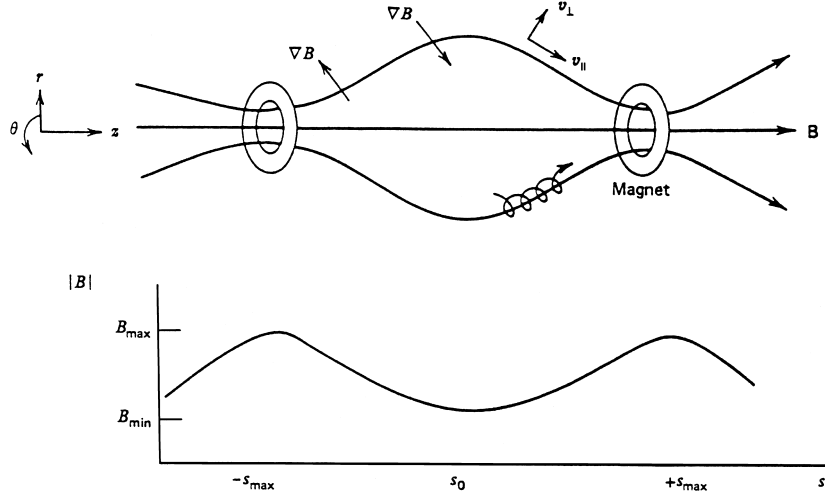


Figure 3.1. Simple mirror configuration

which is conventionally written

$$\mu \equiv \frac{\frac{1}{2}mv_{\perp}^2(s)}{B(s)} = \text{const} \quad (3.3)$$

Combining these relationships yields

$$\frac{1}{2}mv_{\parallel}^2(s) = \text{KE} - \mu B(s) \quad (3.4)$$

indicating that particles for which $\text{KE}/\mu = B(s)$ for $B_{\min} < B(s) < B_{\max}$ will be trapped; that is, v_{\parallel} will vanish for some s in the interval $s_0 < s < s_{\max}$ and for the symmetrical $-s$ in the interval $-s_{\max} < -s < s_0$.

Evaluating the constants KE and μ from the defining relationships at $s = s_0$ yields

$$\frac{1}{2}mv_{\parallel}^2(s) = \left(\frac{1}{2}mv_{\parallel}^2(s_0) + \frac{1}{2}mv_{\perp}^2(s_0) \right) - \frac{1}{2}mv_{\perp}^2(s_0) \frac{B(s)}{B_{\min}} \quad (3.5)$$

The condition for a particle to be trapped depends upon $v_{\perp}(s_0)/v_{\parallel}(s_0)$ and $B(s)/B_{\min}$.

The boundary in velocity (v_{\parallel}, v_{\perp}) space between trapped and untrapped particles can be determined by evaluating the above equation for $v_{\parallel}(s_{\max}) = 0$,

$$v_{\perp}(s_0) = \pm \left(\frac{B_{\max}}{B_{\min}} - 1 \right)^{-\frac{1}{2}} v_{\parallel}(s_0) \quad (3.6)$$

Noting that v_{\perp} is the two-dimensional velocity component in the plane perpendicular to the magnetic field, this equation defines a cone, as depicted in Fig. 3.2.

The “pitch” angle α at any point is defined by

$$\tan \alpha(s) \equiv \frac{v_{\perp}(s)}{v_{\parallel}(s)} = \frac{\sqrt{W_{\perp}(s)}}{\sqrt{W_{\parallel}(s)}} \quad (3.7)$$

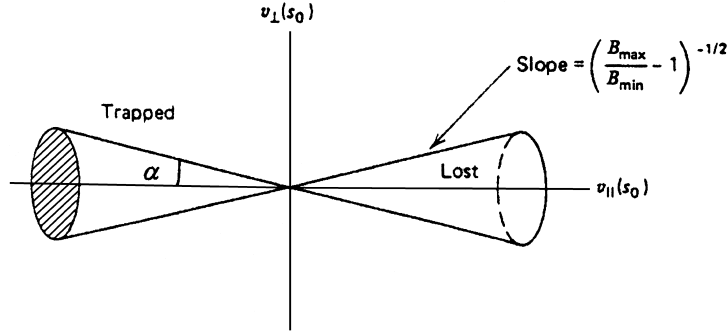


Figure 3.2. Loss cone

For a collection of particles with a uniform velocity distribution, the loss fraction is

$$f_{\text{loss}}(s) = \frac{\int_0^{\alpha_{\text{LC}}} \sin \alpha \, d\alpha}{\int_0^{\frac{\pi}{2}} \sin \alpha \, d\alpha} = 1 - \cos[\alpha_{\text{LC}}(s)] \quad (3.8)$$

where α_{LC} defines the loss-cone boundary at a given position. In particular, for particles at $s = s_0$

$$\alpha_{\text{LC}}(s_0) = \sin^{-1} \left(\sqrt{\frac{B_{\min}}{B_{\max}}} \right) \equiv \sin^{-1} \left(\sqrt{\frac{1}{R_M}} \right) \quad (3.9)$$

where $R_M \equiv B_{\max}/B_{\min}$ is known as the mirror ratio. For $R_M \gg 1$, Eq. (3.8) can be approximated as

$$f_{\text{loss}}(s_0) \approx \frac{1}{2R_M} \quad (3.10)$$

which is a convenient estimate of the loss fraction in terms of the maximum and minimum fields.

Having established that there is a mechanism that could confine particles in an open magnetic well configuration, we must now examine the particle motion for trapped particles. The simple mirror is poloidally symmetric about the centerline. Thus the poloidal angular momentum is a constant of the motion and $\psi = rA_\theta(r, s) = \text{const}$ defines the flux surfaces upon which the trapped particle guiding centers move, to first order. These flux surfaces are the surfaces of revolution about the centerline of the field lines shown in Fig. 3.1.

Now we must examine the effects of drifts upon the particle motion. The curvature and grad- B drifts both produce net currents in the simple mirror. However, for the poloidally symmetric field, $B_\theta = \partial B / \partial \theta = 0$, and the $\mathbf{B} \times \nabla B$ directed drifts and currents are in the poloidal direction and are poloidally symmetric. Consequently, the poloidal coordinate may still be ignored when curvature and grad- B drifts are considered, and the angular momentum is a constant of the net particle motion including drifts. Hence, the trapped

particles move on drift surfaces that are surfaces of revolution about the centerline. As long as the device is designed so that these drift surfaces do not intersect with a material wall, the trapped particles are confined. Thus, mirror-trapped particles can be confined in systems with dimensions that are large compared to a gyroradius. The curvature and grad- B drifts are given by Eqs. (2.24) and (2.44), which are repeated here.

$$\mathbf{v}_c = -\frac{mv_{\parallel}^2}{eR_c} \frac{\mathbf{B} \times \mathbf{n}_c}{B^2} = \frac{mv_{\parallel}^2}{eR_c B} \mathbf{n}_{\theta} \quad (3.11)$$

$$\mathbf{v}_{\nabla B} = \frac{\frac{1}{2}mv_{\perp}^2}{e} \frac{\mathbf{B} \times \nabla B}{B^3} = \frac{\frac{1}{2}mv_{\perp}^2}{e} \frac{|\nabla B|}{B^2} \mathbf{n}_{\theta} \quad (3.12)$$

These drifts are seen to be in the θ -direction, resulting in rotation about the axis of symmetry, but no net radial motion. Hence, the drifts do not destroy confinement.

Particles with $v_{\perp}(s_0)/v_{\parallel}(s_0)$ which fall within the loss cone shown in Fig. 3.2 are lost immediately. Other particles scatter into the loss cone and then are lost. Thus, the confinement time is proportional to the time required for a particle to scatter into the loss cone. This time is related to the 90° deflection time in the lab, $(\tau_{90})_L$,

$$(\tau_p) = (\tau_{90})_L \log_{10} \left(\frac{B_{\max}}{B_{\min}} \right) \quad (3.13)$$

Since $(\tau_{90}^{ii})_L \simeq \sqrt{m_i/m_e}(\tau_{90}^{ee})_L$ the electrons scatter into the loss cone and escape much faster than do the ions. This creates a positive net charge in the plasma which results in a positive electrostatic potential that acts to confine electrons in the loss cone until ions escape. Thus, the particle confinement time for ions and electrons in a simple mirror is proportional to the ion 90° deflection time,

$$\tau_p \simeq (\tau_{90}^{ii})_L \log_{10} \left(\frac{B_{\max}}{B_{\min}} \right) \quad (3.14)$$

The plasma density is maintained by reinjecting ions at somewhat higher energy.

The simple mirror is unstable against flute-type radial perturbations of the plasma. Consider the idealized force balance on the plasma surface illustrated in Fig. 3.3. The internal kinetic pressure p exerts an outward force which is balanced in equilibrium by the inward force of the magnetic pressure, $B^2/2\mu_0$. Now imagine that the surface is perturbed, as indicated by the dashed line in Fig. 3.3, outward into a region of weaker magnetic field. The outward force of the kinetic pressure remains the same, but now the inward force of the magnetic pressure is reduced, leading to further surface deformation and ultimately to destruction of confinement.

3.1.1.1 Minimum- B Mirrors

The flute instability can be suppressed if the field increases, rather than decreases, away from the plasma, that is, if the plasma sits in a three-dimensional magnetic well. In this case the deformation of Fig. 3.3 results in the inward force of the magnetic pressure being

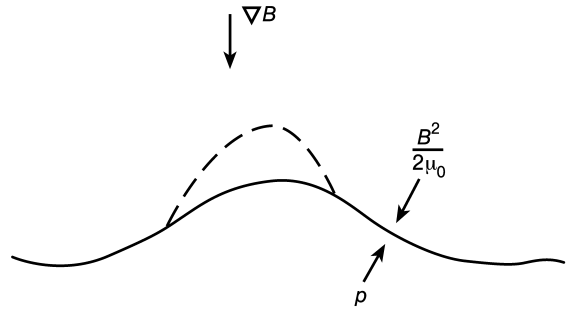


Figure 3.3. Flute instability

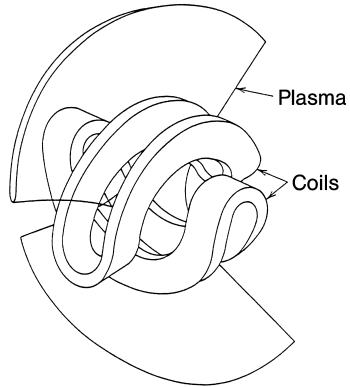


Figure 3.4. Schematic of mirror confinement configuration with yin-yang magnetic coils

stronger than the outward force of the kinetic pressure, thus acting to restore the surface to its equilibrium position.

Minimum- B stabilization of mirror plasmas has evolved through a number of magnetic configurations. The final stage of this evolution makes use of a set of “yin-yang” coils wound somewhat like the seams of a baseball (Fig. 3.4).

The principles of confinement in a minimum- B mirror are essentially the same as those described previously for the simple mirror, namely, confinement is governed by ions scattering into the loss cone. The estimate given previously for confinement time is valid. The drifts are considerably more complicated, but it is possible to show that they do not result in particle motion out of the confinement region.

The basic minimum- B mirror is unstable against “loss-cone” instabilities driven by the relaxation of the anisotropic velocity distribution. The process is illustrated in Fig. 3.5.

Scattering events tend to cause the distribution of Fig. 3.5(a) to relax toward that of Fig. 3.5(b), which has less free energy. The difference in free energy is converted into plasma kinetic energy during the relaxation process, thus constituting an instability which

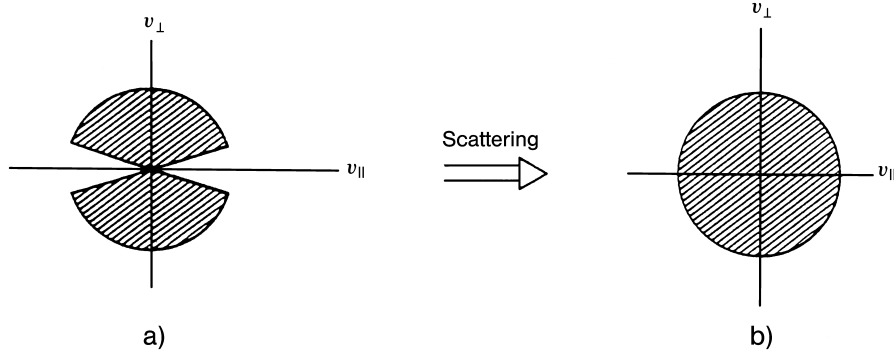


Figure 3.5. Relaxation of loss cone velocity distribution

destroys confinement. This loss-cone instability can be suppressed by filling in the distribution of Fig. 3.5(a) by injecting ions with $v_{\parallel}/v_{\perp} \gg 1$.

The minimum- B mirror has been thoroughly studied and is reasonably well understood. The most favorable performance projected for a minimum- B mirror leads to a plasma power amplification factor of $Q_p \simeq 1$ to 2. Noting that $Q_p \gtrsim 15$ is required for positive power balance on a reactor, it follows that the reactor prospects for a minimum- B mirror reactor for electricity production are poor. The minimum- B mirror has potential applications as a neutron source for materials testing or producing fissile material by nuclear transmutation of thorium-232 or uranium-238.

3.1.2 Tandem Mirrors*

The most promising use of minimum- B mirrors, however, is as end plugs to confine ions electrostatically in a central solenoidal cell. (Recall that the simple and minimum- B mirrors operate with a slight positive charge because electrons deflect into the loss cone faster than ions.)

The basic idea of the tandem mirror, illustrated in Fig. 3.6, is to create a potential difference ϕ_i between the end plugs and the central cell by creating a density difference. According to the Maxwell–Boltzmann distribution

$$n_e(z) = n_0 \exp\left(\frac{e\phi}{T_e}\right) \quad (3.15)$$

Using the subscripts p and c to refer to the end plug and the central cell, respectively, this relation can be used to obtain

$$e\phi_i \equiv e(\phi_p - \phi_c) = T_e \ln\left(\frac{n_p}{n_c}\right) = T_e \ln\left(\frac{\beta_p B_p^2}{\beta_c B_c^2}\right) \quad (3.16)$$

where the definition

$$\beta \equiv \frac{nT}{B^2/2\mu_0} \quad (3.17)$$

has been used.

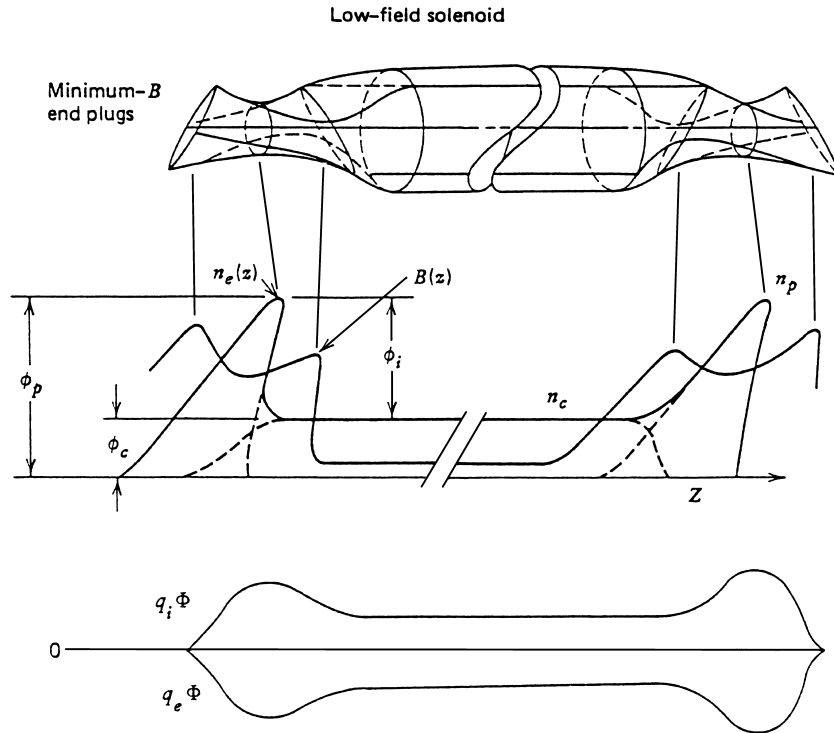


Figure 3.6. Tandem mirror with minimum- B end plugs

The basic tandem mirror concept has been established experimentally. Since most of the plasma volume in the tandem mirror is in the central cell, the power density ($\propto n^2 \langle \sigma v \rangle$) is proportional to $(\beta_c B_c^2)^2$. Thus, in order to achieve large confining potential and an adequate power density, it is necessary to have a large $\beta_p B_p^2$. Calculations indicate that magnetic fields in excess of 20 T may be required in the end plugs, which would put a severe demand upon superconducting magnet technology. In addition, penetration of the dense end plug plasmas would require neutral beam energies of the order of 1 MeV.

A reduction of technological requirements can be achieved, in principle, by the addition of two thermal barrier cells. The original idea of the thermal barrier is shown in Fig. 3.7. It is produced by adding a simple mirror (the barrier coil) to each end of the solenoid, thus partially isolating the end plugs from the solenoid. The intention is to insulate thermally hotter electrons in the end plug from relatively colder electrons in the central cell. If a higher electron temperature can be sustained in the plugs by intense electron heating (e.g., with microwaves at the electron–cyclotron frequency), then the potential peak in the plug necessary to confine the ions escaping from the solenoid can be generated with a much lower density n_p in the end plugs. A large reduction in the plug density reduces the power consumed in the plugs (hence improving Q_p) and opens up options for less demanding magnet and neutral beam technology.

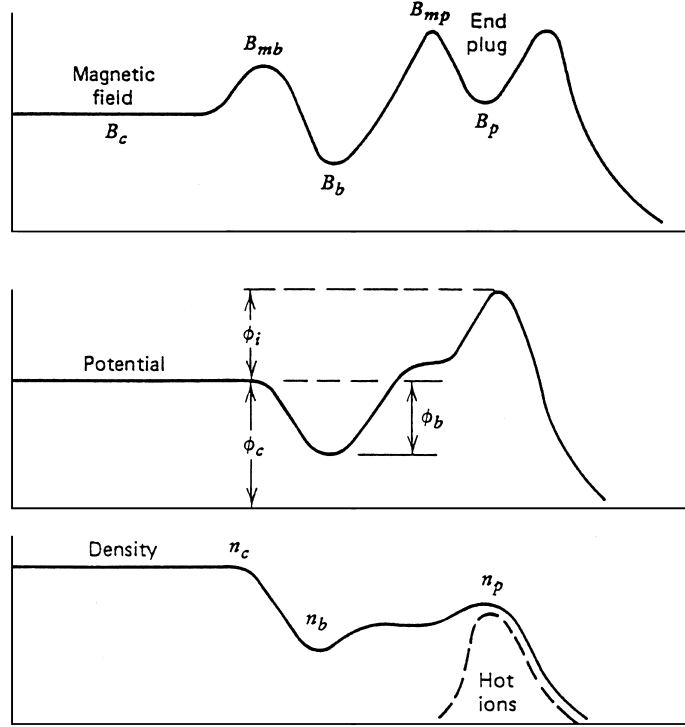


Figure 3.7. Magnetic field, potential, and density in a tandem mirror with thermal barrier

Electrons coming from the central solenoid into the barrier see a negative potential ϕ_b , which can be derived from the Maxwell–Boltzmann distribution

$$e\phi_b = T_c \ln \left(\frac{n_c}{n_b} \right) \quad (3.18)$$

Electrons coming from the plug into the barrier see a negative potential $\phi_i + \phi_b$, given by

$$e(\phi_i + \phi_b) = T_p \ln \left(\frac{n_p}{n_b} \right) \quad (3.19)$$

Combining these two relations yields

$$e\phi_i = T_p \ln \left(\frac{n_p}{n_c} \right) + (T_p - T_c) \ln \left(\frac{n_c}{n_b} \right) \quad (3.20)$$

Confinement in the central solenoid is described by

$$(n\tau_p)_c (\text{cm}^{-3} \cdot \text{s}) \simeq 10^{11} (T_c)^{\frac{1}{2}} \left(\frac{e\phi_i}{T_c} \right) \exp \left(\frac{e\phi_i}{T_c} \right) \quad (3.21)$$

where T is expressed in keV. This is substantially larger than for single-cell mirrors when $e\phi_i/T_c \simeq 2$ to 3.

3.2 Closed Toroidal Confinement Systems

3.2.1 Confinement

The basis for the magnetic confinement of a plasma is the fact that charged particles spiral about magnetic field lines. The radius of the spiral, or gyroradius, is inversely proportional to the strength of the magnetic field, so that in a strong field charged particles move along magnetic field lines, as shown in Fig. 3.8.

The magnetic field lines may be configured to remain completely within a confinement chamber by the proper choice of position and currents in a set of magnetic coils. The simplest such configuration is the torus, shown in Fig. 3.9. A set of coils can be placed to produce a toroidal field B_ϕ . Particles following along the closed toroidal field lines would remain within the toroidal confinement chamber.

The curvature and nonuniformity of the toroidal field produce forces which act upon the charged particles to produce “drift” motions that are radially outward, which would, if uncompensated, cause the particles to hit the wall. A poloidal magnetic field must be superimposed upon the toroidal magnetic field in order to compensate these drifts, result-

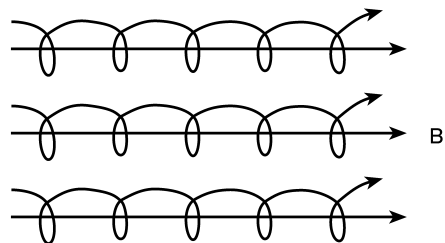


Figure 3.8. Motion of charged particles along magnetic field lines

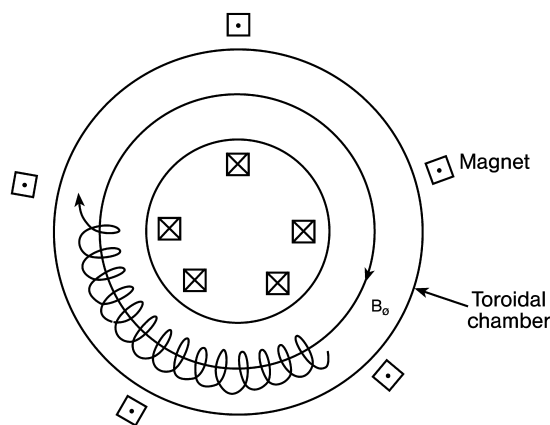


Figure 3.9. Closed toroidal confinement

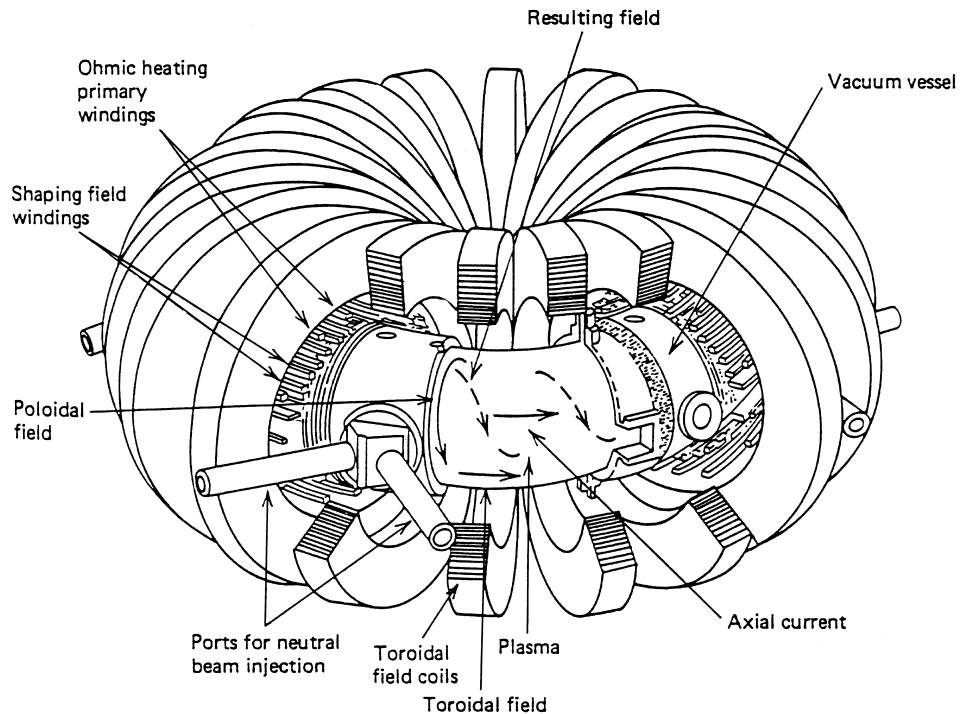


Figure 3.10. Tokamak schematic

ing in a helical magnetic field which is entirely contained within the toroidal confinement chamber. This poloidal field may be produced by a toroidal current flowing in the plasma (tokamak) or in external coils (stellarator, etc.).

The tokamak concept, which was invented in the USSR in the mid-1960s, has been the most extensively investigated worldwide and is the most advanced. This concept is illustrated in Fig. 3.10. The toroidal field is produced by a set of toroidal field coils which encircle the plasma. The poloidal field is produced by an axial, or toroidal, current in the plasma which is induced by the transformer action of a set of primary poloidal field, or “ohmic heating,” coils.

If the field lines do not enter or leave the confinement region (i.e., are closed, in an ergodic sense), then particles are obviously confined with respect to their lowest order guiding center motion along the field lines. The simplest “closed field” configuration is a torus.

An axisymmetric toroidal field can be formed, conceptually, by taking a flexible solenoidal coil and bending it around until the two ends meet. The axial field of the solenoid is thereby deformed into an axisymmetric toroidal field. A cross section of such a configuration is shown in Fig. 3.11. The cross section of the original solenoidal coil has also been deformed into the “D”-shape that is more natural for a torus. The toroidal field is produced by a current flowing in the field coil. Using Ampere’s law and taking a line inte-

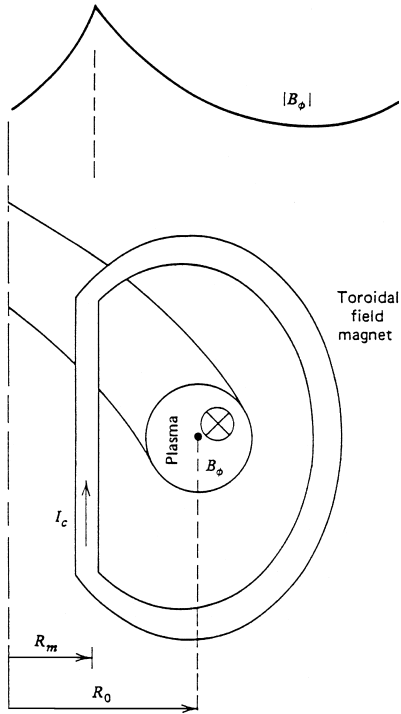


Figure 3.11. Toroidal configuration

gral of B_ϕ around any circular loop in Fig. 3.9 that encloses the inner, but not the outer, legs of the N toroidal field coils each carrying current I yields $\mu_0 NI = 2\pi RB_\phi = 2\pi R_0 h(r, \theta) B_\phi(r, \theta)$. This field has a maximum value, B_ϕ^{\max} , at the inner leg of the coil, $R = R_m$, and falls off as $1/R$ across the confinement region. Denoting the value of B_ϕ at the center of the confinement region, $R = R_0$, as B_ϕ^0 , the magnitude of the toroidal field in the confinement region varies as

$$B_\phi = \frac{B_\phi^0}{h(r, \theta)} \quad (3.22)$$

where

$$h(r, \theta) \equiv 1 + \frac{r}{R_0} \cos \theta \equiv 1 + \epsilon \cos \theta \quad (3.23)$$

The toroidal field is curved, by definition, and nonuniform, by necessity. Thus curvature and grad- B drifts must be taken into consideration in examining confinement. From Eqs. (3.11) and (3.12),

$$\mathbf{v} \nabla B = \frac{W_\perp}{e} \frac{\mathbf{B} \times \nabla B}{B^3} \quad (3.24)$$

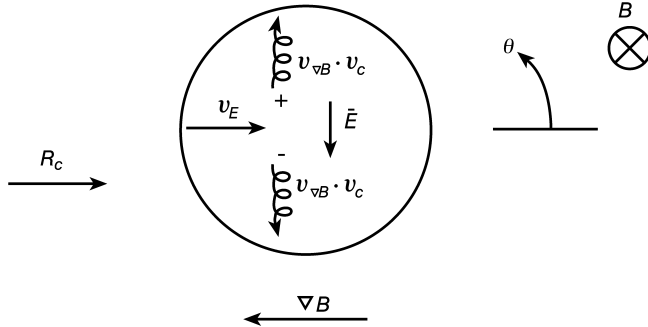


Figure 3.12. Curvature and grad- B drifts in a simple toroidal system

and

$$\mathbf{v}_c = -\frac{2W_{||}}{e} \frac{\mathbf{B} \times \mathbf{R}_c}{B^2 R_c^2} \quad (3.25)$$

These drifts cause charge separation, as depicted in Fig. 3.12, by carrying positive particles up and negative particles down. This charge separation produces an electric field which inhibits the particles from curvature or grad- B drifting out of the confinement region. However, the introduction of the electrostatic field produces an $\mathbf{E} \times \mathbf{B}$ drift, $v_E = \mathbf{E} \times \mathbf{B} / B^2$, which carries ions and electrons radially outward into the chamber wall. Thus particles are not confined in a simple toroidal system. (If the toroidal field in Fig. 3.12 was reversed, the grad- B and curvature drifts for ions and electrons and the direction of the electrostatic field would be reversed, but the confinement destroying $\mathbf{E} \times \mathbf{B}$ drift would still be radially outward.)

In order to achieve confinement in a toroidal field configuration, it is necessary to superimpose a poloidal (θ) field to cause the curvature and grad- B drifts to cancel, on the average. The net field is then helical,

$$\mathbf{B} = B_\phi \hat{n}_\phi + B_\theta \hat{n}_\theta \quad (3.26)$$

Usually, $|B_\theta| \ll |B_\phi|$. A particle guiding center following the helical field line then spirals about the confinement region in the poloidal direction and in the toroidal direction. The upward grad- B and curvature drift of an ion carries it radially outward when the ion is in the upper hemisphere, $0 \leq \theta \leq \pi$, and carries it radially inward when it is in the lower hemisphere, $\pi \leq \theta \leq 2\pi$. If the ion spends an equal time in the upper and lower hemispheres, the radial drift cancels out over the time required for the ion to follow a field line through a full poloidal rotation, $\theta = 2\pi$. A similar argument can be made for the electron drift.

The pitch of the helical toroidal field line configuration is characterized by the rotational transform, ι , which is the poloidal angle, $\Delta\theta$, that is turned by the field line in one toroidal revolution, $\Delta\phi = 2\pi$. If the field line pitch becomes too tight (i.e., if ι becomes too large) the plasma becomes unstable against kink-type perturbations. This has led to the

definition of a safety factor,

$$q \equiv \frac{2\pi}{\iota} \quad (3.27)$$

The safety factor is equal to the number of times a particle goes around the torus in the ϕ -direction before it goes around the torus once in the θ -direction (i.e. $\Delta\theta = 2\pi$). As we will see in chapter 8, stability against kink-type perturbations requires that $q \geq 1$ everywhere in the plasma and that $q \gtrsim 3.0$ at the edge of the plasma.

The pitch of the helical field lines is not necessarily the same for all the field lines. In general, the pitch increases as a function of the small radius from the centerline of the confinement region. Denoting the rotational transform at $r = 0$ by ι_0 , we can write

$$\iota(r) = \iota_0 + \frac{\partial \iota}{\partial r} \delta r \equiv \iota_0 + 2\pi S \delta r \quad (3.28)$$

The quantity S , defined by Eq. (3.28), is known as the shear of the helical toroidal field configuration. It is a measure of the change in pitch of the field lines as a function of radial position.

The poloidal field can be produced by a set of poloidal coils which carry a toroidally directed current or by a toroidal current flowing in the plasma. Devices based upon the former principle are known as stellarators, whereas devices based upon the latter principle are known as tokamaks. Since tokamaks are relatively simpler and of greater current interest, we will concentrate on them.

3.2.2 Flux Surfaces

The toroidal current flowing in a tokamak plasma produces a toroidal vector potential

$$\mathbf{A} = A_\phi \hat{\mathbf{n}}_\phi \quad (3.29)$$

which leads to a poloidal magnetic field

$$\mathbf{B}_\theta = (\nabla \times \mathbf{A}) \cdot \hat{\mathbf{n}}_\theta = \frac{1}{h} \frac{\partial}{\partial r} (h A_\phi) \quad (3.30)$$

In toroidal geometry, the thickness of a “unit” cross sectional slice varies as $h(r, \theta)$. This fact manifests itself in the form of $B_\theta(r, \theta)$, which follows from the solenoidal law equation in toroidal geometry

$$\mathbf{0} = \nabla \cdot \mathbf{B}_\theta = \frac{R_0}{r} \frac{\partial}{\partial \theta} (h B_\theta) \quad (3.31)$$

which leads to

$$B_\theta(r, \theta) = \frac{B_\theta^0(r)}{h(r, \theta)} \quad (3.32)$$

Using the form of Eq. (3.32), Eq. (3.30) may be integrated to obtain

$$A_\phi(r, \theta) = \frac{1}{h} \int B_\theta^0 dr \equiv \frac{A_\phi^0(r)}{h(r, \theta)} \quad (3.33)$$

With this form of $A_\phi(r, \theta)$, there is no radial field; that is,

$$B_r = (\nabla \times \mathbf{A}) \cdot \hat{\mathbf{n}}_r = -\frac{1}{hr} \frac{\partial}{\partial \theta} (h A_\phi) = 0$$

The flux surfaces in toroidal coordinates are

$$\psi(r, \theta) = h(r, \theta) R_0 A_\phi(r, \theta) = R_0 A_\phi^0(r) \quad (3.34)$$

This may be verified by considering

$$\mathbf{B} \cdot \nabla \psi = (B_\phi \hat{\mathbf{n}}_\phi + B_\theta \hat{\mathbf{n}}_\theta) \cdot \left(\hat{\mathbf{n}}_r R_0 \frac{\partial A_\phi^0}{\partial r} + \hat{\mathbf{n}}_\theta \frac{R_0}{r} \frac{\partial A_\phi^0}{\partial \theta} \right) = 0 \quad (3.35)$$

Amperé's law and Eq. (3.30) and Eq. (3.32) relate the vector potential to the toroidal current density

$$\begin{aligned} \mu_0 j_\phi(r, \theta) &= (\nabla \times \mathbf{B}) \cdot \hat{\mathbf{n}}_\phi \equiv \frac{1}{r} \frac{\partial(r B_\theta)}{\partial r} \\ &= \frac{1}{r} \frac{\partial}{\partial r} \left[\frac{r}{h} \frac{\partial}{\partial r} (h A_\phi) \right] \end{aligned} \quad (3.36)$$

From the first part of Eqs. (3.36) and (3.32) we see that

$$j_\phi(r, \theta) \simeq \frac{j_\phi^0(r)}{h(r, \theta)} \quad (3.37)$$

Assuming that the current density distribution is uniform, Eq. (3.36) may be integrated to obtain

$$A_\phi(r, \theta) = \frac{1}{4} \frac{\mu_0 r^2 j_\phi^0}{h(r, \theta)} \quad (3.38)$$

Substituting Eq. (3.38) into Eq. (3.30) yields

$$B_\theta(r, \theta) = \frac{1}{2} \frac{\mu_0 r j_\phi^0}{h(r, \theta)} \quad (3.39)$$

Thus the flux surfaces are concentric annuli

$$\psi(r) = R A_\phi = \text{const} \times r^2 R_0 \quad (3.40)$$

in this approximation. A more rigorous analysis, that accounted for higher order toroidal effects, would show that the centers of successive flux surfaces are shifted successively outward in the major radius (chapter 6).

In an axisymmetric torus, the toroidal coordinate can be ignored. Hence the toroidal angular momentum is a constant of the motion. This may be written, in the cylindrical (R, z, ϕ) coordinate system shown in Fig. 3.13, as

$$P_\phi = R_0 h(m v_\phi + e A_\phi) = \text{const} \quad (3.41)$$

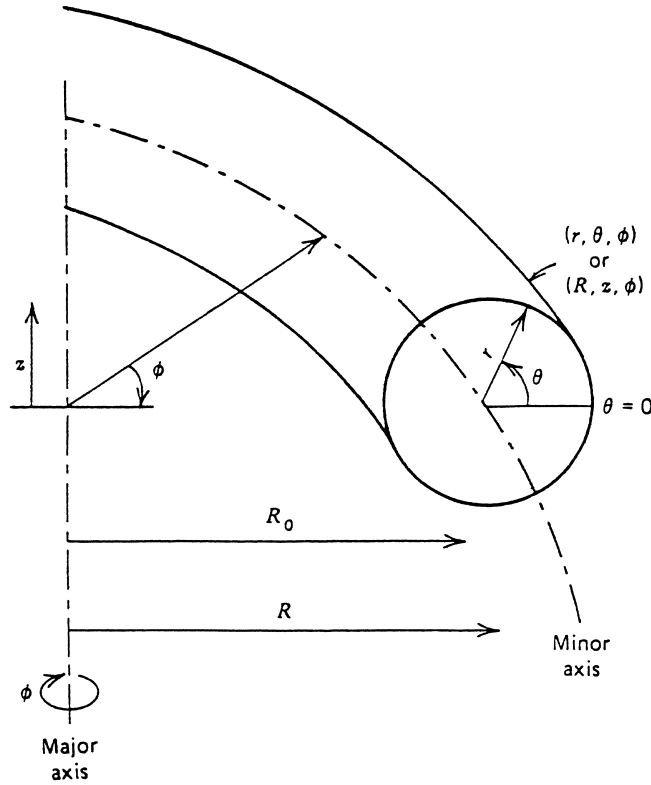


Figure 3.13. Toroidal (r, θ, ϕ) and cylindrical (R, z, ϕ) coordinate systems

Now we wish to examine the implication of Eq. (3.41) for particle motion. Forming the ratio of the first and last terms in Eq. (3.41) yields,

$$\frac{mv_\phi}{eA_\phi} \approx \frac{mv_{\text{th}}}{erB_\theta} \approx \frac{r_{\text{L}\theta}}{r} \quad (3.42)$$

where we have used the constant- j_ϕ approximations.

Thus particles move on flux surfaces, $\psi = R_0 h A$, except for excursions of the order of the gyroradius in the poloidal field, to lowest order. These flux surfaces are approximately $r = \text{const}$, annular, toroidal surfaces. We have seen that the grad- B and curvature drifts produce no average radial displacement. Thus the guiding centers of particles that are free to follow the helical field lines about the toroidal confinement region move on annular toroidal flux surfaces and are confined. Note that the confinement is produced by the poloidal field, and that the toroidal field has not entered our arguments.

3.2.3 Trapped Particles

Our considerations up to this point have been based upon the motion of particles that are free to follow the helical field lines as they encircle both the major and minor axes of the

torus. Such particles constitute the majority of all particles in a tokamak. However, there is a class of particles which are trapped in a magnetic well formed by the poloidal variation of the magnetic field. Since the toroidal and poloidal fields are stronger on the inside of the torus ($\theta = \pi$) than on the outside ($\theta = 0$), as given by Eqs. (3.22) and (3.32), a particle moving along a field line experiences a field variation as shown in Fig. 3.14. In a static field, the total energy is constant. If we neglect any poloidal variation in the electrostatic potential, the kinetic energy, W , is constant. Thus, the parallel velocity along the field line is given by

$$v_{\parallel}(\theta) = \left[\frac{2}{m} \left(W - \frac{\bar{\mu} B^0}{h(\theta)} - e\Phi \right) \right]^{\frac{1}{2}} \quad (3.43)$$

where Φ is the electrostatic potential and $B^0 = [(B_\theta^0)^2 + (B_\phi^0)^2]^{\frac{1}{2}} \approx B_\phi^0$ is the magnitude of the total magnetic field. If

$$\frac{\bar{\mu} B^0}{W - e\Phi} \geq h(\theta = \pi) = 1 - \epsilon \quad (3.44)$$

then v_{\parallel} can become zero, and the particle will be reflected. The results previously derived for particle trapping in mirrors can be applied directly to this situation. A particle is trapped if its pitch angle, α , at $\theta = 0$ satisfies

$$\sin \alpha_0 \equiv \sqrt{\frac{W_{\perp}(\theta = 0)}{W}} \geq \sqrt{\frac{B_{\min}}{B_{\max}}} = \sqrt{\frac{1 - \epsilon}{1 + \epsilon}} \quad (3.45)$$

The fraction of trapped particles can be estimated from

$$f_{\text{trap}} = \left(1 - \int_0^{\alpha_{\text{LC}}} \sin \alpha \, d\alpha \right) = \frac{2}{\pi} \sqrt{1 - \frac{1 - \epsilon}{1 + \epsilon}} \approx \frac{2\sqrt{2\epsilon}}{\pi} \quad (3.46)$$

where α_{LC} is given by Eq. (3.9), and we have assumed an isotropic particle distribution. The turning point in the orbit, θ_t , is the solution of $v_{\parallel}(\theta_t) = 0$. Using Eq. (3.43), we find

$$\theta_t = \pm \frac{1}{\epsilon} \cos^{-1} \left(\frac{\bar{\mu} B^0}{W - e\Phi} - 1 \right) \quad (3.47)$$

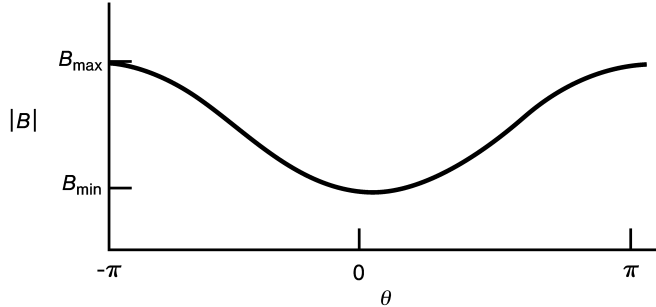


Figure 3.14. Field variation in a tokamak

The conservation of angular momentum can be used to estimate certain features of the trapped particle orbits. We assume $|B_\phi| \gg |B_\theta|$, so that the toroidal and parallel directions are very close. Using the uniform current density result

$$A_\phi(r, \theta) = \frac{1}{2} \frac{r B_\theta^0(r)}{h(r, \theta)} \quad (3.48)$$

Equation (3.41) can be written

$$P_\phi \simeq R_0 h(r, \theta) \left[m v_{\parallel} + \frac{1}{2} \frac{e r B_\theta^0}{h(r, \theta)} \right] = \text{const} \quad (3.49)$$

which can be rearranged to

$$\frac{h(\theta) v_{\parallel}(\theta)}{\Omega_\theta} + \frac{1}{2} r(\theta) = \text{const} \equiv \frac{h(0) v_{\parallel}(0)}{\Omega_\theta} + \frac{1}{2} r(0) \quad (3.50)$$

where Ω_θ is the gyrofrequency in the poloidal field. Noting that $h(0) \equiv h(\theta = 0) = 1 + \epsilon$, this result can be used to obtain an expression for the radial excursion of a particle guiding center from the flux surface as a function of θ ,

$$\Delta r(\theta) \equiv r(\theta) - r(0) = \frac{2v_{\parallel}(0)}{\Omega_\theta} \left[1 + \epsilon - \frac{v_{\parallel}(\theta)}{v_{\parallel}(0)} h(\theta) \right] \quad (3.51)$$

Equation (3.43) can be used to express

$$v_{\parallel}^2(\theta) \simeq v_{\parallel}^2(0) \left[1 - \frac{4}{m} \frac{\bar{\mu} B^0}{v_{\parallel}^2(0)} \epsilon \sin^2 \frac{\theta}{2} \right] \quad (3.52)$$

where we have now neglected the electrostatic potential. The bounce time for trapped particles can be defined in terms of a line integral over the closed trapped-particle orbit

$$\tau_b \equiv \omega_b^{-1} \equiv \int \frac{dl}{v_{\parallel}} = \frac{2r}{v_{\parallel}(0)} \int_{-\theta_t}^{\theta_t} \frac{d\theta}{\left[1 - \frac{4}{m} \frac{\bar{\mu} B^0}{v_{\parallel}^2(0)} \epsilon \sin^2 \frac{\theta}{2} \right]^{\frac{1}{2}}} \quad (3.53)$$

We can distinguish three limiting cases, which give rise to the orbits shown in Fig. 3.15.

3.2.3.1 Well Trapped Particles

The particles are trapped on the outside of the torus and bounce back and forth between small values of $\pm\theta_t$. This requires, from Eq. (3.52), that $v_{\parallel}^2(0) \ll (4\bar{\mu} B^0 \epsilon)/m$. In this case Eq. (3.52) yields

$$\frac{v_{\parallel}(\theta)}{v_{\parallel}(0)} \simeq \pm \left[1 - \frac{1}{m} \frac{\bar{\mu} B^0}{v_{\parallel}^2(0)} \epsilon \theta^2 \right]^{\frac{1}{2}} \quad (3.54)$$

The maximum excursion occurs at $\theta = 0$ when $v_{\parallel}(\theta)/v_{\parallel}(0) < 0$. From Eq. (3.51)

$$\Delta r_{\max} = \frac{2v_{\parallel}(0)}{\Omega_\theta} [(1 + \epsilon) + (1 + \epsilon)] \simeq \frac{4v_{\parallel}(0)}{\Omega_\theta} \quad (3.55)$$

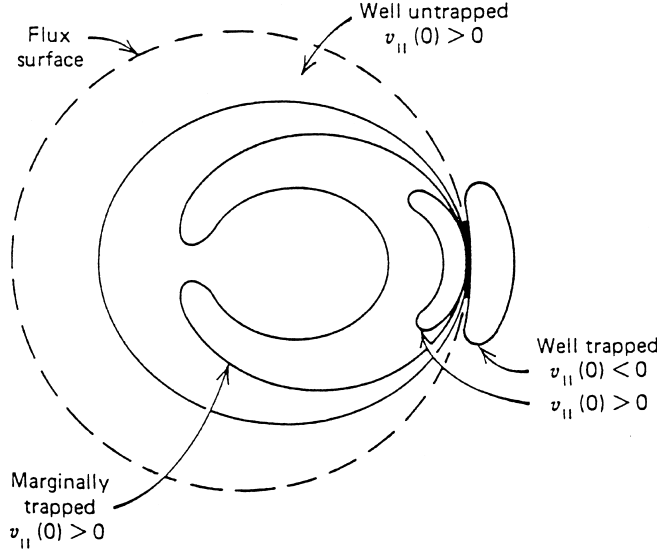


Figure 3.15. Particle orbits in a tokamak projected onto the r - θ plane (B_ϕ and I into page, B_θ clockwise)

3.2.3.2 Marginally Trapped and Untrapped Particles

The particles are trapped at $\theta \approx \pi$. For $v_{\parallel}(\theta = \pi) = 0$, Eq. (3.52) yields

$$v_{\parallel}^2(0) \simeq \frac{4}{m} \bar{\mu} B^0 \epsilon \quad (3.56)$$

and Eq. (3.52) becomes

$$\frac{v_{\parallel}(\theta)}{v_{\parallel}(0)} \simeq \pm \left(1 - \sin^2 \frac{\theta}{2} \right)^{\frac{1}{2}} = \pm \cos \frac{\theta}{2} \quad (3.57)$$

The maximum excursion again occurs at $\theta = 0$ for $v_{\parallel}(\theta)/v_{\parallel}(0) < 0$ and is

$$\Delta r_{\max} \simeq \frac{4v_{\parallel}(0)}{\Omega_\theta} \quad (3.58)$$

Using Eq. (3.56) and recalling that the perpendicular velocity, which we associate with random thermal motion, is given by

$$v_{\perp} \simeq v_{\text{th}} = \left(\frac{2}{m} \bar{\mu} B^0 \right)^{\frac{1}{2}} \quad (3.59)$$

Eq. (3.58) becomes

$$\Delta r_{\max} = \frac{4v_{\perp}}{\Omega_\theta} \sqrt{2\epsilon} = 4r_{L\theta} \sqrt{2\epsilon} \quad (3.60)$$

where $r_{L\theta}$ is the gyroradius in the poloidal field.

Equations (3.56) and (3.57) also obtain for marginally untrapped particles. However, untrapped particles do not change direction, so $v_{\parallel}(\theta)/v_{\parallel}(0) < 0$, and the maximum excursion is

$$\Delta r_{\max} = \frac{2v_{\parallel}(0)}{\Omega_{\theta}} = 2r_{L\theta}\sqrt{2\epsilon} \quad (3.61)$$

at $\theta = \pi$.

3.2.3.3 Far Untrapped Particles

In this case,

$$v_{\parallel}^2(0) \gg \frac{4}{m}\bar{\mu}B^0\epsilon \quad (3.62)$$

$v_{\parallel}(\theta) \simeq v_{\parallel}(0)$, there is no reflection, and Δr_{\max} occurs at $\theta = \pi$

$$\Delta r_{\max} \simeq \frac{2v_{\parallel}(0)}{\Omega_{\theta}} [(1 + \epsilon) - (1 - \epsilon)] = \frac{4v_{\parallel}(0)}{\Omega_{\theta}}\epsilon \quad (3.63)$$

The cancellation of curvature and grad- B drifts by the poloidal rotation of the field lines also occurs for the trapped particles, since they too spend equal times in the upper and lower halves of the torus (in the absence of a toroidal electric field). However, the upward and downward trajectories do not coincide, but are displaced from each other, because the sign of v_{\parallel} changes upon reflection and canonical angular momentum is conserved. The maximum displacement, Δr_{\max} , occurs at the horizontal midplane. The net result is a banana-shaped orbit projected onto the r - θ plane, as shown in Fig. 3.15.

When the effect of the toroidal electric field, which is necessary to produce the toroidal plasma current, is taken into account, the banana orbits are no longer symmetric. An ion spends more time in the lower half of the torus drifting radially inward than in the upper half drifting radially outward. A net inward drift of trapped particles occurs; this is known as the Ware pinch effect.

3.2.4 Transport Losses

Collisions are not as detrimental to confinement in a tokamak as we found them to be in mirror confinement. The effect of a collision is to displace a particle from an orbit associated with one flux surface to an orbit associated with another flux surface. The displacements associated with the scattering of trapped particles are generally larger by a factor ϵ^{-1} than the displacements associated with the scattering of untrapped particles, as may be seen by comparing Eq. (3.58) and Eq. (3.63).

The radial motion of particles then occurs as a result of a series of collisional displacements, each of which may displace the particle orbit guiding center radially inward or outward, depending on where along the orbit the collision takes place. The maximum radial displacements of guiding center orbits occurs when a trapped particle becomes untrapped,

or vice versa. Thus the radial motion is diffusive in nature and may be characterized by a diffusion coefficient

$$D \approx \frac{(\text{characteristic displacement})^2}{\text{characteristic time}} = \frac{(\Delta x)^2}{\tau} \quad (3.64)$$

The characteristic time is the scattering time. For trapped particles, this is the time required to scatter through the pitch angle $\alpha \approx \epsilon$ and become untrapped; in terms of the 90° scattering time, τ_{90} , this is $\tau \approx \alpha \tau_{90} \approx \epsilon \tau_{90}$. For untrapped particles this characteristic time is the time for marginally untrapped particles to scatter through a similar angle and become trapped, or $\tau \approx \epsilon \tau_{90}$.

The characteristic displacements can be taken as proportional (say 1/2 times) to the maximum displacements given by Eqs. (3.60) and (3.61) for marginally trapped and marginally untrapped particles, respectively. The fraction of trapped particles which can scatter through an angle $\alpha \sim \epsilon$ and become untrapped in time $\epsilon \tau_{90}$ is given by Eq. (3.46), and a similar derivation gives a similar result for the fraction of untrapped particles which can scatter through angle $\alpha \sim \epsilon$ and become trapped in time $\epsilon \tau_{90}$. Thus the fraction of particles capable of undergoing these large displacements associated with going from a trapped orbit to an untrapped orbit, and vice versa, is approximately $2\sqrt{\epsilon}$.

Thus for a tokamak with a trapped particle population, the diffusion coefficient may be estimated from Eq. (3.64) as

$$D_1 \approx \frac{(r_{L\theta} \sqrt{2\epsilon})^2 \times (2\sqrt{\epsilon})}{\epsilon \tau_{90}} \approx \sqrt{\epsilon} r_{L\theta}^2 v_{90} = \epsilon^{-\frac{3}{2}} r_L^2 q^2 v_{90} \quad (3.65)$$

where the explicit form of the previously introduced safety factor

$$q = \epsilon \frac{B_\phi}{B_\theta} \quad (3.66)$$

has been used in converting to a gyroradius in the toroidal field. In the above $v_{90} = (\tau_{90})^{-1}$.

The far untrapped particles would have to scatter through an angle of the order of 90° to become trapped and undergo the large displacement given by Eq. (3.61). This would require a time of the order of τ_{90} . The fraction of such particles is $\sim 1 - 2\sqrt{\epsilon} \sim 1$. The diffusion coefficient for such particles is

$$D_2 \approx \frac{(r_{L\theta} \sqrt{2\epsilon})^2}{\tau_{90}} \approx \epsilon r_{L\theta}^2 v_{90} \quad (3.67)$$

which is of order $\sqrt{\epsilon}$ smaller than the diffusion coefficient associated with marginally trapped or marginally untrapped particles. The displacement associated with far untrapped particles is smaller by a factor $\sim \epsilon$ than the displacement associated with marginally trapped or untrapped particles, so the diffusion of far untrapped particles is smaller by a factor $\sqrt{\epsilon}$ than the diffusion due to marginally trapped or untrapped particles. Thus, when there is a trapped particle population, the net radial diffusion is dominated by the trapped

and marginally untrapped particle displacements, and Eq. (3.65) provides an estimate of the diffusion coefficient for the plasma.

Trapped particle orbits of the type shown in Fig. 3.15 can only exist when the average time (τ_c) between collisions is long compared to the time (τ_b) required for a particle to complete an orbit. This latter time can be estimated from the length of the closed orbit for a marginally trapped particle, $2qR_0$, divided by the parallel velocity from Eq. (3.56), $\sqrt{2\epsilon}v_{th}$; that is,

$$\tau_b \equiv \omega_b^{-1} \simeq \sqrt{2} \frac{qR_0}{\sqrt{\epsilon}v_{th}} \quad (3.68)$$

The time between collisions is $(\tau_c) \simeq \epsilon\tau_{90}$. Thus trapped orbits of the type shown in Fig. 3.15 exist and the diffusion is governed by Eq. (3.65) when

$$v^* \simeq \frac{qR_0}{v_{th}\tau_{90}} < \epsilon^{\frac{3}{2}} \quad (\text{collisionless regime}) \quad (3.69)$$

The plasma regime for which Eq. (3.69) is satisfied is known as the collisionless, or banana, regime.

If the time between collisions is less than the time required for a particle to complete an untrapped orbit, then the form of the trapped orbit cannot be relevant to the diffusion process and the plasma is in a collisional regime. Noting that the time required to complete an untrapped orbit is qR_0/v_{th} , the condition for the plasma to be in the collisional regime can be written

$$v^* > 1 \quad (\text{collisional regime}) \quad (3.70)$$

In the collisional regime, particles move along the field lines between collisions. The upward grad- B and curvature drift of a positive ion is radially inward in the lower half of the torus and outward in the upper half, and vice versa for electrons. The drift velocity is of magnitude $v_D \simeq r_L v_{th}/R$. Since this drift reverses direction when the particle goes from the upper to the lower half of the torus, and vice versa, the characteristic displacement that is pertinent to radial diffusion is $v_D t_{1/2}$, where $t_{1/2}$ is the characteristic time for the particle to move along the field line through an angle $\theta = \pi$, which is a distance $\sim qR$. The movement of the particle along the field line is a random walk process in the collisional regime. The step size for the random walk along the field line is $v_{th}\tau_{90}$ and the characteristic time is τ_{90} , so that the time required to diffuse a distance qR along the field line is

$$t_{1/2} = \frac{1}{\tau_{90}} \left(\frac{qR}{v_{th}} \right)^2 \quad (3.71)$$

Thus we may finally estimate the radial diffusion coefficient from Eq. (3.64)

$$D_{PS} \simeq \frac{(v_D t_{1/2})^2}{t_{1/2}} = q^2 r_L^2 v_{th} \quad (3.72)$$

where the subscript PS denotes Pfirsch–Schlüter, the name by which this form of the diffusion coefficient is usually known.

It is interesting to note that simple random walk arguments for particles spiraling about field lines with gyroradius r_L lead to the classical diffusion coefficient

$$D_c \simeq r_L^2 \tau_{90} \quad (3.73)$$

Thus the toroidal field curvature effect is seen to enhance the collisional diffusion by a factor $q^2 \approx 10$ over the classical value.

The regime intermediate between the collisional and collisionless regime is known as the plateau regime and is defined by

$$\epsilon^{\frac{3}{2}} < v^* < 1 \quad (\text{plateau regime}) \quad (3.74)$$

These estimates for the diffusion coefficients lead to a rough estimate of the confinement time in tokamaks with a plasma radius a ,

$$\tau_{\text{conf}} \simeq \frac{a^2}{D} \simeq \begin{cases} \frac{a^2}{q^2 r_L^2} \tau_{90} & v^* > 1 \quad (\text{collisional}) \\ \frac{\epsilon^{\frac{3}{2}} a^2}{q^2 r_L^2} \tau_{90} & v^* < \epsilon^{\frac{3}{2}} \quad (\text{collisionless}) \end{cases} \quad (3.75)$$

A similar estimate of confinement time for a plasma confined by a straight, uniform axial field in a cylinder would use the gyroradius, r_L , for the mean displacement and τ_{90} for the characteristic time between displacements to obtain $\tau_{\text{conf}} \approx a^2 \tau_{90} / r_L$. By comparison with the first of Eq. (3.75), the confinement is reduced by a factor of q^2 (about 10) in a torus relative to a cylinder. This reduction is due to the curvature and grad- B drifts which are present in the torus but not in the cylinder. The collisionless ($v^* < \epsilon^{\frac{3}{2}}$) confinement time in Eq. (3.75) is a factor of $\epsilon^{\frac{3}{2}}$ (about 10) smaller than the collisional ($v^* > 1$) confinement time in a torus, due to the large mean displacements that arise from the banana orbits of the relatively small fraction ($\approx \epsilon^{\frac{1}{2}}$) of trapped particles. These transport effects are developed more fully in chapter 9.

Problems for Chapter 3

1. A deuterium plasma with $T = 10 \text{ keV}$, $n_D = n_e = 5 \times 10^{19} \text{ m}^{-3}$ is confined in a simple mirror field with $B_{\min} = 3 \text{ T}$ and $B_{\max} = 5 \text{ T}$. Estimate the loss fraction.
2. Calculate the confinement time for the plasma in problem 1.
3. A deuterium plasma with $T = 5 \text{ keV}$, $n_D = n_e = 5 \times 10^{19} \text{ m}^{-3}$ is confined in the central solenoidal cell with field $B_c = 5 \text{ T}$ of a tandem mirror. The end-plug plasma has $T = 10 \text{ keV}$, $n_D = n_e = 1 \times 10^{21} \text{ m}^{-3}$ and a confining field $B_p = 20 \text{ T}$. Calculate the confining potential difference between the end plugs and the central solenoid.

4. Calculate the toroidal vector potential, A_ϕ , and the poloidal magnetic field, B_θ , in a toroidal plasma in which the toroidal current density varies linearly with minor radius, $j(r) = j_0(1 - r/a)$ for $0 \leq r \leq a$. Describe the corresponding flux surfaces.
5. Estimate the trapped particle fraction at minor radius $r = 60$ cm in a tokamak with major radius $R = 1.7$ m.
6. Estimate the confinement time of a deuterium plasma with $T = 10$ keV, $n_D = n_e = 5 \times 10^{19} \text{ m}^{-3}$ confined in a tokamak with minor radius $a = 70$ cm and major radius $R = 1.7$ m, a toroidal magnetic field $B_\phi = 5$ T and a plasma current $I_\phi = 3$ MA.
7. Explain why it is not possible to confine a plasma in a purely toroidal magnetic field. Explain why the problem can be resolved by the addition of a small poloidal magnetic field.
8. Calculate the magnitude of the drifts you would expect to find in a tokamak plasma with $R_0 = 3.5$ m, $a = 1.0$ m, $B_{\phi 0} = 4$ T at R_0 , $T = 10$ keV and $I = 1.5$ MA. Take into account the poloidal dependence of the toroidal magnetic field.
9. Estimate the particle confinement time in the tokamak of problem 8 with a uniform deuterium ion density of $n_i = 1 \times 10^{20} \text{ m}^{-3}$. Take into account the collisionality regime.

4 Kinetic Theory

In principle, the characteristics of a plasma can be completely determined by solving for the position and velocity of all the particles in the confinement region. Such an approach is totally impractical, except for a few special situations, because of the large number of particles. We proceed, instead, by assuming that there is a joint statistical distribution function, F_N , that describes the joint probability of particle 1 being in volume element Δx_1 and velocity space element $\Delta \mathbf{v}_1$, of particle 2 being in Δx_2 and $\Delta \mathbf{v}_2$, and so on, for all the N particles in the system. This joint distribution function is governed by a modified version of Liouville's equation

$$\frac{dF_N}{dt}(x_1, \dots, x_N, \mathbf{v}_1, \dots, \mathbf{v}_N, t) = C_N(x_1, \dots, x_N, \mathbf{v}_1, \dots, \mathbf{v}_N, t) + S_N(x_1, \dots, x_N, \mathbf{v}_1, \dots, \mathbf{v}_N, t) \quad (4.1)$$

Note that two or more of these particles may be of the same type.

The term C_N represents the changes in the N -particle distribution function due to those close encounters that are treated as collisions, resonant interactions with electromagnetic waves, and other interactions that take place on a time scale that is short compared to the other phenomena of interest. The term S_N represents sources and sinks of particles. All of the long-range, collective particle interactions and the interaction of the N particles with the electric and magnetic fields are contained within the LHS, which can be written, by chain differentiation,

$$\frac{dF_N}{dt} = \frac{\partial F_N}{\partial t} + \sum_{j=1}^N \mathbf{v}_j \cdot \nabla_{x_j} F_N + \sum_{j=1}^N \mathbf{a}_j \cdot \nabla_{\mathbf{v}_j} F_N = C_N + S_N \quad (4.2)$$

The acceleration, $\mathbf{a}_j \equiv \dot{\mathbf{v}}_j$, can be expressed in terms of the electrical and Lorentz forces acting on a particle

$$\mathbf{a}_j = \frac{1}{m_j} \mathbf{F}_j = \frac{e_j}{m_j} (\mathbf{E} + \mathbf{v}_j \times \mathbf{B}) \quad (4.3)$$

We can define a single-particle distribution function, f_1 , by integrating F_N over the spatial and velocity coordinates of all the $N - 1$ other particles

$$f_1(x_1, \mathbf{v}_1, t) \equiv \int F_N(x_1, \dots, x_N, \mathbf{v}_1, \dots, \mathbf{v}_N, t) dx_2, \dots, dx_N d\mathbf{v}_2, \dots, d\mathbf{v}_N \quad (4.4)$$

The single-particle distribution function specifies the probability that a particle of type 1 is within volume element Δx_1 and velocity space element $\Delta \mathbf{v}_1$, at time t , without regard to the location and velocity of the other particles. The distribution f_1 obviously

has the normalization

$$\int f_1(x_1, \mathbf{v}_1, t) dx_1 d\mathbf{v}_1 = 1 \quad (4.5)$$

If there are n_σ indistinguishable particles of the same type as particle 1 in the confinement region, they must all have the same distribution function. Thus, we can extend our concept of a distribution function by defining

$$f_\sigma(x_\sigma, \mathbf{v}_\sigma, t) = n_\sigma f_1(x_1, \mathbf{v}_1, t) \quad (4.6)$$

which is the probability of finding n_σ particles within $(\Delta x_1, \Delta \mathbf{v}_1) = (\Delta x_\sigma, \Delta \mathbf{v}_\sigma)$. The quantity f_σ can be normalized to have the normalization of Eq. (4.5).

4.1 Boltzmann and Vlasov Equations

If Eq. (4.2) is integrated over the spatial and velocity coordinates of all particles except one, and the generalization of the distribution function described by Eq. (4.6) is used, the resulting equation is

$$\frac{df_\sigma}{dt}(x_\sigma, \mathbf{v}_\sigma, t) = \int C_N dx_2, \dots, dx_N, d\mathbf{v}_2, \dots, d\mathbf{v}_N + S_\sigma(x_\sigma, \mathbf{v}_\sigma, t) \quad (4.7)$$

The distribution functions for particles of species $\sigma' \neq \sigma$ are absent from the LHS of Eq. (4.7) because all long-range interactions among particles have been represented by fields. The coordinates of all other particles are required in order to evaluate the collision term. In general, the integral of the collision term in Eq. (4.7) can be written

$$\int C_N dx_2, \dots, dx_n, d\mathbf{v}_2, \dots, d\mathbf{v}_n \equiv C_\sigma = \sum_{\sigma'} C_{\sigma\sigma'}(f_\sigma, f_{\sigma'}) \quad (4.8)$$

in the two-body collision approximation. The sum in Eq. (4.8) is over all different particle species. Thus Eq. (4.7) can be written

$$\frac{\partial f_\sigma}{\partial t} + \mathbf{v}_\sigma \cdot \nabla f_\sigma + \frac{e_\sigma}{m_\sigma} (\mathbf{E} + \mathbf{v}_\sigma \times \mathbf{B}) \cdot \nabla_{\mathbf{v}\sigma} f_\sigma = C_\sigma + S_\sigma \quad (4.9)$$

Equation (4.9) is known as the Boltzmann equation. When collisions may be neglected ($C_\sigma = 0$), Eq. (4.9) reduces to the collisionless Boltzmann, or Vlasov, equation. These equations govern the evolution of the distribution function for the position and velocity of the particles of species σ .

4.2 Drift Kinetic Approximation

Solutions to the Boltzmann or, when appropriate, the Vlasov equation provide a complete description of the plasma in terms of which the properties of the plasma can be evaluated. However, as these equations are quite complicated, such solutions are quite difficult to obtain in practice, except under the simplest of conditions.

We have seen that the motion of particles in a magnetized plasma can be decomposed into the motion of guiding centers and a superimposed gyromotion about the guiding center orbit. The motion of the guiding centers consists of motion along the field and drift motion across the field. Furthermore, we know that there are certain constants of the motion. A more tractable description of the plasma can be obtained in terms of a distribution function for the velocity and position of particle guiding centers. The constants of the motion and the drift velocity provide a convenient “natural” coordinate system. Thus, we define a guiding center distribution function for particles of species σ

$$\hat{f}_\sigma = \hat{f}_\sigma(W_\sigma, \bar{\mu}_\sigma, r) \quad (4.10)$$

where W_σ is the energy

$$W_\sigma \equiv \frac{1}{2}m_\sigma \left[(v_{\sigma\parallel})^2 + (v_{\sigma\perp})^2 \right] + e_\sigma \Phi \equiv W_\sigma^k + e_\sigma \Phi \quad (4.11)$$

Φ is the electrostatic potential, and $\bar{\mu}_\sigma$, is the magnitude of the magnetic moment

$$\bar{\mu}_\sigma \equiv \frac{1}{2} \frac{m_\sigma}{B} (v_{\sigma\perp})^2 \quad (4.12)$$

In order to motivate an equation for \hat{f}_σ , we consider the relationship between the guiding center distribution function, \hat{f}_σ , and the particle distribution function, f_σ . If \hat{f}_σ is considered as an average of f_σ over the circular area πr_L^2 surrounding the guiding center position, the normal to which is in the field direction, then it follows that \hat{f}_σ satisfies an averaged version of the equation satisfied by f_σ , or

$$\frac{d\hat{f}_\sigma}{dt} = \hat{C}_\sigma + \hat{S}_\sigma \quad (4.13)$$

Using the functional dependence specified in Eq. (4.10), Eq. (4.13) becomes

$$\begin{aligned} \frac{d\hat{f}_\sigma}{dt} &= \frac{\partial \hat{f}_\sigma}{\partial t} + \frac{\partial \hat{f}_\sigma}{\partial W_\sigma} \left[\left\langle \frac{dW_\sigma^k}{dt} \right\rangle + e_\sigma \frac{\partial \Phi}{\partial t} \right] + \frac{\partial \hat{f}_\sigma}{\partial \bar{\mu}_\sigma} \left\langle \frac{d\bar{\mu}_\sigma}{dt} \right\rangle + (\mathbf{v}_{\sigma\text{dr}} + \mathbf{v}_{\sigma\parallel}) \cdot \nabla \hat{f}_\sigma \\ &= \hat{C}_\sigma + \hat{S}_\sigma \end{aligned} \quad (4.14)$$

where $\langle \rangle$ denotes the gyroperiod average, $\mathbf{v}_{\sigma\text{dr}}$ is the drift velocity and $\mathbf{v}_{\sigma\parallel}$ is the parallel velocity. The third term vanishes because the gyroperiod average of $\bar{\mu}$ is a constant of the motion. In order to evaluate the second term, we interpret $\langle dW_\sigma^k / dt \rangle$ as the average rate of change of kinetic energy over a gyroperiod.

The gyro-orbit is not quite closed in the presence of drifts, but has the shape seen in Fig. 4.1(a). This orbit can be represented approximately by a closed circle (I) and a drift displacement (II), as seen in Fig. 4.1(b).

To find $\langle dW_\sigma^k / dt \rangle$, we take the equation of motion (dropping the subscripts momentarily) $m d\mathbf{v} / dt = e(\mathbf{E} + \mathbf{v} \times \mathbf{B})$ and dot \mathbf{v} into it to obtain

$$e\mathbf{v} \cdot \mathbf{E} = m\mathbf{v} \cdot \frac{d\mathbf{v}}{dt} = \frac{d}{dt} \left(\frac{1}{2} m \mathbf{v} \cdot \mathbf{v} \right) \equiv \frac{dW_\sigma^k}{dt} \quad (4.15)$$

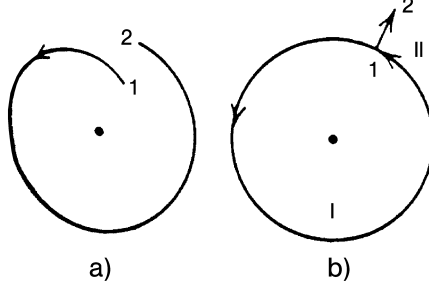


Figure 4.1. Gyro-orbits in the presence of drifts

The gyroperiod average of Eq. (4.15) is

$$\begin{aligned}
 \left\langle \frac{dW^k}{dt} \right\rangle &= -\frac{e\Omega}{2\pi} \oint_I E \cdot d\mathbf{l} + e(\mathbf{v}_{\parallel} + \mathbf{v}_{dr}) \cdot \mathbf{E} \\
 &= -\frac{e\Omega}{2\pi} \int_I \nabla \times \mathbf{E} \cdot ds + e(\mathbf{v}_{\parallel} + \mathbf{v}_{dr}) \cdot \mathbf{E} \\
 &= \frac{e\Omega}{2\pi} \int_I \frac{\partial \mathbf{B}}{\partial t} \cdot ds + e(\mathbf{v}_{\parallel} + \mathbf{v}_{dr}) \cdot \mathbf{E} \\
 &\simeq \bar{\mu} \frac{\partial B}{\partial t} + e(\mathbf{v}_{\parallel} + \mathbf{v}_{dr}) \cdot \mathbf{E}
 \end{aligned} \tag{4.16}$$

Using Eq. (4.16), Eq. (4.14) becomes

$$\begin{aligned}
 \frac{\partial \hat{f}_\sigma}{\partial t} + \frac{\partial \hat{f}_\sigma}{\partial W_\sigma} \left[\bar{\mu}_\sigma \frac{\partial B}{\partial t} + e_\sigma (\mathbf{v}_{\sigma dr} + \mathbf{v}_{\sigma \parallel}) \cdot \mathbf{E} + e_\sigma \frac{\partial \Phi}{\partial t} \right] + (\mathbf{v}_{\sigma dr} + \mathbf{v}_{\sigma \parallel}) \cdot \nabla \hat{f}_\sigma \\
 = \hat{C}_\sigma + \hat{S}_\sigma
 \end{aligned} \tag{4.17}$$

Equation (4.17) is one form of the drift-kinetic equation. Now we consider some further approximations that are appropriate in a large aspect ratio tokomak.

The conservation of toroidal angular momentum

$$\frac{d}{dt} P_\phi = \left(\frac{\partial}{\partial t} + \mathbf{v} \cdot \nabla \right) [R_0 h(mv_\phi + eA_\phi)] = 0 \tag{4.18}$$

in toroidal geometry can be used to derive approximate expressions for the radial and poloidal drift velocities in an axisymmetric tokamak field configuration. Making use of

$$B_\theta = (\nabla \times \bar{A}_\phi)_\theta = -\frac{1}{h} \frac{\partial(hA_\phi)}{\partial r}$$

the above equation can be written

$$m \left[\left(v_{\parallel} \frac{B_\theta}{B} + v_{dr}^\theta \right) \frac{1}{r} \frac{\partial(hv_{\parallel})}{\partial \theta} + v_{dr}^r \frac{\partial(hv_{\parallel})}{\partial r} \right] = ehv_{dr}^r B_\theta$$

where $h = 1 + \epsilon \cos \theta$. Noting that $|v_{\text{dr}}| \ll |v_{\parallel}|$ and $|eB/m| \gg 1$, the leading order terms in this equation are the first term on the left and the term on the right, yielding an expression for the radial drift velocity

$$v_{\text{dr},r} = \frac{mv_{\parallel}}{eB^0} \frac{1}{r} \frac{\partial}{\partial \theta} (hv_{\parallel}) \quad (4.19)$$

When this result is used to evaluate the second order terms, we obtain an expression for the poloidal drift velocity

$$v_{\text{dr},\theta} = -\frac{mv_{\parallel}}{eB^0} \frac{\partial}{\partial r} (hv_{\parallel}) \quad (4.20)$$

Noting that $\hat{\mathbf{n}}_{\parallel} \cdot \hat{\mathbf{n}}_{\theta} = B_{\theta}/B$, recalling that $q \equiv rB/RB_{\theta}$, limiting our attention to situations in which $\partial B/\partial t = 0$, and noting that $|v_{\parallel}| \gg |v_{\text{dr}}|$, Eq. (4.17) for the drift kinetic equation becomes

$$\begin{aligned} \frac{\partial \hat{f}_{\sigma}}{\partial t} + \left(\frac{\partial \hat{f}_{\sigma}}{\partial W_{\sigma}} \right) e_{\sigma} \left(v_{\sigma\parallel} E_{\parallel} + \frac{\partial \Phi}{\partial t} \right) \\ + \frac{mv_{\sigma\parallel}}{e_{\sigma} B^0} \left[\left(\frac{1}{r} \frac{\partial (hv_{\sigma\parallel})}{\partial \theta} \right) \left(\frac{\partial \hat{f}_{\sigma}}{\partial r} \right) - \left(\frac{\partial}{\partial r} (hv_{\sigma\parallel}) \right) \left(\frac{1}{r} \frac{\partial \hat{f}_{\sigma}}{\partial \theta} \right) \right] \\ + \frac{v_{\sigma\parallel}}{Rq} \frac{\partial \hat{f}_{\sigma}}{\partial \theta} = \hat{C}_{\sigma} + \hat{S}_{\sigma} \end{aligned} \quad (4.21)$$

4.3 Fokker–Planck Theory of Collisions

If the collisional time scale is short compared to the time scale of other phenomena that affect the distribution function, then we are justified in considering the change in the distribution function due to collisions alone and then using this result to evaluate the collision term, C_{σ} , in the Boltzmann or drift-kinetic equation, under the assumption that collisional effects are instantaneous on the time scale of interest for these equations. In order to evaluate the collision term that appears in the Boltzmann or drift-kinetic equations, we define the probability, $P(\mathbf{v}, \Delta \mathbf{v})$, that a particle with velocity \mathbf{v} undergoes a change in velocity $\Delta \mathbf{v}$ in time Δt as a result of a collision. The time evolution of the particle distribution function due to collisions satisfies

$$f(\mathbf{v}, t) = \int f(\mathbf{v} - \Delta \mathbf{v}, t - \Delta t) P(\mathbf{v} - \Delta \mathbf{v}, \Delta \mathbf{v}) d(\Delta \mathbf{v}) \quad (4.22)$$

Since multiple, small-angle scattering is the dominant collisional phenomenon, $\Delta \mathbf{v}$ may be considered as small when Δt is small. This fact allows a Taylor's series expansion to be made of the integrand in Eq. (4.22), leading to the Fokker–Planck equation

$$\frac{\partial f}{\partial t} \Big|_c = \frac{\partial}{\partial \mathbf{v}} \cdot \left\langle \frac{\Delta \mathbf{v}}{\Delta t} \right\rangle_P f(\mathbf{v}, t) + \frac{1}{2} \sum_{\epsilon, \gamma} \frac{\partial^2}{\partial v_{\xi} \partial v_{\gamma}} \left[\left\langle \frac{\Delta v_{\xi} \Delta v_{\gamma}}{\Delta t} \right\rangle_P f(\mathbf{v}, t) \right] \quad (4.23)$$

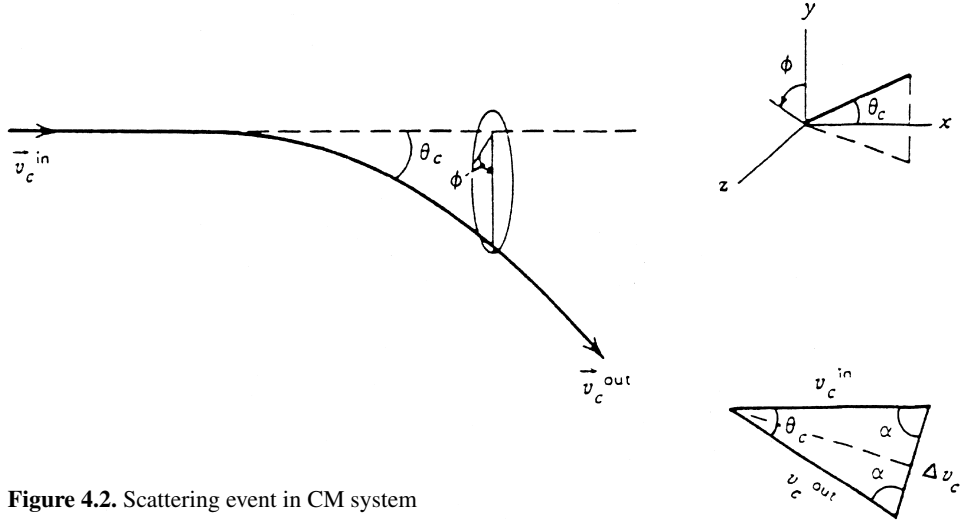


Figure 4.2. Scattering event in CM system

where

$$\left\langle \frac{\Delta \mathbf{v}}{\Delta t} \right\rangle_P \equiv \frac{1}{\Delta t} \int P(\mathbf{v}, \Delta \mathbf{v}) (\Delta \mathbf{v}) d(\Delta \mathbf{v}) \quad (4.24)$$

and

$$\left\langle \frac{\Delta v_\xi \Delta v_\gamma}{\Delta t} \right\rangle_P \equiv \frac{1}{\Delta t} \int P(\mathbf{v}, \Delta \mathbf{v}) (\Delta v_\xi \Delta v_\gamma) d(\Delta \mathbf{v}) \quad (4.25)$$

are moments of the velocity change. The subscripts ξ, γ refer to the coordinate directions (e.g., x, y, z).

The physics of the scattering process is contained in the velocity change moments defined by Eqs. (4.24) and (4.25). We will use the Coulomb scattering results that were developed in chapter 1. The scattering event is illustrated schematically in Fig. 4.2.

For an elastic collision, $|\mathbf{v}_c^{\text{in}}| = |\mathbf{v}_c^{\text{out}}|$. The trigonometric relation $\alpha + \theta_c/2 = \pi/2$ and the small-angle scattering assumption $|\Delta \mathbf{v}_c| \simeq |v_c^{\text{in}} \theta_c| \ll |v_c^{\text{in}}|$ may be used to write the components of the velocity change

$$\begin{aligned} \Delta v_{c,x} &\equiv \hat{\mathbf{n}}_x \cdot \Delta \mathbf{v}_c = -|\Delta \mathbf{v}_c| \sin \frac{\theta_c}{2} \simeq -|v_c \theta_c| \frac{\theta_c}{2} \\ \Delta v_{c,y} &\equiv \hat{\mathbf{n}}_y \cdot \Delta \mathbf{v}_c = |\Delta \mathbf{v}_c| \cos \frac{\theta_c}{2} \sin \phi \simeq -|v_c \theta_c| \sin \phi \\ \Delta v_{c,z} &\equiv \hat{\mathbf{n}}_z \cdot \Delta \mathbf{v}_c = |\Delta \mathbf{v}_c| \cos \frac{\theta_c}{2} \cos \phi \simeq -|v_c \theta_c| \cos \phi \end{aligned} \quad (4.26)$$

for a particle initially moving in the $+x$ -direction. The scattering angle, θ_c , is related to the impact parameter, x , in the limit of small θ_c , by

$$\theta_c = \frac{|e_1 e_2|}{m_r v_c^2 x 2\pi\epsilon_0}, \quad \text{where} \quad m_r \equiv \frac{m_1 m_2}{m_1 + m_2} \quad (4.27)$$

and the subscripts 1 and 2 refer to the particle whose deflection we wish to calculate and to the other particle responsible for the scattering, respectively.

The mean value of Δv_ξ for a “test” particle of type 1 that travels a distance $L \equiv v_c \Delta t$ through a medium of particle density n_2 is

$$\overline{\Delta v_{\xi c}} = n_2 v_c \Delta t \int_{\theta_{\min}}^{\theta_{\max}} \sin \theta \, d\theta \int_0^{2\pi} d\phi \Delta v_\xi = n_2 v_c \Delta t \int_0^{2\pi} d\phi \int_{x_{\min}}^{x_{\max}} x \, dx \Delta v_{\xi c} \quad (4.28)$$

Using Eq. (4.26) and Eq. (4.27), we obtain

$$\overline{\Delta v_{xc}} = \frac{-n_2 e_1^2 e_2^2 \Delta t \ln \Lambda}{4\pi \epsilon_0^2 m_r^2 v_c^2}, \quad \overline{\Delta v_{yc}} = \overline{\Delta v_{zc}} = 0 \quad (4.29)$$

where the maximum and minimum values of the impact parameter have been chosen as the Debye length and the 90° scattering value, respectively, as discussed in chapter 1.

This result must be transformed into the laboratory frame. Recalling the definitions of the velocity of the CM system relative to the lab system

$$\mathbf{v}_{CM} \equiv \frac{m_1}{m_1 + m_2} \mathbf{v}_1 + \frac{m_2}{m_1 + m_2} \mathbf{v}_2 \quad (4.30)$$

and of the relative velocity, which is the same in both systems,

$$\mathbf{v}_c \equiv \mathbf{v}_{c1} - \mathbf{v}_{c2} = \mathbf{v}_1 - \mathbf{v}_2 = \mathbf{v} \quad (4.31)$$

it follows that the initial velocity of the scattering particle in the lab is

$$\mathbf{v}_1 = \mathbf{v}_{CM} + \frac{m_2}{m_1 + m_2} \mathbf{v} \quad (4.32)$$

and that the change in lab system velocity is

$$\Delta \mathbf{v}_1 = \frac{m_2}{m_1 + m_2} \Delta \mathbf{v}_c \quad (4.33)$$

Consequently, Eq. (4.24) may be evaluated from

$$\overline{\left(\frac{\Delta \mathbf{v}_1}{\Delta t} \right)} = -\frac{n_2 (e_1 e_2)^2 \mathbf{v} \ln \Lambda}{4\pi \epsilon_0^2 m_r m_1 v^3} \quad (4.34)$$

A similar analysis leads to

$$\begin{aligned} \overline{(\hat{\mathbf{n}}_x \cdot \Delta \mathbf{v}_c)(\hat{\mathbf{n}}_x \cdot \Delta \mathbf{v}_c)} &\ll \overline{(\hat{\mathbf{n}}_y \cdot \Delta \mathbf{v}_c)(\hat{\mathbf{n}}_y \cdot \Delta \mathbf{v}_c)} = \overline{(\hat{\mathbf{n}}_z \cdot \Delta \mathbf{v}_c)(\hat{\mathbf{n}}_z \cdot \Delta \mathbf{v}_c)} \\ &= \frac{n_2 (e_1 e_2)^2 \ln \Lambda}{4\pi \epsilon_0^2 m_r^2 v} \Delta t \end{aligned} \quad (4.35)$$

and

$$\overline{(\hat{\mathbf{n}}_\xi \cdot \Delta \mathbf{v}_c)(\hat{\mathbf{n}}_\gamma \cdot \Delta \mathbf{v}_c)} = 0 \quad \text{if } \xi \neq \gamma \quad (4.36)$$

This result transforms into the lab system as

$$\overline{\Delta v_{\xi 1} \Delta v_{\gamma 1}} = \frac{n_2 (e_1 e_2)^2 \Delta t \ln \Lambda}{4\pi \epsilon_0^2 m_1^2 v} \left(\delta_{\xi \gamma} - \frac{v_{\xi 1} v_{\gamma 1}}{(v)^2} \right) \quad (4.37)$$

Equations (4.34) and (4.37) prescribe the appropriate moments for the scattering of a particle of type 1, with velocity \mathbf{v}_1 , by a particle of type 2, with velocity \mathbf{v}_2 . These results must now be averaged over the velocity distribution of the type 2 particles to finally obtain the appropriate coefficients for the Fokker–Planck equation,

$$\begin{aligned} \left\langle \frac{\Delta v_{\xi 1}}{\Delta t} \right\rangle_p &\equiv \int f_2(\mathbf{v}_2) \overline{\left(\frac{\Delta \mathbf{v}_1}{\Delta t} \right)} d\mathbf{v}_2 \\ &= -\frac{n_2 (e_1 e_2)^2 \ln \Lambda}{4\pi \epsilon_0^2 m_r m_1} \int f_2(\mathbf{v}_2) \frac{(\mathbf{v}_1 - \mathbf{v}_2)}{|\mathbf{v}_1 - \mathbf{v}_2|^3} d\mathbf{v}_2 \end{aligned} \quad (4.38)$$

and

$$\begin{aligned} \left\langle \frac{\Delta v_{\xi 1} \Delta v_{\gamma 1}}{\Delta t} \right\rangle_p &\equiv \frac{1}{\Delta t} \int f_2(\mathbf{v}_2) (\overline{\Delta v_{\xi 1} \Delta v_{\gamma 1}}) d\mathbf{v}_2 \\ &= \frac{n_2 (e_1 e_2)^2}{4\pi \epsilon_0^2 m_1^2} \ln \Lambda \frac{\partial^2}{\partial v_{\xi 1} \partial v_{\gamma 1}} \int f_2(\mathbf{v}_2) |\mathbf{v}_1 - \mathbf{v}_2| d\mathbf{v}_2 \end{aligned} \quad (4.39)$$

The integrals occurring in these expressions lead to the Rosenbluth potentials,

$$g_2(\mathbf{v}_1) \equiv \int f_2(\mathbf{v}_2) |\mathbf{v}_1 - \mathbf{v}_2| d\mathbf{v}_2 \quad (4.40)$$

and

$$h_2(\mathbf{v}_1) \equiv \frac{m_1}{m_r} \int \frac{f_2(\mathbf{v}_2)}{|\mathbf{v}_1 - \mathbf{v}_2|} d\mathbf{v}_2 \quad (4.41)$$

These results can readily be generalized to the scattering of particles of type 1 by particles of several other types and by other particles of type 1, as well. Hence the general form of Eq. (4.23), the Fokker–Planck equation, is

$$\begin{aligned} \left. \frac{\partial f_1(\mathbf{v}_1)}{\partial t} \right|_c &= \sum_i \Gamma_{1i} \left[- \sum_{\xi=1}^3 \frac{\partial}{\partial v_{\xi 1}} \left(f_1(\mathbf{v}_1) \frac{\partial h_i(\mathbf{v}_1)}{\partial v_{\xi 1}} \right) \right. \\ &\quad \left. + \frac{1}{2} \sum_{\xi=1}^3 \sum_{\gamma=1}^3 \frac{\partial^2}{\partial v_{\xi 1} \partial v_{\gamma 1}} \left(f_1(\mathbf{v}_1) \frac{\partial^2 g_i(\mathbf{v}_1)}{\partial v_{\xi 1} \partial v_{\gamma 1}} \right) \right] \end{aligned} \quad (4.42)$$

where

$$\Gamma_{1i} \equiv \frac{n_i (e_1 e_i)^2 \ln \Lambda}{4\pi \epsilon_0^2 m_1^2} \quad (4.43)$$

Equation (4.42) describes the change in the velocity distribution of particles of type 1 due to Coulomb collisional interactions. This description is appropriate for a fully ionized

plasma, in which all scattering events are via the Coulomb interaction. The first term in Eq. (4.42) represents a drag and the second term represents diffusion, both in velocity space. The scattering term in the Boltzmann or drift-kinetic equation is

$$C_\sigma \equiv \frac{\partial f_\sigma}{\partial t}(\mathbf{v}_\sigma)|_c \quad (4.44)$$

where Eq. (4.42) is used to evaluate the RHS.

Now we consider some specializations that reduce Eq. (4.42) to a simpler form. For electrons scattering by ions or for hot ions scattering by cool ions, $|\mathbf{v}_1| \gg |\mathbf{v}_2|$. Approximating $|\mathbf{v}_1 - \mathbf{v}_2| \simeq |\mathbf{v}_1|$, Eq. (4.40) and Eq. (4.41) become

$$h_2(\mathbf{v}_1) \simeq \frac{m_1 + m_2}{m_2} \int \frac{f_2(\mathbf{v}_2)}{|\mathbf{v}_1|} d\mathbf{v}_2 = \frac{m_1 + m_2}{m_2} \frac{1}{|\mathbf{v}_1|} \quad (4.45)$$

and

$$g_2(\mathbf{v}_1) \simeq \int f_2(\mathbf{v}_2) |\mathbf{v}_1| d\mathbf{v}_2 = |\mathbf{v}_1| \quad (4.46)$$

so that

$$\frac{\partial h_2}{\partial v_{\xi 1}} = -\frac{m_1 + m_2}{m_2} \frac{v_{\xi 1}}{|\mathbf{v}_1|^3} \quad (4.47)$$

and

$$\frac{\partial^2 g_2}{\partial v_{\xi 1} \partial v_{\gamma 1}} = \int f_2(\mathbf{v}_2) \left(\frac{\delta_{\xi \gamma}}{|\mathbf{v}_1|} - \frac{v_{\xi 1} v_{\gamma 1}}{|\mathbf{v}_1|^3} \right) d\mathbf{v}_2 = \left(\frac{\delta_{\xi \gamma}}{|\mathbf{v}_1|} - \frac{v_{\xi 1} v_{\gamma 1}}{|\mathbf{v}_1|^3} \right) \quad (4.48)$$

Making use of the identities

$$|\mathbf{v}_1| = \left[\sum_{\xi=1}^3 v_\xi^2 \right]^{\frac{1}{2}}, \quad \frac{\partial v_\gamma}{\partial v_\xi} = \delta_{\gamma \xi}, \quad \sum_{\xi=1}^3 \frac{\partial v_\xi}{\partial v_\xi} = 3 \quad (4.49)$$

Eq. (4.42) becomes, for $|\mathbf{v}_1| \gg |\mathbf{v}_2|$,

$$\frac{\partial f_1}{\partial t} \Big|_c = \sum_i \Gamma_{1i} \sum_{\xi=1}^3 \frac{\partial}{\partial v_{\xi 1}} \left[\frac{m_1}{m_i} \frac{v_{\xi 1}}{|\mathbf{v}_1|^3} f_1(\mathbf{v}_1) + \frac{1}{2} \sum_{\gamma=1}^3 \left(\frac{\delta_{\xi \gamma}}{|\mathbf{v}_1|} - \frac{v_{\xi 1} v_{\gamma 1}}{|\mathbf{v}_1|^3} \right) \frac{\partial f_1(\mathbf{v}_1)}{\partial v_{\gamma 1}} \right] \quad (4.50)$$

For certain cases (e.g., electron scattering by ions), $m_1 \ll m_2$. In this limit, the first term in Eq. (4.50) is negligible. The resulting equation describes the scattering by cold, infinite-mass particles and is known as the Lorentz model. In this model there is no energy transfer because of the infinite-mass approximation, and the effect of scattering is to alter the directional distribution of particle velocities.

The Lorentz model is useful for illustrating the tendency of scattering to produce an isotropic velocity distribution. For the scattering of particles of type 1 by particles of type 2, the Lorentz model is

$$\frac{\partial f_1}{\partial t} \Big|_c = \frac{1}{2} \Gamma_{12} \sum_{\xi=1}^3 \frac{\partial}{\partial v_{\xi 1}} \left[\sum_{\gamma=1}^3 \left(\frac{\delta_{\xi \gamma}}{|v_1|} - \frac{v_{\xi 1} v_{\gamma 1}}{|v_1|^3} \right) \frac{\partial f_1(v_1)}{\partial v_{\gamma 1}} \right] \quad (4.51)$$

Scattering will alter the particle velocity distribution until the RHS vanishes. It is easy to demonstrate that the RHS vanishes for an isotropic velocity distribution. An isotropic distribution is a function of only $|v_1|^2$; that is, $f_1 = f_1(|v_1|^2)$. For such a distribution

$$\frac{\partial f_1}{\partial v_{\gamma 1}} = 2v_{\gamma 1} \frac{\partial f_1}{\partial v_1^2}$$

which is sufficient to cause the RHS of Eq. (4.51) to vanish.

Next we consider an improvement to the above model which accounts for the thermal motion of the scattering centers. Instead of $|v_1 - v_2| \simeq |v_1|$, which was used in deriving Eq. (4.50), we expand

$$|v_1 - v_2| = |v_1| \left(1 - 2 \frac{v_1 \cdot v_2}{v_1^2} + \frac{v_2^2}{v_1^2} \right)^{\frac{1}{2}}$$

under the assumption $|v_1| \gg |v_2|$ and retain first order terms in $|v_2|$. The resulting Fokker–Planck equation is

$$\begin{aligned} \frac{\partial f_1}{\partial t} \Big|_c &= \sum_i \Gamma_{1i} \left\{ \sum_{\xi=1}^3 \frac{\partial}{\partial v_{\xi 1}} \left[\frac{m_i}{m_i} \frac{v_{\xi 1}}{|v_1|^3} f_1(v_1) \right. \right. \\ &\quad + \frac{1}{2} \sum_{\gamma=1}^3 \left(\frac{\delta_{\xi \gamma}}{|v_1|} - \frac{v_{\xi 1} v_{\gamma 1}}{|v_1|^3} \right) \frac{\partial f_1(v_1)}{\partial v_{\gamma 1}} \\ &\quad \left. \left. + \frac{1}{2} \sum_{\gamma=1}^3 \left(\frac{3v_{\xi 1} v_{\gamma 1} T_i}{m_i |v_1|^5} - \frac{\delta_{\xi \gamma} T_i}{m_i |v_1|^3} \right) \frac{\partial f_1(v_1)}{\partial v_{\gamma 1}} \right] \right\} \end{aligned} \quad (4.52)$$

This equation differs from Eq. (4.50) by the last term, which accounts for the nonzero velocity of the target (type i) particles. The “temperature” in Eq. (4.52) is defined

$$\frac{3}{2} T_i \equiv \int f_i(v_i) \left(\frac{m_i v_i^2}{2} \right) d v_i \quad (4.53)$$

The first term in Eq. (4.52) is a drag term, which vanishes in the Lorentz model limit, $m_1 \gg m_2$. The second term represents velocity-space diffusion and vanishes for an isotropic distribution. The third term also represents diffusion in velocity-space and specifically accounts for the thermal motion of the scattering particles.

As an illustration, we will solve Eq. (4.52) for the case of energetic ions slowing down in a cooler, single-species plasma. An isotropic source of energetic ions of strength S_0 and speed v_1^0 is postulated. Because we are treating the relaxation in speed of an isotropic distribution, the second term can be dropped and the previously mentioned properties of an isotropic distribution can be used to simplify the other terms in Eq. (4.52), so that we obtain

$$\frac{\partial f_1}{\partial t} \Big|_c = \Gamma_{12} \sum_{\xi=1}^3 \frac{\partial}{\partial v_{\xi 1}} \left\{ \frac{v_{\xi 1}}{|\mathbf{v}_1|^3} \left[\frac{m_1}{m_2} f_1(\mathbf{v}_1) + \frac{2T_2}{m_2} \frac{\partial f_1(\mathbf{v}_1)}{\partial v_1^2} \right] \right\} + \frac{S_0 \delta(v_1 - v_1^0)}{v_1^2} \quad (4.54)$$

This equation is solved most conveniently by transforming to spherical coordinates in velocity space, because there is no directional (angular) dependence. The first term in Eq. (4.54) has the form of a divergence

$$\sum_{\xi=1}^3 \frac{\partial}{\partial v_{\xi 1}} [v_{\xi 1} H(\mathbf{v}_1)] = \nabla_{v_1} \cdot [\mathbf{v}_1 H(\mathbf{v}_1)] \Rightarrow \frac{1}{v_1^2} \frac{\partial}{\partial v_1} [v_1^3 H(\mathbf{v}_1)]$$

where we indicate how such a term transforms. The transformed equation is

$$\frac{\partial f_1}{\partial t} \Big|_c = \frac{\Gamma_{12}}{v_1^2} \frac{\partial}{\partial v_1} \left[\frac{m_1}{m_2} f_1(v_1^2) + \frac{2T_2}{m_2} \frac{\partial f_1(v_1^2)}{\partial v_1^2} \right] + \frac{S_0 \delta(v_1 - v_1^0)}{v_1^2} \quad (4.55)$$

The asymptotic form of the distribution function must satisfy Eq. (4.55) with the LHS equal to zero, which leads to an equation for the asymptotic distribution function

$$0 = \Gamma_{12} \left[\frac{m_1}{m_2} f_1(v_1^2) + \frac{2T_2}{m_2} \frac{\partial f_1(v_1^2)}{\partial v_1^2} \right] + \begin{cases} 0 & \text{for } v_1 > v_1^0 \\ S_0 & \text{for } v_1 < v_1^0 \end{cases} \quad (4.56)$$

This equation can be integrated to obtain the asymptotic distribution functions. (Physically unreasonable solutions that arise because we have not included a sink for particles after they slow down must be discarded.)

$$f_1(v_1^2) = \begin{cases} \frac{S_0 m_2}{\Gamma_{12} m_1} \left[1 - \exp \left(-\frac{m_2 v_1^2}{2T_2} \right) \right] & v_1 < v_1^0 \\ \frac{S_0 m_2}{\Gamma_{12} m_1} \left[1 - \exp \left(-\frac{m_2 (v_1^0)^2}{2T_2} \right) \right] \exp \left\{ -\frac{m_2 [v_1^2 - (v_1^0)^2]}{2T_2} \right\} & v_1 > v_1^0 \end{cases} \quad (4.57)$$

This solution is sketched in Fig. 4.3. Note the existence of some ions with energies greater than the source energy; these arise because of energy transfer from the cooler plasma ions. The distribution function is relatively flat for $v_1 < v_1^0$ if

$$\frac{m_2 v_1^2}{2T} \equiv \frac{v_1^2}{v_2^2} \gg 1$$

which is an assumption of the model.

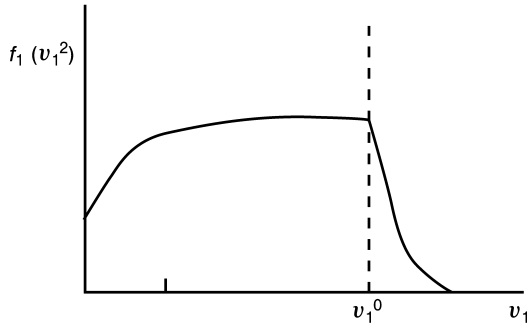


Figure 4.3. Energetic ion distribution function

4.4 Plasma Resistivity

As an application of the use of the Fokker–Planck equation, an exact expression for the plasma resistivity can be derived in the Lorentz-gas approximation.

The electron distribution is approximately Maxwellian

$$f_{e0} = n_e \left(\frac{m_e}{2\pi T_e} \right)^{\frac{3}{2}} \exp \left(-\frac{m_e v^2}{2T_e} \right) = f_e^m \quad (4.58)$$

We let this equilibrium be slightly perturbed by the application of the small electric field in the z -direction. The electric field will cause electrons to accelerate at a rate $-eE/m$, and so the velocity distribution function at time t can be expressed in terms of the distribution function at a slightly earlier time, $t - \Delta t$, by

$$f_e(\mathbf{v}, t) = f_e(\mathbf{v} + eE \Delta t / m, \quad t - \Delta t) \quad (4.59)$$

For small Δt , the distribution function can be expanded

$$f_e(\mathbf{v}, t) - f_e(\mathbf{v}, t - \Delta t) = \frac{eE}{m} \cdot \frac{\partial f_e}{\partial \mathbf{v}} \Delta t$$

which leads to

$$\left(\frac{\partial f_e}{\partial t} \right)_E = \frac{eE}{m} \cdot \frac{\partial f_{e0}}{\partial \mathbf{v}} \quad (4.60)$$

Here, the subscript E indicates a rate of change of f_e due to the effect of the E -field alone. It has also been assumed that the electric field E gives rise to only a small perturbation of the velocity distribution, so that $f_e \approx f_{e0}$ may be substituted in the term containing E .

When the electrons reach a steady-state in which the accelerating force of the electric field is balanced by the collisional drag from the ions, the following balance obtains

$$0 = \frac{\partial f_e}{\partial t} = \left(\frac{\partial f_e}{\partial t} \right)_E + \left(\frac{\partial f_e}{\partial t} \right)_c \quad (4.61)$$

i.e.

$$-\frac{e\mathbf{E}}{m} \cdot \frac{\partial f_{e0}}{\partial \mathbf{v}} = \left(\frac{\partial f_e}{\partial t} \right)_c \quad (4.62)$$

This equation must be solved for the non-Maxwellian part of f_e , which we will denote f_{e1} . Choosing some convenient direction for z , and writing $v_z = v \cos \theta$, $v_x = v \sin \theta \cos \phi$ and $v_y = v \sin \theta \sin \phi$, the standard expressions for the gradient and divergence operators in spherical coordinates can be used to transform the Fokker–Planck equation in the Lorentz approximation to the form

$$\left(\frac{\partial f_e}{\partial t} \right)_c = \frac{n_i z^2 e^4 \ln \Lambda}{8\pi \epsilon_0^2 m^2 v^3} \left[\frac{1}{\sin \theta} \frac{\partial}{\partial \theta} \left(\sin \theta \frac{\partial f_e}{\partial \theta} \right) + \frac{1}{\sin^2 \theta} \frac{\partial^2 f_e}{\partial \phi^2} \right] \quad (4.63)$$

This expression contains only the non-Maxwellian part of the distribution function, f_{e1} , since we know that collisions can have no effect on a Maxwellian f_{e0} . For the present calculation, which uses the Lorentz-gas form of the Fokker–Planck expression, the isotropic property of the Maxwellian distribution is all that is needed to establish that only f_{e1} , and not f_{e0} , enters into the Fokker–Planck expression.

The distribution f_{e1} will be symmetric with respect to the azimuthal angle about the z velocity direction (i.e. there can be no dependence on ϕ), since \mathbf{E} is in the z -direction and the equation itself is symmetric in ϕ . Substituting the Maxwellian for f_{e0} , the equation to be solved is

$$\frac{eEv f_{e0}}{T_e} \cos \theta = \frac{n_i z^2 e^4 \ln \Lambda}{8\pi \epsilon_0^2 m^2 v^3} \frac{1}{\sin \theta} \frac{\partial}{\partial \theta} \left(\sin \theta \frac{\partial f_{e1}}{\partial \theta} \right) \quad (4.64)$$

which has the solution

$$f_{e1} = -\frac{4\pi \epsilon_0^2 m^2 E v^4 f_{e0} \cos \theta}{n_i z^2 e^3 T_e \ln \Lambda} \quad (4.65)$$

The total electron distribution function obtained by adding the θ -independent Maxwellian distribution f_{e0} to the θ -dependent perturbation f_{e1} is a slightly asymmetric (in θ) distribution in which there are more electrons with $\pi > \theta > \frac{\pi}{2}$ than with $\frac{\pi}{2} > \theta > 0$. In terms of Cartesian coordinates, there are slightly more electrons with $v_z < 0$ than with $v_z > 0$. This is what would be expected for an electric field in the z -direction, which accelerates negatively charged electrons in the negative z -direction.

The current density in the z -direction is

$$\begin{aligned} j_z &= -e \int f_{e1} v \cos \theta d^3 v \\ &= \frac{8\pi^2 \epsilon_0^2 m^2 E}{n_i z^2 e^2 T_e \ln \Lambda} \int_0^\infty v^7 f_{e0} dv \int_0^\pi \cos^2 \theta \sin \theta d\theta \\ &= \frac{32\pi^{\frac{1}{2}} \epsilon_0^2 E (2T_e)^{\frac{3}{2}}}{m^{\frac{1}{2}} z e^2 \ln \Lambda} \end{aligned} \quad (4.66)$$

where $d^3v = 2\pi v^2 \sin \theta d\theta dv$ and charge neutrality, $n_e = Zn_i$, have been used. The integrals in Eq. (4.66) are straightforward to carry out: the integral over θ is done by writing $\sin \theta d\theta = -d(\cos \theta)$; the integral over v is done by first writing $v^7 dv = v^6 dv^2/2$, then noting that $f_{e0} \sim \exp(-v^2/2v_{th}^2)$ so that the integral over $v^2/2$ can be done by repeated integrations by parts. Thus, the plasma resistivity in the Lorentz-gas approximation is obtained.

$$\eta = \frac{m^{\frac{1}{2}}ze^2 \ln \Lambda}{32\pi^{\frac{1}{2}}\epsilon_0^2(2T_e)^{\frac{3}{2}}} \quad (4.67)$$

To obtain the actual resistivity, electron-electron collisions must be included, and this calculation can only be done numerically. The resulting resistivity for a hydrogen plasma is about 1.7 times larger than the Lorentz-gas resistivity given by Eq. (4.67).

4.5 Coulomb Collisional Energy Transfer

A very important consequence of collisions among plasma particles is the transfer of energy. We first consider the limiting case of energetic electrons scattering by collisions with cold ions ($T_e \gg T_i$), then extend the development to include thermal motion of the ions.

When a light particle of mass m and initial velocity v_0 collides with a heavy particle of mass M initially at rest, the maximum energy and momentum transfer to the heavy particle occur for 180° scattering (i.e. a “head-on” collision). For this case of exactly 180° scattering, the conservation of momentum and energy gives

$$mv_0 + mv_1 = MV \quad (4.68)$$

$$\frac{1}{2}mv_0^2 - \frac{1}{2}mv_1^2 = \frac{1}{2}MV^2 \quad (4.69)$$

where v_1 (backward) and V (forward) are the final velocities of the light and heavy particle, respectively. Combining these two equations yields $v_1 \approx v_0$ and

$$\frac{1}{2}MV^2 \approx \left(\frac{4m}{M}\right) \frac{mv_0^2}{2} \quad (4.70)$$

thus, only a fraction $\sim 4m/M$ of the energy of the light particle is transferred to the heavy particle.

The change Δv in the velocity of an electron as a result of a Coulomb collision with an ion initially at rest can be related by momentum conservation to the velocity ΔV acquired by the ion:

$$m\Delta v = -M\Delta V \quad (4.71)$$

The ions gains momentum, $M\Delta V$, at the expense of a corresponding loss of the impinging electrons's momentum, $m\Delta v$, resulting from the deflection of the electron away from its initial trajectory. However, averaged over many such isotropically disturbed electrons, each

of them deflected in a different direction, there can be no net gain in ion momentum. If the ions are all initially at rest, however, each collision also results in a small gain in the ion energy. These increases in ion energy will accumulate, i.e. each colliding electron will contribute something, and the contributions from different electrons will not cancel out, as they do in the case of the (vector) momentum. From Eq. (4.71), the increase in ion energy occurring in a single collision is given by

$$\frac{1}{2}M|\Delta\mathbf{V}|^2 = \frac{m^2}{2M}|\Delta\mathbf{v}|^2 \quad (4.72)$$

The change $\Delta\mathbf{v}$ in the velocity of the electron is mainly in a direction perpendicular to its initial velocity vector, and the magnitude of this velocity change is denoted Δv_y . The contribution from the change in electron velocity in the direction of motion, Δv_x , is smaller, since $v\Delta v_x \sim (\Delta v_y)^2$. Accordingly, the electron energy transferred to the ion in this particular collision is $(m^2/2M)(\Delta v_y)^2$.

Now consider the case where there are many electrons colliding with many ions, as in a plasma. We allow the electron and ion densities, n_e and n_i , respectively, to be unequal, as they must be, for example, in a plasma with $Z \neq 1$. An average electron with velocity \mathbf{v} is deflected by its many encounters with ions according to

$$\frac{d\langle(\Delta v_y)^2\rangle}{dt} = \frac{n_i z^2 e^4 \ln \Lambda}{2\pi\epsilon_0^2 m^2 v} \quad (4.73)$$

Integrating over a Maxwellian distribution of electrons (see Eq. (4.58)), we obtain the total rate of energy loss from the electrons by collisional transfer to ions, namely

$$\frac{dW_e}{dt} = -\frac{m^2}{2M} \int \frac{d\langle(\Delta v_y)^2\rangle}{dt} f_{eo}(v) d^3v \quad (4.74)$$

where $W_e = \frac{3}{2}n_e T_e$ is the energy density in electrons. In each collision, the energy is transferred to a single ion, but this energy must then be shared among the entire population of ions, which are also assumed to be Maxwellian. The increase of the energy density in the ions, $W_i = \frac{3}{2}n_i T_i$, must balance the energy loss from the electrons, i.e.

$$\frac{dW_i}{dt} = -\frac{dW_e}{dt} \quad (4.75)$$

Since only the average energies, and therefore the temperatures T_i and T_e , are changed by elastic Coulomb collisions, we obtain an expression for the rate of increase of ion temperature:

$$\frac{dT_i}{dt} = \frac{m^2}{3Mn_i} \int \frac{d\langle(\Delta v_y)^2\rangle}{dt} f_{eo}(v) d^3v \quad (4.76)$$

$$= \frac{z^2 e^4 \ln \Lambda}{6\pi\epsilon_0^2 M} \int \frac{f_{eo}(v)}{v} d^3v \quad (4.77)$$

For a Maxwellian f_{eo} the integral in Eq. (4.77) is straightforward to evaluate

$$\int \frac{f_{eo}(v)}{v} d^3v = \left(\frac{2}{\pi}\right)^{\frac{1}{2}} \frac{n_e m^{1/2}}{T_e^{1/2}} \quad (4.78)$$

giving the result

$$\frac{dT_i}{dt} = \frac{T_e}{\tau_{eq}} \quad (4.79)$$

where

$$\tau_{eq}^{-1} = \frac{n_e z^2 e^4 m^{1/2} \ln \Lambda}{3\pi(2\pi)^{1/2} \epsilon_0^2 M T_e^{3/2}} \quad (4.80)$$

Comparing this “temperature equilibration rate” to the average electron–ion collision frequency defined earlier, we see that

$$\tau_{eq}^{-1} \approx 2 \frac{m}{M} \langle v_{ei} \rangle \quad (4.81)$$

Next, we use the Fokker–Planck equation to calculate the rate at which energy is transferred from a population of energetic ions to a background plasma or the rate at which energy is transferred among the various ion species and electrons in a plasma. We will consider a background plasma of ions and electrons with Maxwellian velocity distributions f_i^M and f_e^M , where the Maxwellian distribution is given by Eq. (4.58). Rather than attempt to solve the Fokker–Planck equation for the time evolution of the distribution function, we will take the first velocity moment to obtain an equation for the quantity

$$U_1 \equiv \int f_i(v_1) v_1 dv_1 \quad (4.82)$$

which is related to the total energy of the particles of type 1. The resulting equation for energetic ions of species 1 slowing down in a background ion–electron plasma is

$$\begin{aligned} \frac{\partial U_1}{\partial t} &= \Gamma_{1e} \frac{\partial}{\partial U_1} \left[\frac{1}{U_1} \Phi \left(U_1 \sqrt{\frac{m_e}{2T_e}} \right) \left(1 + \frac{m_1}{m_e} \right) \right] \\ &\quad + \Gamma_{1i} \frac{\partial}{\partial U_1} \left[\frac{1}{U_1} \Phi \left(U_1 \sqrt{\frac{m_i}{2T_i}} \right) \left(1 + \frac{m_1}{m_i} \right) \right] \end{aligned} \quad (4.83)$$

where the Γ are given by Eq. (4.43) and

$$\Phi(x) \equiv \frac{2}{\sqrt{\pi}} \int_0^x e^{-y^2} dy \quad (4.84)$$

is the error function. The two terms in Eq. (4.83) represent energy transfer from the energetic ions to the background plasma electrons and ions, respectively.

Characteristic energy transfer times, in which the energetic ion will give up a large part of its energy, can be defined from

$$\tau_E^{-1} \equiv -\frac{1}{U_1} \frac{\partial U_1}{\partial t} \quad (4.85)$$

When $U_1 > (T_e/m_e)^{\frac{1}{2}} \gg (T_i/m_i)^{\frac{1}{2}}$

$$\tau_E \simeq \frac{4\pi\epsilon_0^2 m_1^2 U_1^3}{n_e (e_1 e_e)^2 \left(2 + \frac{m_1}{m_e}\right) \ln \Lambda} \quad (4.86)$$

In this limit, the energy transfer is mainly to the electrons and is insensitive to the plasma temperature. When $(T_e/m_e)^{\frac{1}{2}} > U_1 > (T_i/m_i)^{\frac{1}{2}}$,

$$\tau_E \simeq \frac{4\pi\epsilon_0^2 m_1^2}{n_e (e_1 e_e)^2 \left[\frac{z}{U_1^3} \left(1 + \frac{m_1}{m_i}\right) + \frac{4}{3\sqrt{\pi}} \left(1 + \frac{m_1}{m_e}\right) \left(\frac{m_e}{2T_e}\right)^{3/2} \right] \ln \Lambda} \quad (4.87)$$

When $(T_e/m_e)^{\frac{1}{2}} \gg (T_i/m_i)^{\frac{1}{2}} > U_1$,

$$\tau_E \simeq \frac{3(\pi)^{3/2} m_1^2}{n_e (e_1 e_e)^2 \left[\left(1 + \frac{m_1}{m_e}\right) \left(\frac{m_e}{2T_e}\right)^{3/2} + z \left(1 + \frac{m_1}{m_i}\right) \left(\frac{m_i}{2T_i}\right)^{3/2} \right] \ln \Lambda} \quad (4.88)$$

In this latter limit, the energy exchange time increases with the plasma temperature. The slowing down is mainly due to collisions with plasma ions, unless $T_i/T_e > (m_i/m_e)^{\frac{1}{3}}$. In the above $|e_i| = z|e_e|$.

As an illustration, we consider energetic deuterons slowing down in a deuterium plasma of density $n = 10^{20} \text{ m}^{-3}$ and temperature $T = 1 \text{ keV}$. The differential rate of energy transfer between the energetic deuteron and the plasma deuterons is shown in Fig. 4.4.

Now consider an ion-electron plasma with both species in Maxwellian distributions, but at different temperatures. The energy transfer between the ions and the electron distribution can be calculated by considering the ion as the test particle and retaining only the first term in Eq. (4.83)

$$\frac{\partial U_i}{\partial t} = \Gamma_{ie} \frac{\partial}{\partial U_i} \left[\frac{1}{U_i} \Phi \left(U_i \sqrt{\frac{m_e}{2T_e}} \right) \left(1 + \frac{m_i}{m_e}\right) \right] \quad (4.89)$$

An approximation to this equation that displays the physical sense of the result more transparently is

$$\frac{\partial U_i}{\partial t} = \frac{n_e (e_i e_e)^2 m_e \ln \Lambda \left(1 - \frac{2U_i}{3T_e}\right)}{2\pi\epsilon_0^2 (2\pi m_e T_e)^{\frac{1}{2}} m_i \left[1 + \frac{4\sqrt{\pi}}{3} \left(\frac{m_e U_i}{m_i T_e}\right)^{3/2}\right]} \quad (4.90)$$

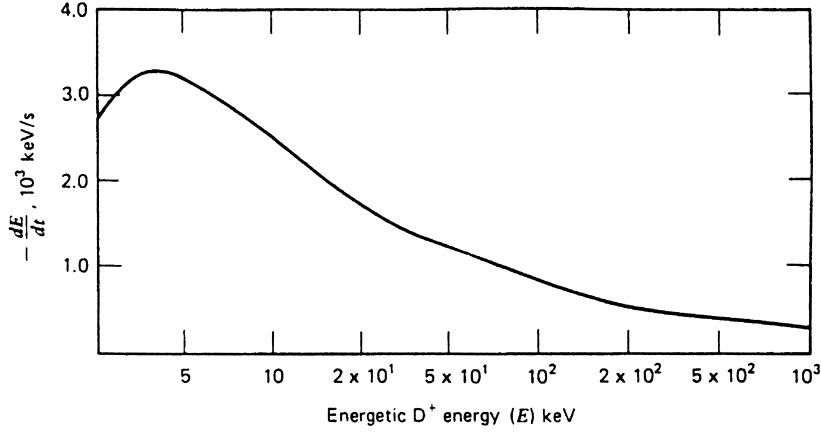


Figure 4.4. Differential energy transfer: Energetic deuterons on plasma deuterons ($n = 10^{20} \text{ m}^{-3}$, $T = 1 \text{ keV}$)

Noting that $U_i = \frac{3}{2} T_i$, we see that Eq. (4.90) is of the form

$$\frac{dT_i}{dt} = \text{const} \frac{(T_e - T_i)}{T_e^{\frac{3}{2}}} \quad (4.91)$$

which displays the plausible characteristic of energy transfer from the hotter to the colder species, that is, from electrons to ions when $T_e > T_i$, and from ions to electrons when $T_e < T_i$.

4.6 Krook Collision Operators

The Fokker–Planck collision operator, the RHS of Eq. (4.42), is rather complex. A number of simpler collision operators have been developed in order to have a more computationally tractable means of representing collisions in the Boltzmann or drift-kinetic equations. We will consider four collision operators that retain, to an increasing extent, the properties of the Fokker–Planck operator.

The first model is

$$\left. \frac{\partial f_1}{\partial t} \right|_c = -v_{12} \left[f_1(\mathbf{v}_1) - f_1^M(v_1^2) n_1^0 \right] \quad (4.92)$$

where $v_{12} = (\tau_{90}^{12})^{-1}$ is the 90° scattering frequency and n_1 and n_1^0 are the instantaneous and average, respectively, particle densities. (Note that the Maxwellian distribution function of Eq. (4.58) is normalized so that $\int f_1^M d^3 v = 1$, while $\int f_1 d^3 v = n_1$.) This model expresses the tendency of a distribution to relax towards a Maxwellian in a characteristic time v_{12}^{-1} , but does not conserve (relative to the Fokker–Planck operator) particle density, momentum, or energy.

A second model is

$$\frac{\partial f_1}{\partial t} \Big|_c = -v_{12} \left[f_1(\mathbf{v}_1) - n_1 f_1^M(v_1^2) \right] \quad (4.93)$$

This model conserves particle density, but not momentum or energy, in addition to the properties of the first model.

A third model, which conserves particle density and momentum, is

$$\frac{\partial f_1}{\partial t} \Big|_c = -v_{12} \left[f_1(\mathbf{v}_1) - n_1 f_1^M(v_1^2) \left(1 + \frac{\langle \mathbf{v}_1 \rangle \cdot \mathbf{v}_1 m_1}{T_1} \right) \right] \quad (4.94)$$

where

$$\langle \mathbf{v}_1 \rangle \equiv \int \frac{f_1(\mathbf{v}_1) \mathbf{v}_1 d\mathbf{v}_1}{n_1} \quad (4.95)$$

Finally, a fourth model, which conserves particle density, momentum, and energy is

$$\frac{\partial f_1}{\partial t} \Big|_c = -v_{12} \left[f_1(\mathbf{v}_1) - n_1 f_1^M(\mathbf{v}_1 - \langle \mathbf{v}_1 \rangle) \right] \quad (4.96)$$

Each of these models is useful for studying a certain class of problems. Their great virtue lies in their relative simplicity.

Problems for Chapter 4

1. Derive Eq. (4.19) and Eq. (4.20) for the radial and poloidal components of the drift velocity.
2. Derive Eq. (4.35) and Eq. (4.36) for the second moments in the Fokker–Planck collision operator.
3. Derive Eq. (4.50) from Eq. (4.42).
4. Prove that $\frac{\partial f}{\partial t} \Big|_c = 0$ for an isotropic distribution function, for the Lorentz model.
5. Calculate the ion–electron temperature equilibration rate for a deuterium plasma with $T = 5 \text{ keV}$, $n_D = n_e = 5 \times 10^{19} \text{ m}^{-3}$.
6. Derive an expression for the collisional friction momentum exchange rate, $m_1 \int \mathbf{v}_1 \frac{\partial f}{\partial t} \Big|_c d\mathbf{v}_1$, using the first Krook collision operator.

5 Fluid Theory

The properties of a plasma can be completely determined by solving the Boltzmann equation

$$\frac{\partial f_\sigma}{\partial t} + \mathbf{v} \cdot \nabla f_\sigma + \frac{e_\sigma}{m_\sigma} (\mathbf{E} + \mathbf{v} \times \mathbf{B}) \cdot \nabla_{\mathbf{v}} f_\sigma \equiv C_\sigma + S_\sigma \quad (5.1)$$

for each species and then computing the appropriate quantities from the distribution function. Such a procedure is not practical, except in rare cases.

Fortunately, a knowledge of the macroscopic, or average, properties suffices to describe many plasma phenomena. A number of important macroscopic quantities can be defined as averages over the distribution function of the form

$$(A)_\sigma \equiv \int f_\sigma(\mathbf{v}) A(\mathbf{v}) d^3 v \quad (5.2)$$

In particular, the particle density of species σ is

$$n_\sigma = \int f_\sigma(\mathbf{v}) d^3 v \quad (5.3)$$

and the average velocity associated with species σ is

$$\mathbf{v}_\sigma = \int f_\sigma(\mathbf{v}) \mathbf{v} d^3 v / n_\sigma \quad (5.4)$$

By taking appropriate velocity moments of Eq. (5.1), equations are obtained which can be solved directly for the macroscopic quantities, thus considerably simplifying the computational task. We develop such equations in this chapter and use them in our study of fusion plasmas in subsequent chapters.

5.1 Moments Equations

The first four moment equations are obtained by multiplying Eq. (5.1) by $z_n(\mathbf{v})$ and integrating over velocity, where

$$\begin{aligned} z_0 &= 1 \\ z_1 &= m\mathbf{v} \\ z_2 &= \frac{1}{2}m(\mathbf{v} \cdot \mathbf{v}) \\ z_3 &= \frac{1}{2}m(\mathbf{v} \cdot \mathbf{v})\mathbf{v} \end{aligned} \quad (5.5)$$

The resulting equations are:

$n = 0$ (**Continuity**)

$$\frac{\partial n_\sigma}{\partial t} + \nabla \cdot n_\sigma \mathbf{v}_\sigma = \mathbf{S}_\sigma^0 \quad (5.6)$$

$n = 1$ (**Momentum Balance**)

$$m_\sigma \frac{\partial (n_\sigma \mathbf{v}_\sigma)}{\partial t} + \nabla \cdot \mathbf{M}_\sigma - n_\sigma e_\sigma (\mathbf{E} + \mathbf{v}_\sigma \times \mathbf{B}) = \mathbf{R}_\sigma^1 + \mathbf{S}_\sigma^1 \quad (5.7)$$

$n = 2$ (**Energy Balance**)

$$\frac{1}{2} \frac{\partial}{\partial t} (Tr \mathbf{M}_\sigma) + \nabla \cdot \mathbf{Q}_\sigma = n_\sigma e_\sigma \mathbf{v}_\sigma \cdot \mathbf{E} + \mathbf{R}_\sigma^2 + \mathbf{S}_\sigma^2 \quad (5.8)$$

and

$n = 3$ (**Energy Flux**)

$$\frac{\partial \mathbf{Q}_\sigma}{\partial t} + \nabla \cdot \boldsymbol{\theta}_\sigma - \frac{1}{2} \frac{e_\sigma}{m_\sigma} (Tr \mathbf{M}_\sigma) \mathbf{E} - \frac{e_\sigma}{m_\sigma} \mathbf{M}_\sigma \cdot \mathbf{E} - \frac{e_\sigma}{m_\sigma} \mathbf{Q}_\sigma \times \mathbf{B} = \mathbf{R}_\sigma^3 + \mathbf{S}_\sigma^3 \quad (5.9)$$

In Eqs. (5.6) to (5.9) we have defined:

$$\mathbf{M}_\sigma \equiv n_\sigma m_\sigma (\mathbf{v} \mathbf{v})_\sigma \quad \text{momentum stress tensor} \quad (5.10)$$

$$Tr \mathbf{M}_\sigma \equiv n_\sigma m_\sigma (\mathbf{v} \cdot \mathbf{v})_\sigma \quad \text{scalar trace of } \mathbf{M}_\sigma \quad (5.11)$$

$$\mathbf{Q}_\sigma \equiv \frac{1}{2} n_\sigma m_\sigma [(\mathbf{v} \cdot \mathbf{v}) \mathbf{v}]_\sigma \quad \text{energy flow} \quad (5.12)$$

$$\boldsymbol{\theta}_\sigma \equiv \frac{1}{2} n_\sigma m_\sigma [(\mathbf{v} \cdot \mathbf{v}) \mathbf{v} \mathbf{v}]_\sigma \quad \text{energy flux tensor} \quad (5.13)$$

$$\mathbf{R}_\sigma^n \equiv \int C_\sigma z_n(\mathbf{v}) d^3 v \quad \text{collisional friction} \quad (5.14)$$

and

$$\mathbf{S}_\sigma^n \equiv \int S_\sigma z_n(\mathbf{v}) d^3 v \quad \text{source moment} \quad (5.15)$$

The quantity $(y)_\sigma \equiv \int y f_\sigma d^3 v$

The velocity, \mathbf{v} , of a particle of species σ can be decomposed into the average velocity of all particles of species σ , \mathbf{v}_σ , and the random velocity about the average, \mathbf{W} , which latter is associated with “thermal” motion:

$$\mathbf{v} = \mathbf{v}_\sigma + \mathbf{W} \quad (5.16)$$

It follows that

$$\mathbf{W}_\sigma \equiv \int f_\sigma(\mathbf{v}) \mathbf{W} d^3 v = 0 \quad (5.17)$$

The velocity decomposition of Eq. (5.16) can be used to decompose the above terms into parts associated with the net flow of the plasma (\mathbf{v}_σ) and parts associated with the

random, internal motion of the particles (\mathbf{W}). The stress tensor can be written as

$$\mathbf{M}_\sigma = n_\sigma m_\sigma \mathbf{v}_\sigma \mathbf{v}_\sigma + \mathbf{P}_\sigma \quad (5.18)$$

where

$$\mathbf{P}_\sigma \equiv n_\sigma m_\sigma (\mathbf{W} \mathbf{W})_\sigma \quad (5.19)$$

is the pressure tensor, which can be further decomposed into a diagonal and a non-diagonal part

$$\mathbf{P}_\sigma = \frac{1}{3} (Tr \mathbf{P}_\sigma) \mathbf{I} + \pi_\sigma \equiv \frac{1}{3} n_\sigma m_\sigma (\mathbf{W} \cdot \mathbf{W})_\sigma \mathbf{I} + n_\sigma m_\sigma [(\mathbf{W} \mathbf{W})_\sigma - \frac{1}{3} (\mathbf{W} \cdot \mathbf{W})_\sigma \mathbf{I}] \quad (5.20a)$$

where \mathbf{I} is the unit dyadic. To ensure that the meaning is clear, we will write Eq. (5.20a) out in detail for an xyz coordinate system.

$$\begin{aligned} n_\sigma m_\sigma & \begin{bmatrix} (W_x W_x)_\sigma \hat{\mathbf{n}}_x \hat{\mathbf{n}}_x & (W_x W_y)_\sigma \hat{\mathbf{n}}_x \hat{\mathbf{n}}_y & (W_x W_z)_\sigma \hat{\mathbf{n}}_x \hat{\mathbf{n}}_z \\ (W_y W_x)_\sigma \hat{\mathbf{n}}_y \hat{\mathbf{n}}_x & (W_y W_y)_\sigma \hat{\mathbf{n}}_y \hat{\mathbf{n}}_y & (W_y W_z)_\sigma \hat{\mathbf{n}}_y \hat{\mathbf{n}}_z \\ (W_z W_x)_\sigma \hat{\mathbf{n}}_z \hat{\mathbf{n}}_x & (W_z W_y)_\sigma \hat{\mathbf{n}}_z \hat{\mathbf{n}}_y & (W_z W_z)_\sigma \hat{\mathbf{n}}_z \hat{\mathbf{n}}_z \end{bmatrix} \\ &= \frac{1}{3} n_\sigma m_\sigma (W^2)_\sigma \begin{bmatrix} \hat{\mathbf{n}}_x \hat{\mathbf{n}}_x & 0 & 0 \\ 0 & \hat{\mathbf{n}}_y \hat{\mathbf{n}}_y & 0 \\ 0 & 0 & \hat{\mathbf{n}}_z \hat{\mathbf{n}}_z \end{bmatrix} + n_\sigma m_\sigma \\ &\times \begin{bmatrix} [(W_x^2)_\sigma - \frac{1}{3} (W^2)_\sigma] \hat{\mathbf{n}}_x \hat{\mathbf{n}}_x & (W_x W_y)_\sigma \hat{\mathbf{n}}_x \hat{\mathbf{n}}_y & (W_x W_z)_\sigma \hat{\mathbf{n}}_x \hat{\mathbf{n}}_z \\ (W_y W_x)_\sigma \hat{\mathbf{n}}_y \hat{\mathbf{n}}_x & [(W_y^2)_\sigma - \frac{1}{3} (W^2)_\sigma] \hat{\mathbf{n}}_y \hat{\mathbf{n}}_y & (W_y W_z)_\sigma \hat{\mathbf{n}}_y \hat{\mathbf{n}}_z \\ (W_z W_x)_\sigma \hat{\mathbf{n}}_z \hat{\mathbf{n}}_x & (W_z W_y)_\sigma \hat{\mathbf{n}}_z \hat{\mathbf{n}}_y & [(W_z^2)_\sigma - \frac{1}{3} (W^2)_\sigma] \hat{\mathbf{n}}_z \hat{\mathbf{n}}_z \end{bmatrix} \end{aligned} \quad (5.20b)$$

where $(W^2)_\sigma \equiv (W_x^2)_\sigma + (W_y^2)_\sigma + (W_z^2)_\sigma$. It is informative to examine the term $\nabla \cdot \mathbf{P}$. Using Eq. (5.19)

$$\begin{aligned} \nabla \cdot \mathbf{P}_\sigma &= m_\sigma \sum_{\alpha, \beta} \frac{\partial}{\partial x_\sigma} [n_\sigma (W_\alpha W_\beta)_\sigma] \\ &= m_\sigma \sum_{\alpha=\beta} \frac{\partial}{\partial x_\sigma} [n_\sigma (W_\alpha^2)_\sigma] + m_\sigma \sum_{\alpha \neq \beta} \frac{\partial}{\partial x_\sigma} [n_\sigma (W_\alpha W_\beta)_\sigma] \end{aligned}$$

where α, β refer to the coordinate directions. If the distribution function is isotropic, then

$$(W_\alpha W_\beta)_\sigma \equiv \int W_\alpha W_\beta f(v_\alpha, v_\beta, v_\gamma) d^3 v = 0, \quad \alpha \neq \beta$$

Thus for an isotropic distribution function, for which the equipartition of energy requires

$$\begin{aligned} W_\alpha^2 &= W_\beta^2 = W_\gamma^2 = \frac{1}{3} W^2 \\ \nabla \cdot \mathbf{P}_\sigma &= \frac{2}{3} \sum_{\alpha} \frac{\partial}{\partial x_\alpha} \left[\frac{1}{2} m_\sigma n_\sigma (W^2)_\sigma \right] = \sum_{\alpha} \frac{\partial}{\partial x_\alpha} (n_\sigma T_\sigma) = \nabla p_\sigma \end{aligned}$$

where p_σ is the isotropic pressure for species σ . Thus we associate the pressure with $\frac{1}{3} (Tr \mathbf{P}_\sigma)$ in Eq. (5.20a) and interpret π_σ as the anisotropic shear. This interpretation is

useful even when the distribution is not isotropic, in which case π_σ will have nonvanishing diagonal elements as well as off-diagonal elements.

Similarly, the energy flow becomes

$$\mathbf{Q}_\sigma = \frac{1}{2} n_\sigma m_\sigma (\mathbf{v}_\sigma \cdot \mathbf{v}_\sigma) \mathbf{v}_\sigma + \mathbf{v}_\sigma \cdot \mathbf{P}_\sigma + \frac{1}{2} \mathbf{v}_\sigma (Tr P_\sigma) + \mathbf{q}_\sigma \quad (5.21a)$$

or

$$\mathbf{Q}_\sigma = \frac{1}{2} n_\sigma m_\sigma (\mathbf{v}_\sigma \cdot \mathbf{v}_\sigma) \mathbf{v}_\sigma + \frac{5}{2} p_\sigma \mathbf{v}_\sigma + \mathbf{v}_\sigma \cdot \pi_\sigma + \mathbf{q}_\sigma \quad (5.21b)$$

where

$$\mathbf{q}_\sigma \equiv \frac{1}{2} n_\sigma m_\sigma [(\mathbf{W} \cdot \mathbf{W}) \mathbf{W}]_\sigma \quad (5.22)$$

is the heat conduction.

Finally, the heat flux becomes

$$\begin{aligned} \mathbf{H}_\sigma &= \frac{1}{2} n_\sigma m_\sigma (\mathbf{v}_\sigma \cdot \mathbf{v}_\sigma) \mathbf{v}_\sigma \mathbf{v}_\sigma + \frac{1}{2} (\mathbf{v}_\sigma \cdot \mathbf{v}_\sigma) \mathbf{P}_\sigma + (\mathbf{v}_\sigma \cdot \mathbf{P}_\sigma) \mathbf{v}_\sigma + \mathbf{v}_\sigma (\mathbf{P}_\sigma \cdot \mathbf{v}_\sigma) \\ &\quad + \mathbf{v}_\sigma \cdot \mathbf{G}_\sigma + \frac{1}{2} (Tr P_\sigma) \mathbf{v}_\sigma \mathbf{v}_\sigma + \mathbf{q}_\sigma \mathbf{v}_\sigma + \mathbf{v}_\sigma \mathbf{q}_\sigma + \mathbf{H}_\sigma \end{aligned} \quad (5.23)$$

where

$$\mathbf{G}_\sigma \equiv n_\sigma m_\sigma (\mathbf{W} \mathbf{W} \mathbf{W})_\sigma \quad (5.24)$$

and

$$\mathbf{H}_\sigma \equiv \frac{1}{2} n_\sigma m_\sigma [(\mathbf{W} \cdot \mathbf{W}) \mathbf{W} \mathbf{W}]_\sigma \quad (5.25)$$

Equations (5.6) and (5.18) to (5.22) can be used to rewrite the momentum and energy equations (5.7) and (5.8), as

$$\begin{aligned} n_\sigma m_\sigma \frac{\partial \mathbf{v}_\sigma}{\partial t} + m_\sigma n_\sigma (\mathbf{v}_\sigma \cdot \nabla) \mathbf{v}_\sigma + \nabla p_\sigma + \nabla \cdot \pi_\sigma &= n_\sigma e_\sigma (\mathbf{E} + \mathbf{v}_\sigma \times \mathbf{B}) + \mathbf{R}_\sigma^1 \\ &\quad + \left(\mathbf{S}_\sigma^1 - m_\sigma \mathbf{v}_\sigma \mathbf{S}_\sigma^0 \right) \end{aligned} \quad (5.26)$$

and

$$\begin{aligned} \frac{3}{2} \frac{\partial p_\sigma}{\partial t} + (\mathbf{P}_\sigma \cdot \nabla) \cdot \mathbf{v}_\sigma + \frac{3}{2} \nabla \cdot (\mathbf{v}_\sigma p_\sigma) + \nabla \cdot \mathbf{q}_\sigma &= \mathbf{R}_\sigma^2 + \mathbf{S}_\sigma^2 - \mathbf{v}_\sigma \cdot (\mathbf{R}_\sigma^1 + \mathbf{S}_\sigma^1) \\ &\quad + \frac{1}{2} m_\sigma (\mathbf{v}_\sigma \cdot \mathbf{v}_\sigma) \mathbf{S}_\sigma^0 \end{aligned} \quad (5.27)$$

Finally, it is convenient for subsequent use to define a “temperature,” T_σ , which includes inertial and pressure contributions,

$$n_\sigma T_\sigma \equiv \frac{1}{3} Tr M_\sigma \quad (5.28)$$

and then subtract $\frac{5}{2}(T_\sigma/m_\sigma)$ times Eq. (5.7) from Eq. (5.9) and write the resulting equation as

$$\begin{aligned} \frac{\partial}{\partial t} \left(\mathbf{Q}_\sigma - \frac{5}{2} n_\sigma T_\sigma \mathbf{v}_\sigma \right) + n_\sigma \mathbf{v}_\sigma \frac{\partial T_\sigma}{\partial t} + \nabla \cdot \boldsymbol{\theta}_\sigma - \frac{5}{2} \frac{T_\sigma}{m_\sigma} \nabla \cdot \mathbf{M}_\sigma \\ - \frac{e_\sigma}{m_\sigma} \left(\mathbf{Q}_\sigma - \frac{5}{2} n_\sigma T_\sigma \mathbf{v}_\sigma \right) \times \mathbf{B} - \frac{e_\sigma}{m_\sigma} \mathbf{E} \cdot [\mathbf{M}_\sigma - \frac{1}{3}(Tr \mathbf{M}_\sigma) \mathbf{I}] \\ = \left(\mathbf{R}_\sigma^3 - \frac{5}{2} \frac{T_\sigma}{m_\sigma} \mathbf{R}_\sigma^1 \right) + \left(\mathbf{S}_\sigma^3 - \frac{5}{2} \frac{T_\sigma}{m_\sigma} \mathbf{S}_\sigma^1 \right) \end{aligned} \quad (5.29)$$

One notable characteristic of the moments equations is that an $n + 1$ moment always appears in the n th moment equation. Thus the moments equations are not closed.

5.2 One-Fluid Model

The moments equations define a multispecies fluid approximation. An even simpler description of the plasma is obtained by appropriate summation of the moments equations over all species present in the plasma.

Multiplying Eq. (5.6) by m_σ and summing over species results in

$$\frac{\partial \rho}{\partial t} + \nabla \cdot \rho \mathbf{u} = S_\rho^0 \quad (5.30)$$

where

$$\rho \equiv \sum_{\sigma} n_{\sigma} m_{\sigma} \quad \text{mass density} \quad (5.31)$$

$$\mathbf{u} \equiv \sum_{\sigma} n_{\sigma} m_{\sigma} \mathbf{v}_{\sigma} / \rho \quad \text{mass velocity} \quad (5.32)$$

$$S_\rho^0 \equiv \sum_{\sigma} S_{\sigma}^0 m_{\sigma} \quad \text{mass source} \quad (5.33)$$

Equation (5.30) is the mass continuity equation for the plasma.

A charge continuity equation can be obtained by multiplying Eq. (5.6) by e_σ and summing over species.

$$\frac{\partial \Sigma}{\partial t} + \nabla \cdot \mathbf{j} = S_\Sigma^0 \quad (5.34)$$

where

$$\Sigma \equiv \sum_{\sigma} n_{\sigma} e_{\sigma} \quad \text{charge density} \quad (5.35)$$

$$\mathbf{j} \equiv \sum_{\sigma} n_{\sigma} e_{\sigma} \mathbf{v}_{\sigma} \quad \text{current density} \quad (5.36)$$

A momentum conservation equation for the plasma is obtained by summing Eq. (5.7) over species. In this case it is convenient to choose a somewhat different decomposition

than Eq. (5.16), namely

$$\mathbf{v} = \mathbf{u} + \mathbf{y} \quad (5.37)$$

so that \mathbf{y} contains the random thermal motion and the relative motion of the various species with respect to the common mass velocity. Using this decomposition, defining the pressure tensor as before, except in terms of \mathbf{y} rather than \mathbf{W} , and making use of Eq. (5.30), finally leads to

$$\rho \frac{\partial \mathbf{u}}{\partial t} + \rho (\mathbf{u} \cdot \nabla) \mathbf{u} + \nabla \cdot \mathbf{P} = \Sigma \mathbf{E} + \mathbf{j} \times \mathbf{B} + \mathbf{S}_\rho^1 - \mathbf{S}_\rho^0 \mathbf{u} \quad (5.38)$$

where

$$\mathbf{S}_\rho^1 \equiv \sum_{\sigma} \mathbf{S}_{\sigma}^1 \quad (5.39)$$

The collisional friction term does not appear in Eq. (5.38) because $\sum_{\sigma} \mathbf{R}_{\sigma}^1 = 0$ from momentum conservation in elastic collisions.

To obtain a one-fluid equation for the current density, we multiply Eq. (5.7) by e_{σ}/m_{σ} and sum over species. Using the velocity decomposition of Eq. (5.37), defining the pressure tensor in terms of \mathbf{y} instead of \mathbf{W} , and making use of the fact that $m_e/m_{\sigma} \ll 1$ for $\sigma \neq e$ leads to

$$\begin{aligned} \frac{m_e}{n_e e_e^2} & \left[\frac{\partial \mathbf{j}}{\partial t} + \nabla \cdot \left(\mathbf{u} \mathbf{j} + \mathbf{j} \mathbf{u} - \Sigma \mathbf{u} \mathbf{u} + \frac{\mathbf{j} \mathbf{j}}{n_e e_e} \right) \right] + \frac{1}{n_e e_e} \nabla \cdot \mathbf{P}_e \\ &= \left[\mathbf{E} + \left(1 - \frac{\Sigma}{n_e e_e^2} \right) \mathbf{u} \times \mathbf{B} + \frac{1}{n_e e_e} \mathbf{j} \times \mathbf{B} \right] - \eta \mathbf{j} + \frac{m_e}{n_e e_e^2} \mathbf{S}_q^1 \end{aligned} \quad (5.40)$$

where

$$\eta \mathbf{j} \equiv -\frac{m_e}{n_e e_e^2} \sum_{\sigma} e_{\sigma} \int \mathbf{v} C_{\sigma} d^3 v \quad (5.41)$$

$$\mathbf{S}_q^1 \equiv \sum_{\sigma} \frac{e_{\sigma}}{m_{\sigma}} \mathbf{S}_{\sigma}^1 \quad (5.42)$$

The quantity η defined by Eq. (5.41) is the plasma resistivity. The subscript e refers to electrons.

Equations (5.38) and (5.40) can be simplified further when the length (L) and time (τ) scales of interest are large compared to certain characteristic parameters of the plasma. Since the potential of a charge is Debye-shielded, the plasma is effectively neutral on a length scale $L \gg \lambda_D$, so that the quasineutrality approximation, $\Sigma \rightarrow 0$, can be used.

In many situations of practical interest, it can be shown that the distribution function is an isotropic Maxwellian plus a small correction of the order of $\delta \equiv r_{Li}/L$. In such cases, since the RHS of Eq. (5.4) vanishes for an isotropic distribution, \mathbf{v}_{σ} and u are of first order

in δ . Multiplying Eq. (5.38) by L/ρ , the terms are of order (relative to v_{th}^2)

$$\begin{aligned} \left| L \frac{\partial \mathbf{u}}{\partial t} \right| &\sim \frac{1}{\Omega_i \tau} \\ |L(\mathbf{u} \cdot \nabla) \mathbf{u}| &\sim \delta^2 \\ \left| \frac{L}{\rho} \nabla \cdot \mathbf{P} \right| &\sim 1 \\ \left| \frac{L}{\rho} \mathbf{j} \times \mathbf{B} \right| &\sim \left| \frac{\delta}{\delta} \right| \sim 1 \end{aligned}$$

where Ω_i is the ion gyrofrequency. It can be shown that it is the scalar pressure component of $\nabla \cdot \mathbf{P} = \nabla p + \nabla \cdot \pi$ that is order unity and that the anisotropic shear is of order δ or higher. Assuming that the source is no larger than first order in δ , we see that for times $\tau \gg \Omega_i^{-1}$, the lowest order form of Eq. (5.38) is

$$\nabla p = \mathbf{j} \times \mathbf{B} \quad (5.43)$$

This equation is valid for scale lengths $L \gg r_{Li}$, the ion gyroradius.

Noting that $\mathbf{j} \cdot \nabla p = \mathbf{B} \cdot \nabla p = 0$ from Eq. (5.43), we conclude that the current and magnetic field lines lie in isobaric surfaces. The $\mathbf{j} \times \mathbf{B}$ force just balances the pressure gradient in a confined plasma. We examine the consequences of Eq. (5.43) in the next chapter.

To simplify Eq. (5.40), we consider the ratio of various terms, making use of Eq. (5.43),

$$\begin{aligned} \frac{1}{n_e e_e} \frac{|\mathbf{j} \times \mathbf{B}|}{|\mathbf{u} \times \mathbf{B}|} &\sim \frac{1}{n_e e_e} \frac{|\nabla \cdot \mathbf{P}_e|}{|\mathbf{u} \times \mathbf{B}|} \sim \delta \\ \frac{m_e}{n_e e_e^2} \frac{|\nabla \cdot (\mathbf{u} \mathbf{j} + \mathbf{j} \mathbf{u} - \Sigma \mathbf{u} \mathbf{u})|}{|\mathbf{u} \times \mathbf{B}|} &\sim \frac{m_e}{m_i} \delta^2 \\ \frac{m_e}{n_e e_e^2} \frac{\left| \frac{\partial \mathbf{j}}{\partial t} \right|}{|\mathbf{u} \times \mathbf{B}|} &\sim \frac{m_e}{m_i} \frac{1}{\Omega_i \tau} \end{aligned}$$

Thus the terms in the first bracket in Eq. (5.40) are seen to be much smaller than the $\mathbf{u} \times \mathbf{B}$ term by virtue of $m_e/m_i \ll 1$, $\delta \ll 1$, and $\tau \gg \Omega_i^{-1}$. The $\nabla \cdot \mathbf{P}_e$ and $\mathbf{j} \times \mathbf{B}$ terms are smaller by order δ than the $\mathbf{u} \times \mathbf{B}$ term, and the former are referred to as finite gyroradius corrections that must be retained when length scales $L \sim r_{Li}$ are important. When length scales $L \gg r_{Li}$ are of interest, Eq. (5.40) becomes to lowest order

$$\mathbf{E} + \mathbf{u} \times \mathbf{B} + \frac{m_e}{n_e e_e^2} \mathbf{S}_q^1 = \eta \mathbf{j} \quad (5.44)$$

Equation (5.44) is an Ohm's law for the plasma. It states that plasma currents may be driven by electric fields, by $\mathbf{u} \times \mathbf{B}$ flows, and by external momentum sources.

For predominantly ion phenomena that evolve sufficiently slowly that the electrons can reach a dynamic equilibrium along the magnetic field, electron momentum can be

neglected. Setting $m_e = 0$ and assuming charge neutrality $\Sigma = 0$ and $S_q^1 = 0$ in Eq. (5.40) for such phenomena yields another form of a generalized Ohm's Law

$$\mathbf{E} + \mathbf{u} \times \mathbf{B} = \eta \mathbf{j} + \frac{\nabla \mathbf{P}_i}{ne} \quad (5.45)$$

where Eq. (5.43) and $e_e = -e$ have been used. Since the right side will not in general vanish, this equation requires that either \mathbf{E} or \mathbf{u} , or both, be non-zero. Thus, in a plasma in equilibrium at rest ($\mathbf{u} = 0$), there must be an electric field. Conversely, a plasma in equilibrium without an electric field must be in motion.

Equation (5.45) can be solved for

$$\mathbf{u}_\perp = \frac{\mathbf{E} \times \mathbf{B}}{B^2} + \frac{\mathbf{B} \times \nabla \mathbf{P}_i}{neB^2} - \eta \frac{\mathbf{j} \times \mathbf{B}}{neB^2} \quad (5.46)$$

The first term is just the $\mathbf{E} \times \mathbf{B}$ drift. The second term is the ion diamagnetic drift. The third term, which vanishes as $\eta \sim T^{-3/2} \rightarrow 0$, is a flow normal to the isobaric surfaces, as may be seen from Eq. (5.43).

An energy balance equation for the plasma is obtained by using the velocity decomposition of Eq. (5.37) in Eq. (5.38) and summing over species

$$\begin{aligned} \frac{\partial}{\partial t} \left(\frac{1}{2} \rho u^2 + \frac{3}{2} p \right) + \nabla \cdot \left(\rho u^2 \mathbf{u} + \mathbf{P} \cdot \mathbf{u} + \frac{3}{2} p \mathbf{u} + \mathbf{q} \right) \\ = \mathbf{j} \cdot \mathbf{E} + \sum_{\sigma} \left(R_{\sigma}^2 + S_{\sigma}^2 \right) \end{aligned} \quad (5.47)$$

The kinetic energy terms can be eliminated by taking the scalar product of Eq. (5.38) multiplying Eq. (5.30) by $\mathbf{u}^2/2$, and subtracting both from Eq. (5.47)

$$\begin{aligned} \frac{3}{2} \frac{\partial p}{\partial t} + \frac{5}{2} \nabla \cdot (p \mathbf{u}) - \mathbf{u} \cdot (\nabla \cdot \mathbf{P}) + \nabla \cdot \mathbf{q} = \mathbf{j} \cdot (\mathbf{E} + \mathbf{u} \times \mathbf{B}) - \Sigma \mathbf{u} \cdot \mathbf{E} + \sum_{\sigma} \left(R_{\sigma}^2 + S_{\sigma}^2 \right) \\ - \mathbf{u} \cdot \mathbf{S}_{\rho}^1 + \frac{1}{2} \mathbf{u}^2 \mathbf{S}_{\rho}^0 \end{aligned} \quad (5.48)$$

The first two terms on the RHS represent a dissipative, or ohmic, heating of the plasma. The second term vanishes by quasineutrality when lengths $L \gg \lambda_D$ are of interest. The R_{σ}^2 term represents collisional frictional heating, and the remaining terms on the RHS are related to the net heating associated with an external source.

Equation (5.48) governs the internal energy of the plasma (note that $p \sim nT = \frac{2}{3}U$). It contains a higher moment, the heat conduction, \mathbf{q} . The next higher moment equation governs \mathbf{q} , but it too contains a higher moment, ad infinitum. In practice, the form for \mathbf{q} is determined by considering the $n = 3$ moment equation under special, simplifying conditions, and only the $n = 0, 1$, and 2 moment equations are actually solved.

In the absence of heat conduction ($\mathbf{q} = 0$), ohmic heating [$\mathbf{j} \cdot (\mathbf{E} + \mathbf{u} \times \mathbf{B}) = 0$], net collisional frictional heating $\sum_{\sigma} R_{\sigma}^2 = 0$ and any external sources of heat, momentum or

particles, Eq. (5.48) reduces to

$$\frac{3}{2} \frac{\partial p}{\partial t} + \frac{5}{2} \nabla \cdot (p \mathbf{u}) - \mathbf{u} \cdot \nabla p = 0 \quad (5.49)$$

for an isotropic distribution. This equation can be combined with the source-free version of Eq. (5.30) to obtain

$$\frac{d}{dt} \left(\frac{p}{\rho^{5/3}} \right) \equiv \left(\frac{\partial}{\partial t} + \mathbf{u} \cdot \nabla \right) \left(\frac{p}{\rho^{5/3}} \right) = 0 \quad (5.50)$$

which is the equation of state for an adiabatic gas. Thus, under the conditions cited above, a plasma obeys the adiabatic gas law.

5.3 Magnetohydrodynamic Model

A specialization of the one-fluid model that is frequently used, together with Maxwell's equations, for the analysis of plasmas is known as the magnetohydrodynamic (MHD) model. The MHD model consists of

$$\frac{\partial \rho}{\partial t} + \nabla \cdot \rho \mathbf{u} = 0 \quad \text{continuity} \quad (5.51)$$

$$\rho \frac{\partial \mathbf{u}}{\partial t} + \nabla p = \mathbf{j} \times \mathbf{B} \quad \text{momentum} \quad (5.52)$$

$$\eta \mathbf{j} = \mathbf{E} + \mathbf{u} \times \mathbf{B} \quad \text{Ohm's law} \quad (5.53)$$

$$\left. \begin{aligned} \nabla \times \mathbf{E} &= -\frac{\partial \mathbf{B}}{\partial t} \\ \mu_0 \mathbf{j} &= \nabla \times \mathbf{B} \end{aligned} \right\} \quad \text{Maxwell's equations} \quad (5.54)$$

$$(5.55)$$

and a suitable "equation of state" instead of the energy balance equation such as

$$\frac{d}{dt} \left(\frac{p}{\rho^{5/3}} \right) = 0 \quad \text{adiabatic} \quad (5.56)$$

or

$$\nabla \cdot \mathbf{u} = 0 \quad \text{incompressible} \quad (5.57)$$

or

$$\frac{d}{dt} \left(\frac{p}{\rho} \right) = 0 \quad \text{isothermal} \quad (5.58)$$

From our previous derivation of the one-fluid equations, we can conclude that certain assumptions are implicit in the MHD model. The use of a scalar pressure assumes an isotropic distribution to lowest order in $\delta \equiv r_{Li}/L$. A source-free problem is obviously assumed. Neglect of Σ implies that the model is valid for spatial scales $L \gg \lambda_D$, and neglect of certain other terms indicates that $L \gg r_{Li}$ is a requirement for validity. The use of a one-fluid model implies that the electrons and ions respond together. This implies the model is valid on time scales that are long compared to the inverse of the lowest of the

plasma characteristic frequencies discussed in chapters 1 and 2, which is the ion frequency; that is, $\tau \gg \Omega_i^{-1}$. In fact, the MHD ordering is

$$1 \gg \frac{1}{\tau \Omega_i} \gg \delta^2 \quad (5.59)$$

We now explore some consequences of the MHD equations. First, we generalize the adiabatic equation of state

$$\frac{d}{dt} (p \rho_m^{-\gamma}) = 0 \quad (5.60)$$

where the quantity γ is the ratio of specific heats and $\gamma = 2 + \delta/\delta$ (δ is the number of degrees of freedom) is 5/3 in the three-dimensional case $\delta = 3$. Combined with Eq. (5.51), this becomes

$$\frac{\partial p}{\partial t} + (\mathbf{u} \cdot \nabla) p + \gamma p \nabla \cdot \mathbf{u} = 0 \quad (5.61)$$

The incompressibility condition

$$\nabla \cdot \mathbf{u} = 0 \quad (5.62)$$

can be used instead of Eq. (5.61) if $|(\partial \rho / \partial t)/\rho| \ll |\nabla \cdot \mathbf{u}|$.

An energy conservation law can be derived from Eqs. (5.52) and (5.53)

$$\frac{1}{\mu_0} \nabla \cdot (\mathbf{E} \times \mathbf{B}) + \frac{\partial}{\partial t} \left(\frac{\mathbf{B}^2}{2\mu_0} \right) + \mathbf{E} \cdot \mathbf{j} = 0 \quad (5.63)$$

From Eq. (5.53), the third term in Eq. (5.63) becomes

$$\mathbf{E} \cdot \mathbf{j} = \eta j^2 + (\mathbf{j} \times \mathbf{B}) \cdot \mathbf{u} \quad (5.64)$$

By use of Eq. (5.52) (but retaining the $\rho(\mathbf{u} \cdot \nabla)\mathbf{u}$ term) and Eq. (5.51), the Lorentz term in Eq. (5.63) can be expressed as

$$(\mathbf{j} \times \mathbf{B}) \cdot \mathbf{u} = \frac{\partial}{\partial t} \left(\frac{\rho u^2}{2} \right) + \nabla \cdot \left(\frac{\rho u^2}{2} \mathbf{u} \right) + \mathbf{u} \cdot \nabla p \quad (5.65)$$

From Eq. (5.61), it follows that

$$-\nabla \cdot (p \mathbf{u}) = \frac{\partial p}{\partial t} + (\gamma - 1) p \nabla \cdot \mathbf{u}$$

and

$$\mathbf{u} \cdot \nabla p = \frac{\partial}{\partial t} \left(\frac{p}{\gamma - 1} \right) + \nabla \cdot \left(\frac{p}{\gamma - 1} + p \right) \mathbf{u}$$

Therefore the energy conservation law of Eq. (5.63) is reduced to

$$\begin{aligned} \nabla \cdot (\mathbf{E} \times \mathbf{H}) + \frac{\partial}{\partial t} \left(\frac{\rho u^2}{2} + \frac{p}{\gamma - 1} + \frac{\mathbf{B}^2}{2\mu_0} \right) + \eta j^2 \\ + \nabla \cdot \left(\frac{\rho u^2}{2} + \frac{p}{\gamma - 1} + p \right) \mathbf{u} = 0 \end{aligned} \quad (5.66)$$

An equation for the diffusion of the magnetic field in the plasma can be derived from the substitution of Eq. (5.53) into Eq. (5.54)

$$\begin{aligned}\frac{\partial \mathbf{B}}{\partial t} &= \nabla \times (\mathbf{u} \times \mathbf{B}) - \eta \nabla \times \mathbf{j} \\ &= \nabla \times (\mathbf{u} \times \mathbf{B}) + \frac{\eta}{\mu_0} \nabla^2 \mathbf{B} \\ &= -(\mathbf{u} \cdot \nabla) \mathbf{B} - \mathbf{B} (\nabla \cdot \mathbf{u}) + (\mathbf{B} \cdot \nabla) \mathbf{u} + \frac{\eta}{\mu_0} \nabla^2 \mathbf{B}\end{aligned}\quad (5.67)$$

The quantity $\eta/\mu_0 = v_m$ is called magnetic viscosity.

The substitution of Eq. (5.55) into Eq. (5.52) yields

$$\rho \frac{d\mathbf{u}}{dt} = -\nabla \left(p + \frac{B^2}{2\mu_0} \right) + \frac{1}{\mu_0} (\mathbf{B} \cdot \nabla) \mathbf{B} \quad (5.68)$$

the equation of motion for the plasma.

The ratio of the first term to the second term on the RHS of the second form of Eq. (5.67)

$$\frac{|\nabla \times (\mathbf{u} \times \mathbf{B})|}{\left| \nabla^2 \mathbf{B} \left(\frac{\eta}{\mu_0} \right) \right|} \approx \frac{\frac{uB}{L}}{\left(\frac{B}{L^2} \right) \left(\frac{\eta}{\mu_0} \right)} = \frac{\mu_0 u L}{\eta} \equiv R_m \quad (5.69)$$

is called the magnetic Reynolds number, where L is a typical plasma dimension. The magnetic Reynolds number is equal to the ratio of the magnetic diffusion time $\tau_R = \mu_0 L^2 / \eta$ to the Alfvén transit time $\tau_H = L/v_A$, that is, $R_m = \tau_R / \tau_H$. When $R_m \ll 1$, the magnetic field in a plasma changes according to a diffusion equation.

When $R_m \gg 1$, the lines of magnetic force are frozen in the plasma. Let the magnetic flux within the surface element ΔS be $\Delta\Phi$, and take the z -axis in the \mathbf{B} -direction. Then $\Delta\Phi$ is given by $\Delta\Phi = \mathbf{B} \cdot \hat{\mathbf{n}} \Delta S = \mathbf{B} \Delta x \Delta y$.

As the boundary of ΔS moves, the rate of change of ΔS is

$$\begin{aligned}\frac{d}{dt}(\Delta x) &= \frac{d}{dt}(x + \Delta x - x) = u_x(x + \Delta x) - u_x(x) = \frac{\partial u_x}{\partial x} \Delta x \\ \frac{d}{dt}(\Delta S) &= \left(\frac{\partial u_x}{\partial x} + \frac{\partial u_y}{\partial y} \right) \Delta x \Delta y\end{aligned}$$

The rate of change of the flux $\Delta\Phi$ is

$$\begin{aligned}\frac{d}{dt}(\Delta\Phi) &= \frac{dB}{dt} \Delta S + B \frac{d}{dt}(\Delta S) \\ &= \left(\frac{d\mathbf{B}}{dt} + \mathbf{B} (\nabla \cdot \mathbf{u}) - (\mathbf{B} \cdot \nabla) \mathbf{u} \right)_z \Delta S = \frac{\eta}{\mu_0} \Delta B_z(\Delta S)\end{aligned}\quad (5.70)$$

When $R_m \rightarrow \infty$, $\eta \rightarrow 0$, the rate of change of the flux becomes zero, i.e., $d(\Delta\Phi)/dt \rightarrow 0$. This means the magnetic flux is frozen in the plasma.

5.4 Anisotropic Pressure Tensor Model*

The off-diagonal, shear terms in the pressure tensor are of the form

$$(P_{\alpha\beta})_{\sigma} = n_{\sigma} m_{\sigma} (W_{\alpha} W_{\beta})_{\sigma} \quad \alpha \neq \beta$$

In a strong magnetic field, ions have a small gyroradius and a rapid gyration, which tends to make $(W_{\alpha} W_{\beta})_{\sigma} \simeq 0$ when the α and β directions are in the plane perpendicular to the field. When either α or β is along the field direction, $(W_{\alpha} W_{\beta})_{\sigma}$ will not vanish unless collisions are sufficiently frequent to randomize the motions perpendicular and parallel to the field. Thus, in a relatively collisionless plasma, the pressure tensor can be anisotropic and can be represented in terms of the parallel (P_{\parallel}) and perpendicular (P_{\perp}) pressure components.

$$\begin{aligned} \mathbf{P} &= \begin{bmatrix} [P_{\perp} + (P_{\parallel} - P_{\perp})]\hat{\mathbf{n}}_x\hat{\mathbf{n}}_x & (P_{\parallel} - P_{\perp})\hat{\mathbf{n}}_x\hat{\mathbf{n}}_y & (P_{\parallel} - P_{\perp})\hat{\mathbf{n}}_x\hat{\mathbf{n}}_z \\ (P_{\parallel} - P_{\perp})\hat{\mathbf{n}}_y\hat{\mathbf{n}}_x & [P_{\perp} + (P_{\parallel} - P_{\perp})]\hat{\mathbf{n}}_y\hat{\mathbf{n}}_y & (P_{\parallel} - P_{\perp})\hat{\mathbf{n}}_y\hat{\mathbf{n}}_z \\ (P_{\parallel} - P_{\perp})\hat{\mathbf{n}}_z\hat{\mathbf{n}}_x & (P_{\parallel} - P_{\perp})\hat{\mathbf{n}}_z\hat{\mathbf{n}}_y & [P_{\perp} + (P_{\parallel} - P_{\perp})]\hat{\mathbf{n}}_z\hat{\mathbf{n}}_z \end{bmatrix} \\ &= P_{\perp} \mathbf{I} + (P_{\parallel} - P_{\perp})\hat{\mathbf{n}}_{\parallel}\hat{\mathbf{n}}_{\parallel} \end{aligned} \quad (5.71)$$

To develop the moments equations appropriate for an anisotropic pressure model it is necessary to take moments of the Boltzmann equation with respect to $1, m\mathbf{v}_{\parallel}, m\mathbf{v}_{\perp}, \frac{1}{2}m\mathbf{v}_{\parallel}^2, \frac{1}{2}m\mathbf{v}_{\perp}^2$, and so on, and to define velocity decompositions of the form of Eqs. (5.16) and (5.37) for both \mathbf{v}_{\parallel} and \mathbf{v}_{\perp} . The algebra is tedious, but straightforward, and the resulting first-moment equations are

$$\begin{aligned} m_{\sigma} n_{\sigma} \frac{\partial \mathbf{v}_{\parallel\sigma}}{\partial t} + m_{\sigma} n_{\sigma} \mathbf{v}_{\sigma} \cdot \nabla \mathbf{v}_{\perp\sigma} + \nabla \cdot \mathbf{P}_{\parallel\sigma} &= n_{\sigma} e_{\sigma} \mathbf{E}_{\parallel} + \mathbf{R}_{\parallel\sigma}^1 \\ &\quad + \mathbf{S}_{\parallel\sigma}^1 - m_{\sigma} \mathbf{v}_{\parallel\sigma} \mathbf{S}_{\sigma}^0 \end{aligned} \quad (5.72)$$

and

$$\begin{aligned} m_{\sigma} n_{\sigma} \frac{\partial \mathbf{v}_{\perp\sigma}}{\partial t} + m_{\sigma} n_{\sigma} \mathbf{v}_{\sigma} \cdot \nabla \mathbf{v}_{\perp\sigma} + \nabla \cdot \mathbf{P}_{\perp\sigma} &= n_{\sigma} e_{\sigma} (\mathbf{E} + \mathbf{v}_{\sigma} \times \mathbf{B})_{\perp} \\ &\quad + \mathbf{R}_{\perp\sigma}^1 + \mathbf{S}_{\perp\sigma}^1 - m_{\sigma} \mathbf{v}_{\perp\sigma} \mathbf{S}_{\sigma}^0 \end{aligned} \quad (5.73)$$

The corresponding one-fluid first moment equations are

$$\frac{\partial(\rho \mathbf{u}_{\parallel})}{\partial t} + \nabla \cdot \rho \mathbf{u}_{\parallel} \mathbf{u} + \nabla \cdot \mathbf{P}_{\parallel} = \Sigma \mathbf{E}_{\parallel} + \sum_{\sigma} (\mathbf{R}_{\parallel\sigma}^1 + \mathbf{S}_{\parallel\sigma}^1) \quad (5.74)$$

and

$$\frac{\partial(\rho \mathbf{u}_{\perp})}{\partial t} + \nabla \cdot \rho \mathbf{u}_{\perp} \mathbf{u} + \nabla \cdot \mathbf{P}_{\perp} = \Sigma \mathbf{E}_{\perp} + (\mathbf{j} \times \mathbf{B})_{\perp} + \sum_{\sigma} (\mathbf{R}_{\perp\sigma}^1 + \mathbf{S}_{\perp\sigma}^1) \quad (5.75)$$

The parallel and perpendicular pressures are defined by

$$P_{\parallel} \equiv \sum_{\sigma} n_{\sigma} m_{\sigma} (y_{\parallel}^2)_{\sigma} \quad (5.76)$$

$$P_{\perp} \equiv \sum_{\sigma} n_{\sigma} m_{\sigma} (y_{\perp}^2)_{\sigma} \quad (5.77)$$

and the other quantities are defined as before, except with respect to \mathbf{v}_{\parallel} or \mathbf{v}_{\perp} instead of \mathbf{v} .

The second moment equations are

$$\begin{aligned} \frac{1}{2} \frac{\partial P_{\parallel\sigma}}{\partial t} + \frac{1}{2} \mathbf{v}_{\sigma} \cdot \nabla P_{\parallel\sigma} + \frac{1}{2} P_{\parallel\sigma} \nabla \cdot \mathbf{v}_{\perp\sigma} + \frac{3}{2} P_{\parallel\sigma} \nabla \cdot \mathbf{v}_{\parallel\sigma} + \nabla \cdot \mathbf{q}_{\parallel\sigma} \\ = R_{\perp\sigma}^2 + S_{\perp\sigma}^2 - \mathbf{v}_{\perp\sigma} \cdot (\mathbf{R}_{\perp\sigma}^1 + \mathbf{S}_{\perp\sigma}^1) + \frac{1}{2} m_{\sigma} (v_{\perp})_{\sigma}^2 \mathbf{S}_{\perp\sigma}^1 \end{aligned} \quad (5.78)$$

and

$$\begin{aligned} \frac{\partial P_{\perp\sigma}}{\partial t} + \mathbf{v}_{\sigma} \cdot \nabla P_{\perp\sigma} + 2 P_{\perp\sigma} \nabla \cdot \mathbf{v}_{\perp\sigma} + P_{\perp\sigma} \nabla \cdot \mathbf{v}_{\parallel\sigma} + \nabla \cdot \mathbf{q}_{\perp\sigma} \\ = R_{\perp\sigma}^2 + S_{\perp\sigma}^2 - \mathbf{v}_{\perp\sigma} \cdot (\mathbf{R}_{\perp\sigma}^1 + \mathbf{S}_{\perp\sigma}^1) + \frac{1}{2} m_{\sigma} (v_{\perp})_{\sigma}^2 \mathbf{S}_{\perp\sigma}^1 \end{aligned} \quad (5.79)$$

where

$$q_{\parallel\sigma} \equiv \frac{1}{2} n_{\sigma} m_{\sigma} (W_{\parallel}^2 \mathbf{W}_{\parallel})_{\sigma} \quad (5.80)$$

$$q_{\perp\sigma} \equiv \frac{1}{2} n_{\sigma} m_{\sigma} (W_{\perp}^2 \mathbf{W}_{\perp})_{\sigma} \quad (5.81)$$

The one-fluid second-moment equations are

$$\begin{aligned} \frac{1}{2} \frac{\partial P_{\parallel}}{\partial t} + \frac{1}{2} \mathbf{u} \cdot \nabla P_{\parallel} + \frac{1}{2} P_{\parallel} \nabla \cdot \mathbf{u}_{\perp} + \frac{3}{2} P_{\parallel} \nabla \cdot \mathbf{u}_{\parallel} + \nabla \cdot \mathbf{q}_{\parallel} = \mathbf{j}_{\parallel} \cdot \mathbf{E}_{\parallel} - \Sigma \mathbf{u}_{\parallel} \cdot \mathbf{E}_{\parallel} \\ + \sum_{\sigma} \left[(R_{\parallel\sigma}^2 + S_{\parallel\sigma}^2) - \mathbf{u}_{\parallel} \cdot (\mathbf{R}_{\parallel\sigma}^1 + \mathbf{S}_{\parallel\sigma}^1) - \frac{1}{2} u_{\parallel}^2 S_{\sigma}^0 \right] \end{aligned} \quad (5.82)$$

and

$$\begin{aligned} \frac{\partial P_{\perp}}{\partial t} + \mathbf{u} \cdot \nabla P_{\perp} + 2 P_{\perp} \nabla \cdot \mathbf{u}_{\perp} + P_{\perp} \nabla \cdot \mathbf{u}_{\parallel} + \nabla \cdot \mathbf{q}_{\perp} = (\mathbf{j}_{\perp} + \Sigma \mathbf{u}_{\perp}) \cdot (\mathbf{E} + \mathbf{u} \times \mathbf{B})_{\perp} \\ + \sum_{\sigma} \left[(R_{\perp\sigma}^2 + S_{\perp\sigma}^2) - \mathbf{u}_{\perp} \cdot (\mathbf{R}_{\perp\sigma}^1 + \mathbf{S}_{\perp\sigma}^1) - \frac{1}{2} u_{\perp}^2 S_{\sigma}^0 \right] \end{aligned} \quad (5.83)$$

In the absence of external sources or heating, Joule heating, collisional heating, and heat conduction, Eqs. (5.81) and (5.82) reduce to

$$\frac{\partial P_{\parallel}}{\partial t} + \mathbf{u} \cdot \nabla P_{\parallel} + P_{\parallel} \nabla \cdot \mathbf{u}_{\perp} + 3 P_{\parallel} \nabla \cdot \mathbf{u}_{\parallel} = 0 \quad (5.84)$$

and

$$\frac{\partial P_{\perp}}{\partial t} + \mathbf{u} \cdot \nabla P_{\perp} + 2 P_{\perp} \nabla \cdot \mathbf{u}_{\perp} + P_{\perp} \nabla \cdot \mathbf{u}_{\parallel} = 0 \quad (5.85)$$

These two equations can be combined with the source-free form of Eq. (5.30) to obtain

$$\frac{d}{dt} \left(\frac{P_{\perp}^2 P_{\parallel}}{\rho^5} \right) = 0 \quad (5.86)$$

The invariancy of magnetic moment density

$$\mu_{\perp} \equiv \sum_{\sigma} n_{\sigma} (\mu_{\perp})_{\sigma} = - \frac{\sum_{\sigma} \frac{1}{2} n_{\sigma} m_{\sigma} (v_{\perp}^2)_{\sigma}}{B} \quad (5.87)$$

leads to

$$\frac{d}{dt} \left(\frac{P_{\perp}}{\rho B} \right) = 0 \quad (5.88)$$

which can be used to reduce Eq. (5.86) to

$$\frac{d}{dt} \left(\frac{P_{\parallel} B^2}{\rho^3} \right) = 0 \quad (5.89)$$

Equations (5.88) and (5.89) are the Double-Adiabatic model of a plasma.

5.5 Strong Field, Transport Time Scale Ordering

We have seen that one-fluid equations can be simplified under certain conditions by identifying terms that are small and can be neglected. In this section, we will develop similar simplifications of the multispecies moments equations. To be specific, we identify the relevant gradient scale length, $L \simeq |\nabla \ln p|^{-1}$, recall the definitions of thermal velocity and gyrofrequency

$$v_{th} \equiv \sqrt{\frac{2T}{m}}, \quad \Omega \equiv \frac{eB}{m}$$

identify a characteristic transient frequency, $\omega = v_{th}/L$, and recall the definition of the gyroradius

$$r_L = \frac{v_{\perp}}{\Omega} \simeq \frac{v_{th}}{\Omega}$$

In a strong magnetic field

$$\delta \equiv \frac{r_L}{L} \ll 1 \quad (5.90)$$

This is the fundamental assumption for strong field, or small gyroradius, ordering.

Anticipating the discussion of transport in chapter 9, we assume

$$\frac{\partial}{\partial t} \ln n \simeq \frac{\partial}{\partial t} \ln T \sim \frac{\partial}{\partial t} \ln p = O(\delta^2 \omega) \quad (5.91)$$

and

$$\frac{E}{v_{th} B} = O(\delta) \quad (5.92)$$

Equations (5.91) and (5.92) serve to define the time scale of interest in transport problems. Faster processes (e.g., MHD instabilities when $E/v_{th} B = O(1)$) are assumed to have evolved to an equilibrium.

It can be shown from kinetic theory that relations in Eqs. (5.90) to (5.92) are sufficient to ensure that the particle distribution function can be written as an isotropic Maxwellian plus a correction of $O(\delta)$,

$$f(\mathbf{v}) = f^{\max}(v^2) + f^1(\mathbf{v}), \quad f^1 = O(\delta) \quad (5.93)$$

Equation (5.93) can be used to estimate the order of the quantities that were defined in section 5.1, by noting that an odd velocity moment of an isotropic distribution vanishes. We find immediately from Eqs. (5.3), (5.4), and (5.10) to (5.13) that

$$n_\sigma = O(1) \quad (5.94)$$

and

$$\{n_\sigma \mathbf{v}_\sigma, \mathbf{Q}, \mathbf{M} - \frac{1}{3}(Tr M)\mathbf{I}, \boldsymbol{\theta} - \frac{5}{2} \frac{p_\sigma T_\sigma}{m_\sigma} \mathbf{I}\} = O(\delta) \quad (5.95)$$

From chapter 4 we recall that the scattering operator depends on the distribution functions of both species so that a linearized expansion leads to

$$C_{\sigma\sigma'}(f_\sigma, f_{\sigma'}) = C_{\sigma\sigma'}(f_\sigma^{\max}, f_{\sigma'}^{\max}) + C_{\sigma\sigma'}(f_\sigma^{\max}, f_{\sigma'}^1) + C_{\sigma\sigma'}(f_\sigma^1, f_{\sigma'}^{\max}) + O(\delta^2)$$

from which we conclude that $R_\sigma^n = O(\delta)$ or higher.

The current density is

$$\mathbf{j} = \sum_\sigma e_\sigma n_\sigma \mathbf{v}_\sigma = O(\delta)$$

and the vector potential was defined in chapter 1 as an integral over the current distribution, so that $\mathbf{A} = O(\delta)$. We postulate that the external source terms are $O(\delta)$ or higher. Collecting these results

$$\{R_\sigma^n, \mathbf{j}, \mathbf{A}, S_\sigma^n\} = O(\delta) \quad (5.96)$$

From Eq. (5.21b) we see that

$$\mathbf{q}_\sigma = \left(\mathbf{Q}_\sigma - \frac{5}{2} p_\sigma \mathbf{v}_\sigma \right) [1 + O(\delta)] \quad (5.97)$$

Relations in Eq. (5.91) and Eq. (5.96) lead to the conclusion that

$$\mathbf{E} = -\nabla\Phi - \frac{\partial \mathbf{A}}{\partial t} = -\nabla\Phi + O(\delta^2) \quad (5.98)$$

Equation (5.26) and Eq. (5.29) can be used to examine the variation of certain quantities along field lines by taking the scalar product with \mathbf{B} and using Eq. (5.94) to Eq. (5.98). The resulting relations are

$$\frac{\mathbf{B}}{B} \cdot (\nabla p_\sigma + n_\sigma e_\sigma \nabla\Phi) = O(\delta) \quad (5.99)$$

and

$$\mathbf{B} \cdot \left[\frac{5}{2} \nabla \left(\frac{p_\sigma T_\sigma}{m_\sigma} \right) - \frac{5}{2} \frac{T_\sigma}{m_\sigma} \nabla p_\sigma \right] = \mathbf{B} \cdot \left(\frac{5}{2} \frac{p_\sigma}{m_\sigma} \nabla T_\sigma \right) = O(\delta) \quad (5.100)$$

Using Eq. (5.28) and Eq. (5.100) in Eq. (5.99), then summing over species and using quasineutrality ($\sum_\sigma n_\sigma e_\sigma = 0$) leads to the conclusion $\mathbf{B} \cdot \nabla n_\sigma = O(\delta)$. This result and

$\mathbf{B} \cdot \nabla T_\sigma = O(\delta)$ are equivalent to $\mathbf{B} \cdot \nabla p_\sigma = O(\delta)$, which can be used in Eq. (5.99) to obtain $(\mathbf{B}/B) \cdot \nabla \Phi = O(\delta)$. Thus

$$\{n_\sigma, T_\sigma, p_\sigma, \Phi\} = \text{const} + O(\delta) \text{ along } \mathbf{B} \quad (5.101)$$

Particle and heat conduction fluxes perpendicular to the field can be (formally) found by taking the vector product of $\hat{\mathbf{n}}_{\parallel}$ with Eq. (5.26) and Eq. (5.29) and making use of Eq. (5.97). The resulting expressions are

$$\begin{aligned} n_\sigma \mathbf{v}_{\sigma\perp} &= \frac{1}{e_\sigma B} \hat{\mathbf{n}}_{\parallel} \times \left[m_\sigma n_\sigma \frac{\partial \mathbf{v}_\sigma}{\partial t} + m_\sigma n_\sigma (\mathbf{v}_\sigma \cdot \nabla) \mathbf{v}_\sigma + \nabla p_\sigma + \nabla \cdot \boldsymbol{\pi}_\sigma \right. \\ &\quad \left. + n_\sigma e_\sigma (\nabla \Phi - \mathbf{E}^A) - \mathbf{R}_\sigma^1 - (S_\sigma^1 - m_\sigma \mathbf{v}_\sigma S \sigma^0) \right] \end{aligned} \quad (5.102)$$

and

$$\begin{aligned} \mathbf{q}_{\sigma\perp} &= \frac{m_\sigma}{e_\sigma B} \hat{\mathbf{n}}_{\parallel} \times \left\{ \frac{\partial}{\partial t} \left(\mathbf{Q}_\sigma - \frac{5}{2} n_\sigma T_\sigma \mathbf{v}_\sigma \right) + \frac{5}{2} n_\sigma \mathbf{v}_\sigma \frac{\partial T_\sigma}{\partial t} + \nabla \cdot \boldsymbol{\theta}_\sigma \right. \\ &\quad - \frac{5}{2} \frac{T_\sigma}{m_\sigma} \nabla \cdot \mathbf{M}_\sigma - \frac{e_\sigma}{m_\sigma} \mathbf{E} \cdot \left[\mathbf{M}_\sigma - \frac{1}{3} (Tr \mathbf{M}_\sigma) \mathbf{I} \right] \\ &\quad \left. - \left(\mathbf{R}_\sigma^3 - \frac{5}{2} \frac{T_\sigma}{m_\sigma} \mathbf{R}_\sigma^1 \right) - \left(S_\sigma^3 - \frac{5}{2} \frac{T_\sigma}{m_\sigma} S_\sigma^1 \right) \right\} \end{aligned} \quad (5.103)$$

(Note that the δ -ordering is essentially a $1/B$ -ordering; this result is explicit in Eq. (5.102) and Eq. (5.103). To compute $n_\sigma \mathbf{v}_{\sigma\perp}$ and $\mathbf{q}_{\sigma\perp}$ to $O(\delta^n)$, terms on the RHS to $O(\delta^{n-1})$ are required. Making use of relations in Eq. (5.95) and Eq. (5.96), we can see that the lowest order perpendicular fluxes are $O(\delta)$,

$$n_\sigma \mathbf{v}_{\sigma\perp}^1 = \frac{1}{e_\sigma B} \hat{\mathbf{n}}_{\parallel} \times (\nabla p_\sigma + n_\sigma e_\sigma \nabla \Phi) \quad (5.104)$$

and

$$\mathbf{q}_{\sigma\perp}^1 = \frac{5}{2} \frac{p_\sigma}{e_\sigma B} \hat{\mathbf{n}}_{\parallel} \times \nabla T_\sigma \quad (5.105)$$

First-order fluxes along the field line, $n \mathbf{v}_\sigma^1$ and \mathbf{Q}_σ^1 or \mathbf{q}_\parallel^1 , can be determined by using Eq. (5.104) and Eq. (5.105) in solving Eq. (5.6) and the $O(\delta)$ version of Eq. (5.48):

$$\frac{3}{2} \frac{\partial p_\sigma}{\partial t} + \frac{3}{2} \nabla \cdot (\mathbf{v}_\sigma^1 p_\sigma) + \nabla \cdot \mathbf{q}_\sigma^1 = R_\sigma^2 + S_\sigma^2 \quad (5.106)$$

The lowest order one-fluid equilibrium condition can be obtained by using Eqs. (5.104) in the definition of the perpendicular current density,

$$\mathbf{j}_\perp^1 = \sum_\sigma e_\sigma n_\sigma \mathbf{v}_{\sigma\perp} = \frac{1}{B} \hat{\mathbf{n}}_{\parallel} \times \sum_\sigma \nabla p_\sigma = \frac{1}{B} \hat{\mathbf{n}}_{\parallel} \times \nabla p$$

which is equivalent to

$$\mathbf{j}_\perp^1 \times \mathbf{B} = \nabla p \quad (5.107)$$

The consequences of Eq. (5.107) will be examined in the next chapter.

Problems for Chapter 5

1. Derive Eq. (5.6) to Eq. (5.8) by taking the indicated moments of the Boltzmann equation.
2. Derive Eq. (5.19) and Eq. (5.20a) by substituting the decomposition of Eq. (5.16) into Eq. (5.10).
3. Derive Eq. (5.26) and Eq. (5.27) from Eq. (5.7) and Eq. (5.8), respectively.
4. Derive Eq. (5.38) by summing Eq. (5.7) for each species present and using the decomposition of Eq. (5.37).
5. Derive Eq. (5.50) from Eq. (5.48). Make note of all approximations.
6. Derive the energy conservation law of Eq. (5.63).
7. Derive the magnetic field diffusion equation (5.67).
8. Derive the perpendicular particle and energy fluxes given by Eq. (5.102) and Eq. (5.103), respectively.
9. Use ordering arguments to reduce Eq. (5.102) and Eq. (5.103) to the leading order expressions given by Eq. (5.104) and Eq. (5.105), respectively.
10. Calculate the deuterium ion and electron plasma frequencies, gyroradii and gyrofrequencies, and the Alfvén speed for a plasma with density $n_0 = 5 \times 10^{19} \text{ m}^{-3}$, temperature $T = 10 \text{ keV}$, and magnetic field $B = 5 \text{ T}$.
11. What is the lowest order equilibrium force balance equation for a magnetically confined plasma? Can a plasma be confined in a magnetic configuration in which the field lines are aligned along the direction of the pressure gradient?

6 Plasma Equilibria

We explore in this chapter the consequences of the lowest order momentum balance equation,

$$\nabla p = \mathbf{j} \times \mathbf{B} \quad (6.1)$$

as it pertains to plasma equilibrium. The current and the field must also satisfy Maxwell's equations

$$\mu_0 \mathbf{j} = \nabla \times \mathbf{B} \quad (6.2)$$

and

$$\nabla \cdot \mathbf{B} = 0 \quad (6.3)$$

6.1 General Properties

The most immediate consequence of Eq. (6.1) is that the current and magnetic field lie on isobaric surfaces. This follows directly from the observation that $\mathbf{j} \cdot \nabla p = \mathbf{B} \cdot \nabla p = 0$ and ∇p is everywhere normal to the surface $p = \text{const}$. Equation (6.1) does not imply that $\mathbf{j} \times \mathbf{B}$ is constant on an isobaric surface, since ∇p will in general vary over an isobaric surface. Equation (6.1) does state that the force is everywhere normal to the isobaric surface and just balances the pressure gradient force, $-\nabla p$. Although the current and the magnetic field lie in a common flux surface, they can only be parallel in regions where the pressure gradient vanishes. Since currents that are parallel to the field do not contribute to the $\mathbf{j} \times \mathbf{B}$ force, they are known as "force-free currents."

Taking the divergence of Eq. (6.2) yields

$$\nabla \cdot \mathbf{j} = 0 \quad (6.4)$$

which is consistent with the quasineutrality assumption. The vector product of \mathbf{B} with Eq. (6.1) leads to an expression for the current perpendicular to \mathbf{B} ,

$$\mathbf{j}_\perp = \frac{\mathbf{B} \times \nabla p}{B^2} \quad (6.5)$$

We see that there can be no perpendicular current in the absence of a pressure gradient.

Using Eq. (6.2) in Eq. (6.1) leads to a momentum balance expressed in terms of the pressure and magnetic field

$$\nabla \left(p + \frac{B^2}{2\mu_0} \right) = \frac{1}{\mu_0} (\mathbf{B} \cdot \nabla) \mathbf{B} \quad (6.6)$$

The RHS vanishes when the field lines are straight and parallel, in which case Eq. (6.6) reduces to a simple statement that the total (kinetic plus magnetic) pressure is constant everywhere within a confined plasma,

$$p + \frac{B^2}{2\mu_0} \equiv \frac{B^2}{2\mu_0} (1 + \beta) = \text{const} \quad (6.7)$$

where we have introduced the quantity

$$\beta \equiv \frac{p}{B^2/2\mu_0} \quad (6.8)$$

as a measure of the efficiency with which the magnetic field confines the plasma. The magnetic pressure associated with even moderate magnetic fields is quite large. The pressure associated with a field of $B = 1$ T is about 4 atm, and with a field of $B = 5$ T is about 100 atm.

Perhaps the simplest realistic example is the equilibrium pinch, in which currents in a cylindrical plasma column produce the magnetic field, and thus the magnetic pressure, that confines the plasma. In cylindrical geometry, with axial and poloidal symmetry, Eqs. (6.1) and (6.2) become

$$-j_z B_\theta = \frac{dp}{dr} \quad (6.9)$$

and

$$\mu_0 j_z = \frac{1}{r} \frac{d}{dr} (r B_\theta) \quad (6.10)$$

Assuming a uniform current distribution $j_z = \text{const}$, $r < a$, Eq. (6.10) can be integrated to obtain

$$B_\theta = \begin{cases} \frac{\mu_0}{2} j_z r, & r \leq a \\ \frac{\mu_0}{2} j_z \frac{a^2}{r}, & r > a \end{cases} \quad (6.11)$$

where $r = a$ is the fixed plasma radius. The equilibrium pressure distribution that is consistent with a uniform current distribution then follows from integration of Eq. (6.9)

$$p(r) = \frac{1}{4} \mu_0 j_z^2 (a^2 - r^2), \quad r < a \quad (6.12)$$

Combining Eq. (6.9) and Eq. (6.10) shows that the momentum balance condition satisfied everywhere in a pinch equilibrium is

$$p + \frac{B^2}{\mu_0} = \text{const} \quad (6.13)$$

which is consistent with Eq. (6.6), since $(\mathbf{B} \cdot \nabla) \mathbf{B} = (B_\theta^2/r) \hat{\mathbf{n}}_r$.

Our treatment of the cylindrical pinch is somewhat idealized in that we have neglected the ends of the cylinders in making the axial symmetry assumption. In the next section we will consider the equilibrium conditions when the straight cylinder is deformed into a torus.

6.2 Axisymmetric Toroidal Equilibria

We consider an axisymmetric, toroidal plasma with a toroidal plasma current. The isobaric surfaces will be nested toroidal surfaces, not necessarily with circular cross section (see Fig. 6.1). We define a function $\psi = \text{const}$ for each isobaric surface such that $2\pi\psi$ is equal to the poloidal magnetic flux passing through a plane extending from the minor (magnetic) axis out to the isobaric surface and encircling the major axis:

$$2\pi\psi \equiv \int_{S_p} \mathbf{B}_p \cdot d\mathbf{s}_p \quad (6.14)$$

The magnetic axis is the innermost (degenerate) isobaric surface. Recalling that both the current and the field lie in the isobaric surfaces, it follows that the value of ψ is independent of the orientation of the plane, although the area subtended by the plane does depend upon the orientation, in general. We will henceforth label the isobaric surfaces according to the corresponding value of ψ and refer to them as flux surfaces.

Now consider the incremental poloidal flux between adjacent flux surfaces (i.e., the poloidal flux passing through the planar ribbon extending from the isobaric surface labeled ψ to the isobaric surface labeled $\psi + d\psi$ and encircling the major axis). Note that the separation, $d\psi$, between adjacent flux surfaces is independent of poloidal orientation, by definition. However, the spatial separation, dr , between adjacent flux surfaces does depend

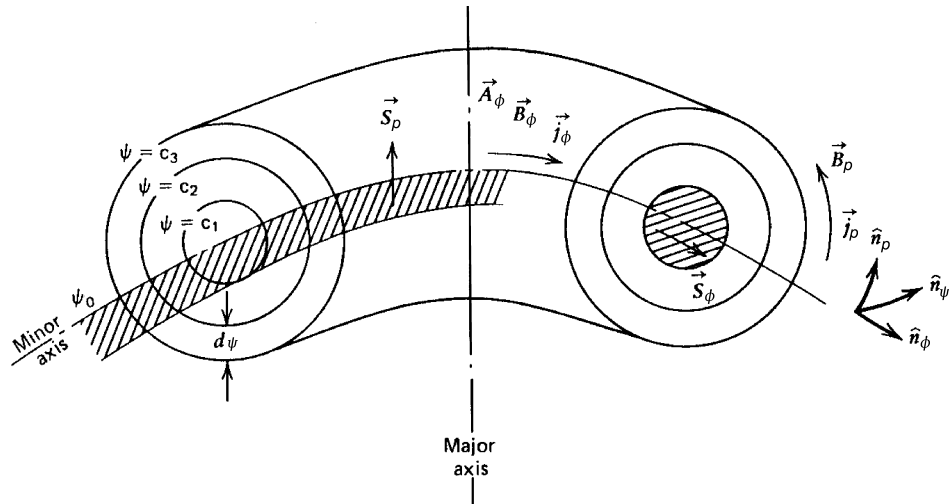


Figure 6.1. Toroidal flux surfaces

upon the poloidal orientation. (Visualizing a contour map of a mountainside may be helpful. The contours are always separated by the same height – $d\psi$ in our case – but the linear separation of the contours on a planar projection will vary with the steepness of the slope.)

$$\begin{aligned} 2\pi(\psi + d\psi) - 2\pi\psi &\equiv \int_{S_p + \delta S_p} \mathbf{B}_p \cdot d\mathbf{s}_p - \int_{S_p} \mathbf{B}_p \cdot d\mathbf{s}_p \\ &= \int_{\delta S_p} \mathbf{B}_p \cdot d\mathbf{s}_p \simeq B_p 2\pi R dr \end{aligned}$$

where R is the major radius from the major axis to the point in question. Thus we see that

$$RB_p = \frac{d\psi}{dr} \equiv |\nabla\psi| \quad (6.15)$$

We are now able to construct a flux surface coordinate system (ψ, χ, ϕ) in which the unit vectors are $\hat{\mathbf{n}}_\psi$ (normal to the flux surface), $\hat{\mathbf{n}}_p$ (in the flux surface and normal to the toroidal direction), and $\hat{\mathbf{n}}_\phi$ (toroidal). Distances in these coordinate directions are $dl_\psi = dr \equiv h_\psi d\psi$, dl_p , and $dl_\phi = R d\phi \equiv h_\phi d\phi$, and the unit vectors are

$$\begin{aligned} \hat{\mathbf{n}}_\psi &= \frac{\nabla\psi}{|\nabla\psi|} = \frac{\nabla\psi}{RB_p} \\ \hat{\mathbf{n}}_p &= \frac{\nabla\phi \times \nabla\psi}{|\nabla\phi \times \nabla\psi|} = \frac{\nabla\phi \times \nabla\psi}{B_p} \end{aligned}$$

and

$$\hat{\mathbf{n}}_\phi = \frac{\nabla\phi}{|\nabla\phi|} = R\nabla\phi \quad (6.16)$$

The volume enclosed by the toroidal flux surface $\psi = \text{const}$ is

$$V(\psi) = \int_{\psi_0}^{\psi} h_\psi d\psi' \oint_{\psi'} dl_p \int_0^{2\pi} h_\phi d\phi = 2\pi \int_{\psi_0}^{\psi} d\psi' \oint_{\psi'} \frac{dl_p}{B_p} \quad (6.17)$$

and the differential volume of the toroidal annulus between ψ and $\psi + d\psi$ is

$$\frac{dV(\psi)}{d\psi} d\psi = 2\pi d\psi \oint_{\psi} \frac{dl_p}{B_p} \equiv 2\pi \hat{V}'(\psi) d\psi \equiv V'(\psi) d\psi \quad (6.18)$$

where ψ_0 labels the magnetic axis. We will henceforth use a prime to denote a derivative with respect to ψ .

Using these results, the magnetic field can be expressed

$$\mathbf{B} = B_\phi + B_p = F\nabla\phi + \nabla\phi \times \nabla\psi \quad (6.19)$$

where

$$F \equiv RB_\phi \quad (6.20)$$

Because, by definition, $p = p(\psi)$, Eq. (6.1) can be written in the flux surface coordinate system as

$$p' \nabla \psi = \mathbf{j} \times \mathbf{B} \quad (6.21)$$

from which we immediately obtain $\mathbf{j} \cdot \nabla \psi = \mathbf{B} \cdot \nabla \psi = 0$. Using the requirement $\mathbf{j} \cdot \nabla \psi = 0$ and Eq. (6.2) leads to

$$0 = (\nabla \times \mathbf{B}) \cdot \frac{\nabla \psi}{|\nabla \psi|} = \frac{1}{h_\phi} \frac{\partial}{\partial l_p} (h_\phi B_\phi) = \frac{1}{R} \frac{\partial F}{\partial l_p} \quad (6.22)$$

We know from axisymmetry that $\partial F / \partial \phi = 0$. Thus we find that $R B_\phi = F = F(\psi)$.

Using Eq. (6.19), the perpendicular current from Eq. (6.5) can be expressed in flux surface coordinates as

$$\mathbf{j}_\perp = \frac{p'}{B^2} \left[F(\nabla \phi \times \nabla \psi) - (RB_p)^2 \nabla \phi \right] \quad (6.23)$$

We conclude immediately that the perpendicular current lies in the flux surface, because $\nabla \psi \cdot \mathbf{j}_\perp = 0$. Thus the total current,

$$\mathbf{j} = \mathbf{j}_\perp + \mathbf{j}_\parallel \quad (6.24)$$

lies in the flux surface, in agreement with our earlier observation.

We now write $\mathbf{j}_\parallel = j_\parallel \hat{\mathbf{n}}_\parallel \equiv j_\parallel \mathbf{B} / B$ and use Eqs. (6.23) and (6.24) in Eq. (6.4) to obtain

$$B_p \frac{\partial}{\partial l_p} \left(\frac{j_\parallel}{B} + p' \frac{F}{B^2} \right) = 0 \quad (6.25)$$

which indicates that the quantity in brackets is a constant on a flux surface, although it may vary with ψ . We evaluate this constant by taking the flux surface average of the quantity in brackets, after multiplying through by B^2 , to obtain finally an expression for the current parallel to the magnetic field

$$\mathbf{j}_\parallel = \left[-\frac{p' F}{B} \left(1 - \frac{B^2}{\langle B^2 \rangle} \right) + \frac{B \langle j_\parallel B \rangle}{\langle B^2 \rangle} \right] \hat{\mathbf{n}}_\parallel \quad (6.26)$$

We have defined the flux surface average of a quantity A by

$$\langle A \rangle_\psi \equiv \oint_\psi \frac{A \, dl_p}{B_p} / \oint_\psi \frac{dl_p}{B_p} = \oint_\psi \frac{A \, dl_p}{B_p} / V'(\psi) \quad (6.27)$$

(We suppress the ψ subscript until its use is required for clarity.) Equation (6.26) contains an unknown constant, $\langle j_\parallel B \rangle$, that must be evaluated from more fundamental considerations involving the overall mass flow of the plasma.

We can construct the toroidal and poloidal currents in the flux surface from Eqs. (6.23) and (6.26).

$$j_\phi \equiv \hat{\mathbf{n}}_\phi \cdot \mathbf{j}_\perp + \hat{\mathbf{n}}_\phi \cdot \mathbf{j}_\parallel = -R \left(1 - \frac{B_\phi^2}{\langle B^2 \rangle} \right) p' + \frac{B_\phi \langle j_\parallel B \rangle}{\langle B^2 \rangle} \quad (6.28)$$

and

$$j_p \equiv \hat{\mathbf{n}}_p \cdot \mathbf{j}_\perp + \hat{\mathbf{n}}_p \cdot \mathbf{j}_\parallel = \frac{B_p F p'}{\langle B^2 \rangle} + \frac{B_p \langle j_\parallel B \rangle}{\langle B^2 \rangle} \quad (6.29)$$

These currents must be consistent with Ampère's law. The toroidal and poloidal components of Eq. (6.2), in flux surface coordinates, are

$$j_\phi = \frac{R}{\mu_0} \nabla \cdot R^{-2} \nabla \psi \quad (6.30)$$

and

$$j_p = -\frac{B_p}{\mu_0} F' \quad (6.31)$$

Equating Eqs. (6.29) and (6.31) results in the equation that must be satisfied by $F(\psi)$,

$$F' = -\mu_0 \left(\frac{F p'}{\langle B^2 \rangle} + \frac{\langle j_\parallel B \rangle}{\langle B^2 \rangle} \right) \quad (6.32)$$

Equating Eqs. (6.28) and (6.30) and using Eq. (6.32) leads to the Grad–Shafranov equation, which governs ψ ,

$$\nabla \cdot R^{-2} \nabla \psi = -\mu_0 p'(\psi) - \frac{F(\psi) F'(\psi)}{R^2} \quad (6.33)$$

Once p' and $\langle j_\parallel B \rangle$ are known, the flux surface topology, $\psi(R, z, \phi)$, in a Euclidian coordinate system can be found by solving Eq. (6.33). The pressure can be determined by solving one of the second moment equations that were derived in the previous chapter.

Equation (6.33) can be integrated to obtain an overall force balance on the plasma. First, we integrate it over the differential volume in the toroidal annulus between adjacent flux surfaces ψ and $\psi + d\psi$ to obtain

$$\frac{\partial}{\partial \psi} \left[\hat{V}'(\psi) \langle B_p^2 \rangle_\psi \right] = -\hat{V}'(\psi) \left[\mu_0 p'(\psi) + \langle R^{-2} \rangle_\psi F(\psi) F'(\psi) \right] \quad (6.34)$$

where we now explicitly denote the flux surface over which the average is taken. Integrating Eq. (6.34) from an arbitrary flux surface, ψ' , to the outermost flux surface, ψ_a , at the plasma surface yields an expression for the pressure on flux surface, ψ' ,

$$\begin{aligned} p(\psi') &= p(\psi_a) + \frac{1}{\mu_0} \left(\langle B_p^2 \rangle_{\psi_a} - \langle B_p^2 \rangle_{\psi'} \right) \\ &+ \frac{1}{\mu_0} \int_{\psi'}^{\psi_a} \frac{\langle B_p^2 \rangle_\psi}{V'(\psi)} \frac{\partial V'(\psi)}{\partial \psi} d\psi + \int_{\psi'}^{\psi_a} \frac{\langle R^{-2} \rangle_\psi}{2\mu_0} \frac{\partial F^2(\psi)}{\partial \psi} d\psi \end{aligned} \quad (6.35)$$

Now Eq. (6.35) can be integrated over the volume of the plasma to obtain an expression for the volume-averaged pressure that can be supported by a given magnetic field and current configuration,

$$\bar{p} = p(\psi_a) + \frac{1}{2\mu_0} \left[\langle B_p^2 \rangle_{\psi_a} + (\langle B_\phi^2 \rangle_{\psi_a} - \hat{B}_\phi^2) \right] + \frac{1}{2\mu_0} \int_{\psi_0}^{\psi_a} \frac{V(\psi)}{V(\psi_a)} \times \left(\langle B_p^2 \rangle_\psi \frac{\partial}{\partial \psi} \ln \left\{ \frac{[\hat{V}'(\psi)]^2 \langle B_p^2 \rangle_\psi}{V(\psi)} \right\} - F^2(\psi) \frac{\partial}{\partial \psi} \langle R^{-2} \rangle_\psi \right) d\psi \quad (6.36)$$

We have defined the volume average pressure

$$\bar{p} \equiv \int_{\psi_0}^{\psi_a} p(\psi) \hat{V}'(\psi) d\psi / \int_{\psi_0}^{\psi_a} \hat{V}'(\psi) d\psi \quad (6.37)$$

$$\langle B_\phi^2 \rangle_{\psi_a} \equiv \langle R^{-2} \rangle_{\psi_a} F^2(\psi_a) \quad (6.38)$$

and

$$\hat{B}_\phi^2 \equiv \int_{\psi_0}^{\psi_a} \langle R^{-2} \rangle_\psi F^2(\psi) \hat{V}'(\psi) d\psi / \int_{\psi_0}^{\psi_a} \hat{V}'(\psi) d\psi \quad (6.39)$$

The first term in Eq. (6.36) is the kinetic pressure at the plasma surface, which vanishes unless the plasma is immersed in a surrounding gas. The last term in Eq. (6.36) vanishes in the limit in which the major radius of the torus becomes very large relative to the plasma radius; it introduces corrections to the pressure balance due to the toroidal geometry. Thus we see that the average kinetic pressure, \bar{p} , is principally balanced by the magnetic pressure associated with the poloidal field, $\langle B_p^2 \rangle_{\psi_a} / 2\mu_0$. The toroidal field contributes to the pressure balance only to the extent that the toroidal field within the plasma is affected by the poloidal currents, j_p , so that the volume average, \hat{B}_ϕ^2 , differs from the average over the plasma surface, $\langle B_\phi^2 \rangle_{\psi_a}$.

A plasma is paramagnetic when $\langle B_\phi^2 \rangle_{\psi_a} - \hat{B}_\phi^2 < 0$ and is diamagnetic when $\langle B_\phi^2 \rangle_{\psi_a} - \hat{B}_\phi^2 > 0$. The paramagnetic and diamagnetic conditions can be shown to correspond to

$$F(\psi) F'(\psi) < 0, \quad \text{paramagnetic}$$

and

$$F(\psi) F'(\psi) > 0, \quad \text{diamagnetic}$$

From Eq. (6.36), we see that paramagnetism decreases and that diamagnetism increases the average plasma pressure associated with a given toroidal plasma current.

Because it is primarily the poloidal magnetic pressure that balances the kinetic pressure, it is useful to define

$$\bar{\beta}_p \equiv \frac{\bar{p}}{\langle B_p^2 \rangle_{\psi_a} / 2\mu_0} \simeq 1 + \frac{\langle B_\phi^2 \rangle_{\psi_a} - \hat{B}_\phi^2}{\langle B_p^2 \rangle_{\psi_a}} \quad (6.40)$$

where Eq. (6.36) with $p(\psi_a) = 0$ has been used in the last step. We see from Eq. (6.40) that $\bar{\beta}_p > 1$ corresponds to a diamagnetic plasma and that $\bar{\beta}_p < 1$ corresponds to a paramagnetic plasma.

In a paramagnetic plasma, the poloidal currents increase the toroidal magnetic field relative to its value in the absence of the plasma. This reduces the allowable plasma kinetic pressure relative to the allowable value if the vacuum toroidal field was present. The converse is true for a diamagnetic plasma, in which the poloidal current decreases the toroidal field and increases the allowable pressure.

Now we return to Fig. 6.1 and define the toroidal magnetic flux across the cross sectional area with $\phi = \text{const}$, $S_\phi(\psi)$, bounded by the flux surface $\psi = \text{const}$,

$$\Phi(\psi) = \int_{S_\phi(\psi)} B_\phi \cdot d\mathbf{s}_\phi \quad (6.41)$$

The differential toroidal flux in the “flux tube” between ψ and $\psi + d\psi$ is

$$d\Phi(\psi) = \int_{S\phi+\delta S_\phi} B_\phi \cdot d\mathbf{s}_\phi - \int_{S_\phi} B_\phi \cdot d\mathbf{s}_\phi \simeq d\psi \oint_\psi h_\psi B_\phi dl_p \quad (6.42)$$

Using our previous results, we can define the ratio of toroidal to poloidal fluxes through the differential volume between adjacent flux surfaces ψ and $\psi + d\psi$

$$q(\psi) \equiv \frac{d\Phi(\psi)}{2\pi d\psi} = \frac{1}{2\pi} \oint_\psi \frac{B_\phi dl_p}{RB_p} = \frac{F(\psi)\hat{V}'(\psi)}{2\pi} \langle R^{-2} \rangle_\psi \quad (6.43)$$

We will find that this q corresponds to the safety factor that we have defined in terms of the pitch of the helical field lines in chapter 3.

Finally, we note that the magnetic field can always be derived from a vector potential, \mathbf{A} , and in particular that

$$\mathbf{B}_p = \nabla \times (A_\phi \hat{\mathbf{n}}_\phi) \quad (6.44)$$

since \mathbf{A} is collinear with the current and there is no current across flux surfaces in the $\hat{\mathbf{n}}_\psi$ direction. Using Eq. (6.44) in Eq. (6.14), we find

$$2\pi\psi = \int_{S_p} \nabla \times (A_\phi \hat{\mathbf{n}}_\phi) \cdot d\mathbf{s}_p = \oint A_\phi \hat{\mathbf{n}}_\phi \cdot d\mathbf{l} = 2\pi(RA_\phi - R_0A_{\phi 0}) \quad (6.45)$$

where the line integral is around the plane S_p shown in Fig. 6.1, and the zero subscript refers to the magnetic axis. Thus the flux surface function, ψ , is related to the vector potential. This result is in agreement with our previous discussion of flux surfaces in chapter 2 (see Eq. (2.73)).

In general, the solution of the Grad–Shafranov Eq. (6.33) for the flux surface geometry and the associated equations of this section must be carried out numerically. A typical solution for the flux surfaces in an elongated tokamak plasma is illustrated in Fig. 6.2.

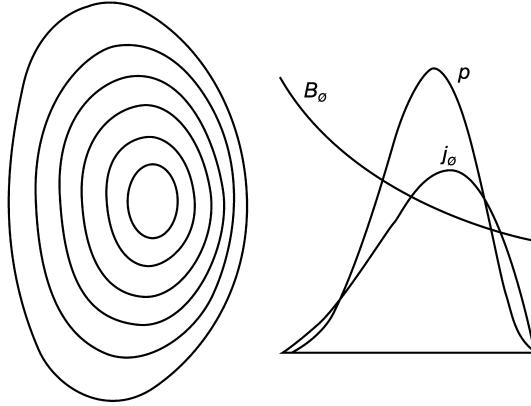


Figure 6.2. Equilibrium flux surfaces, toroidal magnetic field and current density, and pressure in a representative elongated tokamak plasma

6.3 Large Aspect Ratio Tokamak Equilibria

Although solution of the Grad–Shafranov equation for the magnetic flux surface is carried out numerically in practice, it is useful to develop an approximate solution that provides physical insight. In the limit $\epsilon \equiv r/R \ll 1$, it is possible to develop some useful analytical solutions for the equilibria in axisymmetric toroidal plasmas. In this limit, the solution of Eq. (6.33) for the flux surface function, ψ , outside the plasma surface can be written in a form that is independent of the current and pressure distributions within the plasma. In a toroidal (r, θ, ϕ) coordinate system, the solution is

$$2\pi\psi(r, \theta) = -\mu_0 IR \left(\ln \frac{8R}{r} - 2 \right) + \left[-\frac{1}{2}\mu_0 I \left(\ln \frac{8R}{r} - 1 \right) r + \frac{c_1}{r} + c_2 r \right] \cos \theta, \quad r \geq a \quad (6.46)$$

where I is the total toroidal plasma current and c_1 and c_2 are constants to be determined.

The flux surfaces are circles, in this approximation, with centers that are displaced from the minor axis ($r = 0$) by

$$\Delta(r) = -\frac{r^2}{2R} \left(\ln \frac{8R}{r} - 1 \right) + \frac{1}{\mu_0 IR} (c_1 + c_2 r^2) \quad (6.47)$$

From the relationship between the flux function and the vector potential that was discussed at the end of the previous section, we find that the magnetic field in the $r-\theta$ plane can be derived from

$$\mathbf{B} = \nabla \times \left(\frac{\psi}{R} \right) \hat{n}_\phi \quad (6.48)$$

Thus the field outside the plasma is

$$B_\theta \equiv \frac{1}{R} \frac{\partial \psi}{\partial r} = \frac{1}{2\pi} \left[\frac{\mu_0 I}{r} + \frac{1}{R} \left(-\frac{1}{2}\mu_0 I \ln \frac{8R}{r} - \frac{c_1}{r^2} + c_2 \right) \cos \theta \right] \quad (6.49)$$

and

$$B_r \equiv -\frac{1}{R} \frac{1}{r} \frac{\partial \psi}{\partial \theta} = \frac{1}{2\pi R} \left[-\frac{1}{2} \mu_0 I \left(\ln \frac{8R}{r} - 1 \right) + \frac{c_1}{r^2} + c_2 \right] \sin \theta \quad (6.50)$$

This model can help us understand the confinement properties of toroidal plasmas. If the flux function is due entirely to the current flowing in the plasma – that is, there are no external fields – then the natural boundary condition $\psi(r \rightarrow \infty) \rightarrow 0$ requires that $c_2 \equiv 0$. The other boundary condition on ψ , at the plasma surface $r = a$, is the vanishing of the normal component of the magnetic field because the plasma boundary is a flux surface. Requiring $B_r(r = a) = 0$ in Eq. (6.50) leads to

$$c_1 = \frac{\mu_0 I}{2a^2} \left(\ln \frac{8R}{a} - 1 \right) \quad (6.51)$$

In this case, Eq. (6.49) evaluated at the plasma surface is

$$B_\theta(a, \theta) = \frac{\mu_0 I}{2\pi a} \left[1 - \frac{a}{R} \left(\ln \frac{8R}{a} - \frac{1}{2} \right) \cos \theta \right] \quad (6.52)$$

If we now make the assumption that the plasma is a perfect conductor, we can arrive at some useful qualitative insights. Since there is no magnetic field within a perfect conductor, the magnetic pressure, $B_p^2/2\mu_0$, just outside the plasma surface must be balanced by the plasma kinetic pressure, $p(a)$, just inside the plasma surface. Because the plasma pressure is constant on a flux surface and the plasma surface is a flux surface, the kinetic pressure is uniform around the plasma surface $0 \leq \theta \leq 2\pi$. However, the magnetic pressure is obviously (Eq. (6.52)) nonuniform around the plasma surface, being stronger on the inside at $\theta = \pi$ than on the outside at $\theta = 0$, as indicated in Fig. 6.3(a). Thus if the plasma and magnetic pressures were balanced on the average (i.e., satisfied Eq. (6.36)), there would be a net force on the plasma directed radially outward. It is necessary to eliminate this net force by adding a vertical field, as indicated in Fig. 6.3(b), to strengthen the

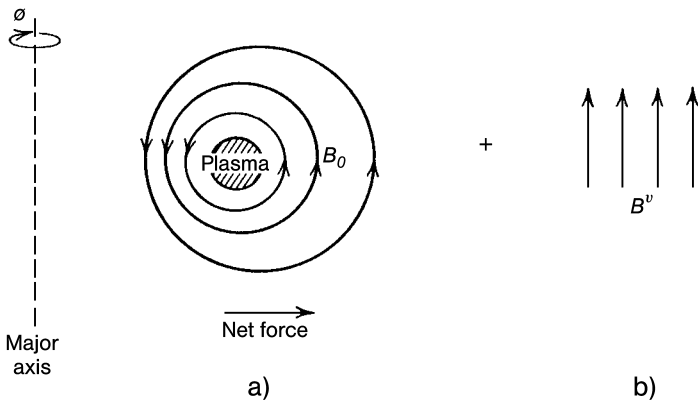


Figure 6.3. Magnetic fields affecting plasma equilibrium

poloidal field on the outside of the torus ($\theta = 0$) and to weaken the poloidal field on the inside of the torus ($\theta = \pi$). This vertical field, B^v , must be provided by coils or a conducting shell located external to the plasma.

Now we reformulate the solution under the assumption that the approximate solution to the Grad–Shafranov equation given by Eq. (6.46) consists of a component due to the currents in the external coils or conducting shell and a component due to the plasma, $\Psi_p = \Psi - \Psi_e$.

$$\Psi_e = c_2 r \cos \theta \quad (6.53)$$

The constants c_1 and c_2 are now determined by requiring that the normal component of the field (B_r) vanishes at the plasma surface and that the tangential component of the field (B_θ) is continuous across the plasma surface. Defining the plasma internal inductance per unit length,

$$l_i \equiv \int_0^{2\pi} d\theta \int_0^a dr \left(B_\theta^2 r / \pi a^2 \langle B_\theta^2 \rangle_{\Psi_a} \right) \quad (6.54)$$

and the parameter

$$\Lambda \equiv \beta_p + \frac{1}{2} l_i - 1 \quad (6.55)$$

the flux surface functions outside the plasma can be written

$$2\pi \Psi_e = \frac{\mu_0 I}{2} \left(\ln \frac{8R_0}{a} + \Lambda - \frac{1}{2} \right) r \cos \theta \quad (6.56)$$

and

$$2\pi \Psi_p = -\mu_0 I R_0 \left(\ln \frac{8R_0}{r} - 2 \right) + \frac{1}{2} \mu_0 I \left[-\ln \frac{8R_0}{r} + 1 - \frac{a^2}{r^2} \left(\Lambda + \frac{1}{2} \right) \right] r \cos \theta \quad (6.57)$$

The components of the field due to the external coils in an (R, z, ϕ) coordinate system, with z the direction along the major axis measured relative to the horizontal symmetry plane, are

$$B_R^v = -\frac{1}{R} \frac{\partial \Psi_e}{\partial z} = -\frac{\mu_0 I}{4\pi R} \left(\ln \frac{8R_0}{a} + \Lambda - \frac{1}{2} \right) \tan \theta, \quad r > a \quad (6.58)$$

and

$$B_z^v = \frac{1}{R} \frac{\partial \Psi_e}{\partial R} = \frac{\mu_0 I}{4\pi R} \left(\ln \frac{8R_0}{a} + \Lambda - \frac{1}{2} \right), \quad r > a \quad (6.59)$$

where we have made use of the relationships (see Fig. 6.4)

$$\begin{aligned} R &= R_0 + r \cos \theta \\ z &= r \sin \theta \end{aligned} \quad (6.60)$$

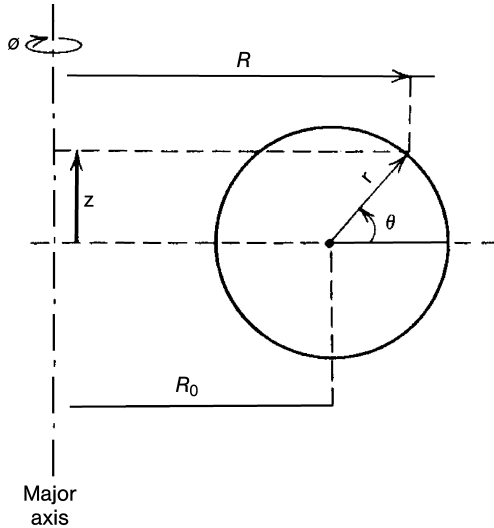


Figure 6.4. Relation of (R, z, θ) and toroidal (r, θ, ϕ) coordinate systems

We now use this model to examine the stability of the plasma equilibrium to vertical (z -direction) and horizontal (R -direction) axisymmetric displacements. If the vertical field lines (due to the external coils) are slightly concave towards the major axis, the interaction of the R -component of the field with the current will produce a restoring force $\mathbf{F} \sim \mathbf{I} \times \mathbf{B}_R$ that opposes the displacement. The requirement that the field be concave can be written as a requirement upon the field index, n (see Fig. 6.5)

$$n \equiv -\frac{R}{B^v} \frac{\partial B^v}{\partial R} > 0 \quad (6.61)$$

When the plasma is vertically elongated, instead of circular, the requirement for stability against vertical displacement is more complex. For an elliptical plasma cross section and a uniform current distribution, the height to width ratio, b/a , is related to the field index, n , in such a way that satisfaction of Eq. (6.61) requires

$$\frac{b}{a} - 1 < \left(\frac{a}{R}\right)^2 \left(\frac{3}{4} \ln \frac{8R}{a} - \frac{17}{16}\right) \quad (6.62)$$

placing an upper limit on the allowable elongation. A perfectly conducting wall (or a feedback stabilization system that simulates one) can stabilize this axisymmetric, vertical displacement instability if the height (b') and width (a') of the conducting wall satisfies

$$\frac{b+a}{b-a} > \left(\frac{b'+a'}{b+a}\right)^2 \quad (6.63)$$

Next we consider a horizontal axisymmetric displacement of the plasma column. At equilibrium, the interaction of the z -component of the external field and the plasma current

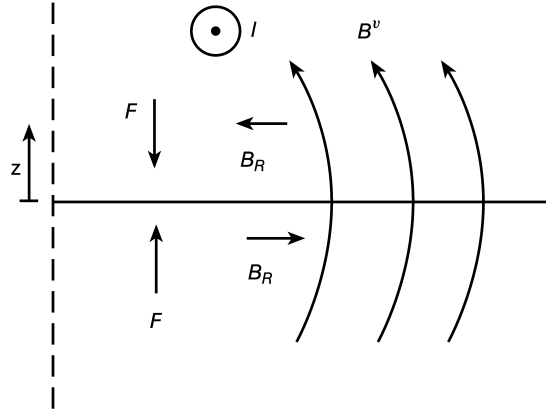


Figure 6.5. Restoring force against vertical displacement

produces a radially inward directed force that just offsets the imbalance in the plasma pressure and poloidal magnetic field pressure,

$$F_R = -IRB_z^v \quad (6.64)$$

The variation of this force with radial position is given by

$$\frac{\partial F_R}{\partial R} = -\left(\frac{\partial I}{\partial R}RB_z^v + IB_z^v + IR\frac{\partial B_z^v}{\partial R}\right) = -IB_z\left(\frac{R}{I}\frac{\partial I}{\partial R} + 1 - n\right) \quad (6.65)$$

If we assume that the magnetic flux within the plasma is unchanged during the displacement, then $n < \frac{3}{2}$ is sufficient to ensure that $\partial F_R / \partial R < 0$ and, thus, that there is a restoring force against horizontal displacements.

Hence we can express the condition for stability of the equilibrium against axisymmetric, or rigid-body, displacements in terms of the field index:

$$0 < n < \frac{3}{2} \quad (6.66)$$

In the limit $R/a \gg 1$, $\bar{\beta}_p \simeq 1$, the flux functions are almost circles $\Psi = r = \text{const}$ and the fields can be approximated by

$$B_\phi(r, \theta) = \frac{B_\phi^0}{1 + \epsilon \cos \theta} \quad B_\theta(r, \theta) = \frac{B_\theta^0}{1 + \epsilon \cos \theta} \quad (6.67)$$

Many of the integral parameters that were defined in the previous section to characterize the equilibrium take on a simple form in this limit. The average β and β_p are

$$\bar{\beta} = \bar{p}/\left(B_\phi^0\right)^2/2\mu_0 \quad (6.68)$$

$$\bar{\beta}_p = \bar{p}/[B_p(a)]^2/2\mu_0 \quad (6.69)$$

Equation (6.2) can be integrated over the plasma cross section (r, θ) to obtain

$$\mu_0 I = \mu_0 \int \mathbf{j}_\phi \cdot d\mathbf{s} = \int \nabla \times \mathbf{B} \cdot d\mathbf{s} = \oint \mathbf{B} \cdot d\mathbf{l}_p = 2\pi al B_p(a) \quad (6.70)$$

where l is the ratio of the poloidal plasma circumference to the circumference of the inscribed circle of radius a .

The function q defined by Eq. (6.43) becomes

$$q(r) = \frac{RB_\phi}{2\pi} \oint \frac{dl_p}{R^2 B_p} = \frac{rlB_\phi}{RB_p(r)} \quad (6.71)$$

which we recognize as the safety factor that was introduced in chapter 3.

Combining Eqs. (6.70) and (6.71) leads to a relation between the plasma current and the toroidal field

$$\mu_0 I = \frac{2\pi(al)^2}{q(a)R} B_\phi^0 \quad (6.72)$$

The plasma momentum balance of Eq. (6.36) becomes

$$\bar{p} = \bar{\beta}_p \frac{1}{2\mu_0} [B_p(a)]^2 = \bar{\beta}_p \frac{\mu_0}{8\pi^2} \left(\frac{I}{al} \right)^2 \quad (6.73)$$

from which we see that, in this approximation, the maximum plasma pressure that can be supported is proportional to the square of the plasma current, which in turn is proportional to the square of the toroidal field.

We have made a number of approximations in this section to reduce the results of the equilibrium analysis to a form that is amenable to direct interpretation. In practice, properties of the equilibrium are evaluated by solving numerically the Grad–Shafranov equation and then performing the appropriate integrals.

If the external vertical field is provided by a conducting shell, then the shape of the shell defines the outermost flux surface, ψ_a , that is, provides a natural boundary condition for the Grad–Shafranov equation. Early tokamaks had a conducting shell, but most present and planned tokamaks use an external coil system to provide the vertical field. When an external coil system is used, the shape of the plasma boundary flux surface is determined jointly by the current distributions in the plasma and among the external coils.

Figure 6.6 illustrates the flux and current contours in a circular plasma with $q(a) = 3$ corresponding to three different levels of the parameter $\bar{\beta}$. The flux functions due to the plasma current, $\psi_p = \psi_{\text{int}}$, and due to the external coils, $\psi_e = \psi_{\text{ext}}$, are shown. The major axis is to the left in these figures. It is clear that as the ratio of plasma to magnetic pressure, $\bar{\beta}$, is increased, the flux surfaces deform from circles and are displaced outward. A corresponding outward displacement of the toroidal current density occurs.

6.4 Safety Factor

In an axisymmetric equilibrium each magnetic field line has a value of q , the safety factor. The field line follows a helical path as it goes round the torus. If at some toroidal angle, ϕ ,

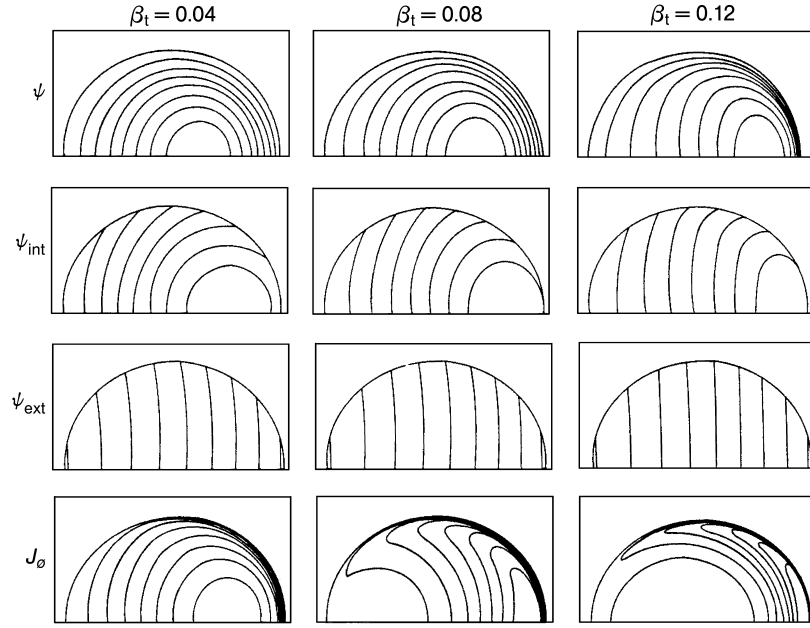


Figure 6.6. Toroidal equilibria for a circular plasma with $q(a) = 3$ and aspect ratio $R/a = 3$

the field line has a certain position in the poloidal plane, it will return to that position in the poloidal plane after change of toroidal angle $\Delta\phi$. The q -value of this field line is defined by

$$q = \frac{\Delta\phi}{2\pi} \quad (6.74)$$

If a magnetic field line returns to its starting position after exactly one toroidal rotation, then $q = 1$. If more than one rotation in ϕ is required, it has a higher value of q .

Rational values of q play an important role in stability. If $q = m/n$, where m and n are integers, the field line “bites its tail” after m toroidal and n poloidal rotations round the torus.

The equation of the field line is

$$\frac{R d\phi}{ds} = \frac{B_\phi}{B_p} \quad (6.75)$$

where ds is the distance moved in the poloidal direction while moving a toroidal distance $R d\phi$, and B_p and B_ϕ are the poloidal and toroidal magnetic fields. Thus from Eq. (6.74)

$$q = \frac{1}{2\pi} \oint \frac{1}{R} \frac{B_\phi}{B_p} ds \quad (6.76)$$

where the integral is carried out over a single poloidal circuit around the flux surface.

It is clear from Eq. (6.74) that q is the same for all magnetic field lines on a magnetic surface; i.e., $q = q(\psi)$ is a flux function.

For a large aspect ratio tokamak of circular cross section Eq. (6.74) becomes

$$q = \frac{rB_\phi}{R_0B_\theta} \quad (6.77)$$

where B_θ is the poloidal magnetic field.

The radial profile of q usually has a minimum value at the magnetic axis and increases outwards. In the case of large aspect ratio and circular cross section the behavior of q is simply determined by the toroidal current density profile, $j(r)$. Writing Ampère's law in the form

$$2\pi r B_\theta = \mu_0 I(r) \quad (6.78)$$

where the current inside r is

$$I(r) = 2\pi \int_0^r j(r')r' dr' \quad (6.79)$$

and using Eq. (6.77) for q yields

$$q(r) = \frac{2\pi r^2 B_\phi}{\mu_0 I(r) R} \quad (6.80)$$

The edge ($r = a$) value of q is

$$q_a = \frac{2\pi a^2 B_\phi}{\mu_0 I R} \quad (6.81)$$

where I is the total current. The central ($r = 0$) value of q is obtained by taking the limit $r \rightarrow 0$ in Eq. (6.80). In this limit $I(r) = \pi r^2 j_0$, where $j_0 = j(0)$, so

$$q_0 = \frac{2B_\phi}{\mu_0 j_0 R} \quad (6.82)$$

Equations (6.81) and (6.82) yield

$$\frac{q_a}{q_0} = \frac{\pi a^2 j_0}{I} = \frac{j_0}{\langle j \rangle_a} \quad (6.83)$$

where $\langle j \rangle_a$ is the average current density over the whole plasma.

Equation (6.80) can be written

$$q(r) = \frac{2B_\phi}{\mu_0 \langle j \rangle_r R} \quad (6.84)$$

where $\langle j \rangle_r$ is the average current density inside the radius r

$$\langle j \rangle_r = \frac{\int_0^r j(r')r' dr'}{r^2/2} \quad (6.85)$$

Differentiating Eq. (6.84) with respect to r yields

$$\frac{q'}{q} = -\frac{\langle j \rangle'_r}{\langle j \rangle_r} \quad (6.86)$$

It follows from Eq. (6.85) that $\langle j \rangle'_r = 2(j - \langle j \rangle_r)/r$. Since a monotonically decreasing current profile has $j < \langle j \rangle_r$, it is seen from Eq. (6.86) that such a current profile has $q' > 0$.

The general behavior of q described above pertains also for non-circular plasmas. The “ q -cylindrical” approximation

$$q_{\text{cyl}} = \frac{2\pi abB_\phi}{\mu_0 IR} \quad (6.87)$$

is defined by analogy with Eq. (6.81), where a and b are the half-width and half-height of the plasma.

A simple model for $q(r)$ is provided by the current distribution

$$j = j_0(1 - r^2/a^2)^\nu \quad (6.88)$$

Ampère's law, $\mu_0 j = (1/r) d(rB_\theta)/dr$, then gives

$$B_\theta = \frac{\mu_0 j_0 a^2}{2(\nu + 1)r} \left[1 - (1 - r^2/a^2)^{\nu+1} \right] \quad (6.89)$$

Using Eq. (6.89) in Eq. (6.77), leads to

$$q(r) = \frac{2(\nu + 1)}{\mu_0 j_0} \frac{B_\phi}{R} \frac{r^2/a^2}{1 - (1 - r^2/a^2)^{\nu+1}} \quad (6.90)$$

With this model

$$\frac{q(a)}{q(0)} = \nu + 1 \quad (6.91)$$

In divertor configurations (see chapter 14) in which the core plasma is enclosed by a separatrix, the q -profile is fundamentally different. The value of q for field lines close to the separatrix is dominated by the contribution close to the X-point. The poloidal magnetic field, B_p , has a null at the X-point, and locally its magnitude is proportional to the distance from the X-point. The magnetic geometry around the X-point is illustrated in Fig. 6.7. The expression in Eq. (6.76) for q has B_p in the denominator of the integrand, which leads to a logarithmic contribution. Defining the shortest distance of a flux surface from the X-point as d , the limiting form of q as $d \rightarrow 0$ is

$$q \rightarrow \frac{B_\phi}{\pi R |\nabla B_p|} \ln \frac{L}{d} (d \rightarrow 0) \quad (6.92)$$

where L is a length characterizing the overall geometry. As the separatrix is approached, $q \rightarrow \infty$ because the smallness of B_p around the X-point inhibits the poloidal displacement of the field lines. The field lines on surfaces close to the separatrix spend almost their entire trajectory close to the X-point.

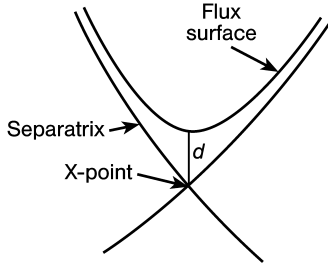


Figure 6.7. Geometry of the flux surface around the X-point when the plasma is bounded by a separatrix

6.5 Shafranov Shift*

For low- β , large aspect ratio tokamak plasmas of nearly circular cross section, the ordering of quantities in terms of the inverse aspect-ratio, $\epsilon = a/R$, is

$$\begin{aligned} B_\phi &= B_{\phi 0}(R_0/R)(1 + O(\epsilon^2)) & B_\theta &\sim \epsilon B_{\phi 0} \\ j_\phi &\sim \epsilon B_{\phi 0}/\mu_0 a & j_\theta &\sim \epsilon^2 B_{\phi 0}/\mu_0 a \\ p &\sim \epsilon^2 B_{\phi 0}^3/\mu_0, (\beta \sim \epsilon^2) & \beta_p &\sim 1 \end{aligned} \quad (6.93)$$

where $B_{\phi 0}$ is the vacuum toroidal magnetic field at the major radius of the plasma, R_0 . The plasma pressure balance equation in the cylindrical limit is

$$\frac{dp}{dr} = j_\phi B_\theta - j_\theta B_\phi \quad (6.94)$$

The equilibrium is specified by $j_\phi(r)$ and $p(r)$ with $p(a) = 0$. The azimuthal field is given by Ampère's law

$$\mu_0 j_\phi = -\frac{1}{r} \frac{d}{dr}(r B_\theta) \quad (6.95)$$

and j_θ is then determined by Eq. (6.94). The flux surfaces are concentric circles in the cylindrical limit.

When toroidal effects are included, the flux surfaces form non-concentric circles as illustrated in Fig. 6.8. Using the toroidal coordinate system shown in Fig. 6.8 the Grad-Shafranov Eq. (6.33) may be written

$$\begin{aligned} \left(\frac{1}{r} \frac{\partial}{\partial r} r \frac{\partial}{\partial r} + \frac{1}{r^2} \frac{\partial^2}{\partial \theta^2} \right) \psi - \frac{1}{R_0 + r \cos \theta} \left(\cos \theta \frac{\partial}{\partial r} - \sin \theta \frac{1}{r} \frac{\partial}{\partial \theta} \right) \psi \\ = -\mu_0 (R_0 + r \cos \theta)^2 p'(\psi) - \mu_0^2 F(\psi) F'(\psi) \end{aligned} \quad (6.96)$$

We expand ψ in ϵ ,

$$\psi = \psi_0(r) + \psi_1(r, \theta) \quad (6.97)$$

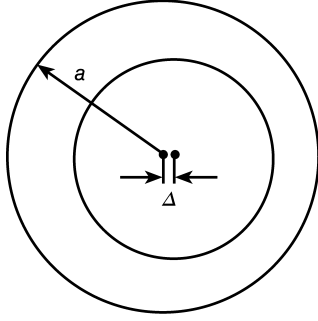


Figure 6.8. Circular flux surface displaced by a distance Δ with respect to the outer flux surface whose center is at a distance R_0 from the major axis

The flux function ψ_0 is given by the leading order part of Eq. (6.96) corresponding to Eq. (6.94)

$$\frac{1}{r} \frac{d}{dr} \left(r \frac{d\psi_0}{dr} \right) = -\mu_0 R_0^2 p'(\psi_0) - \mu_0^2 F(\psi_0) F'(\psi_0) \quad (6.98)$$

and ψ_1 satisfies the first-order part of Eq. (6.96)

$$\begin{aligned} & \left(\frac{1}{r} \frac{\partial}{\partial r} r \frac{\partial}{\partial r} + \frac{1}{r^2} \frac{\partial^2}{\partial \theta^2} \right) \psi_1 - \frac{\cos \theta}{R_0} \frac{d\psi_0}{dr} \\ &= -\mu_0 R_0^2 p''(\psi_0) \psi_1 - \mu_0^2 (F(\psi_0) F'(\psi_0))' \psi_1 \\ & \quad - 2\mu_0 R_0 r \cos \theta p'(\psi_0) \\ &= -\frac{d}{dr} (\mu_0 R_0^2 p'(\psi_0) + \mu_0^2 F(\psi_0) F'(\psi_0)) \frac{dr}{d\psi_0} \psi_1 \\ & \quad - 2\mu_0 R_0 r \cos \theta p'(\psi_0) \end{aligned} \quad (6.99)$$

If the flux surface ψ is displaced a distance $\Delta(\psi_0(r))$, ψ may be written

$$\psi = \psi_0 + \psi_1 = \psi_0 - \Delta(r) \frac{\partial \psi_0}{\partial R} = \psi_0 - \Delta(r) \cos \theta \frac{d\psi_0}{dr} \quad (6.100)$$

Using this form for ψ_1 in Eq. (6.99) leads to

$$\begin{aligned} & -\Delta \frac{d}{dr} \left[\frac{1}{r} \frac{d}{dr} \left(r \frac{d\psi_0}{dr} \right) \right] - \frac{1}{r} \left(\frac{dr}{d\psi_0} \right) \frac{d}{dr} \left[r \left(\frac{d\psi_0}{dr} \right)^2 \frac{d\Delta}{dr} \right] - \frac{1}{R_0} \frac{d\psi_0}{dr} \\ &= \Delta \frac{d}{dr} (\mu_0 R_0^2 p'(\psi_0) + \mu_0^2 F(\psi_0) F'(\psi_0)) - 2\mu_0 R_0 r \frac{dp_0}{dr} \frac{dr}{d\psi_0} \end{aligned} \quad (6.101)$$

From Eq. (6.98), the first terms on the two sides of Eq. (6.101) cancel, leaving

$$\frac{d}{dr} \left(r B_{\theta 0}^2 \frac{d\Delta}{dr} \right) = \frac{r}{R_0} \left(2\mu_0 r \frac{dp_0}{dr} - B_{\theta 0}^2 \right) \quad (6.102)$$

where the definition of the flux function given by Eq. (6.48) has been used to replace $(d\psi_0/dr)/R_0$ by $B_{\theta 0}$.

The solution of the differential equation, Eq. (6.102), with $d\Delta/dr = 0$ at $r = 0$ and $\Delta(a) = 0$ gives the displacement $\Delta(r)$ of the flux surfaces for a leading order pressure $p_0(r)$ and poloidal magnetic field $B_{\theta 0}(r)$. Together with Eq. (6.100), the solution of Eq. (6.102) provides the solution for $\psi(r, \theta)$.

It is seen that the centers of the magnetic flux surfaces are displaced with respect to the center of the bounding surface. This displacement, $\Delta(r)$, is given by the solution of Eq. (6.102). The displacement of the axis, $\Delta_s = \Delta(0)$, is called the Shafranov shift.

The Shafranov shift depends on the forms of $p_0(r)$ and $B_{\theta 0}(r)$ in Eq. (6.102) and must be solved for each case. However, some indication of the behavior can be obtained by using simple analytic forms. Suppressing the subscript zero, and taking

$$p = p_0 \left(1 - \frac{r^2}{a^2}\right) \quad (6.103)$$

and

$$j = j_0 \left(1 - \frac{r^2}{a^2}\right)^v \quad (6.104)$$

Equation (6.102) can be written

$$\frac{d\Delta}{dr} = -\frac{1}{RB_\theta^2} \left(\frac{r^3}{a^2} \beta_p B_{\theta a}^2 + \frac{1}{r} \int_0^r B_\theta^2 r dr \right) \quad (6.105)$$

where $B_{\theta a} = B_\theta(a)$ and the poloidal beta, β_p , is defined by

$$\beta_p = \frac{\bar{p}}{B_{\theta a}^2 / 2\mu_0} = \frac{4\mu_0 \int_0^a pr dr}{a^2 B_{\theta a}^2} \quad (6.106)$$

and $\beta_p = \mu_0 p_0 / B_{\theta a}^2$ in this case. Use of Eq. (6.104) in Ampère's law gives the poloidal field (see Eq. 6.89)

$$B_\theta = B_{\theta a} \frac{1 - \left(1 - \frac{r^2}{a^2}\right)^{v+1}}{r/a} \quad (6.107)$$

Equation (6.105) can now be integrated numerically to obtain Δ_s as a function of β_p and v . However, it is more useful to use the internal inductance, l_i , rather than v . This is defined by

$$l_i = \frac{\bar{B}_\theta}{B_{\theta a}^2} = \frac{2 \int_0^a B_\theta^2 r dr}{a^2 B_{\theta a}^2} \quad (6.108)$$

A graph of $l_i(v)$ is given in Fig. 6.9, and an empirical fit correct to within 2 % is given by

$$l_i = \ln(1.65 + 0.89v) \quad (6.109)$$

The parameter v is related to the ratio of edge and central q values through $q_a/q_0 = v + 1$ and this ratio is also indicated in the figure.

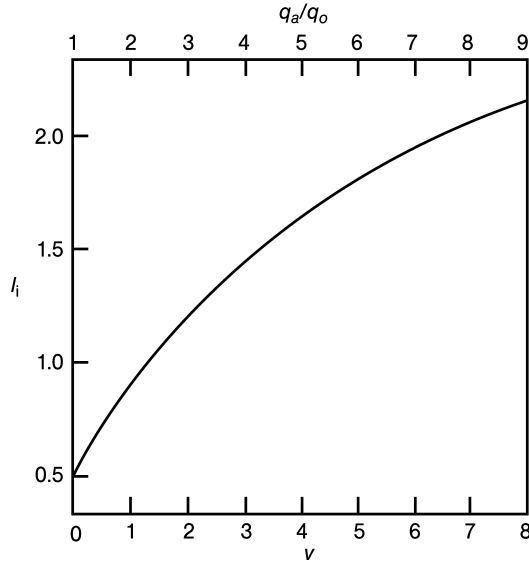


Figure 6.9. Internal inductance of the current $j = j_0(1 - r/a^2)^\nu$ as a function of ν

6.6 Beta

The efficiency of confinement of plasma pressure by the magnetic field is represented by the ratio

$$\beta = \frac{p}{B^2/2\mu_0} \quad (6.110)$$

There are several different measures of this type, arising from different choices of definition and from the need to quantify different equilibrium properties.

The important quantity for a reactor is the thermonuclear power achieved for a given magnetic field. The reaction rate is proportional to $n^2 \langle \sigma v \rangle$. In the temperature range envisaged for a reactor of 10 keV to 15 keV, $\langle \sigma v \rangle$ is roughly proportional to T^2 and the thermonuclear power is then proportional to p^2 . The resulting form of β , called β^* , is defined by

$$\beta^* = \frac{\left(\int p^2 d\tau / \int d\tau\right)^{\frac{1}{2}}}{B_0^2/2\mu_0} \quad (6.111)$$

where the integrals are over the plasma volume and B_0 is the value of the toroidal magnetic field.

The volume average value of β is defined by

$$\langle \beta \rangle = \frac{\int p d\tau / \int d\tau}{B_0^2/2\mu_0} \quad (6.112)$$

The surface-average poloidal β is defined by

$$\beta_p = \frac{\int p dS / \int dS}{B_a^2 / 2\mu_0} \quad (6.113)$$

where the integrals are surface integrals over the poloidal cross section at a given value of ψ (or r) and

$$B_a = \frac{\mu_0 I}{l} \quad (6.114)$$

where I is the plasma current and l is the length of the poloidal perimeter of the plasma. For a large aspect-ratio circular plasma $l = 2\pi a$ and Eq. (6.113) becomes

$$\beta_p = \frac{\int p dS}{\mu_0 I^2 / 8\pi} \quad (6.115)$$

An alternative definition uses the volume average of p rather than the cross-sectional average in Eq. (6.113).

The significance of β_p may be seen by taking a circular cross section and integrating the numerator of Eq. (6.115) by parts to obtain

$$\beta_p = -\frac{8\pi^2}{\mu_0 I^2} \int_0^a \frac{dp}{dr} r^2 dr \quad (6.116)$$

and substituting dp/dr from the approximate pressure balance equation

$$\frac{dp}{dr} + \frac{d}{dr} \left(\frac{B_\phi^2}{2\mu_0} \right) + \frac{B_\theta}{\mu_0 r} \frac{d}{dr}(r B_\theta) = 0 \quad (6.117)$$

to obtain, after integration,

$$\beta_p = 1 + \frac{1}{(a B_{\theta a})^2} \int_0^a \frac{dB_\phi^2}{dr} r^2 dr \quad (6.118)$$

If there are no poloidal currents, the integrand of Eq. (6.118) is zero and $\beta_p = 1$. If $d B_\phi^2 / dr > 0$, so that the toroidal field plays a part in confining the pressure, then $\beta_p > 1$. On the other hand, if $d B_\phi^2 / dr < 0$, the magnetic pressure $B_\phi^2 / 2\mu_0$ displaces some of the plasma pressure and $\beta_p < 1$. This is illustrated in Fig. 6.10.

There is no formal limit to the equilibrium value of β . Consider a perfectly conducting plasma surrounded by a perfectly conducting shell. If the plasma is continually heated, increasing the pressure on the flux surfaces, the plasma surfaces will move but their nested topology will remain unchanged. The plasma boundary is fixed. In principle this process may be continued without limit. However, it should be noted that this procedure leads to an increased plasma current. The experimental situation is of course more complex and in practice raising current ultimately leads to the formation of a separatrix with an X-point on the high field side of the plasma. More to the point, various plasma instabilities place a definite limit on the achievable values of β , as discussed in chapter 8 and chapter 18.

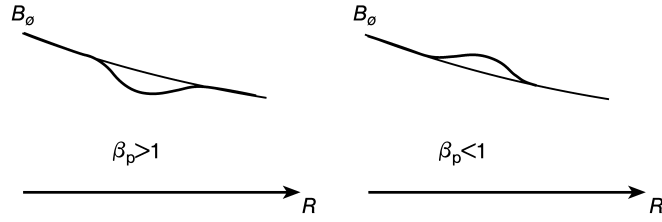


Figure 6.10. Profiles of $\beta_\phi > 1$ and $\beta_p < 1$

6.7 Magnetic Field Diffusion and Flux Surface Evolution*

It is clear from the discussion up to this point that the properties of plasma equilibria are intimately related to the magnetic field configuration and the magnetic flux contours within the plasma. In this section we examine how magnetic fields and flux surfaces can change within a plasma.

Faraday's law

$$\frac{\partial \mathbf{B}}{\partial t} \Big|_x = -\nabla \times \mathbf{E}^A \equiv +\nabla \times \frac{\partial \mathbf{A}}{\partial t} \Big|_x \quad (6.119)$$

describes the time dependence of the magnetic field in response to a change in the currents flowing in the plasma, as represented by the vector potential, \mathbf{A} . Consider the poloidal component of Eq. (6.119), obtained by taking the scalar product of $\hat{\mathbf{n}}_p$ with Eq. (6.119) and using Eq. (6.19) for \mathbf{B} . In flux surface coordinates this is

$$\frac{\partial}{\partial \psi} \left(\frac{\partial \psi}{\partial t} \Big|_x \right) = \frac{\partial}{\partial \psi} (R E_\phi^A)$$

where we must now be careful to indicate that we are considering a time derivative at a fixed spatial point, x . This equation can be integrated to obtain

$$\frac{\partial \psi}{\partial t} \Big|_x = R E_\phi^A + V(t) \quad (6.120)$$

where $V(t)$ is a voltage determined from the boundary conditions on ψ at the plasma surface. This voltage can be related to the transformer voltage by a suitable set of circuit equations.

By definition of a surface with $\psi = \text{const}$

$$0 \equiv \frac{d\psi}{dt} = \frac{\partial \psi}{\partial t} \Big|_x + \mathbf{u}_\psi \cdot \nabla \psi$$

so that the flux surfaces are moving through space with a velocity \mathbf{u}_ψ given by

$$\mathbf{u}_\psi \cdot \nabla \psi = -(R E_\phi^A + V(t)) \quad (6.121)$$

We must, of course, know E_ϕ^A in order to evaluate Eq. (6.121), which requires that we know the currents that produce the changing vector potential.

The diffusion of magnetic field lines in space can be computed directly by taking the curl of Eq. (6.2), using Ohm's law

$$\eta \mathbf{j} = \mathbf{E} + \mathbf{u} \times \mathbf{B} \quad (6.122)$$

to eliminate the current, using Eq. (6.119) to eliminate the electric field, and neglecting terms which are small for time scales that are long compared to $\tau_D \equiv \epsilon_0 \eta$. The resulting equation is

$$\frac{1}{\mu_0} \nabla^2 \mathbf{B} = \frac{1}{\eta} \frac{\partial \mathbf{B}}{\partial t} \Big|_x - \nabla \left(\frac{1}{\eta} \right) \times \mathbf{E} - \nabla \times \mathbf{u} \times \frac{\mathbf{B}}{\eta} \quad (6.123)$$

where \mathbf{u} is the plasma mass velocity. For a uniform plasma, η is space independent and Eq. (6.123) becomes

$$\frac{\eta}{\mu_0} \nabla^2 \mathbf{B} = \frac{\partial \mathbf{B}}{\partial t} \Big|_x - \nabla \times \mathbf{u} \times \mathbf{B} \quad (6.124)$$

In a stationary plasma ($\mathbf{u} \equiv 0$), Eq. (6.124) is a diffusion equation. Thus the magnetic field diffuses in a plasma with a time constant $\tau_m \simeq (\mu_0/\eta)L^2$, where L is a characteristic gradient scale length for the magnetic field. Using Eq. (1.51) of chapter 1, this magnetic diffusion time constant is

$$\tau_m(s) \simeq 40z T_e^{\frac{3}{2}} L^2 \quad (6.125)$$

where T_e is in keV and z is the effective charge of the plasma ions. The quantity τ_m is many hundreds of seconds for thermonuclear plasmas.

On a time scale that is short compared to τ_m , the LHS of Eq. (6.124) can be neglected and that equation describes a magnetic field moving with the plasma flow. We can see this more explicitly by considering the magnetic flux linking a contour that is “painted on the plasma,” that is, a contour that is everywhere moving with the plasma mass velocity, which can vary along the contour (see Fig. 6.11). The magnetic flux that links this contour is

$$\Phi \equiv \int_s \mathbf{B} \cdot d\mathbf{s} \quad (6.126)$$

where the integral can be taken over any single-valued cross sectional area bound by the contour.

The change in Φ in time consists of two components. The first component is due to the change in \mathbf{B} locally, and the second component is due to the change in the contour. The first component is

$$\frac{d\Phi_1}{dt} = \int_s \frac{\partial \mathbf{B}}{\partial t} \Big|_x \cdot d\mathbf{s} = \int_s \left(\frac{\eta}{\mu_0} \nabla^2 \mathbf{B} + \nabla \times \mathbf{u} \times \mathbf{B} \right) \cdot d\mathbf{s} \quad (6.127)$$

The second component is

$$\frac{d\Phi_2}{dt} = \oint \mathbf{B} \cdot (\mathbf{u} \times d\mathbf{l}) = - \oint \mathbf{u} \times \mathbf{B} \cdot d\mathbf{l} = - \int_s (\nabla \times \mathbf{u} \times \mathbf{B}) \cdot d\mathbf{s} \quad (6.128)$$

On time scales $\tau \ll \tau_m$, the first term in the integrand of Eq. (6.127) is negligible, and the two components exactly cancel. Thus we are led to the concept of flux conservation, that

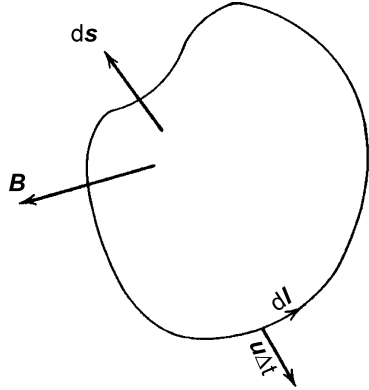


Figure 6.11. Contour in a moving plasma

is, the magnetic field moves with the plasma such that the total magnetic flux associated with a given volume of plasma is conserved. This result is quite general.

Now we return to our consideration of the evolution of flux surfaces in an axisymmetric toroidal plasma. A parameter that characterizes the flux surface topology is $q(\psi, t)$ defined by Eq. (6.43). We can derive an equation for the evolution of q in time relative to the moving flux surfaces from the toroidal component of Faraday's law. Taking the scalar product of $\nabla\phi$ with Eq. (6.119), flux surface averaging, and using Eq. (6.19), yields

$$\left\langle R^{-2} \frac{\partial F}{\partial t} \Big|_x \right\rangle = -\left\langle \nabla \cdot (\mathbf{E}^A \times \nabla\phi) \right\rangle \quad (6.129)$$

We can use the identity for the flux surface average in axisymmetric toroidal geometry,

$$\langle \nabla \cdot \mathbf{g} \rangle = \frac{1}{V'} \frac{\partial}{\partial \psi} (V' \langle \mathbf{g} \cdot \nabla\psi \rangle) \quad (6.130)$$

for any differentiable vector function, and Eq. (6.19) to obtain

$$V' \left\langle R^{-2} \frac{\partial F}{\partial t} \Big|_x \right\rangle = -\frac{\partial}{\partial \psi} (V' \langle \mathbf{E} \cdot \mathbf{B}_p \rangle) = -\frac{\partial}{\partial \psi} \left[V' \left(\langle E_{\parallel} B \rangle - \langle R^{-1} F E_{\phi}^A \rangle \right) \right] \quad (6.131)$$

and use Eq. (6.120) to finally obtain

$$\begin{aligned} \left. \frac{\partial q(\psi, t)}{\partial t} \right|_{\psi} &\equiv \frac{1}{(2\pi)^2} \left[V' \left\langle R^{-2} \frac{\partial F}{\partial t} \Big|_x \right\rangle - \frac{\partial}{\partial \psi} \left(V' \left\langle R^{-2} F \frac{\partial \psi}{\partial t} \Big|_x \right\rangle \right) \right] \\ &= \frac{1}{(2\pi)^2} \frac{\partial}{\partial \psi} \left[V' \left(\langle E_{\parallel} B \rangle + F V \langle R^{-2} \rangle \right) \right] \end{aligned} \quad (6.132)$$

Equation (6.132) indicates that the topology of the moving magnetic field changes due to ohmic dissipation (the $\langle E_{\parallel} B \rangle$ term) and due to the external voltage, $V(t)$. In principle, the external voltage could be selected to compensate the dissipation and maintain $q(\psi, t) = \text{const.}$

6.8 Anisotropic Pressure Equilibria*

Situations exist in which the distribution function for one or more of the plasma species is anisotropic to lowest order. Open (mirror) confinement configurations are an example. We will assume that the distribution function is isotropic with respect to orientation in the plane perpendicular to the field, so that the pressure tensor is given by Eq. (5.71) of chapter 5; that is,

$$\mathbf{P} = p_{\perp} \mathbf{I} + (p_{\parallel} - p_{\perp}) \hat{\mathbf{n}}_{\parallel} \hat{\mathbf{n}}_{\parallel} \quad (6.133)$$

In this situation, the lowest order momentum balance equation for the plasma is

$$\mathbf{j} \times \mathbf{B} = \nabla \cdot \mathbf{P} \quad (6.134)$$

instead of Eq. (6.1). The components of Eq. (6.134) parallel and perpendicular to the field are

$$0 = (\nabla \cdot \mathbf{P})_{\parallel} = \nabla_{\parallel} p_{\parallel} - \frac{(p_{\parallel} - p_{\perp})}{B} (\nabla_{\parallel} B) \quad (6.135)$$

and

$$\mathbf{j} \times \mathbf{B} = (\nabla \cdot \mathbf{P})_{\perp} = \nabla_{\perp} p_{\perp} + \frac{(p_{\parallel} - p_{\perp})}{B} \left[\nabla_{\perp} B + \frac{(\nabla \times \mathbf{B}) \times \mathbf{B}}{B} \right] \quad (6.136)$$

The magnetic field can be represented quite generally by

$$\mathbf{B} = \nabla \alpha \times \nabla \beta \quad (6.137)$$

where α and β are constant along the field lines. We assume that $p_{\parallel} = p_{\parallel}(B, \alpha, \beta)$, so that Eq. (5.88) and Eq. (5.89) lead to

$$\frac{\partial p_{\parallel}}{\partial B} = \frac{p_{\parallel} - p_{\perp}}{B} \quad (6.138)$$

Using Eq. (6.2) in Eq. (6.136) yields

$$[\nabla \times (\sigma \mathbf{B})] \times \mathbf{B} = \nabla_{\perp} p_{\parallel} - \frac{(p_{\parallel} - p_{\perp})}{B} \nabla_{\perp} \mathbf{B} \quad (6.139)$$

where we have defined

$$\sigma \equiv \frac{1}{\mu_0} - \frac{(p_{\parallel} - p_{\perp})}{B^2} \quad (6.140)$$

Now using Eq. (6.138) in Eq. (6.139), using the functional dependence $p_{\parallel} = p_{\parallel}(B, \alpha, \beta)$, and noting that α and β are constant along the field lines yields

$$[\nabla \times (\sigma \mathbf{B})] \times \mathbf{B} = \frac{\partial p_{\parallel}}{\partial \alpha} \nabla \alpha + \frac{\partial p_{\parallel}}{\partial \beta} \nabla \beta \quad (6.141)$$

Comparison of Eq. (6.141) with the equation that is obtained by substituting Eq. (6.2) into Eq. (6.21) suggests defining a current-like quantity

$$\mathbf{K} \equiv \nabla \times (\sigma \mathbf{B}) \quad (6.142)$$

which is the total current minus the magnetization current. The perpendicular component of \mathbf{K} can be determined from Eq. (6.141)

$$\mathbf{K}_\perp = \frac{\hat{\mathbf{n}}_\parallel}{B} \times \left(\frac{\partial p_\parallel}{\partial \alpha} \nabla \alpha + \frac{\partial p_\parallel}{\partial \beta} \nabla \beta \right) \quad (6.143)$$

and the parallel component of \mathbf{K} can be determined from the scalar product of $\hat{\mathbf{n}}_\parallel$ with Eq. (6.142), after substitution of Eq. (6.2) into Eq. (6.142)

$$\mathbf{K}_\parallel = \sigma \mu_0 j_\parallel \hat{\mathbf{n}}_\parallel \quad (6.144)$$

Now we seek to construct a solution of the form

$$\sigma \mathbf{B} = \Psi_1 \nabla \alpha + \Psi_2 \nabla \beta + \nabla \phi \quad (6.145)$$

Using Eq. (6.145) in Eq. (6.141) yields

$$(\mathbf{B} \cdot \nabla \Psi_1) \nabla \alpha + (\mathbf{B} \cdot \nabla \Psi_2) \nabla \beta = \frac{\partial p_\parallel}{\partial \alpha} \nabla \alpha + \frac{\partial p_\parallel}{\partial \beta} \nabla \beta \quad (6.146)$$

from which we find, because α and β are independent,

$$\begin{aligned} \Psi_1(l) &= \int_0^l \frac{dl'}{B} \frac{\partial p_\parallel}{\partial \alpha} \\ \Psi_2(l) &= \int_0^l \frac{dl'}{B} \frac{\partial p_\parallel}{\partial \beta} \end{aligned} \quad (6.147)$$

the integral being taken along the field line. Substituting Eq. (6.145) in Eq. (6.3) yields a “magnetic differential equation” for ϕ ,

$$\nabla^2 \phi - \frac{1}{\sigma} \nabla \sigma \cdot \nabla \phi = -\nabla \cdot (\Psi_1 \nabla \alpha + \Psi_2 \nabla \beta) + \frac{1}{\sigma} \nabla \sigma \cdot (\Psi_1 \nabla \alpha + \Psi_2 \nabla \beta) \quad (6.148)$$

For open field line confinement configurations the field lines pass out of the confinement region into an exterior region of zero pressure for $l > l_c$, so that $\bar{\Psi}_1 \equiv \Psi_1(l_c)$, $\bar{\Psi}_2 \equiv \Psi_2(l_c)$, and $\sigma = \mu_0^{-1}$ are constant in this exterior region. The requirement that there be no current in this exterior region can be written, using Eq. (6.2) and Eq. (6.145) as

$$0 = \mu_0 \mathbf{j} = \left(\frac{\partial \bar{\Psi}_2}{\partial \alpha} - \frac{\partial \bar{\Psi}_1}{\partial \beta} \right) (\nabla \alpha \times \nabla \beta) \quad (6.149)$$

which introduces a constraint condition that is required to specify a unique solution to Eq. (6.147) and Eq. (6.148).

Problems for Chapter 6

1. What can you say about the direction of the current and magnetic field in a region of a confined plasma in which the pressure is uniform (i.e., the pressure gradient vanishes)?
2. What is the kinetic pressure of a plasma in which the magnetic field is $B = 5\text{ T}$ and $\beta = 0.1$?
3. Calculate the radial pressure distribution in a cylindrical plasma of radius $a = 1\text{ m}$ with an axial current of 2 MA distributed as $j(r) = j_0(1 - r/a)$ for $0 \leq r \leq a$.
4. Derive Eq. (6.23) from Eq. (6.5) by using the field representation of Eq. (6.19).
5. Derive Eq. (6.26) for the parallel current in a confined plasma.
6. Derive the Grad–Shafranov equation.
7. Calculate and plot $\beta_p(r)$ and calculate the internal inductance for a tokamak plasma with $T = 5\text{ keV}$, $n_D = n_e = 5 \times 10^{19}\text{ m}^{-3}$ and minor radius $a = 0.6\text{ m}$ that has a toroidal current of 3 MA distributed as $j(r) = j_0(1 - (r/a)^2)$ for $0 \leq r \leq a$.
8. Calculate and plot as a function of the poloidal angle θ the r - and z -components of the vertical magnetic field that is required to achieve horizontal force balance in the tokamak plasma of problem 7 if the major radius $R = 1.7\text{ m}$.
9. Calculate and plot as a function of minor radius, r , the safety factor for the tokamak of problems 7 and 8 if the toroidal magnetic field is 5 T.
10. Calculate the magnetic field diffusion time constant for the plasma of problem 7.

7 Waves

A wide variety of wavelike phenomena can exist in a plasma. We will begin our study of plasma waves in this chapter by considering the simplest types of waves that can exist in a cold plasma by using a multi-fluid description of the plasma. We will then turn to a Vlasov equation description of the plasma to develop a formalism appropriate for the study of high frequency wave phenomena and will study certain effects that are introduced by the fact that the plasma is hot. In all cases, we will ignore collisions, so that we are considering wave phenomena with frequencies much greater than the collision frequency.

7.1 Waves in an Unmagnetized Plasma

7.1.1 Electromagnetic Waves

The simplest case is a uniform, cold plasma in the absence of a magnetic field. We will consider perturbations in the magnetic and electric fields and in the current, relative to an equilibrium condition. The field perturbations are described by Maxwell's equations

$$\nabla \times \mathbf{B} = \mu_0 \mathbf{j} + \frac{1}{c^2} \frac{\partial \mathbf{E}}{\partial t} \quad (7.1)$$

and

$$\nabla \times \mathbf{E} = -\frac{\partial \mathbf{B}}{\partial t} \quad (7.2)$$

which may be combined to obtain

$$\nabla(\nabla \cdot \mathbf{E}) - \nabla^2 \mathbf{E} = -\mu_0 \frac{\partial \mathbf{j}}{\partial t} - \frac{1}{c^2} \frac{\partial^2 \mathbf{E}}{\partial t^2} \quad (7.3)$$

The current density in the plasma is

$$\mathbf{j} \equiv \sum_{\sigma} n_{\sigma} e_{\sigma} \mathbf{v}_{\sigma} \quad (7.4)$$

where the sum is over species. In the multi-fluid approximation, the average species' velocities are determined from the force balance equations Eq. (5.26)

$$m_{\sigma} n_{\sigma} \left(\frac{\partial}{\partial t} + \mathbf{v}_{\sigma} \cdot \nabla \right) \mathbf{v}_{\sigma} = -\nabla p_{\sigma} + n_{\sigma} e_{\sigma} (\mathbf{E} + \mathbf{v}_{\sigma} \times \mathbf{B}) \quad (7.5)$$

For a cold plasma the ∇p_{σ} term is negligible. Because there are no net particle flows or magnetic field in equilibrium, retaining lowest order terms in Eq. (7.5) yields

$$\frac{\partial \mathbf{v}_\sigma}{\partial t} = \frac{e_\sigma}{m_\sigma} \mathbf{E}$$

which can be used, together with Eq. (7.4), to write Eq. (7.3) as

$$\nabla(\nabla \cdot \mathbf{E}) - \nabla^2 \mathbf{E} = -\mu_0 \left(\sum_\sigma \frac{n_\sigma e_\sigma^2}{m_\sigma} \right) \mathbf{E} - \frac{1}{c^2} \frac{\partial^2 \mathbf{E}}{\partial t^2} \quad (7.6)$$

The eigenfunctions of Eq. (7.6) are plane waves with space and time dependences of the form

$$\exp[i(\mathbf{k} \cdot \mathbf{r} - \omega t)] \quad (7.7)$$

Using this form in Eq. (7.6) yields

$$-\mathbf{k}(\mathbf{k} \cdot \mathbf{E}) + k^2 \mathbf{E} = \frac{\omega^2}{c^2} \mathbf{E} - \mu_0 \left(\sum_\sigma \frac{n_\sigma e_\sigma^2}{m_\sigma} \right) \mathbf{E} \quad (7.8)$$

There are two independent wave types that are solutions of Eq. (7.8): longitudinal waves with $\mathbf{k} \parallel \mathbf{E}$; and transverse waves with $\mathbf{k} \perp \mathbf{E}$.

Consider first the longitudinal waves ($\mathbf{k} \parallel \mathbf{E}$). In this case, Eq. (7.8) reduces to

$$\omega^2 = \frac{1}{\epsilon_0} \sum_\sigma \frac{n_\sigma e_\sigma^2}{m_\sigma} \equiv \omega_p^2 \quad (7.9)$$

where ω_p is the plasma frequency which, because of the m_σ^{-1} dependence, is essentially the electron plasma frequency. These waves are purely electrostatic – there is no magnetic field perturbation – and describe nonpropagating plasma oscillations. These are the waves that were derived from simpler considerations in chapter 1.

Now consider the transverse ($\mathbf{k} \perp \mathbf{E}$) waves. In this case Eq. (7.8) becomes

$$\omega^2 = c^2 k^2 + \omega_p^2 \quad (7.10)$$

In the absence of a plasma, the transverse waves would satisfy $\omega^2 = c^2 k^2$. If this wave is incident upon a plasma from a vacuum region, it may be reflected. Since ω remains constant, k^2 must decrease as the wave propagates into a plasma and $\omega_p^2 (\propto n)$ increases, until finally the wave is reflected if $\omega^2 \leq \omega_p^2$.

The cold plasma approximation that we have used is valid when $\nabla p \ll mn(\partial \mathbf{v}/\partial t)$. Using the adiabatic law to relate the perturbed, p , and equilibrium, p_0 , pressures,

$$\frac{p}{p_0} = \gamma \frac{n}{n_0}$$

and using the continuity Eq. (5.6) to relate the perturbed, n , and equilibrium, n_0 , densities when the perturbed solution has the form of Eq. (7.7),

$$\omega n = kv n_0$$

the condition for the validity of the approximation is

$$1 \gg \frac{|\nabla p|}{\left| mn \frac{\partial \mathbf{v}}{\partial t} \right|} \approx \frac{k^2 \gamma}{\omega^2} \frac{p_0}{nm} = \frac{k^2}{\omega^2} v_{th}^2 \quad (7.11)$$

where v_{th} is the thermal speed. For longitudinal waves, $\omega = \omega_p$, so Eq. (7.11) requires

$$\frac{k^2 v_{th}^2}{\omega_p^2} \ll 1 \quad (7.12)$$

From our definition of the Debye length in Chapter 1, it follows that Eq. (7.12) is satisfied whenever the wavelength is much greater than the Debye length. For transverse waves, $\omega \geq ck$, so that Eq. (7.11) is always satisfied.

7.1.2 Ion Sound Waves

Let us now look at another longitudinal ($\mathbf{k} \parallel \mathbf{E}_1$), electrostatic, wave in an unmagnetized plasma. We assume that the frequency is low enough that the ions can participate in the motion, but the more mobile electrons are able to establish nearly exact force balance on the oscillation time scale. To investigate the wave motion, we expand variables about their equilibrium values, $x(r, t) = x_0(r) + x_1(r, t)$. Taking $\mathbf{B}_0 = 0$ and $\mathbf{k} \parallel \mathbf{E}_1$, we have $\mathbf{B}_1 = 0$ as well. The ion fluid equation, for scalar pressure, is then

$$m_i n_i [\mathbf{v}_i + (\mathbf{v}_i \cdot \nabla) \mathbf{v}_i] = e n_i \mathbf{E} - \nabla p_i \quad (7.13)$$

where m_i indicates an ion mass, and we have assumed $z = 1$. We linearize this equation, take advantage of the electrostatic nature of the oscillation to write \mathbf{E}_1 as the gradient of a potential ($\nabla \times \mathbf{E}_1 = 0$), and use the adiabatic gas law equation of state to relate p_{i1} to n_{i1} . We use the plane wave and sinusoidal wave form of Eq. (7.7) and note that in this unmagnetized longitudinal wave, the fluid motion has no reason to be in any direction other than \mathbf{k} , so we treat v_{i1} as a scalar, i.e. the component of \mathbf{v}_{i1} in the \mathbf{k} direction. Equation (7.13) becomes

$$-i\omega m_i n_{i0} v_{i1} = -e n_{i0} ik \phi_1 - \gamma_i T_i ik n_{i1} \quad (7.14)$$

For the electrons, we assume a Boltzmann distribution:

$$\begin{aligned} n_e &= n_{e0} \exp(e\phi_1/T_e) \approx n_{e0}(1 + e\phi_1/T_e) \\ n_{e1} &= n_{e0}(e\phi_1/T_e) \end{aligned} \quad (7.15)$$

From Poisson's equation, we obtain

$$\epsilon_0 \nabla \cdot \mathbf{E}_1 = \epsilon_0 k^2 \phi_1 = e(n_{i1} - n_{e1}) = e[n_{i1} - n_{e0}(e\phi_1/T_e)] \quad (7.16)$$

which is solved for n_{i1} as a function of ϕ_1

$$n_{i1} = \left[n_{i0} (e/T_e) + \epsilon_0 k^2 / e \right] \phi_1 \quad (7.17)$$

where we have used $n_{i0} = n_{e0}$ in the case of $z = 1$. The linearized ion continuity equation is

$$i\omega n_{i1} = n_{i0}ikv_{i1} \quad (7.18)$$

We can now cast all the first-order terms in Eq. (7.14) in terms of n_{i1} , using Eq. (7.17) and Eq. (7.18)

$$\omega m_i n_{i0} \frac{\omega n_{i1}}{k n_{i0}} = \frac{e n_{i0} k n_{i1}}{n_{i0} e / T_e + \epsilon_0 k^2 / e} + \gamma_i T_i k n_{i1} \quad (7.19)$$

which may be rewritten

$$(\omega/k)^2 = \frac{T_e/m_i}{1 + k^2 \lambda_D^2} + \gamma_i T_i / m_i \quad (7.20)$$

where we recall $\lambda_D^2 \equiv \epsilon_0 T_e / n_e e^2$.

In the long wavelength ($k \rightarrow 0$) limit, this wave is very similar to a normal sound wave, in which the electrons and the ions both contribute pressure, but the ions contribute essentially all of the mass. The phase velocity of this wave is of the order of the ion sound speed, so the electrons generally have plenty of time to free-stream and equilibrate their temperature ahead of the wave propagation, which is not the case for the ions. In the limit of sufficient collisions to prevent ion thermal diffusion at speeds close to the sound speed, we should take γ_i to be the usual adiabatic isotropic value of $5/3$. In the absence of collisions, but with $T_i \ll T_e$ so ion thermal motion cannot keep up with the wave, we can assume a one-dimensional adiabatic compression for the ions, equivalent to $\gamma_i = 3$.

7.2 Waves in a Uniformly Magnetized Plasma

7.2.1 Electromagnetic Waves

When the plasma is in a uniform magnetic field, \mathbf{B}_0 , which we choose to be in the z -direction, it is necessary to retain the $\mathbf{v}_\sigma \times \mathbf{B}_0$ term in Eq. (7.5). Assuming the perturbed solutions are of the plane wave form, the Cartesian components of the momentum Eq. (7.5) become

$$\begin{aligned} -i\omega v_{\sigma x} - \Omega_\sigma v_{\sigma y} &= \frac{e_\sigma}{m_\sigma} E_x \\ -i\omega v_{\sigma y} + \Omega_\sigma v_{\sigma x} &= \frac{e_\sigma}{m_\sigma} E_y \\ -i\omega v_{\sigma z} &= \frac{e_\sigma}{m_\sigma} E_z \end{aligned} \quad (7.21)$$

Solving Eq. (7.21) for v_σ and substituting into Eq. (7.4) yields

$$\begin{aligned} j_x &= \sum_{\sigma} \frac{n_{\sigma} e_{\sigma}^2}{m_{\sigma}} \left(\frac{i\omega E_x - \Omega_{\sigma} E_y}{\omega^2 - \Omega_{\sigma}^2} \right) \\ j_y &= \sum_{\sigma} \frac{n_{\sigma} e_{\sigma}^2}{m_{\sigma}} \left(\frac{i\omega E_y - \Omega_{\sigma} E_x}{\omega^2 - \Omega_{\sigma}^2} \right) \\ j_z &= - \sum_{\sigma} \frac{n_{\sigma} e_{\sigma}^2}{m_{\sigma}} \frac{E_z}{i\omega} \end{aligned} \quad (7.22)$$

Choosing, without loss of generality, the coordinate system such that $k_y = 0$ and using Eq. (7.22) in Faraday's Law Eq. (7.3) now leads to

$$\begin{aligned} \left(c^2 k_z^2 - \omega^2 + \sum_{\sigma} \frac{\omega_{p\sigma}^2 \omega^2}{\omega^2 - \Omega_{\sigma}^2} \right) E_x + i \left(\sum_{\sigma} \frac{\omega_{p\sigma}^2 \Omega_{\sigma} \omega}{\omega^2 - \Omega_{\sigma}^2} \right) E_y - \left(c^2 k_x k_z \right) E_z &= 0 \\ -i \left(\sum_{\sigma} \frac{\omega_{p\sigma}^2 \Omega_{\sigma} \omega}{\omega^2 - \Omega_{\sigma}^2} \right) E_x + \left(c^2 k^2 - \omega^2 + \sum_{\sigma} \frac{\omega_{p\sigma}^2 \omega^2}{\omega^2 - \Omega_{\sigma}^2} \right) E_y &= 0 \quad (7.23) \\ - \left(c^2 k_x k_z \right) E_x + \left(c^2 k_x^2 - \omega^2 + \sum_{\sigma} \omega_{p\sigma}^2 \right) E_z &= 0 \end{aligned}$$

To understand the content of Eqs. (7.23), we first consider waves that propagate along the direction of the equilibrium field ($\mathbf{k} \parallel \mathbf{B}_0$), for which $k_x = k_y = 0$. One solution to Eqs. (7.23) is

$$\omega^2 = \sum_{\sigma} \omega_{p\sigma}^2 \quad (7.24)$$

which is the result obtained in the absence of an equilibrium magnetic field. The field has no effect because the motion associated with the wave is in the field direction ($\mathbf{v}_{\sigma} \parallel \mathbf{B}_{\sigma}$) and the term $\mathbf{v}_{\sigma} \times \mathbf{B}_{\sigma}$ vanishes.

Other solutions to Eq. (7.23), with $k_x = 0$, occur when

$$c^2 k^2 - \omega^2 + \sum_{\sigma} \frac{\omega_{p\sigma}^2 \omega}{\omega \pm \Omega_{\sigma}} = 0 \quad (7.25)$$

The plus and minus signs correspond to solutions $E_x = iE_y$ and $E_x = -iE_y$, respectively, which can be written

$$\mathbf{E} = |E| (\hat{\mathbf{n}}_x \cos(\omega t) - \hat{\mathbf{n}}_y \sin(\omega t)) \quad (7.26a)$$

and

$$\mathbf{E} = |E| (\hat{\mathbf{n}}_x \cos(\omega t) + \hat{\mathbf{n}}_y \sin(\omega t)) \quad (7.26b)$$

respectively. Both solutions are circularly polarized waves with a constant amplitude, $|E|$. The electric field vector described by Eq. (7.26a) rotates in the direction of the ion gyration (see Fig. 2.1) and this wave is said to be left circularly polarized. The electric field

vector described by Eq. (7.26b) rotates in the direction of the electron gyration, and this wave is said to be right circularly polarized.

From Eq. (7.25) there are obviously certain resonance values of the wave frequency, $\omega = \pm\Omega_\sigma$, for which the propagation vector goes to infinity. Since $\omega > 0$ and $\Omega_\sigma \equiv e_\sigma B_\sigma / m_\sigma$, the $\omega = +\Omega_\sigma$ resonances must occur at (positive) ion-cyclotron frequencies for the left circularly polarized wave. The $\omega = -\Omega_\sigma$ resonances must occur for the right circularly polarized wave at the electron-cyclotron frequency. At these resonances, the species involved absorbs energy from the wave. This phenomenon provides a means of increasing the energy of the plasma species by launching waves of the proper frequency into the plasma, a subject which will be discussed in chapter 12.

For the nonmagnetized plasma, we found that $\omega > \omega_p$ was required for penetration ($k^2 > 0$) of the wave. From Eq. (7.25) we see that this penetration condition is modified for waves propagating along the magnetic field direction by the presence of the magnetic field. Considering only the electron contribution to the sum in Eq. (7.25), which is valid except in the vicinity of the ion-cyclotron resonance, the penetration condition is

$$\omega^2 > \frac{\omega_{pe}^2}{1 \pm \frac{\Omega_e}{\omega}} \quad (7.27)$$

Solutions of Eqs. (7.23) that describe waves propagating transverse to the equilibrium magnetic field ($\mathbf{k} \perp \mathbf{B}_0$) are rather more complicated. One solution is a plane polarized ($E_x = E_y = 0$) transverse electrostatic wave described by

$$\omega^2 = c^2 k^2 + \sum_\sigma \omega_{p\sigma}^2 \quad (7.28)$$

Since $\mathbf{E} = \mathbf{E}_z$, the motion driven by the wave is along the magnetic field direction and $\mathbf{v}_\sigma \times \mathbf{B}_\sigma = 0$. This is the same wave that existed in the absence of a magnetic field.

Other solutions for waves with $\mathbf{k} \perp \mathbf{B}_0$ correspond to mixed longitudinal and transverse (with respect to the electrical field direction) waves that are described by the dispersion relation

$$c^2 k^2 = \omega^2 - \sum_\sigma \frac{\omega_{p\sigma}^2 \omega^2}{\omega^2 - \Omega_\sigma^2} - \frac{\left(\sum_\sigma \frac{\omega_{p\sigma}^2 \Omega_\sigma}{\omega^2 - \Omega_\sigma^2} \right)^2}{\left(1 - \sum_\sigma \frac{\omega_{p\sigma}^2}{\omega^2 - \Omega_\sigma^2} \right)} \quad (7.29)$$

There are no resonances of Eq. (7.29) at $\omega = \pm\Omega_\sigma$, because of cancellation between the last two terms. However, there are resonances corresponding to the zeros of the denominator of the last term, that is,

$$1 - \sum_\sigma \frac{\omega_{p\sigma}^2}{\omega^2 - \Omega_\sigma^2} = 0 \quad (7.30)$$

For an ion-electron plasma, in almost all cases of interest $\omega_{pi}^2/\Omega_i^2 \gg 1$ and always $\omega_{pi}^2/\Omega_i^2 \gg \omega_{pe}^2/\Omega_e^2$. Thus the roots of Eq. (7.30) divide into a high frequency pair that

satisfy

$$\omega^2 = \omega_{pe}^2 + \Omega_e^2 \quad (7.31)$$

and a low-frequency pair that satisfy

$$\omega^2 = \frac{\omega_{pi}^2 \Omega_e^2}{\omega_{pe}^2 + \Omega_e^2} \quad (7.32)$$

The resonances given by Eqs. (7.31) and (7.32) are known as the upper-hybrid and lower-hybrid, respectively, resonances. When $\omega_{pe} \gg \Omega_e$, Eq. (7.32) becomes

$$\omega_{LH}^2 \simeq |\Omega_e \Omega_i|$$

7.2.2 Shear Alfvén Wave

Consider propagation purely parallel to \mathbf{B}_0 , i.e. $\mathbf{k} \parallel \mathbf{B}_0$ of the left (L) and right (R) circularly polarized waves introduced above. Further take $\mathbf{E}_1 \perp \mathbf{B}_0$, and thus $\mathbf{E}_1 \perp \mathbf{k}$. Note that $\mathbf{E}_1 \parallel \mathbf{B}_0 \parallel \mathbf{k}$ at low frequency, with a warm plasma, just gives the ion acoustic wave studied previously. The ion acoustic wave is decoupled from the low frequency R- and L-waves, propagating parallel to \mathbf{B}_0 in the modes we are considering. Since $\mathbf{B}_0 \parallel \hat{\mathbf{n}}_z$, $E_{z1} = u_{z1} = 0$. The equations of motion reveal that T plays no role in these modes. As a result, the equations of motion yield

$$\begin{aligned} v_{xi1} &= \frac{-(e/m_i)(i\omega E_{x1} - \Omega_i E_{y1})}{\Omega_i^2 - \omega^2} \\ v_{xi1} &= \frac{-(e/m_i)(i\omega E_{y1} + \Omega_i E_{x1})}{\Omega_i^2 - \omega^2} \end{aligned} \quad (7.33)$$

For the electrons we will assume $\omega \lesssim \Omega_e \ll \omega_{pe}$, in which case the electron fluid exhibits pure $\mathbf{E}_1 \times \mathbf{B}_0$ drift:

$$\begin{aligned} v_{xe1} &= \frac{(e/m_e)E_{y1}}{\Omega_e} = \frac{eE_{y1}}{m_i \Omega_i} \\ v_{ye1} &= \frac{-(e/m_e)E_{x1}}{\Omega_e} = \frac{-eE_{x1}}{m_i \Omega_i} \end{aligned} \quad (7.34)$$

The last step in the above equations was motivated by the desire to express frequencies in terms of ion quantities, and it brings a common factor of e/m_i in front of both the ion and the electron equations.

The conductivity tensor is then given by

$$\begin{aligned} \mathbf{j}_1 &= \frac{n_0 e^2}{m_i} \left[\frac{-i\omega}{\Omega_i^2 - \omega^2} \hat{\mathbf{n}}_x \hat{\mathbf{n}}_x + \left(\frac{\Omega_i}{\Omega_i^2 - \omega^2} - \frac{1}{\Omega_i} \right) \hat{\mathbf{n}}_x \hat{\mathbf{n}}_y \right. \\ &\quad \left. - \left(\frac{\Omega_i}{\Omega_i^2 - \omega^2} - \frac{1}{\Omega_i} \right) \hat{\mathbf{n}}_y \hat{\mathbf{n}}_x - \frac{-i\omega}{\Omega_i^2 - \omega^2} \hat{\mathbf{n}}_y \hat{\mathbf{n}}_y \right] \cdot \mathbf{E}_1 \end{aligned} \quad (7.35)$$

For the case of interest here, which has $\mathbf{E}_1 \perp \mathbf{B}_0$, the dispersion relation is

$$\begin{vmatrix} 1 - \tilde{n}^2 + \frac{\omega_{\text{pi}}^2}{\Omega_i^2 - \omega^2} & \frac{i\omega_{\text{pi}}^2 \omega}{\Omega_i(\Omega_i^2 - \omega^2)} \\ \frac{-i\omega_{\text{pi}}^2 \omega}{\Omega_i(\Omega_i^2 - \omega^2)} & 1 - \tilde{n}^2 + \frac{\omega_{\text{pi}}^2}{\Omega_i^2 - \omega^2} \end{vmatrix} = 0 \quad (7.36)$$

A more compact form of the dispersion relation is

$$\tilde{n}^2 = \frac{c^2 k^2}{\omega^2} = 1 + \frac{\omega_{\text{pi}}^2 \Omega_i \mp \omega_{\text{pi}}^2 \omega}{\Omega_i(\Omega_i^2 - \omega^2)} = 1 + \frac{\omega_{\text{pi}}^2}{\Omega_i(\Omega_i \pm \omega)} = \frac{\Omega_i^2 + \omega_{\text{pi}}^2 \pm \Omega_i \omega}{\Omega_i(\Omega_i \pm \omega)} \quad (7.37)$$

where the index of refraction, $\tilde{n} = ck/\omega$, has been introduced. The upper signs go with right-hand polarization (R-wave), the lower signs with left-hand polarization (L-wave).

Thus for the R-wave, dividing top and bottom by Ω_i , we have

$$\tilde{n}^2 = \frac{c^2 k^2}{\omega^2} = \frac{\Omega_i + \frac{\omega_{\text{pi}}^2}{\Omega_i} + \omega}{\Omega_i + \omega} \quad (7.38)$$

The shear-Alfven R-wave has no cutoffs and no resonances in this low frequency range, since neither the numerator nor the denominator can go to zero. As we go up in frequency, the shear-Alfven R-wave smoothly goes over into the whistler, which has its resonance at $\omega = \Omega_e$. At the low frequency end, we have a “simple” light wave propagating in a medium with a large scalar dielectric constant. As $\omega \rightarrow 0$, Eq. (7.38) gives an index of refraction

$$\tilde{n} = \left(1 + \frac{\omega_{\text{pi}}^2}{\Omega_i^2} \right)^{\frac{1}{2}} \quad (7.39)$$

and so a phase velocity

$$v_p = \frac{\omega}{k} = \frac{c}{\tilde{n}} = c \left(1 + \frac{\omega_{\text{pi}}^2}{\Omega_i^2} \right)^{-\frac{1}{2}} \quad (7.40)$$

If we define an “Alfven speed,” v_A , by

$$v_A \equiv \frac{c \Omega_i}{\omega_{\text{pi}}} = \frac{c \frac{eB}{m_i}}{\left(\frac{ne^2}{\epsilon_0 m_i} \right)^{\frac{1}{2}}} = \frac{cB}{\sqrt{\frac{nm_i}{\epsilon_0}}} = \frac{B}{\sqrt{\mu_0 n m_i}} \quad (7.41)$$

then the phase velocity can be written

$$v_p = \frac{c}{\left(1 + \frac{c^2}{v_A^2} \right)^{\frac{1}{2}}}$$

Multiplying top and bottom by v_A/c , and then taking $v_A/c = \Omega_i/\omega_{pi} \ll 1$ (which is correct for $\omega_{pe} \sim \Omega_e$), we have

$$v_p = \frac{v_A}{\left(1 + \frac{v_A^2}{c^2}\right)^{\frac{1}{2}}} \approx v_A \quad (7.42)$$

The left-hand shear Alfvén wave (L-wave) has the dispersion relation

$$\tilde{n}^2 = \frac{c^2 k^2}{\omega^2} = \frac{\Omega_i + \frac{\omega_{pi}^2}{\Omega_i} - \omega}{\Omega_i - \omega} \quad (7.43)$$

This has the same low frequency behavior as the R-wave. At low frequencies, plane polarized shear Alfvén waves exist, and do not undergo Faraday rotation. The L-wave, however, clearly has a resonance at $\omega = \Omega_i$, associated with the left-handed ion-cyclotron motion, and a cutoff at $\omega = \omega_L = \Omega_i + \omega_{pi}^2/\Omega_i$.

In the lowest frequency range ($\omega \ll \Omega_i$), both the ions and the electrons are $E_1 \times B_0$ drifting, and the ions have a simple low frequency polarization drift, which is small compared to their $E_1 \times B_0$ drift. The magnetic field lines themselves also “move” with the same $v_\perp = E_1 \times B_0/B^2$, since the plasma is “frozen” to the field lines. The field lines are twisting – moving circularly in the (x, y) plane – with different phases of rotation along z . The twisting of the field lines pulls the magnetic configuration away from its lowest energy state, and magnetic energy is stored in the “twist.” The ions provide the inertia for this wave, causing the field lines to continue to move circularly, rather than come to rest. The twisting motion of the shear Alfvén mode has $\nabla \cdot v_1 = 0$, so there is no compression, no perturbed pressure, p_1 , and hence no pressure effects on the waves.

7.3 Langmuir Waves and Landau Damping

Consideration of the simplest case of an electrostatic wave in a field-free ($E_0 = B_0 = 0$) uniform plasma provides some insight into some basic plasma wave phenomena, as well as illustrating some of the mathematical techniques that are employed in the linear analysis of plasma waves. Starting with the linearized Vlasov equation,

$$\frac{\partial f_{\sigma 1}}{\partial t} + \mathbf{v} \cdot \nabla f_{\sigma 1} = \frac{e_\sigma}{m_\sigma} \nabla \Phi_1 \cdot \nabla_{\mathbf{v}} f_{\sigma 0} \quad (7.44)$$

that is appropriate for electrostatic waves in an initially field-free plasma, we assume that the perturbed distribution functions and electrostatic potential can be constructed from a superposition of wavelike forms,

$$f_{\sigma 1}(\mathbf{r}, \mathbf{v}, t) \sim f_{\sigma k}(\mathbf{v}) e^{i(\mathbf{k} \cdot \mathbf{r} - \omega t)}$$

and

$$\Phi_1(\mathbf{r}, t) \sim \Phi_k e^{i(\mathbf{k} \cdot \mathbf{r} - \omega t)} \quad (7.45)$$

Substituting the assumed forms into Eq. (7.44) leads to a formal solution for the k -component of the perturbed distribution function for plasma species σ ,

$$f_{\sigma k} = -\frac{\frac{e_\sigma}{m_\sigma}(\mathbf{k} \cdot \nabla_v f_{\sigma 0})}{\omega - \mathbf{k} \cdot \mathbf{v}} \Phi_k \quad (7.46)$$

The dispersion relation follows from using Eq. (7.46) in Poisson's equation

$$\nabla^2 \Phi_k = -\frac{1}{\epsilon_0} \sum_\sigma n_\sigma e_\sigma \int f_{\sigma k} d^3 v \quad (7.47)$$

which leads to

$$D(\omega, k) \equiv 1 + \sum_\sigma \frac{\omega_{p\sigma}^2}{k^2} \int_{-\infty}^{\infty} \frac{\mathbf{k} \cdot \nabla_v f_{\sigma 0}}{\omega - \mathbf{k} \cdot \mathbf{v}} d^3 v = 0 \quad (7.48)$$

The stable solutions of the form of Eqs. (7.45) which persist after long times must have ω almost real, with only a small imaginary part. Writing $\omega = \omega_r + i\gamma$, and requiring $\gamma \ll \omega_r$ allows the velocity integral in Eq. (7.48) to be evaluated by a Taylor series expansion of the integrand about $\omega = \omega_r$

$$\begin{aligned} \int_{-\infty}^{\infty} \frac{\mathbf{k} \cdot \nabla_v f_{\sigma 0} d^3 v}{\mathbf{k} \cdot \mathbf{v} - \omega} &= \lim_{\gamma \rightarrow 0} \int_{-\infty}^{\infty} \frac{\mathbf{k} \cdot \nabla_v f_{\sigma 0} d^3 v}{\mathbf{k} \cdot \mathbf{v} - \omega_r - i\gamma} \\ &\quad + i\gamma \frac{\partial}{\partial \omega_r} \left(\lim_{\gamma \rightarrow 0} \int_{-\infty}^{\infty} \frac{\mathbf{k} \cdot \nabla_v f_{\sigma 0} d^3 v}{\mathbf{k} \cdot \mathbf{v} - \omega_r - i\gamma} \right) + \dots \end{aligned} \quad (7.49)$$

It is convenient to reduce these integrals to one-dimensional integrals over the velocity component, u , along the wave propagation direction, \mathbf{k} , by defining

$$F_{\sigma 0}(u) \equiv \int f_{\sigma 0}(\mathbf{v}) \delta \left(u - \frac{\mathbf{k} \cdot \mathbf{v}}{|\mathbf{k}|} \right) d^3 v \quad (7.50)$$

which reduces the integrals in Eq. (7.46) to

$$\lim_{\gamma \rightarrow 0} \int_{-\infty}^{\infty} \frac{\frac{\partial F_{\sigma 0}}{\partial u} du}{u - \frac{\omega_r}{|\mathbf{k}|} - i\frac{\gamma}{|\mathbf{k}|}}$$

(Evaluation of complex integrals of this type will be discussed in the next section.) Combining these results, the dispersion relation of Eq. (7.48) becomes

$$D(\omega, k) = 1 - \sum_\sigma \frac{\omega_{p\sigma}^2}{k^2} \left(1 + i\gamma \frac{\partial}{\partial \omega_r} \right) \left[\oint \frac{\frac{\partial F_{\sigma 0}}{\partial u} du}{u - \frac{\omega_r}{|\mathbf{k}|}} + i\pi \left(\frac{\partial F_{\sigma 0}}{\partial u} \right)_{u=\frac{\omega_r}{|\mathbf{k}|}} \right] = 0 \quad (7.51)$$

where \oint is the Cauchy principal value integral.

When the phase velocity, ($\frac{\omega}{|k|}$), of the waves is much greater than the thermal velocity, $v_{\sigma\text{th}}$, the principle value integral may be expanded

$$\oint \frac{\frac{\partial F_{\sigma 0}}{\partial u} du}{u - \frac{\omega_r}{|k|}} = - \int \frac{\partial F_{\sigma 0}}{\partial u} \left(\frac{1}{\frac{\omega_r}{|k|}} + \frac{u}{\left(\frac{\omega_r}{|k|}\right)^2} + \frac{u^2}{\frac{\omega_r}{|k|}} + \dots \right) du$$

Using this expansion and a Maxwellian velocity distribution,

$$F_{\sigma 0}(u) = \left(\frac{m_\sigma}{2\pi T_\sigma} \right)^{\frac{1}{2}} e^{-\frac{m_\sigma u^2}{2T_\sigma}}$$

for the one-dimensional velocity distribution in Eq. (17.52) leads to

$$D(\omega, k) \simeq 1 - \sum_{\sigma} \left(1 + i\gamma \frac{\partial}{\partial \omega_r} \right) \left[\frac{\omega_{p\sigma}^2}{\omega_r^2} + \frac{3}{2} \frac{\omega_{p\sigma}^2}{\omega_r^2} k^2 \lambda_{D\sigma}^2 + \dots + i\pi \frac{\omega_{p\sigma}^2}{k^2} \left(\frac{\partial F_{\sigma 0}}{\partial u} \right)_{u=\frac{\omega_r}{|k|}} \right] = 0 \quad (7.52)$$

where the Debye length for species σ has been introduced,

$$\lambda_{D\sigma} \equiv \sqrt{\frac{\epsilon_0 T_\sigma}{n_\sigma e_\sigma^2}} \quad (7.53)$$

Because $\omega_{pe} \gg \omega_{pi}$, only the electron contribution to the sum in the dispersion relation need be retained. Since $k\lambda_{De} \ll 1$ and $\gamma \ll \omega_r$, the reduced dispersion relation can be solved for the oscillation frequency,

$$\omega_r \simeq \omega_{pe} \left(1 + \frac{3}{2} k^2 \lambda_{De}^2 \right) \quad (7.54)$$

and the damping factor,

$$\gamma = -\sqrt{\frac{\pi}{8}} \frac{\omega_{pe}}{|k^3 \lambda_{De}^3|} e^{-\left(\frac{3}{2} + \frac{1}{2k^2 \lambda_{De}^2}\right)} \sim \left(\frac{\partial F_{e0}}{\partial u} \right)_{u=\frac{\omega_r}{|k|}} \quad (7.55)$$

This form of collisionless damping is known as Landau damping and is proportional to the slope of the distribution function evaluated at the wave phase velocity, $u = \frac{\omega_r}{k}$. For a distribution function that decreases with velocity, $\gamma < 0$, which ensures damping of the wave. Physically, when $\frac{\partial F_{e0}}{\partial u} < 0$ there are more particles moving slightly slower than the wave phase velocity than there are moving slightly faster. The slower particles are accelerated by the wave, taking energy from it, while the faster particles are decelerated by the wave, giving energy to it. Thus there is a net damping of the wave when $\frac{\partial F_{e0}}{\partial u} < 0$, and a growth of the wave when $\frac{\partial F_{e0}}{\partial u} > 0$, with the slope of the distribution function being evaluated at the wave phase velocity. It follows from this that a monotonically decreasing distribution function is sufficient to ensure damping. Conversely, waves whose phase velocities coincide with a velocity region where the distribution function increases with velocity might be expected to grow.

7.4 Vlasov Theory of Plasma Waves*

We will study the small amplitude dynamics of a plasma in a uniform magnetic field ($\mathbf{B}_0 = B_0 \hat{\mathbf{n}}_z$) which has an equilibrium distribution function, f_0 , for each species that satisfies the time-independent Vlasov equation

$$\mathbf{v} \cdot \nabla f_0 + \frac{e}{m} (\mathbf{v} \times \mathbf{B}_0) \cdot \nabla_{\mathbf{v}} f_0 = 0 \quad (7.56)$$

and Ampère's law

$$\nabla \times \mathbf{B}_0 = \mu_0 \mathbf{j}_0 \equiv \mu_0 \sum_{\sigma} n_{\sigma} e_{\sigma} \int \mathbf{v} f_{\sigma 0} d^3 v = 0 \quad (7.57)$$

The zero subscript refers to the equilibrium value (except for μ_0). Note that we are treating the case $E_0 = 0$. The quantity n_{σ} is the average particle density. The most general solution of Eq. (7.56) that is isotropic in the plane perpendicular to \mathbf{B}_0 is of the form

$$f_0 = f_0(v_{\perp}^2, v_{\parallel}^2) \quad (7.58)$$

The two-temperature Maxwellian,

$$f_0 = \frac{m}{2\pi T_{\perp}} \left(\frac{m}{2\pi T_{\parallel}} \right)^{\frac{1}{2}} \left[\exp -\frac{m}{2} \left(\frac{v_{\perp}^2}{T_{\perp}} + \frac{v_{\parallel}^2}{T_{\parallel}} \right) \right] \quad (7.59)$$

is a frequently used example.

Since we are considering small amplitude perturbations about the equilibrium, we write

$$f = f_0 + f_1, \mathbf{B} = \mathbf{B}_0 + \mathbf{B}_1, \mathbf{E} = \mathbf{E}_1, \mathbf{j} = \mathbf{j}_0 + \mathbf{j}_1 \quad (7.60)$$

The perturbed quantities must satisfy the linearized Vlasov equation

$$\frac{\partial f_1}{\partial t} + \mathbf{v} \cdot \nabla f_1 + \frac{e}{m} (\mathbf{v} \times \mathbf{B}_0) \cdot \nabla_{\mathbf{v}} f_1 = -\frac{e}{m} (\mathbf{E}_1 + \mathbf{v} \times \mathbf{B}_1) \cdot \nabla_{\mathbf{v}} f_0 \quad (7.61)$$

and Maxwell's equations

$$\nabla \times \mathbf{E} = -\frac{\partial \mathbf{B}_1}{\partial t} \quad (7.62)$$

$$\nabla \times \mathbf{B}_1 - \frac{1}{c^2} \frac{\partial \mathbf{E}_1}{\partial t} = \mu_0 \mathbf{j}_1 \equiv \mu_0 \sum_{\sigma} n_{\sigma} e_{\sigma} \int \mathbf{v} f_{\sigma 1} d^3 v \quad (7.63)$$

and

$$\epsilon_0 \nabla \cdot \mathbf{E}_1 = \sum_{\sigma} n_{\sigma} e_{\sigma} \int f_{\sigma 1} d^3 v \quad (7.64)$$

where the sum is over species.

Equation (7.61) can be solved by integrating along the equilibrium ($\mathbf{B} = \mathbf{B}_0, \mathbf{E} = 0$) particle orbits, which is the method of characteristics. Defining a primed set of coordinates by the equilibrium orbit equations

$$\frac{d\mathbf{r}'}{dt'} = \mathbf{v}' \quad \frac{d\mathbf{v}'}{dt'} = \frac{e}{m} [\mathbf{v}' \times \mathbf{B}_0(\mathbf{r}', t')] \quad (7.65)$$

which coincide with the actual coordinates at time t : $\mathbf{r}'(t' = t) = \mathbf{r}$, $\mathbf{v}'(t' = t) = \mathbf{v}$, Eq. (7.61) can be transformed into the primed coordinate system. Noting that the third term in Eq. (7.61) is

$$\mathbf{a} \cdot \nabla_{\mathbf{v}} f_1 \equiv \frac{d\mathbf{v}}{dt} \cdot \nabla_{\mathbf{v}} f_1$$

the LHS of Eq. (7.61) is seen to be the substantive derivative, $d f_1 / dt$. Thus Eq. (7.61) can be integrated from $t' = -\infty$ to $t' = t$ to obtain

$$f_1(\mathbf{r}, \mathbf{v}, t) = -\frac{e}{m} \int_{-\infty}^t dt' [\mathbf{E}_1(\mathbf{r}', t') + \mathbf{v}' \times \mathbf{B}(\mathbf{r}', t')] \cdot \nabla_{\mathbf{v}'} f_0(\mathbf{r}', \mathbf{v}', t') \quad (7.66)$$

Assuming that the solution for \mathbf{E}_1 and \mathbf{B}_1 can be constructed from a superposition of functions of the form

$$\mathbf{E}_1 \sim \mathbf{E}_k e^{i(k \cdot \mathbf{r} - \omega t)}, \mathbf{B}_1 \sim \mathbf{B}_k e^{i(k \cdot \mathbf{r} - \omega t)} \quad (7.67)$$

(such a form would result from Fourier and Laplace transformation and inversion in the space and time domains, respectively), the corresponding solution to Eq. (7.66) can be constructed from

$$f_1 \sim f_k = -\frac{e}{m} \int_{-\infty}^0 (\mathbf{E}_k + \mathbf{v}' \times \mathbf{B}_k) \cdot \nabla_{\mathbf{v}'} f_0(\mathbf{v}') e^{i[k \cdot (\mathbf{r}' - \mathbf{r}) - \omega(t' - t)]} d(t' - t) \quad (7.68)$$

Equation (7.68) is valid for $\text{Im}(\omega) > 0$. The solution for $\text{Im}(\omega) < 0$ is obtained by analytic continuation.

The $\nabla_{\mathbf{v}} f_0$ term in Eq. (7.68) can be written

$$\nabla_{\mathbf{v}} f_0 = 2v_{\parallel} \frac{\partial f_0}{\partial v_{\parallel}^2} \hat{n}_z + 2(\mathbf{v} - v_{\parallel} \hat{n}_z) \frac{\partial f_0}{\partial v_{\perp}^2} \quad (7.69)$$

when we make use of Eq. (7.58) and note that $\hat{n}_z = \hat{n}_{\parallel}$. Conservation of magnetic moment and of energy in a uniform magnetic field is sufficient to ensure that v_{\perp} is constant along the unperturbed (primed coordinates) orbit, and $E_0 = 0$ insures that v_{\parallel} is constant along the unperturbed orbit. Therefore $f_0(v_{\parallel}^2, v_{\perp}^2)$ is constant along the unperturbed orbits. This allows the terms $\partial f_0 / \partial v_{\perp}^2$ and $\partial f_0 / \partial v_{\parallel}^2$ to be removed from under the integral sign in Eq. (7.68), leaving integrals of the form

$$\int_{-\infty}^0 (\mathbf{v}_{x'}, \mathbf{v}_{y'}, 1) e^{i[k \cdot (\mathbf{r}' - \mathbf{r}) - \omega(t' - t)]} d(t' - t)$$

to be evaluated. We use the results on particle orbits in a uniform magnetic field from chapter 2 to write

$$\begin{aligned} v_{x'} &= v_{\perp} \cos(-\Omega t + \phi) & x' &= x - \frac{v_{\perp}}{\Omega} \sin(-\Omega t + \phi) + \frac{v_{\perp}}{\Omega} \sin \phi \\ v_{y'} &= v_{\perp} \sin(-\Omega t + \phi) & y' &= y + \frac{v_{\perp}}{\Omega} \cos(-\Omega t + \phi) - \frac{v_{\perp}}{\Omega} \cos \phi \\ v_{z'} &= v_{\parallel} & z' &= v_{\parallel}(t' - t) + z \end{aligned} \quad (7.70)$$

where here

$$\Omega \equiv -\frac{eB}{m} \quad (7.71)$$

is the gyrofrequency. Using Eqs. (7.70), integrals of the above type can be performed most conveniently by using the identity

$$\exp \left[\frac{i k_{\perp} v_{\perp}}{\Omega} \sin(-\Omega t + \phi) \right] = \sum_{n=-\infty}^{\infty} J_n \left(\frac{k_{\perp} v_{\perp}}{\Omega} \right) e^{in(\Omega t + \phi)} \quad (7.72)$$

where J_n is the Bessel function of the first kind of order n .

The resulting evaluation of Eq. (7.68) yields

$$f_k = \frac{e}{m} \sum_{n,l} \left\{ \left[\frac{2Zv_{\parallel}J_l + Xv_{\perp}(J_{l+1} + J_{l-1}) - iYv_{\perp}(J_{l+1} + J_{l-1})}{i(\omega - l\Omega - k_{\parallel}v_{\parallel})} \right] \times J_n e^{-i(n-l)\phi} \right\} \quad (7.73)$$

where the arguments of the Bessel functions are given in Eq. (7.72), the “wave vector,” \mathbf{k} , has been decomposed

$$\mathbf{k} = k_{\perp} \hat{\mathbf{n}}_x + k_{\parallel} \hat{\mathbf{n}}_z \quad (7.74)$$

and

$$\begin{aligned} X &\equiv E_{1x} \frac{\partial f_0}{\partial v_{\perp}^2} + \frac{v_{\parallel}}{\omega} (k_{\parallel} E_{1x} - k_{\perp} E_{1z}) \left(\frac{\partial f_0}{\partial v_{\parallel}^2} - \frac{\partial f_0}{\partial v_{\perp}^2} \right) \\ Y &\equiv E_{1y} \frac{\partial f_0}{\partial v_{\perp}^2} + \frac{v_{\parallel}}{\omega} k_{\parallel} E_{1y} \left(\frac{\partial f_0}{\partial v_{\parallel}^2} - \frac{\partial f_0}{\partial v_{\perp}^2} \right) \\ Z &\equiv E_{1z} \frac{\partial f_0}{\partial v_{\parallel}^2} \end{aligned} \quad (7.75)$$

Using the form of Eq. (7.67) in Eq. (7.62) leads to

$$ik \times \mathbf{E}_k = i\omega \mathbf{B}_k \quad (7.76)$$

Using this result and Eq. (7.67) in Eq. (7.61) yields

$$-\mathbf{k} \times \mathbf{k} \times \mathbf{E}_k = \frac{\omega^2}{c^2} \mathbf{E}_k + i\omega \sum_{\sigma} n_{\sigma} e_{\sigma} \int \mathbf{v} f_{\sigma k} d^3 v \quad (7.77)$$

where f_k is given by Eq. (7.73).

Evaluation of the integral in Eq. (7.77) involves performing velocity integrals of the form

$$g_k(p) = \int_{-\infty}^{\infty} \frac{h(u) du}{u - \frac{ip}{|k|}} \quad (7.78)$$

which are strictly defined only for $\text{Re}(p) \geq p_0$, where p_0 is a real, positive constant chosen sufficiently large that the integral

$$\int_0^{\infty} f_k(\mathbf{r}, \mathbf{v}, t) e^{-p_0 t} dt$$

converges. This requirement follows from the requirement that f_k has a solution of the form of Eq. (7.67) with $p = i\omega$ or, equivalently, that the Laplace transform of f_k exists. It is useful to define a function $G_k(p)$ that is identical with $g_k(p)$ for $\text{Re}(p) > p_0$ and that is the analytic continuation of $g_k(p)$ for $\text{Re}(p) < p_0$. We can generally limit our considerations to functions $h(u)$ that are analytic for all $|u| < \infty$.

The analytic continuation of $g_k(p)$ requires that the path of integration from $-\infty$ to $+\infty$ along the real axis in Eq. (7.78) pass under the pole at $u = ip/|k|$. There are three possible cases, $\text{Re}(p) > 0$, and $\text{Re}(p) = 0$, $\text{Re}(p) < 0$. The corresponding integration paths that must be used in evaluating Eq. (7.78) are shown in Fig. 7.1. The value of $G_k(p)$ is defined differently, depending upon the location of the pole.

$$G_k(p) = \begin{cases} \int_{-\infty}^{\infty} \frac{h(u) du}{u - \frac{ip}{|k|}} & \text{Re}(p) > 0 \\ \oint_{-\infty}^{\infty} \frac{h(u) du}{u - \frac{ip}{|k|}} + \pi i h\left(\frac{ip}{|k|}\right) & \text{Re}(p) = 0 \\ \oint_{-\infty}^{\infty} \frac{h(u) du}{u - \frac{ip}{|k|}} + 2\pi i h\left(\frac{ip}{|k|}\right) & \text{Re}(p) < 0 \end{cases} \quad (7.79)$$

Where

$$\oint_{-\infty}^{\infty} = \lim_{\epsilon \rightarrow 0} \left(\int_{-\infty}^{\frac{ip}{|k|}-\epsilon} + \int_{\frac{ip}{|k|}+\epsilon}^{\infty} \right)$$

is the Cauchy principal value of the integral. The integration in Eqs. (7.79) is along the axis.

A solution of the form of Eqs. (7.67) can be used in Eq. (7.64) to obtain

$$\epsilon_0 \mathbf{k} \cdot \mathbf{E}_k = \sum_{\sigma} n_{\sigma} e_{\sigma} \int f_{\sigma k} d^3 v \quad (7.80)$$

When Eq. (7.73) is used in Eq. (7.77) and Eq. (7.80) and the latter two are combined, a set of three coupled equations for the components $E_{\parallel} = E_z$, E_x and E_y of the electric field

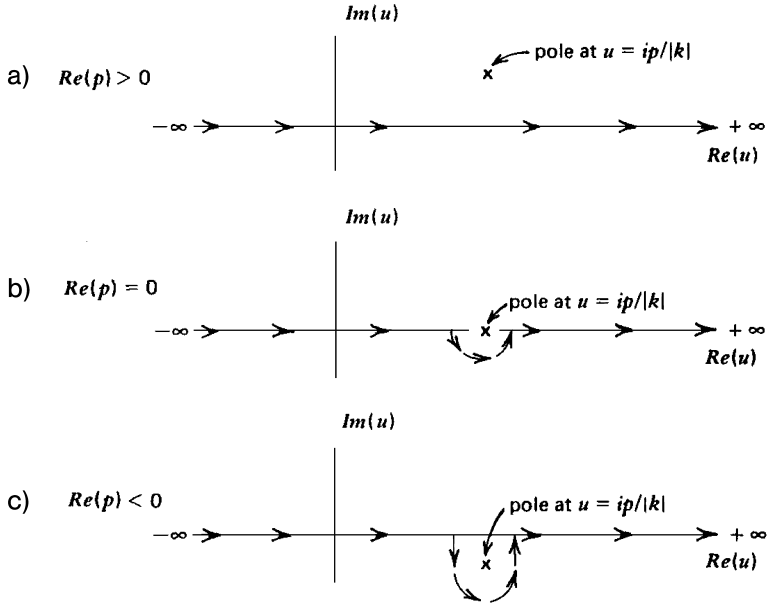


Figure 7.1. Integration paths for evaluating $G_k(p)$ from Eq. (7.59)

is obtained. These equations can be written in matrix format as

$$[D][E] \equiv \begin{bmatrix} D_{xx} & D_{xy} & D_{xz} \\ D_{yz} & D_{yy} & D_{yz} \\ D_{zx} & D_{zy} & D_{zz} \end{bmatrix} \begin{bmatrix} E_x \\ E_y \\ E_z \end{bmatrix} = 0 \quad (7.81)$$

The condition that Eq. (7.81) has a nontrivial solution is that the determinant of the dispersion matrix, $[D]$, vanishes, or

$$\det[D(\omega, \mathbf{k})] = 0 \quad (7.82)$$

Equation (7.82) is the dispersion relation which defines the frequency spectrum $\omega = \omega(\mathbf{k})$. Perturbed solutions of the form given in Eq. (7.67) for which $\text{Im}(\omega) > 0$ grow in time and hence represent unstable perturbations. Thus the dispersion relation can be used to examine a plasma for stability with respect to perturbations with particular values of the displacement vector, \mathbf{k} .

More generally, Eq. (7.66) represent waves propagating in the direction \mathbf{k} with a time dependence characterized by $\omega(\mathbf{k})$. Some specific examples will be considered in the next section.

The elements of the dispersion matrix are

$$\begin{aligned}
D_{xx} &= 1 - \frac{c^2 k_{\parallel}^2}{\omega^2} - \frac{1}{2\omega} \sum_{\sigma} \left(\frac{\omega_{p\sigma}^2}{\Omega_{\sigma}} \right) \sum_n \left\langle \frac{n^2 \Omega_{\sigma}^2}{k_{\perp}^2} J_n^2 \chi_{\sigma} \right\rangle \\
D_{xy} = -D_{yx} &= -\frac{i}{2\omega} \sum_{\sigma} \left(\frac{\omega_{p\sigma}^2}{\Omega_{\sigma}} \right) \sum_n \left\langle \frac{n \Omega_{\sigma}^2 v_{\perp}}{k_{\perp}} J_n^2 \chi_{\sigma} \left[\frac{dJ_n}{d \frac{k_{\perp} v_{\perp}}{\Omega_{\sigma}}} \right] \right\rangle \\
D_{xz} &= \frac{c^2 k_{\parallel} k_{\perp}^2}{\omega^2} - \frac{1}{2\omega} \sum_{\sigma} \left(\frac{\omega_{p\sigma}^2}{\Omega_{\sigma}} \right) \sum_n \left\langle \frac{n \Omega_{\sigma} v_{\parallel} J_n^2}{k_{\perp}} \Lambda_{\sigma n} \right\rangle \\
D_{yy} &= 1 - \frac{c^2 (k_{\parallel} + k_{\perp})}{\omega^2} - \frac{1}{2\omega} \sum_{\sigma} \left(\frac{\omega_{p\sigma}^2}{\Omega_{\sigma}} \right) \sum_n \left\langle \Omega_{\sigma} v_{\perp}^2 \chi_{\sigma} \left[\frac{dJ_n}{d \frac{k_{\perp} v_{\perp}}{\Omega_{\sigma}}} \right]^2 \right\rangle \quad (7.83) \\
D_{yz} &= \frac{i}{2\omega} \sum_{\sigma} \left(\frac{\omega_{p\sigma}^2}{\Omega_{\sigma}} \right) \sum_n \left\langle \Omega_{\sigma} v_{\perp} v_{\parallel} J_n \Lambda_{\sigma n} \left[\frac{dJ_n}{d \frac{k_{\perp} v_{\perp}}{\Omega_{\sigma}}} \right] \right\rangle \\
D_{zx} &= \left(\frac{c^2 k_{\parallel} k_{\perp}}{\omega^2} \right) - \frac{1}{2\omega} \sum_{\sigma} \left(\frac{\omega_{p\sigma}^2}{\Omega_{\sigma}} \right) \sum_n \left\langle \frac{v_{\parallel} n \Omega_{\sigma}^2}{k_{\perp}} \chi_{\sigma} J_n^2 \right\rangle \\
D_{zy} &= -\frac{i}{2\omega} \sum_{\sigma} \left(\frac{\omega_{p\sigma}^2}{\Omega_{\sigma}} \right) \sum_n \left\langle v_{\parallel} v_{\perp} \Omega_{\sigma} \chi_{\sigma} J_n \left[\frac{dJ_n}{d \frac{k_{\perp} v_{\perp}}{\Omega_{\sigma}}} \right] \right\rangle \\
D_{zz} &= 1 - \frac{c^2 k_{\perp}^2}{\omega^2} - \frac{1}{2\omega} \sum_{\sigma} \left(\frac{\omega_{p\sigma}^2}{\Omega_{\sigma}} \right) \sum_n \left\langle v_{\parallel}^2 \Omega_{\sigma} \Lambda_{\sigma n} J_n^2 \right\rangle
\end{aligned}$$

In Eqs. (7.83), the operation $\langle \rangle$ is defined as

$$\langle F(v) \rangle \equiv \int_{-\infty}^{\infty} dv_{\parallel} \int_0^{\infty} dv_{\perp} \frac{2v_{\perp} F(v_{\perp}, v_{\parallel})}{k_{\parallel} v_{\parallel} + n \Omega_{\sigma} - \omega} \quad (7.84)$$

where the integrals are evaluated along the contours that were discussed in relation to Fig. 7.1. The other quantities introduced in Eqs. (7.83) with a species index are

$$\chi_{\sigma} \equiv \frac{\partial f_{\sigma 0}}{\partial v_{\perp}^2} \left(1 - \frac{k_{\parallel} v_{\parallel}}{\omega} \right) + \frac{k_{\parallel} v_{\parallel}}{\omega} \frac{\partial f_{\sigma 0}}{\partial v_{\parallel}^2} \quad (7.85)$$

$$\Lambda_{\sigma n} \equiv \frac{\partial f_{\sigma 0}}{\partial v_{\parallel}^2} - \frac{n \Omega_{\sigma}}{\omega} \left(\frac{\partial f_{\sigma 0}}{\partial v_{\parallel}^2} - \frac{\partial f_{\sigma 0}}{\partial v_{\perp}^2} \right) \quad (7.86)$$

and the plasma frequency

$$\omega_{p\sigma} \equiv \sqrt{\frac{e_\sigma^2 n_\sigma}{m_\sigma \epsilon_0}} \quad (7.87)$$

7.5 Electrostatic Waves*

There is a class of wave phenomena in plasmas for which the magnetic field is unperturbed, $\mathbf{B}_1 = 0$. For such purely electrostatic waves the perturbed electric field can be represented by a scalar potential and the development and evaluation of a dispersion relation is considerably simplified. In this section we specialize the formalism of the previous section to the simpler form that is appropriate for electrostatic waves and examine several types of such waves.

We will consider a uniform magnetic field, $\mathbf{B}_0 = B_0 \hat{n}_z$, in the z -direction. For the moment, we treat only the electron dynamics and consider the ions as a cold, fixed background. Single-charged ions are assumed throughout this section.

It is convenient to specifically designate the non-oscillatory part of the time dependence of the perturbation by replacing ω with $\omega + i\gamma$ in Eq. (7.67), where γ is a real constant which determines the growth or damping of the wave amplitude. A development similar to that which led to Eq. (7.73) then leads to

$$f_{ek} = -\frac{e}{m_e} \Phi_k e^{-\frac{ik_\perp v_\perp \sin \phi}{\Omega_e}} \sum_n \frac{J_n \left(2n\omega \frac{\partial f_{e0}}{\partial v_\perp^2} + k \frac{\partial f_{e0}}{\partial v_\parallel} \right) e^{in\phi}}{k_\parallel v_\parallel - (\omega + i\gamma) + n\Omega_e} \quad (7.88)$$

where Φ_k is the k -component of the perturbed electrostatic potential.

Assuming that the unperturbed electron distribution function is a Maxwellian,

$$f_{e0}(v) = \left(\frac{m_e}{2\pi T_e} \right)^{\frac{3}{2}} e^{-\frac{m_e v^2}{2T_e}} \quad (7.89)$$

using the identity of Eq. (7.72), and defining

$$\begin{aligned} X_n \left(\frac{k_\perp^2 T_e}{m_e \Omega_e^2} \right) &\equiv \int_0^\infty \left[2\pi v_\perp dv_\perp \frac{m_e}{2\pi T_e} e^{-\frac{m_e v_\perp^2}{2T_e}} J_n^2 \left(\frac{k_\perp v_\perp}{\Omega_e} \right) \right] \\ &= I_n \left(\frac{k_\perp^2 T_e}{m_e \Omega_e^2} \right) e^{-\frac{k_\perp^2 T_e}{m_e \Omega_e^2}} \end{aligned} \quad (7.90)$$

where I_n is the Bessel function of the second type, the perturbed electron density can be calculated from

$$n_{ek} \equiv n_e \int f_k d^3v$$

$$= \frac{en_e \Phi_k}{T_e} \left\{ 1 + \sum_n X_n \int_{-\infty}^{\infty} dv_{\parallel} \left[\frac{(\omega + i\gamma) \left(\frac{m_e}{2\pi T_e} \right)^{\frac{1}{2}} e^{-\frac{m_e v_{\parallel}^2}{2T_e}}}{k_{\parallel} v_{\parallel} - (\omega + i\gamma) + n\Omega_e} \right] \right\} \quad (7.91)$$

It is convenient to transform variables by defining

$$y \equiv \frac{\omega - n\Omega_e}{k_{\parallel} \sqrt{\frac{T_e}{m_e}}}$$

$$x \equiv \sqrt{\frac{m_e}{T_e}} v_{\parallel}$$

$$\epsilon \equiv \frac{\gamma}{k_{\parallel}} \sqrt{\frac{m_e}{T_e}}$$

$$b \equiv \frac{k_{\perp}^2 T_e}{m_e \Omega_e^2}$$

$$Z(y) \equiv \int_{-\infty}^{\infty} \frac{dx}{\sqrt{2\pi}} \frac{e^{-\frac{x^2}{2}}}{x - y - i\epsilon} \quad (7.92)$$

With this change of variables, Eq. (7.91) becomes

$$n_{ek} = \frac{en_e \Phi_k}{T_e} \left[1 + \sum_n X_n(b) Z(y) \sqrt{\frac{m_e}{T_e}} \frac{\omega + i\gamma}{k_{\parallel}} \right] \quad (7.93)$$

Now we make the cold plasma approximation that b is small. In this case $I_n(b) \sim T_e^{-1} b^n$, and we are justified in keeping only the $n = 0, \pm 1$ terms in the sum in Eq. (7.93). For small γ , these terms can be approximately evaluated to obtain a simple expression for the k -component of the perturbed electron density,

$$n_{ek} = -en_e \Phi_k \left[\frac{k_{\perp}^2}{m_e(\omega^2 - \Omega_e^2)} + \frac{k_{\parallel}^2}{m_e \omega^2} \right] \quad (7.94)$$

Perturbations in the electron density produce a local charge density concentration, en_{ek} , because $n_e = n_i$ in equilibrium and we are considering a model in which the ions are fixed. This charge concentration produces an electric field according to Eq. (7.64) which, in the case of electrostatic fields, becomes Poisson's equation

$$-\nabla^2 \Phi_k \equiv k^2 \Phi_k = \frac{en_{ek}}{\epsilon_0} \quad (7.95)$$

Substitution of Eq. (7.94) into Eq. (7.95) yields the dispersion relation for small amplitude electrostatic waves in a cold, uniform plasma with a uniform magnetic field,

$$1 = \frac{k_{\perp}^2 \omega_{pe}^2}{k^2(\omega^2 - \Omega_e^2)} + \frac{k_{\parallel}^2 \omega_{pe}^2}{k^2 \omega^2} \quad (7.96)$$

For weak magnetic fields, $|\omega_{pe}| \gg |\Omega_e|$. For waves with $|\omega| \approx |\omega_{pe}|$, Eq. (7.96) reduces to

$$\omega^2 \simeq \omega_{pe}^2 + \frac{k_\perp^2}{k^2} \Omega_e^2 \quad (7.97)$$

The first term arises from the motion of electrons parallel to the magnetic field in response to charge separation. (Recall that in chapter 1 we found that an unmagnetized plasma responded to a charge separation by oscillating at the electron plasma frequency, ω_{pe} .) The second term in Eq. (7.97) arises from the electron gyromotion perpendicular to the magnetic field. For waves with $|\omega| \simeq |\Omega_e| \ll |\omega_{pe}|$, Eq. (7.96) reduces to

$$\omega^2 \simeq \frac{k_\parallel^2}{k^2} \Omega_e^2 \quad (7.98)$$

a mode which obviously is associated with the electron gyromotion.

For strong magnetic fields and/or low plasma densities (that is, low- β plasmas), $|\Omega_e| \gg |\omega_{pe}|$. For waves with $|\omega| \simeq |\Omega_e|$, Eq. (7.96) reduces to

$$\omega^2 = \omega_{pe}^2 \frac{k_\parallel^2}{k^2} + \Omega_e^2 \quad (7.99)$$

When the wave propagates perpendicular to the magnetic field ($k_\parallel = 0$), Eq. (7.99) describes the upper-hybrid electron–cyclotron wave with $\omega \simeq \pm \Omega_e$. For, waves with $|\omega| \simeq |\omega_{pe}| \ll \Omega_e$, Eq. (7.96) becomes

$$\omega^2 = \omega_{pe}^2 \frac{k_\parallel^2}{k^2} \quad (7.100)$$

For waves propagating almost perpendicular to the magnetic field, ion effects (which are not included in this analysis) become important and must be included in the analysis. The wave described by (7.100) is the lower-hybrid wave.

Now the analysis is generalized to include ion motion. A development of the same type that led to Eq. (7.93) yields an expression for the k -component of the ion density perturbation

$$n_{ik} = \frac{en_i\Phi_k}{T_i} \left(1 + \sum_n X_n(b_i) Z(y_i) \sqrt{\frac{m_i}{T_i}} \frac{\omega + i\gamma}{k_\parallel} \right) \quad (7.101)$$

where variables are defined as before, but now in terms of the plasma ion properties instead of the electron properties. We will use the subscripts e and i to distinguish the two sets of variables.

If we consider “hot” electrons, so that y_e is small, then $\text{Re}[Z(y_e)]$ is small in Eq. (7.93), and that equation reduces to

$$\text{Re}(n_e k) \simeq \frac{en_e\Phi_k}{T_e} \quad (7.102)$$

Limiting our consideration to low-frequency ion cyclotron waves, for which $|\omega| \simeq |\Omega_i|$, the assumption of “cold” ions allows us to treat Eq. (7.101) in the same way that

Eq. (7.93) was treated in reducing it to Eq. (7.94) to obtain a expression for the real part of the k -component of the perturbed ion density

$$\text{Re}(n_{ik}) \simeq en_i\Phi_k \left[\frac{k_\perp^2\omega^2}{m_i\Omega_i^2(\omega^2 - \Omega_i^2)} + \frac{k_\parallel^2}{m_i\omega^2} \right] \quad (7.103)$$

The dispersion relation is obtained from the quasineutrality condition by using Eq. (7.102) and Eq. (7.103),

$$\text{Re}(n_{ek} - n_{ik}) \simeq 0 \simeq en\Phi_k \left[\frac{1}{T_e} - \frac{k_\perp^2\omega^2}{m_i\Omega_i^2(\omega^2 - \Omega_i^2)} - \frac{k_\parallel^2}{m_i\omega^2} \right] \quad (7.104)$$

(In the limit of low-frequency waves that we are considering, the simpler quasineutrality condition is equivalent to Poisson's equation.) For waves propagating almost perpendicular to the field ($k_\perp \gg k_\parallel$) with $|\omega - \Omega_i| \ll |\omega|$, Eq. (7.104) reduces to the dispersion relation for the electrostatic ion cyclotron wave,

$$\omega^2 \simeq \Omega_i^2 + \frac{k_\perp^2 T_e}{m_i} \quad (7.105)$$

In order to examine the growth or damping of the ion cyclotron wave it is necessary to include the imaginary parts of n_{ik} and n_{ek} in the quasineutrality condition. Making the same approximations that were used to arrive at Eq. (7.102) and Eq. (7.103), but now retaining the imaginary parts, leads to the quasineutrality condition

$$0 = n_{ek} - n_{ik} = en\Phi_k \left[\frac{1}{T_e} \left(1 + \frac{i\omega\sqrt{\frac{\pi}{2}}}{k_\parallel\sqrt{\frac{T_e}{m_e}}} \right) - \left(\frac{k_\perp^2}{m_i(\omega^2 - \Omega_i^2)} + \frac{k_\parallel^2}{m_i\omega^2} \right. \right. \\ \left. \left. - \frac{iX_1(b_i)\omega\sqrt{\frac{\pi}{2}} e^{-\frac{m_i(\omega-\Omega_i)^2}{2k_\parallel^2 T_i}}}{T_i k_\parallel \sqrt{\frac{T_i}{m_i}}} \right) \right] \quad (7.106)$$

from which we extract the dispersion relation

$$[D(\omega, k)] = \frac{1}{T_e} \left(1 + \frac{i\omega\sqrt{\frac{\pi}{2}}}{k_\parallel\sqrt{\frac{T_e}{m_e}}} \right) \\ - \left[\frac{k_\perp^2}{m_i(\omega^2 - \Omega_i^2)} + \frac{k_\parallel^2}{m_i\omega^2} - \frac{iX_1(b_i)\omega\sqrt{\frac{\pi}{2}} e^{-\frac{m_i(\omega-\Omega_i)^2}{2k_\parallel^2 T_i}}}{T_i k_\parallel \sqrt{\frac{T_i}{m_i}}} \right] \quad (7.107)$$

Representing $\omega = \omega_r + i\gamma$, where ω_r and γ are real numbers representing the real and imaginary parts, respectively, of ω , the assumption $|\gamma| \ll |\omega_r|$ allows $D(\omega, k)$ to be expanded about $\omega = \omega_r$ to obtain

$$\frac{\gamma \partial \operatorname{Re}[D(\omega_r)]}{\partial \omega} = -\operatorname{Im}[D(\omega_r)] \quad (7.108)$$

Using Eq. (7.105) for ω and Eq. (7.107) for $D(\omega)$ leads to an expression for the damping factor,

$$\gamma \simeq -\sqrt{\frac{\pi}{8}} \frac{k_\perp^2}{k_\parallel} \sqrt{\frac{T_e}{m_i}} \left[\sqrt{\frac{m_e}{m_i}} + \frac{1}{2} \frac{k_\perp^2 T_i}{m_i \Omega_i^2} \left(\frac{T_e}{T_i} \right)^2 e^{-\frac{m_i(\omega-\Omega_i)^2}{2k_\parallel^2 T_i}} \right] \quad (7.109)$$

for the electrostatic ion cyclotron wave. The mechanism for this collisionless, ion cyclotron damping is a wave-particle interaction related to the shape of the particle distribution function in the vicinity of the wave phase velocity. A similar phenomenon was discussed in section 7.3 in connection with Landau damping.

Next we consider waves in the frequency range $|\Omega_i| \ll |\omega| \ll |\Omega_e|$. For “cold” electrons ($\omega/k_\parallel \ll \sqrt{T_e/m_e}$), Eq. (7.94) becomes

$$n_{ek} \simeq e n_e \Phi_k \left(\frac{k_\perp^2}{m_e \Omega_e^2} - \frac{k_\parallel^2}{m_e \omega^2} \right) \quad (7.110)$$

For “cold” ions ($\omega/k \gg \sqrt{T_i/m_i}$), the equivalent of Eq. (7.103) in which the imaginary parts are retained becomes

$$n_{ik} \simeq e n_i \Phi_k \left(\frac{k^2}{m_i \omega^2} \right) \quad (7.111)$$

Using Eqs. (7.110) and (7.111) in Poisson’s equation,

$$\nabla^2 \Phi_k = -k^2 \Phi_k = \frac{e}{\epsilon_0} (n_{ek} - n_{ik}) = \frac{e^2 n \Phi_k}{\epsilon_0} \left(\frac{k_\perp^2}{m_e \Omega_e^2} - \frac{k_\parallel^2}{m_e \omega^2} - \frac{k^2}{m_i \omega^2} \right) \quad (7.112)$$

leads to the dispersion relation for the lower-hybrid wave,

$$\omega^2 = \frac{\Omega_e^2 \omega_{pe}^2 k^2}{k_\perp^2 \omega_{pe}^2 + k^2 \Omega_e^2} \left(\frac{k_\parallel^2}{k^2} + \frac{m_e}{m_i} \right) \quad (7.113)$$

The ions enter this expression only through the m_e/m_i term, so this is predominantly an electron wave. When the wave propagates perpendicular to the magnetic field ($k_\parallel = 0$), Eq. (7.113) reduces to

$$\omega_{LH}^2 = \frac{\Omega_e^2 \omega_{pe}^2}{\omega_{pe}^2 + \Omega_e^2} \cdot \frac{m_e}{m_i} \quad (7.114)$$

We have used the subscript LH because this quantity is referred to as the lower-hybrid frequency.

Still considering the frequency range $|\Omega_i| \ll |\omega| \ll |\Omega_e|$, but now considering “hot” electrons ($\omega/k_{\parallel} \ll \sqrt{T_e/m_e}$) and “cold” ions ($\omega/k_{\parallel} \gg \sqrt{T_i/m_i}$), we can use Eqs. (7.102) and (7.111) in Poisson’s equation to obtain the dispersion relation for an ion acoustic wave,

$$\omega^2 = \frac{k^2 T_e}{m_i \left(1 + \frac{k^2 T_e}{m_e \omega_{pe}^2} \right)} \quad (7.115)$$

This sampling of electrostatic waves gives some indication of the variety of wave phenomena which can exist in a plasma. Some of these waves are important in the wave heating of plasmas, as will be discussed in chapter 12.

Problems for Chapter 7

1. Derive Eq. (7.8) from Eq. (7.6).
2. Derive Eq. (7.14) from Eq. (7.13).
3. Derive Eqs. (7.23) from Eq. (7.3) to Eq. (7.5).
4. Calculate the electron and ion plasma frequencies, the electron and ion cyclotron frequencies, the upper and lower hybrid frequencies and the Alfvén speed for a deuterium plasma with $T = 10 \text{ keV}$, $n_D = n_e = 5 \times 10^{19} \text{ m}^{-3}$ and $B = 5 \text{ T}$.
5. Calculate the cut-off frequency for the shear Alfvén L-wave in the plasma of problem 4.
6. Derive the dispersion relation for the lower hybrid wave from Eqs. (7.94), (7.103) and (7.112). Justify any assumptions.
7. Calculate some electromagnetic wave frequencies at which you could heat a plasma with $R_0 = 3.5 \text{ m}$, $a = 1.0 \text{ m}$, $B_{\phi 0} = 4 \text{ T}$ at R_0 , $T = 10 \text{ keV}$ and $I = 1.5 \text{ MA}$.

8 Instabilities

A confined plasma is not in thermodynamic equilibrium. Thus we are led to examine ways in which a confined plasma can evolve towards states of lower free energy, in the process converting free energy into kinetic energy. We must also examine constraints that inhibit these destabilizing transitions. We have already studied one process by means of which the plasma evolves towards a state of lower free energy – collisions reduce the internal energy of the plasma and drive transport particle and heat fluxes across flux surfaces. The time scale for collisional transport processes is the reciprocal of the momentum exchange collision frequency, ν . In this chapter we consider other processes that operate on a shorter time scale to destroy plasma equilibrium.

A uniform, infinite plasma with an isotropic, Maxwellian velocity distribution and the vacuum magnetic field configuration that would exist in the absence of the plasma represent the thermodynamic equilibrium towards which a magnetically confined plasma would tend to evolve in the absence of constraints. Three classes of free energy sources that are available to drive instabilities in a magnetically confined plasma are: (1) relaxation of a non-Maxwellian, nonisotropic velocity distribution; (2) relaxation of a spatial inhomogeneity or expansion; and (3) rearrangement of the magnetic field configuration. There are three classes of constraints which inhibit transitions to states of lower free energy: (1) The MHD, or perfect conductivity, constraint freezes plasma to field lines to the extent that resistivity is negligible; (2) conservation of magnetic moment constrains motions with characteristic frequencies less than the gyrofrequency; and (3) the Liouville equation or equation of state constrains possible motions to those that do not change the entropy.

Some general considerations of these free energy sources and constraints are useful as an introduction to plasma instabilities. The Liouville or state equation constraint can take many forms. For example, consider a functional $S(f)$ of the plasma distribution function, f , of the form

$$S(f) = \int G(f) d^3r d^3v \quad (8.1)$$

The total time derivative is

$$\begin{aligned} \frac{dS}{dt} &= \int \left(\frac{\partial G}{\partial t} + \boldsymbol{v} \cdot \nabla G + \boldsymbol{a} \cdot \nabla_v G \right) d^3r d^3v \\ &= \int \left(\frac{\partial f}{\partial t} + \boldsymbol{v} \cdot \nabla f + \boldsymbol{a} \cdot \nabla_v f \right) \frac{\partial G}{\partial f} d^3r d^3v \end{aligned} \quad (8.2)$$

Because the quantity in brackets vanishes for any distribution function that satisfies the Vlasov equation, Eq. (8.2) also vanishes for such functions.

If the distribution function depends only on the particle energy, $f = f(W)$, and not on position or velocity orientation, then

$$\frac{dS}{dt} = 0 = \int \left(\frac{\partial f}{\partial t} + \frac{\partial f}{\partial W} \frac{\partial W}{\partial t} \right) \frac{\partial G}{\partial f} d^3 r d^3 v \quad (8.3)$$

for any function, f , that satisfies the Vlasov equation. For small perturbations, $f_1(W, t)$, about the solution, $f_0(W)$, of the steady-state Vlasov equation, the linearized Eq. (8.3) becomes

$$0 = \int \left(\frac{\partial f_1}{\partial t} + \frac{\partial f_0}{\partial W} \frac{\partial W}{\partial t} \right) \frac{\partial G}{\partial f} d^3 r d^3 v \quad (8.4)$$

A growing perturbation ($\partial f_1 / \partial t > 0$) increases the internal energy of the plasma (that is, $\partial W / \partial t > 0$) if ($\partial f_0 / \partial W < 0$) and decreases the internal energy of the plasma if ($\partial f_0 / \partial W > 0$). A decrease in the internal energy provides kinetic energy to drive an instability. Thus it follows that ($\partial f_0 / \partial W < 0$) for all W (that is, f_0 is a monotonically decreasing function of energy) is sufficient to ensure the stability of any distribution function, $f_0(W)$, against perturbations that satisfy the Vlasov equation. We obtained a similar result in the previous chapter.

In a confined plasma the distribution function depends upon other variables in addition to the energy. For perturbations with characteristic frequency ω and characteristic spatial nonuniformity scale L , if $\omega < \Omega$ (Ω = gyrofrequency) and $L > r_L$ (r_L = gyroradius), then the magnetic moment, averaged over the gyroperiod, $\langle \mu \rangle$, is a constant of the motion, as we saw in chapter 2. Thus a distribution function $f = f(\bar{\mu}, W)$ is more plausible ($\bar{\mu} \equiv -\langle \mu \rangle$). The particle density is

$$n(B) = \int f(v_{\parallel}, v_{\perp}) d^3 v = \frac{2}{m^2} \int dW d\bar{\mu} \frac{B(r)f(\bar{\mu}, W)}{\left\{ \frac{2}{m}[W - \bar{\mu}B(r)] \right\}^{\frac{1}{2}}} \quad (8.5)$$

where the spatial dependence is implicit in the spatial dependence of $B(r)$. It can be shown from differentiation of Eq. (8.5) that the sufficient condition for stability, $\partial f / \partial W < 0$, implies that $(d/dB)(n/B) < 0$. Because the density normally decreases outward from the center of the plasma, the field must increase outward from the center of the plasma to insure stability. Such a field configuration is called a minimum- B field.

Instabilities that are driven by the rearrangement of magnetic field are inhibited by the perfect-conductivity constraint that the field moves with the plasma. The lowest magnetic free energy state corresponds to the vacuum field configuration. In a low- β plasma the field due to external coils is much greater than the field due to currents in the plasma. Because of the perfect conductivity constraint, any motion of the plasma would cause a rearrangement of the externally generated field and the free energy would, in general, increase. Thus it is unlikely that magnetic field rearrangement could be a source of free energy in low- β plasmas. However, in high- β plasmas the fields produced by the plasma currents are significant relative to the externally generated fields, and plasma motion may produce field rearrangements that decrease the free energy and thereby drive instabilities.

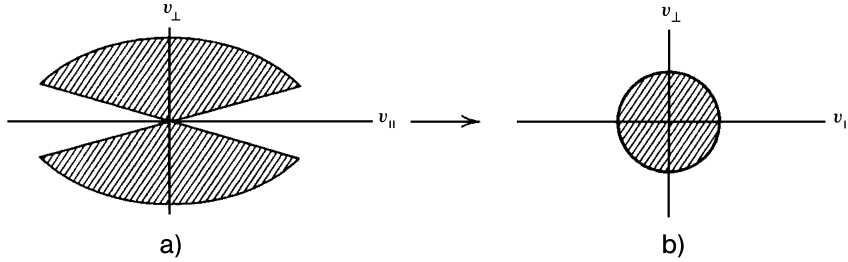


Figure 8.1. Relaxation of an anisotropic velocity distribution

Relaxation of an anisotropic velocity distribution, such as the loss-cone distribution in a mirror-confined plasma shown in Fig. 8.1(a) to the isotropic distribution shown in Fig. 8.1(b) that conserves volume in velocity space would reduce the plasma free energy and thereby drive an instability. Conservation of magnetic moment inhibits the change in $W_{\perp} = \frac{1}{2}mv_{\perp}^2$ for frequencies $\omega < \Omega$. Thus instabilities driven by the relaxation of anisotropic velocity distributions would have characteristic frequencies $\omega > \Omega$.

Relaxation of a spatial nonuniformity can provide free energy. An estimate of the energy potentially available to drive instabilities can be obtained by considering the plasma as an ideal gas with energy content

$$U = \frac{p}{\rho(1-\gamma)} \quad (8.6)$$

where p is the pressure, ρ is the mass density and γ is the gas constant ($\gamma = (\delta + 2)/\delta$, where δ is the number of degrees of freedom in the expansion). The energy per unit volume in an adiabatic expansion is

$$\frac{U}{V} \equiv U\rho \sim \frac{p}{\rho} \rho \sim \rho^{\gamma} \quad (8.7)$$

Consider the relaxation of the linear density gradient shown in Fig. 8.2 to a uniform distribution. Assume a three-dimensional relaxation. The energy per unit volume before and after the relaxation are

$$\begin{aligned} \left(\frac{U}{V}\right)_{\text{before}} &= \int_{r_0-\Delta r}^{r_0+\Delta r} \left[\rho_0 + \left(\frac{\partial \rho}{\partial r} \right)_{r_0} (r - r_0) \right]^{\frac{5}{3}} dr \\ \left(\frac{U}{V}\right)_{\text{after}} &= \rho_0^{\frac{5}{3}} \int_{r_0-\Delta r}^{r_0+\Delta r} dr \end{aligned}$$

so that the available free energy is

$$\Delta E = \left(\frac{U}{V}\right)_{\text{after}} - \left(\frac{U}{V}\right)_{\text{before}} \simeq \left(\frac{1}{\rho} \frac{\partial \rho}{\partial r} \right)^2 p(\Delta r)^3 \quad (8.8)$$

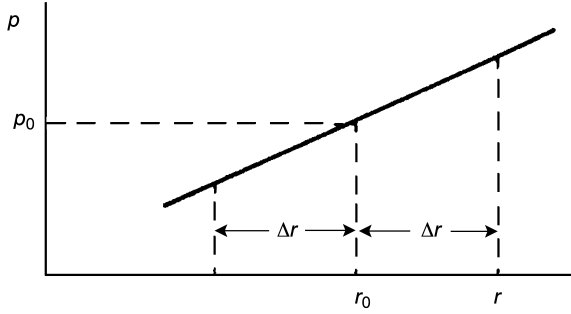


Figure 8.2. Density gradient relaxation

The instability has a displacement

$$\delta r \simeq \delta r_0 e^{\omega t} \quad (8.9)$$

a velocity

$$\delta v = \frac{\partial}{\partial t}(\delta r) \simeq \omega \delta r_0 e^{\omega t} \quad (8.10)$$

and a kinetic energy

$$\delta W \simeq (\rho_0 \Delta r)(\delta v)^2 \sim \rho_0 \omega^2 (\Delta r)^3 \quad (8.11)$$

where we have assumed that the displacement scale is comparable to the relaxation scale (i.e., $\delta r \simeq \Delta r$).

The free energy, ΔE , released by the gradient relaxation must provide at least this kinetic energy, δW , of the displacement. The characteristic frequency range of such instabilities can thus be determined from the condition $\Delta E > \delta W$ and is

$$\omega < \left(\frac{1}{\rho} \frac{\partial \rho}{\partial r} \right) \sqrt{\frac{p}{\rho}} \simeq \left(\frac{1}{\rho} \frac{\partial \rho}{\partial r} \right) v_{\text{th}}^i = \frac{v_{\text{th}}^i}{L} = \delta_i \Omega_i \quad (8.12)$$

where δ_i is the ratio of the ion gyroradius to the scale length of the density gradient, and Ω_i is the ion gyrofrequency. Usually $\delta_i \ll 1$, so that Eq. (8.12) implies that $\omega \ll \Omega_i$ for instabilities driven by the relaxation of density gradients. Such instabilities would be constrained by the conservation of the magnetic moment.

In the sections that follow, a number of specific instabilities will be examined. A variety of methods for analyzing stability are developed in the process.

8.1 Hydromagnetic Instabilities

We first consider the linear dynamics of low-frequency $\omega < \Omega_i$ instabilities in a uniform plasma imbedded in a uniform magnetic field. The general procedure is to expand about the equilibrium solution and assume that the perturbed quantities can be constructed from a superposition of functions of the form $\xi_k e^{i(\mathbf{k} \cdot \mathbf{r} - \omega t)}$, as we did in the previous chapter.

Here, \mathbf{k} is the wave propagation vector, ξ_k is the amplitude coefficient and ω is the corresponding characteristic frequency. This form of the solution is used in the linearized equations that govern the plasma motion and the magnetic field. (Because we are considering low frequency waves, we do not need to include the electric field in the analysis; we saw in the previous chapter that electrostatic waves are high frequency.) The final result is a dispersion relation $D(\omega, \mathbf{k}) = 0$ from which we can determine whether $\text{Im}(\omega) > 0$ (instability) or $\text{Im}(\omega) < 0$ (stability).

8.1.1 MHD Theory

We begin our study with one of the simplest hydromagnetic waves, the Alfvén wave. We assume cold, uniform, incompressible, perfectly conducting plasma in a uniform magnetic field. The momentum balance for such a plasma is given by Eq. (5.38), which, on setting the pressure to zero (cold plasma approximation) and using Ampère's law, becomes

$$\rho \frac{\partial \mathbf{u}}{\partial t} + \rho \mathbf{u} \cdot \nabla \mathbf{u} = \mathbf{j} \times \mathbf{B} = \frac{1}{\mu_0} (\nabla \times \mathbf{B}) \times \mathbf{B} \quad (8.13)$$

The magnetic field must satisfy Faraday's law

$$\begin{aligned} -\frac{\partial \mathbf{B}}{\partial t} &= \nabla \times \mathbf{E} = \nabla \times (\mathbf{u} \times \mathbf{B}) \\ &= (\mathbf{B} \cdot \nabla) \mathbf{u} - (\mathbf{u} \cdot \nabla) \mathbf{B} + \mathbf{u} (\nabla \cdot \mathbf{B})^0 - \mathbf{B} (\nabla \cdot \mathbf{u})^0 \end{aligned} \quad (8.14)$$

where the perfect conductivity form of Ohm's law has been used in going from the second to third equality, and one of Maxwell's equations and the incompressibility assumption, respectively, cause the last two terms to vanish.

Denoting equilibrium and perturbed quantities by 0 and 1 subscripts and noting that $\mathbf{u}_0 = 0$ and for a uniform field $\nabla \times \mathbf{B}_0 = 0$, the linearized Eqs. (8.13) and (8.14) are

$$\rho \frac{\partial \mathbf{u}_1}{\partial t} = \frac{1}{\mu_0} (\nabla \times \mathbf{B}_1) \times \mathbf{B}_0 \quad (8.15)$$

and

$$-\frac{\partial \mathbf{B}_1}{\partial t} = \frac{1}{\mu_0} (\mathbf{B}_0 \cdot \nabla) \mathbf{u}_1 \quad (8.16)$$

Assuming the form indicated previously for the perturbed solutions and choosing a coordinate system with $\mathbf{B}_0 = B_0 \hat{\mathbf{n}}_z$ allows Eq. (8.15) to be written in component form as

$$\begin{aligned} \rho \omega u_{kx} &= \frac{B_{0z}}{\mu_0} (k_x B_{kz} - k_z B_{kx}) \\ \rho \omega u_{ky} &= \frac{B_{0z}}{\mu_0} (k_y B_{kz} - k_z B_{ky}) \\ \rho \omega u_{kz} &= 0 \end{aligned} \quad (8.17)$$

and allows Eq. (8.16) to be written

$$\begin{aligned}\omega B_{kx} &= -B_{0z} k_z u_{kx} \\ \omega B_{ky} &= -B_{0z} k_z u_{ky} \\ \omega B_{kz} &= -B_{0z} k_z u_{kz}\end{aligned}\quad (8.18)$$

Equations (8.17) and (8.18) may be solved for the dispersion relation

$$\omega = \pm \frac{B_{0z} k_z}{\sqrt{\mu_0 \rho}} \quad (8.19)$$

There is a perturbed solution for \mathbf{u}_k and \mathbf{B}_k with components in the x - and y -directions –perpendicular to the field – which propagates along the field (z -direction) with phase velocity

$$\frac{\omega}{k_z} = \frac{B_{0z}}{\sqrt{\mu_0 \rho}} \equiv V_A \quad (8.20)$$

This wave is known as the Alfvén wave, and V_A is the Alfvén speed. Because $\text{Im}(\omega) = 0$, the Alfvén wave will not grow or diminish in time, but will persist indefinitely. Thus we do not find an instability associated with the Alfvén wave.

8.1.2 Chew–Goldberger–Low Theory

Now the cold-plasma approximation is relaxed by including a pressure gradient term in Eq. (8.13). Because we are treating a uniform plasma, $\nabla p_0 = 0$ and instead of Eq. (8.15), we now have

$$\rho \frac{\partial \mathbf{u}_1}{\partial t} = -\nabla p_1 + \frac{1}{\mu_0} (\nabla \times \mathbf{B}_1) \times \mathbf{B}_0 \quad (8.21)$$

Having introduced another variable, the pressure, we must provide an equation for it. The adiabatic law serves our purpose:

$$\frac{d}{dt} \left(\frac{p}{\rho^\gamma} \right) = \left(\frac{\partial}{\partial t} + \mathbf{u} \cdot \nabla \right) \left(\frac{p}{\rho^\gamma} \right) = 0 \quad (8.22)$$

If an anisotropic pressure distribution is possible, then Eq. (8.13) must be replaced by

$$\rho \frac{\partial \mathbf{u}}{\partial t} + \rho \mathbf{u} \cdot \nabla \mathbf{u} = -\nabla \cdot \mathbf{P} + \frac{1}{\mu_0} (\nabla \times \mathbf{B}) \times \mathbf{B} \quad (8.23)$$

Using the Chew–Goldberger–Low form

$$\mathbf{P} = p_\perp \mathbf{I} + \frac{p_\parallel - p_\perp}{B^2} \mathbf{B} \mathbf{B} \quad (8.24)$$

allows the representation

$$\nabla \cdot \mathbf{P} = \nabla p_\perp + \left(\frac{p_\parallel - p_\perp}{B^2} \right) (\mathbf{B} \cdot \nabla) \mathbf{B} + \mathbf{B} (\mathbf{B} \cdot \nabla) \left(\frac{p_\parallel - p_\perp}{B^2} \right) \quad (8.25)$$

Further improving the model by removing the incompressibility assumption ($\nabla \cdot \mathbf{u} = 0$), the last term in Eq. (8.14) must be retained. In this case, an equation for the density – the continuity equation – must be used,

$$\frac{\partial \rho}{\partial t} + \nabla \cdot (\rho \mathbf{u}) = 0 \quad (8.26)$$

We must also provide equations for p_{\parallel} and p_{\perp} . The double adiabatic equations that were derived in chapter 5 can be used:

$$\frac{d}{dt} \left(\frac{p_{\perp} p_{\parallel}^2}{\rho^3} \right) = 0 \quad (8.27)$$

and

$$\frac{d}{dt} \left(\frac{p_{\perp}}{\rho B} \right) = 0 \quad (8.28)$$

A similar type of linear analysis as that carried through previously when applied to Eq. (8.23), Eq. (8.26) to Eq. (8.28), and Eq. (8.14) with the last term retained yields

$$\begin{aligned} \omega^2 = & \frac{k^2}{2\rho_0} \left\{ \left(\frac{B_0^2}{\mu_0} + p_{\perp 0} + 2p_{\parallel 0} \cos^2 \theta + p_{\perp 0} \sin^2 \theta \right) \right. \\ & \left. \pm \left[\left(\frac{B_0^2}{\mu_0} + p_{\perp 0}(1 + \sin^2 \theta) - 4p_{\parallel 0} \cos^2 \theta \right)^2 + 4p_{\perp 0}^2 \sin^2 \theta \cos^2 \theta \right]^{\frac{1}{2}} \right\} \end{aligned} \quad (8.29)$$

where θ is the angle at which the perturbation propagates with respect to the unperturbed field (that is, $B_0 k \cos \theta = \mathbf{B}_0 \cdot \mathbf{k}$).

For waves propagating perpendicular to B_0 (i.e., $\theta = \pi/2$),

$$\omega^2 = \frac{2k_{\perp}^2}{\rho_0} \left(\frac{B_0^2}{2\mu_0} + p_{\perp 0} \right) \quad (8.30)$$

This wave is the magnetosonic wave and reduces in the limit $\beta_{\perp} \equiv p_{\perp 0} 2\mu_0 / B_0^2 \ll 1$ to the Alfvén wave whose dispersion relation is given by Eq. (8.19), except that the magnetosonic wave propagates perpendicular to the field. Because $\text{Im}(\omega) = 0$, these waves are not unstable.

There are two solutions of Eq. (8.29) for waves propagating along \mathbf{B}_0 ,

$$\omega^2 = \frac{k_{\parallel}^2}{\rho_0} \left(\frac{B_0^2}{\mu_0} + p_{\perp 0} - p_{\parallel 0} \right) \quad (8.31)$$

and

$$\omega^2 = \frac{6k_{\parallel}^2 p_{\parallel 0}}{\rho_0} \quad (8.32)$$

When the pressure is isotropic ($p_{\perp 0} = p_{\parallel 0}$), Eq. (8.31) is the Alfvén wave given by Eq. (8.19). In general, Eq. (8.31) has a growing solution with $\text{Im}(\omega) > 0$ unless

$$p_{\parallel 0} < p_{\perp 0} + \frac{B_0^2}{\mu_0} \quad (8.33)$$

The wave that propagates along the field direction with growing amplitude when Eq. (8.33) is not satisfied is known as the firehose instability because of its analogy with the hydrodynamic wave that is sometimes seen to propagate along a firehose.

The second solution, Eq. (8.32), is the ion acoustic wave, which propagates along the unperturbed field direction with phase velocity

$$V = \frac{\omega}{k_{\parallel}} = \sqrt{\frac{6p_{\parallel 0}}{\rho_0}} \quad (8.34)$$

It is apparent from the development up to this point that the less restrictive the assumptions of the model, the more varied are the wave phenomena predicted. When the equilibrium is isotropic (i.e., in a closed confinement system in which the equilibrium has been established by collisions over times that are long compared to the reciprocal collision frequency) and when heat conduction and heat sources are negligible, the use of a scalar pressure and of the adiabatic law to describe it is justified. If the collision time is short compared to the growth rate of the relevant instabilities that are being studied and compared to the transient time along field lines, Eq. (8.22) (the adiabatic law) may be a valid approximation. Approximations that use Eq. (8.22), the perfect conductivity Ohm's law in Faraday's law (Eq. (8.14)), and the momentum balance (Eq. 8.13) are known as MHD stability theory. MHD theory is generally valid when the distribution function is locally isotropic and the instability depends only on the pressure, not on any details of the distribution function.

The double adiabatic approximation, often known as Chew–Goldberger–Low (CGL) theory, can treat situations in which the distribution is locally isotropic in the plane perpendicular to the magnetic field direction. Eqs. (8.14), (8.23) and (8.26) to (8.28) constitute the CGL theory. This theory is valid for instabilities that depend on an anisotropy between the perpendicular and parallel pressures, such as may occur in an open confinement system for which the transient time along field lines is infinite, but the collision time may be short enough compared to the growth rate of the instability that the distribution of mirror-trapped particles is isotropic in the plane perpendicular to the field. However, the CGL theory cannot treat instabilities that depend on the details of the distribution function.

8.1.3 Guiding Center Theory

Some of the restrictions introduced into the CGL theory can be removed if, instead of using the double adiabatic theory to evaluate p_{\parallel} and p_{\perp} , these quantities are evaluated directly from the defining relations. The distribution function can be calculated from the

drift kinetic equation that is appropriate for the study of low frequency waves. In the collisionless, source-free case, Eq. (4.17) becomes

$$\frac{\partial \hat{f}}{\partial t} + \left[\bar{\mu} \frac{\partial B}{\partial t} + e(\mathbf{v}_{\text{dr}} + \mathbf{v}_{\parallel}) \cdot \mathbf{E} \right] \frac{\partial \hat{f}}{\partial W} + (\mathbf{v}_{\text{dr}} + \mathbf{v}_{\parallel}) \cdot \nabla \hat{f} = 0 \quad (8.35)$$

The limits $\omega \ll \Omega_i$ and $r_L \ll L$ can be realized in this equation by the strategem of taking $r_L \rightarrow L$ and $\Omega_i \rightarrow \infty$. But $r_L \rightarrow 0$ and $\Omega_i \rightarrow \infty$ are mathematically equivalent to $e^{-1} \rightarrow 0$, as follows from the definitions of r_L and Ω_i . The grad- B curvature and polarization drifts vanish in the limit $e^{-1} \rightarrow 0$, as can be verified from the expressions given in chapter 2 (that is, Eqs. (2.25), (2.30) and (2.41), leaving only the $\mathbf{E} \times \mathbf{B}$ drift in this limit. With the use of Maxwell's equations, Eq. (8.35) can be written in the $e^{-1} \rightarrow 0$ limit as

$$\begin{aligned} & \frac{\partial \hat{f}}{\partial t} + (\mathbf{v}_{\parallel} + \mathbf{v}_E) \cdot \nabla \hat{f} \\ & + \left[eE_{\parallel}\mathbf{v}_{\parallel} - \bar{\mu}B(\nabla \cdot \mathbf{v}_E) + (mv_{\parallel}^2 - \bar{\mu}B)\mathbf{v}_E \cdot (\hat{\mathbf{n}}_{\parallel} \cdot \nabla)\hat{\mathbf{n}}_{\parallel} \right] \frac{\partial \hat{f}}{\partial W} = 0 \end{aligned} \quad (8.36)$$

Eqs. (8.36) replaces (8.13) or (8.23) in the guiding center (GC) stability theory.

By analogy with our previous procedure, we consider displacements of particle position that can be constructed by the superposition of displacements of the form

$$\delta \mathbf{r} \equiv \xi \sim \xi_k e^{i(\mathbf{k} \cdot \mathbf{r} - \omega t)} \quad (8.37)$$

The perturbed drift velocity can then be constructed

$$\mathbf{v}_{E1} = \frac{d(\xi)}{dt} = -i\omega\xi \quad (8.38)$$

The linearized Faraday's law, Eq. (8.14), is

$$\mathbf{B}_1 = (\mathbf{B}_0 \cdot \nabla)\xi - \mathbf{B}_0(\nabla \cdot \xi) \quad (8.39)$$

In writing Eq. (8.39), we have assumed that the plasma mass flow, \mathbf{u}_E , has the same form as the individual species drift, \mathbf{v}_E . We also have used the fact that $\mathbf{v}_{E0} = 0$ at equilibrium. (Note that the plasma has not been assumed to be incompressible, but that the uniform field restriction has been retained.)

In the equilibrium, with no electric field, the particle energy is a constant. In the low-frequency range under study the magnetic moment is a constant. Thus particles move on flux surfaces with constant W and $\bar{\mu}$ in the equilibrium, and it is natural to choose these variables as coordinates, that is, $\hat{f} = \hat{f}(W, \bar{\mu})$.

We will find in chapter 9 that to lowest order in $\delta \equiv r_L/L$ the drift kinetic equation is satisfied by the Maxwellian

$$\hat{f}^0 = \hat{f}^{\max} = \frac{n}{(2\pi m T)^{\frac{3}{2}}} e^{-[m(v_{\parallel}^2 + v_{\perp}^2)/2T]} \quad (8.40)$$

Expanding $\hat{f} = f^0 + \hat{f}^1$ and using Eq. (8.38), the linearized Eq. (8.36) can be used to obtain

$$\hat{f}^1 = -\frac{\frac{\partial \hat{f}^0}{\partial W}(ev_{\parallel}E_{\parallel} + \bar{\mu}B_0i\omega\nabla \cdot \xi)}{i(\omega - k_{\parallel}v_{\parallel})} \quad (8.41)$$

To simplify the problem, we let $\omega \rightarrow 0$, which limits the applicability to marginally stable or unstable, low frequency waves. We further restrict the type of instability under consideration by assuming no electric field parallel to the magnetic field. With these simplifications, we find $\hat{f}^1 = 0$. Linearizing Eq. (8.23), using Eq. (8.39), making the usual postulate about constructing the perturbed solutions from the superposition of wavelike solutions, and using Eq. (8.40) to evaluate

$$p_{\perp 1} = \frac{1}{2} \int d^3v \hat{f}^0 m v_{\perp}^2 \quad (8.42)$$

and so on, leads to the dispersion relation

$$\omega^2 = \frac{k_{\perp}^2}{\rho_0} \left[\frac{B_0^2}{\mu_0} - 2p_{\perp 0} \left(\frac{p_{\perp 0}}{p_{\parallel 0}} - 1 \right) \right] + \frac{k_{\parallel}^2}{\rho_0} \left(\frac{B_0^2}{\mu_0} + p_{\perp 0} - p_{\parallel 0} \right) \quad (8.43)$$

When $p_{\perp 0} = p_{\parallel 0}$, Eq. (8.43) reduces to the Alfvén wave propagating along and perpendicular to the field direction. For propagation along the field ($k_{\perp} \ll k_{\parallel}$) Eq. (8.43) reduces to the CGL dispersion relation given by Eq. (8.31), which led to the firehose stability criterion of Eq. (8.33). For propagation perpendicular to the field ($k_{\perp} \gg k_{\parallel}$),

$$p_{\perp 0} \left(\frac{p_{\perp 0}}{p_{\parallel 0}} - 1 \right) < \frac{B_0^2}{2\mu_0} \quad (8.44)$$

is sufficient to ensure that there is not an unstable, growing wave with $\text{Im}(\omega) > 0$. The growing wave which would propagate perpendicular to the field if the inequality of Eq. (8.44) was not satisfied is driven by the mirror reflection of particles in the perturbed magnetic fields and is known as the mirror instability.

The analysis of stability has become more complex as we have proceeded through this section from the MHD theory to the CGL theory, and finally to this last guiding center (GC) analysis. The added complexity has been associated with the removal of assumptions and has had the effect of including more information about the plasma dynamics in the analysis. The added information in the analysis has led to the identification of additional waves.

A general statement can be made about the stability criteria given by the different theories for the same wave. The MHD criterion will be more stringent than the GC criterion, and the GC criterion, in turn, will be more stringent than the CGL criterion. We can intuitively understand the first part of this statement by contrasting the MHD and GC theories. In both cases, particles are frozen to field lines and the cross-field drift is the $\mathbf{E} \times \mathbf{B}$ drift. However, in the MHD theory there is no distinction between the velocities parallel and perpendicular to the magnetic field, whereas v_{\parallel} and v_E are treated explicitly in the

GC theory. The isotropic Maxwellian distribution, which is assumed in the MHD theory, corresponds to the lowest state of free energy for the plasma. Any other distribution corresponds to a state of higher free energy. Thus the MHD theory would predict that more kinetic energy was available to drive instabilities than would the GC (or CGL) theory. Consequently, the MHD stability criterion is a sufficient, but not necessary, condition for the stability of a given wave. Unfortunately, the MHD stability analysis does not identify all of the potentially unstable waves. Nevertheless, the MHD stability theory is a valuable and widely used methodology.

In this section, waves that would exist in a uniform plasma imbedded in a uniform magnetic field have been examined. Since a nonuniform magnetic field is the rule for confined plasmas and the density and temperature of a confined plasma are, in general, not uniform, the waves identified in this section are only suggestive of waves that will be found in confined plasmas. We remove these restrictions in the next section, and we investigate effects which arise in nonuniform plasmas in sections 8.6 and 8.8.

8.2 Energy Principle

The idea of perturbations reducing the plasma field free energy to provide kinetic energy to drive instabilities can be utilized to analyze stability. In this section we develop an expression for the change in free energy, δW , of the plasma-magnetic field system when it is perturbed from an equilibrium. If $\delta W < 0$, we conclude that kinetic energy is available to drive an instability.

We use the MHD theory to construct an expression for δW . It is possible, in principle, to construct an energy principle using CGL or GC theory, but the MHD theory is widely used because it is less complex and has the virtue of providing a sufficient condition for stability. We relax our previous assumptions of a uniform plasma in a uniform field and treat the general case of a nonuniform plasma and a nonuniform magnetic field.

The basic equations of the MHD theory are

$$\rho \frac{\partial \mathbf{u}}{\partial t} + \mathbf{u} \cdot \nabla \mathbf{u} = -\nabla p + \frac{1}{\mu_0} (\nabla \times \mathbf{B}) \times \mathbf{B} \quad \text{momentum and Ampere's law} \quad (8.45)$$

$$\frac{\partial \mathbf{B}}{\partial t} \nabla \times (\mathbf{u} \times \mathbf{B}) \quad \text{Faraday's and Ohm's laws} \quad (8.46)$$

$$\frac{\partial \rho}{\partial t} + \nabla \cdot \rho \mathbf{u} = 0 \quad \text{continuity} \quad (8.47)$$

and

$$\left(\frac{\partial}{\partial t} + \mathbf{u} \cdot \nabla \right) \frac{p}{\rho^\gamma} = 0 \quad \text{adiabatic law} \quad (8.48)$$

The perturbed displacement of the fluid element is represented as

$$\delta \mathbf{r}(r, t) = \xi(r) e^{-i\omega t} \quad (8.49)$$

so that

$$\mathbf{u} = \frac{d(\delta\mathbf{r})}{dt} = -i\omega\xi(\mathbf{r})e^{-i\omega t} \quad (8.50)$$

The perturbed field, density and pressure are assumed to be representable as

$$\begin{aligned}\delta\mathbf{B} &= \mathbf{B}_1(\mathbf{r})e^{-i\omega t} \\ \delta\rho &= \rho_1(\mathbf{r})e^{-i\omega t} \\ \delta p &= p_1(\mathbf{r})e^{-i\omega t}\end{aligned} \quad (8.51)$$

Using Eq. (8.50) and Eq. (8.51) in the linearized Eq. (8.45) to Eq. (8.48) leads to

$$-\rho_0\omega^2\xi = -\nabla p_1 + \left[\frac{1}{\mu_0}(\nabla \times \mathbf{B}_1) \times \mathbf{B}_0 + \mathbf{j}_0 \times \mathbf{B}_1 \right] \quad (8.52)$$

where $\mathbf{j}_0 = \mu_0^{-1}\nabla \times \mathbf{B}_0$, and to

$$\mathbf{B}_1 = \nabla \times (\xi \times \mathbf{B}_0) \quad (8.53)$$

$$\rho_1 = -\nabla \cdot (\rho_0\xi) \quad (8.54)$$

and

$$p_1 = -(\xi \cdot \nabla)p_0 - \gamma p_0 \nabla \cdot \xi \quad (8.55)$$

Taking the scalar product of ξ with Eq. (8.52) and integrating over the volume of the system leads to

$$\begin{aligned}\delta W &\equiv \omega^2 \int d^3r \rho_0 \xi^2 \\ &= \int d^3r \left[\xi \cdot \nabla p_1 + \frac{1}{\mu_0}(\xi \times \mathbf{B}_0) \cdot (\nabla \times \mathbf{B}_1) - \xi \cdot \mathbf{j}_0 \times \mathbf{B}_1 \right]\end{aligned} \quad (8.56)$$

If, for any choice of ξ , the RHS of Eq. (8.56) is positive, then $\text{Im}(\omega) = 0$ and that displacement does not lead to an instability. The RHS of Eq. (8.56) is the change in free energy of the plasma magnetic field system associated with the perturbation ξ . The perturbed pressures and field appearing in Eq. (8.56) can be calculated from Eqs. (8.53) and (8.55), for a given ξ .

The first term on the RHS of Eq. (8.56) can be integrated by parts,

$$\int d^3r \xi \cdot \nabla p_1 = \int d^3r \nabla \cdot (\xi p_1) - \int d^3r p_1 (\nabla \cdot \xi)$$

and then transformed by Gauss' theorem and Eq. (8.55) into

$$\int d^3r \xi \cdot \nabla p_1 = \int ds \xi_n p_1 + \int d^3r [(\xi \cdot \nabla)p_0 + \gamma p_0 (\nabla \cdot \xi)] (\nabla \cdot \xi) \quad (8.57)$$

where ξ_n is the outward component of the displacement on the plasma surface. The second term on the RHS of Eq. (8.56) can be transformed by a similar procedure and the use of

the linearized Ohm's and Faraday's laws, Eq. (8.53), into

$$\begin{aligned} \frac{1}{\mu_0} \int d^3r (\boldsymbol{\xi} \times \mathbf{B}_0) \cdot (\nabla \times \mathbf{B}_1) &= \frac{1}{\mu_0} \int ds (\mathbf{B}_1 \cdot \mathbf{B}_0) \xi_n \\ &\quad + \frac{1}{\mu_0} \int d^3r [\nabla \times (\boldsymbol{\xi} \times \mathbf{B}_0)]^2 \end{aligned} \quad (8.58)$$

where we have required that the normal component of the equilibrium field ($\mathbf{B}_0 \cdot \hat{n}$) vanish on the exterior surface of the plasma because that surface is a flux surface.

Now we must consider the boundary conditions that are relevant to a plasma that is surrounded by a vacuum region and then a conducting wall. Consider the idealized interface illustrated in Fig. 8.3. In the vacuum region, the perturbed field can be represented in terms of a vector potential, \mathbf{A}_1 :

$$\mathbf{B}_{1v} = \nabla \times \mathbf{A}_1 \quad (8.59)$$

At the plasma side of the plasma–vacuum interface, the linearized, perfect conductivity Ohm's law is

$$\mathbf{E}_1 + \mathbf{u}_1 \times \mathbf{B}_0 = 0 \quad (8.60)$$

The tangential component of the electric field in the frame moving with velocity \mathbf{u}_1 , $\mathbf{E}' = \mathbf{E} + \mathbf{u}_1 \times \mathbf{B}$, must be continuous across the plasma–vacuum interface, which leads to the requirement,

$$\hat{n} \times (\mathbf{E}_{1v} + \mathbf{u}_1 \times \mathbf{B}_{0v}) = \hat{n} \times (\mathbf{E}_1 + \mathbf{u}_1 \times \mathbf{B}_0) = 0 \quad (8.61)$$

where the v subscript refers to the vacuum region, and the last equality follows from Eq. (8.60). Assuming a time dependence of the form of Eq. (8.51) for \mathbf{A}_1 , Eq. (8.59) can be used in Faraday's law, and the result and Eq. (8.50) can be used to reduce Eq. (8.61) to

$$\hat{n} \times \mathbf{A}_1 = \xi_n \mathbf{B}_{0v} \quad (8.62)$$

at the plasma–vacuum interface. At a perfectly conducting wall, the tangential electric field must vanish, a requirement which can be written after using Eq. (8.59) in Faraday's law as

$$\hat{n} \times \mathbf{A}_1 = 0 \quad (8.63)$$

at the vacuum–wall interface.

The pressure balance across the plasma–vacuum interface is

$$\left(p + \frac{B^2}{2\mu_0} \right)_{\text{plasma}} = \left(\frac{B^2}{2\mu_0} \right)_{\text{vac}} \quad (8.64)$$

The perturbed pressure balance contains terms due to changes δp and δB and terms due to the change in location of the interface into a region of different B . The linearized pressure

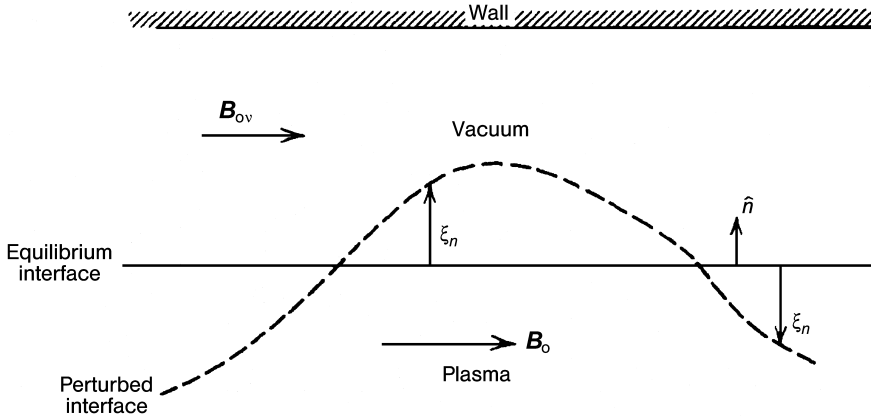


Figure 8.3. Plasma–vacuum–wall interface

balance across the perturbed interface is

$$p_1 + \left(\frac{\mathbf{B}_0 \cdot \mathbf{B}_1}{\mu_0} \right) + \xi_n \hat{n} \cdot \nabla \left(p_0 + \frac{B_0^2}{2\mu_0} \right) = \left(\frac{\mathbf{B}_{0v} \cdot \mathbf{B}_{1v}}{\mu_0} \right) + \xi_n \hat{n} \cdot \nabla \left(\frac{B_{0v}^2}{2\mu_0} \right) \quad (8.65)$$

This equation can be multiplied by ξ_n and integrated over the plasma–vacuum interface, and the integral can be converted to a volume integral over the vacuum region. Using Eq. (8.59) and Eq. (8.62) and the requirement that the tangential electric field vanishes at the wall leads to

$$\begin{aligned} \int d\mathbf{s} \xi_n \frac{\mathbf{B}_0 \cdot \mathbf{B}_1}{\mu_0} &= - \int d\mathbf{s} \xi_n p_1 - \int d\mathbf{s} \xi_n^2 \hat{n} \cdot \nabla \left(p_0 + \frac{B_0^2}{2\mu_0} - \frac{B_{0v}^2}{2\mu_0} \right) \\ &\quad + \frac{1}{\mu_0} \int_{\text{vac}} d^3 r (\nabla \times \mathbf{A}_1) \cdot (\nabla \times \mathbf{A}_1) \end{aligned} \quad (8.66)$$

where the volume integral is over the vacuum region.

These results may be combined to write Eq. (8.56) as

$$\begin{aligned} \delta W(\xi) &\equiv \omega^2 \int d^3 r \rho_0 \xi^2 \\ &= \int \left\{ [(\xi \cdot \nabla) p_0 + \gamma p_0 (\nabla \cdot \xi)] (\nabla \cdot \xi) \right. \\ &\quad \left. + \frac{1}{\mu_0} (|\nabla \times (\xi \times \mathbf{B}_0)|)^2 - \xi \cdot \mathbf{j}_0 \times \nabla \times (\xi \times \mathbf{B}_0) \right\} d^3 r \\ &\quad + \frac{1}{\mu_0} \int_{\text{vac}} (|\nabla \times \mathbf{A}_1|)^2 d^3 r \\ &\quad + \int \left[\xi_n^2 \hat{n} \cdot \nabla \left(\frac{B_{0v}^2}{2\mu_0} - p_0 - \frac{B_0^2}{2\mu_0} \right) \right] d\mathbf{s} \end{aligned} \quad (8.67)$$

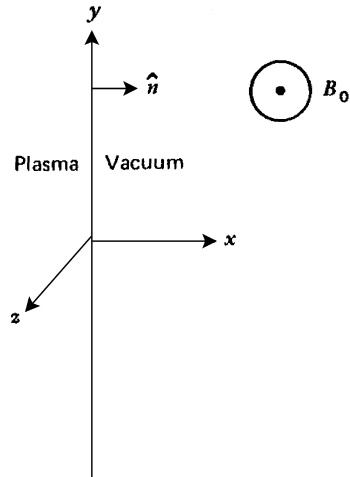


Figure 8.4. Plasma–vacuum interface

The first term in Eq. (8.67) is a volume integral over the plasma. The first term in the integrand can lead to pressure-driven instabilities by contributing a negative contribution to δW . The second term in Eq. (8.67) is a volume integral over the vacuum region of the perturbed field and is always stabilizing. The last term in Eq. (8.67) is a surface integral over the plasma–vacuum interface and can be stabilizing or destabilizing, depending on the field configuration and the perturbation.

Application of the energy principle to a simple problem serves to illustrate an important point. Consider a plasma confined with uniform pressure in the region $x < 0$ by a field B_0 which vanishes for $x < 0$ (see Fig. 8.4). In this case, the plasma current must flow along the plasma–vacuum surface. Equation (8.67) for this situation is

$$\delta W = \int \gamma p_0 (\nabla \cdot \xi)^2 d^3 r + \frac{1}{\mu_0} \int_{\text{vac}} (|\nabla \times A_1|)^2 d^3 r + \int \xi_n^2 \hat{n} \cdot \nabla \left(\frac{B_{0v}^2}{2\mu_0} \right) ds \quad (8.68)$$

The first two terms in Eq. (8.68) cannot contribute negative terms. This configuration is surely stable if the last term is nonnegative, which will be the case if the vacuum field increases away from the plasma. Thus we are led again to the concept of minimum- B stabilization, that is, confinement of a plasma in a magnetic field configuration that increases in magnitude away from the plasma.

8.3 Pinch and Kink Instabilities

A plasma column which is confined entirely by the poloidal magnetic field produced by the axial current flowing in the plasma is unstable with respect to perturbations of the type seen in Fig. 8.5 in which the surface of the column alternately contracts and bulges out. Recalling that the poloidal field, B_θ , that is produced at the surface of the plasma is related

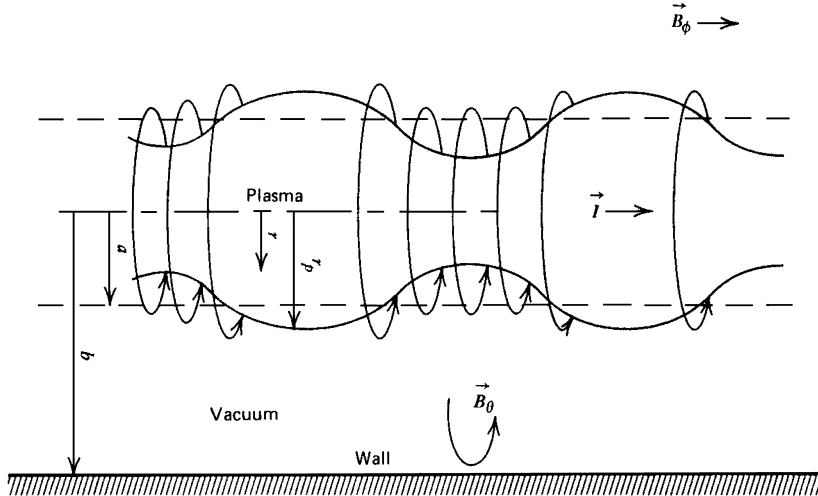


Figure 8.5. Pinch instability

to the axial current, I , by Ampère's law,

$$B_\theta(r_p) = \frac{\mu_0 I}{2\pi r_p} \quad (8.69)$$

we see that B_θ increases in the contracted region and decreases in the bulging region. The radially inward force due to the poloidal magnetic pressure, $B_\theta^2/2\mu_0$, thus increases in the contracted region and decreases in the bulge region, which causes further contraction and bulging. This “pinch” instability can be inhibited by the presence of a sufficiently strong axial field, B_ϕ . This toroidal field exerts a pressure, $B_\phi^2/2\mu_0$, perpendicular to the field lines and a tension of the same magnitude along the field lines. Since the toroidal field moves with the plasma (in the perfectly conducting plasma limit) so that the magnetic flux $\Phi = \pi r_p^2 B_\phi$ within the plasma column is constant, the toroidal field pressure increases in the contracted region to oppose the contraction and decreases in the bulged region to reduce the bulging. The stabilizing $B_\phi \sim 1/r_p^2$ dependence is stronger than the destabilizing $B_\theta \sim 1/r_p$ dependence.

A plasma column can also be unstable with respect to the corkscrew, or kink, type of perturbations seen in Fig. 8.6. The mechanism is similar to that for pinch instabilities; B_θ is stronger on the inside than on the outside of the bend, which produces a net force that further kinks the plasma column. The tension in the toroidal field lines resists the kinking, so that if the toroidal field is sufficiently strong relative to the poloidal field, the kink instability can be suppressed. Kink instabilities thus place an upper limit on the plasma current, for a given toroidal field. For a tokamak, this limit can be characterized in terms of the safety factor,

$$q(r) \equiv \frac{r B_\phi(r)}{R_0 B_\theta(r)} \quad (8.70)$$

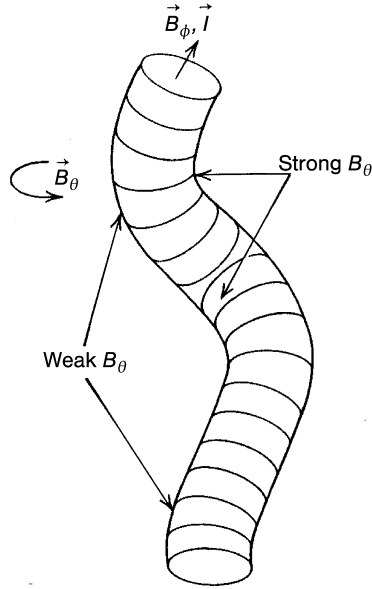


Figure 8.6. Kink instability

The nonlocal, helical perturbations of the type seen in Fig. 8.6 can be represented in a plasma cylinder or a tokamak by

$$\delta r = \xi(r, \theta, \phi) e^{-i\omega t} = \xi(r) e^{i(m\theta - n\phi)} e^{-i\omega t} \quad (8.71)$$

where θ and ϕ are the poloidal and toroidal angles, respectively. For displacements of this form, the energy principle in a plasma cylinder can be written

$$\begin{aligned} \delta W = \frac{B_\phi^2}{\mu_0 R_0} & \left\{ \int_0^a \left[\left(r \frac{d\xi}{dr} \right)^2 + (m^2 - 1)\xi^2 \right] \left(\frac{n}{m} - \frac{1}{q} \right)^2 r dr \right. \\ & \left. + \left[\frac{2}{q(a)} \left(\frac{n}{m} - \frac{1}{q(a)} \right) + (1 + m\lambda) \left(\frac{n}{m} - \frac{1}{q(a)} \right)^2 \right] a^2 \xi_a^2 \right\} \end{aligned} \quad (8.72)$$

where

$$\lambda \equiv \frac{1 + \left(\frac{a}{b} \right)^{2m}}{1 - \left(\frac{a}{b} \right)^{2m}} \quad (8.73)$$

The region $r < a$ is plasma, and $a < r < b$ is vacuum, in equilibrium, as shown in Fig. 8.5. The wall is assumed to be perfectly conducting.

The modes usually referred to as kink modes are the surface kink modes, which can only occur if there is a vacuum region between the plasma and the wall. Only the second,

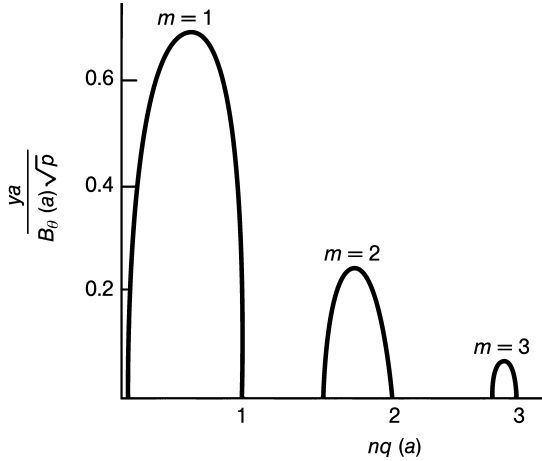


Figure 8.7. Normalized growth rates for parabolic current distribution

surface term in Eq. (8.72) can contribute a negative term to δW . Any kink mode (n, m) is stable ($\delta W > 0$) if $q(a) > m/n$. Since $n \geq 1$ for kink modes ($n = 0$ is the axisymmetric mode discussed in chapter 6), $q(a) > m$ is a sufficient condition for stability against mode m .

The basic variable characterizing stability, $q(r)$, is related to the toroidal current distribution. For a current distribution of the form

$$j_\phi(r) = j_{\phi 0} \left(1 - \frac{r^2}{a^2}\right)^\nu \quad (8.74)$$

the growth rates, γ , of the various kink modes have been computed as function of $nq(a)$. The results for $\nu = 1$ (parabolic distribution) are shown Fig. 8.7. The unstable bands ($\gamma > 0$) are seen to be increasingly localized and the growth rate decreases in amplitude as m increases. (For a uniform current distribution the growth rate is independent of m .) The perturbation becomes increasingly localized at the plasma surface as m increases.

Numerical evaluations of Eq. (8.72) for different current density distributions, characterized by the parameter ν in Eq. (8.74), have been made for the case of no conducting wall (i.e., $b \rightarrow \infty$). The stability ($\delta W > 0$) conditions are summarized in Fig. 8.8. With regard to this figure, note that with the current profiles given by Eq. (8.74), the following relations obtain

$$I = \frac{1}{\nu + 1} A j_{\phi 0} \quad (8.75)$$

where A is the plasma cross section area, and

$$\frac{qa}{q_0} \equiv \frac{q(a)}{q(0)} = \nu + 1 \quad (8.76)$$

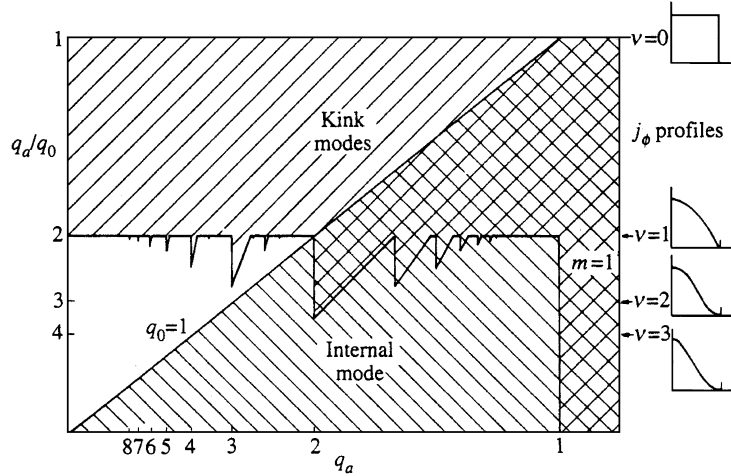


Figure 8.8. Stability diagram for kink instabilities

A current profile at least as peaked as parabolic ($v \geq 1$) is necessary to insure stability against surface kink modes. The $m = 1$ mode is unstable for $q(a) < 1$. The condition $q(a) > 1$ is a minimal condition for stability, and is known as the Kruskal–Shafranov stability limit. The stability of modes with $m > 1$ depends more on the peaking of the current distribution than on $q(a)$. Complete stability against all surface kink modes can be obtained when $q(a) > 1$ by using a sufficiently peaked current profile $v > 2.5$. Profiles only slightly more peaked than parabolic $v = 1$ are sufficient to stabilize all kink modes with $m > 3$. Stability of the $m = 2$ mode can be assured if $q(a)/q(0) \gtrsim 3.5$. We note that these conclusions are based upon MHD theory and thus represent sufficient, not necessary, conditions for stability.

8.4 Interchange (Flute) Instabilities

Interchange instabilities are localized perturbations that are driven principally by the relaxation of pressure gradients or by expansion. The characteristic feature of the perturbation is the interchange of magnetic field lines without bending or otherwise distorting them in such a way as to produce a restoring magnetic force. We will investigate interchange instabilities in mirrors, from the viewpoint of free energy and from the viewpoint of drifts, and in tokamaks, where they are a form of internal, or fixed-boundary, kink modes.

Consider a configuration such as the simple mirror shown in Fig. 8.9 with a flutelike perturbation in the field. If the plasma pressure is small compared to the magnetic pressure $\beta \ll 1$ the field in the plasma is nearly the same as would exist in the absence of a plasma. Any distortion of the field would increase the field energy, contributing a positive term to δW . Thus the least stable (or most unstable) perturbations are those that interchange the plasma and field lines, which are assumed to be frozen into the plasma, between regions I and II without distortion of the field lines. We will analyze this situation.

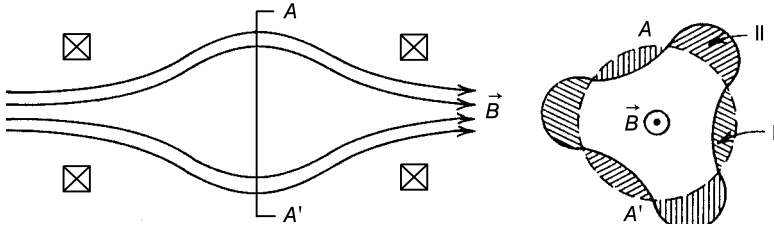


Figure 8.9. Flute modes in a simple mirror

The magnetic energy in a flux tube – a volume of plasma with no field lines crossing the “side” surfaces – is

$$W_M = \int \frac{B^2}{2\mu_0} d^3r = \int \frac{B^2}{2\mu_0} A dl \quad (8.77)$$

where l is the length along the flux tube, and $A(l)$ is the cross sectional area of the flux tube. By definition, the flux enclosed in a flux tube

$$\Phi = B(l)A(l) = \text{const} \quad (8.78)$$

When the plasma in volume I is displaced into volume II, the magnetic flux in volume I is also displaced into volume II, and vice versa. The change in magnetic energy that results from interchanging the plasma in volumes I and II is

$$\delta W_M = \frac{1}{2\mu_0} \left[\left(\Phi_I^2 \int_{II} \frac{dl}{A} + \Phi_{II}^2 \int_I \frac{dl}{A} \right) - \left(\Phi_I^2 \int_I \frac{dl}{A} + \Phi_{II}^2 \int_{II} \frac{dl}{A} \right) \right] \quad (8.79)$$

The least stable interchanges are those that leave W_M unchanged; that is $\delta W_M = 0$. This is the case when $\Phi_I = \Phi_{II}$. For such interchanges, the volume

$$V = \int A dl = \Phi \int \frac{dl}{B} \quad (8.80)$$

associated with a flux tube varies as

$$V_{II} - V_I = \delta V = \Phi \delta \left(\int \frac{dl}{B} \right) \quad (8.81)$$

The plasma internal energy is, in the ideal gas approximation,

$$W_p = \frac{pV}{\gamma - 1} \quad (8.82)$$

An adiabatic expansion of the plasma satisfies

$$\frac{d}{dt}(pV^\gamma) = 0 \quad (8.83)$$

Hence, the change in plasma internal energy when the flux tubes are interchanged is

$$\delta W_p = \frac{1}{\gamma - 1} \left[\left(\frac{p_I V_I^\gamma V_{II}}{V_{II}^\gamma} + \frac{p_{II} V_{II}^\gamma V_I}{V_I^\gamma} \right) - (p_I V_I + p_{II} V_{II}) \right] \quad (8.84)$$

Writing $p_{II} = p_I + \delta p$, $V_{II} = V_I + \delta V$, Eq. (8.84) becomes

$$\delta W_p = \delta p \delta V + \gamma p \frac{(\delta V)^2}{V} = V^{-\gamma} \delta(p V^\gamma) \delta V \quad (8.85)$$

The necessary condition for MHD stability is $\delta W_p > 0$. Because the second term in Eq. (8.85) is always positive,

$$\delta p \delta V = \delta p \Phi \delta \left(\int \frac{dl}{B} \right) > 0 \quad (8.86)$$

is a sufficient condition for stability.

In the usual case for confined plasmas, the pressure decreases from the center outwards, so that $\delta p < 0$ for the interchange depicted in Fig. 8.9. In this case, Eq. (8.86) yields

$$\delta \left(\int \frac{dl}{B} \right) < 0 \quad (8.87)$$

as a sufficient condition for stability. This criterion can be related to the curvature of the field lines

$$\frac{\mathbf{R}_c}{R_c^2} \equiv -\frac{(\mathbf{B} \cdot \nabla) \mathbf{B}}{B^2} \quad (8.88)$$

which reduces for the geometry of Fig. 8.10 to

$$\frac{\delta B}{B} = -\frac{d}{R_c} \quad (8.89)$$

In a vacuum, $\nabla \times \mathbf{B} = 0$, and \mathbf{B} can be constructed from a scalar magnetic potential, $\mathbf{B} = -\nabla\Phi_m$. In this case, the differential $B dl$ is the same along any two field lines between equipotential surfaces, and the interchange of field lines is characterized by $\delta(B dl) = 0$. (This is strictly valid only in a vacuum, but we will use it as an approximation in a low- β plasma.) Using this result allows Eq. (8.87) to be written

$$\int \delta \left(\frac{1}{B^2} \right) B dl = - \int \frac{2\delta B}{B^2} dl < 0 \quad (8.90)$$

The flux in an annular flux tube, $\Phi = 2\pi r dB$ is a constant. Using this result and Eq. (8.89) in Eq. (8.90) leads to the sufficient condition for stability of interchange modes,

$$\int \frac{dl}{R_c r B^2} < 0 \quad (8.91)$$

In Fig. 8.10, stabilizing regions with $R_c < 0$ correspond to the field lines being concave into the plasma, and, conversely, destabilizing regions with $R_c > 0$ correspond to the field

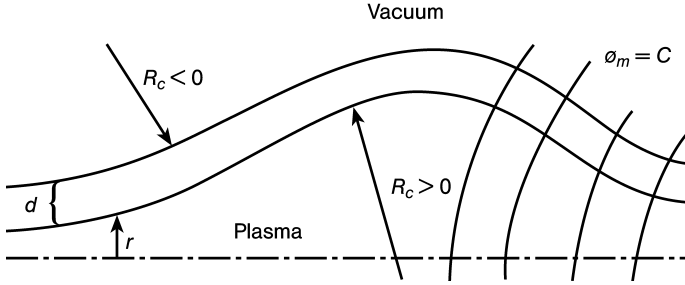


Figure 8.10. Field line curvature

lines being convex away from the plasma. In the simple mirror of Fig. 8.9, the $(rB^2)^{-1}$ weighting favors the destabilizing central regions over the stabilizing regions under the coils. The simple mirror is unstable to flute modes. The more complicated, minimum- B mirror field configurations constructed with Joffee bars or yin-yang coils have good curvature everywhere – the field lines are everywhere concave into the plasma.

It is instructive to examine the interchange instability in a simple mirror in terms of the particle drifts. Assume that a flute perturbation has been established, as shown in Fig. 8.11. The angular displacement, $\Delta\theta$, of a particle during one transit time between mirror reflection points (see Fig. 8.11) is

$$\Delta\theta \equiv \int \frac{\dot{\theta} dl}{v_{\parallel}} \quad (8.92)$$

The angular displacement is a result of curvature and grad- B drifts. Using the vacuum ($\nabla \times \mathbf{B} = 0$) values of these drifts,

$$\begin{aligned} \mathbf{v}_c &= -\frac{2W_{\parallel}}{e} \frac{\mathbf{B} \times \mathbf{R}_c}{B^2 R_c^2} \\ \mathbf{v}_{\nabla B} &= -\frac{W_{\perp}}{e} \frac{\mathbf{B} \times \mathbf{R}_c}{B^2 R_c^2} \end{aligned} \quad (8.93)$$

the angular velocity can be written

$$\mathbf{v}_{\theta} = r\dot{\theta} = \frac{1}{eB} \frac{(2W_{\parallel} + W_{\perp})}{R_c} \quad (8.94)$$

with the positive sense of θ as shown in the figure. Positive charges will move counter-clockwise ($v_{\theta} > 0$) and negative charges will move clockwise ($v_{\theta} < 0$) in regions with $R_c > 0$, and conversely for regions with $R_c < 0$. This produces a charge separation as indicated in Fig. 8.11, which in turn produces an electric field and a drift,

$$\mathbf{v}_E = \frac{\mathbf{E} \times \mathbf{B}}{B^2} \quad (8.95)$$

that increases the flute perturbation.

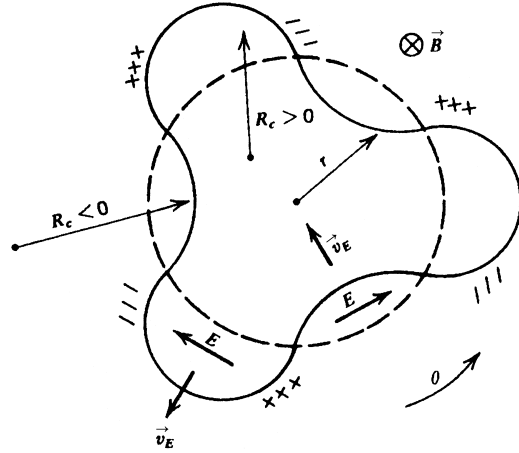


Figure 8.11. Flute instability in a simple mirror

On a given field line, the angular displacement, $\Delta\theta$, is a function of W and $\bar{\mu}$. The average angular displacement is

$$\langle \Delta\theta \rangle = \int d\bar{\mu} dW N(\bar{\mu}, W) \Delta\theta(\bar{\mu}, W) \quad (8.96)$$

where $N(\bar{\mu}, W) d\bar{\mu} dW$ is the number of particles on a field line within the phase space element $d\bar{\mu} dW$. Because the particle flow along a flux tube $\hat{f} v_{\parallel} A = \hat{f} v_{\parallel} \Phi / B = \text{const}$, where $f(\bar{\mu}, W, l)$ is the particle density distribution function, and because $\Phi = \text{const}$, it follows that

$$\hat{f}(\bar{\mu}, W, l) \propto N(\bar{\mu}, W) \frac{B(l)}{v_{\parallel}(l)} \quad (8.97)$$

Making use of Eqs. (8.92), (8.94) and (8.97), Eq. (8.96) becomes

$$\langle \Delta\theta \rangle \propto \int dl \int d\bar{\mu} dW \frac{(2W_{\parallel} + W_{\perp})}{erR_c B^2} \hat{f}(\bar{\mu}, W, l) \quad (8.98)$$

Recalling the definition of the parallel and perpendicular pressures,

$$\begin{aligned} p_{\parallel}(l) &\equiv \int d\bar{\mu} dW \hat{f}(\bar{\mu}, W, l) 2W_{\parallel} \\ p_{\perp}(l) &\equiv \int d\bar{\mu} dW \hat{f}(\bar{\mu}, W, l) W_{\perp} \end{aligned} \quad (8.99)$$

we can use the condition $\langle \Delta\theta \rangle < 0$ for stability to arrive at the stability criterion

$$\int dl \frac{[p_{\perp}(l) + p_{\parallel}(l)]}{erR_c(l) B^2(l)} < 0 \quad (8.100)$$

which is similar to the result (Eq. (8.91) found from the fluid analysis.

This interpretation of the flute instability in terms of charge separation implies that if the field lines were “shorted” at the ends of the mirror, then charge separation and hence the flute instability could be inhibited. This “line-tying” could be achieved by a metal plate located at the reflection plane, but this would create a significant impurity source.

The simple mirror is generally unstable because B is largest where $R_c < 0$ and smallest where $R_c > 0$. Thus, the $(rB^2)^{-1}$ weighting in Eq. (8.91) or Eq. (8.100) is unfavorable. As mentioned previously, this deficiency can be overcome by a minimum- B mirror field configuration with $R_c < 0$ almost everywhere.

Thus, a plasma in a curved magnetic field has the potential for charge separation and unstable growth of flute perturbations when the radius of curvature vector is directed oppositely from the direction of the pressure gradient. This situation can occur whenever a plasma is confined in a magnetic field that is concave towards the plasma. The tokamak field configuration obviously has bad curvature.

The toroidal curvature is favorable (convex towards the plasma) on the small R inner side and unfavorable (concave towards the plasma) on the large R outer side. The $1/R$ weighting of the small R -side is slightly greater than the weighting of the large R -side, so the net effect is stabilizing. However, there is a mechanism for shorting out the charge separation which would otherwise build up. Since a field line traced many times around the torus will map out a flux surface, there can be no charge build up on a flux surface because of the rapid transport along the field lines. The poloidal field thus inhibits the natural tendency towards interchange instability that would be a feature of purely toroidal field configurations. The rational surfaces, $q = m/n$, are unique exceptions, because the field lines close upon themselves and do not map out a flux surface when followed many times around the torus. Thus charge build up is not inhibited on rational surfaces. If displacements which conform to the field line pitch of a rational surface, and which interchange field lines without distorting them, are generated, internal interchange instabilities will grow on the rational surface. The growth of these modes will be inhibited if neighboring flux surfaces have a different field line pitch – this is known as “shear stabilization.” Pressure gradients are the principal energy source for driving interchange instabilities in tokamaks.

For large m -numbers (assuming a perturbation of the form of Eq. (8.71)), the interchange modes are localized about the internal rational surfaces. These modes are internal kink modes in a tokamak or a cylindrical plasma. The energy principle can be written for a cylindrical plasma,

$$\delta W = \frac{1}{2} \int \left[f \left(\frac{d\xi}{dr} \right)^2 + g \xi^2 \right] dr \quad (8.101)$$

where f and g are functions of the mode number of the plasma equilibrium. δW is minimized by the displacement, ξ , satisfying

$$\frac{d}{dr} \left(f \frac{d\xi}{dr} \right) - g\xi = 0$$

This equation can be expanded about the rational surface on which $q \equiv rB_\phi/RB_\theta = m/n$. It can be shown from the expanded equation that there are no radially localized

displacements, ξ , which make $\delta W < 0$ if

$$\frac{dp}{dr} + \frac{rB_\phi^2}{8\mu_0} \left(\frac{1}{q} \frac{dq}{dr} \right)^2 > 0 \quad (8.102)$$

This is the Suydam criterion for the stability of high- m , localized interchange modes in a cylinder. Since $dp/dr < 0$, usually, the pressure gradient is destabilizing. The shear, $(1/q)(dq/dr)$, is required to stabilize these modes.

An extension of this type of analysis to an axisymmetric toroidal configuration leads to the Mercier criterion for the stability of large- m interchange modes. An approximate form of this criterion, valid in the low- β , large aspect ratio limit, is

$$-\left(\frac{dp}{dr}\right)(q^2 - 1) + \frac{rB_\phi^2}{8\mu_0} \left(\frac{1}{q} \frac{dq}{dr} \right)^2 > 0 \quad (8.103)$$

In the usual case, with $(dp)/(dr) < 0$, both the pressure gradient and shear term are stabilizing if $q(r) > 1$. For toroidal current density distributions that peak at the center of the plasma and decrease with minor radius, r , the safety factor, $q(r)$, increases with r . Thus, $q(0) > 1$ is sufficient to ensure the stability of localized, high- m interchange modes, as long as $(dp)/(dr) < 0$. This requirement is indicated by the “internal mode” instability region in Fig. 8.8.

The interchange modes in a tokamak are internal kink modes. Since such modes must vanish on the surface, only the volume integral term obtains in the energy principle of Eq. (8.72), which is rewritten here with a zero subscript to denote the fact that it is based on a cylindrical, or zero-order in ϵ approximation:

$$\delta W_0 = \frac{B_\phi^2}{\mu_0 R_0} \int_0^a \frac{1}{q^2} \left[\left(r \frac{d\xi}{dr} \right)^2 + (m^2 - 1)\xi^2 \right] \left(\frac{nq}{m} - 1 \right)^2 r dr \quad (8.104)$$

$O(\epsilon^0)$, $\delta W \geq 0$, and stability must be determined from an $O(\epsilon)$ expression for δW . These higher order terms can only affect the value of δW when $\delta W_0 \approx 0$. There are three different situations in which this can occur: (1) for $m = 1$, $\delta W_0 \simeq 0$ if $(d\xi)/(dr)$ is small everywhere except near the rational surface $nq(r_s) = 1$; (2) for m large, $\delta W_0 \simeq 0$ if $(d\xi)/(dr)$ and ξ are small everywhere except near the rational surface $nq(r_s) = m$, where $((nq)/m - 1)$ is small; and (3) for $m > 1$ but not large, a nonlocal analysis is required to determine when $\delta W_0 \simeq 0$. The Mercier criterion applies to the second situation. Analyses of the first and third situations have led to a similar result, namely that $q(0) > 1$ is sufficient to ensure the stability of interchange modes in tokamaks.

8.5 Ballooning Instabilities

At sufficiently large values of the plasma pressure, the pressure gradient may become large enough in regions of bad curvature in a tokamak to produce a “ballooning” instability. The deformation is flutelike and is larger on the outside of the torus, as indicated in Fig. 8.12. This deformation bends the field lines, which provides a restoring force. If

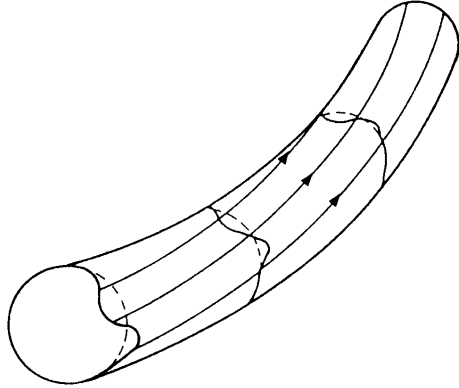


Figure 8.12. Ballooning mode

the driving force, which is proportional to the product of the pressure gradient and the curvature (inverse major radius), is greater than the restoring force due to the resistance of the field lines to bending, then these ballooning modes will limit the achievable plasma pressure.

In the interchange instability discussed in the previous section, the parallel component of the propagation vector, $k_{\parallel} = \mathbf{k} \cdot \mathbf{B} / B$, is zero, and an average minimum- B configuration may be sufficient for stability. Suydam's criterion and other local mode stability conditions apply to this situation in which $k_{\parallel} = 0$. However, it is possible that a mode with $k_{\parallel} \neq 0$ can grow locally in the region of bad curvature, even in an average minimum- B configuration. This type of instability is known as a ballooning instability.

We use the energy integral

$$\delta W = \frac{1}{2\mu_0} \int ([\nabla \times (\xi \times \mathbf{B}_0)]^2 - [\xi \times (\nabla \times \mathbf{B}_0)] \cdot \nabla \times (\xi \times \mathbf{B}_0) + \gamma \mu_0 p_0 (\nabla \cdot \xi)^2 + \mu_0 (\nabla \cdot \xi)(\xi \cdot \nabla p_0)) d\mathbf{r} \quad (8.105)$$

and represent the perturbation

$$\xi = \frac{\mathbf{B}_0 \times \nabla \phi}{B_0^2} \quad (8.106)$$

where ϕ is understood to be the time average of the perturbed electrostatic potential. Since

$$\xi \times \mathbf{B}_0 = \nabla_{\perp} \phi \quad (8.107)$$

Eqs. (8.105) can be reduced to

$$\delta W = \frac{1}{2\mu_0} \int \left[(\nabla \times \nabla_{\perp} \phi)^2 - \left(\frac{(\mathbf{B}_0 \times \nabla_{\perp} \phi) \times \mu_0 \mathbf{j}_0}{B_0^2} \right) \right] \nabla \times \nabla_{\perp} \phi + \gamma \mu_0 p_0 (\nabla \cdot \xi)^2 + \mu_0 (\nabla \cdot \xi)(\xi \cdot \nabla p_0) d\mathbf{r} \quad (8.108)$$

and $\nabla \cdot \xi$ can be written

$$\begin{aligned}\nabla \cdot \xi &= \nabla \cdot \left(\frac{\mathbf{B}_0 \times \nabla_{\perp} \phi}{B_0^2} \right) \\ &= \nabla \phi \cdot \nabla \times \left(\frac{\mathbf{B}_0}{B_0^2} \right) \\ &= \nabla \phi \cdot \left[\left(\nabla \frac{1}{B^2} \right) \times \mathbf{B} + \frac{1}{B^2} \nabla \times \mathbf{B} \right]\end{aligned}\quad (8.109)$$

The second term is small compared to the first term, except for very high β . Making use of the equilibrium force balance $\nabla p_0 = j_0 \times \mathbf{B}_0$, Eq. (8.108) becomes

$$\begin{aligned}\delta W &= \frac{1}{2\mu_0} \int (\nabla \times \nabla_{\perp} \phi)^2 + \frac{\mu_0 \nabla p_0 \cdot (\nabla_{\perp} \phi \times \mathbf{B}_0)}{B_0^2} \left(\frac{\mathbf{B}_0 \cdot \nabla \times \nabla_{\perp} \phi}{B_0^2} \right) \\ &\quad - \frac{\mu_0 (\mathbf{j}_0 \cdot \mathbf{B}_0)}{B_0^2} \nabla_{\perp} \phi \cdot \nabla \times \nabla_{\perp} \phi + \gamma \mu_0 p_0 \left[\nabla \left(\frac{1}{B_0^2} \right) \cdot (\mathbf{B}_0 \times \nabla_{\perp} \phi) \right]^2 \\ &\quad + \frac{\mu_0 \nabla p_0 \cdot (\mathbf{B}_0 \times \nabla_{\perp} \phi)}{B_0^2} \left[\nabla \left(\frac{1}{B_0^2} \right) \cdot (\mathbf{B}_0 \times \nabla_{\perp} \phi) \right] dr\end{aligned}\quad (8.110)$$

Identifying the z -directions along the field lines, θ as the poloidal angle direction perpendicular to z in the cylindrical flux surface, and r as the radial direction, we can write $\nabla p_0 = \hat{\mathbf{n}}_r \partial p_0 / \partial r$, $\mathbf{B} = B_\theta \mathbf{n}_\theta + B_0 (1 - r/R_c(z)) \mathbf{n}_\phi$, and $\nabla \phi = (\partial \phi / \partial r) \mathbf{n}_r + (\partial \phi / r \partial \theta) \mathbf{n}_\theta + (\partial \phi / \partial z) \mathbf{n}_z$. Here, $R_c(z)$ is the radius of curvature of the magnetic field line

$$\frac{1}{R_c(z)} = \frac{1}{R_0} \left(-\omega + \cos 2\pi \frac{z}{L} \right)\quad (8.111)$$

When $R_c(z) < 0$, the curvature is referred to as “good,” and conversely when $R_c(z) > 0$ the curvature is referred to as “bad.” If the configuration is average minimum- B , then $1 > \omega > 0$ and $R_0 > 0$.

Representing the θ -dependence of the perturbed electrostatic potential as $\phi(r, \theta, z) = \phi(r, z) \exp(im\theta)$ and neglecting the small quantities B_θ / B_0 , r / R_0 , and r / L , where L is the length of the cylindrical plasma, Eq. (8.110) can be reduced to

$$\delta W = \frac{1}{2\mu_0} \int \frac{m^2}{r^2} \left\{ \left[\frac{\partial \phi(r, z)}{\partial z} \right]^2 - \frac{\beta}{L_p R_c(z)} [\phi(r, z)]^2 \right\} 2\pi r dr dz\quad (8.112)$$

where $L_p = -p_0 / (\partial p_0 / \partial r)$ and $\beta = p_0 / (B_0^2 / 2\mu_0)$. The second term is stabilizing when $R_c(z) < 0$ and destabilizing when $R_c(z) > 0$, hence the “good” and “bad” curvature designations.

The Euler equation of this form of δW (i.e., the equation satisfied by ϕ which makes $\delta W = 0$) is

$$\frac{d^2\phi}{dz^2} + \frac{\beta}{L_p R_c(z)}\phi = 0 \quad (8.113)$$

This is a Mathieu differential equation, which has an eigenvalue of the form

$$\omega = F(\beta L^2 / 2\pi L_p R_0) \quad (8.114)$$

where

$$F \equiv \mathbf{k} \cdot \mathbf{B} = \frac{m}{r} B_\theta + k B_z \quad (8.115)$$

Since $F(x) \rightarrow x/4$ when $x \ll 1$ and $f(x) \rightarrow 1 - x^{-\frac{1}{2}}$ when $x \gg 1$, we can develop an approximation for the threshold value of β for ballooning instability

$$\beta_c \simeq \frac{4\omega}{(1+3\omega)(1-\omega)^2} \frac{2\pi^2 L_p R_0}{L^2} \quad (8.116)$$

Since the eigenvalue is of the order $\omega \sim O(L_p/2R_0)$ and the connection length in toroidal geometry is $L \approx 2\pi R_0 q$, the threshold β is

$$\beta_c \sim \left(\frac{L_p}{R} \right) \Big/ q^2 \quad (8.117)$$

If $\beta < \beta_c$, then $\delta W > 0$ and the plasma is stable.

Note that the above derivation was for a cylindrical, not toroidal, plasma, until the very end when the toroidal expression for the connection length was used. As a consequence of the cylindrical plasma, magnetic shear did not enter the derivation. A similar treatment in toroidal geometry of ballooning modes with large toroidal mode number $n \gg 1$ and $m - nq \approx 0$ leads to the identification of a stability boundary in a phase space defined by the shear parameter

$$S = \frac{r}{q} \frac{dq}{dr} \quad (8.118)$$

and the normalized pressure gradient

$$\alpha = -\frac{q^2 R}{B^2/2\mu_0} \frac{dp}{dr} = \beta \Big/ \left[\left(\frac{L_p}{R} \right) \Big/ q^2 \right] \quad (8.119)$$

as shown in Fig. 8.13.

In the region of large S , the stability boundary can be approximately represented by the straight line $\alpha \approx 0.6S$. Since

$$\beta = \frac{1}{B_0^2/2\mu_0} \frac{1}{\pi a^2} \int_0^a p 2\pi r dr = -\frac{1}{B_0^2/2\mu_0} \frac{1}{a^2} \int_0^a \frac{dp}{dr} r^2 dr \quad (8.120)$$

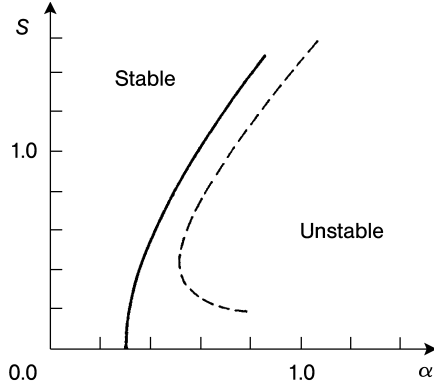


Figure 8.13. The maximum stable pressure gradient α versus the magnetic shear S . (Dotted line indicates result when more restrictive boundary conditions are imposed on perturbation)

use of the straight line approximation yields

$$\beta_c \simeq 0.6 \frac{a}{R} \left(\frac{1}{a^3} \int_0^a \frac{1}{q^3} \frac{dq}{dr} r^3 dr \right) \quad (8.121)$$

Under an optimal current profile, the maximum ballooning mode stable β for $q_a > 2$ and $q(0) = 1$ is

$$\beta_{\max} \sim 0.28 \frac{a}{R q_a} \quad (q_a > 2) \quad (8.122)$$

Note that the ballooning mode is stable in the negative shear region $S < 0$. Since

$$q(r) = \frac{B_0 2\pi r^2}{\mu_0 I(r) R_0} = \frac{B_0 r^2}{\mu_0 R_0 \int_0^r r' j(r') dr'} \quad (8.123)$$

a negative shear region can be realized by a current density profile that increases with radius.

8.6 Drift Wave Instabilities

Drift wave instabilities are driven by a plasma nonuniformity (e.g. a density gradient) and thus are universally present in magnetically confined plasmas. A dissipation mechanism (e.g. resistivity) is necessary to make a drift wave unstable, however. Drift waves do not involve a significant magnetic perturbation, except at high β , so we will treat them as electrostatic (i.e. $\mathbf{E} = -\nabla\phi$).

The generalized Ohm's law of chapter 5 is

$$\mathbf{E} + \mathbf{u} \times \mathbf{B} = \eta \mathbf{j} + \frac{\mathbf{j} \times \mathbf{B} - \nabla p_e}{ne} \quad (8.124)$$

The perpendicular component can be solved for the mass flow perpendicular to the field by neglecting the terms on the right to obtain the $\mathbf{E} \times \mathbf{B}$ drift

$$\mathbf{u}_\perp \simeq \frac{\mathbf{E} \times \mathbf{B}}{B^2} \quad (8.125)$$

and the parallel component is

$$E_\parallel = \eta j_\parallel - \frac{1}{ne} \nabla_\parallel p_e \quad (8.126)$$

We consider slab geometry with a straight uniform field in the z -direction and plasma properties that vary in the x -direction. Expanding about an equilibrium solution, $A(x, t) = A_0(x) + A_1(x) \exp(-i\omega t + ik_y y + ik_z z)$ in Eq. (8.125) and Eq. (8.126) yields

$$\begin{aligned} u_x &= \frac{E_y}{B_{z0}} = -ik_y \frac{\phi}{B_{z0}} \\ E_z &= \eta j_z - \frac{ik_z p_{e1}}{ne} \end{aligned} \quad (8.127)$$

which can be combined to obtain

$$k_z B_{z0} u_x = k_y \left(\eta j_z - \frac{ik_z T_{e0}}{ne} n_{e1} \right) \quad (8.128)$$

Any temperature perturbation along the field line has been assumed to be rapidly damped by thermal conduction.

A similar expansion in the electron density and parallel momentum balance and linearization leads to

$$-i\omega n_{e1} + u_x \frac{dn_{e0}}{dx} + ik_z n_{e0} u_z = 0 \quad (8.129)$$

and

$$-i\omega \rho_0 u_z = -ik_z T_{e0} n_{e1} \quad (8.130)$$

which can be combined with Eq. (8.128) to obtain

$$\left(1 - \frac{k_y v_{de}}{\omega - k_z^2 c_s^2 / \omega} \right) u_x = \frac{k_y \eta}{k_z B_{z0}} j_z \quad (8.131)$$

where

$$v_{de} = -\frac{1}{n_{e0} e B_{z0}} \frac{dp_{e0}}{dx} \quad (8.132)$$

is the electron diamagnetic drift velocity.

A similar expansion in the plasma (ion plus electron) momentum balance and linearization yields

$$\begin{aligned} -i\omega\rho_0u_x &= -\frac{\partial p_1}{\partial x} + j_{y1}B_{z0} \\ -i\omega\rho_0u_y &= -ik_y p_1 - j_{x1}B_{z0} \end{aligned} \quad (8.133)$$

which may be combined to eliminate the plasma pressure

$$-i\omega\left(\frac{\partial}{\partial x}(\rho_0u_y) - ik_y\rho_0u_x\right) = -B_{z0}\left(\frac{\partial j_{x1}}{\partial x} + ik_yj_{y1}\right) \quad (8.134)$$

Using $\nabla \cdot \mathbf{j} = 0$ to replace the term on the right with $ik_zj_zB_{z0}$ and requiring that \mathbf{u}_\perp is incompressible leads to

$$\frac{\partial u_x}{\partial x} + ik_yu_y = 0 \quad (8.135)$$

and using a WKB approximation to write $\partial/\partial x \approx -ik_x$ leads to

$$j_z = \frac{i\omega\rho_0}{k_yk_zB_{z0}}k_\perp^2u_x \quad (8.136)$$

where $k_\perp^2 = k_x^2 + k_y^2$.

Using Eq. (8.136) in Eq. (8.131) yields the dispersion relation for electrostatic drift waves in slab geometry

$$\omega - k_yv_{de} - \frac{k_z^2c_s^2}{\omega} = \left(\frac{i\eta k_\perp^2}{\mu_0}\right)\left(\frac{\omega^2 - k_z^2c_s^2}{k_z^2V_A^2}\right) \quad (8.137)$$

where V_A is the Alfvén speed and c_s is the speed of sound.

When $k_yv_{de} \gg k_zc_s$, $\omega \approx k_yv_{de}$ and the growth rate of the drift wave instability is

$$\gamma = \frac{\eta k_\perp^2 k_y^2 v_{de}^2}{\mu_0 k_z^2 V_A^2} \quad (8.138)$$

The energy source for drift wave instabilities is provided by the thermal energy dissipation of the plasma as it expands across the magnetic field. The plasma resistivity causes a phase shift between the electron density and the electrostatic potential perturbations that enables the thermal energy available in the electron pressure gradient to be transferred to the energy of the drift wave flow, resulting in the unstable growth of the drift wave.

Drift waves have finite wavelengths along field lines. The plasma motion is not tightly coupled to motion of the magnetic field because of the resistivity, thus avoiding energetically unfavorable field line distortions. These features distinguish the drift waves from the interchange, or flute, modes discussed previously.

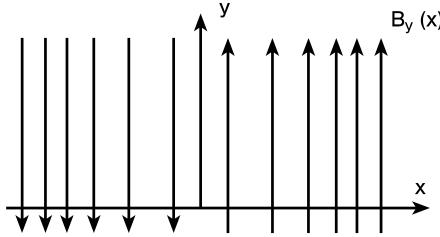


Figure 8.14. Magnetic field lines for the “plasma current sheet” equilibrium.
(There is also a strong uniform field B_z)

8.7 Resistive Tearing Instabilities*

The perfect conductivity constraint that the magnetic field lines move with the plasma no longer exists when finite resistivity is present. Relaxation of this constraint allows the possibility of magnetic field perturbations that can more effectively draw energy out of the magnetic field produced by currents in the plasma to drive instabilities, as we just saw for drift waves. The most important of such instabilities is the resistive tearing mode.

8.7.1 Slab Model

The essential physics of the resistive tearing instability can be seen in a simple thin slab plasma configuration with a current parallel to a straight, uniform magnetic field in the z -direction

$$j_z = \begin{cases} j_{z0} & -a < x < a \\ 0 & x < -a, x > a \end{cases} \quad (8.139)$$

By Ampère’s law

$$\frac{dB_y(x)}{dx} = \mu_0 j_z(x) \quad (8.140)$$

this current produces a magnetic field

$$B_y(x) = \begin{cases} \mu_0 j_{z0}x & -a < x < a \\ -\mu_0 j_{z0}a & x < -a \\ \mu_0 j_{z0}a & x > a \end{cases} \quad (8.141)$$

This configuration is indicated in Fig. 8.14. Any spatial nonuniformity is assumed to be in the x -direction.

Since the magnetic energy associated with the current slab, $B_y^2/2\mu_0$, integrated over some small region, $-\Delta \leq x \leq \Delta$, about $x = 0$ would be reduced if the positive and negative B_y on opposite sides of $x = 0$ diffused together to reduce $|B_y| \rightarrow 0$, such field diffusion would free magnetic energy to drive an instability. The perfect conductivity constraint against such field diffusion is relaxed by the presence of finite resistivity.

Making the usual expansion about the equilibrium solution, $A(x, y, z, t) = A_0(x) + A_1(x) \exp(-i\omega t + ik_y y + ik_z z)$ in the generalized Ohm's law

$$\mathbf{E} + \mathbf{u} \times \mathbf{B} = \eta \mathbf{j} \quad (8.142)$$

and in Faraday's law leads to an equation for the x -component of the perturbed magnetic field

$$\omega B_x = -k B_{y0} u_x + \frac{i\eta}{\mu_0} \frac{\partial^2 B_x}{\partial x^2} \quad (8.143)$$

where the “1” subscripts have been suppressed on u_x and B_x , $k_z = 0$ is assumed and $k_y \rightarrow k$, and $\nabla^2 \rightarrow \partial^2/\partial x^2$ in anticipation that the main gradient in B_x is in the x -direction near $x = 0$.

The resistive term in Eq. (8.143) is important only where $\partial^2 B_x / \partial x^2$ is large; i.e. in a thin resistive layer about $x = 0$. Thus, we consider the plasma to consist of two “MHD” regions ($x > \Delta$ and $x < -\Delta$) in which the resistive term is unimportant separated by a layer $-\Delta < x < \Delta$, where 2Δ is greater than the resistive layer about $x = 0$.

Integrating $\nabla \cdot \mathbf{B} = 0$ over the domain $-\Delta < x < \Delta$ and a distance in y much less than the characteristic wavelength of any perturbation yields the continuity boundary condition

$$B_x(x \rightarrow \Delta) = B_x(x \rightarrow -\Delta) \quad (8.144)$$

from which it is plausible to assume $B_x(y)$ is constant across the resistive boundary layer at $x = 0$.

Integrating $\nabla \times \mathbf{B}_1 = \mu_0 \mathbf{j}$ over the same domain yields the discontinuity condition

$$B_{y1}(x \rightarrow \Delta) - B_{y1}(x \rightarrow -\Delta) = \mu_0 j_{z1} \Delta \quad (8.145)$$

From

$$\nabla \cdot \mathbf{B}_1 = \frac{\partial B_x}{\partial x} + ik B_{y1} = 0 \quad (8.146)$$

it is clear that a discontinuity in B_{y1} implies a discontinuity in $\partial B_x / \partial x$. The solutions in the MHD regions ($x > \Delta$ and $x < -\Delta$) determine the magnitude of this discontinuity

$$\Delta' \equiv \frac{1}{B_x} \left[\frac{\partial B_x}{\partial x} \right]_{x=0} \equiv \frac{1}{B_x} \left(\frac{\partial B_x}{\partial x} \Big|_{x=\Delta} - \frac{\partial B_x}{\partial x} \Big|_{x=-\Delta} \right) \quad (8.147)$$

8.7.2 MHD Regions

The usual expansion may be used in the linearized plasma momentum balance

$$\rho_0 \frac{\partial \mathbf{u}_1}{\partial t} = -\nabla p_1 + (\mathbf{j} \times \mathbf{B})_1 \quad (8.148)$$

and in Ampère's law, and Eq. (8.146) can then be used, to obtain

$$-i\omega\rho_0u_x = -\frac{\partial}{\partial x} \left(p_1 + \frac{B_{z0}B_{z1} + B_{y0}B_{y1}}{\mu_0} \right) + \frac{1}{\mu_0}ikB_{y0}B_x \quad (8.149)$$

and

$$-i\omega\rho_0u_y = -ik \left(p_1 + \frac{B_{z0}B_{z1} + B_{y0}B_{y1}}{\mu_0} \right) - \frac{1}{\mu_0} \left(B_{y0}\frac{\partial B_x}{\partial x} - B_x\frac{\partial B_{y0}}{\partial x} \right) \quad (8.150)$$

Differentiating Eq. (8.150) with respect to x and subtracting the result from ik times Eq. (8.149), using Eq. (8.143) with $\eta \rightarrow 0$, using Eq. (8.146) and the incompressibility requirement ($\nabla \cdot \mathbf{u}_1 = 0$), and rearranging leads to

$$\frac{\partial}{\partial x} \left[(\rho_0\mu_0\omega^2 - k^2B_{y0}^2)\frac{\partial u_x}{\partial x} \right] - k^2(\rho_0\mu_0\omega^2 - k^2B_{y0}^2)u_x = 0 \quad (8.151)$$

This equation describes a stable, oscillatory "shear Alfvén" wave with frequency $\omega \approx (k_y B_{y0}/B_{z0})V_A$. Possible solutions include discrete modes with $\omega > k|B_{y0}|_{\max}/(\rho_0\mu_0)^{\frac{1}{2}}$ and a continuum of modes with smaller oscillation frequencies.

Using Eq. (8.143) with $\eta \rightarrow 0$ in Eq. (8.151) and omitting inertial terms yields

$$\frac{\partial}{\partial x} \left[B_{y0}^2 \frac{\partial}{\partial x} \left(\frac{B_x}{B_{y0}} \right) \right] - k^2 B_{y0}^2 B_x = 0 \quad (8.152)$$

In the region $x > a$, where $B_y = \mu_0 j_{z0}a$, this equation becomes

$$\frac{\partial^2 B_x}{\partial x^2} - k^2 B_x = 0 \quad (8.153)$$

which has the solutions

$$B_x(x) = C \exp(-kx) \quad (8.154)$$

satisfying the physical boundary condition $B_x(x \rightarrow \infty) \rightarrow 0$.

In the region $0 < x < a$, where $B_y = \mu_0 j_{z0}x$, Eq. (8.152) can be shown to reduce to Eq. (8.153), which has the general solution

$$B_x(x) = A \exp(kx) + D \exp(-kx) \quad (8.155)$$

The solution Eq. (8.154) for $x > a$ must match the solution Eq. (8.155) for $x < a$ at $x = a$. We have previously argued that it is plausible to take B_x as continuous across the resistive layer. Thus, integrating Eq. (8.152) across the boundary layer at $x = a$ yields

$$B_x(x = a+) = B_x(x = a-)$$

and

$$\frac{\partial}{\partial x} \left(\frac{B_x}{B_{y0}} \right) \Big|_{x=a+} = \frac{\partial}{\partial x} \left(\frac{B_x}{B_{y0}} \right) \Big|_{x=a-} \quad (8.156)$$

which may be used to eliminate two of the constants of integration

$$\begin{aligned} A &= \frac{C}{2ka} \exp(-2ka) \\ D &= \frac{C}{2ka}(2ka - 1) \end{aligned} \quad (8.157)$$

Similar considerations may be used to match solutions for $x < -a$ and $x > -a$ at $x = -a$, enabling evaluation of the quantity Δ' given by Eq. (8.147)

$$\Delta' a = \frac{2ka[\exp(-2ka) - 2ka + 1]}{[\exp(-2ka) + 2ka - 1]} \quad (8.158)$$

8.7.3 Resistive Layer

The solution in the outer MHD regions must be related to the solution in the resistive layer by the discontinuity condition Δ' . Denoting the approximately constant value of B_x in the resistive layer as B_x^* and using it on the left in Eq. (8.143), integration of that equation across the resistive layer yields

$$\Delta' \bar{B}_x = \left[\frac{\partial B_x}{\partial x} \right]_{x=0} = \frac{\mu_0}{i\eta} \int (i\gamma \bar{B}_x + k\mu_0 j_{z0} x u_x) dx \quad (8.159)$$

where $\omega = i\gamma$ has been used in anticipation of a nonoscillatory solution. This equation can be solved for the growth rate, γ , using Eq. (8.158) for Δ' , once the solution for the x -component of the mass flow, u_x , in the resistive layer is known.

An equation for u_x in the resistive layer can be derived from the momentum balance equation, following a derivation similar to that used for the derivation of Eq. (8.151), but now retaining finite resistivity in Eq. (8.143) and assuming that y -derivatives (k -terms) can be neglected relative to x -derivatives

$$\gamma\eta\rho_0 \frac{\partial^2 u_x}{\partial x^2} = k\mu_0 j_{z0} x (i\gamma \bar{B}_x + k\mu_0 j_{z0} x u_x) \quad (8.160)$$

This equation indicates that u_x will be an odd function of x and will decrease as $u_x \sim 1/x$ as the term on the left becomes small away from the resistive layer. A characteristic width for the resistive layer can be estimated by equating the term on the left with the second term on the right

$$\delta_R = (\gamma\eta\rho_0)^{\frac{1}{4}} / (k\mu_0 j_{z0})^{\frac{1}{2}} \quad (8.161)$$

This expression shows that the resistive layer becomes thicker as the resistivity or the plasma density increases.

An explicit solution of Eq. (8.160) is

$$U(X) = -\frac{X}{2} \int_0^{\frac{\pi}{2}} \exp\left(-\frac{X^2}{2} \cos \theta\right) [\sin \theta]^{\frac{1}{2}} d\theta \quad (8.162)$$

where

$$\begin{aligned} X &\equiv -x/\delta_R \\ U &\equiv (\gamma\eta\rho_0)^{\frac{1}{4}}(k\mu_0 j_{z0})^{\frac{1}{2}}u_x/i\gamma\bar{B}_x \end{aligned} \quad (8.163)$$

Expressing Eq. (8.159) in terms of these transformed variables and evaluating the resulting integral numerically leads finally to an expression for the growth rate of resistive tearing modes

$$\gamma = 0.55 \left[(\Delta')^4 \eta^3 (k j_{z0})^2 / \rho_0 \mu_0^2 \right]^{\frac{1}{5}} = 0.55 \left[\frac{(\Delta' a)^4}{\tau_A^2 \tau_R^3} \right]^{\frac{1}{5}} \quad (8.164)$$

where the MHD region solution for Δ' given by Eq. (8.158) must be used to evaluate the discontinuity condition. The last form of Eq. (8.164) results from the identification of the resistive magnetic diffusion time

$$\tau_R \approx a^2 \mu_0 / \eta \quad (8.165)$$

and the characteristic growth time for shear Alfvén waves

$$\tau_A = \omega_A^{-1} \approx \left(\frac{B_{z0}}{k \mu_0 j_{z0} a} \right) \frac{1}{V_A} \approx \frac{(\rho_0 \mu_0)^{\frac{1}{2}}}{k \mu_0 j_{z0} a} \quad (8.166)$$

Thus, tearing modes grow much faster than the resistive magnetic diffusion time, but much slower than shear Alfvén waves and other MHD instabilities.

$\Delta' a > 0$ is the requirement for resistive tearing modes to be unstable. This quantity is plotted vs. ka in Fig. 8.15. Hence, resistive tearing modes of sufficiently long wavelength, k^{-1} , would be unstable in the slab model.

In order to extrapolate these results for a slab model to a tokamak, the latter is considered as a cylinder of length $2\pi R$ with periodic axial boundary conditions, so that $k = n/R$. The equivalent of the “resonant” surface in the slab at $x = 0$, where $\mathbf{k} \cdot \mathbf{B} = k B_{y0} = 0$ in a tokamak is the rational surface surface r where $\mathbf{k} \cdot \mathbf{B} = m B_\theta / r - n B_\phi / R$. These surfaces occur at values of r_{mn} for which $q(r_{mn}) = r B_\phi / R B_\theta(r_{mn}) = m/n$. Since Fig. 8.15 shows that the longest wavelength modes will be the most unstable, the $m = n = 1$ tearing mode is the most dangerous, but this mode can be present only if $q(0) < 1$. Other low- m modes can occur for $q(0) \geq 1$.

8.7.4 Magnetic Islands

A dramatic change in the magnetic field topology is produced by the tearing modes. The equilibrium field for the “plasma current sheet” equilibrium is shown in Fig. 8.14. There is also a strong B_z which is not shown.

The tearing mode instability produces an x -component of the magnetic field

$$B_x(y, t) = \bar{B}_x e^{\gamma t} \sin ky \quad (8.167)$$

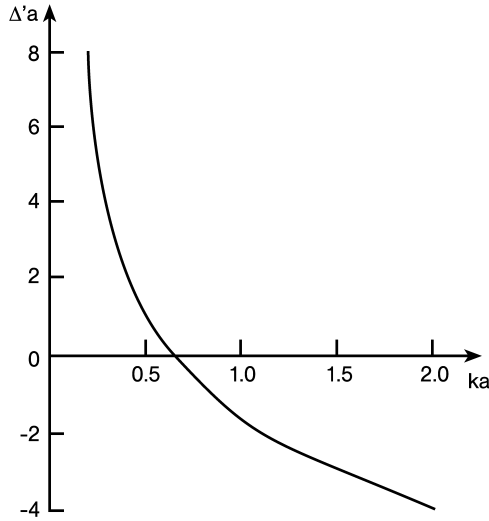


Figure 8.15. The discontinuity function $\Delta'a$ for resistive tearing modes (unstable for $\Delta'a > 0$)

and the y -component of the field can be approximated by the equilibrium value $B_y \approx \mu_0 j_{z0} x$. The field line equation

$$\frac{dx}{dy} = \frac{B_x}{B_y} = \frac{\bar{B}_x \sin ky}{\mu_0 j_{z0} x} \quad (8.168)$$

can be integrated within the resistive layer around $x = 0$ to obtain

$$\frac{1}{2} \mu_0 j_{z0} x^2 + \frac{\bar{B}_x}{k} e^{\gamma t} \cos ky = \text{const} \quad (8.169)$$

For small values of the constant, corresponding to small values of x , the second term is dominant, and Eq. (8.169) describes closed field lines in the $x-y$ plane. For large values of the constant, the first term on the left is dominant, and the field lines differ only slightly from the equilibrium values. This magnetic field topology is illustrated in Fig. 8.16. The closed field lines plotted from Eq. (8.169) are called “magnetic islands.”

The half-width, w , of the largest magnetic island is found by solving Eq. (8.169) for x at $ky = \pi$

$$w = 2 \left(\frac{\bar{B}_x}{k \mu_0 j_{z0}} \right)^{\frac{1}{2}} e^{\frac{1}{2} \gamma t} \quad (8.170)$$

This quantity increases in time until nonlinear effects limit further island growth when the value given by Eq. (8.170) becomes comparable with the width of the resistive layer given by Eq. (8.161).

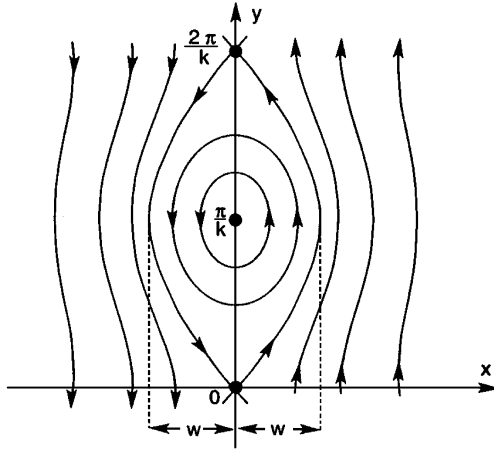


Figure 8.16. Magnetic islands produced by the resistive tearing instability

8.8 Kinetic Instabilities*

There are some instabilities that are sensitive to the shape of the velocity distribution and that cannot be described adequately by a fluid theory that represents only moments of the velocity distribution. Such distributions must be treated with kinetic theory.

8.8.1 Electrostatic Instabilities

Many such instabilities involve the growth of high-frequency plasma oscillations in which the electron motion creates a self-consistent oscillatory electric field either along or in the absence of a magnetic field. For frequencies above the ion plasma frequency, $\omega_{pi} = ne^2/\epsilon_0 m_i$, the ions are unable to respond to the oscillating electric field, and for oscillation frequencies above the collision frequency, scattering may be ignored. Such waves are usually analyzed using the Vlasov equation and Poisson's equation. In slab geometry these are

$$\frac{\partial f}{\partial t} + v \frac{\partial f}{\partial x} - \frac{e}{m} E \frac{\partial f}{\partial v} = 0 \quad (8.171)$$

and

$$\frac{\partial E}{\partial x} = \frac{\sigma}{\epsilon_0} \equiv \frac{1}{\epsilon_0} \left[\int f(v) dv - n_{i0} \right] \quad (8.172)$$

where σ is here used to represent the local charge density due to the electron motion.

We look for a plane wave solution propagating in the x -direction

$$E(x, t) = E \exp(-i\omega t + ikx) \quad (8.173)$$

Expanding

$$f(v, t) = f_0(v) + f_1(v, t) \quad (8.174)$$

about an equilibrium distribution normalized such that $\int f_0(v) dv = n_{e0} = n_{i0}$, Laplace transforming in time and Fourier transforming in space leads to

$$D(k, s)\tilde{E}(s) = \frac{ie}{k\epsilon_0} \int_{-\infty}^{\infty} \frac{f_1(v, t=0)}{s + ikv} dv \quad (8.175)$$

where the dispersion function is

$$D(k, s) \equiv 1 - \frac{ie^2}{mk\epsilon_0} \int_{-\infty}^{\infty} \frac{\partial f_0/\partial v}{s + ikv} dv \quad (8.176)$$

and \tilde{E} is the Laplace transform of the electric field. The integral in Eq. (8.176) must be evaluated as discussed in section 7.4

Using $s = -i\omega$, the dispersion function becomes

$$D(k, \omega) = 1 + \frac{e^2}{mk\epsilon_0} \left[\oint_{-\infty}^{\infty} \frac{\partial f_0/\partial v}{\omega - kv} dv - \frac{\pi i}{k} \frac{\partial f_0}{\partial v} \Big|_{v=\omega/k} \right] \quad (8.177)$$

where the integral is the Cauchy principal value integral.

Assuming that the equilibrium distribution is approximately Maxwellian everywhere except in a small region about $v = \omega/k$ to evaluate the integral, Eq. (8.177) becomes

$$D(k, \omega) = 1 - \frac{\omega p_c^2}{\omega^2} - \frac{\pi i e^2}{mk^2 \epsilon_0} \frac{\partial f_0}{\partial v} \Big|_{v=\omega/k} \quad (8.178)$$

which leads to the dispersion relation ($D(k, \omega) = 0$)

$$\omega = \omega_{pe} + \frac{\pi i \omega_{pe}^2}{2nk^2} \frac{\partial f_0}{\partial v} \Big|_{v=\omega/k} \quad (8.179)$$

The first term describes an electron plasma oscillation at the electron plasma frequency. The presence of the second, imaginary term introduces a real, positive growth rate for the wave if $\partial f_0/\partial v > 0$ in the region about $v = \omega/k$. Waves with phase velocity ω/k in a region of positive $\partial f_0/\partial v$ will extract energy from the “resonant” particles (i.e. those with $v = \omega/k$).

This instability is the inverse of the Landau damping of plasma waves that occurs when $\partial f_0/\partial v < 0$ in the region about $v = \omega/k$. Basically, when there are more slow particles than fast particles ($\partial f_0/\partial v < 0$) in a small region about $v = \omega/k$, the wave energy is extracted to accelerate the slower particles (Landau damping). However, where there are more fast particles than slow particles ($\partial f_0/\partial v > 0$) in a small region about $v = \omega/k$, the fast particle energy is extracted into the wave, leading to a growing wave amplitude (an instability).

8.8.2 Collisionless Drift Waves

Now we reconsider the electrostatic waves driven by a density gradient that were discussed in section 8.6, but now in the absence of dissipative collisions. We use a slab model and

postulate an equilibrium with an electron density gradient in the x -direction and no electric field. Instead of the Vlasov equation, the drift kinetic equation is used to describe the guiding center distribution function. With a straight uniform equilibrium field in the z -direction, the leading order drift is $\mathbf{v}_{E \times B} = \mathbf{E} \times \mathbf{B}/B^2 = E_y/B_z$, leading to the drift kinetic equation

$$\frac{\partial f_e}{\partial t} + \frac{E_y}{B_z} \frac{\partial f_e}{\partial x} + v_z \frac{\partial f_e}{\partial z} - \frac{e}{m_e} E_z \frac{\partial f_e}{\partial v_z} = 0 \quad (8.180)$$

Assuming $f_e(x, v, t) = f_{e0}(v) + f_{e1}(x, v, t)$, approximating $f_{e0}(v)$ as a Maxwellian, for which $\partial f_{e0}/\partial v = (f_{e0}/n_{e0})\partial n_{e0}/\partial x$ and $\partial f_{e0}/\partial v_z = (v_z/v_{\text{the}}^2)f_{e0}$, and using the traveling wave representation of Eq. (8.173) for all perturbed quantities reduces Eq. (8.180) to

$$-i(\omega - k_z v_z) f_{e1} + \frac{E_{y1}}{B_{z0}} \frac{f_{e0}}{n_{e0}} \frac{\partial n_{e0}}{\partial x} + \frac{e}{m_e} E_z \left(\frac{v_z}{v_{\text{th}, e}^2} \right) f_{e0} = 0 \quad (8.181)$$

which can be solved for

$$f_{e1} = \frac{e\phi f_{e0}}{T_{e0}} \left(1 - \frac{\omega - k_y v_{\text{de}}}{\omega - k_z v_z} \right) \quad (8.182)$$

when $E_{1y} = -ik_y\phi$ and $E_{1z} = -ik_z\phi$ have been used to represent the perturbed electrostatic field. Here, $v_{\text{de}} = -(T_{e0}/n_{e0}eB_{z0})\partial n_{e0}/\partial x$ is the electron diamagnetic drift for uniform T_{e0} .

The perturbed electron density is

$$n_{e1} \equiv \int f_{e1} d^3v = \frac{n_{e0}e\phi}{T_{e0}} - \frac{e\phi}{T_{e0}} (\omega - k_y v_{\text{de}}) \int \frac{f_{e0} d^3v}{\omega - k_z v_z} \quad (8.183)$$

We define a one-dimensional Maxwellian distribution function, as in the previous chapter,

$$F_{e0}(v_z) = n_{e0} \left(\frac{m_e}{2\pi T_0} \right)^{\frac{1}{2}} \exp \left(-\frac{mv_z^2}{2T_{e0}} \right) \quad (8.184)$$

in terms of which the integral in Eq. (8.183) can be written

$$\int \frac{f_{e0} d^3v}{\omega - k_z v_z} = \int_{-\infty}^{\infty} \frac{F_{e0}(v_z) dv_z}{\omega - k_z v_z} \simeq -i \left(\frac{\pi}{2} \right)^{\frac{1}{2}} \frac{n_{e0}}{|k_z| v_{\text{the}}} \quad (8.185)$$

which leads to an expression for the perturbed electron density

$$n_{e1} = \frac{n_{e0}e\phi}{T_{e0}} \left[1 + i \left(\frac{\pi}{2} \right)^{\frac{1}{2}} \frac{(\omega - k_y v_{\text{de}})}{|k_z| v_{\text{the}}} \right] \quad (8.186)$$

The ions are treated as a cold fluid with $\mathbf{E} \times \mathbf{B}$ and polarization drifts

$$\mathbf{u}_\perp = \frac{\mathbf{E} \times \mathbf{B}}{B^2} + \frac{m_i \dot{\mathbf{E}}_\perp}{eB^2} \quad (8.187)$$

an equation of motion along the field lines

$$m_i \frac{du_z}{dt} = eE_z \quad (8.188)$$

and a continuity equation

$$\frac{\partial n_i}{\partial t} + \nabla \cdot (n_i \mathbf{u}) = 0 \quad (8.189)$$

Making the usual expansion about the equilibrium solution, $n_i = n_{i0} + n_{i1}$, and assuming a plane wave form of the solution for the perturbed quantities, Eq. (8.187) to Eq. (8.189) yield

$$\begin{aligned} n_{i1} &= -\frac{k_y \phi}{\omega B_{z0}} \frac{dn_{i0}}{dx} + \frac{n_{i0} e k_z^2 \phi}{m_i \omega^2} - \frac{n_{i0} (k_x^2 + k_y^2) m_i \phi}{e B_{z0}^2} \\ &= \frac{n_{i0} e \phi}{T_{e0}} \left(\frac{k_y v_{de}}{\omega} + \frac{k_z^2 c_{se}^2}{\omega^2} - (k_x^2 + k_y^2) r_L^2 \right) \end{aligned} \quad (8.190)$$

where we use the slightly different definitions $c_{se} = (T_{e0}/m_i)^{\frac{1}{2}}$ and $r_L = (m_i T_{e0})^{\frac{1}{2}}/e B_{z0}$.

Using the above results in the charge neutrality requirement, $n_{e1} = n_{i1}$, leads to the dispersion relation for collisionless drift waves

$$\omega [1 + (k_x^2 + k_y^2) r_L^2] - k_y v_{de} - \frac{k_z^2 c_{se}^2}{\omega} = -i \left(\frac{\pi}{2} \right) \frac{\omega(\omega - k_y v_{de})}{|k_z| v_{the}} \quad (8.191)$$

Letting $\omega = \omega_r + i\gamma$ in Eq. (8.191) leads to the expression for the growth rate of collisionless drift waves

$$\gamma = \left(\frac{\pi}{2} \right)^{\frac{1}{2}} \frac{k_y^2 v_{de}^2}{|k_z| v_{the}} \left[(k_x^2 + k_y^2) r_L^2 - \frac{k_y^2 c_{se}^2}{k_y^2 v_{de}^2} \right] \quad (8.192)$$

showing that these waves are unstable ($\gamma > 0$) only if $(k_x^2 + k_y^2) r_L^2 > (k_z c_{se})^2 / (k_y v_{de})^2$. The $(k_x^2 + k_y^2) r_L^2$ term, which must be nonzero in order for an instability to exist, arises from the polarization drift.

8.8.3 Electron Temperature Gradient Instabilities

The results of the previous section can be extended to the case in which gradients in both the electron density and electron temperature exist. In slab geometry, the gradient of the equilibrium Maxwellian distribution is

$$\frac{\partial f_{e0}}{\partial x} = \frac{f_{e0}}{n_{e0}} \frac{dn_{e0}}{dx} \left[1 - \frac{\left(\frac{1}{T_{e0}} \frac{dT_{e0}}{dx} \right)}{\left(\frac{1}{n_{e0}} \frac{dn_{e0}}{dx} \right)} \left(\frac{3}{2} - \frac{v^2}{2v_{the}^2} \right) \right] \quad (8.193)$$

Proceeding as in the previous section and limiting consideration to waves with $\omega \ll k_z v_{de}$, we now obtain for the perturbed electron distribution function

$$n_{e1} \simeq \frac{n_{e0} e \phi}{T_{e0}} \left[1 + i \left(\frac{\pi}{2} \right)^{\frac{1}{2}} \left(\frac{\omega - k_y v_{de}(1 - \eta_e/2)}{k_z v_{the}} \right) \right] \quad (8.194)$$

instead of Eq. (8.186). Comparing the two expressions, we see that the effect of the electron temperature gradient is represented by the term

$$\eta_e \equiv \left(\frac{1}{T_{e0}} \frac{d T_{e0}}{dx} \right) \Bigg/ \left(\frac{1}{n_{e0}} \frac{d n_{e0}}{dx} \right) \quad (8.195)$$

in Eq. (8.194).

The treatment of ion density perturbation in the cold fluid approximation, leading to Eq. (8.190), remains unchanged.

Using Eq. (8.194) in the charge neutrality requirement now leads to the dispersion relation

$$\omega [1 + (k_x^2 + k_y^2)r_L^2] - k_y v_{de} - \frac{k_z^2 c_{se}^2}{\omega} = -i \left(\frac{\pi}{2} \right)^{\frac{1}{2}} \frac{\omega [\omega - k_y v_{de}(1 - \eta_e/2)]}{|k_z| v_{the}} \quad (8.196)$$

The η_e term fundamentally changes the stability characteristics. For example, the imaginary part of the frequency no longer vanishes in the limit $(k_x^2 + k_y^2)^{\frac{1}{2}} r_L \ll 1$ and $k_z c_{se} \ll k_y v_{de}$, but instead becomes

$$\gamma \simeq - \left(\frac{\pi}{2} \right)^{\frac{1}{2}} \frac{k_y^2 v_{de}^2}{|k_z| v_{the}} \eta_e \quad (8.197)$$

When the electron density and temperature gradients are in the same direction, $\eta_e > 0$, the effect of the temperature gradient is to damp the electron drift wave. However, if the equilibrium density and temperature gradients are oppositely directed, the presence of the temperature gradient causes a growing instability.

8.8.4 Ion Temperature Gradient Instabilities

Up to this point, we have examined electron drift wave instabilities that were driven by the transfer of energy from “resonant” electrons to the wave in an inverse Landau damping process. We now examine ion drift waves driven by a similar process involving resonant ions. Since the frequency of ion oscillations will be considerably less than the oscillation frequencies of the electron waves considered previously, we assume that electrons relax completely to a Boltzmann distribution along the field lines, $n_e \approx n_{e0} \exp(e\phi/T_{e0})$, in which case the imaginary term in Eq. (8.186) and Eq. (8.194) is of order m_e/m_i and can be neglected, leading to

$$n_{e1} \simeq \frac{n_{e0} e \phi}{T_{e0}} \quad (8.198)$$

The ions must now be analyzed using a drift kinetic approximation similar to that used for the electrons (i.e. Eq. (8.180))

$$\frac{\partial f_i}{\partial t} + \frac{E_y}{B_z} \frac{\partial f_i}{\partial x} + v_z \frac{\partial f_i}{\partial z} + \frac{e}{m_i} E_z \frac{\partial f_i}{\partial v_z} = 0 \quad (8.199)$$

Following the same procedure used for treating electrons in the previous two sections, this equation may be solved for the perturbed ion density. Allowing both ion density and temperature gradients, this leads to

$$n_{i1} = -\frac{n_{i0} e \phi}{T_{i0}} + \frac{e \phi}{T_{i0}} \int_{-\infty}^{\infty} \frac{F_{i0}(v_z) dv_z}{\omega - k_z v_z} \left\{ \omega - k_y v_{di} \left[1 - \eta_i \left(\frac{1}{2} - \frac{v_z^2}{2v_{thi}^2} \right) \right] \right\} \quad (8.200)$$

where F_{i0} is the one-dimensional ion Maxwellian distribution function defined by Eq. (8.184) but with $e \rightarrow i$, $v_{di} = (T_{i0}/n_{i0} e B_{z0}) \partial T_{i0} / \partial x$ is the ion diamagnetic drift velocity, and

$$\eta_i \equiv \left(\frac{1}{T_{i0}} \frac{dT_{i0}}{dx} \right) \Big/ \left(\frac{1}{n_{i0}} \frac{dn_{i0}}{dx} \right) \equiv \frac{L_{n_{i0}}}{L_{T_{i0}}} \quad (8.201)$$

Again, the dispersion relation follows from the charge neutrality requirement $n_{i1} = n_{e1}$

$$1 + \frac{T_{i0}}{T_{e0}} = \frac{1}{n_{i0}} \int_{-\infty}^{\infty} \frac{F_{i0}(v_z) dv_z}{\omega - k_z v_z} \left\{ \omega - k_y v_{di} \left[1 - \frac{\eta_i}{2} \left(1 - \frac{v_z^2}{v_{thi}^2} \right) \right] \right\} \quad (8.202)$$

Evaluation of this dispersion relation is quite involved. However, the final result indicates that the condition for an unstable wave being driven by energy extracted from resonant ions in an inverse Landau damping process is

$$\eta_i > 2 + \left(\frac{4k_z^2 v_{thi}^2}{\eta_i k_y^2 v_{di}^2} \right) \frac{T_{i0}}{T_{e0}} \left(1 + \frac{T_{i0}}{T_{e0}} \right) \quad (8.203)$$

Since there is the possibility of the existence of ion drift waves with a wide range of values of $(k_z/k_y)^2$, in general, unstable ion drift waves are possible if $\eta_i > 2$; i.e. if the ion density gradient scale length is greater than twice the ion temperature gradient scale length. Note that this result is for a slab model. In toroidal geometry, the condition for instability of ion temperature gradient (ITG) modes is $L_{T_{i0}} < L_{T_{i\text{crit}}} \simeq 0.1 R$, where R is the major radius and $L_{T_{i0}}^{-1} = (dT_{i0}/dr)/T_{i0}$.

8.8.5 Loss-Cone and Drift-Cone Instabilities

The ion velocity distribution in a mirror plasma is characterized by the absence of ions in the loss cone, a condition which can be written

$$f(\mathbf{v}) = 0 \quad |v_{\parallel}| > \alpha |v_{\perp}| \quad (8.204)$$

where α is a constant that depends on the field configuration. The electron distribution function is approximately isotropic, because $v_{ei} \simeq \sqrt{m_i/m_e} v_{ii}$, so the instabilities will

have $\omega < \Omega_e$. We concluded in the introduction to this chapter that such instabilities would have $\omega > \Omega_i$. Thus the instabilities we expect to be driven by the relaxation of an anisotropic ion distribution function in a mirror-confined plasma will have characteristic frequencies in the range $\Omega_e > \omega > \Omega_i$.

The distribution function, $f(\mathbf{v})$, can be reduced to a one-dimensional function, $F(u)$, of the velocity component parallel to the wave propagation vector ($u = k \cdot \mathbf{v}/|k|$) by integrating over velocity. Making the assumption that the velocity distribution is isotropic in the plane perpendicular to the field, this integration is

$$F(u) \equiv \int_{-\infty}^{\infty} dv_{\parallel} \int_u^{\infty} v_{\perp} dv_{\perp} \int_0^{2\pi} f(v_{\perp}^2, v_{\parallel}) \delta(v_{\perp} \sin \phi - u) d\phi \quad (8.205)$$

where ϕ is the angle between the propagation and magnetic field directions ($\cos \phi = (u/v_{\parallel})^{-1}$) and δ is the Dirac-delta function. Equation (8.205) can be written

$$\begin{aligned} F(u) &= \int_u^{\infty} \frac{v_{\perp} dv_{\perp}}{(v_{\perp}^2 - u^2)^{\frac{1}{2}}} \int_{-\alpha v_{\perp}}^{\alpha v_{\perp}} f(v_{\perp}^2, v_{\parallel}) dv_{\parallel} \\ &\equiv \int_u^{\infty} \frac{v_{\perp} H(v_{\perp}) dv_{\perp}}{(v_{\perp}^2 - u^2)^{\frac{1}{2}}} \end{aligned} \quad (8.206)$$

The function $H(v_{\perp})$ is just the number of ions with a given v_{\perp} (note that the integral is over the region of v_{\parallel} , space outside the loss cone). The functional dependence of $H(v_{\perp})$ and $\partial H/\partial v_{\perp}$ on v_{\perp} are illustrated qualitatively in Fig. 8.17.

Equation (8.206) can be integrated by parts, and $H(v_{\perp}) \rightarrow 0$ as $v_{\perp} \rightarrow \infty$ can be used, to obtain

$$F(u) = - \int_u^{\infty} (v_{\perp}^2 - u^2)^{\frac{1}{2}} \left(\frac{\partial H}{\partial v_{\perp}} \right) dv_{\perp} \quad (8.207)$$

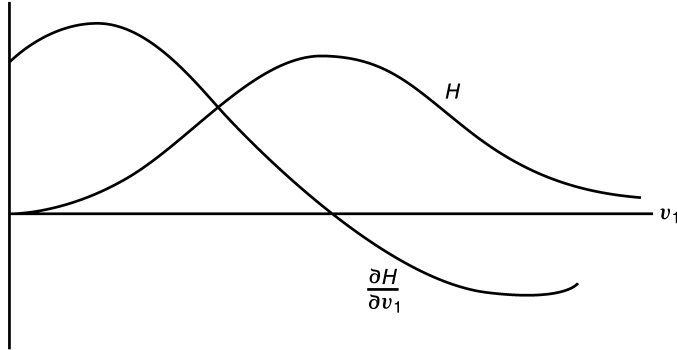


Figure 8.17. Functional dependence of H on v_{\perp}

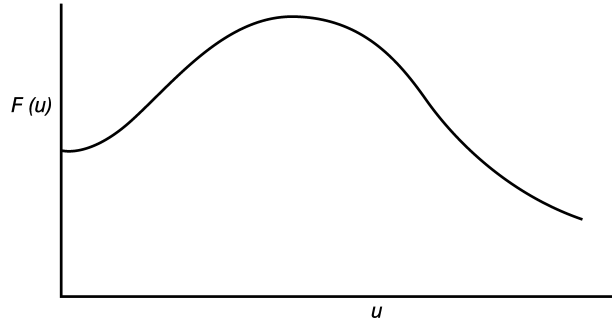


Figure 8.18. Functional dependence of F on u

which can be differentiated to obtain,

$$\frac{\partial F}{\partial u} = u \int_u^\infty \frac{(\partial H/\partial v_\perp)}{(v_\perp^2 - u^2)^{\frac{1}{2}}} dv_\perp \quad (8.208)$$

The general shape of $F(u)$, shown in Fig. 8.18, is such that $\partial F/\partial u > 0$ at small u and $\partial F/\partial u < 0$ at large u .

We will investigate electrostatic modes in a plasma that has a density gradient perpendicular to the field direction, which is representative of the situation in mirror-confined plasmas. The perturbation can be represented by an electrostatic potential

$$\Phi(y, z, t) = \hat{\Phi} e^{-i(\omega t - k_{\parallel} z - k_y y)} \quad (8.209)$$

This potential gives rise to a number of drifts. There is a polarization drift,

$$v_{py} = \frac{m}{eB^2} \dot{E} = -\frac{m}{eB^2} (ik_y)(-i\omega) \Phi = \frac{\omega k_y}{\Omega B} \Phi \quad (8.210)$$

Because $\Omega_e > \omega > \Omega_i$, the ions cannot respond, and only the electrons are affected by the polarization drift. There is an $\mathbf{E} \times \mathbf{B}$ drift,

$$v_{Ex} = -\frac{ik_y}{B} \Phi \quad (8.211)$$

and parallel motion in response to the electrostatic field,

$$v_z = v_{\parallel} = -\frac{e}{m} \int_0^t \nabla \Phi dt' = -\frac{ek_{\parallel}\Phi}{\omega m} \quad (8.212)$$

The electron continuity equation can be linearized, and an $e^{-i\omega t}$ time dependence can be specified for the perturbed density to obtain,

$$n_{e1} = -n_{e0} \left(\frac{\partial v_y}{\partial y} + \frac{\partial v_z}{\partial z} \right) - \frac{\partial n_{e0}}{\partial x} v_x \quad (8.213)$$

Using Eq. (8.210) to Eq. (8.212) for the velocity components leads to

$$n_{e1} = \left[n_{e0} \left(\frac{ek_y^2}{m_e \Omega_e^2} - \frac{ek_{\parallel}^2}{m_e \omega^2} \right) - \frac{\partial n_{e0}}{\partial x} \frac{k_y}{\omega B} \right] \Phi \quad (8.214)$$

The Vlasov equation for the one-dimensional ion distribution function is

$$\frac{\partial F(u)}{\partial t} + \mathbf{u} \cdot \nabla F(u) = \frac{e}{m_i} \nabla \Phi \cdot \nabla_u F(u) \quad (8.215)$$

This equation can be integrated, using the method of Green's functions, to obtain

$$F(u) = \frac{e}{m_i} \frac{\left(\frac{\partial F}{\partial u} \right) \Phi}{\left(u - \frac{\omega}{k_y} - \frac{i\gamma}{k_y} \right)} \quad (8.216)$$

where γ is the real part of the frequency, ω .

The perturbed ion density is

$$n_{i1} = n_{i0} \int F(u) du = \frac{n_{i0} e}{m_i} \int \frac{\left(\frac{\partial F}{\partial u} \right) \Phi}{u - \frac{\omega}{k_y} - \frac{i\gamma}{k_y}} du \quad (8.217)$$

Poisson's equation is the consistency relation among the perturbed ion and electron densities and the perturbed electrostatic potential:

$$\nabla^2 \Phi = -k^2 \Phi = -(k_{\parallel}^2 + k_y^2) \Phi = \frac{e(n_{e1} - n_{i1})}{\epsilon_0} \quad (8.218)$$

Assuming quasineutrality ($n_{i0} \simeq n_{e0}$) and using Eqs. (8.214) and (8.217) in Eq. (8.218) leads to the dispersion relation

$$0 = \left(1 + \frac{k_y^2 \omega_{pe}^2}{k^2 \Omega_e^2} - \frac{k_{\parallel}^2 \omega_{pe}^2}{k^2 \omega^2} \right) + \left(\frac{\omega_{pe}^2}{\omega \Omega_e} \frac{k_y L_n^{-1}}{k^2} \right) - \left[\frac{\omega_{pi}^2}{k^2} \int \frac{(\partial F / \partial u) du}{u - \frac{\omega}{k_y} - \frac{i\gamma}{k_y}} \right] \quad (8.219)$$

where ω_{pe} is the electron plasma frequency and L_n is the characteristic length of the unperturbed density gradient.

When the plasma density is uniform $L_n^{-1} \rightarrow 0$ and $k_{\parallel} \neq 0$, Eq. (8.219) reduces to the dispersion relation for the loss-cone instability. When the plasma density is nonuniform $L_n^{-1} \neq 0$ and propagation is perpendicular to the field ($k_{\parallel} = 0$), Eq. (8.219) reduces to the dispersion relation for the drift-cone instability.

8.9 Sawtooth Oscillations*

Relaxation oscillations, known as “sawtooth oscillations” because of their effect on several measurements, are frequently found throughout tokamak plasmas. Oscillations in the center of the plasma are out of phase with oscillations in the outer region. The temperature in the center of the plasma increases with heating during the ramp-up, followed by a sharp collapse in the central temperature and a simultaneous sharp increase in the outer temperature, in a repetitive cycle. The collapse phase is typically about 100 μs , which is much less than the conventional resistive time constant of about 10 ms, in present tokamaks.

The collapse is caused by an instability with an $m = 1, n = 1$ structure associated with the $q = 1$ surface. Sawtooth oscillations typically begin when the $q = 1$ surface first appears. The current density near the axis increases and $q(0)$ decreases during the ramp-up phase, and conversely during the collapse, typically by a few percent.

Many features of the sawtooth oscillations can be explained by a fast magnetic reconnection model. The magnetic field lines on the $q = 1$ surface define a helical sheet which has $d\theta/d\phi = 1$, as shown in Fig. 8.19. Magnetic field lines with $q = 1$ lie in this sheet, and $q \neq 1$ field lines intersect the sheet.

The unit vectors normal to the sheet are

$$\begin{aligned} n_\theta &= \frac{1}{\sqrt{1 + r^2/R^2}} \\ n_\phi &= -\frac{r/R}{\sqrt{1 + r^2/R^2}} \end{aligned} \quad (8.220)$$

which enables the helical magnetic field to be expressed

$$\begin{aligned} B^* &= B_\theta - (r/R)B_\phi \\ &= B_\theta(1 - q) \end{aligned} \quad (8.221)$$

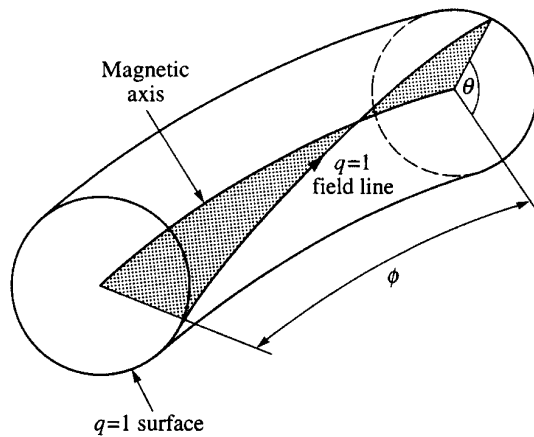


Figure 8.19. The helical sheet that contains the magnetic axis and the $q = 1$ flux surface

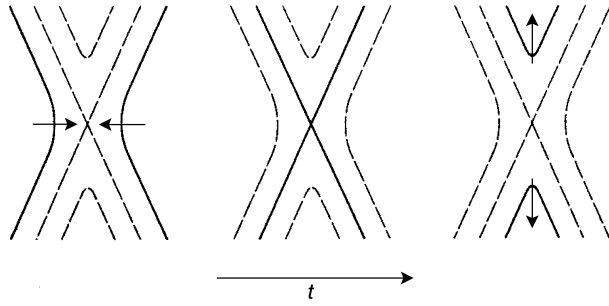


Figure 8.20. The flux surfaces (solid lines) break and join to form a reconnected surface

and the helical flux is $d\psi/dr = B^*$. This helical field changes sign at the $q = 1$ surface and the helical flux between the axis and the $q = 1$ flux surface reconnects with an equal and opposite flux outside the $q = 1$ surface, as indicated in Fig. 8.20.

The flux is progressively reconnected, the structure passing through a sequence of configurations as illustrated in Fig. 8.21. The reconnected flux forms an island which grows and eventually replaces the nested flux surfaces.

The reconnection takes place in a narrow layer of thickness δ , as shown in Fig. 8.22. There is a current sheet in this layer that is driven by the motional electric field $v_1 B^*$, where v_1 is the velocity of the plasma flow. This causes a current

$$j \simeq v_1 B^*/\eta \quad (8.222)$$

Using Ampère's law

$$j \simeq B^*/\mu_0 \delta \quad (8.223)$$

then leads to

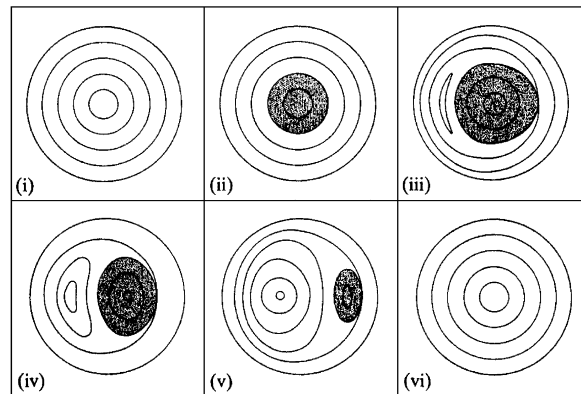


Figure 8.21. Evolution of magnetic field topology during a sawtooth oscillation

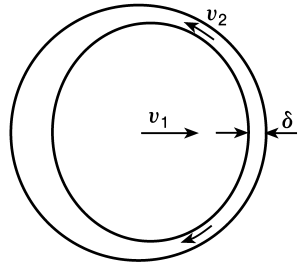


Figure 8.22. Reconnection geometry. (Central core plasma moves into reconnection layer with velocity v_1 and leaves with velocity v_2)

$$v_1 = \frac{\eta}{\mu_0 \delta} \quad (8.224)$$

The displaced core transmits a pressure $\approx B^{*2}/2\mu_0$, which causes a flow along and out of the layer with velocity v_2 , given by momentum balance

$$\rho v_2^2 \simeq B^{*2}/2\mu_0 \quad (8.225)$$

Letting the flow into the layer take place over a length $\approx r_1$, continuity requires

$$v_1 r_1 \sim v_2 \delta \quad (8.226)$$

Eliminating the two velocities using Eq. (8.224) and Eq. (8.225) yields

$$\delta^2 \sim \frac{\eta}{\mu_0} \frac{\sqrt{\mu_0 \rho}}{B^*} r_1 \quad (8.227)$$

Defining the resistive and Alfvén times

$$\begin{aligned} \tau_R &\equiv \frac{\mu_0}{\eta} r_1^2 \\ \tau_A &\equiv \frac{r_1}{B^*/\sqrt{\mu_0 \rho}} \end{aligned} \quad (8.228)$$

this may be rewritten

$$\delta \sim \left(\frac{\tau_A}{\tau_R} \right)^{\frac{1}{2}} r_1 \quad (8.229)$$

The characteristic time for the collapse is the time for the core to move across r_1

$$\tau_K \sim \frac{r_1}{v_1} \quad (8.230)$$

Then the velocity v_2 can be obtained using Eqs. (8.224) and (8.229)

$$\tau_K \sim (\tau_R \tau_A)^{\frac{1}{2}} \quad (8.231)$$

Since $\tau_A \ll \tau_R$, the resistive time, this model predicts that the collapse times are comparable to the observed values.

Problems for Chapter 8

1. Derive the energy principle of Eq. (8.67).
2. Derive the form of the energy principle for kink modes given by Eq. (8.72).
3. Discuss the kink mode stability of a tokamak plasma with $T = 5 \text{ keV}$, $n_D = n_e = 5 \times 10^{19} \text{ m}^{-3}$, major radius $R = 1.7 \text{ m}$, minor radius $a = 0.6 \text{ m}$, central safety factor $q_0 = 1$ and toroidal magnetic field $B = 5 \text{ T}$ that has a toroidal current of 3 MA distributed as $j(r) = j_0(1 - (r/a)^2)^\nu$ for $0 \leq \nu \leq 3$.
4. Evaluate the Mercier criterion for stability against interchange modes in the tokamak of problem 3 for a $\nu = 1$ current distribution. (Hint: Evaluate the radial pressure gradient from the equilibrium condition.)
5. Evaluate the ballooning mode stability of the tokamak of problem 3 for a $\nu = 1$ current distribution.
6. Calculate the growth rate of drift wave instabilities in the tokamak of problem 3 as a function of the square of the wave propagation vector $k^2 = k_x^2 = k_y^2 = k_z^2$.
7. A tokamak plasma with major radius $R = 3 \text{ m}$ and minor radius $a = 0.8 \text{ m}$ has a toroidal plasma current of 2 MA. What value of toroidal magnetic field is needed for MHD stability?
8. Discuss the kink-mode stability of the circular plasma with $R_0 = 3.5 \text{ m}$, $a = 1.0 \text{ m}$, $B_{\phi 0} = 4 \text{ T}$ at R_0 , $T = 10 \text{ keV}$ and $I = 1.5 \text{ MA}$.
9. Discuss how surface and internal MHD kink-mode instabilities limit the allowable values of the safety factor in a tokamak.

9 Neoclassical Transport

Collisions produce net fluxes of particles, momentum and energy along and across field lines in a magnetized plasma. Those transport fluxes that exist in uniform and straight magnetic field configurations and that arise solely from collisions are referred to as “classical.”

Additional parallel currents must flow to balance the particle drifts perpendicular to the field lines that exist in toroidal plasmas. In a collisional plasma the balance is not complete, and the resulting charge separation produces an electric field which in turn interacts with the magnetic field to create further particle drifts perpendicular to the magnetic field. Inclusion of these geometrical effects modifies the collisional transport fluxes, and the modified fluxes are referred to as “Pfirsch–Schlüter,” or sometimes as “neoclassical.”

At higher temperatures, the plasma becomes “collisionless” in the sense that a particle can travel many times around the torus before colliding. Particles with velocity nearly perpendicular to the magnetic field are then trapped on the outside of the torus because they are reflected by the higher magnetic field on the inside of the torus. These particles trace out banana orbits, as discussed in chapter 3, with large radial excursions from the flux surface. Because of the large radial displacements that arise when collisions do occur, these particles dominate in the determination of radial transport. This transport is referred to as “neoclassical,” or sometimes as “banana-plateau.”

9.1 Collisional Transport Mechanisms

Before undertaking a formal development, we present some physical arguments for the types of forces and transport fluxes that might be expected in a simple configuration of a homogeneous plasma in a straight and uniform magnetic field in the z -direction.

9.1.1 Particle Fluxes

9.1.1.1 Motion Along Field Lines

In the absence of a magnetic field, or for particle motion along the field line, the particles will free stream at their thermal speed, v_{th} , until they have a collision after traversing an average distance equal to the collision mean free path, $\lambda = v_{th}\tau_{90}$, where τ_{90} is the mean time between collisions that can reverse a particle’s direction along the field line (e.g. mean time for 90° deflection). We will suppress the “90” in the following development.

With respect to Fig. 9.1, the partial particle flux to the right at $z_0(\Gamma_+)$ can be written as the product of the particle 90° deflection collision rate per unit distance, n/τ , and the probability 1/2 that the particle emerges to the right, integrated over the mean distance to the left of z_0 that the particle would travel to the right without a collision. A similar

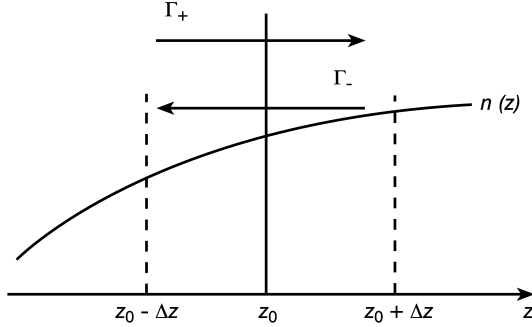


Figure 9.1. Particle fluxes along field lines

expression describes the partial flux to the left at z_0 (Γ_-). We henceforth suppress the zero subscript and write

$$\Gamma_+(z) = \frac{1}{2} \int_{z-\lambda}^z \frac{n(z')}{\tau(z')} dz', \quad \Gamma_-(z) = \frac{1}{2} \int_z^{z+\lambda} \frac{n(z')}{\tau(z')} dz' \quad (9.1)$$

A density gradient along z will cause an imbalance in the partial fluxes to the right and left at z . Since $\tau \sim T^{\frac{3}{2}}$, a temperature gradient will also cause an imbalance in the partial fluxes. Making a Taylor's series expansion of the integrands about z , Eqs. (9.1) can be integrated to obtain an expression for the net flux in the positive direction along the field lines

$$\Gamma_{||} \equiv \Gamma_+ - \Gamma_- \simeq -\frac{1}{2} \frac{\lambda^2}{\tau} \left(\frac{\partial n}{\partial z} - \frac{3}{2} \frac{n}{T} \frac{\partial T}{\partial z} \right) \quad (9.2)$$

This particle flux has a diffusive form with parallel diffusion coefficient $D_{||} = \lambda^2/2\tau$. The second term on the right represents “thermal diffusion.” In the absence of a density or temperature gradient, the partial fluxes are of the same magnitude and the net flux vanishes.

9.1.1.2 Motion Across Field Lines

Motion in the plane perpendicular to the field lines is dominated by the gyromotion about the field lines imposed by the $\mathbf{v} \times \mathbf{B}$ force. With each collision, the guiding center of the gyromotion is displaced slightly. The cumulative displacement due to many small displacements over time $\tau (= \tau_{90})$ is about r_L , the gyroradius. This may be visualized by considering the displacement of the origin of the gyroradius vector when the direction is rotated 90° about the tip.

The partial fluxes can be formulated as in Eqs. (9.1), except now the maximum displacement of the guiding center in the $x-y$ plane perpendicular to the field is r_L ; i.e. r_L replaces λ in the limits on the integrals. The corresponding net particle flux in the x -direction produced by a gradient in the x -direction is

$$\Gamma_{\perp x} = -\frac{1}{2} \frac{r_L^2}{\tau} \left(\frac{\partial n}{\partial x} - \frac{3}{2} \frac{n}{T} \frac{\partial T}{\partial x} \right) \quad (9.3)$$

and $\Gamma_{\perp y}$ is given by a similar expression involving gradients in the y -direction. Again, this is a diffusive expression, with the cross-field diffusion coefficient $D_{\perp} = r_L^2/2\tau = (r_L/\lambda)^2 D_{\parallel} \ll D_{\parallel}$.

9.1.2 Heat Fluxes

9.1.2.1 Motion Along Field Lines

The net heat flux along the field lines can be constructed by a similar procedure as that used to construct the particle flux along field lines, but now including $3T(z)/2$ under the integrals in Eqs. (9.1) to define partial heat fluxes, leading to

$$Q_{\parallel} = \frac{3}{2} T \Gamma_{\parallel} - \frac{\lambda^2}{2\tau} \frac{3}{2} n \frac{\partial T}{\partial z} \quad (9.4)$$

We identify the last term with thermal conduction, since the first term is obviously convection. Thus,

$$q = -\frac{3}{2} n \frac{\lambda^2}{2\tau} \frac{\partial T}{\partial z} \equiv -\kappa_{\parallel} \frac{\partial T}{\partial z} \quad (9.5)$$

where the parallel heat conductivity $\kappa_{\parallel} = (3/2)n\lambda^2/2\tau \sim nD_{\parallel}$. Since $v_{\text{th}}^2 \sim T$ and $\tau \sim T^{3/2}$, $\kappa_{\parallel} \sim T^{5/2}$ is strongly temperature dependent.

9.1.2.2 Motion Across Field Lines

The same argument used above to justify the replacement of λ by r_L in the limits on the partial particle flux integrals because of the gyromotion constraint when calculating the particle flux across field lines can be used to convert the previous expression for heat flux along field lines to heat flux in the plane perpendicular to the field lines. Thus, the x -directed gradients produce x -directed convective and conductive heat fluxes

$$Q_{\perp} = \frac{3}{2} T \Gamma_{\perp x} - \kappa_{\perp} \frac{\partial T}{\partial x} \equiv \frac{3}{2} T \Gamma_{\perp x} + q_{\perp x} \quad (9.6)$$

where the cross-field heat conductivity $\kappa_{\perp} = (3/2)n r_L^2 / 2\tau = (r_L/\lambda)^2 \kappa_{\parallel} \ll \kappa_{\parallel}$. A similar expression obtains in the y -direction.

9.1.2.3 Gyromotion

A temperature gradient in the x -direction will drive a heat flux in the other (y)-direction in the plane perpendicular to the field lines because of the gyromotion, as indicated in Fig. 9.2. The heat flux in the $x-y$ plane due to gyrating particles is $Q_{\Omega} = (3/2)n T \Omega r_L \sim n T v_{\text{th}} \sim T^{3/2}$. If T is uniform, the downward (y -directed) heat flux carried by particles with guiding centers to the left just balances the upward heat flux carried by particles

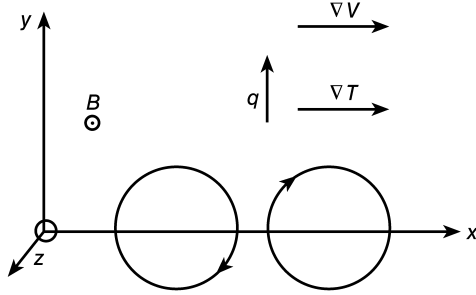


Figure 9.2. Fluxes due to gyromotion

with guiding centers to the right. However, if there is a temperature gradient in the x -direction (left to right), as shown, then the upward heat flux exceeds the downward heat flux, producing a net upward heat flux associated with the gyromotion

$$Q_{\Omega y} = \frac{\partial Q_{\Omega}}{\partial x} r_L = \frac{3}{2} n \frac{r_L \lambda}{\tau} \frac{\partial T}{\partial x} = \kappa_{\Omega} \frac{\partial T}{\partial x} \quad (9.7)$$

where the gyroconductivity $\kappa_{\Omega} \approx (\lambda/r_L)\kappa_{\perp} \gg \kappa_{\perp}$, but $\kappa_{\Omega} \approx (r_L/\lambda)\kappa_{\parallel} \ll \kappa_{\perp\parallel}$.

9.1.3 Momentum Fluxes

9.1.3.1 Motion Along Field Lines

The partial momentum fluxes in the z -direction can be derived following the same type of development as for the partial particle fluxes along field lines

$$M_{+zz} = \frac{1}{2} \int_{z-\lambda}^z dz' \frac{n(z')}{\tau(z')} m v_z(z'), \quad M_{-zz} = \frac{1}{2} \int_z^{z+\lambda} dz' \frac{n(z')}{\tau(z')} m v_z(z') \quad (9.8)$$

Making a Taylor's series expansion of the integrands about z , the net z -directed flux of z -momentum along the field lines may be written

$$\pi_{zz} = M_{+zz} - M_{-zz} = m v_z \Gamma_{\parallel} - \eta_{\parallel} \frac{\partial v_z}{\partial z} \quad (9.9)$$

The first term on the right represents momentum convection, and the second term represents momentum diffusion with parallel viscosity coefficient $\eta_{\parallel} = nm\lambda^2/2\tau = nmD_{\parallel}$.

9.1.3.2 Motion Across Field Lines

Now suppose that the velocity along the field lines, $v_z(x)$, varies in the x -direction perpendicular to the field lines. Using the same arguments that were made in computing partial particle fluxes across the field lines, the $(+x)$ -directed partial flux of z -momentum to the right arises from the displacement to the right of the guiding centers of half of the particles that have collided in the interval $(x - r_L, x)$ in time τ , and the $(-x)$ -directed partial flux

of z -momentum to the left arises from the displacement to the left of the guiding centers of half the particles that have collided in the interval $(x, x + r_L)$ in time τ

$$M_{+zx} = \int_{x-r_L}^x dx' \frac{n}{\tau} m v_z(x'), \quad M_{-zx} = \int_x^{x+r_L} dx' \frac{n}{\tau} m v_z(x') \quad (9.10)$$

If n , T and v_z are uniform in x , these two partial fluxes are equal in magnitude and the net x -directed flux of z -momentum vanishes. Any x -dependence of n or T will result in a convective flux of z -momentum in the x -direction. Any x -dependence of v_z will result in a net diffusive flux of z -momentum in the x -direction that is found by making a Taylor's series expansion of $v_z(x')$ about x in Eqs. (9.10) to obtain

$$\pi_{zx} = M_{+zx} - M_{-zx} = -\eta_{\perp} \frac{\partial v_z}{\partial x} \quad (9.11)$$

where the perpendicular viscosity coefficient $\eta_{\perp} = nmr_L^2/2\tau = (r_L/\lambda)^2 \eta_{\parallel} \ll \eta_{\parallel}$.

Now consider the case in which one perpendicular velocity component, v_y , depends on the other perpendicular direction, x . The x -directed partial fluxes of y -momentum can be constructed in the same way as the x -directed partial fluxes of z -momentum given by Eqs. (9.10), but with v_z replaced by v_y . Arguments similar to those used to arrive at Eq. (9.11) then lead to an expression for the net x -directed diffusive flux of y -momentum

$$\pi_{yx} = M_{+yx} - M_{-yx} = -\eta_{\perp} \frac{\partial v_y}{\partial x} \quad (9.12)$$

Finally, consider the case in which one of the perpendicular velocities, v_x , depends on the direction along the magnetic field lines, z . Because gyromotion in the $x-y$ plane will convert x -momentum into y -momentum, the ordered x -momentum will be destroyed in the time required to complete a small fraction (i.e. $< 1/4$ of a gyro-orbit, only those particles in the intervals $(z-r_L, z)$ and $(z, z+r_L)$ will be able to contribute to the z -directed partial fluxes of x -momentum at z , so that these partial fluxes are

$$M_{+xz} \simeq \int_{z-r_L}^z dz' \frac{n}{\tau} m v_x(z'), \quad M_{-xz} \simeq \int_z^{z+r_L} dz' \frac{n}{\tau} m v_x(z') \quad (9.13)$$

Making the usual Taylor's series expansion leads to an expression for the z -directed diffusive flux of x -momentum

$$\pi_{xz} = M_{+xz} - M_{-xz} \simeq -\eta_{\perp} \frac{\partial v_x(z)}{\partial z} \quad (9.14)$$

There is also a convective component, which would have been obtained as well had we considered variations in n along the field lines. A z -directed diffusive flux of y -momentum is obtained by exchanging x and y .

9.1.3.3 Gyromotion

With reference to Fig. 9.2, consider the case in which a velocity perpendicular to the field $v_y(x)$ varies in the other direction x perpendicular to the field. Gyrating particles carry a

y -momentum flux $(nmv_y)\Omega r_L = nmv_y v_{\text{th}}$, which for ions is upward ($+y$ -direction) for particles with guiding centers to the right ($+x$ -direction) and is downward ($-y$ -direction) for particles with guiding centers to the left ($-x$ -direction). If v_y does not depend on x , these two fluxes are equal in magnitude and the net y -directed flux of y -momentum is zero. For a $v_y(x)$ increasing to the right in Fig. 9.2, the upward flux arising from guiding centers to the right is greater than the downward flux arising from guiding centers to the left, resulting in a net upward ($+y$ -direction) flux of y -momentum

$$\pi_{yy} = nmv_{\text{th}}(v_y(x + r_L) - v_y(x - r_L)) \simeq \eta_\Omega \frac{\partial v_y(x)}{\partial x} \quad (9.15)$$

where a Taylor's series expansion has been made and $\eta_\Omega \approx 2nmv_{\text{th}}r_L$ is the gyroviscosity coefficient. $\eta_\Omega \approx (r_L/\lambda)\eta_{\parallel}$ $\ll \eta_{\parallel}$, but $\eta_\Omega \approx (\lambda/r_L)\eta_{\perp} \gg \eta_{\perp}$. The same type of momentum flux obviously obtains when v_x is dependent on y , leading to an x -directed flux of x -momentum given by Eq. (9.15) but with y and x interchanged.

Similarly, there is a net y -directed flux of z -momentum when v_z depends on x

$$\pi_{zy} = nmv_{\text{th}}(v_z(x + r_L) - v_z(x - r_L)) \simeq \eta_\Omega \frac{\partial v_z(x)}{\partial x} \quad (9.16)$$

9.1.4 Friction Force

In collisions between ions and electrons with ordered average velocities \mathbf{v}_i and \mathbf{v}_e , the electrons lose their ordered momentum in the time required for a 90° deflection in the lab, $\tau = \tau_{90ei}$. The rate of momentum loss is a negative (with respect to the direction of \mathbf{v}_e) force acting on the electrons by the ions

$$\mathbf{R}_{ei} = -\frac{n_e m_e (v_e - v_i)}{\tau_{ei}^{90}} \quad (9.17)$$

From momentum conservation, the force that the electrons produce on the ions must be equal and opposite in direction; i.e. $\mathbf{R}_{ie} = -\mathbf{R}_{ei}$.

9.1.5 Thermal Force

The temperature dependence of the 90° deflection time, $\tau \sim T^{\frac{3}{2}}$, leads to a thermal force. Because of the differences in mass, ions move much slower than electrons at comparable temperatures and can be approximated as being at rest, in which case Eq. (9.17) may be written $\mathbf{R}_{ei} \approx -m_e \Gamma_e / \tau$.

9.1.5.1 Motion Along Field Lines

Consider the case in which the electron temperature increases with direction z along the magnetic field lines (i.e. as shown in Fig. 9.1 for n). The net electron flux in the z -direction is the difference between the partial fluxes Γ_+ to the right coming from half of the collisions in the interval $(z, z - \lambda)$ in time τ and Γ_- to the left coming from half of the collisions

in the interval $(z + \lambda, z)$ in time τ

$$\Gamma_{ez}(z) = \Gamma_{+z}(z) - \Gamma_{-z}(z) = \frac{1}{2} \int_{z-\lambda}^z dz' \frac{n}{\tau(z')} - \frac{1}{2} \int_z^{z+\lambda} dz' \frac{n}{\tau(z')} \quad (9.18)$$

This expression may be used to evaluate the frictional force exerted by the almost stationary ions on the electrons by making Taylor's series expansions

$$R_{eiz}^T = -\frac{m_e \Gamma_{ez}}{\tau} = -\frac{3}{2} n \left(\frac{\frac{1}{2} m_e v_{th e}^2}{T_e} \right) \frac{\partial T_e}{\partial z} = -\frac{3}{2} n \frac{\partial T_e}{\partial z} \quad (9.19)$$

The corresponding force exerted on the ions by the electrons is, from momentum conservation, $R_{iez}^T = -R_{eiz}^T$. Note that the thermal force is a collisional friction force, although the collision time does not appear in the final expression.

9.1.5.2 Gyromotion

Now consider the situation shown for electrons in Fig. 9.3 in which the electron temperature increases in the x -direction perpendicular to the field line. The thermal speed of electrons with guiding centers to the right is greater than the thermal speed of electrons with guiding centers to the left, producing a net electron flux in the $-y$ -direction

$$\Gamma_{ey} = n [v_{th e}(x - r_L) - v_{th e}(x + r_L)] \simeq -n v_{th e} r_{Le} \frac{1}{T_e} \frac{\partial T_e}{\partial x} \quad (9.20)$$

which in turn produces a downward $-y$ -direction thermal force due to collisions with ions

$$R_{ey}^T = -\frac{r_{Le}}{T_e} \frac{\partial T_e}{\partial x} m_e n_e v_{th e} = -\frac{n_e}{\Omega_e \tau} \frac{\partial T_e}{\partial x} \quad (9.21)$$

where $\Omega_e = v_{th e}/r_{Le}$ is the electron gyrofrequency. The thermal force exerted by the electrons on the ions is $R_{iy}^T = -R_{ey}^T$, by conservation of momentum.

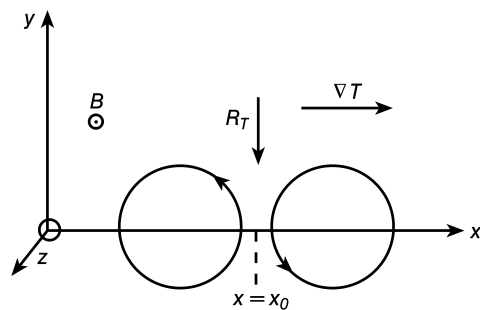


Figure 9.3. Thermal force from gyromotion

9.2 Classical Transport

We now develop classical collisional transport theory from fluid theory for a plasma confined in a cylinder with an axial magnetic field and an axial current, as shown in Fig. 9.4. The starting point is the momentum balance equation, Eq. (5.26). We consider the source free, steady state, isotropic pressure version of this equation

$$\nabla p_\sigma = n_\sigma e_\sigma (\mathbf{E} + \mathbf{v}_\sigma \times \mathbf{B}) + \mathbf{R}_\sigma^1 \quad (9.22)$$

An equation of this form is obtained for each particle species in the plasma. In writing Eq. (9.22), we have neglected terms of $O(\delta^2)$ and have also neglected the pressure anisotropy term $\nabla \cdot \boldsymbol{\pi}_\sigma$.

We will investigate the consequences of Eq. (9.22) for particle fluxes in a poloidally symmetric cylinder of plasma, in which the flux surfaces are concentric cylindrical annuli. Consider the radial component of Eq. (9.22) in (r, θ, z) coordinates,

$$\frac{\partial p_\sigma}{\partial r} = n_\sigma e_\sigma (E_r + v_{\sigma\theta} B_z - v_{\sigma z} B_\theta) + R_\sigma^1 \quad (9.23)$$

Because R_σ^1 is of $O(\delta)$ and the other terms are of $O(1)$ (see chapter 5, section 5.5 we may neglect R_σ^1 to lowest order. Further requiring $B_\theta/B_z \ll 1$, this equation can be solved for the poloidal flow

$$v_{\sigma\theta} = \frac{1}{n_\sigma e_\sigma B_z} \left(\frac{\partial p_\sigma}{\partial r} - n_\sigma e_\sigma E_r \right) \quad (9.24)$$

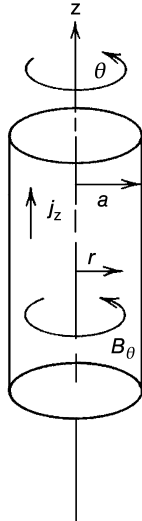


Figure 9.4. Cylindrical plasma column

Now consider the θ -component of Eq. (9.22) and make use of poloidal symmetry $\left(\frac{\partial p_\sigma}{\partial \theta} = 0, E_0 = -\frac{1}{r} \frac{\partial \Phi}{\partial \theta} = 0\right)$ to obtain

$$0 = \frac{1}{r} \frac{\partial p_\sigma}{\partial \theta} - n_\sigma e_\sigma E_\theta = -n_\sigma e_\sigma v_{\sigma r} B_z + R_{\sigma \theta}^1 \quad (9.25)$$

from which we find an expression for the radial particle flux that is driven by the poloidal friction

$$n_\sigma v_{\sigma r} = \frac{R_{\sigma \theta}^1}{e_\sigma B_z} \quad (9.26)$$

The net radial current is

$$j_r \equiv \sum_\sigma n_\sigma e_\sigma v_{\sigma r} = \frac{1}{B_z} \sum_\sigma R_{\sigma \theta}^1 = 0 \quad (9.27)$$

where conservation of momentum in elastic collisions is sufficient to ensure the last equality. Thus, the collisional radial transport produces no net current and is said to be ambipolar.

In order to evaluate the collisional friction operator,

$$R_\sigma^1 = m_\sigma \int C_\sigma \mathbf{v} d^3 v = m_\sigma \sum_{\sigma' \neq \sigma} C_{\sigma \sigma'}(f_\sigma, f_{\sigma'}) \mathbf{v} d^3 v \quad (9.28)$$

we use the results of chapter 4. In particular, we make use of the assumptions $m_\sigma \ll m_{\sigma'}$ and $|\mathbf{v}|_\sigma \gg |\mathbf{v}|_{\sigma'}$, which led to Eq. (4.51). Making the assumption that the distribution function is a perturbation about a Maxwellian

$$f_\sigma = f_\sigma^{\max} (1 + v_{\sigma'}/v_{\text{th}}^{\sigma'}) \quad (9.29)$$

where $v_{\text{th}}^{\sigma'}$ is the thermal speed of species σ' , and $v_{\sigma'} \sim \delta v_{\text{th}}^{\sigma'}$ in evaluating $C_{\sigma \sigma'}/c$ from Eq. (4.51) leads to

$$R_\sigma^1 = - \sum_{\sigma' \neq \sigma} \left(\Gamma_{\sigma \sigma'} n_{\sigma'} m_\sigma \int \frac{\mathbf{v} f_\sigma(\mathbf{v}) d^3 v}{|\mathbf{v}|^3} - m_\sigma n_\sigma v_{\sigma \sigma'} \mathbf{v}_{\sigma'} \right) \quad (9.30)$$

where

$$\nu_{\sigma \sigma'} \equiv \frac{4 \Gamma_{\sigma \sigma'} n_{\sigma'}}{3 \sqrt{\pi} (v_{\text{th}}^\sigma)^2} = \frac{n_{\sigma'} (e_\sigma e_{\sigma'})^2 \ln \Lambda}{3 (3\pi T_\sigma)^{\frac{3}{2}} m_\sigma^{\frac{1}{2}} \epsilon_0^2} \quad (9.31)$$

is the momentum-exchange collision frequency for a particle of species σ scattering off particles of species σ' . We further approximate Eq. (9.30)

$$\begin{aligned} R_\sigma^1 &\simeq - \sum_{\sigma' \neq \sigma} \left(\Gamma_{\sigma \sigma'} \frac{n_{\sigma'} m_\sigma n_\sigma \mathbf{v}_\sigma}{(v_{\text{th}}^\sigma)^3} - m_\sigma n_\sigma v_{\sigma \sigma'} \mathbf{v}_{\sigma'} \right) \\ &\simeq - \sum_{\sigma' \neq \sigma} n_\sigma m_\sigma v_{\sigma \sigma'} (\mathbf{v}_\sigma - \mathbf{v}_{\sigma'}) \end{aligned} \quad (9.32)$$

Using this form for $R_{\sigma\theta}$ and Eq. (9.24) for $v_{\sigma\theta}$, Eq. (9.26) becomes

$$n_\sigma v_{\sigma r} = - \sum_{\sigma' \neq \sigma} \frac{n_\sigma m_\sigma v_{\sigma\sigma'}}{e_\sigma B_z^2} \left(\frac{1}{n_\sigma e_\sigma} \frac{\partial p_\sigma}{\partial r} - \frac{1}{n_{\sigma'} e_{\sigma'}} \frac{\partial p_{\sigma'}}{\partial r} \right) \quad (9.33)$$

We see that the radial particle flux is driven by differences in radial pressure gradients among the particle species present. The radial electric field does not drive a radial particle flux.

Specializing the above result to a plasma consisting only of one ($z = 1$) ion species i and electrons e and writing $p = p_i + p_e$ leads to ($\tau_{90}^{-1} = v_{\sigma\sigma'}$)

$$n_i v_{ir} = - \frac{m_i (\tau_{90}^{ie})_L^{-1}}{e^2 B_z^2} \frac{\partial p}{\partial r}$$

and

$$n_e v_{er} = - \frac{m_e (\tau_{90}^{ei})_L^{-1}}{e^2 B_z^2} \frac{\partial p}{\partial r} \quad (9.34)$$

Since $n_e m_e (\tau_{90}^{ei})_L^{-1} = n_i m_i (\tau_{90}^{ie})_L^{-1}$ from conservation of momentum

$$n_e v_{er} = n_i v_{ir} \quad (9.35)$$

and the radial current vanishes,

$$j_r \equiv e n_i v_{ir} + (-e) n_e v_{er} = 0 \quad (9.36)$$

Vanishing of the radial current is known as ambipolarity and is necessary to ensure charge neutrality.

The relative contribution of collisions with species σ' to the radial particle flux of species σ varies as $v_{\sigma\sigma'}$. It is instructive to examine the relative magnitudes of the inter-species collision frequency for a plasma made up of electrons (e), hydrogen ions (i), and heavy-mass impurity ions (z). Taking the collision frequency for electrons from ions, v_{ei} , as a base, it follows from Eq. (9.31) that

$$\begin{aligned} v_{iz} &= \frac{n_z z^2}{n_i} \sqrt{\frac{m_e}{m_i}} v_{ei}, & v_{ez} &= \frac{n_z z^2}{n_i} v_{ei} \\ v_{ie} &= \frac{n_e}{n_i} \left(\frac{m_e}{m_i} \right) v_{ei}, & v_{ze} &= \frac{n_z z^2}{n_i} \left(\frac{m_e}{m_z} \right) v_{ei} \\ v_{zi} &= z^2 \sqrt{\frac{m_e}{m_z}} v_{ei} \end{aligned} \quad (9.37)$$

A relatively small impurity concentration,

$$\frac{n_z z^2}{n_i} > \sqrt{\frac{m_e}{m_i}} \simeq \frac{1}{40} \quad (9.38)$$

is sufficient for ion–impurity collisions to be more important than ion–electron collisions in driving radial ion fluxes. The impurity flux is governed almost entirely by collisions

with ions. The radial electron fluxes driven by collisions with impurities and ions are in the ratio $n_z z^2 / n_i$.

In the absence of sources, a steady state solution would require the radial particle fluxes to vanish. Equation (9.33) implies that the steady state radial profiles are related by

$$\left(\frac{n_{\sigma'}(r)}{n_{\sigma'}(0)} \right)^{e_{\sigma}} = \left(\frac{n_{\sigma}(r)}{n_{\sigma}(0)} \right)^{e_{\sigma'}} \quad (9.39)$$

if the temperatures of both species are uniform. In an electron–ion impurity plasma in which Eq. (9.38) is satisfied, Eq. (9.39) becomes

$$\frac{n_z(r)}{n_z(0)} = \left(\frac{n_i(r)}{n_i(0)} \right)^z \quad (9.40)$$

where z is the charge of the impurity ion. Equation (9.40) predicts that if the ion profile is moderately peaked towards the center of the plasma, then the impurity profile is sharply peaked towards the center. This result implies that impurities will tend to concentrate at the center of the plasma, which would cause radiative cooling of the plasma. However, the effects of temperature gradients and of the particle sources required to sustain a steady state may both mitigate this result.

9.3 Neoclassical Transport – Toroidal Effects in Fluid Theory

When a cylinder is deformed into an axisymmetric torus, the poloidal symmetry is lost because the toroidal field is stronger on the inside than on the outside of the torus. This loss of poloidal symmetry has a profound effect upon transport fluxes, which we examine in this section.

The toroidal magnetic field, in the limit $\beta_p \approx 1$, varies as $1/R$ across the plasma region, because of the general $1/R$ dependence of the field around a current-carrying conductor. Thus, it follows from Ampère's law that

$$B_{\phi}(r, \theta) = B_{\phi}^0(r)h^{-1}(r, \theta) \quad (9.41)$$

where (see Fig. 9.5)

$$h(r, \theta) \equiv 1 + \frac{r}{R_0} \cos \theta \equiv 1 + \epsilon \cos \theta \quad (9.42)$$

Ampère's law can also be used to show that $B_{\theta}(r, \theta)h(r, \theta) = f(r) \sim I_{\text{enclosed}}$, so that,

$$B_{\theta}(r, \theta) = B_{\theta}^0(r)h^{-1}(r, \theta) \quad (9.43)$$

This result was derived from a different point of view in chapter 3 (see Eq. 3.32). The 0 superscript on B_{ϕ} and B_{θ} indicates the value at R_0 , or at $\theta = \pi/2$, respectively.

Because particles move freely along field lines and because, excepting rational surfaces, the locus of a field line traced many times around the torus covers a flux surface, we expect particle densities and temperatures and the electrostatic potential to be constant on

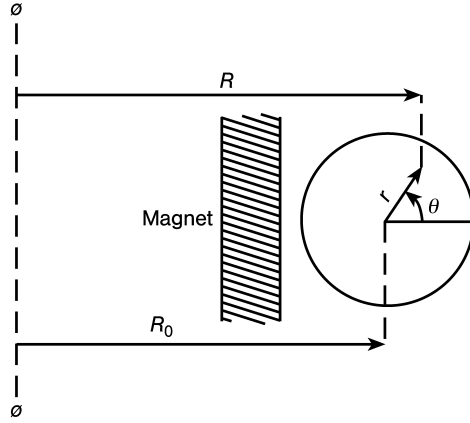


Figure 9.5. Toroidal coordinate system

a flux surface. (This was proven to be the case, to lowest order in δ , the ratio of the gyroradius to the gradient scale length, in section 5.5. Equation (9.22) can be used to demonstrate that the lowest order flow perpendicular to the field

$$n_\sigma \mathbf{v}_{\sigma\perp} = \frac{1}{e_\sigma B} \hat{\mathbf{n}}_\parallel \times (\nabla p_\sigma + n_\sigma e_\sigma \nabla \Phi) \quad (9.44)$$

lies in the flux surface. In the large aspect ratio, low- β approximation the flux surfaces are the annuli with $r = \text{const}$. Thus the particle continuity equation

$$\nabla \cdot n_\sigma \mathbf{v}_\sigma = 0 \quad (9.45)$$

may be solved by neglecting the radial flow. Making use of axisymmetry, the solution of Eq. (9.45) in toroidal geometry is

$$v_{\sigma\theta}(r, \theta) = v_{\sigma\theta}^0(r) h^{-1}(r, \theta) \quad (9.46)$$

The poloidal component of Eq. (9.22) yields

$$n_\sigma v_{\sigma r} = \frac{h R_{\sigma\theta}^1}{e_\sigma B_\phi^0} - \frac{h}{e_\sigma B_\phi^0} \left(\frac{1}{r} \frac{\partial p_\sigma}{\partial \theta} + n_\sigma e_\sigma \frac{1}{r} \frac{\partial \Phi}{\partial \theta} \right) \quad (9.47)$$

The first term in Eq. (9.47) corresponds to the result obtained for the classical transport in a cylinder, Eq. (9.26), except for a higher order (in ϵ) correction. The second term, which disappeared for the cylinder because of poloidal symmetry, drives neoclassical transport fluxes. This latter term can be evaluated from the component of Eq. (9.22) parallel to the field, to obtain

$$n_\sigma v_{\sigma r} = \frac{h R_{\sigma\theta}^1}{e_\sigma B_\phi^0} - \frac{h R_{\sigma\parallel}^1}{e_\sigma B_\theta^0} \equiv (n_\sigma v_{\sigma r})_c + (n_\sigma v_{\sigma r})_{NC} \quad (9.48)$$

Thus a classical transport flux is driven by poloidal collisional friction, and a neoclassical transport flux is driven by parallel collisional friction.

There are two important neoclassical effects within the second term in Eq. (9.48). The first effect, which is always present, is due to the toroidal geometry. The second effect is due to the influence of trapped particles on the friction term. The trapped-particle effect is present only when the collision frequency is less than the bounce frequency of the trapped particles. The transport fluxes due to the toroidal geometry effect are known as Pfirsch–Schlüter (PS) fluxes, and the transport fluxes due to the trapped particle effect are known as banana-plateau (BP) fluxes.

We consider first the Pfirsch–Schlüter transport. A more accurate expression for the collisional friction term than Eq. (9.32) will be used. This expression can be derived from the Fokker–Planck theory of chapter 4. To simplify the notation, we consider a plasma consisting of only two species, σ and σ' ; generalization is straightforward. The expression for the parallel friction is

$$R_{\sigma\parallel} = -R_{\sigma'\parallel} = -C_1 m_\sigma n_\sigma v_{\sigma\sigma'} u_\parallel - C_2 n_\sigma \nabla_\parallel T_\sigma \quad (9.49)$$

where

$$u_\parallel \equiv v_{\sigma\parallel} - v_{\sigma'\parallel} \quad (9.50)$$

The first term in Eq. (9.49) is essentially the result of Eq. (9.32). The second term arises from accounting for the thermal force. The constants are of order unity and will be defined later.

Consider the radial component of Eq. (9.22):

$$\frac{1}{n_\sigma e_\sigma} \frac{\partial p_\sigma}{\partial r} + \frac{\partial \Phi}{\partial r} = (v_{\sigma\theta} B_\phi - v_{\sigma\phi} B_\theta) \quad (9.51)$$

Noting that $B_\theta/B_\phi = \epsilon/q$ and using Eqs. (9.41), (9.43) and (9.46) yields to $O(\epsilon^0)$.

$$v_{\sigma\theta}^0 = \frac{1}{n_\sigma e_\sigma B_\phi^0} \left(\frac{\partial p_\sigma}{\partial r} + n_\sigma e_\sigma \frac{\partial \Phi}{\partial r} \right) \quad (9.52)$$

which is the result of Eq. (9.24). Thus we could recover the classical flux of Eq. (9.25) from the first term in Eq. (9.48) by using Eq. (9.32) for $R_{\sigma\theta}^1$. Subtracting Eq. (9.51) for σ and σ' yields

$$(u_\theta B_\phi - u_\phi B_\theta) = \frac{1}{n_\sigma e_\sigma} \frac{\partial p_\sigma}{\partial r} - \frac{1}{n_{\sigma'} e_{\sigma'}} \frac{\partial p_{\sigma'}}{\partial r} \quad (9.53)$$

The parallel relative velocity can be constructed from

$$u_\parallel = \hat{n}_\parallel \cdot \hat{n}_\phi u_\phi + \hat{n}_\parallel \cdot \hat{n}_\theta u_\theta = \frac{B_\phi^0}{B^0} u_\phi + \frac{B_\theta^0}{B^0} u_\theta \quad (9.54)$$

Using Eqs. (9.43), (9.46), and (9.53) and noting that $B_\phi^0/B^0 = 1 + 0(\epsilon)$, Eq. (9.54) yields

$$u_\parallel = -\frac{2\epsilon \cos \theta}{B_\theta^0} \left(\frac{1}{n_\sigma e_\sigma} \frac{\partial p_\sigma}{\partial r} - \frac{1}{n_{\sigma'} e_{\sigma'}} \frac{\partial p_{\sigma'}}{\partial r} \right) \quad (9.55)$$

To evaluate the parallel temperature gradient in Eq. (9.49), it is necessary to consider the lowest order, $0(\delta)$, heat conduction flux, given by Eq. (5.105),

$$\mathbf{q}_{\sigma\perp} = \frac{5}{2} \frac{p_\sigma}{e_\sigma B} \hat{\mathbf{n}}_{\parallel} \times \nabla T_\sigma \quad (9.56)$$

and the lowest order parallel heat conduction. An expression for the latter that was derived on a basis that is consistent with the parallel friction term of Eq. (9.49) is, for the lighter species,

$$\mathbf{q}_{\sigma\parallel} = \left(C_2 n_\sigma T_\sigma u_{\parallel} - C_3 \frac{n_\sigma T_\sigma}{m_\sigma v_{\sigma\sigma'}} \nabla_{\parallel} T_\sigma \right) \hat{\mathbf{n}}_{\parallel} \quad (9.57)$$

and for the heavier species,

$$\mathbf{q}_{\sigma'\parallel} = - \left(3.9 \frac{n_{\sigma'} T_{\sigma'}}{m_{\sigma'} v_{\sigma'\sigma}} \nabla_{\parallel} T_{\sigma'} \right) \hat{\mathbf{n}}_{\parallel} \quad (9.58)$$

where $m_\sigma \ll m_{\sigma'}$ and C_3 is a constant.

Note from Eq. (9.56) that the perpendicular heat conduction flux lies entirely in the flux surfaces with $r = \text{const}$. If we assume divergence-free heat conduction,

$$\nabla \cdot \mathbf{q}_\sigma = 0 \quad (9.59)$$

we can make use of axisymmetry to find that

$$q_{\sigma\theta}(r, \theta) = q_{\sigma\theta}^0(r) h^{-1}(r, \theta) \quad (9.60)$$

The poloidal heat conduction flux can be constructed from

$$q_{\sigma\theta} = \hat{\mathbf{n}}_\theta \cdot \hat{\mathbf{n}}_{\parallel} q_{\sigma\parallel} + \hat{\mathbf{n}}_\theta \cdot \hat{\mathbf{n}}_{\perp} q_{\sigma\perp} = \frac{B_\theta^0}{B^0} q_{\sigma\parallel} + \frac{5}{2} \frac{p_\sigma}{e_\sigma B} \left(\frac{B_\phi^0}{B^0} \right) \frac{\partial T_\sigma}{\partial r} \quad (9.61)$$

Using Eqs. (9.56) and (9.57) and noting that

$$\nabla_{\parallel} T_\sigma \simeq \frac{B_\theta^0}{B^0} \frac{1}{r} \frac{\partial T_\sigma}{\partial \theta} \quad (9.62)$$

Equation (9.61) can be used to identify

$$q_{\sigma\theta}^0 \simeq \frac{5}{2} \frac{p_\sigma}{e_\sigma B^0} \frac{\partial T_\sigma}{\partial r} \quad (9.63)$$

This result, together with Eq. (9.57), can now be used in Eq. (9.61) to obtain

$$\begin{aligned} \nabla_{\parallel} T_\sigma &\simeq - \frac{2\epsilon \cos \theta m_\sigma v_{\sigma\sigma'}}{B_\theta^0} \\ &\times \left[\frac{C_2}{C_3} \left(\frac{1}{n_\sigma e_\sigma} \frac{\partial p_\sigma}{\partial r} - \frac{1}{e_{\sigma'} n_{\sigma'}} \frac{\partial p_{\sigma'}}{\partial r} \right) - \frac{1}{e_\sigma} \frac{1}{C_3} \frac{5}{2} \frac{\partial T_\sigma}{\partial r} \right] + 0(\epsilon^2) \end{aligned} \quad (9.64)$$

Equations (9.55) and (9.64) allow us to evaluate the parallel collisional friction Eq. (9.49) and thus determine the Pfirsch–Schlüter transport flux from the second term in Eq. (9.48).

A more useful quantity is the average radial flux over the flux surface with $r = \text{const}$. The flux surface average, defined by Eq. (6.27), takes on a simple form in the approximations for toroidal flux surface with $r = \text{const}$,

$$\langle A \rangle = \frac{1}{2\pi} \int_0^{2\pi} h(r, \theta) A(r, \theta) d\theta \quad (9.65)$$

The neoclassical, Pfirsch–Schlüter radial transport flux, averaged over the flux surface, is

$$\begin{aligned} \Gamma_{\sigma r}^{\text{PS}} \equiv \langle n_\sigma v_{\sigma r}^{\text{PS}} \rangle &\simeq -\frac{2e^2 n_\sigma m_\sigma v_{\sigma\sigma'}}{(e_\sigma B_\theta^0)^2} \\ &\times \left[\left(C_1 + \frac{C_2^2}{C_3} \right) \left(\frac{1}{n_\sigma} \frac{\partial p_\sigma}{\partial r} - \frac{1}{z n_{\sigma'}} \frac{\partial p_{\sigma'}}{\partial r} \right) - \frac{5}{2} \frac{C_2}{C_3} \frac{\partial T_\sigma}{\partial r} \right] \end{aligned} \quad (9.66)$$

where $z \equiv e_{\sigma'}/e_\sigma$. It follows directly from the first equality in Eq. (9.49), which is a statement of momentum conservation in elastic collisions, that

$$\Gamma_{\sigma' r}^{\text{PS}} \equiv \langle n_{\sigma'} v_{\sigma' r}^{\text{PS}} \rangle = -\frac{1}{z} \Gamma_{\sigma r}^{\text{PS}} \quad (9.67)$$

The Pfirsch–Schlüter fluxes display many of the same characteristics that were noted for the classical fluxes. Equation (9.66) demonstrates that the flow of species σ driven by collisions with species σ' is proportional to $v_{\sigma\sigma'}$. A generalization of our results to multiple species would show that the relative fluxes of species σ driven by collisions with other species σ' scales as the relative $v_{\sigma\sigma'}$, so that the conclusions that were drawn from Eqs. (9.37) and (9.38) also apply to the Pfirsch–Schlüter fluxes. The requirement that the radial particle flux vanish in steady state applied to Eq. (9.66) would lead to Eq. (9.40) and the associated conclusion about impurity concentration at the center of the plasma, if the temperature gradient term is ignored in Eq. (9.66). This thermal force term was introduced by a better treatment of the collisional friction, and would also appear in the expression for the classical flux that was developed from the same basis; it is not a neoclassical effect. It is clear that the temperature gradient can alter the particle flux and, hence, alter our previous conclusion about impurity concentration at the center.

Comparing Eqs. (9.33) and (9.66), and noting that the constants C_1, C_2, C_3 are of order unity, leads to an estimate of the relative magnitudes of the Pfirsch–Schlüter and classical radial particle fluxes

$$\Gamma_{\sigma r}^{\text{PS}} \simeq 2 \left(\frac{\epsilon B_\phi^0}{B_\theta^0} \right)^2 \Gamma_{\sigma r}^C = 2q^2 \Gamma_{\sigma r}^C \quad (9.68)$$

Since q varies from ~ 1 at the plasma center to 3–4 at the edge, we see that the Pfirsch–Schlüter fluxes are an order of magnitude larger than the classical fluxes. Thus the toroidal geometry effects result in an order-of-magnitude enhancement of the radial transport fluxes over the classical values, in agreement with the estimates made in chapter 3.

The radial heat conduction can be constructed from

$$q_{\sigma r} = \hat{\mathbf{n}}_r \cdot \hat{\mathbf{n}}_{\perp} q_{\sigma \perp} + \hat{\mathbf{n}}_r \cdot \hat{\mathbf{n}}_{\parallel} q_{\sigma \parallel} \quad (9.69)$$

by using Eqs. (9.56) and (9.57), or for the more massive species, Eq. (9.58). The resulting expression can be averaged over the flux surface with $r = \text{const}$ to obtain

$$\langle q_{\sigma r} \rangle = \frac{5 n_{\sigma} m_{\sigma} v_{\sigma \sigma'} T_{\sigma} (2\epsilon^2)}{2 (e_{\sigma} B_{\theta}^0)^2} \left[\frac{C_2}{C_3} \left(\frac{1}{n_{\sigma}} \frac{\partial p_{\sigma}}{\partial r} - \frac{1}{z n_{\sigma'}} \frac{\partial p_{\sigma'}}{\partial r} \right) - \frac{5}{2} \frac{1}{C_3} \frac{\partial T_{\sigma}}{\partial r} \right] \quad (9.70)$$

The radial heat conduction for the heavier species, σ' , depends upon whether there is strong collisional temperature equilibration on the flux surface, in which case $T_{\sigma'} = T_{\sigma}$ on the flux surface, or whether there is weak collisional temperature equilibration on the flux surface, in which case $T_{\sigma'} \neq T_{\sigma}$ on the flux surface. The radial heat conduction can be constructed from

$$q_{\sigma' r} = \hat{\mathbf{n}}_r \cdot \hat{\mathbf{n}}_{\perp} q_{\sigma' \perp} + \hat{\mathbf{n}}_r \cdot \hat{\mathbf{n}}_{\parallel} q_{\sigma' \parallel} \simeq -\frac{5}{2} \frac{p_{\sigma'}}{e_{\sigma'} B} \frac{1}{r} \frac{\partial T_{\sigma'}}{\partial \theta} \quad (9.71)$$

In the strong equilibration case, Eq. (9.64) for species σ can be used to evaluate $\partial T_{\sigma'}/\partial \theta \simeq \partial T_{\sigma}/\partial \theta$. The resulting flux surface averaged heat conduction flux is

$$\langle q_{\sigma' r}^{\text{PS}} \rangle \simeq \frac{n_{\sigma'}}{z n_{\sigma}} \langle q_{\sigma r} \rangle \quad (\text{strong equilibration}) \quad (9.72)$$

In the weak equilibration case, the same procedure that was used to arrive at Eq. (9.70) can be used, except that Eq. (9.58) is used instead of Eq. (9.57). The resulting expression for the flux surface averaged radial heat conduction flux is

$$\langle q_{\sigma' r}^{\text{PS}} \rangle = -\frac{5}{2} \frac{n_{\sigma'} m_{\sigma'} v_{\sigma' \sigma'} T_{\sigma'} (2\epsilon^2)}{3.9 (e_{\sigma'} B_{\theta}^0)^2} \left(\frac{5}{2} \frac{\partial T_{\sigma'}}{\partial r} \right) \quad (\text{weak equilibration}) \quad (9.73)$$

The constants C_1 , C_2 , and C_3 can be found by interpolating in Table (9.1) for a plasma in which electron–ion collisions are dominant. The quantity z is the effective charge of the plasma ions.

Table 9.1. Transport constants

z	1	2	3	4	∞
C_1	0.513	0.441	0.397	0.375	0.295
C_2	0.711	0.905	1.016	1.090	1.521
C_3	3.162	4.890	6.064	6.920	12.471

For a plasma in which the transport is dominated by ion–impurity collisions, the constants can be fit by

$$\begin{aligned} C_1 + \frac{C_2^2}{C_3} &= 0.47 + \frac{0.35}{0.66 + \alpha} \\ \frac{5}{2} \frac{C_2}{C_3} &= 0.30 + \frac{0.41}{0.58 + \alpha} \\ \frac{25}{4C_3} &= \frac{1.13}{\alpha} + 0.50 + \frac{0.56}{0.56 + \alpha} \end{aligned} \quad (9.74)$$

where

$$\alpha \equiv \frac{n_{\sigma'}}{n_{\sigma}} \left(\frac{e_{\sigma'}}{e_{\sigma}} \right)^2 \equiv \frac{n_{\sigma'}}{n_{\sigma}} z^2 \quad (9.75)$$

This geometric, or Pfirsch–Schlüter, neoclassical effect on transport is always present in toroidal plasmas. However, the effects of particle orbits, in particular trapping, are dominant when they are present. Thus, only when the effective time for large angle collisional deflection, $(v_{90})^{-1}$, is less than the time, qR_0/v_{th} , required for a particle to complete an untrapped orbit, or

$$v^* \equiv \frac{v_{90} q R_0}{v_{\text{th}}} > 1 \quad (\text{Pfirsch–Schlüter}) \quad (9.76)$$

would the Pfirsch–Schlüter transport effects be dominant.

At the other extreme is the case where the time, $\epsilon(v_{90})^{-1}$, required to scatter through a small angle $\sim \epsilon$ into or out of a trapped-particle orbit is greater than the time, $qR_0/\sqrt{\epsilon}v_{\text{th}}$, required to complete a marginally-trapped-particle orbit, or

$$v^* < \epsilon^{\frac{3}{2}} \quad (\text{Banana}) \quad (9.77)$$

In this instance, the transport is determined by the effect of the guiding center motion of the trapped particles upon the particle distribution function.

The intermediate regime

$$\epsilon^{\frac{3}{2}} < v^* < 1 \quad (\text{Plateau}) \quad (9.78)$$

is one in which the effects of the untrapped-particle orbits are dominant in determining the transport process.

These particle orbit effects, for $v^* < 1$, affect the multifluid momentum balance in two ways. First, they determine the form of the collisional friction term \mathbf{R}_{σ}^1 . Second, they introduce viscous shear, so that the pressure gradient in Eq. (9.22) must be replaced by the divergence of the pressure tensor.

9.4 Multifluid Transport Formalism*

A general formalism for particle and heat transport can be developed formally from the moments equations. This formalism extends and consolidates many of the basic characteristics of transport processes that have been discussed previously in this chapter. We specify an axisymmetric toroidal plasma and assume the existence of flux surfaces. We will further assume the high-field ordering that was described in chapter 5, and assume that all faster transients have evolved to an asymptotic state so that the time-independent moments equations can be used.

Particle transport is governed by the momentum balance equation

$$\nabla \cdot \mathbf{P} = ne(\mathbf{E} + \mathbf{v} \times \mathbf{B}) + \mathbf{R}^1 + (\mathbf{S}^1 - m\mathbf{v}\mathbf{S}^0) \quad (9.79)$$

and heat transport is governed by the heat flux equation

$$\begin{aligned} \nabla \cdot \boldsymbol{\theta} - \frac{5}{2} \frac{T}{m} \nabla \cdot \mathbf{M} &= \frac{e}{m} (\mathbf{Q} - \frac{5}{2} m T \mathbf{v}) \times \mathbf{B} \\ &+ \frac{e}{m} \mathbf{E} \cdot \left[\mathbf{M} - \frac{1}{3} (Tr M) \mathbf{I} \right] + \left(\mathbf{R}^3 - \frac{5}{2} \frac{T}{m} \mathbf{R}^1 \right) + \left(\mathbf{S}^3 - \frac{5}{2} \frac{T}{m} \mathbf{S}^1 \right) \end{aligned} \quad (9.80)$$

where quantities were defined in chapter 4, and the species subscript has been suppressed to simplify the notation. Strong rotation effects have been neglected.

As we saw in section 5.5, these equations may be solved directly for the particle and heat conduction fluxes perpendicular to the field

$$n\mathbf{v}_\perp = \frac{1}{eB} \hat{\mathbf{n}}_\parallel \times [\nabla p + \nabla \cdot \boldsymbol{\pi} + ne(\nabla\Phi - \mathbf{E}^A) - \mathbf{R}^1 - \mathbf{S}^1] + 0(\delta^3) \quad (9.81)$$

and

$$\begin{aligned} \mathbf{q}_\perp &= \frac{m}{eB} \hat{\mathbf{n}}_\parallel \times \left[\nabla \cdot \boldsymbol{\theta} - \frac{5}{2} \frac{T}{m} \nabla \cdot \mathbf{M} - \left(\mathbf{R}^3 - \frac{5}{2} \frac{T}{m} \mathbf{R}^1 \right) - \left(\mathbf{S}^3 - \frac{5}{2} \frac{T}{m} \mathbf{S}^1 \right) \right] \\ &+ 0(\delta^3) \end{aligned} \quad (9.82)$$

Because p and Φ are constant on a flux surface to $0(\delta)$, the lowest-order fluxes perpendicular to the field,

$$n\mathbf{v}_\perp^1 = \frac{1}{eB} \hat{\mathbf{n}}_\parallel \times (\nabla p + ne\nabla\Phi) = \frac{p' + ne\Phi'}{eB} \hat{\mathbf{n}}_\parallel \times \nabla\psi \quad (9.83)$$

and

$$\mathbf{q}_\perp^1 = \frac{5}{2} \frac{p}{eB} \hat{\mathbf{n}}_\parallel \times \nabla T = \frac{5}{2} \frac{pT'}{eB} \hat{\mathbf{n}}_\parallel \times \nabla\psi \quad (9.84)$$

lie within the flux surfaces (i.e., $\nabla\psi \cdot n\mathbf{v}_\perp^1 = \nabla\psi \cdot \mathbf{q}_\perp^1 = 0$). (Recall that a prime indicates a derivative with respect to ψ .) Because $n\mathbf{v}_\parallel^1$ and \mathbf{q}_\parallel^1 lie in the flux surface, by definition, we conclude that the lowest-order $-0(\delta)$ – particle and heat conduction fluxes lie within the flux surfaces.

Thus the transport fluxes across flux surfaces must be of $0(\delta^2)$ or higher. We can identify the transport fluxes across the flux surfaces by taking the scalar product of $\nabla\psi$ with Eqs. (9.81) and (9.82). Because we ultimately require the flux surface average transport flux, we also take the flux surface average to obtain

$$\begin{aligned} \langle \nabla\psi \cdot n\mathbf{v}_\perp \rangle &= \left\langle \frac{(\hat{\mathbf{n}}_\parallel \times \nabla\psi) \cdot (\mathbf{R}^1 + \mathbf{S}^1 + ne\mathbf{E}^A)}{eB} \right\rangle \\ &- \left\langle \frac{(\hat{\mathbf{n}}_\parallel \times \nabla\psi) \cdot (\nabla p + \nabla \cdot \boldsymbol{\pi} + ne\nabla\Phi)}{eB} \right\rangle \end{aligned} \quad (9.85)$$

and

$$\begin{aligned} \langle \nabla \psi \cdot \mathbf{q}_\perp \rangle &= \frac{m}{e} \left\langle \frac{(\hat{\mathbf{n}}_\parallel \times \nabla \psi) \cdot \left[\left(\mathbf{R}^3 - \frac{5T}{2m} \mathbf{R}^1 \right) + \left(\mathbf{S}^3 - \frac{5T}{2m} \mathbf{S}^1 \right) \right]}{B} \right\rangle \\ &\quad - \frac{m}{e} \left\langle \frac{(\hat{\mathbf{n}}_\parallel \times \nabla \psi) \cdot \left(\nabla \cdot \boldsymbol{\theta} - \frac{T}{m} \nabla \cdot \mathbf{M} \right)}{B} \right\rangle + 0(\delta^3) \quad (9.86) \end{aligned}$$

The vector $\hat{\mathbf{n}}_\parallel \times \nabla \psi$ is perpendicular to the field and lies in the flux surface. We will refer to this direction as the perpendicular direction. The first terms in Eqs. (9.85) and (9.86) represent transport fluxes driven by perpendicular momentum exchange or electromagnetic fields. These terms survive in the cylindrical limit and are generalizations of the classical fluxes discussed in section 9.2 of this chapter. Note that the momentum exchange due to the external momentum source, \mathbf{S} , is entirely equivalent to the momentum exchange due to interspecies collisions, \mathbf{R} , in driving transport fluxes.

The second terms in Eqs. (9.85) and (9.86) represent transport fluxes driven by perpendicular gradients in the pressure tensor, electrostatic potential, energy flux tensor, and momentum stress tensor. These fluxes are associated with neoclassical and/or other nonclassical effects. It can be shown that these nonclassical fluxes are driven by momentum exchange parallel to the field by making use of the identity

$$\hat{\mathbf{n}}_\parallel \times \nabla \psi \cdot \nabla Q = RB_\phi \hat{\mathbf{n}}_\parallel \cdot \nabla Q \quad (9.87)$$

which is valid for any axisymmetric scalar, Q . Taking the scalar product of $\hat{\mathbf{n}}_\parallel/B$ with Eqs. (9.79) and (9.80) and using Eqs. (9.87), (9.85) and (9.86) become

$$\begin{aligned} \langle \nabla \psi \cdot n \mathbf{v}_\perp \rangle &= \left\langle \frac{(\hat{\mathbf{n}}_\parallel \times \nabla \psi) \cdot (\mathbf{R}^1 + \mathbf{S}^1 + ne\mathbf{E}^A)}{eB} \right\rangle \\ &\quad - RB_\phi \left\langle \frac{\hat{\mathbf{n}}_\parallel \cdot (\mathbf{R}^1 + \mathbf{S}^1 + ne\mathbf{E}^A)}{eB} \right\rangle + 0(\delta^3) \quad (9.88) \end{aligned}$$

and

$$\begin{aligned} \langle \nabla \psi \cdot \mathbf{q}_\perp \rangle &= \frac{m}{e} \left\langle \frac{(\hat{\mathbf{n}}_\parallel \times \nabla \psi) \cdot \left[\left(\mathbf{R}^3 - \frac{5T}{2m} \mathbf{R}^1 \right) + \left(\mathbf{S}^3 - \frac{5T}{2m} \mathbf{S}^1 \right) \right]}{B} \right\rangle \\ &\quad - \frac{mRB_\phi}{e} \left\langle \frac{\hat{\mathbf{n}}_\parallel \cdot \left[\left(\mathbf{R}^3 - \frac{5T}{2m} \mathbf{R}^1 \right) + \left(\mathbf{S}^3 - \frac{5T}{2m} \mathbf{S}^1 \right) \right]}{B} \right\rangle + 0(\delta^3) \quad (9.89) \end{aligned}$$

We have used the high-field ordering results of section 5.5 to simplify Eqs. (9.88) and (9.89). The second terms in Eqs. (9.88) and (9.89) represent nonclassical transport fluxes

driven by momentum exchange parallel to the field. The Pfirsch–Schlüter fluxes in the large aspect ratio approximation that were derived in section 9.3 of this chapter are a special case of such nonclassical transport fluxes.

Because of charge neutrality ($\sum_{\sigma} n_{\sigma} e_{\sigma} = 0$) and conservation of momentum in elastic collisions ($\sum_{\sigma} \mathbf{R}_{\sigma}^1 = 0$), the first and second terms in Eq. (9.88) are separately ambipolar if

$$\sum_{\sigma} \left\langle \frac{(\hat{\mathbf{n}}_{\parallel} \times \nabla \psi) \cdot \mathbf{S}^1}{eB} \right\rangle = \sum_{\sigma} \left\langle \frac{\hat{\mathbf{n}}_{\parallel} \cdot \mathbf{S}^1}{eB} \right\rangle = 0 \quad (9.90)$$

It can be demonstrated that momentum conservation in the flux surface requires the $0(\delta)$ flows to adjust so that Eq. (9.90) is satisfied, so that the transport fluxes across the flux surfaces are ambipolar.

9.5 Closure of Fluid Transport Equations*

The fluid theory discussed in the previous sections and more generally in chapter 5 would provide a complete set of equations for the calculation of the transport of particles momentum and energy in a plasma if the frictional forces, viscous fluxes and heat fluxes were known. These latter quantities can be calculated from kinetic theory, thus providing the needed “closure” relations for the multifluid transport theory.

We describe in this section the general development of the Chapman–Enskog method from the kinetic theory of gases for application to plasmas pioneered by Braginskii. This methodology has been developed under the assumptions: (1) that the time between collisions, τ_{90} , is short compared to the time scale of other phenomena which affect transport; (2) that the inverse gyrofrequency \mathcal{Q}^{-1} , is much less than τ_{90} ; (3) that the collisional mean free path, $l = v_{\text{th}} \tau_{90}$, is much less than the gradient scale length along the field lines, and (4) that the gyroradius, r_L , is much less than the gradient scale length perpendicular to the field lines, L_{\perp} . When these orderings are satisfied, the distribution function can be expanded in the corresponding small parameters, $f_{\sigma} = f_{\sigma 0} + f_{\sigma 1} + \dots$, where the lowest order solution is the local Maxwellian

$$f_{\sigma 0}(\mathbf{r}, \mathbf{v}, t) = n_{\sigma}(\mathbf{r}, t) \left(\frac{m_{\sigma}}{2\pi T_{\sigma}(\mathbf{r}, t)} \right)^{\frac{3}{2}} \exp \left\{ \frac{m_{\sigma} [\mathbf{v} - \mathbf{V}_{\sigma}(\mathbf{r}, t)]}{2T_{\sigma}(\mathbf{r}, t)} \right\} \quad (9.91)$$

where \mathbf{V}_{σ} is the local average velocity of species σ .

9.5.1 Kinetic Equations for Ion–Electron Plasma

It is more convenient to work in a frame of reference moving with velocity \mathbf{V}_{σ} , which requires a coordinate transformation $(\mathbf{r}, \mathbf{v}, t) \rightarrow (\mathbf{r}, \mathbf{v}'_{\sigma}, t)$, where $\mathbf{v}'_{\sigma} = \mathbf{v} - \mathbf{V}_{\sigma}$ is the velocity variable in the moving coordinate system. The derivatives transform as

$$\frac{\partial}{\partial t} \rightarrow \frac{\partial}{\partial t} - \frac{\partial \mathbf{V}_{\sigma}}{\partial t} \cdot \frac{\partial}{\partial \mathbf{v}'_{\sigma}}, \frac{\partial}{\partial \mathbf{r}} \rightarrow \frac{\partial}{\partial \mathbf{r}} - \frac{\partial \mathbf{V}_{\sigma j}}{\partial \mathbf{r}} \frac{\partial}{\partial \mathbf{v}'_{\sigma j}}, \frac{\partial}{\partial \mathbf{v}} = \frac{\partial}{\partial \mathbf{v}'_{\sigma}} \quad (9.92)$$

In this moving frame, the Boltzmann kinetic equation for species σ is

$$\frac{df_\sigma}{dt} + \mathbf{v}'_\sigma \cdot \nabla f_\sigma + \left[\frac{e_\sigma}{m_\sigma} (\mathbf{E}' + \mathbf{v}'_\sigma \times \mathbf{B}) - \frac{dV_\sigma}{dt} \right] \cdot \frac{\partial f_\sigma}{\partial \mathbf{v}'_\sigma} - v'_\sigma j \frac{\partial V_{\sigma k}}{\partial r_j} \frac{\partial f_\sigma}{\partial v'_{\sigma k}} = C_\sigma(f_\sigma) \quad (9.93)$$

where $\mathbf{E}' = \mathbf{E} + \mathbf{V}_\sigma \times \mathbf{B}$ is the electric field measured in the moving frame, and

$$\frac{d}{dt} = \frac{\partial}{\partial t} + \mathbf{V}_\sigma \cdot \nabla \quad (9.94)$$

is the convective derivative. Summation over the three spatial directions ($i, k = x_1, x_2, x_3$) is implied by the Einstein summation convention in this section. The largest terms are those involving the collision operator and the magnetic field, which reflects the ordering of high collision frequency and small gyroradius. Collecting these large terms on the left-hand side gives the following equation for electrons ($e_e = -e$),

$$C_{ee}(f_e) + C_{ei}^0(f_e) + \frac{e}{m_e} \mathbf{v}'_e \times \mathbf{B} \cdot \frac{\partial f_e}{\partial \mathbf{v}'_e} = \frac{d f_e}{dt} + \mathbf{v}'_e \cdot \nabla f_e - \left(\frac{e}{m_e} \mathbf{E}' + \frac{dV_e}{dt} \right) \cdot \frac{\partial f_e}{\partial \mathbf{v}'_e} - v'_e j \frac{\partial V_{ek}}{\partial r_j} \frac{\partial f_e}{\partial v'_{ek}} - C_{ei}^1(f_e) \quad (9.95)$$

where we have considered the term in the collision operator as small and put it on the right-hand side.

The next step is to solve this equation perturbatively by expanding the distribution function, $f_e = f_{e0} + f_{e1} + \dots$. In lowest order, the left-hand side must vanish, which forces the distribution to be a Maxwellian at rest in the moving frame,

$$f_{e0} = n_e \left(\frac{m_e}{2\pi T_e} \right)^{\frac{3}{2}} e^{-m_e v_e'^2 / 2T_e} \quad (9.96)$$

In the next order, we insert this distribution on the right-hand side of Eq. (9.95) and obtain an equation for the correction f_{e1}

$$\begin{aligned} C_{ee}(f_{e1}) + C_{ei}^0(f_{e1}) + \frac{e}{m_e} \mathbf{v} \times \mathbf{B} \cdot \frac{\partial f_{e1}}{\partial \mathbf{v}} \\ = \left[\frac{d \ln n_e}{dt} + \left(x^2 - \frac{3}{2} \right) \frac{d \ln T_e}{dt} + \mathbf{v} \cdot \nabla \ln n_e + \left(x^2 - \frac{3}{2} \right) \mathbf{v} \cdot \nabla \ln T_e \right. \\ \left. + \frac{m_e \mathbf{v}}{T_e} \cdot \left(\frac{e}{m_e} \mathbf{E}' + \frac{dV_e}{dt} \right) + \frac{m_e v_j v_k}{T_e} \frac{\partial V_{ek}}{\partial r_j} + v_{ei} \frac{m_e \mathbf{v} \cdot \mathbf{u}}{T_e} \right] f_{e0} \end{aligned} \quad (9.97)$$

where we have now written \mathbf{v} instead of \mathbf{v}'_e , where $\mathbf{u} = \mathbf{V}_e - \mathbf{V}_i$ is the mean velocity of the electrons relative to the ions, and where $x^2 = m_e v_e'^2 / 2T_e$. Integrating Eq. (9.97) over velocity space gives the fluid continuity Eq. (5.6) without sources, which implies

that $d\ln n_e/dt$ can be replaced by $-\nabla \cdot \mathbf{V}_e$. The $m_e \mathbf{v}$ -moment gives the fluid momentum Eq. (5.26) without sources or the inertial or viscous terms, and can be used to eliminate $d\mathbf{V}_e/dt$ and \mathbf{E}' by

$$\frac{d\mathbf{V}_e}{dt} + \frac{e\mathbf{E}'}{m_e} = \frac{\mathbf{R}_e - \nabla(n_e T_e)}{m_e n_e} \quad (9.98)$$

The energy moment finally gives the fluid energy Eq. (5.27) without sources, heat conduction, viscous terms or energy exchange.

$$\frac{3}{2} \frac{d\ln T_e}{dt} + \nabla \cdot \mathbf{V}_e = 0 \quad (9.99)$$

and this can be used to eliminate dT_e/dt in Eq. (9.97).

Eliminating time derivatives from Eq. (9.97) in this manner gives the following kinetic equation for f_{e1} in the electron rest frame,

$$\begin{aligned} C_{ee}(f_{e1}) + C_{ei}^0(f_{e1}) + \frac{e}{m_e} \mathbf{v} \times \mathbf{B} \cdot \frac{\partial f_{e1}}{\partial \mathbf{v}} \\ = \left[\left(x^2 - \frac{5}{2} \right) \mathbf{v} \cdot \nabla \ln T_e + \mathbf{v} \cdot \left(\frac{\mathbf{R}_e}{p_e} + \frac{m_e v_{ei} \mathbf{u}}{T_e} \right) \right. \\ \left. + \frac{m_e}{2T_e} \left(v_j v_k - \frac{v^2}{3} \delta_{jk} \right) W_{jk}^e \right] f_{e0} \quad (9.100) \end{aligned}$$

where now x is defined with ion parameters and

$$W_{jk}^\sigma \equiv \frac{\partial V_{\sigma j}}{\partial r_k} + \frac{\partial V_{\sigma k}}{\partial r_j} - \frac{2}{3} (\nabla \cdot V_\sigma) \delta_{jk} \quad (9.101)$$

is the rate-of-strain tensor. Note that there are three driving terms on the right: the temperature gradient, which we have encountered before as a thermal force; the term involving the friction force; and the tensor W_{jk} which gives rise to plasma viscosity.

The ion analysis is slightly simpler since the entire ion-electron collision operator can be regarded as small, which implies that the friction \mathbf{R}_{ie} is negligible in the ion kinetic problem. The analog of Eq. (9.100) for ions is thus

$$\begin{aligned} C_{ii}(f_{i1}) - \frac{e}{m_i} \mathbf{v} \times \mathbf{B} \cdot \frac{\partial f_{i1}}{\partial \mathbf{v}} \\ = \left[\left(x^2 - \frac{5}{2} \right) \mathbf{v} \cdot \nabla \ln T_i + \frac{m_i}{2T_i} \left(v_j v_k - \frac{v^2}{3} \delta_{jk} \right) W_{jk}^i \right] f_{i0} \quad (9.102) \end{aligned}$$

The distribution function can be expanded in any complete set of functions of the velocity variable. A useful set of such functions are the Sonine polynomials, or generalized Laguerre polynomials,

$$L_j^{(m)}(x) \equiv \frac{1}{j!} \frac{e^x}{x^m} \frac{d^j}{dx^j} (x^{j+m} e^{-x}) \quad (9.103)$$

The lower index is an integer, $j = 0, 1, \dots$, and here we shall only need polynomials with $m = 3/2$ for the upper index,

$$\begin{aligned} L_0^{(\frac{3}{2})}(x) &= 1 \\ L_1^{(\frac{3}{2})}(x) &= \frac{5}{2} - x \\ L_2^{(\frac{3}{2})}(x) &= \frac{35}{8} - \frac{7x}{2} + \frac{x^2}{2} \end{aligned} \quad (9.104)$$

Sonine polynomials are orthogonal in the sense

$$\int_0^\infty L_j^{(m)}(x)L_k^{(m)}(x)x^m e^{-x} dx = \frac{\Gamma(j+m+1)}{j!} \delta_{jk} \quad (9.105)$$

where $\Gamma(n)$ is the Gamma function, which satisfies $\Gamma(1/2) = \pi^{1/2}$, $\Gamma(n+1) = n\Gamma = n!$. In terms of the velocity-space average,

$$\{F(v)\} \equiv \int F \frac{mv_\parallel^2}{nT} f_M d^3 v = \frac{8}{3\sqrt{\pi}} \int_0^\infty F(x) e^{-x^2} x^4 dx \quad (9.106)$$

the orthogonality relation for Sonine polynomials can be expressed as

$$\left\{ L_j^{(\frac{3}{2})}(x^2) L_k^{(\frac{3}{2})}(x^2) \right\} = \frac{\Gamma(j+\frac{5}{2})}{j! \Gamma(\frac{5}{2})} \delta_{jk} \quad (9.107)$$

The meaning of $\{ \}$ is seen by comparing Eqs. (9.105) and (9.107). The integral

$$\int f_\sigma(v) v_\parallel L_j^{(\frac{3}{2})}(x_\sigma^2) d^3 v$$

with $x_\sigma^2 = m_\sigma v^2 / 2T_\sigma$ is equal to the particle flux of species σ if $j = 0$, and is equal to the negative heat flux divided by T if $j = 1$. Accordingly, if $f_{\sigma 1}$ is expanded as

$$f_{\sigma 1} = f_\sigma - f_{\sigma 0} = f_{\sigma 0} \frac{m_\sigma v_\parallel}{T_\sigma} \sum_j u_{\sigma j} L_j^{(\frac{3}{2})}(x_\sigma^2) \quad (9.108)$$

where $f_{\sigma 0}$ is a stationary Maxwellian, then the first two coefficients $u_{\sigma j}$ are very simply related to the parallel mean velocity V_\parallel and conductive heat flux $q_{\sigma \parallel}$ by

$$u_{\sigma 0} = V_{\sigma \parallel}, \quad u_{\sigma 1} = -\frac{2q_{\sigma \parallel}}{5p_\sigma} \quad (9.109)$$

We define the matrix elements of the collision operator

$$\begin{aligned} M_{\sigma\sigma'}^{jk} &\equiv \frac{\tau_{\sigma\sigma'}}{n_\sigma} \int v_\parallel L_j^{(\frac{3}{2})}(x_\sigma^2) C_{\sigma\sigma'} \left[\frac{m_\sigma v_\parallel}{T_\sigma} L_k^{(\frac{3}{2})}(x_\sigma^2) f_{\sigma 0}, f_{\sigma' 0} \right] d^3 v \\ N_{\sigma\sigma'}^{jk} &\equiv \frac{\tau_{\sigma\sigma'}}{n_\sigma} \int v_\parallel L_j^{(\frac{3}{2})}(x_\sigma^2) C_{\sigma\sigma'} \left[f_{\sigma 0}, \frac{m_{\sigma'} v_\parallel}{T_{\sigma'}} L_k^{(\frac{3}{2})}(x_{\sigma'}^2) f_{\sigma' 0} \right] d^3 v \end{aligned} \quad (9.110)$$

where $\tau_{\sigma\sigma'} = 3\pi^{\frac{1}{2}}/4\hat{\nu}_{\sigma\sigma'}$ and $\nu_{\sigma\sigma'} = n_\sigma e_{\sigma'}^2 e_\sigma^2 \ln \Lambda / 4\epsilon_0^2 m_\sigma^2 v_{\text{th}\sigma}^2$. The calculation of the matrix elements from the full Coulomb collision operator is straightforward if one uses the generating function for Sonine polynomials,

$$(1-y)^{-m-1} \exp\left(\frac{-xy}{1-y}\right) = \sum_{j=0}^{\infty} y^j L_j^{(m)}(x) \quad (9.111)$$

Making use of these quantities, integral equation transport problems, e.g. the Spitzer problem for parallel transport in a multi-species plasma,

$$\sum_{\sigma'} [C_{\sigma\sigma'}(f_{\sigma 1}, f_{\sigma' 0}) + C_{\sigma\sigma'}(f_{\sigma 0}, f_{\sigma' 1})] = v_{\parallel} \left[A_{\sigma 1} L_0^{(\frac{3}{2})}(x_{\sigma}^2) - A_{\sigma 2} L_1^{(\frac{3}{2})}(x_{\sigma}^2) \right] f_{\sigma 0} \quad (9.112)$$

can be transformed into an algebraic system of equations for the coefficients $u_{\sigma j}$ by multiplying by $(m_{\sigma} v_{\parallel} / T_{\sigma}) L_j^{(\frac{3}{2})}(x_{\sigma}^2)$ and integrating over velocity-space

$$\sum_{\sigma' k} \frac{m_{\sigma}}{\tau_{\sigma\sigma'} T_{\sigma}} \left(M_{\sigma\sigma'}^{jk} u_{\sigma k} + N_{\sigma\sigma'}^{jk} u_{\sigma' k} \right) = A_{\sigma 1} \delta_{j0} - \frac{5}{2} A_{\sigma 2} \delta_{j1} \quad (9.113)$$

where we have used the orthogonality of the Sonine polynomials. Note that the ‘‘driving terms’’ on the right only appear in the first two ($j = 0, 1$) equations. As a result of this property the Sonine polynomial expansion tends to converge very quickly. The system of equations can usually be truncated after only a few (typically three) equations with very little loss of accuracy.

9.5.2 Transport Parameters

Solving Eqs. (9.100) and (9.102) using the polynomial expansion method leads to the following results. The force \mathbf{R}_e acting on electrons consists of a friction force and a thermal force

$$\mathbf{R}_e = \mathbf{R}_u + \mathbf{R}_T \quad (9.114)$$

$$\mathbf{R}_u = -\frac{m_e n_e}{\tau_e} (0.51 \mathbf{u}_{\parallel} + \mathbf{u}_{\perp}) \quad (9.115)$$

$$\mathbf{R}_T = -0.71 n_e \nabla_{\parallel} T_e + \frac{3n_e}{2\Omega_e \tau_e} \hat{\mathbf{n}}_{\parallel} \times \nabla T_e \quad (9.116)$$

where $\mathbf{u} \equiv \mathbf{V}_e - \mathbf{V}_i$, $\hat{\mathbf{n}}_{\parallel} \equiv \mathbf{B}/B$, and, because of momentum conservation in Coulomb collisions, $\mathbf{R}_i = -\mathbf{R}_e$. The parallel friction coefficient in Eq. (9.116) is seen to be smaller than the perpendicular one by a factor of 0.51, linked to the fact that the collision frequency decreases with velocity, ($\tau_e \sim v^3$), causing electrons with large parallel velocities to be more distorted from the Maxwellian distribution than slower ones. The fast electrons then contribute more to the relative velocity, and less to the friction since their collisionality

is relatively low. The parallel thermal force of Eq. (9.116) is also a consequence of the fact that the collision frequency falls off with increasing energy, and the second term in Eq. (9.116) is smaller than the first one by a factor of $1/\Omega_e \tau_e \ll 1$.

The electron heat flux also has two parts

$$\mathbf{q}_e = \mathbf{q}_e^u + \mathbf{q}_e^T \quad (9.117)$$

$$\mathbf{q}_e^u = 0.71 n_e T_e \mathbf{u}_{\parallel} - \frac{3n_e T_e}{2\Omega_e \tau_e} \hat{\mathbf{n}}_{\parallel} \times \mathbf{u}_{\perp} \quad (9.118)$$

$$\mathbf{q}_e^T = -\kappa_{\parallel}^e \nabla_{\parallel} T_e - \kappa_{\Omega}^e \hat{\mathbf{n}}_{\parallel} \times \nabla T_e - \kappa_{\perp}^e \nabla_{\perp} T_e \quad (9.119)$$

where $\tau_e \equiv v_{ei}^{-1} = 3\sqrt{m_e} T_e^{3/2} \epsilon_0^2 / 4\sqrt{2\pi} \ln \Lambda_e e^4 z_i^2 n_i$, and the heat conductivities are

$$\kappa_{\parallel}^e = 3.16 \frac{n_e T_e \tau_e}{m_e} \quad (9.120)$$

$$\kappa_{\Omega}^e = \frac{5n_e T_e}{2m_e \Omega_e} \quad (9.121)$$

$$\kappa_{\perp}^e = 4.66 \frac{n_e T_e}{m_e \Omega_e^2 \tau_e} \quad (9.122)$$

The ion heat flux only has terms related to ∇T_i

$$\mathbf{q} = -\kappa_{\parallel}^i \nabla_{\parallel} T_i + \kappa_{\Omega}^i \hat{\mathbf{n}}_{\parallel} \times \nabla T_i - \kappa_{\perp}^i \nabla_{\perp} T_i \quad (9.123)$$

where

$$\kappa_{\parallel}^i = 3.9 \frac{n_i T_i \tau_i}{m_i} \quad (9.124)$$

$$\kappa_{\Omega}^i = \frac{5n_i T_i}{2m_i \Omega_i} \quad (9.125)$$

$$\kappa_{\perp}^i = 2 \frac{n_i T_i}{m_i \Omega_i^2 \tau_i} \quad (9.126)$$

where $\tau_i \equiv v_{ii}^{-1} = 3\sqrt{m_i} T_i^{3/2} \epsilon_0^2 / 4\sqrt{\pi} \ln \Lambda_i e^4 z_i^2 n_i$.

The conductivities κ_{\parallel} , κ_{Ω} , and κ_{\perp} are consecutively separated by the large factor $\Omega \tau$ for both species. The first and third terms in the expressions for \mathbf{q}_e^T and \mathbf{q}_i are parallel to the gradients that drive them and will therefore tend to relax these gradients. This relaxation occurs on widely separate time scales in the two directions. Perpendicular to the magnetic field, the ion contribution is dominant. Parallel to the field, on the other hand, the electron heat flux dominates. Of intermediate magnitude is the diamagnetic heat flux term $\mathbf{q}_{\Omega} = \pm \kappa_{\Omega} \hat{\mathbf{n}}_{\parallel} \times \nabla T$, carrying heat across the field perpendicular to the gradient.

The heat exchanged between the species,

$$Q_{ie} = -Q_{ei} - \mathbf{R}_e \cdot \mathbf{u} = \frac{3n_e m_e}{m_i \tau_e} (T_e - T_i) \quad (9.127)$$

is a result of temperature equilibration on the slow time scale τ_{ie} and frictional generation of heat.

We now turn to the flux of momentum, π . When the flow velocity is large, $V_\sigma \sim v_{\text{th}\sigma}$, the flux of momentum is driven by gradients of this flow. Just as in the Navier–Stokes equation for an ordinary fluid, the viscosity tensor is

$$\pi_{jk} = \eta W_{jk} + \xi \delta_{jk} \nabla \cdot \mathbf{V} \quad (9.128)$$

Here η and ξ are viscosity coefficients, and W_{jk} is the rate-of-strain tensor

$$W_{jk}^\sigma = \frac{\partial V_{\sigma j}}{\partial r_k} + \frac{\partial V_{\sigma k}}{\partial r_j} - \frac{2}{3}(\nabla \cdot \mathbf{V}_\sigma) \delta_{jk} \quad (9.129)$$

The last term is nonzero only for flow velocity fields with nonvanishing divergence, i.e., for non-compressible fluid flows.

In a magnetized plasma, the viscosity tensor is more complicated because the transport of momentum occurs at very different rates in different directions. Each species has its own rate-of-strain tensor, and the viscosity tensors are of the form

$$\pi_{xx} = -\frac{\eta_0}{2}(W_{xx} + W_{yy}) - \frac{\eta_1}{2}(W_{xx} - W_{yy}) - \eta_3 W_{xy} \quad (9.130)$$

$$\pi_{yy} = -\frac{\eta_0}{2}(W_{xx} + W_{yy}) - \frac{\eta_1}{2}(W_{yy} - W_{xx}) + \eta_3 W_{xy} \quad (9.131)$$

$$\pi_{xy} = \pi_{yx} = -\eta_1 W_{xy} + \frac{\eta_3}{2}(W_{xx} - W_{yy}) \quad (9.132)$$

$$\pi_{xz} = \pi_{zx} = -\eta_2 W_{xz} - \eta_4 W_{yz} \quad (9.133)$$

$$\pi_{yz} = \pi_{zy} = -\eta_2 W_{yz} + \eta_4 W_{xz} \quad (9.134)$$

$$\pi_{zz} = -\eta_0 W_{zz} \quad (9.135)$$

where the coordinate system (x, y, z) is taken to be aligned with the magnetic field, $\hat{\mathbf{n}}_\parallel = (0, 0, 1)$.

All terms in the viscosity tensor are small (by factors of r_L/L_\perp or $v_{\text{th}}\tau/L_\parallel$) in comparison with the other terms in the momentum equation. Thus,

$$\nabla \cdot \pi \ll \nabla p \sim \mathbf{R} \quad (9.136)$$

since the lowest-order Maxwellian distribution does not contribute to the viscosity. Nevertheless, this does not mean that viscosity is unimportant. For instance, in a tokamak the parallel pressure gradient vanishes in leading order and parallel viscosity plays a crucial role in determining the parallel flow velocity. The viscosity coefficients for ions are

$$\eta_\parallel^i: \quad \eta_0^i = 0.96 n_i T_i \tau_i \quad (9.137)$$

$$\eta_\perp^i: \quad \eta_1^i = \frac{3n_i T_i}{10\Omega_i^2 \tau_i} = \eta_2^i/4 \quad (9.138)$$

$$\eta_\Omega^i: \quad \eta_4^i = \frac{n_i T_i}{\Omega_i} = 2\eta_3^i \quad (9.139)$$

and for electrons

$$\eta_{\parallel}^e: \quad \eta_0^e = 0.73 n_e T_e \tau_e \quad (9.140)$$

$$\eta_{\perp}^e: \quad \eta_1^e = 0.51 \frac{n_e T_e}{\Omega_e^2 \tau_e} = \eta_2^e / 4 \quad (9.141)$$

$$\eta_{\Omega}^e: \quad \eta_4^e = \frac{n_e T_e}{\Omega_e} = 2\eta_3^e \quad (9.142)$$

As in the case of the heat flux, we see that the viscosity contains terms with different dependences on the collision frequency. First, there is a part proportional to τ , $\eta_0 \sim n T \tau$, similar to that for an ordinary gas. This scaling is identical to that of parallel heat conduction and reflects transport of momentum due to random walk with a step size equal to the mean free path. Second, there are entries in the viscosity tensor proportional to η_1 and η_2 , which scale as the perpendicular heat conduction coefficient κ_{\perp} . They come from random walk transport of momentum with a step size equal to the Larmor radius, and are therefore smaller than the parallel viscosity η_0 by a factor of $(\Omega \tau)^2$. Finally, there is the contribution from “gyroviscosity” proportional to η_3 and η_4 . This contribution is inversely proportional to the gyrofrequency but is completely independent of the collision frequency. Gyroviscosity represents a diamagnetic flow of momentum across the field, and is analogous to the term q_{Ω} in the heat flux.

9.6 Neoclassical Transport – Trapped Particles

When a tokamak plasma has sufficiently long mean time, τ_{90} , between collisions that the particles can execute the type of trapped particle orbits described in chapter 3, a second type of neoclassical transport effect becomes important.

The starting point for our investigation of trapped particle effects is the drift-kinetic equation, Eq. (4.21). We consider the time-independent problem with no electric field and with no source, in which case the drift-kinetic equation is

$$(\mathbf{v}_{\text{dr}} + \mathbf{v}_{\parallel}) \cdot \nabla \hat{f} = C = \left. \frac{\partial \hat{f}}{\partial t} \right|_c \quad (9.143)$$

The guiding center distribution function, $\hat{f} = \hat{f}(r, \theta, \bar{\mu}, W)$, is a function of the poloidal angle, θ , the minor radius, r , the particle magnetic moment,

$$\bar{\mu} = \frac{1}{2} \frac{m v_{\perp}^2}{B} \quad (9.144)$$

and the particle energy,

$$W = \frac{1}{2} m (v_{\perp}^2 + v_{\parallel}^2) \quad (9.145)$$

The parallel velocity, v_{\parallel} , is given by

$$v_{\parallel} \simeq \left\{ \frac{2}{m} \left[W - \bar{\mu} B^0 \left(1 - \frac{r}{R_0} \cos \theta \right) \right] \right\}^{\frac{1}{2}} \quad (9.146)$$

and is not an independent variable, but is a function $v_{\parallel} = v_{\parallel}(r, \theta, \bar{\mu}, W)$ of other variables. (Species subscripts are suppressed in this section.)

If we make the plausible assumption that $|v_{\parallel}| \gg |v_{\text{dr}}|$, then the θ -component of \mathbf{v}_{dr} can be neglected, and the r -component of \mathbf{v}_{dr} from Eq. (4.21),

$$v_{\text{dr},r} = \frac{mv_{\parallel}}{eR_0B^0} \frac{1}{r} \frac{\partial(Rv_{\parallel})}{\partial\theta} \quad (9.147)$$

can be used in Eq. (9.143) to obtain

$$\frac{mv_{\parallel}}{eR_0B^0} \frac{1}{r} \frac{\partial(Rv_{\parallel})}{\partial\theta} \frac{\partial\hat{f}}{\partial r} + v_{\parallel} \frac{B_\theta^0}{B^0} \frac{1}{r} \frac{\partial\hat{f}}{\partial\theta} = \frac{\partial\hat{f}}{\partial t} \Big|_c \quad (9.148)$$

The collision operator will be evaluated using the Fokker–Planck theory introduced in chapter 4. If the principal scattering of interest involves light particles (e.g., electrons) from heavy particles (e.g., ions), then the scattering event produces a change in $\bar{\mu}$ but a negligible change in W for the scattering particle. We assume this type of “pitch-angle” scattering to be dominant. Since the scattering event takes place without a change in spatial location, the only variable that changes during pitch-angle scattering is $\bar{\mu}$.

Define a distribution function, $g(\bar{\mu})$, and a probability, $P(\bar{\mu}, \Delta\bar{\mu})$, that a particle with magnetic moment, $\bar{\mu}$, will undergo a change of magnetic moment, $\Delta\bar{\mu}$, in unit time. The distribution function must satisfy

$$g(\bar{\mu}, t) = \int g(\bar{\mu} - \Delta\bar{\mu}, t - \Delta t) P(\bar{\mu} - \Delta\bar{\mu}, \Delta\bar{\mu}) d\Delta\bar{\mu} \quad (9.149)$$

Because of the preponderance of small-angle-deflection scattering events, $\Delta\bar{\mu} \rightarrow 0$ when $\Delta t \rightarrow 0$. This enables a Taylor’s series expansion to be made in Eq. (9.149), leading to the Fokker–Planck equation appropriate to this problem,

$$\frac{\partial g}{\partial t} \Big|_c = -\frac{\partial}{\partial\bar{\mu}} [g(\bar{\mu})\langle\Delta\bar{\mu}\rangle] + \frac{1}{2} \frac{\partial^2}{\partial\bar{\mu}^2} \left[g(\bar{\mu}) \langle (\Delta\bar{\mu})^2 \rangle \right] \quad (9.150)$$

where

$$\begin{aligned} \langle\Delta\bar{\mu}\rangle &\equiv \frac{1}{\Delta t} \int P(\bar{\mu}, \Delta\bar{\mu})(\Delta\bar{\mu}) d(\Delta\bar{\mu}) \\ \langle(\Delta\bar{\mu})^2\rangle &\equiv \frac{1}{\Delta t} \int P(\bar{\mu}, \Delta\bar{\mu})(\Delta\bar{\mu})^2 d(\Delta\bar{\mu}) \end{aligned} \quad (9.151)$$

Detailed balance must obtain in an equilibrium situation – the rate of scattering from the phase space volume element about $\bar{\mu}$ into the phase volume element about $\bar{\mu} + \Delta\bar{\mu}$ must equal the rate for the inverse process. The phase space volume element is

$$d^3v = (dv_{\parallel})(2\pi v_{\perp} dv_{\perp}) = \pi dv_{\parallel} dv_{\perp}^2 = \pi J dW d\bar{\mu} \quad (9.152)$$

where

$$J = \frac{2B}{m^2 |v_{\parallel}|} \quad (9.153)$$

is the Jacobian of the transformation between $(v_{\parallel}, v_{\perp})$ -space and $(W, \bar{\mu})$ -space. Using Eq. (9.153), the principle of detailed balance can be written

$$P(\bar{\mu}, \Delta\bar{\mu})\pi J(\bar{\mu}) dW d\bar{\mu} = P(\bar{\mu} + \Delta\bar{\mu}, -\Delta\bar{\mu})\pi J(\bar{\mu} + \Delta\bar{\mu}) dW d\bar{\mu} \quad (9.154)$$

Taking a $\Delta\bar{\mu}$ moment of Eq. (9.154), making use of Eq. (9.153), and making a Taylor expansion yields

$$\frac{\partial}{\partial\bar{\mu}} \left[\left(\frac{\langle \Delta\bar{\mu} \rangle}{v_{\parallel}} \right) - \frac{1}{2} \frac{\partial}{\partial\bar{\mu}} \left(\frac{\langle (\Delta\bar{\mu})^2 \rangle}{v_{\parallel}} \right) \right] = 0 \quad (9.155)$$

where $\langle \Delta\bar{\mu} \rangle$, $\langle (\Delta\bar{\mu})^2 \rangle$ and v_{\parallel} are considered as functions of $\bar{\mu}$. This equation can be integrated once. The constant of integration must vanish because $\langle \Delta\bar{\mu} \rangle$ physically cannot depend on the sign of v_{\parallel} . The resulting equation – the quantity in square brackets in Eq. (9.155) set equal to zero – can be used to simplify Eq. (9.150) to

$$\frac{\partial g}{\partial t} \Big|_c = \frac{1}{2} \frac{\partial}{\partial\bar{\mu}} \left[\frac{\langle (\Delta\bar{\mu})^2 \rangle}{v_{\parallel}} \frac{\partial}{\partial\bar{\mu}} (v_{\parallel} g) \right] \quad (9.156)$$

Noting that

$$\hat{f}(\mathbf{v}) d^3v = \hat{f}(\mathbf{v}) \pi J(\bar{\mu}) dW d\bar{\mu} = g(\bar{\mu}) dW d\bar{\mu} \quad (9.157)$$

we see that $gv_{\parallel} \sim \hat{f}$, the particle distribution function. Thus Eq. (9.156) becomes

$$\frac{\partial \hat{f}}{\partial t} \Big|_c = \frac{1}{2} v_{\parallel} \frac{\partial}{\partial\bar{\mu}} \left[\frac{\langle (\Delta\bar{\mu})^2 \rangle}{v_{\parallel}} \frac{\partial \hat{f}}{\partial\bar{\mu}} \right] \quad (9.158)$$

The moments $\langle (\Delta\bar{\mu})^2 \rangle$ can be evaluated by an analysis similar to that of section 4.3 for Coulomb scattering. The result is, for the Lorentz model,

$$\langle (\Delta\bar{\mu})^2 \rangle = \frac{v(W)m}{B} v_{\parallel}^2 \bar{\mu} \quad (9.159)$$

where $v(W)$ is the 90° collision frequency, τ_{90}^{-1} , as given e.g. by Eq. (9.31). Substituting Eq. (9.159) in Eq. (9.158) provides a representation of the Fokker–Planck collision operator that can be used in the drift-kinetic equation, Eq. (9.143), to obtain

$$\frac{mv_{\parallel}}{eR_0 B^0} \frac{1}{r} \frac{\partial(Rv_{\parallel})}{\partial\theta} \frac{\partial \hat{f}}{\partial r} + v_{\parallel} \frac{B_{\theta}^0}{B^0} \frac{1}{r} \frac{\partial \hat{f}}{\partial\theta} = \frac{\partial \hat{f}}{\partial t} \Big|_c = \frac{mvv_{\parallel}}{B} \frac{\partial}{\partial\bar{\mu}} \left(v_{\parallel} \bar{\mu} \frac{\partial \hat{f}}{\partial\bar{\mu}} \right) \quad (9.160)$$

To solve Eq. (9.160) analytically, we resort to a hierarchy of expansions in small parameters. Three small parameters may be identified: (1) if the magnetic field is large, then the ratio, δ , of the gyroradius to perpendicular gradient scale length is a small parameter; (2) if the plasma is sufficiently hot and insufficiently dense, then the ratio, $v^* = vrB^0/v_{\parallel}B_{\theta}^0$, of the collision frequency to the bounce frequency of a trapped particle is a small parameter;

(3) if the aspect ratio is large, the ratio $\epsilon = r/R_0$ is a small parameter. We postulate that these three conditions obtain. We expand the distribution function to first order in δ ,

$$\hat{f} = \hat{f}^0 + \hat{f}^1 \quad (9.161)$$

where the superscript indicates the order in δ , and note that the first term in Eq. (9.160) is of one order higher in δ than are the other two terms. The Maxwellian distribution

$$\hat{f}^0 = f^{\text{Max}} = \frac{n(r)}{(2\pi m T)^{\frac{3}{2}}} e^{-(\frac{v}{T})} \quad (9.162)$$

satisfies $(\partial \hat{f}^0 / \partial t)|_c = \partial \hat{f}^0 / \partial \theta = 0$. (We could allow the temperature, T , to be spatially dependent and obtain temperature gradient terms as well as density gradient terms in the final expression for the particle flux. However we use a uniform T , for simplicity). Using Eqs. (9.161) and (9.162) in Eq. (9.160), the $0(\delta)$ equation is

$$v_{\parallel} \frac{B_{\theta}^0}{B^0} \frac{1}{r} \frac{\partial \hat{f}^1}{\partial \theta} + \frac{mv_{\parallel}}{eR_0 B^0} \frac{1}{r} \frac{\partial(Rv_{\parallel})}{\partial \theta} \frac{\hat{f}^0}{n} \frac{\partial n}{\partial r} = \frac{\partial \hat{f}^1}{\partial t} \Big|_c = \frac{mvv_{\parallel}}{B} \frac{\partial}{\partial \bar{\mu}} \left(v_{\parallel} \bar{\mu} \frac{\partial \hat{f}^1}{\partial \bar{\mu}} \right) \quad (9.163)$$

Now the $0(\delta)$ distribution function, \hat{f}^1 , is expanded to first order in v^* ,

$$\hat{f}^1 = \hat{f}_0^1 + \hat{f}_1^1 \quad (9.164)$$

where the subscript indicates the order in v^* . Note the RHS of Eq. (9.163) is of one order higher in v^* than the LHS, so to lowest order in v^* , $0(1)$, we obtain

$$v_{\parallel} \frac{B_{\theta}^0}{B^0} \frac{1}{r} \frac{\partial \hat{f}_0^1}{\partial \theta} = - \frac{mv_{\parallel}}{eR_0 B^0} \frac{1}{r} \frac{\partial(Rv_{\parallel})}{\partial \theta} \frac{\hat{f}^0}{n} \frac{\partial n}{\partial r} \quad (9.165)$$

which may be integrated to obtain

$$\hat{f}_0^1(r, \theta, \bar{\mu}, W) = - \frac{mv_{\parallel}}{eB_{\theta}^0} \frac{\hat{f}^0}{n} \frac{\partial n}{\partial r} + C_1(\bar{\mu}, W) \quad (9.166)$$

To first order in v^* Eq. (9.163) yields

$$v_{\parallel} \frac{B_{\theta}^0}{B^0} \frac{1}{r} \frac{\partial \hat{f}_1^1}{\partial \theta} = \frac{\partial \hat{f}_0^1}{\partial t} \Big|_c = \frac{mvv_{\parallel}}{B} \frac{\partial}{\partial \bar{\mu}} \left(v_{\parallel} \bar{\mu} \frac{\partial C_1}{\partial \bar{\mu}} \right) + \frac{mvv_{\parallel}}{eB_{\theta}^0} \frac{\hat{f}^0}{n} \frac{\partial n}{\partial r} \quad (9.167)$$

This equation may be integrated over a period in θ , and the requirement that \hat{f}_1^1 be a single-valued function of θ can be used to obtain

$$0 = \frac{B_{\theta}^0}{B^0} \frac{1}{r} \oint \frac{\partial \hat{f}_1^1}{\partial \theta} d\theta = \oint \frac{1}{v_{\parallel}} \frac{\partial \hat{f}_0^1}{\partial t} \Big|_c d\theta \quad (9.168)$$

The $\oint d\theta/v_{\parallel}$ -integration of the second term on the RHS of Eq. (9.167) is different for trapped and untrapped particles.

$$\frac{mv}{eB_{\theta}^0} \frac{\hat{f}^0}{n} \frac{\partial n}{\partial r} \oint d\theta \begin{cases} = 0 & \text{(trapped)} \\ = \frac{2\pi mv}{eB_{\theta}^0} \frac{\hat{f}^0}{n} \frac{\partial n}{\partial r} & \text{(untrapped)} \end{cases} \quad (9.169)$$

Thus, for trapped particles, Eq. (9.168) requires

$$\frac{mv}{B^0} \frac{\partial}{\partial \bar{\mu}} \left[\bar{\mu} \left(\oint v_{\parallel} d\theta \right) \frac{\partial C_1}{\partial \bar{\mu}} \right] = 0 \quad (9.170)$$

which is satisfied by

$$C_1(\bar{\mu}, W) = 0, \quad \bar{\mu} \geq \bar{\mu}_t \quad (9.171)$$

where

$$\bar{\mu}_t = \frac{W}{B^0(1 + \epsilon)} \quad (9.172)$$

is the smallest value of $\bar{\mu}$ for which a particle can be trapped. For untrapped particles, Eq. (9.168) requires

$$\frac{1}{B^0} \frac{\partial}{\partial \bar{\mu}} \left[\bar{\mu} \left(\oint v_{\parallel} d\theta \right) \frac{\partial C_1}{\partial \bar{\mu}} \right] + \frac{2\pi}{eB_{\theta}^0} \frac{\hat{f}^0}{n} \frac{\partial n}{\partial r} = 0 \quad (9.173)$$

which may be integrated to obtain

$$\frac{\partial C_1(\bar{\mu}, W)}{\partial \bar{\mu}} = -\frac{2\pi B^0 f^0}{eB_{\theta}^0} \frac{1}{n} \frac{\partial n}{\partial r} \quad (9.174)$$

where the constant of integration was set to zero to make the equation regular at $\bar{\mu} = 0$. Equation (9.174) can be integrated from $\bar{\mu}_t$ to $\bar{\mu}$ (i.e., over the untrapped space) to obtain

$$C_1(\bar{\mu}, W) = \int_{\bar{\mu}_t}^{\bar{\mu}} \frac{2\pi B^0 f^0}{eB_{\theta}^0} \frac{1}{n} \frac{\partial n}{\partial r} d\bar{\mu}' \quad (9.175)$$

where the condition $C_1(\bar{\mu}_t, W) = 0, \bar{\mu} \geq \bar{\mu}_t$ has been used. This expression for C_1 can be used in Eq. (9.166) to obtain an expression for the distribution function,

$$\hat{f}_0^1(r, \theta, \bar{\mu}, W) = -\frac{m \hat{f}^0}{eB_{\theta}^0} \frac{1}{n} \frac{\partial n}{\partial r} \left(v_{\parallel} - \int_{\bar{\mu}_t}^{\bar{\mu}} \frac{2\pi B^0}{m \oint v_{\parallel} d\theta} d\bar{\mu}' \right) \quad (9.176)$$

for untrapped particles, $\bar{\mu} < \bar{\mu}_t$. The last term in the brackets is missing in the distribution function for trapped particles.

The particle flux across the flux surface, averaged over the flux surface, is

$$\Gamma \equiv \langle nv_r \rangle = \frac{1}{2\pi} \int h d\theta d^3v \hat{f} v_{dr,r} \quad (9.177)$$

Using Eq. (9.147) for $v_{dr,r}$ and the transformation of Eq. (9.152), integrating by parts over θ and making use of the fact that $\partial \hat{f}^0 / \partial \theta = 0$, leads to

$$\Gamma = -\frac{1}{emR_0 r} \int d\theta d\bar{\mu} dW \frac{v_\parallel^2}{|v_\parallel|} R \frac{\partial \hat{f}^1}{\partial \theta} \quad (9.178)$$

Using Eq. (9.163), this becomes

$$\begin{aligned} \Gamma = & -\frac{B^0}{emR_0 B_\theta^0} \int d\theta d\bar{\mu} dW \frac{(Rv_\parallel)}{|v_\parallel|} \left. \frac{\partial \hat{f}^1}{\partial t} \right|_c \\ & + \frac{1}{(eR_0)^2 r B_\theta^0} \int d\bar{\mu} dW \int d\theta (Rv_\parallel) \frac{\partial (Rv_\parallel)}{\partial \theta} \hat{f}^0 \end{aligned} \quad (9.179)$$

The integrand in the last term in Eq. (9.179) is a perfect differential over θ and therefore vanishes upon integration because of the requirement that Rv_\parallel be single-valued.

We see from the first, nonvanishing, term in Eq. (9.179) that particle fluxes are driven across flux surfaces by collisional friction, in agreement with the result obtained previously from an analysis of the moments equations. Using the transformation of Eq. (9.152) again, this result becomes,

$$\Gamma = -\frac{1}{eB_\theta^0 R_0 2\pi} \int R d\theta \int d^3v m v_\parallel \left. \frac{\partial \hat{f}^1}{\partial t} \right|_c \quad (9.180)$$

a form which lends itself to the interpretation that a transport flux is driven across flux surfaces by a collisional exchange of angular momentum with other species. Note that the integral over d^3v must vanish for like-particle collisions because of conservation of momentum, so that like-particle collisions do not produce a transport flux, in this $0(\delta)$ approximation.

Now, Eq. (9.163) can be used to represent the Fokker–Planck collision operator in Eq. (9.179) or Eq. (9.180), and Eq. (9.176) can be used to obtain the results to lowest order in v^*

$$\Gamma = -\frac{1}{(eB_\theta^0)^2 m R_0} \int d\theta d\bar{\mu} dW \frac{\bar{\mu} v R B^2}{|v_\parallel|} \left(1 - \frac{2\pi v_\parallel}{\phi v_\parallel d\theta} \right) \hat{f}^0 \quad (9.181)$$

where the second term in the brackets only obtains for untrapped particles; that is, for $\bar{\mu} < \bar{\mu}_t$.

In the large aspect ratio limit, $\epsilon \ll 1$, the integral appearing in Eq. (9.181) for untrapped particles can be evaluated

$$\begin{aligned} \oint v_{\parallel}(\bar{\mu}) d\theta &= \oint \left\{ \frac{2}{m} \left[W - \bar{\mu} B^0 (1 - \epsilon \cos \theta) \right] \right\}^{\frac{1}{2}} d\theta \\ &\simeq 2\pi \left[\frac{2}{m} (W - \bar{\mu} B^0) \right]^{\frac{1}{2}} \left[1 + O(\epsilon^2) \right] \\ &= 2\pi v_{\parallel}^0 \left[1 + O(\epsilon^2) \right] \end{aligned} \quad (9.182)$$

so that the term in brackets is $O(\epsilon^2)$ for untrapped particles. For the trapped particles, which constitute a fraction $\sim \epsilon^{\frac{1}{2}}$ of the total particles and for which $\bar{\mu} B \simeq W$, the quantity in brackets is unity. Thus, to lowest order in ϵ , Eq. (9.181) becomes

$$\Gamma \simeq \frac{1}{(eB_{\theta}^0)^2} \int d\theta \int d\bar{\mu} dW \frac{BvW\hat{f}^0}{m|v_{\parallel}|} = -\frac{\epsilon^{\frac{1}{2}} \frac{\partial n}{\partial r} m}{(eB_{\theta}^0)^2} \int d\theta \int \frac{d^3 v v W \hat{f}^0}{2\pi n} \quad (9.183)$$

The integral in Eq. (9.183) has the form of an average of vW over the distribution function. Defining an effective collision frequency, \bar{v} , Eq. (9.183) can be approximated by

$$\Gamma \simeq -\bar{v} \left(\frac{mv_{\text{th}}}{eB_{\theta}^0} \right)^2 \epsilon^{\frac{1}{2}} \frac{\partial n}{\partial r} \simeq -\bar{v} r_L^2 q^2 \epsilon^{-\frac{3}{2}} \frac{\partial n}{\partial r} = -D^{\text{BP}} \frac{\partial n}{\partial r} \quad (9.184)$$

where $r_L \equiv (mv_{\perp}/eB^0)$ is the gyroradius and $q \equiv \epsilon B^0 / B_{\theta}^0$ is the safety factor. A similar development leads to a neoclassical expression for the thermal conductivity

$$\chi^{\text{BP}} = \bar{v} r_L^2 q^2 \epsilon^{-\frac{3}{2}} \quad (9.185)$$

where ‘‘BP’’ indicates banana-plateau.

By way of comparison, the classical transport flux developed in section 9.2 and the neoclassical, Pfirsch–Schlüter flux developed in section 9.3 can be written

$$\Gamma^C \simeq -\bar{v} r_L^2 \frac{\partial n}{\partial r}, \quad \Gamma^{\text{PS}} \simeq -\nu r_L^2 2q^2 \frac{\partial n}{\partial r} \quad (9.186)$$

when temperature gradients are neglected. These fluxes could be derived from the drift-kinetic theory, also, by making the approximation $v^* \gg 1$. Thus, the first neoclassical effect, due to the toroidal geometry, introduces a q^2 enhancement of the classical transport flux. The second neoclassical effect, due to trapped particles, introduces an additional $\epsilon^{-\frac{3}{2}}$ enhancement of the transport flux when $v^* \ll 1$.

9.7 Chang–Hinton Ion Thermal Conductivity*

It is clear from the previous development of neoclassical transport theory that there are numerous factors which affect the form of the theory. An expression for the ion thermal

conductivity which incorporates finite aspect ratio effects, interpolates between banana and Pfirsch–Schlüter collisionality regimes, and allows for the effects of impurities is the Chang–Hinton formula

$$\chi_i = \frac{n_i \epsilon^{-\frac{3}{2}} q^2 r_{Li}}{\tau_i} \left\{ \left[\frac{0.66(1 + 1.54\alpha) + (1.88\epsilon^{\frac{1}{2}} - 1.54\epsilon)(1 + 3.75\alpha)}{1 + 1.03\mu_{*i}^{\frac{1}{2}} + 0.31\mu_{*i}} \right] g_1 + \frac{0.58\mu_{*i}\epsilon}{(1 + 0.74\mu_{*i}\epsilon^{\frac{3}{2}})} \left[1 + \frac{1.33\alpha(1 + 0.60\alpha)}{1 + 1.79\alpha} \right] (g_1 - g_2) \right\} \quad (9.187)$$

where $\epsilon = r/R$, $r_{Li} = (2T_i/m_i)^{\frac{1}{2}}/e_i B/m_i$, $\alpha = n_i Z_i^2/n_i Z_i^2$ measures the effect of impurity ions with charge Z_i and density n_i , and $\mu_{*i} = v_{*i}(1 + 1.54\alpha)$, with $v_{*i} = v_i Rq/\epsilon^{\frac{3}{2}} v_{th,i}$ being a collisionality parameter allowing the interpolation between collision regimes. The first term in Eq. (9.187) contains a factor

$$g_1 = \frac{1 + \frac{3}{2}(\epsilon^2 + \epsilon\Delta') + \frac{3}{8}\epsilon^3\Delta'}{1 + \frac{1}{2}\epsilon\Delta'} \quad (9.188)$$

with $\Delta' = d\Delta/dr$ being the derivative of the Shafranov shift (section 6.5). This term describes the neoclassical contributions from the banana and plateau regimes and the transition between them as μ_{*i} varies.

The corrections proportional to $\epsilon^{\frac{1}{2}}$ and to ϵ represent the effects of energy scattering terms in the collision operator which play a role at finite aspect ratio when the fraction of trapped particles is not small. The second term in Eq. (9.187), which has a factor $g_1 - g_2$, where

$$g_2 = \frac{\sqrt{1 - \epsilon^2} \left(1 + \frac{\epsilon\Delta'}{2} \right)}{1 - \frac{\Delta'}{\epsilon} \left(\sqrt{1 - \epsilon^2} - 1 \right)} \quad (9.189)$$

represents the Pfirsch–Schlüter contribution.

9.8 Extended Neoclassical Transport – Fluid Theory*

In the previous discussion of transport in this chapter, the plasma has been considered as a closed system with no external sources or sinks of particles, momentum, or energy. Most plasmas are heated by external means; e.g., by neutral beams, which are a source of particles, momentum, and energy. Such external sources can have a profound effect on transport, which we examine in this section by formally deriving expressions for cross-field particle transport from the multifluid momentum balance equations extended to include external momentum input and cross-field momentum transport

$$n_j m_j (\mathbf{v}_j \cdot \nabla) \mathbf{v}_j + \nabla p_j + \nabla \cdot \pi_j = -n_j e_j \nabla \Phi + n_j e_j (\mathbf{v}_j \times \mathbf{B}) + \mathbf{R}_j + \mathbf{M}_j \quad (9.190)$$

where \mathbf{M} is any external momentum input (e.g., from NBI) or loss (e.g., from charge-exchange) and the other symbols are standard. This multifluid model is supplemented

by constitutive relations from kinetic theory for the collisional interspecies momentum exchange

$$\mathbf{R}_j = -n_j m_j \sum_{k \neq j} v_{jk} (\mathbf{v}_j - \mathbf{v}_k) \quad (9.191)$$

and for the neoclassical parallel viscous force

$$\mathbf{B} \cdot \nabla \cdot \pi_j = 3 \langle (\hat{\mathbf{n}}_\parallel \cdot \nabla \mathbf{B})^2 \rangle \left[\frac{R q n_j m_j v_{\text{th},j} v_j^*}{(1 + v_j^*)(1 + \epsilon^{\frac{3}{2}} v_j^*)} \right] \frac{\mathbf{v}_j \cdot \mathbf{B}_\theta}{B_\theta^2} \quad (9.192)$$

where $v_j^* \equiv v_{jj} q R / \epsilon^{\frac{3}{2}} v_{\text{th},j}$. In toroidal geometry $\langle (\hat{\mathbf{n}}_\parallel \cdot \nabla \mathbf{B})^2 \rangle = \frac{1}{2} (\epsilon/qR)^2 B^2$, where $\epsilon = r/R$. The flux surface averaged toroidal component of the neoclassical viscous torque will be written

$$\langle R^2 \nabla \phi \cdot \nabla \cdot \pi_j \rangle = R n_j m_j v_{\text{d},j} v_{\phi,j} \quad (9.193)$$

We will discuss the evaluation of this toroidal viscous force in the next chapter.

9.8.1 Radial Electric Field

The component of the radial electric field which is constant over the flux surface is obtained self-consistently from the flux surface averaged toroidal projection of the momentum balance equation summed over species. At this point, we specialize the formalism to a main ion species “*i*” and an impurity species “*I*” in order to simplify (note that we are assuming that the impurity concentration is sufficient that Eq. (9.38) is satisfied and collisions with electrons can be ignored). With this specialization, the radial electric field may be written

$$\begin{aligned} \frac{E_r}{B_\theta} = & \left[\{\hat{\mu}_i + \hat{\mu}_I(1 + \xi_i)\} \hat{M}_{\phi I} + \{\hat{\mu}_I + \hat{\mu}_i(1 + \xi_I)\} \hat{M}_{\phi i} \right. \\ & + \{\beta_i + \beta_I(1 + \xi_i)\} \hat{\mu}_I P'_I + \{\beta_I + \beta_i(1 + \xi_I)\} \hat{\mu}_i P'_i \Big] \\ & \div [\hat{\mu}_i \{\beta_I + \beta_i(1 + \xi_I)\} + \hat{\mu}_I \{\beta_i + \beta_I(1 + \xi_i)\}] \end{aligned} \quad (9.194)$$

where $M_{\phi,j}$ is the normalized toroidal projection of the neutral beam (or other) momentum input on the given flux surface, P'_j is the normalized radial pressure gradient across the given flux surface, and

$$\begin{aligned} \hat{\mu}_j & \equiv \frac{\frac{3}{2} \sqrt{\epsilon} (v_{jj}/v_{jk})}{(1 + v_j^*)(1 + \epsilon^{\frac{3}{2}} v_j^*)} & P'_j & \equiv \frac{1}{n_j e_j B_\theta} \frac{\partial p_j}{\partial r} \\ \beta_j & \equiv \frac{v_{\text{d},j}}{v_{jk}} & \xi_j & \equiv \hat{\mu}_j + \beta_j \hat{M}_{\phi j} \equiv \frac{M_{\phi j}}{n_j m_j v_{jk}} \end{aligned} \quad (9.195)$$

9.8.2 Toroidal Rotation

The parallel flux surface averaged component of Eq. (9.190) can now be solved for the impurity toroidal velocity on the flux surface

$$\begin{aligned} v_{\phi I} = & \left[\left\{ \hat{M}_{\parallel} + (1 + \xi_i) \hat{M}_{\parallel} \right\} - \left\{ \hat{\mu}_I (1 + \xi_i) P'_I + \hat{\mu}_i P'_i \right\} \right. \\ & \left. + \left\{ \hat{\mu}_I (1 + \xi_i) + \hat{\mu}_i \right\} \left(\frac{E_r}{B_\theta} \right) \right] \Big/ [\xi_i (1 + \xi_I) + \xi_I] \end{aligned} \quad (9.196)$$

and for the (small) difference in main ion and impurity toroidal velocities,

$$v_{\phi i} - v_{\phi I} = \left[(\hat{\mu}_i + \hat{\mu}_I) (\beta_I \hat{M}_{\parallel} - \beta_i \hat{M}_{\parallel}) - \hat{\mu}_i \hat{\mu}_I (\beta_i + \beta_I) (P'_i - P'_I) \right] \quad (9.197)$$

9.8.3 Transport Fluxes

The toroidal component of the momentum balance equation for each species can be flux surface averaged to obtain an expression for the cross field (radial) transport flux $\Gamma_{rj} \equiv n_j \mathbf{v}_{rj}$,

$$\begin{aligned} e_j \Gamma_j = & \left\langle R^2 \nabla \phi \cdot \nabla p_j \right\rangle + \left\langle R^2 \nabla \phi \cdot \nabla \cdot \pi_j \right\rangle - \left\langle R^2 \nabla \phi \cdot \mathbf{M}_j \right\rangle \\ & + \left\langle R^2 \nabla \phi \cdot (n_j m_j (\mathbf{v}_j \cdot \nabla) \mathbf{v}_j) \right\rangle + \left\langle R^2 \nabla \phi \cdot n_j e_j \nabla \Phi \right\rangle \\ & - \left\langle R^2 \nabla \phi \cdot \mathbf{R}_j \right\rangle \end{aligned} \quad (9.198)$$

Using Eq. (9.196) and Eq. (9.197) for toroidal rotation velocities, this expression for the radial particle flux may be written in a form that associates various terms with conventional neoclassical fluxes or with one of the various effects discussed previously. For the impurities

$$\Gamma_I \equiv \Gamma_I^{\text{PS}} + \Gamma_I^{\text{nc}} + \Gamma_I^M + \Gamma_I^I + \Gamma_I^{\Phi'} + \Gamma_I^{\tilde{\Phi}} \quad (9.199)$$

Explicit expressions for the various terms in Eq. (9.199) are given below for the “two-species” approximation. The value B_θ is positive or negative depending on whether the toroidal current is parallel or antiparallel, respectively, with the toroidal magnetic field, and the value of M_ϕ or M_{\parallel} is positive or negative depending on whether the beam injection direction is parallel or antiparallel, respectively, to the toroidal magnetic field.

The first two terms correspond to the Pfirsch–Schlüter and trapped particle “neoclassical” fluxes of conventional neoclassical theory

$$\begin{aligned} \Gamma_I^{\text{PS}} = & \frac{n_I m_I v_{Ii} \epsilon^2}{e_I B_\theta} \left[\left\{ \left(\frac{1 + 2q^2}{q^2} \right) + \tilde{n}_i^c \right\} P'_i \right. \\ & \left. - \left\{ \left(\frac{1 + 2q^2}{q^2} \right) + \tilde{n}_I^c \right\} (1 + \beta_I) P'_I \right] \end{aligned} \quad (9.200)$$

and

$$\begin{aligned}\Gamma_I^{nc} = & \frac{n_I m_I v_{Ii}}{e_I B_\theta d} \left[\left\{ \hat{\mu}_i \hat{\mu}_I + \epsilon^2 \hat{\mu}_i ((1 + \beta_I) \tilde{n}_I^c - \tilde{n}_i^c) \right\} P'_i \right. \\ & \left. - \left\{ \hat{\mu}_I (\xi_i + \beta_I (1 + \xi_i)) + \epsilon^2 \mu_I (\tilde{n}_i^c - \tilde{n}_I^c) \right\} P'_I \right] \end{aligned}\quad (9.201)$$

where

$$d \equiv \xi_i + \xi_I (1 + \xi_i) \quad (9.202)$$

For a negative main ion pressure gradient ($P'_i < 0$), these fluxes are generally inward for impurities and outward for main ions. The corresponding main ion transport fluxes are given by similar expressions with the i and I subscripts interchanged.

The third flux component in Eq. (9.199) is the contribution resulting directly from momentum exchange between beam ions and plasma and impurity ions,

$$\begin{aligned}\Gamma_I^M = & -\frac{n_I m_I v_{Ii}}{e_I B_\theta d} \times \left[\hat{M}_{\phi I} \left\{ \hat{\mu}_I (1 + \xi_i) + \epsilon^2 (d + (1 + d) \tilde{n}_I^c - (1 + \xi_i) \tilde{n}_i^c) \right\} \right. \\ & \left. + \hat{M}_{\phi i} \left\{ \hat{\mu}_I + \epsilon^2 \left(\left(1 + \frac{1}{2} (\beta_I + \xi_I) \right) \tilde{n}_I^c - \tilde{n}_i^c \right) \right\} \right] \end{aligned}\quad (9.203)$$

The corresponding main ion flux component is given by a similar express with i and I interchanged. Both the impurity and main ion fluxes are generally inward for co-injection ($M_\phi > 0$) and outward for counterinjection ($M_\phi < 0$), when the toroidal current is in the same direction as the toroidal magnetic field, and conversely when the toroidal current and magnetic field are antiparallel.

The fourth flux component in Eq. (9.199) results from the inertial ($nm(\mathbf{v} \cdot \nabla)\mathbf{v}$) term in the momentum balance equation, which produces $O(\epsilon^2)$ terms in the rotation velocities, which in turn contribute an $O(\epsilon^2)$ flux component

$$\Gamma_I^I = -\frac{n_I m_I v_{Ii} \epsilon^2 B_\phi}{e_I B_\theta B^2 d} \left[(\xi_i + \beta_I (1 + \xi_i)) \langle \hat{G}_I \rangle - \hat{\mu}_I \langle \hat{G}_I \rangle \right] \quad (9.204)$$

where

$$\langle \hat{G}_I \rangle \equiv \frac{1}{2} \left(\frac{B_\phi}{q R v_{Ii}} \right) \left[\left\{ \left(\frac{B_\phi}{B_\theta} v_{\theta I} \right)^2 + w^2 + 2\delta_1 w \right\} \tilde{n}_I^s + \{2\delta_2 w\} \tilde{n}_i^s \right] \quad (9.205)$$

and

$$\delta_1 \equiv \frac{(\alpha/z_I)}{(1 + (\alpha/z_I)) e_I B_\theta} \left[\frac{1}{n_I} \frac{\partial p_I}{\partial r} - \frac{T}{(1 + (\alpha/z_I))} \left\{ \left(\frac{\alpha}{z_I} \right) \frac{1}{n_I} \frac{\partial n_I}{\partial r} + \frac{1}{n_i} \frac{\partial n_i}{\partial r} \right\} \right] \quad (9.206)$$

$$\delta_2 \equiv \frac{1}{(1 + (\alpha/z_I)) e_I B_\theta} \left[\frac{1}{n_i} \frac{\partial p_i}{\partial r} - \frac{T}{(1 + (\alpha/z_I))} \left\{ \frac{1}{n_I} \frac{\partial n_I}{\partial r} + \frac{1}{n_i} \frac{\partial n_i}{\partial r} \right\} \right] \quad (9.207)$$

and

$$w \equiv P'_I - \frac{E_r}{B_\theta} \quad (9.208)$$

The expression for $\langle \hat{G}_i \rangle$ is obtained from Eq. (9.205) by interchanging i and I subscripts and interchanging δ_1 and δ_2 . The corresponding transport flux component for main ions is obtained by interchanging i and I in Eq. (9.204).

The \tilde{n}_j^c and \tilde{n}_j^s are the cosine and sine components of the relative density variation over the flux surface and $v_{\theta j}$ is the poloidal velocity, all of which must be calculated from the poloidal component of the momentum balance equations (see chapter 10).

The fifth term describes the radial impurity flux that is driven directly by the radial electric field

$$\Gamma_I^{\Phi'} = \frac{n_I m_I v_{Ii}}{e_I B_\theta} \left[\hat{\mu}_I \gamma_I + \epsilon^2 \left\{ \beta_I \left(\frac{1+2q^2}{q^2} \right) + (\beta_I + \gamma_I) \tilde{n}_I^c - \gamma_I \tilde{n}_i^c \right\} \right] \left(\frac{E_r}{B_\theta} \right) \quad (9.209)$$

where

$$\gamma_I = \frac{\beta_i + \beta_I(1 + \xi_i)}{\xi_i + \xi_I(1 + \xi_i)} \quad (9.210)$$

The corresponding main ion flux component is obtained by interchanging I and i . This flux component will generally have the same sign as the radial electric field (e.g., outward for $E_r > 0$). Since E_r tends to be positive for injection parallel to the toroidal current and negative for injection antiparallel to the toroidal current, this flux component would be expected to have corresponding behavior.

The last term in Eq. (9.199) is the impurity transport driven by the poloidal variation in the electrostatic potential over the flux surface, is of $O(\alpha/z_I)$, and can usually be neglected.

The net particle flux depends upon a competition among the different flux components and may be inward or outward, depending on the specific operating conditions.

External particle sources also modify the expressions for the particle transport flux, and external heat sources or sinks modify the expressions for the heat fluxes.

9.9 Electrical Currents*

9.9.1 Bootstrap Current

A fraction $\approx \epsilon^{1/2}$ of the particles in a tokamak are trapped. These particles have a reduced parallel velocity $\approx \epsilon^{1/2} v_{th}$ and execute a banana orbit of width $w_b \approx \epsilon^{-1/2} qr_L$. When a radial density gradient exists, these particles produce a current similar to the diamagnetic current due to untrapped particles, but parallel to the magnetic field.

$$j_{\text{trap}} \simeq -e \epsilon^{1/2} (\epsilon^{1/2} v_{th}) w_b \frac{dn}{dr} \simeq -q \frac{\epsilon^{1/2}}{B} T \frac{dn}{dr} \quad (9.211)$$

Trapped ions and trapped electrons each produce such a current. There is a transfer of momentum from the trapped to passing particles of both species which modifies the velocities of the passing particles. A toroidal “bootstrap” current, j_{bs} , is produced by the difference in modified velocities of the passing ions and electrons.

The momentum exchange rate between passing ions and electrons is $m_e j_{bs}/e\tau_{ei}$. The passing electrons are also affected by a momentum exchange with the trapped electrons, which are localized in a small $\sim \epsilon^{1/2}$ region of $v_\perp - v_\parallel$ velocity space, so that their effective collision frequency is determined by the time needed to scatter out of this localized region in velocity space, $\tau_{eff} \approx \epsilon\tau_{ee}$. Thus the momentum exchange rate between trapped and passing electrons is $\approx m_e j_{trap}/e(\epsilon\tau_{ee})$. Balancing the momentum exchange of passing electrons with passing ions and with trapped electrons yields an approximate expression for the bootstrap current

$$j_{bs} \simeq \frac{\tau_{ei}}{\tau_{ee}} \frac{j_{trap}}{\epsilon} \simeq -\frac{\epsilon^{1/2}}{B_\theta} T \frac{dn}{dr} \quad (9.212)$$

which is parallel to the magnetic field.

A more rigorous derivation leads to a more precise expression

$$j_{bs} = -\frac{\epsilon^{1/2} n}{B_\theta} \left[2.44(T_e + T_i) \frac{1}{n} \frac{dn}{dr} + 0.69 \frac{dT_e}{dr} - 0.42 \frac{dT_i}{dr} \right] \quad (9.213)$$

In the opposite limit $\epsilon \rightarrow 1$, when most particles are trapped, the bootstrap current is driven entirely by the pressure gradient

$$j_{bs} = -\frac{1}{B_\theta} \frac{dp}{dr} \quad (9.214)$$

rather than by the density gradient. Equation (9.213) indicates that the bootstrap current fraction of the total current scales as

$$f_{bs} \equiv \frac{I_{bs}}{I} = c\epsilon^{1/2} \beta_p \quad (9.215)$$

with $c \approx 1/3$.

9.9.2 Total Current

The conductivity along the field lines is the Spitzer value, $\sigma_{Sp} = 1.96 ne^2 \tau_{ei}/m_e$, in a cylindrical plasma. However, in a tokamak the current is reduced by the trapped particles, which are not able to move freely along field lines in response to an electric field. The fraction of trapped particles, $\approx \epsilon^{1/2}$, varies with radius. Thus, in a large aspect ratio approximation, the total current density parallel to the magnetic field is

$$j_\parallel = \sigma_{Sp}(1 - \epsilon^{1/2}) E_\parallel + j_{bs} \quad (9.216)$$

In a multi-ion species plasma, $Z_{eff} = \Sigma_{ions} n_j z_j^2 / n_e$ is included in the numerator of the above expression for σ_{Sp} .

9.10 Orbit Distortion

Effects associated with the trapped particle “banana” orbits have been shown to dominate neoclassical transport. It stands to reason that any distortion of these orbits would have an important effect on neoclassical transport theory. Three such distortions are examined in this section.

9.10.1 Toroidal Electric Field – Ware Pinch

The toroidal electric field that is induced by transformer action to drive the plasma current in a tokamak also causes a displacement of the banana orbit of trapped particles, which in turn causes an inward particle flux known as the Ware pinch. The inward flow of trapped particles follows directly from the toroidal momentum balance equation

$$\frac{d}{dt}(m_j v_{\phi j}) = e_j (E_\phi + (\mathbf{v}_j \times \mathbf{B})_\phi) \quad (9.217)$$

For trapped particles, the integral over the bounce period, and consequently the time average, of the term on the left vanishes, so that

$$-E_\phi = \hat{n}_\phi \cdot \langle \mathbf{v}_j \times \mathbf{B}_j \rangle = \langle v_{\psi j} \rangle B_\theta \quad (9.218)$$

where ψ indicates the coordinate perpendicular to the flux surface (r in toroidal coordinates). Thus, the time averaged pinch velocity of the trapped particles is

$$\langle v_{\psi j} \rangle = -\frac{E_\phi}{B_\theta} \quad (9.219)$$

Since the trapped particle fraction is $\approx \epsilon^{\frac{1}{2}}$, there is an inward particle flux

$$\Gamma \simeq -\epsilon^{\frac{1}{2}} n E_\phi / B_\theta \quad (9.220)$$

The physical cause of this flux is the displacement of the banana orbit shown in Fig. 9.6.

The equation of motion along the magnetic field direction is

$$\frac{ds}{dt} = -\omega_b^2 s + e_j E_\phi / m_j \quad (9.221)$$

where the bounce frequency is

$$\omega_b = \frac{v_\psi}{qR} \left(\frac{r}{2R} \right)^{\frac{1}{2}} \quad (9.222)$$

Since the distance along the field line, $s = (B/B_\theta)r\theta$, integration of Eq. (9.221) yields

$$\theta = \theta_b \sin \omega_b t + \frac{e_j B_\theta E_\phi}{m_j \omega_b^2 r B} \quad (9.223)$$

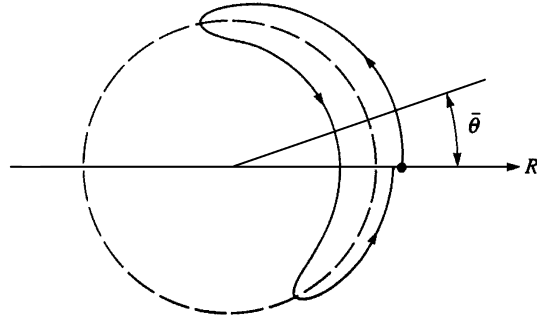


Figure 9.6. Displacement of a trapped particle orbit caused by a toroidal electric field.
(I out of the page)

where θ_b is the orbit turning point given by Eq. (3.47). The orbit is displaced poloidally by a mean angle

$$\bar{\theta} = \frac{e_j B_\theta E_\phi}{m_j \omega_b^2 r B} \quad (9.224)$$

As a result of this displacement, the effect of the grad- B and curvature drifts is not symmetric about the midplane, as it was in the discussion of banana orbits in chapter 3. Consequently, the trapped particle undergoes a radially inward drift (while it is in the upper half plane) for a longer time than it undergoes a radially outward drift (while it is in the lower half plane). The resulting radial velocity is

$$v_{rj} = -v_{dj} \sin \theta \simeq -v_{dj} \theta = -v_{dj} \left(\theta_b \sin \omega_b t + \frac{e_j B_\theta E_\phi}{m_j \omega_b^2 r B} \right) \quad (9.225)$$

where the \simeq indicates the result for deeply trapped particles. Using the expressions for the curvature drift $v_{dj} = 1/2 m_j v_{thj}^2 / e_j R B$, the bounce frequency $\omega_b = (v_{thj}/qR)(r/2R)^{1/2}$, and $q = rB/RB_\theta$ then leads to the time averaged inward velocity

$$\langle v_{rj} \rangle = -\frac{E_\phi}{B_\theta} \quad (9.226)$$

9.10.2 Potato Orbits

The trapped particle orbit effects on neoclassical transport have been derived on the basis of orbits that remained relatively close to a given magnetic surface (i.e. the minor radius is nearly constant). However, for particles near the magnetic axis, the banana orbit width $\Delta r_{ban} \approx \epsilon^{1/2} r_L B_\phi / B_\theta$ can become as large as r . These orbits, shown in Fig. 9.7, indicate that trapped particle orbits near the magnetic axis become quite fat, resembling a potato rather than a banana. Thus, we might expect neoclassical theory to break down near the magnetic axis.

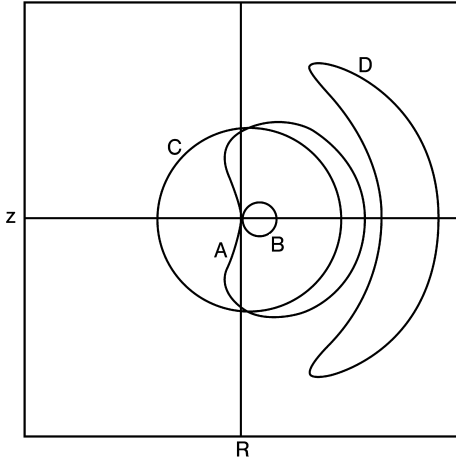


Figure 9.7. Trapped particle orbits near the magnetic axis. (A) Trapped “potato” orbits that pass through the magnetic axis; (B) untrapped orbits that remain within a few r_L of the magnetic axis; (C) untrapped orbits that stay near a particular flux surface; (D) trapped particle banana orbits at a distance $(q^2 r_L^2 R)^{1/3}$ from the magnetic axis

9.10.3 Orbit Squeezing

In the conventional transport ordering ($r_L \ll L$ = characteristic radial gradient scale length) it is implicitly assumed that the density, temperature, electric field and other quantities of interest vary slowly on the gyroradius scale length. Situations may occur in which a sharp variation in the electrostatic potential occurs on the gyroradius scale length. Such a strong variation in electrostatic potential can distort, or “squeeze,” trapped ion orbits.

Consider a situation in which there is a uniform, straight B -field in the z -direction and a transverse electrostatic potential $\phi(x)$ that varies with x , giving rise to an electric field $E = -d\phi/dx$. The Lagrangian of the system is

$$L = \frac{1}{2}m(\dot{x}^2 + \dot{y}^2 + \dot{z}^2) - eBx\dot{y} - e\phi(x) \quad (9.227)$$

The canonical momenta are $p_x = m\dot{x}$, $p_y = m\dot{y} - eB\dot{x}$, and $p_z = m\dot{z}$. p_y and p_z are constants of the motion since the Lagrangian is independent of y and z . The quantity

$$\bar{x} = -p_y/eB = x - v_y/\Omega \quad (9.228)$$

with $v_y = \dot{y}$ and $\Omega = eB/m$, is thus constant along the orbit. In the absence of an electric field, \bar{x} corresponds to the x -coordinate of the guiding center. Since L is time independent, the total energy

$$TE = \frac{1}{2}mv^2 + e\phi(x) = \frac{1}{2}m(\dot{x}^2 + \dot{z}^2) + V(x) \quad (9.229)$$

is also constant along the orbit, where the potential

$$V(x) = \frac{1}{2}m\Omega^2(x - \bar{x})^2 + e\phi(x) \quad (9.230)$$

forms a well that confines the particle in the x -direction. The Hamiltonian governing the x -component of the motion

$$H_x(x, p_x) = \frac{p_x^2}{2m} + V(x) \quad (9.231)$$

is also a constant of the motion.

We expand the potential in a Taylor's series and keep terms through second order

$$\phi(x) \simeq \phi_0 + x \frac{d\phi_0}{dx} + \frac{1}{2} x^2 \frac{d^2\phi_0}{dx^2} \quad (9.232)$$

We assume that the shear in the electric field, $dE/dx = -d^2\phi/dx^2$, is nearly constant over the region of interest, even though the electric field, $E = -d\phi/dx$, may be large and rapidly varying. This assumption makes the potential parabolic about X defined by $dV(X)/dx = 0$,

$$X = \frac{x - (v_y - v_E)/\Omega}{S} \quad (9.233)$$

where $v_E = (-d\phi_0/dx)/B$ is the $\mathbf{E} \times \mathbf{B}$ velocity at $x = 0$, and

$$S = 1 + \frac{m(d^2\phi_0/dx^2)}{eB_\theta^2} \quad (9.234)$$

is the "squeezing factor." The expression for the potential is

$$V(x) = \frac{m\Omega^2 S}{2}(x - X)^2 + \text{const} \quad (9.235)$$

A sheared radial electric field distorts the banana orbits of trapped particles if $S \neq 1$. This will affect radial transport. For example, the ion thermal conductivity is reduced by $S^{-\frac{3}{2}}$ relative to the standard neoclassical (e.g. Chang–Hinton) value.

9.11 Transport in a Partially Ionized Gas*

To gain insight into the effect of a neutral gas upon the ion transport in the boundary region, we will consider an idealized transport model in which ions scatter from fixed, neutral particles. This model, known as the Lorentzian gas model, is applicable for ion transport in a neutral or partially ionized gas in which the ions scatter principally from the neutrals.

The Boltzmann equation for the ion distribution function is

$$\mathbf{v} \cdot \nabla f + \frac{e}{m}(\mathbf{E} + \mathbf{v} \times \mathbf{B}) \cdot \nabla_{\mathbf{v}} f = \left. \frac{\partial f}{\partial t} \right|_c \quad (9.236)$$

The basic Lorentzian assumption is

$$\left. \frac{\partial f}{\partial t} \right|_c = -v_n f \quad (9.237)$$

where v_n is the momentum transfer (90° deflection) frequency for collisions with fixed neutral particles.

Assuming, momentarily, an unmagnetized plasma, these equations lead to an expression for the ion flux

$$\Gamma \equiv \int \mathbf{v} f(\mathbf{v}) d^3 v = - \int \mathbf{v} \left(\frac{\mathbf{v} \cdot \nabla f}{\nu_n} + \frac{e}{m \nu_n} \mathbf{E} \cdot \nabla_{\mathbf{v}} f \right) d^3 v \quad (9.238)$$

For an isotropic distribution,

$$v_x^2 = v_y^2 = v_z^2 \equiv \frac{1}{3} v^2 \quad (9.239)$$

Choosing the x -axis to coincide with the gradient direction, the first term in Eq. (9.238) is

$$\sum_{i=1}^3 \hat{\mathbf{n}}_i \int \frac{v_i v_x}{\nu_n} \frac{\partial f}{\partial x} d^3 v = \hat{\mathbf{n}}_x \int \frac{v^2}{3 \nu_n} \frac{\partial f}{\partial x} d^3 v \quad (9.240)$$

This form suggests defining a diffusion coefficient

$$D \equiv \int \frac{v^2 f(\mathbf{v})}{3 \nu_n} d^3 v / \int f(\mathbf{v}) d^3 v \quad (9.241)$$

Choosing the electric field along the y -axis, the second term in Eq. (9.238) is

$$\frac{e}{m} \sum_{i=1}^3 \hat{\mathbf{n}}_i E_y \int \frac{v_i}{\nu_n} \frac{\partial f}{\partial v_y} d^3 v = -\frac{e}{m} \hat{\mathbf{n}}_y E_y \int_0^\infty \frac{\partial}{\partial v} \left(\frac{4 \pi v^3}{3 \nu_n} \right) f(v) dv \quad (9.242)$$

where we have transformed $d^3 v = 4 \pi v^2 dv$ to spherical coordinates in velocity space. This form suggests defining a mobility coefficient

$$\mu \equiv \frac{e}{m} \int_0^\infty \frac{\partial}{\partial v} \left(\frac{4 \pi v^3}{3 \nu_n} \right) f(v) dv / \int f(\mathbf{v}) d^3 v \quad (9.243)$$

Generalizing these results, we write Eq. (9.238) as

$$\Gamma \equiv -\nabla(Dn) + \mathbf{E}(\mu n) \quad (9.244)$$

The first term is the diffusive flux and the second term is the mobility flux.

A similar development in the presence of a magnetic field leads to an extension of Eq. (9.244)

$$\Gamma \equiv -\nabla \cdot (\mathbf{D}n) + \mathbf{E}(\mu n) \quad (9.245)$$

where

$$\mathbf{D} = \begin{bmatrix} D_{\perp} \hat{\mathbf{n}}_x \hat{\mathbf{n}}_x & -D_H \hat{\mathbf{n}}_x \hat{\mathbf{n}}_y & 0 \\ D_H \hat{\mathbf{n}}_y \hat{\mathbf{n}}_x & D_{\perp} \hat{\mathbf{n}}_y \hat{\mathbf{n}}_y & 0 \\ 0 & 0 & D_{\parallel} \hat{\mathbf{n}}_z \hat{\mathbf{n}}_z \end{bmatrix}$$

and

$$\boldsymbol{\mu} = \begin{bmatrix} \mu_{\perp} \hat{\mathbf{n}}_x \hat{\mathbf{n}}_x & -\mu_H \hat{\mathbf{n}}_x \hat{\mathbf{n}}_y & 0 \\ \mu_H \hat{\mathbf{n}}_y \hat{\mathbf{n}}_x & \mu_{\perp} \hat{\mathbf{n}}_y \hat{\mathbf{n}}_y & 0 \\ 0 & 0 & \mu_{\parallel} \hat{\mathbf{n}}_z \hat{\mathbf{n}}_z \end{bmatrix} \quad (9.246)$$

when the magnetic field is along the z -axis. The components in the tensors are

$$\begin{aligned} D_{\perp} &\equiv \int \frac{v_n}{v_n^2 + \Omega^2} \left(\frac{v^2}{3} \right) f(\mathbf{v}) d^3 v / \int f(\mathbf{v}) d^3 v \\ D_H &\equiv \int \frac{\Omega}{v_n^2 + \Omega^2} \left(\frac{v^2}{3} \right) f(\mathbf{v}) d^3 v / \int f(\mathbf{v}) d^3 v \\ D_{\parallel} &\equiv \int \frac{1}{v_n} \left(\frac{v^2}{3} \right) f(\mathbf{v}) d^3 v / \int f(\mathbf{v}) d^3 v \end{aligned} \quad (9.247)$$

and

$$\begin{aligned} \mu_{\perp} &\equiv -\frac{4\pi e}{3m} \int_0^{\infty} \frac{v^3 v_n}{v_n^2 + \Omega^2} \frac{\partial f}{\partial v} dv / \int f(\mathbf{v}) d^3 v \\ \mu_H &\equiv -\frac{4\pi e}{3m} \int_0^{\infty} \frac{v^3 \Omega}{v_n^2 + \Omega^2} \frac{\partial f}{\partial v} dv / \int f(\mathbf{v}) d^3 v \\ \mu_{\parallel} &\equiv -\frac{4\pi e}{3m} \int_0^{\infty} \frac{v^3}{v_n} \frac{\partial f}{\partial v} dv / \int f(\mathbf{v}) d^3 v \end{aligned} \quad (9.248)$$

The magnetic field does not affect motion along the magnetic field lines. The motion perpendicular to the field lines is driven by particle density gradients and electric fields along the direction of motion (the D_{\perp} and μ_{\perp} terms), and density gradients and electric fields perpendicular to both the direction of motion and the magnetic field (the D_H and μ_H terms). This latter effect, known as the Hall effect, is due to gyromotion.

Problems for Chapter 9

1. Estimate the particle and heat fluxes along the field lines for a plasma with $T = 5$ keV, $n_D = n_e = 5 \times 10^{19} \text{ m}^{-3}$ and magnetic field $B = 5$ T for density and temperature gradient scale lengths $((-\text{d}n/\text{d}z)/n)^{-1} = ((-\text{dT}/\text{dz})/T)^{-1} = 5 \text{ cm}$ and 1 m .
2. Calculate the radial particle fluxes of deuterium and carbon in a cylindrical plasma with $T = 5$ keV, $n_D = n_e = 5 \times 10^{19} \text{ m}^{-3}$, $n_{\text{carbon}} = 1 \times 10^{18} \text{ m}^{-3}$, an axial magnetic field $B = 5$ T and pressure gradient scale lengths of 50 cm for the deuterium and 150 cm for the carbon.
3. Calculate the Pfirsch–Schlüter radial particle flux for a tokamak plasma with the same parameters as the plasma in problem 2 and a toroidal plasma current of 3 MA distributed as $j(r) = j_0(1 - (r/a)^2)$.

4. Calculate the three viscosity coefficients parallel, gyroviscous and perpendicular for a plasma with $T = 5 \text{ keV}$, $n_D = n_e = 5 \times 10^{19} \text{ m}^{-3}$ and a magnetic field $B = 5 \text{ T}$.
5. Calculate the relative variation in the magnetic field from the outboard side ($\theta = 0$) of the plasma to the inboard side of the plasma in a tokamak with minor radius $a = 60 \text{ cm}$ and major radius $R = 1.7 \text{ m}$. Estimate the fraction of trapped particles.
6. Would there be a radial transport flux in a tokamak with an isotropic distribution function?
7. Use the Chang–Hinton formula to calculate the ion thermal conductivity at $r/a = 0.5$ and $q = 1.8$ for a tokamak plasma with $R = 1.7 \text{ m}$, $a = 0.6 \text{ m}$, $B = 3 \text{ T}$, $T_e = T_i = 5 \text{ keV}$, $n_D = n_e = 5 \times 10^{19} \text{ m}^{-3}$, $n_{\text{carbon}} = 1 \times 10^{18} \text{ m}^{-3}$ (assume $\Delta' = 0$).
8. Calculate the bootstrap current in the tokamak plasma of problem 3 for density and temperature gradient scale lengths $((-dn/dr)/n)^{-1} = ((-dt/dr)/T)^{-1} = 1 \text{ cm}$ and 10 cm .
9. A tokamak plasma with major radius $R = 1.7 \text{ m}$, minor radius $a = 0.75 \text{ m}$ and toroidal magnetic field $B = 2.2 \text{ T}$ is heated to a steady state density and temperature distribution by a neutral beam injecting 5 MW of power, all of which is deposited inside plasma radius $r = 0.55 \text{ m}$. The plasma is gettered and strongly pumped, so that an insignificant fraction of the plasma ions escaping the plasma are recycled as a neutral influx to the plasma. The ion density and temperature at plasma radius $r = 0.60 \text{ m}$ are measured to be $n_i = 0.4e20 \text{ m}^{-3}$ and $T_i = 250 \text{ eV}$, and the corresponding gradient scale lengths are measured to be $L_{n_i}^{-1} = 6 \text{ cm}$ and $L_{T_i}^{-1} = 10 \text{ cm}$ at the same location. The radiation from the core region $r < 0.60 \text{ m}$ is measured to be 1.0 MW . What value of the ion thermal conductivity, χ_i , at $r = 0.60 \text{ m}$ would you infer from these measurements?
10. Calculate the neoclassical $\chi_i = \epsilon^{\frac{1}{2}} \rho_{i\theta} v_{iz}$ at $r = 0.60 \text{ m}$ in the above problem and compare with the value inferred from experiment, where $\rho_{i\theta}$ is the gyroradius in the poloidal field B_θ . Assume that the plasma current $I = 1 \text{ MA}$ is uniformly distributed over the plasma cross section. The measured carbon impurity concentration at $r = 0.60 \text{ m}$ is $n_c = 0.8e18 \text{ m}^{-3}$.

10 Plasma Rotation*

Rotation velocities are determined by solving the momentum balance equation, or equation of motion, for each species, from Eq. (5.26)

$$\begin{aligned} n_\sigma m_\sigma \frac{\partial \mathbf{v}_\sigma}{\partial t} + n_\sigma m_\sigma (\mathbf{v}_\sigma \cdot \nabla) \mathbf{v}_\sigma + \nabla p_\sigma + \nabla \cdot \boldsymbol{\pi}_\sigma \\ = n_\sigma e_\sigma (\mathbf{E} + \mathbf{v}_\sigma \times \mathbf{B}) + \mathbf{R}_\sigma^1 + \mathbf{S}_\sigma^1 - m_\sigma \mathbf{v}_\sigma \mathbf{S}_\sigma^0 \quad (10.1) \end{aligned}$$

We wish to solve these equations for the axisymmetric toroidal geometry of a tokamak.

In order to solve these equations for the toroidal velocities, we will take the flux surface average of the toroidal component, and in order to solve for the poloidal velocities, we will take the flux surface average of the poloidal component. Thus, we need expressions for the toroidal viscous force (note $\mathbf{n}_\phi \equiv R \nabla \phi$) $R \nabla \phi \cdot \nabla \cdot \boldsymbol{\pi}$ and the poloidal viscous force $\mathbf{n}_\theta \cdot \nabla \cdot \boldsymbol{\pi}$. We construct the appropriate neoclassical (in the sense of geometry) expressions for $\boldsymbol{\pi}$ by extending the formalism of section 9.5 to toroidal geometry.

10.1 Neoclassical Viscosity

10.1.1 Rate-of-Strain Tensor in Toroidal Geometry

The elements of the general rate-of-strain tensor of fluid theory may be written

$$W_{\alpha\beta} \equiv \hat{\mathbf{n}}_\alpha \cdot \nabla \mathbf{v} \cdot \hat{\mathbf{n}}_\beta + \hat{\mathbf{n}}_\beta \cdot \nabla \mathbf{v} \cdot \hat{\mathbf{n}}_\alpha - \frac{2}{3} \delta_{\alpha\beta} \nabla \cdot \mathbf{v} \quad (10.2)$$

where \mathbf{v} is the fluid velocity and $\hat{\mathbf{n}}_\alpha$ is the unit vector in the α direction. The elements of the rate-of-strain tensor can be written generally as

$$W_{\alpha\beta} = \left(\frac{\partial v_\beta}{\partial l_\alpha} + \sum_k \Gamma_{\beta k}^\alpha v_k \right) + \left(\frac{\partial v_\alpha}{\partial l_\beta} + \sum_k \Gamma_{\alpha k}^\beta v_k \right) - \frac{2}{3} \delta_{\alpha\beta} \nabla \cdot \mathbf{v} \quad (10.3)$$

where dl_α are the differential elements in the α -coordinate directions and $\Gamma_{\alpha k}^\beta$ are the Christoffel symbols. The nonvanishing Christoffel symbols for an axisymmetric, tokamak,

flux surface geometry are

$$\begin{aligned}\Gamma_{\psi p}^{\psi} &= RB_p \frac{\partial(RB_p)^{-1}}{\partial l_p} = -\Gamma_{p\psi}^{\psi} \\ \Gamma_{\psi p}^p &= -\frac{1}{h_p} \frac{\partial h_p}{\partial l_\psi} = -\Gamma_{p\psi}^p \\ \Gamma_{\psi\phi}^{\phi} &= -\frac{1}{R} \frac{\partial R}{\partial l_\psi} = -\Gamma_{\phi\psi}^{\phi} \\ \Gamma_{p\phi}^{\phi} &= -\frac{1}{R} \frac{\partial R}{\partial l_p} = -\Gamma_{\phi p}^{\phi}\end{aligned}\tag{10.4}$$

We adopt an orthogonal (ψ, p, ϕ) flux surface coordinate system with $dl_\psi = h_\psi d\psi = (RB_p)^{-1} d\psi$, $dl_p = h_p dp$, $dl_\phi = h_\phi d\phi = R d\phi$, where R is the major radius and B_p is the poloidal magnetic field. We also make use of toroidal symmetry. The elements of the traceless rate-of-strain tensor in this coordinate system are

$$\begin{aligned}W_{\psi\psi} &= -\frac{2}{3} \frac{\partial v_p}{\partial l_p} + \left(\frac{4}{3} RB_p \frac{\partial(RB_p)^{-1}}{\partial l_p} - \frac{2}{3} \frac{1}{R} \frac{\partial R}{\partial l_p} \right) v_p \\ W_{\psi p} &= h_p \frac{\partial}{\partial l_\psi} (v_p h_p^{-1}) = W_{p\psi} \\ W_{\psi\phi} &= R \frac{\partial}{\partial l_\psi} (v_\phi R^{-1}) = W_{\phi\psi} \\ W_{pp} &= \frac{4}{3} \frac{\partial v_p}{\partial l_p} - \frac{2}{3} \left(RB_p \frac{\partial(RB_p)^{-1}}{\partial l_p} + \frac{1}{R} \frac{\partial R}{\partial l_p} \right) v_p \\ W_{p\phi} &= \frac{R \partial(v_\phi R^{-1})}{\partial l_p} = W_{\phi p} \\ W_{\phi\phi} &= -\frac{2}{3} \frac{\partial v_p}{\partial l_p} + \left(\frac{4}{3} \frac{1}{R} \frac{\partial R}{\partial l_p} - \frac{2}{3} RB_p \frac{\partial(RB_p)^{-1}}{\partial l_p} \right) v_p\end{aligned}\tag{10.5}$$

10.1.2 Viscous Stress Tensor

We follow section 9.5 in computing the elements of the viscous stress tensor for a plasma in a magnetic field from the corresponding rate-of-strain tensor elements:

$$\begin{aligned}\Pi_{\alpha\beta} &= -\eta_0 W_{\alpha\beta}^0 - [(\eta_1 W_{\alpha\beta}^1 + \eta_2 W_{\alpha\beta}^2)] + [(\eta_3 W_{\alpha\beta}^3 + \eta_4 W_{\alpha\beta}^4)] \\ &\equiv \Pi_{\alpha\beta}^0 + \Pi_{\alpha\beta}^{12} + \Pi_{\alpha\beta}^{34}\end{aligned}\tag{10.6}$$

where the prescription for construction of the $W_{\psi\beta}^n$ ($n = 0, 1, 2, 3, 4$) from the rate-of-strain tensor elements of Eq. (10.5) are based on the Braginskii decomposition of the viscous stress tensor into parallel (η_0), perpendicular (η_1 and η_2), and gyroviscous (η_3

and η_4) components given by Eq. (10.6), where

$$\begin{aligned} W_{\alpha\beta}^0 &\equiv \frac{3}{2} \left(f_\alpha f_\beta - \frac{1}{3} \delta_{\alpha\beta} \right) \left(f_\mu f_\nu - \frac{1}{3} \delta_{\mu\nu} \right) W_{\mu\nu} \\ W_{\alpha\beta}^1 &\equiv \left(\delta_{\alpha\mu}^\perp \delta_{\beta\nu}^\perp + \frac{1}{2} \delta_{\alpha\beta}^\perp f_\mu f_\nu \right) W_{\mu\nu} \\ W_{\alpha\beta}^2 &\equiv \left(\delta_{\alpha\mu}^\perp f_\beta f_\nu + \delta_{\beta\nu}^\perp f_\alpha f_\mu \right) W_{\mu\nu} \\ W_{\alpha\beta}^3 &\equiv \frac{1}{2} \left(\delta_{\alpha\mu}^\perp \epsilon_{\beta\gamma\nu} + \delta_{\beta\nu}^\perp \epsilon_{\alpha\gamma\mu} \right) f_\gamma W_{\mu\nu} \\ W_{\alpha\beta}^4 &\equiv (f_\alpha f_\mu \epsilon_{\beta\gamma\nu} + f_\beta f_\nu \epsilon_{\alpha\gamma\mu}) f_\gamma W_{\mu\nu} \\ \delta_{\alpha\beta}^\perp &\equiv \delta_{\alpha\beta} - f_\alpha f_\beta \end{aligned} \quad (10.7)$$

$\epsilon_{\alpha\beta\gamma}$ is the antisymmetric unit tensor, $f_\alpha \equiv B_\alpha/B$, and the Einstein summation convention is employed. The viscosity coefficients ($\eta_0^i \simeq n_i T_i \tau_i$, $\eta_{1,2}^i \simeq n_i T_i \tau_i / (\Omega_i \tau_i)^2$, $\eta_{3,4}^i \simeq n_i T_i \tau_i / (\Omega_i \tau_i)$) are defined in Eqs. (9.137) to (9.139).

The stress tensor elements in this form naturally decompose into a “parallel” term $\Pi_{\alpha\beta}^0$, a “perpendicular” term $\Pi_{\alpha\beta}^{12}$, and a “gyroviscous” term $\Pi_{\alpha\beta}^{34}$. The particle motions producing these stresses are discussed in section 9.1. The parallel viscosity coefficient η_0 scales inversely with self-collision frequency; the perpendicular viscosity coefficients, η_1 and η_2 , scale directly with collision frequency and inversely as the square of the magnetic field; and the gyroviscous coefficients, η_3 and η_4 , are independent of collision frequency and scale inversely with the magnetic field.

We assume $f_\phi \equiv |B_\phi|/|B| \simeq 1$, $f_p \equiv |B_p|/|B| \ll 1$. The viscosity tensor elements can then be represented as given in Table 10.1.

10.1.3 Toroidal Viscous Force

The toroidal component of the viscous force can be written, by specializing the representation in general curvilinear coordinates to flux surface coordinates, as

$$R^2 \nabla \phi \cdot \nabla \cdot \Pi = \frac{1}{Rh_p} \frac{\partial}{\partial l_\psi} (R^2 h_p \Pi_{\psi\phi}) + B_p \frac{\partial}{\partial l_p} \left(\frac{R \Pi_{p\phi}}{B_p} \right) \quad (10.8)$$

Recall that $\Pi_{\alpha\beta} \equiv \hat{n}_\alpha \cdot \Pi \cdot \hat{n}_\beta$.

The flux surface average of this force is

$$\langle R^2 \nabla \phi \cdot \nabla \cdot \Pi \rangle = \left\langle \frac{1}{Rh_p} \frac{\partial}{\partial l_\psi} (R^2 h_p \Pi_{\psi\phi}) \right\rangle \quad (10.9)$$

We note that, since Π is a symmetric tensor,

$$\langle R^2 \nabla \phi \cdot \nabla \cdot \Pi \rangle = \frac{1}{V'} \frac{\partial}{\partial \psi} \left(V' \langle R^2 \nabla \phi \cdot \Pi \cdot \nabla \psi \rangle \right) \quad (10.10)$$

Making use of Table 10.1, we find that the parallel (η_0) viscosity contribution to the toroidal viscous force vanishes, that the perpendicular ($\eta_1 \eta_2$) viscosity contribution can

Table 10.1. The viscosity tensor elements, where

$A_0 = 2 \left\{ -\frac{1}{3} (\partial v_p / \partial l_p) + \left[(1/R) (\partial R / \partial l_p) + \frac{1}{3} (1/B_p) (\partial B_p / \partial l_p) \right] v_p + f_p R [\partial(v_\phi R^{-1}) / \partial l_p] \right\}$			
Parallel	Perpendicular	Gyroviscous	
$\Pi_{\alpha\beta}^0 \equiv -\eta_0 W_{\alpha\beta}^0$	$\Pi_{\alpha\beta}^{12} \equiv -(\eta_1 W_{\alpha\beta}^1 + \eta_2 W_{\alpha\beta}^2)$	$\Pi_{\alpha\beta}^{34} \equiv (\eta_3 W_{\alpha\beta}^3 + \eta_4 W_{\alpha\beta}^4)$	
$\Pi_{\psi\psi}$	$\frac{1}{2} \eta_0 A_0$	$\eta_1 \left((RB_p)^{-1} \frac{\partial(RB_p v_p)}{\partial l_p} - f_p R \frac{\partial(v_\phi R^{-1})}{\partial l_p} \right)$	$-\eta_3 \left(h_p \frac{\partial(v_p h_p^{-1})}{\partial l_\psi} - f_p R \frac{(v_\phi R^{-1})}{\partial l_\psi} \right)$
$\Pi_{\psi p} = \Pi_{p\psi}$	0	$-\eta_1 h_p \frac{\partial(v_p h_p^{-1})}{\partial l_\psi} + (\eta_2 - \eta_1) f_p R \frac{\partial(v_\phi R^{-1})}{\partial l_\psi}$	$-\eta_3 (RB_p)^{-1} \frac{\partial(RB_p v_p)}{\partial l_p} - (\eta_4 - \eta_3) f_p R \frac{\partial(v_\phi R^{-1})}{\partial l_p}$
$\Pi_{\psi\phi} = \Pi_{\phi\psi}$	0	$-\eta_2 R \frac{\partial(v_\phi R^{-1})}{\partial l_\psi}$	$-\eta_4 R \frac{\partial(v_\phi R^{-1})}{\partial l_p}$
Π_{pp}	$\frac{1}{2} \eta_0 A^0$	$-\eta_1 (RB_p)^{-1} f_p \frac{\partial(RB_p v_p)}{\partial l_p} + (\eta_1 - 2\eta_2) f_p R \frac{\partial(v_\phi R^{-1})}{\partial l_p}$	$\eta_3 h_p \frac{\partial(v_p h_p^{-1})}{\partial l_\psi} + (2\eta_4 - \eta_3) f_p R \frac{\partial(v_\phi R^{-1})}{\partial l_\psi}$
$\Pi_{p\phi} = \Pi_{\phi p}$	$-\frac{3}{2} \eta_0 f_p A^0$	$-\eta_2 R \frac{\partial(v_\phi R^{-1})}{\partial l_p}$	$\eta_4 R \frac{\partial(v_\phi R^{-1})}{\partial l_\psi}$
$\Pi_{\phi\phi}$	$-\eta_0 A^0$	$2\eta_2 f_p R \frac{\partial(v_\phi R^{-1})}{\partial l_p}$	$-2\eta_4 f_p R \frac{\partial(v_\phi R^{-1})}{\partial l_\psi}$

be written (to leading terms in $f_p \ll 1$) as

$$\langle (R^2 \nabla \phi \cdot \nabla \cdot \pi)_{12} \rangle \simeq - \left\langle \frac{1}{Rh_p} \frac{\partial}{\partial l_\psi} \left(R^3 h_p \eta_2 \frac{\partial(v_\phi R^{-1})}{\partial l_p} \right) \right\rangle \quad (10.11)$$

and the gyroviscous ($\eta_3 \eta_4$) contribution can similarly be written as

$$\langle (R^2 \nabla \phi \cdot \nabla \cdot \Pi)_{34} \rangle \simeq - \left\langle \frac{1}{Rh_p} \frac{\partial}{\partial l_\psi} \left(R^3 h_p \eta_4 \frac{\partial(v_\phi R^{-1})}{\partial l_p} \right) \right\rangle \quad (10.12)$$

We note that if the plasma rotated as a rigid body, then $v_\phi(\psi, p) = R(\psi, p)\Omega$, and both of the viscous forces would vanish. Thus, it is the departure from rigid-body rotation within a flux surface $\partial(v_\phi R^{-1})/\partial l_p \neq 0$ that drives the gyroviscous force, and it is the departure from radially uniform rigid-body rotation, $\partial(v_\phi R^{-1})/\partial l_\psi \neq 0$, that drives the perpendicular viscous force.

In the large aspect ratio, low- β , circular flux surface approximation [$\{\epsilon = r/R_0 \ll 1, p \rightarrow \theta, h_p \rightarrow r, \psi \rightarrow r, R \rightarrow R_0(1 + \epsilon \cos \theta)\}$] Eq. (10.11) reduces to

$$\langle R^2 \nabla \phi \cdot \nabla \cdot \Pi_{12} \rangle \simeq -R_0 \frac{1}{r} \frac{\partial}{\partial r} \left(\eta_2^0 r \frac{\partial v_\phi^0}{\partial r} \right) + O(\epsilon^2) \quad (10.13)$$

In order to further reduce Eq. (10.11), it is necessary to specify the form of the poloidal dependence of the various quantities appearing under the poloidal derivative. Noting that $\eta_4 \simeq nmT/eB$, we expand

$$n(r, \theta) = \bar{n}(r) \{1 + \epsilon [\tilde{n}^c \cos \theta + \tilde{n}^s (\sin \theta)]\} \quad (10.14)$$

make a similar expansion for v_ϕ , and assume that $T \neq T(\theta)$ because of rapid heat conduction along field lines.

Assuming that the radial flow velocity is small compared to the toroidal v_ϕ and poloidal v_θ flow velocities, the radial component of Eq. (10.1) yields an expression which may be used to calculate the poloidal dependence of the toroidal rotation velocity

$$v_{\phi j}(r, \theta) = \left(\frac{B_\phi}{B_\theta} \right) v_{\theta j}(r, \theta) - \Phi'(r, \theta) - P'_j(r, \theta) \quad (10.15)$$

where we have included a species subscript “ j ” and

$$\begin{aligned} \Phi' &\equiv \frac{1}{B_\theta} \frac{\partial \Phi}{\partial r} \\ P'_j &\equiv \frac{1}{B_\theta n_j e_j} \frac{\partial p_j}{\partial r} \end{aligned} \quad (10.16)$$

In the subsequent development, we will use Eq. (10.15) to represent the poloidal dependence of the toroidal velocity in terms of the poloidal dependence of the other quantities

appearing in that equation, then use the flux surface average of this equation

$$\bar{\Phi}'(r) \equiv \frac{B_\phi^0}{B_\theta^0} \bar{v}_{\theta j}(r) - \bar{v}_{\phi j}(r) - \bar{P}'_j(r) \quad (10.17)$$

to replace $\bar{\Phi}'$ with $\bar{v}_{\phi j}$, $\bar{v}_{\theta j}$ and pressure gradient terms in the final result.

Noting that $|v_\phi, v_\theta| \gg |v_r|$ and assuming axisymmetry, the continuity equation $\nabla \cdot n\mathbf{v} = 0$ yields

$$\frac{1}{r} \frac{\partial}{\partial \theta} [(1 + \epsilon \cos \theta) n_j v_{\theta j}] = 0 \quad (10.18)$$

in toroidal geometry. This equation can be integrated to obtain a “surface function of integration,” $K_j(\theta)$. K_j can be determined by flux surface averaging the resulting equation and setting it equal to the average value over the flux surface of the poloidal velocity, $\bar{v}_{\theta j}$, yielding finally

$$v_{\theta j}(r, \theta) = \frac{\bar{n}_j(r) \bar{v}_{\theta j}(r)}{n_j(r, \theta)(1 + \epsilon \cos \theta)} \quad (10.19)$$

Thus, the θ -dependence of the poloidal velocity depends on the θ -dependence of the density and on the toroidal geometry metric $(1 + \epsilon \cos \theta)$. We will develop equations for the determination of $\bar{v}_{\theta j}$ in section 10.2.

The poloidal dependence of the electrostatic potential is represented as

$$\Phi(r, \theta) = \bar{\Phi}(r) \left[1 + \epsilon (\tilde{\Phi}^s(r) \sin \theta + \tilde{\Phi}^c(r) \cos \theta + \dots) \right] \quad (10.20)$$

and the poloidal component of the electron momentum balance is used to relate the Fourier coefficients for the electrostatic potential to the Fourier coefficients of the ion densities

$$\left(\frac{e \bar{\Phi}}{T_e} \right) \tilde{\Phi}^s = \tilde{n}_e^s = \sum_j^{\text{ions}} z_j \frac{\bar{n}_j}{\bar{n}_e} \tilde{n}_j^s \quad (10.21)$$

Finally, Eq. (10.12) can be written

$$\begin{aligned} \langle R^2 \nabla \phi \cdot \nabla \cdot \pi_{34j} \rangle &= - \left\langle \frac{1}{R h_\theta} \frac{\partial}{\partial l_\psi} \left(R^3 h_\theta \eta_{4j} \frac{\partial(v_{\phi j} R^{-1})}{\partial l_\theta} \right) \right\rangle \\ &= \frac{1}{2} \tilde{\theta}_j G_j \frac{n_j m_j T_j}{e_j B} \frac{v_{\phi j}}{R} \equiv R n_j m_j v_{dj} v_{\phi j} \end{aligned} \quad (10.22)$$

where

$$\begin{aligned} \tilde{\theta}_j &\equiv (4 + \tilde{n}_j^c) \tilde{v}_{\phi j}^s + \tilde{n}_j^s (1 - \tilde{v}_{\phi j}^c) \\ &= (4 + \tilde{n}_j^c) \left[-\hat{v}_{\theta j} \hat{v}_{\phi j}^{-1} (\tilde{\Phi}^s + \tilde{n}_j^s) + \tilde{\Phi}^s \right] \\ &\quad + \tilde{n}_j^s \left[\hat{v}_{\theta j} \hat{v}_{\phi j}^{-1} (2 + \tilde{\Phi}^c + \tilde{n}_j^c) - \tilde{\Phi}^c \right] \end{aligned} \quad (10.23)$$

and

$$G_j(r) \equiv -\frac{r}{\eta_{4j} v_{\phi j}} \frac{\partial(\eta_{4j} v_{\phi j})}{\partial r} \quad (10.24)$$

where $\hat{v}_{\phi j} \equiv v_{\phi j}/v_{\text{thj}}$, $\hat{v}_{\theta j} \equiv v_{\theta j}/\beta v_{\text{thj}}$ ($\beta \equiv B_\theta/B_\phi$) and $\eta_{4j} = n_j m_j T_j/e_j B$.

Both the “perpendicular” toroidal viscous force of Eq. (10.13) and the “gyroviscous” toroidal viscous force of Eq. (10.22) contribute formally to the radial transport of momentum. However, since η_Ω is usually 3–4 orders of magnitude larger than η_\perp , only the gyroviscous component need be retained in practice.

Thus, in order to evaluate the gyroviscous component of the toroidal viscous force needed for calculation of the toroidal rotation velocity, it is first necessary to calculate the flux surface averaged poloidal rotation velocities and the poloidal variation of the density ($\tilde{n}_j^c, \tilde{n}_j^s$) for all species in the plasma. Before undertaking this calculation, which will require solution of moments of the poloidal component of the momentum balance Eq. (10.1), we need to develop an expression for the parallel viscous force.

10.1.4 Parallel Viscous Force

The parallel viscous force in flux surface coordinates is represented as

$$\begin{aligned} \mathbf{B} \cdot \nabla \cdot \Pi = B_p \left[\frac{1}{Rh_p^2} \frac{\partial}{\partial l_\psi} (Rh_p^2 \Pi_{\psi p}) + B_p \frac{\partial}{\partial l_p} \left(\frac{\Pi_{pp}}{B_p} \right) - \left(\frac{1}{R} \frac{\partial R}{\partial l_p} \right) \Pi_{\phi\phi} \right. \\ \left. - \left(RB_p \frac{\partial (RB_p)^{-1}}{\partial l_p} \right) \Pi_{\psi\psi} \right] \\ + \frac{B_\phi}{R} \left[\frac{1}{Rh_p} \frac{\partial}{\partial l_\psi} (R^2 h_p \Pi_{\psi\phi}) + B_p \frac{\partial}{\partial l_p} \left(\frac{R\Pi_{p\phi}}{B_p} \right) \right] \quad (10.25) \end{aligned}$$

Comparison with Eq. (10.8) shows that the second term in Eq. (10.25) is B_ϕ/R times the toroidal viscous force of Eq. (10.8). (The second term in Eq. (10.25) is dominant when $|B_p| \ll |B_\phi|$). Thus, we see immediately that the toroidal viscous forces caused by the radial transfer of toroidal momentum, which are necessary to explain the rotation measurements, also contribute to the parallel viscous force.

Making use of the viscous stress tensor representation given in Table 10.1 and retaining only the leading terms ($f_p \ll f_\phi \simeq 1$), we find the parallel (η_0) viscous force contribution,

$$\begin{aligned} (\mathbf{B} \cdot \nabla \cdot \Pi)_0 \simeq -2B_p \frac{\partial}{\partial l_p} \left\{ \eta_0 \left[-\frac{1}{3} \frac{\partial v_p}{\partial l_p} + \left(\frac{1}{R} \frac{\partial R}{\partial l_p} + \frac{1}{3} \frac{1}{B_p} \frac{\partial B_p}{\partial l_p} \right) v_p + f_p R \frac{(v_\phi R^{-1})}{\partial l_p} \right] \right\} \\ + 3\eta_0 \left(\frac{\partial B_p}{\partial l_p} \right) \left[-\frac{1}{3} \frac{\partial v_p}{\partial l_p} + \left(\frac{1}{R} \frac{\partial R}{\partial l_p} + \frac{1}{3} \frac{1}{B_p} \frac{\partial B_p}{\partial l_p} \right) v_p + f_p R \frac{\partial(v_\phi R^{-1})}{\partial l_p} \right] \quad (10.26) \end{aligned}$$

the perpendicular (η_1, η_2) viscous force contribution,

$$\begin{aligned} (\mathbf{B} \cdot \nabla \cdot \Pi)_{12} \simeq \frac{B_\phi}{R} \left[\frac{1}{Rh_p} \frac{\partial}{\partial l_\psi} \left(R^3 h_p \eta_2 \frac{\partial(v_\phi R^{-1})}{\partial l_\psi} \right) + B_p \frac{\partial}{\partial l_p} \left(\frac{R^2 \eta_2}{B_p} \frac{\partial(v_\phi R^{-1})}{\partial l_p} \right) \right] \\ \equiv (B_\phi/R)(R^2 \nabla \phi \cdot \nabla \cdot \Pi)_{12} \quad (10.27) \end{aligned}$$

and the gyroviscous (η_3, η_4) force contribution

$$\begin{aligned} (\mathbf{B} \cdot \nabla \cdot \boldsymbol{\Pi})_{34} &\simeq \frac{B_\phi}{R} \left[\frac{1}{Rh_p} \frac{\partial}{\partial l_\psi} \left(R^3 h_p \eta_4 \frac{\partial(v_\phi R^{-1})}{\partial l_p} \right) + B_p \frac{\partial}{\partial l_p} \left(\frac{R^2 \eta_4}{B_p} \frac{\partial(v_\phi R^{-1})}{\partial l_p} \right) \right] \\ &\equiv (B_\phi/R)(R^2 \nabla \phi \cdot \nabla \cdot \boldsymbol{\Pi})_{34} \end{aligned} \quad (10.28)$$

Making use of the continuity equation $\nabla \cdot n\mathbf{v} = 0$ to write $n v_p = K(\psi) B_p$, Eq. (10.25) can be used to write the flux surface average of the leading, parallel viscous force contribution as

$$\begin{aligned} \langle (\mathbf{B} \cdot \nabla \cdot \boldsymbol{\Pi})_0 \rangle &= 3 \left\langle \eta_0 \left(\frac{\partial B_p}{\partial l_p} \right) \left(\frac{1}{R} \frac{\partial R}{\partial l_p} \right) v_p \right\rangle + \left\langle \eta_0 \left(\frac{\partial B_p}{\partial l_p} \right) \left(\frac{1}{n} \frac{\partial n}{\partial l_p} \right) v_p \right\rangle \\ &\quad + 3 \left\langle \eta_0 f_p \left(\frac{\partial B_p}{\partial l_p} \right) R \frac{\partial(v_\phi R^{-1})}{\partial l_p} \right\rangle \end{aligned} \quad (10.29)$$

Note that in a low- β equilibrium where $R B_p$ is a surface quantity,

$$\frac{1}{R} \frac{\partial R}{\partial l_p} = - \frac{1}{B_p} \frac{\partial B_p}{\partial l_p} \quad (10.30)$$

The second term in Eq. (10.29) arises because of a variation of the particle density over the flux surface, and the third term arises from the departure from rigid rotation over the flux surface; both of these effects are associated with a strongly rotating plasma.

10.1.5 Neoclassical Viscosity Coefficients

The classical viscosity theory of section 9.5 has been extended to toroidal geometry in the foregoing sections of this chapter. However, there is a second phenomenon – the effect of trapped particles – that must be taken into account to obtain a fully neoclassical theory of viscosity. Detailed investigations indicate that trapped particle effects do not alter the magnitude of the perpendicular viscosity coefficients ($\eta_\perp = \eta_{1,2}$), and the gyroviscosity arises from gyromotion, not collisions, and hence is independent of collisionality. Thus, we are left with the effect of trapped particles on the parallel viscosity coefficient, η_0 , to examine.

Writing

$$\mathbf{B} \cdot \nabla \cdot \boldsymbol{\pi} \equiv \int d^3 v \frac{1}{2} m v^2 (\hat{\mathbf{n}}_\parallel \cdot \nabla B) f_1 \quad (10.31)$$

where $\hat{\mathbf{n}}_\parallel = \mathbf{B}/B$, and the perturbed distribution function f_1 is the solution of

$$D(f_1) - C(f_1) = v'_\parallel \frac{\partial}{\partial \theta} \left(\frac{I v'_\parallel}{\mathcal{Q}} \right) \Big|_{E,\mu} \left(\frac{1}{JB} \frac{\partial f_0}{\partial \psi} \right) \quad (10.32)$$

where D is the streaming operator, C is the collision operator, J is the Jacobian, $I = RB_\phi$, \mathcal{Q} is the gyroradius, and f_0 is the Maxwellian distribution function which is shifted owing

to rotation. In the strong rotation case

$$f_0 = n \left(\frac{m}{2\pi T} \right)^{\frac{3}{2}} \exp \left[-\frac{m}{2T} (v'^2 + v'^2_{\parallel}) - \frac{e\tilde{\Phi}}{T} + \frac{m}{2T} \tilde{u}^2 \right] \quad (10.33)$$

Here, n and T are the density and temperature components which are uniform over the flux surface, $v'^2 = v'^2_{\parallel} - u$, Φ is the electrostatic potential,

$$u \equiv - \left(\frac{I}{B} \right) \frac{\partial}{\partial \psi} \Phi(\psi, \theta) \quad (10.34)$$

is the parallel flow due to the radial electric field, and the poloidally varying components are

$$\tilde{\Phi} \equiv \Phi - \langle \Phi \rangle \quad \tilde{u}^2 = u^2 - \langle u^2 \rangle \quad (10.35)$$

where $\langle \cdot \rangle$ denotes a flux surface average. Note that this expression for f_0 contains the term $(m/2T)\tilde{u}^2$, which corresponds to the inertial term of the fluid theory.

To solve Eq. (10.31), let

$$f_1 = - \frac{Iv'_{\parallel}}{\Omega} \frac{\partial f_0}{\partial \psi} + \frac{v'_{\parallel}}{v} S(\psi, v') \frac{B}{\sqrt{\langle B^2 \rangle}} f_0 + h_1 \quad (10.36)$$

where S is a smooth function of energy, and h_1 is a localized function of pitch angle, which is due to the plateau resonance $D - C = 0$. For a given S , the equation for h_1 is

$$(D - C)h_1 = \frac{1}{2} v' \frac{(\hat{n}_{\parallel} \cdot \nabla B)}{\sqrt{\langle B^2 \rangle}} S f_0 \quad (10.37)$$

For circular flux surfaces, with minor radius r and major radius R , where $B_p = B_p^0(r)/(1 + \epsilon \cos \theta)$, and $\hat{n}_{\parallel} \cdot \nabla B = (B_p^0/r)\epsilon \sin \theta (\epsilon = r/R)$, Eq. (10.37) has the solution

$$h_1 = \frac{1}{2} \epsilon S \left(\frac{v_s}{\omega_t} \right)^{-\frac{1}{3}} \frac{B}{\sqrt{\langle B^2 \rangle}} f_0 \int_0^\infty \sin(\theta - p\tau) \exp(-\tau^3/6) d\tau \quad (10.38)$$

where the resonance integral has the property

$$\int_{-1}^1 d\lambda' \int_0^\infty \cos(p\tau) \exp(-\tau^3/6) d\tau = \pi (v_s/\omega_t)^{\frac{1}{3}} \quad (10.39)$$

Here, λ is the pitch-angle variable, $d^3v = 2\pi v^2 dv d\lambda$; v_s is the collisional pitch-angle scattering frequency; $\omega_t = v_{th}/Rq$ is the transit frequency; q is the safety factor; and $p \equiv (v_s/\omega_t)^{-\frac{1}{3}} (v'_{\parallel}/v')$ is normalized such that $p = 1$ for resonant particles.

Finally, the driving term $S(\psi, v')$ can be determined self-consistently from the $v_{\parallel} L_0$ and $v_{\parallel} L_1$, moments of Eq. (10.36), using the expansion

$$S(\psi, v') = \frac{2v'}{v_{th}} (A_0 L_0 + A_1 L_1 + \dots) \quad (10.40)$$

where the Sonine polynomials $L_0 = 1$, $L_1 = \frac{5}{2} - (v')^2/v_{th}^2$, etc. In this case, the term h_1 , which is localized in pitch angle, can be neglected. We thus obtain expressions for A_0

and A_2 in terms of v_{\parallel} and q_{\parallel} , the parallel particle and heat flows. These flows are related through the fluid equations to the radial pressure gradient.

Using Eq. (10.33), Eq. (10.36), Eq. (10.38) and Eq. (10.40) in Eq. (10.31) yields the final result for the parallel viscous force

$$\mathbf{B} \cdot \nabla \cdot \boldsymbol{\pi} = \langle \mathbf{B} \cdot \nabla \cdot \boldsymbol{\pi} \rangle 2 \sin^2 \theta \quad (10.41)$$

where the flux surface averaged viscous force is

$$\langle \mathbf{B} \cdot \nabla \cdot \boldsymbol{\pi} \rangle = 3 (\langle \hat{\mathbf{n}}_{\parallel} \cdot \nabla B \rangle)^2 \mu_1 \mathbf{v} \cdot \mathbf{B}_p / B_p^2 \quad (10.42)$$

where, for species “ j ,”

$$\mu_{1j} \equiv \frac{R q n_j m_j v_{thj} v_{*j}}{(1 + v_{*j})(1 + \epsilon^{3/2} v_{*j})} \quad (10.43)$$

For circular flux surfaces

$$\langle (\hat{\mathbf{n}} \cdot \nabla B)^2 \rangle = \frac{1}{2} (\epsilon / R q)^2 (B^0)^2 \quad (10.44)$$

The above development is appropriate for a strongly rotating plasma ($v_{\phi} \approx v_{th}$, $E \approx B_{\theta}$) with sharp gradients ($L \equiv [(-1/p)(\partial p / \partial r)]^{-1} \approx r_{L\theta} \equiv mv_{th}/eB_{\theta}$), and make the usual tokamak assumptions about the ratio of the poloidal and toroidal magnetic fields ($\beta \equiv B_{\theta}/B_{\phi} \ll 1$) and the magnitude of the minor to major radii ($\epsilon \equiv r/R < 1$).

10.2 Rotation Calculations

10.2.1 Poloidal Rotation and Density Asymmetries

We use the simple Lorentz model for the collisional momentum exchange

$$\mathbf{R}_j = -n_j m_j \sum_{k \neq j} v_{jk} (\mathbf{v}_j - \mathbf{v}_k) \quad (10.45)$$

The neoclassical parallel viscosity tensor is obtained by extending the classical rate-of-strain tensor formalism to toroidal geometry and using the neoclassical parallel viscosity coefficient of the previous section that takes banana–plateau collisionality effects into account

$$\eta_{0j} = \frac{n_j m_j v_{thj} q R \epsilon^{-3/2} v_{jj}^*}{(1 + \epsilon^{-3/2} v_{jj}^*)(1 + v_{jj}^*)} \equiv n_j m_j v_{thj} q R f_j(v_{jj}^*) \quad (10.46)$$

where $q = |r B_{\phi} / R B_{\theta}| = \epsilon / |\beta|$ is the safety factor and the normalized collision frequency is $v_{jk}^* = v_{jk} q R / v_{thj}$. The poloidal component of the divergence of the parallel viscosity tensor, which is the only component that we will need, can be written

$$\hat{\mathbf{n}}_{\theta} \cdot \nabla \cdot \boldsymbol{\pi}_j = \eta_{0j} \left(\frac{1}{2} A_{0j} \right) \left\{ \frac{1}{r} \frac{\partial \ln(\eta_{0j} A_{0j})}{\partial \theta} - \frac{3 \sin \theta}{R} \right\} \quad (10.47)$$

where

$$\frac{1}{2} A_{0j} = \left\{ -\frac{1}{3} \frac{1}{r} \frac{\partial v_{\theta j}}{\partial \theta} + v_{\theta j} \left(\frac{1}{R} \frac{1}{r} \frac{\partial R}{\partial \theta} + \frac{1}{3} \frac{1}{B_\theta} \frac{1}{r} \frac{\partial B_\theta}{\partial \theta} \right) + \left(\frac{B_\theta}{B_\phi} \right) \frac{R}{r} \frac{\partial (v_{\phi j}/R)}{\partial \theta} \right\} \quad (10.48)$$

Since $\eta_0 \gg \eta_\Omega \gg \eta_\perp$, we only include the parallel viscosity contribution.

Taking into account that the particle fluxes in the flux surface are much greater than the particle flux across the flux surface to drop v_r terms, we can write the poloidal component of the inertial term, which is the only one that we will need, as

$$\hat{n}_\theta \cdot (\mathbf{v}_j \cdot \nabla) \mathbf{v}_j \simeq \frac{1}{2} \frac{1}{r} \frac{\partial v_{\theta j}^2}{\partial \theta} + \frac{v_{\phi j}^2}{R} \sin \theta \quad (10.49)$$

We develop equations for determining the $\hat{v}_{\theta j}$ and the \tilde{n}_j^s by taking moments of the poloidal component of the steady-state version of Eq. (10.1) weighted by 1, $\cos \theta$, $\sin \theta$, ... and flux surface averaging.

$$\langle (\hat{n}_\theta \cdot \text{Eq. (10.1)}) X \rangle \quad X = 1, \sin \theta, \cos \theta, \dots \quad (10.50)$$

After considerable algebraic reduction, retaining terms through quadratic in the small quantities $(\epsilon, \epsilon \tilde{n}_j^c, \tilde{\Phi}^s)$, these equations can be written, to leading order, as

$$\begin{aligned} \hat{v}_{\theta j} & \left[-q\epsilon \hat{v}_{\phi j} (\tilde{n}_j^s + \tilde{\Phi}^s) - q^2 f_j f_p \left(1 + \tilde{\Phi}^c + \frac{2}{3} \tilde{n}_j^c \right) + f_p \sum_{k \neq j} v_{jk}^* \right] \\ & - f_p \sum_{k \neq j} v_{jk}^* \sqrt{\frac{m_j}{m_k}} \hat{v}_{\theta k} = -q\epsilon \hat{v}_{\phi j} \left[(\hat{P}'_j + \hat{v}_{\phi j}) \tilde{\Phi}^s + \frac{1}{2} \hat{v}_{\phi j} \tilde{n}_j^s \right] \\ & - q^2 f_j f_p \tilde{\Phi}^c (\hat{P}'_j + \hat{v}_{\phi j}) - \frac{1}{4} q\epsilon \tilde{n}_j^s \\ & - \frac{1}{4} q\epsilon \hat{\Phi}_j \left[(1 + \tilde{n}_j^c) \tilde{\Phi}^s - \tilde{n}_j^s \tilde{\Phi}^c \right] - \hat{v}_{rj} \end{aligned} \quad (10.51)$$

$$\begin{aligned} \tilde{n}_j^c & \left[\frac{2}{3} q^2 f_j f_p \hat{v}_{\theta j} - \epsilon^2 f_p \sum_{k \neq j} v_{jk}^* \sqrt{\frac{m_j}{m_k}} \hat{v}_{\theta k} + \epsilon^2 \hat{v}_{rj} \right] \\ & + \tilde{n}_j^s \left[q\epsilon \left(\frac{1}{2} - f_p^2 \hat{v}_{\theta j}^2 \right) \right] = -\epsilon^2 f_p \sum_{k \neq j} v_{jk}^* \hat{v}_{\theta j} \tilde{n}_k^c - \frac{1}{2} q\epsilon \hat{\Phi}_j \tilde{\Phi}^s \\ & - q^2 f_j f_p \left[(1 + \tilde{\Phi}^c) \hat{v}_{\theta j} - \tilde{\Phi}^c (\hat{P}'_j + \hat{v}_{\phi j}) \right] \end{aligned} \quad (10.52)$$

and

$$\begin{aligned} \tilde{n}_j^s & \left[\frac{2}{3}q^2 f_j f_p \hat{v}_{\theta j} - \epsilon^2 f_p \sum_{k \neq j} v_{jk}^* \sqrt{\frac{m_j}{m_k}} \hat{v}_{\theta k} + \epsilon^2 \hat{v}_{rj} \right] \\ & + \tilde{n}_j^c \left[-q\epsilon \left(\frac{1}{2} - f_p^2 \hat{v}_{\theta j}^2 \right) \right] = -\epsilon^2 f_p \sum_{k \neq j} v_{jk}^* \hat{v}_{\theta k} \tilde{n}_k^s \\ & - q\epsilon f_p^2 \hat{v}_{\theta j}^2 + \frac{1}{2} q\epsilon \hat{\Phi}_j \tilde{\Phi}^c \\ & - q^2 f_j f_p \left(\hat{v}_{\theta j} - \hat{v}_{\phi j} - \hat{P}'_j \right) \tilde{\Phi}^s - q\epsilon f_p^2 \hat{v}_{\phi j}^2 \end{aligned} \quad (10.53)$$

where

$$\begin{aligned} f_p & \equiv \frac{B_\theta}{B_\phi} & \hat{v}_{\theta j} & \equiv \frac{\bar{v}_{\theta j}}{f_p v_{thj}} & \hat{v}_{\phi j} & \equiv \frac{\bar{v}_{\phi j}}{v_{thj}} \\ \hat{v}_{rj} & = \left(\frac{e_j B_\phi}{m_j v_{thj}} \right) \left(\frac{q \bar{R}}{v_{thj}} \right) \bar{v}_{rj} & v_{jk}^* & = \frac{q \bar{R} \bar{v}_{jk}}{v_{thj}} \\ \hat{P}'_j & \equiv \frac{1}{\bar{n}_j e_j \bar{B}_\theta v_{thj}} \frac{\partial \bar{p}_j}{\partial r} & \hat{\Phi}_j & \equiv \frac{e_j \bar{\Phi}}{T_j} \\ f_j & \equiv \frac{\epsilon^{-\frac{3}{2}} v_{jj}^*}{(1 + \epsilon^{-\frac{3}{2}} v_{jj}^*)(1 + v_{jj}^*)} \end{aligned} \quad (10.54)$$

There is a set of Eqs. (10.51) to (10.53) for each ion species, and these sets of equations for the different ion species are coupled through the friction and electrostatic potential terms.

10.2.2 Radial Electric Field and Toroidal Rotation Velocities

The steady-state momentum balance Eq. (10.1) can be written for each ion species as

$$\begin{aligned} n_j m_j (\nu_j \cdot \nabla) \nu_j + \nabla p_j + \nabla \cdot \Pi_j \\ = -n_j e_j \nabla \Phi + n_j e_j \nu_j \times \mathbf{B} + \mathbf{R}_j + \mathbf{M}_j - m_j \nu_j S_j^0 \end{aligned} \quad (10.55)$$

where $\mathbf{R}_j = -n_j m_j \nu_{jk} (\nu_j - \nu_k)$ is the interspecies collisional friction and \mathbf{M}_j is the net external momentum input. Taking the flux surface average of the radial component of Eq. (10.55), evaluating the inertial term using

$$n_j m_j [(\nu_j \cdot \nabla) \nu_j]_r = n_j m_j \left[-\cos \theta \frac{\nu_{\phi j}^2}{R} - \frac{\nu_{\theta j}^2}{r} + \frac{1}{2} \frac{\partial \nu_{rj}^2}{\partial r} + \frac{\nu_{\theta j}}{r} \frac{\partial \nu_{rj}}{\partial \theta} \right] \quad (10.56)$$

and assuming $\nu_{rj} \ll \nu_{\theta j} < \nu_{\phi j}$ to justify dropping the last two terms leads to an expression for the flux surface averaged radial electric field

$$\frac{\bar{E}_r}{B_\theta^0} = \nu_{\phi j}^0 - \frac{B_\phi^0}{B_\theta^0} \nu_{\theta j}^0 + \bar{P}'_j - \frac{\bar{I}_j}{B_\theta^0} \quad (10.57)$$

where the inertial contribution is

$$\bar{I}_j \equiv \frac{m_j \epsilon v_{thj}^2}{e_j R_0} \left[\hat{v}_{\phi j} - \hat{v}_{\theta j} (\tilde{\Phi}^c + \tilde{n}_j^c + 2) + \tilde{\Phi}^c (\hat{v}_{\phi j} + \hat{P}_j) + \frac{\hat{v}_{\theta j}^2}{2q^2} \right] \quad (10.58)$$

and the overbar or zero superscript indicates the average value over the flux surface. The requirement that Eq. (10.57) must yield the same value for the radial electric field when the RHS is evaluated for different ion species is a consistency check on the solutions.

The flux surface average of the toroidal component of Eq. (10.55) for each species ‘ j ’ can be written

$$n_j^0 m_j \bar{v}_{jk} \left[(1 + \beta_j) v_{\phi j}^0 - v_{\phi k}^0 \right] = n_j^0 e_j E_\phi^A + e_j B_\theta^0 \Gamma_j + \bar{M}_{\phi j} \equiv n_j^0 m_j \bar{v}_{jk} y_j \quad (10.59)$$

where radial transport of toroidal momentum is represented by the parameter

$$\beta_j \equiv \frac{\bar{v}_{dj}^* + v_{nj} + S_{nbj}/n_j^0}{\bar{v}_{jk}} \quad (10.60)$$

where S_{nb} is e.g. the local neutral beam source rate which arises from the use of the continuity equation to evaluate the radial particle flux needed to evaluate the inertial term, and

$$v_{nj} \equiv v_{rj} \left[\frac{1}{R_0} - \frac{1}{L_{v\phi}} \right] - \frac{1}{2} \frac{\epsilon v_{\theta j}^0}{R_0} \left[-\tilde{v}_{\theta j}^c (\tilde{v}_{\phi j}^s + \tilde{n}_j^s) + v_{\theta j}^s (2 + \tilde{v}_{\phi j}^c + \tilde{n}_j^c) + (\tilde{v}_{\theta j}^s + \tilde{v}_{\phi j}^s + \tilde{n}_j^s) \right] \quad (10.61)$$

S_{nbj}/n_j^0 is the rate of radial transport of toroidal angular moment due to momentum convection and v_{nj} is the rate of radial transport of toroidal angular moment due to inertial effects. The ion-electron friction term has been neglected. A sum over other species ‘ k ’ is implied and the collisional momentum conservation requirement $n_j^0 m_j \bar{v}_{jk} = n_k^0 m_k \bar{v}_{kj}$ has been used in Eq. (10.59).

Using the radial momentum balance Eq. (10.57) in the toroidal momentum balance Eq. (10.59) to eliminate the $v_{\phi j}^0$ and summing over species yields another expression for the radial electrostatic field when only two species are present

$$\frac{\bar{E}_r}{B_\theta^0} = \frac{\left\{ \hat{M}_{\phi k} + \hat{M}_{\phi j} \right\} + \beta_{\sigma j} \left\{ \bar{P}'_j - \frac{B_\phi^0}{B_\theta^0} v_{\theta j}^0 \right\} + \beta_k \left\{ \bar{P}'_k - \frac{B_\phi^0}{B_\theta^0} v_{\theta k}^0 \right\} - \frac{I_j + I_k}{B_\theta^0}}{\beta_j + \beta_k} \quad (10.62)$$

that displays the dependence on momentum input, pressure and poloidal rotation velocity.

10.3 Momentum Confinement Times

10.3.1 Theoretical

For our purposes, gyroviscous momentum transport across a flux surface in a tokamak for ion species "j" may be characterized by the frequency

$$\nu_{dj} = \frac{T_j \tilde{\theta}_j r (L_{nj}^{-1} + L_{Tj}^{-1} + L_{v_{\phi j}}^{-1})}{2R_0^2 Z_j e B} \quad (10.63)$$

where $\tilde{\theta}_j$ is given by Eq. (10.23) and the $L_x = -x / (dx/dr)$ are gradient scale lengths. The poloidal rotation speeds and sine and cosine components of the density and potential variation needed to evacuate $\tilde{\theta}_j$ may be evacuated from poloidal momentum balance, as discussed in the previous section.

Using this expression for the toroidal momentum radial transport rate to evaluate the definition of momentum confinement time yields

$$\begin{aligned} \tau_{\phi}^{gv} &\equiv \frac{2\pi R \sum_j \int_0^a \langle R n_j m_j v_{\phi j} \rangle r dr}{2\pi R \sum_j \int_0^a \langle R^2 \nabla \phi \cdot \nabla \cdot \Pi_j^{gv} \rangle r dr} \\ &= \frac{2R_0^2 e B h_{nvT}}{T_0} \frac{\left(\sum_j \frac{n_j}{n_e} m_j \right)_{av}}{\left(\sum_j \frac{n_j}{n_e} \frac{m_j}{Z_j} \tilde{\theta}_j r (L_{nj}^{-1} + L_{Tj}^{-1} + L_{v_{\phi j}}^{-1}) \right)_{av}} \end{aligned} \quad (10.64)$$

where the h_{xy} are profile factors resulting from writing $n(r) = n_0 f_n(r)$, etc. For example,

$$h_{nv}^{-1} \equiv \frac{(2\pi R) \int_0^a f_n(r) f_v(r) 2\pi r dr}{(2\pi R) \int_0^a 2\pi r dr} = \frac{2}{a^2} \int_0^a f_n(r) f_v(r) r dr \quad (10.65)$$

and the subscript av indicates an appropriate average of the quantity that may then be removed from under the integral to facilitate the approximate evaluation.

There is also a convective momentum confinement time associated with the convective flux of angular momentum carried by the outward (or inward) particle flux. The total momentum confinement time may be written as

$$\begin{aligned} \tau_{\phi}^{\text{th}} &\equiv \frac{2\pi R \sum_j \int_0^a \langle R n_j m_j v_{\phi j} \rangle r dr}{2\pi \sum_j \int_0^a \langle R^2 \nabla \phi \cdot \nabla \cdot \pi_j^{gv} \rangle r dr + 2\pi R \sum_j \int_0^a \left\langle R \frac{\partial}{\partial r} (n_j m_j v_{\phi j} v_{rj}) \right\rangle r dr} \\ &= \frac{\tau_{\phi}^{gv}}{1 + C} \end{aligned} \quad (10.66)$$

where the ratio of the gyroviscous to convective momentum confinement times is

$$C \equiv \frac{\int_0^a \sum_j \left\langle R \frac{\partial}{\partial r} (n_j m_j v_{\phi j} v_{rj}) \right\rangle r dr}{\int_0^a \sum_j \langle R^2 \nabla \phi \cdot \nabla \cdot \Pi_j \rangle r dr} \quad (10.67)$$

The input torque from the neutral beams is related to the momentum confinement time and the angular momentum of the plasma by

$$\Gamma_\phi = \frac{(2\pi R) \int_0^a \langle R \sum_j^{\text{ions}} n_j m_j v_{\phi j} \rangle 2\pi r dr}{\tau_\phi^{\text{th}}} \quad (10.68)$$

The theoretical momentum confinement time of Eq. (10.66) and the neutral beam torque input can be combined to obtain an expression for the central rotation frequency,

$$\Omega_{\phi 0}^{\text{th}} \equiv \frac{v_{\phi 0}^{\text{th}}}{R} = \frac{\Gamma_\phi \tau_\phi^{\text{th}} h_{nv}}{2\pi^2 a^2 R^3 \left(\sum_j^{\text{ions}} \frac{n_j}{n_e} m_j \right)_{av} n_{e0}} \quad (10.69)$$

10.3.2 Experimental

If the central toroidal rotation frequency and density and the rotation and density profiles are measured, then an experimental angular momentum confinement time can be constructed from an expression which is based on the same relationship among input torque, angular momentum and momentum confinement time as in Eqs. (10.68) and (10.69), namely

$$\begin{aligned} \tau_\phi^{\text{exp}} &\equiv \frac{(2\pi R) \int_0^a \left\langle R \sum_j^{\text{ions}} n_j m_j v_{\phi j} \right\rangle 2\pi r dr}{\Gamma_\phi - (2\pi R) \int_0^a R \sum_j^{\text{ions}} m_j \frac{d}{dt} (n_j v_{\phi j}) 2\pi r dr} \\ &= \frac{2\pi^2 a^2 R^3 \left(\sum_j^{\text{ions}} \frac{n_j}{n_e} m_j \right)_{av} n_{e0} \Omega_{\phi 0}^{\text{exp}}}{\Gamma_\phi h_{nv} - 2\pi^2 a^2 R^3 \left(\sum_j^{\text{ions}} \frac{n_j}{n_e} m_j \right)_{av} \frac{d}{dt} (n_{e0} \Omega_{\phi 0}^{\text{exp}})} \end{aligned} \quad (10.70)$$

This expression, when evaluated with measured quantities, is the appropriate quantity for comparison with the theoretical expressions of Eq. (10.66).

Problems for Chapter 10

- Using the minor radius, a , and ϵ times the poloidal connection length, $\epsilon 2\pi a$, as estimates of the radial and poloidal gradient scale lengths, respectively, estimate the ratio of the perpendicular and gyroviscous toroidal viscous forces from Eqs. (10.11) and (10.12) for a tokamak plasma with $T = 5 \text{ keV}$, $n_D = n_e = 5 \times 10^{19} \text{ m}^{-3}$ and a toroidal magnetic field $B = 5 \text{ T}$.
- Calculate and plot the parallel viscosity function $f_j(v_{jj}^*)$ of Eq. (10.46) vs. v_{jj}^* over the range $10^{-4} < v_{jj}^* < 10^1$.
- Calculate the torque injected into a tokamak plasma by 10 MW of 80 keV neutral beams with a radius at the point of tangency $R_{\tan} = 1.85 \text{ m}$ (R_{\tan} is the perpendicular distance from the centerline of the tokamak [$R = 0$] to the trajectory of the beam path).

4. Calculate the gyroviscous momentum confinement time in the tokamak plasma of problem 1 with $R = 1.7\text{ m}$, $a = 0.7\text{ m}$, $r_{av} = a/2$, $\tilde{\theta} = 0.1\epsilon$ and in which the radial distributions of n , T and v_ϕ are parabolic $X(r) = X_0(1 - (r/a)^2)$.
5. Calculate the central rotation velocity in the tokamak plasma of problems 1, 3 and 4.
6. If a current of 3 MA is distributed as $j(r) = j_0(1 - (r/a)^2)$ in the plasma of problems 1, 3 and 4, and the measured values at $r/a = 0.5$ of the toroidal and poloidal rotation velocities are $v_\phi = 2 \times 10^5 \text{ m} \cdot \text{s}^{-1}$ and $v_\theta = 1 \times 10^4 \text{ m} \cdot \text{s}^{-1}$ and of the pressure gradient scale length is 20 cm, calculate the radial electric field.

11 Turbulent Transport

The neoclassical transport described in chapter 9 sets the lower limit on the transport loss rate. In practice, the measured loss rate in tokamaks is almost always greater than the neoclassical rate for electrons and is usually greater than the neoclassical rate for ions. The excess over the neoclassical rate is usually referred to as “anomalous” transport because it is not yet fully understood. This additional transport is widely believed to be associated with the turbulent fluctuations in density, the electric field and the magnetic field which are usually observed experimentally.

Although the most conspicuous instabilities observed in tokamaks are the long wavelength, low- m MHD modes such as those responsible for disruptions (chapter 18), there appears to be little, if any, correlation between the intensity of these modes and the observed electron loss rates in macroscopically stable plasmas. Such modes doubtless affect the local transport in the vicinity of their resonant surfaces but do not appear to contribute to the overall electron loss rate. Consequently, investigations have focused on short wavelength fluctuations referred to as microturbulence. The relative density fluctuations are generally observed to be $\leq 1\%$, in the center and to increase radially to 10 to 100 %, in the plasma edge, while the radial magnetic fluctuations are generally $\leq 10^{-4}$ in the edge and increase into the plasma.

There are two obvious ways that microturbulence can lead to enhanced particle and energy radial transport rates: (1) the $E \times B$ drift across the confining field lines resulting from fluctuating electric fields, or (2) the motion along magnetic field lines with a fluctuating radial component. The most effort has been devoted to understanding turbulent transport arising from the $E \times B$ drift produced by various electrostatic drift waves.

An intensive research effort has been devoted to the area of turbulent transport over the past two decades. Linear and nonlinear analyses, in various idealizations, have led to numerous models for turbulent transport coefficients. The effort to identify specific microinstabilities that produce observed transport rates has been difficult, but there is substantial supporting evidence for resistive ballooning drift waves as the primary cause of turbulent transport in ohmic heated tokamaks and for ion temperature gradient (ITG) drift waves as the primary cause of turbulent transport in auxiliary heated tokamaks. The major thrust of current research has now turned to the numerical calculation of the nonlinear evolution to a saturated state of many coupled microinstability modes in realistic geometry.

11.1 Electrostatic Drift Waves

11.1.1 General

First, we consider the two-fluid (ion–electron) description of electrostatic drift waves. We postulate an equilibrium (with parameters denoted by the 0 subscript) in which $E_0 =$

$\mathbf{v}_0 = 0$. Then we consider fluctuations about the equilibrium values. The electrostatic assumption allows us to write the fluctuating electric field as $\mathbf{E} = -\nabla\phi$. If we neglect, or average over, the gyromotion, the fluctuating ion guiding center velocity perpendicular to the magnetic field can be written as the sum of the fluctuating $\mathbf{E} \times \mathbf{B}$ and polarization drifts

$$\mathbf{v}_{i\perp} = -\frac{\nabla\phi \times \mathbf{B}}{B^2} - \frac{m_i}{eB^2} \frac{d}{dt}(\nabla_{\perp}\phi) \quad (11.1)$$

The fluctuating ion guiding center velocity along the field lines is determined by the linearized parallel ion momentum balance equation

$$n_o m_i \frac{dv_{i\parallel}}{dt} = -\nabla_{\parallel}(n_o e\phi + \tilde{n}_i T_i) \quad (11.2)$$

where n_0 is the value of the local equilibrium ion and electron densities. The fluctuating ion density, \tilde{n}_i^* , satisfies the linearized continuity equation

$$\frac{\partial \tilde{n}_i}{\partial t} + \nabla \cdot (n_o \mathbf{v}_i) = 0 \quad (11.3)$$

The Boltzmann description of the electron response to a potential fluctuation is

$$\frac{\tilde{n}_e}{n_o} = \left[\exp\left(\frac{e\phi}{T_e}\right) - 1 \right] = \frac{e\phi}{T_e}(1 - i\delta) \simeq \frac{e\phi}{T_e} \quad (11.4)$$

Although the last form of Eq. (11.4) is commonly used, it is important in drift wave analysis to take into account that any dissipation (e.g. resistance, resonant electrons, trapped electrons) introduces an out of phase addition (the $i\delta$ term) to the electron Boltzmann distribution, which can be determined by analysis of the electron momentum balance.

Consideration of the above equations, in toroidal geometry and without dissipation in the last equation, for the simple wave

$$\phi(x, y, z, t) = \phi(x) \exp[i(k_y y + k_{\parallel} z - \omega t)] \quad (11.5)$$

is instructive. Here x is the flux surface or radial coordinate, y is the coordinate perpendicular (\perp or θ) in the flux surface, and z is the parallel coordinate. Using quasi-neutrality and the last form of Eq. (11.4) allows \tilde{n}_i to be replaced by ϕ . Assuming uniform temperature along field lines, Eq. (11.2) and (11.3) can then be solved for the two components of the fluctuating ion velocity in terms of ϕ , resulting finally in a dispersion relation.

The drift wave is essentially the ion acoustic wave in a nonuniform plasma. The restoring forces are the electrostatic potential and ion pressure gradients – see Eq. (11.2). In a uniform plasma, the ion acoustic waves occur as oscillations parallel to the magnetic field with frequency

$$\omega_{ac}^2 = \frac{k_{\parallel}^2 c_s^2}{1 + \frac{1}{2} k_{\perp}^2 \rho_i^2 r_T} \quad (11.6)$$

where $r_T = T_e/T_i$, ρ_i is the ion gyroradius, and $c_s = [(T_e + T_i)/m_i]^{1/2}$.

The dispersion relation for ion acoustic waves with a perpendicular wave number k_{\perp} is derived from consideration of the polarization currents

$$\mathbf{j}_p = \frac{\sum_j \tilde{n}_j m_j}{B^2} \frac{d\mathbf{E}_{\perp}}{dt} \quad (11.7)$$

A consequence of a large polarization current across the magnetic field is that transverse electromagnetic waves with $\omega < \Omega_i$, the ion gyrofrequency, propagate as Alfvén waves. In the absence of a radial nonuniformity, the ion acoustic waves are strongly damped by Landau damping from the wave-ion resonance because the parallel phase velocity $\omega/k_{\parallel} \approx c_s$ is comparable to the peak of the parallel velocity distribution.

In a nonuniform plasma, the density is also perturbed by the $\mathbf{E} \times \mathbf{B}$ drift, which convects plasma along the equilibrium density gradient, giving rise to a $\omega\omega^*$ term, where $\omega^* = -(k_y T_e / e B n_0) (dn_0 / dx)$, which is important only for waves propagating nearly perpendicular to the magnetic field, $k_{\parallel}/k \leq \rho_i/L_n$, where $L_n = -n_0/(dn_0/dr)$. Inclusion of the density gradient term leads to separate dispersion relations for fast and slow ion acoustic waves. The slow waves are strongly damped, $\omega \approx -k_{\parallel}^2 c_s^2 / k_y v_{de}$, where $v_{de} = -(T_e / e B n_0) (dn_0 / dx) = \omega^*/k_y$ is the electron drift velocity. For the fast waves, on the other hand,

$$\omega_D = \frac{k_y v_{de}}{1 + k_{\perp}^2 \rho_i^2} + \frac{k_{\parallel}^2 c_s^2}{k_y v_{de} (1 + k_{\perp}^2 \rho_i^2)} \gg k_{\parallel} c_s \quad (11.8)$$

This dispersion relation determines the formation and propagation of drift waves in tokamaks when the ion temperature and ion temperature gradient are not important. This drift wave propagates fast along the field lines and slow across the magnetic field. The $k_{\perp}^2 \rho_i^2$ term arises from the ion polarization drift and is only important for short wavelengths.

When the drift wave becomes unstable, it extracts plasma compressional energy, which is transferred to the wave via parallel current flow. In a uniform plasma this current would extract energy from the wave via ohmic dissipation or Landau damping, thus damping the wave. However, in a nonuniform plasma, the $\mathbf{E} \times \mathbf{B}$ drift converts some of the radial pressure gradient into a pressure gradient along the magnetic field lines. These parallel gradients then drive an electron current the phase of which is such that it does work on the wave electric field, increasing the wave energy. Any dissipation introduces an out of phase addition (i.e. the δ term in Eq. (11.4)) which will cause the density peak to lead the potential peak when $\delta > 0$, resulting in exponential growth, or to follow the potential peak, causing exponential decay, or damping, when $\delta < 0$.

Analysis of the parallel electron momentum balance shows that in the collisional regime the plasma resistivity produces a positive δ . For the collisionless regime, the effects of particle trapping and the resonant electron-wave interactions usually produce a positive δ .

11.1.2 Ion Temperature Gradient Drift Waves

It is important to retain the separate representation of low- Z impurities in developing a dispersion relation for ion temperature gradient (ITG) instabilities. The electrostatic kinetic dispersion relation for multiple charged species (electrons, ions, impurities) all distributed in local Maxwellian distributions, is

$$D(\mathbf{k}, \omega) = \sum_j \frac{n_j e_j^2}{T_j} \left[1 - \left\langle \frac{\omega - \omega_j^*(\epsilon_j)}{\omega - \omega_{Dj} - k_{\parallel} v_{\parallel}} J_0^2 \right\rangle \right] \quad (11.9)$$

where the $\langle \rangle$ indicates an average over a Maxwellian distribution, $\epsilon_j = m_j v^2 / 2T_j$, J_0 is the Bessel function, and the density and temperature gradients enter through

$$\omega_j^* = \frac{k_y T_j}{e_j n_{0j} B} \left(\frac{\partial n_{0j}}{\partial r} \right) \left[1 + \eta_j \left(\epsilon_j - \frac{3}{2} \right) \right] \quad (11.10)$$

where

$$\eta_j = \frac{1}{T_j} \frac{\partial T_j}{\partial r} / \frac{1}{n_{0j}} \frac{\partial n_{0j}}{\partial r} = \frac{L_{nj}}{L_{Tj}} \quad (11.11)$$

The wave-particle resonance is determined by the resonance denominator $\omega - k_{\parallel} v_{\parallel} = \omega_{Dj}$, where the guiding center drift frequency is

$$\omega_{Dj} = \frac{k_y T_j}{e_j B R} \left(\frac{m_j v_{\perp}^2}{2T_j} + \frac{m_j v_{\parallel}^2}{T_j} \right) \quad (11.12)$$

An important feature of the ion temperature gradient (ITG) modes is that in certain plasma regimes there is a critical value η_c above which there is a strong drift wave instability. In general, this critical value of the temperature gradient is a complicated function of the plasma parameters, but there is a useful approximation in the limit $k_{\parallel} v_{\text{thi}} / \omega_{Di} \rightarrow 0$

$$\eta_c = \frac{4}{3} \frac{L_n}{R} \left(1 + \frac{T_i}{T_e} \right) (1 + k_y^2 \rho_i^2) \quad (11.13a)$$

and another in the limit of small toroidicity $L_n / R \rightarrow 0$

$$\eta_c = 1 - \frac{2}{3} \frac{L_n}{R} \left(1 + \frac{T_i}{T_e} \right) (1 + k_y^2 \rho_i^2) \quad (11.13b)$$

11.1.3 Quasilinear Transport Analysis

In the quasilinear approach, the various plasma parameters (in fluid theory) or the distribution function (in kinetic theory) are formally expanded as the time independent equilibrium solution plus a term that is first order in the fluctuation amplitude plus higher order terms. Using a general wave form like Eq. (11.5) implies a sine or cosine variation in the plane perpendicular to x (in toroidal geometry x is the flux surface or radial coordinate, y is

the coordinate perpendicular to the magnetic field in the flux surface, and z is the parallel coordinate). Thus, averages over the flux surface of terms that are linear in the first-order fluctuations vanish, and the leading order surviving terms in the particle and heat fluxes are second order in the fluctuations.

There are two types of terms that are second order in the fluctuation amplitudes: (1) products of two terms that are each first order in the fluctuation amplitude; and (2) individual higher order terms which are intrinsically second order in the fluctuation amplitude. In quasilinear theory the type-2 terms are neglected.

Formally, the kinetic theory expression for the flux surface average particle flux arising from the $\mathbf{E} \times \mathbf{B}$ drift is

$$\Gamma = \left\langle \int f_1 \left(\frac{E_y}{B} \right) dv \right\rangle \quad (11.14)$$

where (E_y/B) is the $\mathbf{E} \times \mathbf{B}$ drift, which is first order in the fluctuation amplitude, and f_1 is the first order in fluctuation amplitude component of the distribution function, which in cylindrical geometry is

$$f_1 = -\frac{1}{\omega - k_{\parallel} v_{\parallel}} \frac{k_y}{B} (\phi - v_{\parallel} A_{\parallel}) \frac{\partial f_M}{\partial r} \quad (11.15)$$

where f_M is the Maxwellian distribution and ϕ and A_{\parallel} are the electrostatic potential and the parallel component of the vector potential, both of which are first order in the fluctuation amplitude. For electrostatic fluctuations, $A_{\parallel} = 0$. When trapped particles are present, $k_{\parallel} v_{\parallel}$ in the denominator averages to zero over the flux surface, and the denominator in Eq. (11.15) must be modified to account for the precessional drift of trapped particles and their Coulomb detrappling rate.

In fluid theory, the quasilinear expressions for the flux surface average particle and energy transport arising from electrostatic turbulence can be formally written

$$\Gamma_j = \frac{1}{S} \int_s \tilde{n}_j \mathbf{v}_E \cdot d\mathbf{s} \quad (11.16)$$

and

$$q_j = \frac{1}{S} \int_s \frac{3}{2} \tilde{n}_j T_j \mathbf{v}_E \cdot d\mathbf{s} \quad (11.17)$$

In a cylindrical model, the electron particle flux becomes

$$\Gamma_e = \frac{1}{2\pi} \int_0^{2\pi} \tilde{n}_e \left[\frac{\mathbf{E} \times \mathbf{B}_0}{B_0^2} \right]_r d\theta = -\frac{1}{2\pi r B_0} \int_0^{2\pi} \tilde{n}_e \frac{\partial \phi}{\partial \theta} d\theta \quad (11.18)$$

Using Eq. (11.4) and assuming the dissipation term is small, $\delta \ll 1$, yields

$$\Gamma_e = \frac{n_0 T_e}{e B} k_\theta \delta \left\langle \left(\frac{\tilde{n}_e}{n_0} \right)^2 \right\rangle \quad (11.19)$$

where we recall that \tilde{n}_e is the fluctuating part of the electron density. The linear growth rate of the drift wave is $\gamma = \delta \omega^*$, where $\omega^* = -(k_y T_e / e B n_0) (\partial n_0 / \partial x)$, which when

used in Eq. (11.19) results in a diffusive electron particle flux

$$\Gamma_e = -L_n^2 \nu \left\langle \left(\frac{\tilde{n}_e}{n_0} \right)^2 \right\rangle \frac{\partial n_0}{\partial r} \equiv -D \frac{\partial n_0}{\partial r} \quad (11.20)$$

with a diffusion coefficient which depends upon the flux surface average of the fractional electron density fluctuation level

$$D = L_n^2 \nu \left\langle \left(\frac{\tilde{n}_e}{n_0} \right)^2 \right\rangle \quad (11.21)$$

When the saturated density fluctuation level is known from experiment, Eq. (11.20) and a similarly derived equation for the heat flux provide an estimate of the electrostatic drift wave turbulent transport rates.

11.1.4 Saturated Fluctuation Levels

Determination of the saturated fluctuation level and the corresponding transport rate is quite difficult. However, there are a number of dimensional scaling and plausibility arguments that lead to useful analytical results.

If the turbulence is on the microscopic spatial scale of the ion gyroradius (ρ_i), then dimensional analysis leads to scalings for the fluctuations (e.g. in electrostatic potential)

$$\frac{e\phi}{T_e} = \frac{\rho_i}{L_n} F(v^*, \beta, \dots) \quad (11.22)$$

and to corresponding gyro-Bohm diffusion coefficients

$$D = D_{gB} F = \frac{\rho_i}{L_n} \left(\frac{T_e}{eB} \right) F \quad (11.23)$$

On the other hand, if the fluctuations have a spatial scale $\Delta \sim a$, instead of ρ_i , such that $a/\rho_i \gg 1$, then

$$\frac{e\phi}{T_e} = \frac{\Delta}{a} F(v^*, \beta, \dots) \quad (11.24)$$

and the corresponding Bohm diffusion coefficient is

$$D = D_B F = \left(\frac{T_e}{eB} \right) F \quad (11.25)$$

Although there have been many attempts to correlate measured transport rates with Bohm and gyro-Bohm scaling, which are quite different, there is not a consensus on this issue. The calculation of specific forms for the function F requires a model for the nonlinear saturation mechanism.

A model for the nonlinear saturation mechanism is also needed for the calculation of saturated fluctuation levels. However, a simple physical argument can provide some guidance. An upper bound on transport is given by Kadomtsev's mixing length estimate, in which it is assumed that the instability cannot grow beyond the amplitude at which the fluctuation density gradients are large enough to reverse the equilibrium density gradient that is driving the fluctuation, giving an upper bound $k_{\perp} \tilde{n}_e \leq n_0 / L_n$. When used in Eq. (11.21) this bound leads to

$$D \simeq \frac{\gamma}{k_{\perp}^2} \quad (11.26)$$

This result can also be derived from a balance between the linear growth rate of a mode and its stabilization rate due to turbulent diffusion, $k_{\perp}^2 D$.

With weak turbulence, a balance between the wave energy growth rate, $\gamma |\phi|^2$, and the nonlinear wave scattering due to ions can be invoked. The damping arises from the $(\mathbf{E} \times \mathbf{B} / B^2) - \nabla f_1$ nonlinearity in the ion kinetic equation and leads to a damping rate $k_{\perp}^4 |\phi|^4 / \omega^* B^2$, where $\omega^* = k_{\perp} T / BL_n$ is the diamagnetic frequency. The balance leads to

$$\left| \frac{e\phi}{T} \right|^2 \simeq \frac{\gamma}{\omega^*} \frac{1}{k_{\perp}^2 L_n^2} \quad (11.27)$$

Use of Eqs. (11.27) and (11.4) in Eq. (11.21) yields the weak turbulence estimate of the diffusion coefficient

$$D \simeq \frac{\gamma^2}{\omega^* k_{\perp}^2} \quad (11.28)$$

Note that both the mixing length estimate of Eq. (11.26) and the weak turbulence estimate of Eq. (11.28) require a specific model of the microinstability for calculation of the linear growth rate, γ .

11.2 Magnetic Fluctuations

A magnetic perturbation of the form

$$\tilde{B}_r = \tilde{B} \cos(m\theta - n\phi) \quad (11.29)$$

is resonant at a magnetic surface at $r = r_{mn}$ where the condition $q = m/n$ obtains. In the presence of such a perturbation, the resonant magnetic surface is destroyed and a magnetic island is formed, as indicated in Fig. 11.1.

In toroidal geometry, the island on the $r = r_{mn}$ surface winds helically about the torus, as shown in Fig. 11.2 for the ($m = 3, n = 1$) island.

The radial width, w_{mn} , of the magnetic island that replaces the rational surface at r_{mn} is given by

$$w_{mn} = \left(\frac{L_s r_{mn}}{m} \frac{\tilde{B}_r}{B} \right)^{\frac{1}{2}} \quad (11.30)$$

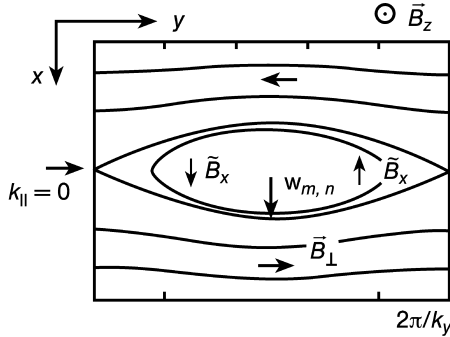


Figure 11.1. Magnetic island formed at a mode rational surface. Local Cartesian coordinates (x,y) correspond to radial and poloidal coordinates, respectively

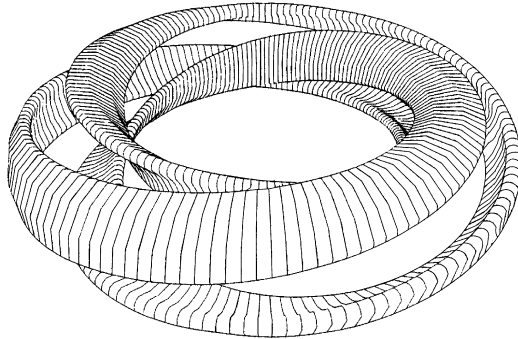


Figure 11.2. The ($m = 3, n = 1$) magnetic island in a toroidal plasma

where $L_s = Rq/r(dq/dr)$ is the shear length. As the perturbation \tilde{B}_r is increased, the width of each island increases and more of the region between the islands is affected, becoming ergodic. The parameter

$$\alpha = \frac{1}{2} \frac{w_{mn} + w_{m'n'}}{|r_{mn} - r_{m'n'}|} \quad (11.31)$$

characterizes the ergodic nature of the region between resonant surfaces (m, n) and (m', n'), with the field line structure becoming predominantly ergodic when $\alpha \rightarrow 1$. When $\alpha \gg 1$, many islands overlap and the field line structure becomes stochastic, and the parameter α may be generalized to

$$\alpha = \sum_{m,n} w_{mn}/\Delta r \quad (11.32)$$

where the sum is over all rational surfaces within Δr (i.e. those for which $nq(r) < m < nq(r) + n(dq/dr)\Delta r$, so that $\alpha = \Sigma_n w_{mn}n[dq/dr]$ independent of m).

If the field perturbation, \tilde{B}_r , remains in the same direction (in or out) for a distance L_M in the toroidal direction (i.e. L_M is a magnetic correlation length), then the radial displacement of the field over a toroidal distance equal to L_M is $\delta r \approx (\tilde{B}_r/B)L_M$. If the direction (in or out) of \tilde{B}_r over successive correlation lengths is uncorrelated, then particles traveling along the field lines undergo a radial random walk process. In the collisionless limit, when the collisional mean free path $\lambda > L_M$, a particle moves freely along the field line with velocity v_{\parallel} for an average distance L_M before the direction of the perturbation \tilde{B}_r changes, becoming displaced radially a distance $\delta r \approx (\tilde{B}_r/B)L_M$ in a characteristic time L_M/v_{\parallel} . This collisionless random walk process can be characterized by a diffusion coefficient

$$D \approx \frac{(\delta r)^2}{(L_M/v_{\parallel})} = \left(\frac{\tilde{B}_r}{B} \right)^2 L_M v_{\parallel} \simeq \left(\frac{\tilde{B}_r}{B} \right)^2 q R v_{\parallel} \quad (11.33)$$

We have used the weak turbulence result for the correlation length, $L_M \approx qR$, in the last form of this equation.

If, on the other hand $\lambda < L_M$, a particle will move along a field line under the influence of a constant inward or outward \tilde{B}_r only for the mean distance λ before it has a collision. Assuming that the collision displaces the particle's guiding center to an uncorrelated field line, the particle performs a random walk radially with step size $\delta r_c \approx (\tilde{B}_r/B)\lambda$ in characteristic time λ/v_{\parallel} , leading to an estimate of a collisional diffusion coefficient

$$D \approx \frac{(\delta r_c)^2}{(\lambda/v_{\parallel})} = \left(\frac{\tilde{B}_r}{B} \right)^2 \lambda v_{\parallel} \quad (11.34)$$

Relating the term (\tilde{B}_r/B) to the island width by Eq. (11.30) and estimating a radial gradient scale length as an island width leads to the estimate

$$(\delta r)^2/L_M \approx \frac{k_{\perp} w_{mn}^3}{R q / r (dq/dr)}$$

There are a number of island width theories that suggest $w_{mn} \sim 1/n$, in which case

$$D \approx \left(\frac{v_{\parallel} R}{q^3 s^2} \right) \left(\frac{r}{R} \right) \left(\frac{\alpha_s}{N} \right) \quad (11.35)$$

where $s = (r/q)(dq/dr)$ is the shear, $\alpha_s \approx 1$, and N is the number of toroidal modes in Δr . The ion and electron heat diffusivities are similarly derived, and for this case $\chi_i \approx D$ and $\chi_e \approx (m_i/m_e)^{1/2} \chi_i$.

11.3 Candidate Microinstabilities

Widespread belief that turbulent transport is dominant in tokamaks has led to an intensive and still ongoing search for the microinstabilities which produce the observed transport rates. The transport rates predicted by some of the current favorites are summarized in this section.

11.3.1 Drift Waves and ITG Modes

For ohmic and L-mode plasmas the combination of electrostatic trapped electron drift waves and ion temperature gradient (ITG) modes, with a contribution from resistive ballooning modes near the edge, is probably currently the leading candidate.

The principal electron drift wave instabilities arise from trapped electron effects when the collisionality parameter $v_e^* = v_e/\epsilon^{3/2}(v_{the}/qR) < 1$. These waves typically have $k_\theta \rho_i \approx 0.3$ and $\omega \approx \omega_e^* = -(k_\theta T_e/eBn_0)(dn_0/dx)$. When $v_e^* > 1$, the mode becomes the collisional drift wave destabilized by circulating particles. There are many models for the associated thermal diffusivity, depending on whether toroidicity is included in the mode structure and the saturation mechanism approximation. These diffusivity expressions have the gyro-Bohm form of Eq. (11.23). A representative expression, which includes the transition from the dissipative trapped electron mode to the collisionless mode driven by the precessional drift resonance as $v_e^* \rightarrow 0$, is

$$\chi_e \simeq \frac{5}{2} \frac{\epsilon^{3/2}}{v_e} \frac{c_s^2 \rho_i^2}{L_n L_{Te}} \frac{1}{1 + 0.1/v_e^*} \quad (11.36)$$

While this expression reproduces certain observed features of ohmic and L-mode transport rates, it predicts a radial profile that decreases towards the plasma edge, contrary to the trend inferred from experimental observations.

The ITG mode, with $k_\perp \rho_i \leq 1$, becomes unstable when $\eta_i = L_n/L_{Ti}$ becomes sufficiently large. In slab geometry, the instability condition is just $\eta_i \geq 1$, but in toroidal geometry the more relevant instability criterion is $L_{Ti} < L_{Ticrit} \approx 0.1R$. Several gyro-Bohm expressions for the ion thermal diffusivity take the form

$$\chi_i \simeq \frac{5}{2} \left(\frac{1}{RL_{Ti}} \right)^{1/2} \left(\frac{T_e}{m_i} \right) \left(\frac{m_i}{e_i B} \right)^{1/2} \rho_i H \left(\frac{1}{L_{Ti}} - \frac{1}{L_{Ticrit}} \right) \quad (11.37)$$

where H is the Heaviside function which is unity when $L_{Ti} < L_{Ticrit} \approx 0.1R$ and zero otherwise. This expression has had some success in matching observed ohmic and L-mode transport rates, particular with versions for which the function $F \sim q$.

One possible consequence of a critical temperature gradient, above which the transport increases significantly, is that once the critical gradient is exceeded the enhanced transport will cause the temperature gradient to relax back towards the critical gradient. This would result in a certain “stiffness” in the temperature profile, which is consistent with experimental observation.

11.3.2 Trapped Ion Modes

Trapped ion modes (TIM) are predicted to be unstable in collisionless plasmas for which $v_i^* = v_i/\epsilon^{3/2}(v_{thi}/qR) < 1$. The ion thermal diffusivity for the TIM instability is

$$\chi_i \simeq \frac{3}{2\sqrt{2}} \frac{\rho_i^2 c_s R}{L_n^2} \sqrt{\frac{m_e}{m_i}} \frac{\epsilon^{1/2} q}{s^2 v_e^*} \quad (11.38)$$

11.3.3 Electron Temperature Gradient Modes

In addition to unstable electron drift waves with $k_{\perp}\rho_i \leq 1$, there is also an electron temperature gradient (ETG) mode with $k_{\perp} \leq \omega_{pe}/c$ which is unstable for $\eta_e = L_n/L_{Te} \geq 1$. A gyro-Bohm-like expression for the electron thermal diffusivity is

$$\chi_e \simeq 0.13 \left(\frac{c_s}{\omega_{pe}} \right)^2 \frac{v_{the}s}{qR} \eta_e (1 + \eta_e) \quad (11.39)$$

11.3.4 Resistive Ballooning Modes

The resistive ballooning mode is an electrostatic wave destabilized by the pressure gradient in regions of unfavorable curvature. The wave has a magnetic component that can lead to a stochastic magnetic field. The electron thermal diffusivity arising from these modes is given by

$$\chi_e \simeq C \eta \left(\beta \frac{m_i}{m_e} \right)^{\frac{1}{2}} \left(\frac{\alpha}{s} \right)^{\frac{3}{2}} \quad (11.40)$$

where now η is the plasma resistivity, $\beta = p/(B^2/2\mu_0)$, $\alpha = -(2\mu_0 R q^2/B^2)(dp/dr)$ and $C \geq 10$.

11.3.5 Chaotic Magnetic Island Overlap

If islands overlap, the magnetic field becomes ergodic. A semi-empirical RLW model based on a critical electron temperature gradient necessary for the self-sustainment of the chaotic magnetic field was constructed to reproduce the ohmic and L-mode transport observed in JET. The model has an underlying neoclassical value for the electron heat diffusivity and an enhancement that becomes nonzero when $dq/dr > 0$ and the electron temperature gradient exceeds a critical value

$$|\nabla T_{ecrit}| = 0.06 \frac{e}{(\mu_0 m_e^{\frac{1}{2}})^{\frac{1}{2}} q} \left(\frac{\eta j B^3}{n_0 T_e^{\frac{1}{2}}} \right)^{\frac{1}{2}} \quad (11.41)$$

where again η is the plasma resistivity, and j is the plasma current density. The resulting enhancement of the electron heat diffusivity is

$$\begin{aligned} \Delta \chi_e \simeq 0.5 c_s^2 \sqrt{\mu_0 m_i} \frac{(1 - \sqrt{\epsilon})(1 + Z_{eff})^{\frac{1}{2}}}{B R^{\frac{1}{2}}} \left(\frac{T_e}{T_i} \right)^{\frac{1}{2}} \\ \times \left[\left(\frac{1}{T_e} \frac{dT_e}{dr} + \frac{2}{n_0} \frac{dn_0}{dr} \right) \middle/ \frac{1}{q^2} \frac{dq}{dr} \right] \end{aligned} \quad (11.42)$$

11.4 Wave–Wave Interactions*

11.4.1 Mode Coupling

In the development up to this point, wave–wave interactions, or mode coupling, have been neglected. To understand what is meant by this, as well as to develop a basis for including mode coupling, we consider electrostatic waves in a uniform medium, which in the simplest cases can be described by the kinetic Vlasov equation

$$\frac{\partial f}{\partial t} + \mathbf{v} \cdot \frac{\partial f}{\partial \mathbf{r}} - \frac{e}{m} \nabla \phi \cdot \frac{\partial f}{\partial \mathbf{v}} = 0 \quad (11.43)$$

We characterize the procedure that has been used to find a solution as a perturbation expansion of the distribution function, with the fluctuation amplitude as a small parameter,

$$f(\mathbf{r}, \mathbf{v}, t) = f_0(\mathbf{r}, \mathbf{v}) + f_1(\mathbf{r}, \mathbf{v}, t) + f_2(\mathbf{r}, \mathbf{v}, t) + \dots \quad (11.44)$$

In the previous analysis, the f_2 (and higher) terms were neglected.

We now extend the procedure to retain higher order terms. Since the fluctuations are described by linearized equations, they can be represented by a superposition of independent normal modes

$$f_p(\mathbf{r}, \mathbf{v}, t) = \sum_{\mathbf{k}} f_p(\mathbf{k}, \mathbf{v}) \exp[i(\mathbf{k} \cdot \mathbf{r} - \omega(\mathbf{k})t)], \quad p = 1, 2, \dots \quad (11.45)$$

Substituting these expansions in Eq. (11.43), we find in first order that the k -th component is just the linearized solution for f_1 ; e.g. Eq. (11.15). In second order, collecting all terms which vary as $\exp[i(k_y y + k_z z - \omega t)]$ gives an equation for $f_2(\mathbf{k})$

$$\frac{\partial f_2(\mathbf{k})}{\partial t} + \mathbf{v} \cdot \frac{\partial f_2(\mathbf{k})}{\partial \mathbf{r}} = i \left(\frac{e}{m} \right) \sum_{\mathbf{k}_1 + \mathbf{k}_2 = \mathbf{k}} \phi_1(\mathbf{k}_1) \mathbf{k}_1 \cdot \frac{\partial f_1(\mathbf{k}_2)}{\partial \mathbf{v}} \quad (11.46)$$

where the right side is summed over all pairs of waves that satisfy the selection rules $\omega_1 + \omega_2 = \omega$ and $\mathbf{k}_1 + \mathbf{k}_2 = \mathbf{k}$. The selection rules are satisfied only for certain types of dispersion relations, referred to as the decay type. Decay type dispersion allows resonant coupling between different normal modes. The transfer of energy via resonant mode coupling from an unstable \mathbf{k} -mode to a damped \mathbf{k}' -mode can be an important saturation mechanism.

Mode coupling provides the energy sink needed to balance input over the unstable range of waves. Most drift wave instabilities have their maximum growth rate at $k_{\perp} \rho_i = O(1)$, for which the propagation given by Eq. (11.8) is highly dispersive, hence not of the decay type. However, forced beat waves are produced by the wave–wave interaction, and the forced beat waves in turn interact and contribute to normal mode damping in third order, where the selection rules are less stringent. In addition, some of the forced beat waves will have a phase velocity comparable to the ion thermal velocity, giving rise to energy transfer from the waves via resonant wave–particle interactions (i.e. nonlinear Landau damping).

11.4.2 Direct Interaction Approximation

The above perturbation expansion method can be extended to higher order. However, since it is a perturbation method, the higher order solutions will provide successively smaller corrections to the zero-order solution. Moreover, this method will lead, at every order, to a precise dispersion relation between ω and k . While such well-defined modes are sometimes observed when the fluctuations are weak, in most cases the observed spectrum is very diffuse; i.e. for each k -component the time variation corresponds to a wide frequency range $\Delta\omega$, characteristic of strong turbulence. With increasing fluctuation intensity, the effect of mode coupling becomes too strong to be treated as a perturbation.

This difficulty has been circumvented by the “direct interaction approximation” of replacing the higher order nonlinear terms describing the mode coupling with an approximate operator involving an unspecified function to be determined later from self-consistency requirements, which allows the mode coupling term to be included in the zero order operator. To make this clear, we express the fluctuating distribution function as an integral over their Fourier components, $f_k(\mathbf{v}, t)$

$$f(\mathbf{r}, \mathbf{v}, t) = \int_{-\infty}^{\infty} d\mathbf{k} \exp(i\mathbf{k} \cdot \mathbf{r}) f_k(\mathbf{v}, t) \quad (11.47)$$

Substituting this representation into the nonlinear kinetic equation of Eq. (11.43) yields an equation of the form

$$\left[\frac{\partial}{\partial t} + L_k \right] f_k = \int_{-\infty}^{\infty} V_{\mathbf{k}, \mathbf{k}_1} f_{\mathbf{k}_1} f_{\mathbf{k}-\mathbf{k}_1} d\mathbf{k}_1 \quad (11.48)$$

where L_k is the usual linear operator and $V_{\mathbf{k}, \mathbf{k}_1}$ is the coupling operator between Fourier components \mathbf{k} and \mathbf{k}_1 . Multiplying Eq. (11.48) by f_k^* , the complex conjugate Fourier component, yields an equation for the wave amplitude

$$\frac{1}{2} \left[\frac{\partial}{\partial t} + L_k \right] |f_k|^2 = f_k^* \int_{-\infty}^{\infty} V_{\mathbf{k}, \mathbf{k}_1} f_{\mathbf{k}_1} f_{\mathbf{k}-\mathbf{k}_1} d\mathbf{k}_1 \quad (11.49)$$

An assumption of weak coupling between modes allows an expansion of the solution in powers of the $V_{\mathbf{k}, \mathbf{k}_1}$, $f_k = f_k^0 + f_k^1$, where the coupling with other modes enters through f_k^1 . An equation for f_k^1 results from using the expansion in Eq. (11.49) and collecting lowest order terms

$$\left[\frac{\partial}{\partial t} + L_k \right] f_k^1 = \int_{-\infty}^{\infty} V_{\mathbf{k}, \mathbf{k}_1} f_{\mathbf{k}_1}^0 f_{\mathbf{k}-\mathbf{k}_1}^0 d\mathbf{k}_1 \quad (11.50)$$

The corresponding equation for the phase amplitude $|f_k^1|^2$ must include all second-order terms on the right side of Eq. (11.49)

$$\begin{aligned} & \left[\frac{\partial}{\partial t} + L_k \right] |f_k^1|^2 \\ &= \int_{-\infty}^{\infty} V_{\mathbf{k}, \mathbf{k}_1} \left[f_k^1 f_{\mathbf{k}-\mathbf{k}_1}^0 f_k^{*0} + f_{\mathbf{k}_1}^0 f_{\mathbf{k}-\mathbf{k}_1}^1 f_k^{*0} + f_{\mathbf{k}_1}^0 f_{\mathbf{k}-\mathbf{k}_1}^0 f_k^{*1} \right] d\mathbf{k}_1 \end{aligned} \quad (11.51)$$

Assuming there is no phase correlation among the Fourier components of a turbulent spectrum, to lowest order in the coupling operator, the only terms in Eq. (11.51) which survive

the integration contain either the products $|f_{\mathbf{k}1}|^2 \times |f_{\mathbf{k}}|^2$ or $|f_{\mathbf{k}1}|^2 \times |f_{\mathbf{k}-\mathbf{k}1}|^2$. Terms of the first type are referred to as coherent, and those of the second type as incoherent.

If we Fourier transform Eq. (11.48) in time, write the linear operator as $\omega_{\mathbf{k}} f_{\mathbf{k}}$, and represent the coherent coupling terms by the linear operator $-i v_{\mathbf{k}} f_{\mathbf{k}}$, the resulting equation is

$$(\omega - \omega_{\mathbf{k}} + i v_{\mathbf{k}}) f_{\mathbf{k}}(\omega) = i \int_{-\infty}^{\infty} V_{\mathbf{k}, \mathbf{k}1} f_{\mathbf{k}1}(\omega_1) f_{\mathbf{k}-\mathbf{k}1}(\omega - \omega_1) d\mathbf{k}_1 d\omega_1 \quad (11.52)$$

The terms on the right proportional to $|f_{\mathbf{k}}|^2$ define the linear operator $v_{\mathbf{k}}$, and the rest define an incoherent Fourier source component $S_{\mathbf{k}\omega}$.

As a more concrete example of this direct interaction approximation procedure, we express the electrostatic potential by a Fourier series, $\phi(r, t) = \sum_{\mathbf{k}} \phi_{\mathbf{k}}(t) \exp(i \mathbf{k} \cdot \mathbf{r})$, use the last form of Eq. (11.4) to relate the fluctuating electron density and potential, equate the fluctuating electron and ion densities, and finally obtain from the ion continuity Eq. (11.2) the Hasegawa–Mima equation

$$\frac{\partial \phi_{\mathbf{k}}}{\partial t} + i \omega_D \phi_{\mathbf{k}} = \sum_{\mathbf{k}_1 + \mathbf{k}_2 = \mathbf{k}} V_{\mathbf{k}_1, \mathbf{k}_2} \phi_{\mathbf{k}_1} \phi_{\mathbf{k}_2} \quad (11.53)$$

where the mode coupling operator is

$$V_{\mathbf{k}_1, \mathbf{k}_2} = \frac{\rho_i^2}{(1 + k^2 \rho_i^2) B} (\mathbf{k}_1 \times \mathbf{k}_2) \cdot \hat{\mathbf{n}}_z [k_2^2 - k_1^2] \quad (11.54)$$

and ω_D is given by Eq. (11.8).

11.5 Drift Wave Eigenmodes*

In the two-component (ions and electrons) hydrodynamic model of drift waves the ion dynamics can be represented by the fluid particle, momentum and energy balances

$$\frac{\partial n_i}{\partial t} + \mathbf{v}_{\hat{E}} \cdot \nabla n_i + \nabla_{\perp} \cdot \left(\frac{n_i m_i}{e_i B^2} \frac{d\mathbf{E}_{\perp}}{dt} \right) + \nabla_{\parallel}(n_i u_{\parallel}) = 0 \quad (11.55)$$

$$n_i m_i \left(\frac{\partial u_{\parallel}}{\partial t} + \mathbf{v}_E \cdot \nabla u_{\parallel} \right) = e_i n_i E_{\parallel} - \nabla_{\parallel} p_i \quad (11.56)$$

and

$$\frac{3}{2} n_i \left(\frac{\partial T_i}{\partial t} + \mathbf{v}_E \cdot \nabla T_i \right) + n_i T_i (\nabla_{\perp} \cdot \mathbf{v}_E + \nabla_{\parallel} u_{\parallel}) + \nabla \cdot \mathbf{q}_i = 0 \quad (11.57)$$

Inclusion of thermal (T_i and p_i) fluctuations are important when $T_i \geq T_e$ and $\eta_i \geq 2/3$, but will be omitted in the following discussion.

The electron dynamics is generally kinetic, and the kinetic response of electrons to a fluctuating electrostatic potential can be represented by Eq. (11.4) by retaining the $i\delta$ term

to represent dissipation. The two most important cases of dissipation are for trapped electrons for which $\delta_{Te} = (\epsilon^{\frac{3}{2}} c_s / L_n v_e) [\eta_e + k_\perp^2 / (1 + k_\perp^2)]$ and for the plateau regime electrons for which $\delta_{plat} = (\pi m_e / 2m_i)^{\frac{1}{2}} (qR / L_n) [k_\perp^2 / (1 + k_\perp^2) - \eta_e / 2]$.

In the cylindrical limit, the double periodic boundary conditions on θ and $\zeta (= z / 2\pi R)$ imply the Fourier decomposition

$$n(r, \theta, \phi, t) = n_0(r) + \sum_{m,n} \tilde{n}_{mn}(r) \exp[i(m\theta - n\zeta - \omega t)] \quad (11.58)$$

and similarly for the ion fluid velocity u_{\parallel} and the electrostatic potential ϕ .

The rotational transform of the magnetic field line in toroidal geometry is

$$\frac{d\theta}{d\phi} = \frac{1}{q(r)} \frac{RB_\theta}{rB_\phi} \quad (11.59)$$

and the fractional rate of change of the helical twist with radius, the shear, is $s = (r/q) \times (dq/dr)$.

For drift waves, the (m, n) mode numbers in the dominant ϕ_{mn} terms in the Fourier decomposition of the electrostatic potential are aligned with the magnetic field so that $k_{\parallel} = (m - nq)/qR$ is small so that $|k_{\parallel} c_s| \ll \omega^*$ for robust drift waves. An important effect of finite toroidicity ($\epsilon = r/R \neq 0$) is that the $B = B_0/[1 + (r/R) \cos \theta]$ magnetic field variation couples large numbers of m components in Eq. (11.58) to form each toroidal (n) eigenmode. For computational convenience, a ballooning mode transformation

$$\sum_m \phi_m(r) \exp[im\theta] = \exp[inq\theta_0] \times \sum_{l=-\infty}^{+\infty} \phi(\theta - 2\pi l, \theta_0) i n q(r) (\theta - 2\pi l) \quad (11.60)$$

is introduced to create a function that has 2π periodicity in θ and small k_{\parallel} at large mode numbers. The free parameter θ_0 determines the radial orientation of the resulting convective cells.

Drift waves tend to localize to the outside of the torus due both to the unfavorable curvature of the magnetic field lines with respect to the interchange instability and to the resonant interaction with the particles trapped in the magnetic well centered on the outside of the torus. When the drift modes are strongly localized to the outside of the torus, $\phi(n, \theta_0) \approx \exp(-\sigma n^2/2)$ with $\sigma > 1$, then the single $= 0$ term in Eq. (11.60) is sufficient to represent a function that has 2π periodicity in θ and small k_{\parallel} at large mode numbers. Defining the local radial wave number $k_r = -i(d\phi/dr)/\phi$ and taking only the $l = 0$ term and $n \gg 1$, leads to

$$k_r = n \left(\frac{dq}{dr} \right) (\theta - \theta_0) = k_\theta s(\theta - \theta_0) \quad (11.61)$$

Making use of the representations for n , u_{\parallel} and ϕ indicated by Eq. (11.58), Eq. (11.56) can be solved for the fluctuating components of the ion parallel velocity

$$\tilde{u}_{\parallel mn}(r) = \left(\frac{e_i}{m_i} \right) \frac{\left(k_{\parallel} + \frac{k_\theta}{\Omega_i} \frac{du_{\parallel o}}{dr} \right)}{(\omega - k_{\parallel} u_{\parallel o} - k_\theta u_{\theta_0})} \phi_{mn}(r) \quad (11.62)$$

where $k_\theta = m/r$ and $k_{\parallel} = (m - nq)/qR$. For a spectrum of (m, n) modes there exists a set of mode rational surfaces at radial locations $r_{m,n}$ where $nq(r_{m,n}) = m$, such that $k_{\parallel} = 0$. Expanding around this resonant layer leads to

$$k_{\parallel} = k_\theta(r - r_{m,n})qR/s \quad (11.63)$$

Linearizing Eq. (11.55) and using Eq. (11.62) leads to the standard drift wave eigenvalue equation

$$\frac{\rho_i^2}{r} \frac{\partial}{\partial r} \left(r n_0(r) \frac{\partial \phi}{\partial r}(r) \right) + n_0(r) \left[\frac{\omega^*(r)}{\bar{\omega}} - 1 + i\delta_k - k_y^2 \rho_i^2 + \frac{k_{\parallel}^2(r) c_s^2(r)}{\bar{\omega}^2} \right] \phi(r) = 0 \quad (11.64)$$

where $\bar{\omega} = \omega - \mathbf{k} \cdot \mathbf{u}$ and

$$\omega^*(r) = - \left(\frac{k_y T_e(r)}{e B n_0(r)} \right) \left(\frac{dn_0(r)}{dr} \right) \equiv k_y v_{de} \quad (11.65)$$

The increase in the ion acoustic wave term in Eq. (11.64) (the $k_{\parallel}^2 = k_y^2(r - r_{m,n})^2/L_s^2$ term) with distance from the rational surface is so rapid that the modes are effectively localized within the distance $(r - r_{m,n}) = \rho_i(L_s/L_n)^{1/2}$ of the rational surface.

When $\Delta r_n = r_{m+1,n} - r_{m,n} = 1/(n_0 dq/dr) \ll L_n, L_s$ there is a degeneracy, with all neighboring m -modes satisfying essentially the same eigenvalue equation. The complex eigenvalues of such a “single helicity” system are

$$\omega_l = \frac{\omega^* [1 - i(2l + 1)(L_n/L_s)]}{1 + k_y^2 \rho_i^2 - i\delta_k} \quad (11.66)$$

where $L_s = R/s$. These eigenvalues and the corresponding single helicity localized eigenmodes form the basis for many linear and nonlinear drift wave calculations.

11.6 Gyrokinetic and Gyrofluid Simulations

With the dramatic increase in digital computer capacity and speed, it has, over the past decade, become possible to undertake numerical solution of the full set of kinetic equations, or the fluid equations based thereon, without making many of the simplifying approximations discussed above. We first summarize some of the terminology used in describing such calculation models. “Gyrokinetic” refers to a kinetic model in which a multiple time scale perturbation expansion in the ratio of the gyroperiod to the time scales of the phenomena of interest is made. Such a model is more efficient than a “fully kinetic” model that calculates the full particle dynamics including gyromotion. Finite gyroradius effects (e.g. effects that arise when the spatial scales of phenomena of interest are comparable to the gyroradius) are retained nonperturbatively in gyrokinetic models, which distinguishes them from “drift kinetic” models that either ignore such effects or treat them perturbatively.

The gyrokinetic models are based on the Vlasov–Poisson system of equations in the electrostatic limit. A single ion species with input equilibrium density, velocity and temperature distributions and, at present, an adiabatic (no dissipation) electron kinetic response (e.g. Eq. (11.4) with $\delta = 0$) is treated. These equilibrium distributions must either be taken from experiment or calculated with an associated transport code. The spatial domain of the calculation is either a toroidal flux tube (“flux tube”) or the full torus (“global”).

“Gyrofluid” models are a class of fluid models derived by taking moments of the gyrokinetic equations, rather than moments of the standard kinetic equations (e.g. chapter 5). These models are distinguished from the usual fluid models by taking finite gyroradius effects into account nonperturbatively. Those gyrofluid models that incorporate Landau damping and related processes are referred to as “gyro-Landau fluid” models.

There are a number of groups developing and applying different variants of such numerical solution procedures, and the methodology is evolving rapidly. We will describe one of these models, the so-called IFS-PPPL model, as an illustrative example. This model combines a nonlinear gyrofluid simulation of the fluctuation and thermal transport characteristics of toroidal ITG modes and a linear gyrokinetic ballooning mode calculation of linear growth rates, critical temperature gradients and a quasilinear estimate of χ_i and χ_e . The nonlinear gyrofluid equations are based on a reduction of the gyrokinetic equations and include toroidal effects (e.g. curvature drift) and kinetic effects (e.g. toroidal drift resonances, linear and nonlinear finite gyroradius orbit averaging, parallel wave–particle resonances, fine scale sheared poloidal flows) that play an important role in determining the saturated fluctuation amplitude.

The actual implementation of the IFS-PPPL model in transport calculations involves the use of information obtained from theory, linear gyrokinetic simulations and nonlinear gyrofluid simulations to parameterize several critical temperature gradients. The parameter

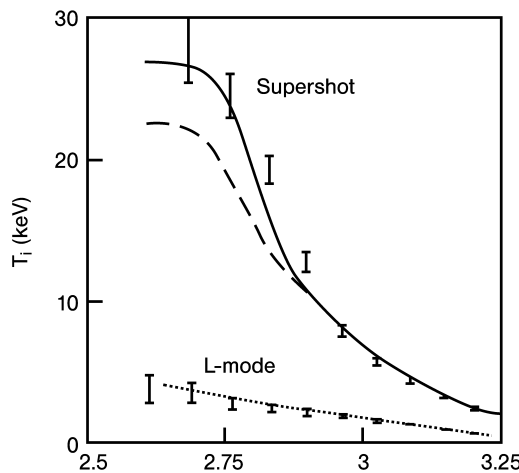


Figure 11.3. Comparison of temperature distributions calculated using the IFS-PPPL model with experiment for L-mode and Supershot discharges in TFTR

list is rather large. These critical temperature gradients are then used as “switches” to turn on or off various terms that contribute to χ_i .

A comparison of predictions of the IFS-PPPL model with experiment for the temperature distributions in L-mode and “Supershot” discharges in TFTR is shown in Fig. 11.3. Experimental values at $r/a = 0.8$ were used as boundary conditions. Clearly the rather complex χ_i model is able to account for the dramatic difference in temperature distribution between the two discharges.

Problems for Chapter 11

1. Calculate the electron density fluctuation in a plasma with electron temperature $T_e = 1 \text{ keV}$ and electrostatic potential $\phi = 3 \text{ V}$.
2. Calculate the critical value of the temperature gradient for ITG modes in a deuterium plasma with $T_e = T_i = 5 \text{ keV}$, $R = 1.7 \text{ m}$, $B = 3 \text{ T}$ and density gradient scale length $L_n = 50 \text{ cm}$, for $k_{\parallel} = k_y = 1, 10$ and 100 cm .
3. Use Kadomtsev’s mixing length estimate to calculate the diffusion coefficient of drift waves with a growth rate of $2 \times 10^3 \text{ s}^{-1}$ and perpendicular wavelength $k_{\perp}^{-1} = 1 \text{ cm}$.
4. Use weak turbulence theory to calculate the diffusion coefficient of the drift waves of problem 3 when $T = 5 \text{ keV}$, $L_n = 50 \text{ cm}$ and $B = 3 \text{ T}$.
5. A current of 3 MA is distributed as $j(r) = j_0[1 - (r/a)^2]$ in a tokamak plasma with $a = 0.65 \text{ m}$, $R = 1.7 \text{ m}$, $T = 5 \text{ keV}$ and $B = 3 \text{ T}$. Calculate the diffusion coefficient due to fluctuating magnetic islands with amplitude $(\tilde{B}_r/B) = 0.2$.
6. Calculate the ion thermal diffusivity due to ITG modes for the plasma of problem 2 with $L_{Ti} = 10 \text{ cm}$.
7. Calculate the electron thermal diffusivity at $r/a = 0.5$ due to ETG modes for the plasma of problems 2 and 5 with $L_{Te} = 50 \text{ cm}$.
8. An instability with linear growth rate $\gamma = 10^3 \text{ s}^{-1}$ and radial wavelength $\lambda = k_{\perp}^{-1} = 2 \text{ cm}$ is present in the edge of a tokamak plasma, where the density gradient scale length is $L_n = 5 \text{ cm}$. The toroidal field is $B = 5 \text{ T}$ and the temperature is $T = 200 \text{ eV}$. Estimate the diffusion coefficient that might characterize the transport associated with this instability.

12 Heating and Current Drive

Two major topics of fusion plasma research are the heating of plasmas to thermonuclear temperatures and, at least in tokamaks, driving the plasma current that is needed for confinement. These topics are related, both because a current flowing in a resistive plasma will heat it and because in many cases the same mechanism that will drive a current in a plasma will also heat it. In this chapter we discuss inductive current drive and (ohmic) heating, adiabatic compression heating, fast ion heating and current drive, and electromagnetic wave heating and current drive in plasmas.

12.1 Inductive

In the normal inductive operation of a tokamak the toroidal plasma current is induced and maintained by a changing magnetic field in a central solenoid (CS), or “ohmic heating” (OH), coil (plus other poloidal field (PF) coils), as illustrated in Fig. 12.1 and Fig. 12.2. In essence, the plasma loop acts as a secondary of a transformer for which the CS is the primary. A changing current in the CS produces a changing B_{OH} which links the plasma and, by Faraday’s law, induces an electromagnetic force, V_p , which in turn drives a current, I_p

$$L_p \dot{I}_p + I_p R_p = V_p = -\dot{\Phi} \quad (12.1)$$

The total change in magnetic flux needed to induce a final current I_p^f is

$$\Delta\Phi_{\text{ind}} = \int_0^{t_f} \dot{\Phi} dt = L_p I_p^f \simeq \mu_0 R_0 \left[\ln \left(\frac{8R_0}{a\sqrt{\kappa}} \right) + \frac{l_i}{2} - 2 \right] \quad (12.2)$$

where L_p and R_p are the plasma inductance and resistance,

$$l_i \simeq \ln [1.65 + 0.89 (q_{95} - 1)] \quad (12.3)$$

is the internal inductance of the plasma and q_{95} is the value of the safety factor on the flux surface that encloses 95 % of the plasma volume.

Additional magnetic flux must be provided to overcome resistive losses during start up

$$\Delta\Phi_{\text{res}} = C_E \mu_0 R_0 I_p^f \quad (12.4)$$

where $C_E \approx 0.4$ is the empirical Ejima coefficient.

In order to maintain the plasma current after start up, Eq. (12.1) indicates that a further change in magnetic flux

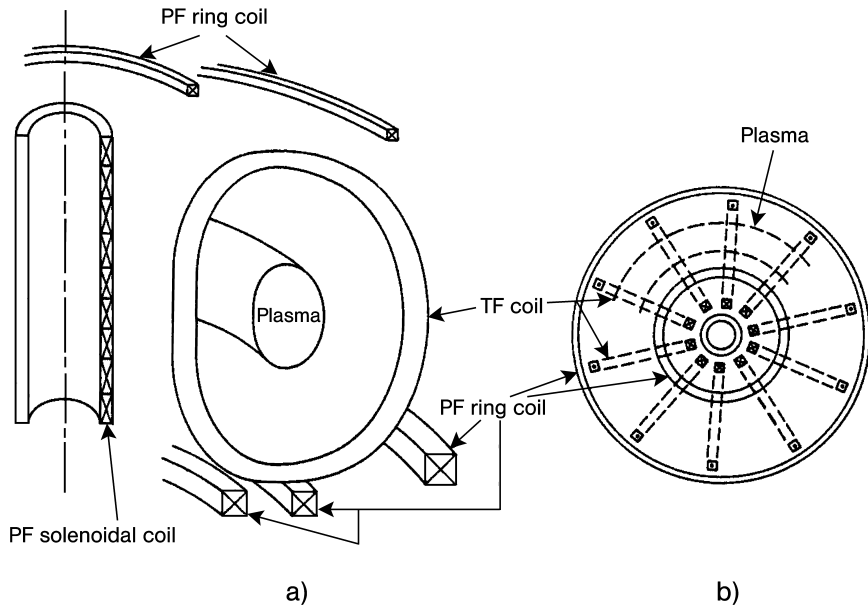


Figure 12.1. Tokamak magnet system configuration: (a) elevation view; (b) plan view

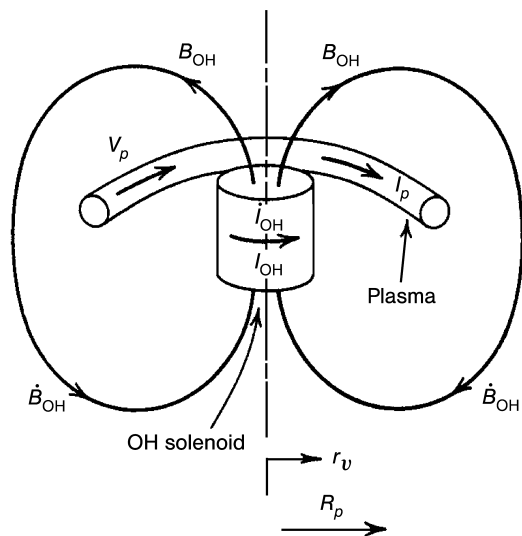


Figure 12.2. Current induction

$$\Delta\Phi_{\text{burn}} = \int_0^t I_p^f R_p dt' \quad (12.5)$$

is required. Since $\Delta\Phi \approx \pi r_v^2 \Delta B_{\text{OH}}$ and there is a technological limit to the maximum value of B_{OH} , the conventional tokamak is inherently a pulsed device.

The toroidal current resistively heats the plasma, strongly at low temperatures and less strongly with increasing temperature because the plasma resistivity $\eta \sim 1/T_e^{3/2}$. This ohmic heating density is $P_\Omega = \eta j^2$. The neoclassical resistivity has a radial dependence due both to the $1/T_e^{3/2}$ dependence of the Spitzer resistivity, η_s , and to the neoclassical factor

$$\eta_n = \frac{\eta_s}{\left(1 - \left(\frac{r}{R}\right)^{\frac{1}{2}}\right)^2} \quad (12.6)$$

which significantly enhances the resistivity.

In order to make an illustrative estimate of ohmic heating, we evaluate the neoclassical factor at the half radius, $r = a/2$, leading to $\eta \approx 8 \times 10^{-8} Z_{\text{eff}}/T_e^{3/2}$ (T_e in keV) for a representative $R/a = 3$. Using a parabola-to-a-power current profile $j(r) = j_0(1 - (r/a)^2)^\nu$, the radially averaged current density squared is $\langle j^2 \rangle = j_0^2/(2\nu + 1)$. For this profile, Ampère's law gives

$$B_\theta(r) = \frac{\mu_0 a^2 j_0}{2(\nu + 1)r} \left[1 - \left(1 - \frac{r^2}{a^2}\right)^{\nu+1} \right] \quad (12.7)$$

Using this equation in the definition $q_a = B_\phi r / B_\theta R$ results in $q_a/q_0 = \nu + 1$. Using $j_0 = 2B_\phi/Rq_0\mu_0$, the radially averaged current density squared is

$$\langle j^2 \rangle = 2 \left(\frac{B_\phi}{\mu_0 R} \right)^2 \frac{1}{q_0 \left(q_a - \frac{1}{2}q_0 \right)} \quad (12.8)$$

The maximum temperature that could be achieved with ohmic heating can now be estimated from the energy balance equation for an ohmic heated plasma $\eta \langle j^2 \rangle = 3nT/\tau_E$

$$T(\text{keV}) = 2.7 \times 10^8 \left(\frac{Z_{\text{eff}}\tau_E}{nq_aq_0} \right)^{\frac{2}{3}} \left(\frac{B_\phi}{R} \right)^{\frac{4}{3}} \quad (12.9)$$

Taking $q_aq_0 = 1.5$, $Z_{\text{eff}} = 1.5$ and $R/a = 3$, and using the above value for η and the Alcator scaling $\tau_E = (n/10^{20})a^2/2$, this equation reduces to $T = 0.87B_\phi^{4/3}$. This expression is plotted in Fig. 12.3. Noting that average temperatures above ≈ 7 keV are necessary before fusion alpha heating is large enough to achieve a significant fusion rate and that the field at the coil will be reduced relative to the plotted field in the plasma, it seems unlikely that tokamaks that would lead to practical reactors can be heated to thermonuclear temperatures by ohmic heating.

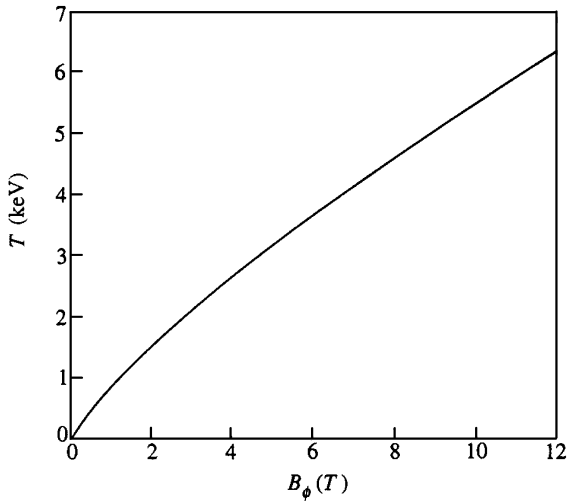


Figure 12.3. Central temperature predicted for ohmic heating with representative tokamak parameters

12.2 Adiabatic Compression*

An increase in magnetic field strength will, in general, compress and heat a plasma. If the compression occurs over a sufficiently long period of time that the reactions that take place within the plasma are reversible, then the compression is adiabatic and obeys the law of adiabatic compression

$$pV^\gamma = \text{const} \quad (12.10)$$

The compression velocity must be small compared to the thermal velocity in order for the compression to be adiabatic. (A compression taking place on a much faster, microsecond, time scale is known as an implosion and is governed by a different set of laws.) The gas constant $\gamma = (2 + \delta)/\delta$, where δ is the number of degrees of freedom of the compression. If the compression is physically in one or two dimensions and the compression time is short compared to the scattering time, v_{90}^{-1} , for large-angle deflection, then $\delta = 1$ or 2. If the compression time is comparable to or greater than v_{90}^{-1} , then the energy increase produced by the compression is shared among all three directions due to scattering deflections, independent of the dimensionality of the physical compression. Because the collision time for electrons is $\sim \sqrt{m_e/m_i}$ times the collision time for ions, it is possible to have a compression with $\delta = 3$ for electrons and $\delta < 3$ for ions.

Noting that the specific volume, V , is proportional to the inverse of the particle density, n^{-1} , and that the pressure, p , is related to the average energy per particle, W , by $p = nW$, we can rewrite Eq. (12.10) as

$$n^{1-\gamma} W = \text{const} \quad (12.11)$$

When the compression time is less than v_{90}^{-1} , only the energy component, W_{\parallel} , in the direction of the compression changes. Denoting initial and final states by superscript 1 and 2, respectively, Eq. (12.11) yields

$$\frac{W_{\parallel}^{(1)}}{W_{\parallel}^{(2)}} = \left(\frac{n^{(2)}}{n^{(1)}} \right)^{1-\gamma} \quad (12.12)$$

For an initially isotropic distribution, $W_{\parallel}^{(1)} = (\delta/3)W^{(1)}$ and $W_{\perp}^{(1)} = (3-\delta)W^{(1)}/3$, where δ is the number of directions of compression. Noting that $W_{\perp}^{(2)} = W_{\perp}^{(1)}$, we find by using Eq. (12.12) that

$$\frac{W^{(2)}}{W^{(1)}} \equiv \frac{W_{\parallel}^{(2)} + W_{\perp}^{(2)}}{W_{\perp}^{(1)} + W_{\parallel}^{(1)}} = \frac{3 - \delta + \delta \left(\frac{n^{(2)}}{n^{(1)}} \right)^{\gamma-1}}{3} \quad (12.13)$$

We see from Eq. (12.13) that, for a given density compression, $n^{(2)}/n^{(1)}$, a one-dimensional compression is more effective than a two-dimensional compression, which in turn is more effective than a three-dimensional compression, in raising the particle energy.

Now these general results are specialized to a tokamak and to a compression time that is long compared to v_{90}^{-1} , so that $\delta = 3$. The basic equation governing the compression is Eq. (12.11), which becomes

$$n^{-\frac{2}{3}} W = \text{const} \quad (12.14)$$

and the equations specifying the conservation of toroidal and poloidal flux (perfect conductivity is assumed),

$$a^2 B_{\phi} = \text{const} \quad (12.15)$$

and

$$q = \text{const} \quad (12.16)$$

By varying the toroidal, poloidal and/or vertical fields it is possible to achieve compression in major and/or minor radius. The other relevant variables scale with major (R) or minor (a) radius as

$$\begin{aligned} n &\sim a^{-2} R^{-1} \\ T &\sim a^{-\frac{4}{3}} R^{-\frac{2}{3}} \\ B_{\phi} &\sim a^{-2} \\ I &\sim R^{-1} \\ B_p &\sim a^{-1} R^{-1} \\ \beta_t &\sim a^{\frac{2}{3}} R^{-\frac{5}{3}} \\ \beta_p &\sim a^{-\frac{4}{3}} R^{\frac{1}{3}} \end{aligned} \quad (12.17)$$

The characteristics of three different types of compression are given in Table 12.1. Compression in the minor radius, by a factor C , at constant R , can be accomplished by increasing the toroidal field, B_ϕ . The vertical field, B_v , must also be increased to maintain an equilibrium pressure balance. This type of compression is denoted type A in the table. Pulsing the toroidal field is impractical because of the large magnetic energy increase ($\sim C^{\frac{4}{3}}$) that is required to achieve a modest temperature increase ($\sim C^{\frac{4}{3}}$). Moreover, if superconducting toroidal magnets were used, the conductor required for pulsed operation would be more complicated than would be necessary for steady state operation of the toroidal coils.

Table 12.1. Adiabatic compression scaling

Quantity	Type compression		
	A	B	C
Minor radius	C^{-1}	C^{-1}	$C^{-\frac{1}{2}}$
Major radius	const	C^{-1}	C^{-1}
Density	C^2	C^3	C^2
Pressure	$C^{\frac{10}{3}}$	C^5	$C^{\frac{10}{3}}$
Plasma, energy	$C^{\frac{4}{3}}$	C^2	$C^{\frac{4}{3}}$
Plasma current	const	C	C
Toroidal field at coil	C^2	C	const
Toroidal field at plasma	C^2	C^2	C
Plasma β_p	$C^{\frac{4}{3}}$	C	$C^{\frac{1}{3}}$
Plasma β_t	$C^{-\frac{2}{3}}$	C	$C^{\frac{4}{3}}$
Magnetic energy	C^4	C^2	const

A combined compression of the minor and major radii by a factor C could be achieved by pulsing the toroidal field, the plasma current and the vertical field. This type of compression, denoted type B in the table, can achieve better heating ($\sim C^2$) with less increase in magnetic energy ($\sim C^2$) than a type A compression. However, relatively large increases in magnetic energy are still required.

Because most of the magnetic energy is in the toroidal field and since it is undesirable to pulse superconducting toroidal field coils, a compression which involves only the vertical field and plasma current (poloidal field) may be the most desirable. The characteristics of such a compression are denoted type C in the table. The plasma is forced to smaller R by increasing the vertical field, moving the plasma into a region of higher toroidal field, which requires a decrease in minor radius to conserve toroidal flux. The increase in magnetic energy is trivial compared to the other two types.

Adiabatic compression has been demonstrated on the Adiabatic Toroidal Compressor (ATC) experiment, thus this technique provides a proven means for increasing the plasma temperature in tokamaks beyond the level that can be achieved by resistive heating alone. However, the nature of the compression process is such that the vacuum chamber must be significantly larger than is needed to accommodate the compressed plasma. This would

result in significant additional costs for the relatively large tokamaks that are envisioned for reactors.

12.3 Fast Ions

12.3.1 Neutral Beam Injection

Injection of high-energy neutral hydrogen atoms is perhaps the most successful technique that has been applied to date for supplemental heating of plasmas. The neutral atoms are converted to ions within the plasma by charge exchange or impact ionization and then give up their energy to the plasma particles via Coulomb collisions. The relevant cross sections for H^0 and D^0 beams incident upon a plasma are plotted in Fig. 12.4 as a function of the incident particle energy. These cross sections are averaged over Maxwellian distributions for the plasma ions and electrons. They are only weakly dependent on the plasma temperature, and then only for low-incident neutral particle energy, except for the electron-impact reaction in which the relative velocity is essentially the electron velocity.

The ion- or electron-impact event produces an energetic ion and a “cold” electron (a few eV) which rapidly ($\sim 10 \mu s$) is heated up by electron-electron scattering with the plasma electrons. The energy required to heat the cold electron is negligible compared to the energy of the hot ion. The charge exchange event produces an energetic ion and a warm (plasma temperature) neutral by exchanging an electron between an incident neutral and a plasma ion. The warm neutral initiates a chain of subsequent charge exchange events which ends either in ionization or, in the case of a small plasma, the escape of a warm neutral. Thus the principal result of an ionization or charge exchange event is to produce an energetic ion which then shares its energy with the plasma ions and electrons.

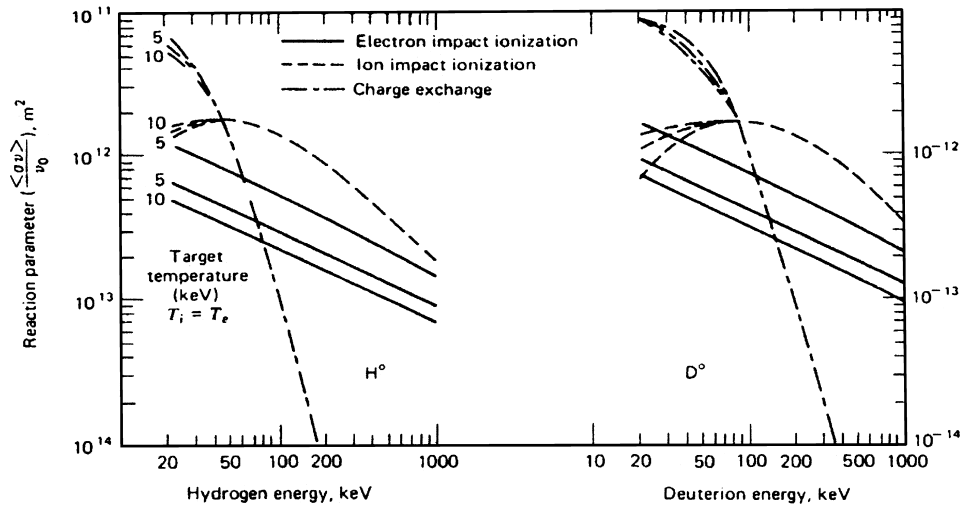


Figure 12.4. Relevant cross sections for H^0 and D^0 beams incident on a $z = 1$ plasma

We will now examine the deposition of energy in a plasma by neutral beam injection by considering first the attenuation of a neutral beam incident upon a plasma and second the transfer of energy from the energetic ion to the plasma ions and electrons. The attenuation of a beam of neutral particles in a plasma is described by

$$\frac{dN_b(s)}{ds} = -N_b(s)n(s)\sigma \quad (12.18)$$

where N_b is the beam particle density, n is the plasma particle density, σ is the total cross section for charge exchange and ionization and s is the path length along the beam direction.

The solution of Eq. (12.18) yields the birthrate distribution of energetic ions. To determine the energy deposition distribution it is necessary to calculate the guiding center motion of the energetic ions. The calculation is similar to that described in chapter 3; conservation of canonical angular momentum, energy and magnetic moment and the expressions for curvature and grad- B drifts are used to establish the energetic ion orbits. Some of these orbits will carry an ion out of the plasma, where it is presumed to be lost, resulting in "loss cones" in velocity space for the energetic ions. Since the drifts depend on the sign as well as the magnitude of the component of the ion velocity in the direction of the magnetic field, counterinjected ($v \cdot B < 0$) particles are more likely to be lost than co-injected ($v \cdot B > 0$) particles. In tokamaks, these loss cones are related to the excursions of marginally trapped particles from flux surfaces and are more important for particles on exterior flux surfaces. The direct loss of energetic ions becomes relatively unimportant for larger plasmas. To a good approximation the energetic ions distribute themselves over the drift surface which passes through their birth point. (A drift surface is a flux surface modified to account for particle drifts.)

Thus the flux surface average of the energetic ion birth distribution calculated from Eq. (12.18) provides a good estimate of the energy deposition distribution. This estimate may be improved by taking into account excursions from the flux surface during the slowing down process, but this effect is not too important in relatively large plasmas.

Energetic neutral D⁰ (or H⁰ or T⁰) beams can be produced in a number of ways, all of which have certain common features: (1) extraction of ions from a plasma ion source; (2) acceleration of these ions to the desired energy; and (3) neutralization of the high energy ions in a gas cell. The most highly developed class of ion sources are those from which atomic (D⁺) and molecular (D₂⁺, D₃⁺) ions are extracted. (The D₂⁺ and D₃⁺ energies will be $\frac{1}{2}$ and $\frac{1}{3}$, respectively, of the D⁺ energy since all three species will be subjected to the same accelerating voltage.) The neutralization efficiency (due to charge exchange) for these ions in a D₂ neutralization cell is plotted as a function of the D⁺ energy in Fig. 12.5. The neutralization efficiencies become small at beam energies of a few 100 keV and are less than 1 % for 1 MeV beams. Since rather large amounts of injected power (~ 100 MW) may be required for fusion reactors, these low efficiencies may be intolerable. (Present injection experiments use beams with energies near 100 keV, and the power injected is several tens of MWs.)

Direct extraction of D⁻ ions that have been formed by electron attachment in a deuterium plasma ion source is one possible means of producing highly energetic neutral

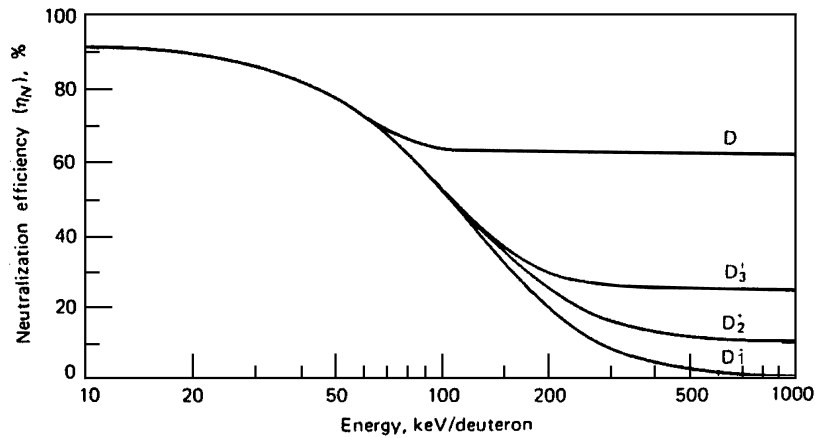


Figure 12.5. Neutralization efficiency of deuterium ions in a gas target

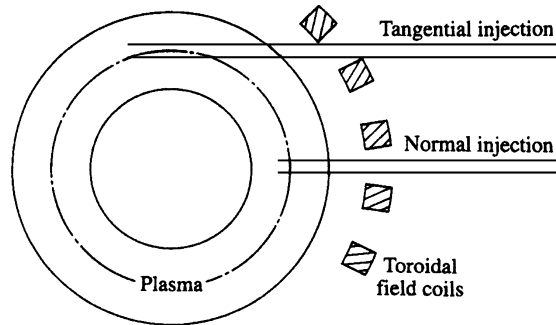


Figure 12.6. Normal and tangential NB injection

beams more efficiently. The neutralization efficiency for D^- ions remains over 60 % for all energies of interest. Negative ion sources are in use today.

It is clear from Fig. 12.4 that the distance of penetration of a neutral beam into a plasma before “ionization” will increase with the energy of the beam particles. Since heating the center of the plasma is desirable, injection normal to the field lines (see Fig. 12.6) will generally be preferable, at least for positive ion neutral beams.

12.3.2 Fast Ion Energy Loss

Fast ions will collisionally transfer their energy to the plasma ions and electrons, heating these particles, until they come into equilibrium. We will assume that the plasma ions and electrons are in Maxwellian distributions and that the number of fast ions, n_b , is negligible relative to the plasma density. We further assume that the fast ions have initial speed V_b

that is much greater than the plasma ion thermal speed, v_{thi} , but much less than the electron thermal speed, v_{the} .

Collisions of the fast ions with the plasma ions and electrons will cause a frictional drag on the latter, causing the fast ions to slow down in energy. Scattering of the fast ions on the plasma ions will also deflect the fast ions in angle.

12.3.2.1 Collisions with Plasma Electrons

In the frame moving with the fast ions, the plasma electrons collide with stationary ions, and the plasma electrons can transfer momentum, but not much energy, to the fast ions. In the moving frame, the fast ions will on average gain momentum in the direction of the average electron momentum, which in this moving frame is oppositely directed to the fast ion motion in the lab frame. In the lab frame, the fast ions will lose directed momentum and slow down because of collisions with electrons, but they will not be deflected significantly in angle.

The loss in fast ion energy is almost entirely due to loss in directed motion. The change in fast ion, ΔV , and electron, $\Delta \mathbf{v}$, velocities are related by conservation of momentum, $\Delta \mathbf{v} = -(M_b/m_e)\Delta V$. The change in fast ion energy $\Delta W_b = (M_b/2)(|V + \Delta V|^2 - V^2) \approx M_b V \cdot \Delta V$ must be equal and opposite in sign to the change in electron energy $\Delta W_e = (m_e/2)(M_b/m_e)^2(|\Delta V|)^2 \approx (M_b^2/2m_e)(|\Delta V|)^2$. Denoting the components of velocity change along and perpendicular to the original fast ion direction ΔV_{\parallel} and ΔV_{\perp} , the energy conservation condition can be written

$$-M_b V \Delta V_{\parallel} = \frac{M_b^2}{2m_e} |\Delta V|^2 = \frac{M_b^2}{2m_e} [(\Delta V_{\parallel})^2 + (\Delta V_{\perp})^2] \quad (12.19)$$

Since $M_b(\Delta V_{\perp})^2/2 < m_e V |\Delta V_{\parallel}| \ll M_b V |\Delta V_{\parallel}|$, the energy associated with the perpendicular velocity change is much less than the energy associated with the parallel velocity change. Since Eq. (12.19) requires $|\Delta V_{\parallel}| < (2m_e/M_b)V$, the fast ion loses a fraction m_e/M_b of its energy in a collision, or an amount of order $m_e V_b^2$. Thus, $(\Delta V_{\perp}) < (2m_e/M_b)V$ also.

The force of the background electrons on the fast ions is mostly of the nature of a frictional drag. Since $\Delta \mathbf{v} = -(M_b/m_e)\Delta V$ and we have assumed a Maxwellian distribution

$$f_e(\mathbf{v}) = n_e \left(\frac{m_e}{2\pi T_e} \right)^{\frac{3}{2}} \exp \left(-\frac{m_e v^2}{2T_e} \right) \quad (12.20)$$

The momentum balance between the population of fast ions and the population of electrons is

$$n_b M_b \frac{d\langle V \rangle}{dt} = -m_e \int \frac{d\langle \mathbf{v} \rangle}{dt} f_e(\mathbf{v}) d^3 v \quad (12.21)$$

The equation of motion for the average velocity of the electron population is

$$\frac{d\langle \mathbf{v} \rangle}{dt} = -v_{eb}(\mathbf{v} - \mathbf{V}) \quad (12.22)$$

where

$$\nu_{eb} = \frac{n_b Z_b^2 e^4 \ln \Lambda}{4\pi \epsilon_0^2 m_e^2 |\mathbf{v} - \mathbf{V}|^3} \quad (12.23)$$

Using this result in Eq. (12.21) yields

$$\frac{d\langle V \rangle}{dt} = \frac{Z_b^2 e^4 \ln \Lambda}{4\pi \epsilon_0^2 m_e M_b} \int \frac{\mathbf{v} - \mathbf{V}}{|\mathbf{v} - \mathbf{V}|^3} f_e d^3 v = -\frac{Z_b^2 e^4 \ln \Lambda}{4\pi \epsilon_0^2 m_e M_b} \frac{\partial I}{\partial V} \quad (12.24)$$

where

$$I(V) = - \int \frac{f_e d^3 v}{|\mathbf{v} - \mathbf{V}|} \quad (12.25)$$

This integral can be evaluated by using Eq. (12.20), or slightly more generally a distribution that is isotropic in velocity space, to obtain

$$\frac{d\langle V \rangle}{dt} = -\frac{2^{\frac{1}{2}} n_e Z_b^2 e^4 m_e^{\frac{1}{2}} \ln \Lambda}{12\pi^{\frac{3}{2}} \epsilon_0^2 M_b T_e^{\frac{3}{2}}} \mathbf{V} \quad (12.26)$$

The frictional drag of the electrons on the fast ions varies as $1/T_e^{\frac{3}{2}}$. The rate at which fast ion energy is reduced can be obtained by taking the scalar product of this equation with $M_b \mathbf{V}$

$$\frac{dW_b}{dt} = -\frac{2^{\frac{1}{2}} n_e Z_b^2 e^4 m_e^{\frac{1}{2}} \ln \Lambda}{6\pi^{\frac{3}{2}} \epsilon_0^2 M_b T_e^{\frac{3}{2}}} W_b \equiv -\frac{W_b}{\tau_{eb}} \quad (12.27)$$

where τ_{eb} is the characteristic time for fast ion slowing down by collisions with electrons.

12.3.2.2 Collisions with Plasma Ions

In contrast to the situation with electrons, both the deflection of fast ions by plasma ions and the parallel energy transfer from fast ions to plasma ions are comparable energy loss mechanisms for the fast ions. If the fast ion mass, M_b , is much greater than the plasma ion mass, m_i , then transfer of parallel energy will be the dominant mechanism, just as for the electrons. The development is as above, leading to

$$\nu_{ib} = \frac{n_b Z^2 Z_b^2 e^4 \ln \Lambda}{4\pi \epsilon_0^2 m_i |\mathbf{v} - \mathbf{V}|^3} \quad (12.28)$$

$$\frac{d\langle V \rangle}{dt} = -\frac{n_i Z^2 Z_b^2 e^4 \ln \Lambda}{4\pi \epsilon_0^2 m_i M_b V^3} \mathbf{V} \quad (12.29)$$

and

$$\frac{dW_b}{dt} = -\frac{2^{\frac{1}{2}} n_i Z^2 Z_b^2 e^4 M_b^{\frac{1}{2}} \ln \Lambda}{8\pi \epsilon_0^2 m_i W_b^{\frac{1}{2}}} \quad (12.30)$$

On the other hand, if $m_i \gg M_b$, deflection of the fast ion velocity, representing the loss of directed energy by pitch-angle scattering, will be the dominant process. Again, conservation of momentum requires $m_i \Delta v = -M_b \Delta V$. The energy acquired by the plasma ion in a collision is $m_i |\Delta v|^2/2 = M_{b/m_i}^2 |\Delta V|^2/2$, which must equal the energy loss by the fast ion. For small angle deflections $|\Delta V|^2 \approx (\Delta V_\perp)^2$, so that the results of the ion-electron slowing down discussion of section 4.5 can be used with a change in subscripts to obtain

$$\frac{d(\Delta V_\perp)^2}{dt} = \frac{n_i Z^2 Z_b^2 e^4 \ln \Lambda}{2\pi \epsilon_0^2 M_b^2 V_b} \quad (12.31)$$

and the fast ion slowing down rate is

$$\frac{dW_b}{dt} = -\frac{M_b^2}{2m_i} \frac{d(\Delta V_\perp)^2}{dt} = -\frac{n_i Z^2 Z_b^2 e^4 \ln \Lambda}{4\pi \epsilon_0^2 m_i V_b} = -\frac{\frac{1}{2} n_i Z^2 Z_b^2 e^4 M_b^{\frac{1}{2}} \ln \Lambda}{8\pi \epsilon_0^2 m_i W_b^{\frac{1}{2}}} \quad (12.32)$$

12.3.2.3 Critical Fast Ion Energy

Combining the results for the slowing down of fast ions by plasma electrons and plasma ions yields

$$\frac{dW_b}{dt} = -\frac{\frac{1}{2} n_e Z_b^2 e^4 m_e^{\frac{1}{2}} \ln \Lambda}{6\pi^{\frac{3}{2}} \epsilon_0^2 M_b} \left(\frac{W_b}{T_e^{\frac{3}{2}}} + \frac{C}{W_b^{\frac{1}{2}}} \right) \quad (12.33)$$

where $C = 3\pi^{\frac{1}{2}} Z M_b^{\frac{3}{2}} / 4m_e^{\frac{1}{2}} m_i \approx 81$ for fast and plasma ions both being deuterons. The first and second terms represent fast ions slowing down by collisions with plasma electrons and ions, respectively. The two terms are equal when the fast ion energy has a “critical” value

$$\frac{W_{b,\text{crit}}}{T_e} = C^{\frac{2}{3}} \approx 19 \quad (12.34)$$

where again fast and plasma ions have been assumed to be deuterons to evaluate C .

Fast ions with $W_b > W_{b,\text{crit}}$ slow down predominantly by heating plasma electrons, and fast ions with $W_b < W_{b,\text{crit}}$ predominantly heat plasma ions.

12.3.3 Fast Ion Distribution

Equations (12.26) and (12.29) describe the first velocity moments, or dynamical friction, terms due to parallel energy loss in collisions with plasma electrons and ions, respectively, that are required in the Fokker–Planck equation for the fast ion distribution, and Eq. (12.31) describes the first velocity moment contribution of pitch-angle scattering with plasma ions. Note that the pitch-angle scattering term is only important if the fast ions have a significant

directed velocity, as would fast ions arising from neutral beam injections, and would vanish for an isotropic source of fast ions such as would arise from fusion alpha particles.

Neglecting the pitch-angle scatter term (i.e. assuming an isotropic fast ion distribution) and second velocity moment (velocity diffusion) terms, the Fokker–Planck equation describing the fast ion distribution is

$$\frac{\partial f_b}{\partial t} = \frac{n_e Z Z_b^2 e^4 \ln \Lambda}{4\pi \epsilon_0^2 M_b m_i} \frac{\partial}{\partial V} \cdot \left[\frac{V}{V^3} \left(1 + \frac{V^3}{V_{\text{crit}}^3} \right) f_b \right] \quad (12.35)$$

where

$$V_{\text{crit}} = (2W_{b,\text{crit}}/M_b)^{\frac{1}{2}} = 3^{\frac{1}{3}} Z^{\frac{1}{3}} (\pi/2)^{\frac{1}{6}} \left[T_e / (m_e^{\frac{1}{3}} m_i^{\frac{2}{3}}) \right]^{\frac{1}{2}} \quad (12.36)$$

is the fast ion velocity at the critical energy, $W_{b,\text{crit}}$. Since we are neglecting non-isotropic effects, it is convenient to transform Eq. (12.35) to spherical coordinates in velocity space

$$\frac{\partial f_b}{\partial t} = \frac{n_e Z Z_b^2 e^4 \ln \Lambda}{4\pi \epsilon_0^2 M_b m_i} \frac{1}{V^2} \frac{\partial}{\partial V} \left[\left(1 + \frac{V^3}{V_{\text{crit}}^3} \right) f_b \right] \quad (12.37)$$

12.3.3.1 Monoenergetic Fast Ion Source

If the fast ions are all introduced into the plasma isotropically and with the same speed V_0 , a source term

$$\left(\frac{\partial f_b}{\partial t} \right)_{\text{source}} = \frac{S \delta(V - V_0)}{4\pi V^2} \quad (12.38)$$

must be added to the right side of Eq. (12.37). (Integrating this source over all velocity space with differential element $4\pi V^2 dV$ yields S .) Having introduced a source, we need also to introduce a sink at $V = 0$ to represent the fast ions becoming plasma ions. (This same problem was solved somewhat more exactly in section 4.3, taking into account the sink and the thermal motion of the background plasma.)

In steady state the term on the right of Eq. (12.35) must vanish away from the source speed, which requires

$$\left(1 + \frac{V^3}{V_{\text{crit}}^3} \right) f_b = C \quad (12.39)$$

for $V < V_0$. For $V > V_0$, f_b must equal zero since we have not allowed for the thermal motion of the plasma ions to upscatter the fast ions in this model (see chapter 4). Including the source term in the steady state Eq. (12.37), multiplying by V^2 and integrating across $V = V_0$ yields an equation for the constant C

$$-C \frac{n_e Z Z_b^2 e^4 \ln \Lambda}{4\pi \epsilon_0^2 M_b m_i} + \frac{S}{4\pi} = 0 \quad (12.40)$$

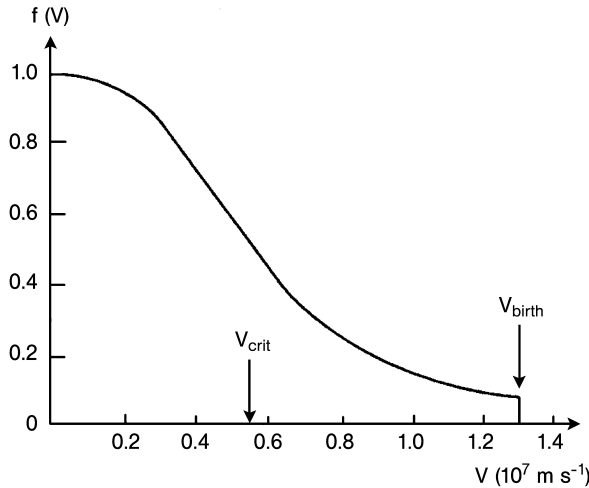


Figure 12.7. Steady-state velocity distribution $f(V)$ of energetic alpha particles in a deuterium-tritium plasma with $T_e = 20 \text{ keV}$. The vertical scale is arbitrary

Thus, the fast ion distribution is described by

$$f_b(V) = \frac{S\epsilon_0^2 m_i M_b}{n_e Z Z_b^2 e^4 \ln \Lambda} \left(\frac{1}{1 + V^3/V_{\text{crit}}^3} \right) \quad V < V_0 \quad (12.41)$$

and is plotted in Fig. 12.7 for the case of fusion alpha particles in a D-T plasma at $T_i = T_e = 20 \text{ keV}$. The alpha source strength is $S_\alpha = n_D n_T \langle \sigma v \rangle_f$ per unit volume. $\langle \sigma v \rangle_f \approx 4.2 \times 10^{-22} \text{ m}^3 \cdot \text{s}^{-1}$ at $T_i = 20 \text{ keV}$, and the source energy is 3.5 MeV, corresponding to $V_0 = 1.3 \times 10^7 \text{ m} \cdot \text{s}^{-1}$. The critical energy is $W_{b,\text{crit}} = 30T_e = 600 \text{ keV}$, above which the alpha particles give up their energy primarily to plasma electrons and below which primarily to plasma ions. The plasma electrons and ions equilibrate (share heating energy) in about 10^{-2} s .

12.3.4 Neutral Beam Current Drive

Neutral beam injection with any tangential component produces a current of fast ions when the neutrals become ions, primarily by charge-exchange at beam energies below about 100 keV for D and by ion-impact ionization for higher energies (see Fig. 12.4). When charge exchange is dominant, the current density of fast ions is $j_f = j_b V_{\parallel} \tau_{\text{cx}} / 2\pi R = S_f \tau_{\text{cx}} e Z_b V_{\parallel}$, where j_b is the neutral beam current density, V_{\parallel} is now the fast ion velocity parallel to the magnetic field, τ_{cx} is the inverse of the charge-exchange frequency, S_f is the fast ion production rate per unit volume and Z_b is the fast ion charge.

When ionization is the dominant fast ion production mechanism, the fast ion current density must be calculated from

$$j_f = \frac{S_f \tau_s e Z_b V_0}{(1 + u_c^2)} \int_0^1 f_1(u) u^3 du \quad (12.42)$$

where τ_s is the fast ion slowing down time and $u = V/V_0$. The fast ion Fokker–Planck equation, in the absence of trapping but with pitch-angle scattering terms retained, can be solved for the fast ion distribution function

$$f_1 = u^{2\beta} \left[\frac{1 + u_c^3}{u^3 + u_c^3} \right]^{1 + \frac{2\beta}{3}} \quad (12.43)$$

where

$$\beta = \frac{m_i Z_{\text{eff}}}{2M_b \bar{Z}} \quad u_c^3 = \frac{3\pi^{\frac{1}{2}}}{4} \frac{m_e \bar{Z} v_{\text{the}}^3}{m_i V_0^3} \quad \bar{Z} = \sum_i \frac{M_b n_i Z_i^2}{m_i n_e} \quad (12.44)$$

The efficiency for producing the fast ion current is

$$\frac{j_f}{P_d} = \frac{2\tau_s e Z_b}{M_b V_0 (1 + u_c^2)} \int_0^1 f_1(u) u^3 du \quad (12.45)$$

where $P_d = (M_b V_0^2 / 2) S_f$. Highest efficiency is achieved by operating at a high electron temperature, low electron density and $u_c \approx 1$.

The slowing down of the fast ions by collisions with electrons produces an electron flow in the direction of the fast ion current, hence an electron current in the opposite direction. The degree of current cancellation depends on the fast ion charge, Z_{eff} , and the fraction of trapped electrons. Fokker–Planck calculations yield

$$\frac{I}{I_f} = 1 - \frac{Z_b}{Z_{\text{eff}}} + 1.46 \frac{\sqrt{\epsilon Z_b}}{Z_{\text{eff}}} A(Z_{\text{eff}}) \quad (12.46)$$

for the ratio of the net driven current to the fast ion current, where the second term accounts for the electron current cancellation in the absence of trapping and the last term takes trapping into account. The quantity A varies from 1.67 for $Z_{\text{eff}} = 1$ to 1.18 for $Z_{\text{eff}} = 4$.

12.3.5 Toroidal Alfvén Instabilities

The presence of fast ions in the plasma introduces the possibility of destabilization of shear Alfvén waves in toroidal geometry. The usual energy principle analysis leads to an equation for the shear Alfvén perturbation in toroidal geometry

$$\frac{d}{dr} \left[(\rho \omega^2 - F^2) r^3 \frac{d\xi}{dr} \right] - (m^2 - 1) \left[\rho \omega^2 - F^2 \right] r \xi + \omega^2 r^2 \frac{d\rho}{dr} \xi = 0 \quad (12.47)$$

where ξ is the radial displacement perturbation, ρ is the plasma density, and $F = (m - nq)B_\theta/r\mu_0^{\frac{1}{2}}$. For a given frequency, ω , the coefficient of the highest derivative in this

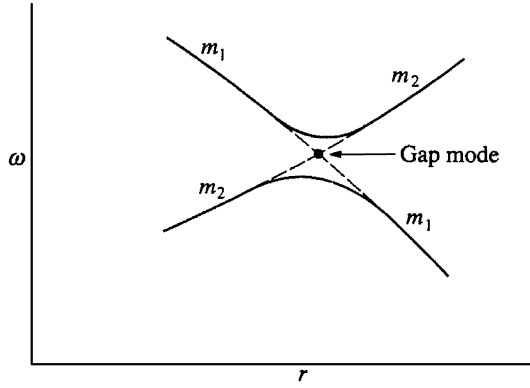


Figure 12.8. The $\omega(r)$ curves, for a given toroidal mode number n . The curves for the cylindrical modes m_1 and m_2 “reconnect” and also produce a discrete “gap” mode at the intersection

equation has a zero at the radius r for which

$$m - nq = \pm \frac{\omega r}{B_\theta / (\mu_0 \rho)^{\frac{1}{2}}} \quad (12.48)$$

with the corresponding solutions of Eq. (12.47) being singular (i.e. unstable) at that radius. These unstable modes thus form a continuum. For a given n , the frequencies of modes corresponding to different m break and join at their intersection, as shown in Fig. 12.8, leaving a gap. A discrete toroidal Alfvén eigenmode (TAE) exists within the gap.

The continuum modes are strongly damped, but the TAE are only weakly damped, and this weak damping can be destabilized by an interaction with fast particles. In particular, the fusion alpha particles could have a resonance interaction with the TAE to release the free energy in the radial alpha particle density gradient, leading to a TAE growth rate

$$\frac{\gamma}{\omega_0} \simeq \frac{9}{4} + \beta_\alpha \left(\frac{\omega_{*\alpha}}{\omega_0} - \frac{1}{2} \right) F \left(\frac{V_A}{V_\alpha} \right) - D \quad (12.49)$$

where $\omega_0 = V_A/2qr$ is the real frequency of the shear Alfvén mode, β_α is the beta of the alpha particles, and

$$\omega_{*\alpha} = -\frac{m}{r} \frac{T_\alpha}{e_\alpha B} \frac{d \ln n_\alpha}{dr} \quad (12.50)$$

is the alpha particle diamagnetic frequency, V_α is the average alpha particle speed, and $F(x) = x(1 + 2x^2 + 2x^4) \exp(-x^2)$.

The four important phenomena represented by the damping term D in Eq. (12.49) are: (1) ion Landau damping, which is only weakly dependent on m ; (2) radiative damping due to coupling with Alfvén waves, which scales as $\exp(-1/m)$; (3) trapped electron collisional damping proportional to m^2 ; and (4) damping due to coupling to the damped continuum modes, which scales as $m^{\frac{-3}{2}}$ at high m .

The form of $F(V_A/V_\alpha)$ indicates that alpha particle velocities near the Alfvén velocity are most dangerous for driving the instability. The Alfvén velocity is $\sim 10^7 \text{ m} \cdot \text{s}^{-1}$ in a plasma with $n = 10^{20} \text{ m}^{-3}$ and $B = 5 \text{ T}$, and the alpha particles have an initial velocity $V_0 = 1.3 \times 10^7 \text{ m} \cdot \text{s}^{-1}$. Thus, the potential for instability exists. This is perhaps the most critical unresolved “burning plasma” issue.

12.4 Electromagnetic Waves

The electric field of an electromagnetic wave propagating in a plasma will accelerate the plasma ions and electrons, which then collisionally convert this directed energy into random heat energy. Since the collisional process scales as $1/T_e^{3/2}$, plasma heating by the direct collisional mechanism saturates with temperature and becomes weak in high temperature plasmas.

On the other hand, there are a number of resonance frequencies at which electromagnetic wave energy is noncollisionally absorbed by the plasma. Because of the nonuniform magnetic field and density in most plasmas, there is resonance reflection as well as resonance absorption. For example, when a wave approaches the resonance location from a lower magnetic field region strong reflection may occur, whereas strong absorption will occur when the same wave approaches from a region of higher magnetic field.

While the different resonance frequencies of a plasma allow a wide variety of wave heating frequencies and hence technologies, all electromagnetic wave heating and current drive technologies consist of a generator of high power electromagnetic waves located at some distance from the plasma, a waveguide or cable for transmission of the wave to the plasma, and a launching horn, antenna or other mechanism for coupling the electromagnetic energy to the plasma by the creation of plasma waves. The plasma waves must then propagate to a local region where the conditions for an absorption resonance are met. We consider here only the physics of the wave propagation and resonance absorption within the plasma.

12.4.1 Wave Propagation

12.4.1.1 Refractive Index

A relatively simple model based on the cold plasma approximation can be used to discuss many of the important features of the propagation of electromagnetic waves in plasmas. Although thermal effects must be taken into account in the region of the resonance absorption, the propagation of the waves to these local absorption regions is adequately described by the cold plasma approximation.

It is convenient, and conventional, to use the *dielectric tensor*, ϵ , to describe electromagnetic wave propagation, and we will now introduce this formalism. Combining Ampère’s and Faraday’s laws

$$\nabla \times \nabla \times \mathbf{E} = -\frac{1}{c^2} \frac{\partial^2 \mathbf{E}}{\partial t^2} - \mu_0 \frac{\partial \mathbf{j}}{\partial t} \quad (12.51)$$

and using the usual wave representation for \mathbf{E} and \mathbf{j}

$$\mathbf{E}(x, t) = \hat{\mathbf{E}} e^{-i(-\omega t + \mathbf{k} \cdot \mathbf{x})} \quad (12.52)$$

leads to a defining relationship for the dielectric tensor

$$-\mathbf{k} \times \mathbf{k} \times \mathbf{E} = \frac{\omega^2}{c^2} \left(\mathbf{E} + \frac{i\epsilon_0}{\omega} \mathbf{j} \right) \equiv \frac{\omega^2}{c^2} \boldsymbol{\epsilon} \cdot \mathbf{E} \quad (12.53)$$

where $\mu_0 c^2 = \epsilon_0$ has been used and the carat has been dropped.

An associated quantity is the *refractive index*, $n = |\mathbf{k}c/\omega|$.

In terms of these quantities, the cold plasma dispersion relationship (see chapter 7 in slab geometry can be written

$$\epsilon_{\perp} n_{\perp}^4 - \left[(\epsilon_{\perp} - n_{\parallel}^2) (\epsilon_{\perp} + \epsilon_{\parallel}) + \epsilon_{xy}^2 \right] n_{\perp}^2 + \epsilon_{\parallel} \left[(\epsilon_{\perp} - n_{\parallel}^2)^2 + \epsilon_{xy}^2 \right] = 0 \quad (12.54)$$

where B_0 is in the z -direction, and x and y are normal to z (e.g. x , y , z refers to the radial, poloidal and toroidal direction in a tokamak). The perpendicular and parallel refractive indices are defined with respect to the z -direction of the equilibrium magnetic field, $n_{\perp/\parallel} = k_{\perp/\parallel} c / \omega$. The nonzero dielectric tensor components are

$$\begin{aligned} \epsilon_{xx} = \epsilon_{yy} = \epsilon_{\perp} &= 1 - \sum_j \frac{\omega_{pj}^2}{(\omega^2 - \Omega_j^2)}, & \epsilon_{zz} = \epsilon_{\parallel} &= 1 - \sum_j \frac{\omega_{pj}^2}{\omega^2} \\ \epsilon_{xy} &= \sum_j \frac{i \omega_{pj}^2 \Omega_j}{\omega (\Omega_j^2 - \omega^2)}, & \text{and} & \epsilon_{yx} = -\epsilon_{xy} \end{aligned} \quad (12.55)$$

The summation is over electrons and all ion species, the gyrofrequency $\Omega_j = z_j e B / m_j$ and the plasma frequency $\omega_{pj} = (n_j z_j^2 e^2 / \epsilon_0 m_j)^{1/2}$ are defined as usual.

The frequency of the wave, ω , is determined by the generator, and the parallel index of refraction is determined by the launching mechanism. A wave will only propagate if $n_{\perp}^2 > 0$. Thus, we can learn something about the propagation of a wave across the equilibrium magnetic field by solving Eq. (12.54) for n_{\perp}^2 for various values of the radial coordinate, using the local values of the magnetic field and plasma density.

For certain combinations of plasma density, magnetic field and wave frequency, $n_{\perp} \rightarrow \infty$, indicating a resonance associated with wave energy absorption. For other combinations, $n_{\perp} \rightarrow 0$, indicating a cut-off surface at which the incident wave is reflected. Beyond a cut-off surface, a wave will decay exponentially with radial position. Such a region, in which the plasma conditions do not support the wave, is referred to as an evanescent region. If the evanescent region is of limited spatial extent and a region in which the wave can once again be supported lies beyond it, the wave will be able to “tunnel through” the evanescent region.

12.4.1.2 Ray Tracing*

The propagation of wave energy in a plasma can be calculated by tracing out the rays followed by wave packets. We consider a Gaussian packet of fast oscillations grouped together in time and space, as illustrated in Fig. 12.9. Each individual wave travels with its own phase velocity. The speed at which the entire packet of waves (i.e. the energy and information content of the all of waves) travels, the group velocity, differs from the phase velocities of the various individual waves in the packet.

The amplitudes of the Gaussian wave packet shown in Fig. 12.9 may be represented by

$$A(x) = \operatorname{Re} \left[\exp(-x^2/2\sigma^2) \exp(ik_0 x) \right] \quad (12.56)$$

where k_0 is the peak of the k -spectrum, and many oscillations within the packet dictate $k_0\sigma \gg 1$. From Fourier transform theory, this amplitude can also be represented as

$$A(x) = \operatorname{Re} \left(\frac{\sigma}{\sqrt{2\pi}} \int_{-\infty}^{\infty} \exp(ikx) \exp[-\sigma^2(k - k_0)^2/2] dk \right) \quad (12.57)$$

which indicates that a wave packet localized in space can be constructed as an integral over plane waves localized in wave number, k . Extending this representation to include time evolution of the plane waves leads to

$$A(x, t) = \operatorname{Re} \left(\frac{\sigma}{\sqrt{2\pi}} \int_{-\infty}^{\infty} \exp \{i[kx - \omega(k)t]\} \exp[-\sigma^2(k - k_0)^2/2] dk \right) \quad (12.58)$$

For a well localized in k wave packet (i.e. large σ), we can expand $\omega(k) = \omega(k_0) + (\partial\omega/\partial k)_{k_0}(k - k_0) + \dots$ and neglect quadratic and higher terms in a dispersive medium to obtain

$$\begin{aligned} A(x, t) &= \operatorname{Re} \left(\exp \{i[k_0(\partial\omega/\partial k)_{k_0} - \omega(k_0)]t\} \right. \\ &\quad \times \left. \frac{\sigma}{\sqrt{2\pi}} \int_{-\infty}^{\infty} \exp \{i[kx - k(\partial\omega/\partial k)_{k_0}t]\} \exp[-\sigma^2(k - k_0)^2/2] dk \right) \end{aligned} \quad (12.59)$$

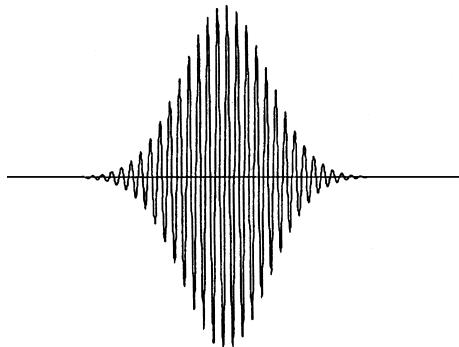


Figure 12.9. Wave packet with a Gaussian envelope, constructed such that $k_0\sigma \gg 1$

The $\sigma/\sqrt{2\pi}$ term is just the instantaneous form of Eq. (12.57) but moving at the group velocity $(d\omega/dk)_{k_0}$ of the wave packet, while the first term represents space-independent oscillations of the individual wave fronts within the packet propagating with their individual phase velocities ω/k , which in general differ from the group velocity of the wave packet.

Nonuniformities in the plasma or magnetic field will cause the trajectory of a wave packet to be curved. Taking \mathbf{k}_0 in the x -direction and considering a wave packet localized both along and perpendicular to \mathbf{k}_0 , the instantaneous wave amplitudes of Eqs. (12.56) and (12.57) become

$$\begin{aligned} A(x) &= \text{Re} \left[\exp \left(-x^2/2\sigma_x^2 - y^2/2\sigma_y^2 - z^2/2\sigma_z^2 \right) \exp(i k_0 x) \right] \\ &= \text{Re} \left(\frac{\sigma_x \sigma_y \sigma_z}{(2\pi)^{\frac{3}{2}}} \int_{-\infty}^{\infty} \exp(i \mathbf{k} \cdot \mathbf{x}) \right. \\ &\quad \times \exp \left[-\sigma_x^2(k_x - k_0)^2/2 - \sigma_y^2 k_y^2/2 - \sigma_z^2 k_z^2/2 \right] d^3 \mathbf{k} \left. \right) \end{aligned} \quad (12.60)$$

Extending to allow time evolution and expanding as before extends the above analysis to three dimensions and indicates a wave packet propagating with a group velocity

$$\mathbf{v}_g = \frac{\partial \omega}{\partial \mathbf{k}} = \hat{\mathbf{n}}_x \frac{\partial \omega}{\partial k_x} + \hat{\mathbf{n}}_y \frac{\partial \omega}{\partial k_y} + \hat{\mathbf{n}}_z \frac{\partial \omega}{\partial k_z} \quad (12.61)$$

We expect $\omega(\mathbf{k}_0)$ to be constant for a time-independent plasma and magnetic field, which implies that

$$\frac{d\omega}{dt} = \mathbf{v}_g \cdot \frac{\partial \omega}{\partial \mathbf{x}} \Big|_{\mathbf{k}} + \frac{d\mathbf{k}_0}{dt} \cdot \frac{\partial \omega}{\partial \mathbf{k}} \Big|_{\mathbf{x}} = 0 \quad (12.62)$$

However, there is no reason to expect the location \mathbf{k}_0 of the peak of the \mathbf{k} -spectrum of the wave packet not to change. Thus the “ray-tracing” equations for the wave packet are

$$\frac{d\mathbf{k}_0}{dt} = - \frac{\partial \omega}{\partial \mathbf{x}} \Big|_{\mathbf{k}}, \quad \frac{d\mathbf{x}_0}{dt} = \frac{\partial \omega}{\partial \mathbf{k}} \Big|_{\mathbf{x}} \quad (12.63)$$

The wave packet’s position in both space \mathbf{x} (x, y, z) and k -space \mathbf{k} (k_x, k_y, k_z) is obtained by integrating these equations forward in time from the initial \mathbf{x}_0 and \mathbf{k}_0 .

12.4.2 Wave Heating Physics

There are two quite different physical processes for transferring the energy of electromagnetic waves into thermal energy. The resonant absorption process involves the transfer of some of the energy of the incident wave to another propagating wave that is resonant in the same spatial regions in a reactive process known as “mode conversion.” There is also a collisionless dissipative wave-particle resonant interaction.

12.4.2.1 Resonance Frequencies

The resonance absorption frequencies can be identified by locating resonances in the solutions of Eq. (12.54). Because this equation is quadratic in n_{\perp}^2 , one of the solutions will tend to infinity when the coefficient of the n_{\perp}^4 term vanishes, so $\epsilon_{\perp} = 0$ is a condition for a resonance to occur, in the cold plasma approximation.

Ion cyclotron resonance heating (ICRH) is the lowest resonance frequency found. A resonance frequency only occurs when two or more ion species are present in the plasma. The ion–ion resonance frequency is

$$\omega_{ii}^2 = \frac{\Omega_1 \Omega_2 (1 + n_2 m_2 / n_1 m_1)}{(m_2 Z_1 / m_1 Z_2 + n_2 Z_2 / n_1 Z_1)} \quad (12.64)$$

where $\Omega_i = z_i e B / m_i$.

Equation (12.64) yields frequencies in the 30 MHz to 120 MHz range, depending on species and magnetic field strength, with corresponding wavelengths of the order of 10 m. Such “radiofrequency” waves are readily generated, but must be transported to the plasma in large waveguides and launched into the plasma with large antenna.

The lower hybrid resonance is between the ion and electron cyclotron frequencies and is given for high density regions in which $\omega_{pi}^2 \gg \Omega_i^2$ by

$$\omega_{LH}^2 \approx \omega_{pi}^2 / \left(1 + \omega_{pe}^2 / \Omega_e^2\right) \quad (12.65)$$

The LHRH range of frequencies is about 1 GHz to 8 GHz, depending on plasma density and magnetic field, with corresponding wavelengths of order 10 cm. High power waves in this frequency range are readily generated, but must be transported to the plasma in waveguides and launched into the plasma with complex gridded waveguide structures.

The highest resonance identified from Eq. (12.54) is the upper hybrid frequency for electron cyclotron resonance heating (ECRH)

$$\omega_{UH}^2 \approx \omega_{pe}^2 + \Omega_e^2 \quad (12.66)$$

In general, $\omega_{pe} \ll \Omega_e$ at the edge of tokamak plasmas, but the two frequencies are comparable in the center. Hence, ECRH requires high power sources in the 100 GHz to 200 GHz range, which are only just becoming available. Since the corresponding wavelength is in the millimeter range, these waves can be readily transported to the plasma in small coaxial cables and launched into the plasma with simple horns.

Electromagnetic wave heating and current drive at the MW–10 MW level has been tested on major tokamaks.

12.4.2.2 Wave Polarization

The electric field polarization of a wave can have a strong impact on the resonance absorption of wave energy to heat the plasma. The energy of waves at the electron or ion cyclotron frequency will be strongly absorbed if a significant fraction of the wave energy is associated with an electric field that is rotating in the same direction as the electron or ion,

respectively. Also, a wave electric field component parallel to the equilibrium magnetic field will have an important effect on transferring wave energy into electron acceleration.

We consider the propagation of waves in slab geometry with the equilibrium field in the z -direction and the plasma and magnetic field nonuniformity in the x -direction. Maxwell's equations can be written in terms of the dielectric tensor ϵ and the index of refraction n as

$$(n^2 \mathbf{I} - \mathbf{n}\mathbf{n} - \boldsymbol{\epsilon})\mathbf{E} = 0 \quad (12.67)$$

where \mathbf{I} is unit dyadic. The vanishing of the determinant of the coefficient multiplying \mathbf{E} defines the dispersion relation, Eq. (12.54). When $k_{\parallel} = 0$,

$$\frac{E_y}{E_x} = \frac{\epsilon_{\perp}}{\epsilon_{xy}} \quad (12.68)$$

Near a resonance surface where $\epsilon_{\perp} \rightarrow 0$, $E_y \ll E_x$. For the two-ion hybrid resonance, even when $k_{\parallel} \neq 0$, Eq. (12.67) leads to

$$n_{\perp} n_{\parallel} E_x + (\epsilon_{\parallel} - n_{\perp}^2) E_z = 0 \quad (12.69)$$

Since $\epsilon_{\parallel} \gg n_{\perp}^2$ for the ion cyclotron frequency range

$$\frac{E_z}{E_x} \simeq -\frac{n_{\perp} n_{\parallel}}{\epsilon_{\parallel}} \ll 1 \quad \text{and} \quad \frac{E_y}{E_x} \simeq -\frac{(\epsilon_{\perp} - n_{\parallel}^2)}{\epsilon_{xy}} \quad (12.70)$$

Near the two-ion hybrid resonance where $\epsilon_{\perp} - n_{\parallel}^2 \rightarrow 0$, the same result $E_y \ll E_x$ obtains under less restrictive conditions.

A wave with significant E along the x -direction of the nonuniformity has transverse polarity, and a wave with significant E along the y -direction normal to both the equilibrium magnetic field z -direction and the transverse x -direction has longitudinal polarity. The polarization of this wave becomes transverse in the resonance region ($E_y \ll E_x$), but is partially transverse and partially longitudinal ($E_y \approx E_x$) away from the resonance region. The longitudinal polarization favors the coupling of the incident wave to longitudinal Bernstein waves that propagate in a narrow band of frequencies about the hybrid resonance frequency. Furthermore, because longitudinal polarization can be decomposed into right and left circular polarization, resonance cyclotron heating of either ions or electrons may occur if the hybrid resonance frequency is sufficiently close to either cyclotron frequency.

12.4.2.3 Solutions of Local Dispersion Relations

The general features of the solutions of the local dispersion relation for any wave near a resonance are given in Fig. 12.10, which shows the square of the perpendicular refractive index for the extraordinary electron cyclotron wave propagating across the equilibrium magnetic field. The extraordinary mode is polarized with its electric field entirely in the plane perpendicular to the equilibrium magnetic field, in contrast to the ordinary mode which is linearly polarized with its electric field aligned with the equilibrium magnetic

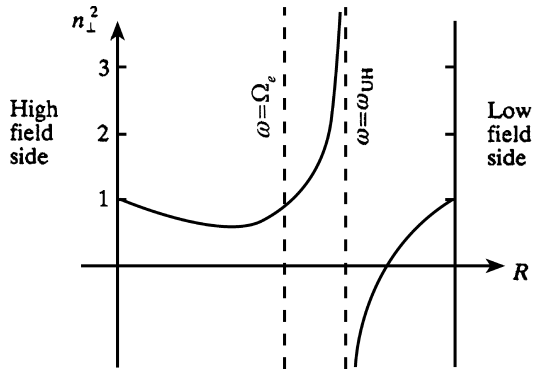


Figure 12.10. n_{\perp}^2 versus major radius for the electron cyclotron X-mode for $n_{\parallel} = 0$ and $\omega \sim \Omega_e$

field. The density variation in Fig. 12.10 is from zero at both the high-field and low-field boundaries to a maximum value in the center. n_{\perp}^2 is obtained by solving Eq. (12.54) with $n_{\parallel} = 0$ and the ion contribution neglected. The separation between the cut-off ($n_{\perp}^2 = 0$) and the upper hybrid resonance increases with plasma density. The existence of the cut off on the low field side (outboard of torus) means that an extraordinary electron cyclotron wave launched on the outboard will have to tunnel through an evanescent region to reach the region of the upper hybrid resonance absorption. Conversely, the absence of a cut off on the high field side means that an extraordinary wave launched from the inboard side will reach the upper hybrid resonance absorption region.

Note that there is no resonance at the electron cyclotron frequency. This is an artifact of using the cold plasma model. A kinetic model of a hot plasma would yield resonances at the electron cyclotron frequency and its harmonics.

12.4.2.4 Wave–Particle Collisionless Dissipation

Collisionless damping of an electromagnetic wave is governed by the wave–particle resonance condition

$$\omega - k_{\parallel} v_{\parallel j} - l |\Omega_j| = 0 \quad (12.71)$$

where $l = 0, 1, 2, 3 \dots$ in general and $l = 0$ corresponds to Landau damping. This equation, with $l = 0$, specifies a resonance between the parallel phase velocity of the wave and the particle velocity. Both the fast ion cyclotron wave and the lower hybrid wave can have phase velocities between the electron thermal velocity and the velocity of light. Wave energy is transferred to the resonant particles through their acceleration by the component of the wave electric field that is parallel to the equilibrium magnetic field.

Significant fast wave energy can also be transferred by the component of the wave magnetic field that is parallel to the equilibrium magnetic field through the transit time damping mechanism, which satisfies the Landau resonance condition, in the ion cyclotron range of frequencies.

The resonance condition with $l \neq 0$ corresponds to the electron or ion cyclotron resonance. Unlike the case with the $l = 0$ Landau resonance, a particle can be in resonance with a cyclotron mode if it is slower or faster than the corresponding cyclotron resonance frequency (i.e. $v_{\parallel} \neq \Omega_j/k_{\parallel}$). The perpendicular energy of the resonant particle is increased by the wave-particle interaction.

A collisionless wave-particle interaction results directly in the dissipation of wave energy by accelerating plasma particles. On the other hand, mode conversion only transfers energy from one wave to another. It is necessary that this converted mode propagate to another region in which the resonance conditions for a wave-particle interaction are satisfied. An absorption resonance is most effective when it is well removed in space from a wave-particle resonance location.

In all of these collisionless wave-particle interaction absorption mechanisms, only the small fraction of particles that have velocities that almost match the resonance condition gain energy from the wave. This small fraction of accelerated particles subsequently collide with other, primarily nonresonant, plasma particles and thereby share the wave energy. If the collision rate is sufficiently large, the overall effect is to preserve the Maxwellian distribution of the plasma particles and to increase the plasma temperature; i.e. to heat the plasma. However, the collision rate scales as $1/T_e^{3/2}$. If the energy transfer rate to the resonant particles is greater than the collision rate among the resonant and nonresonant particles, as it will tend to be as the electromagnetic power input increases, an unheated thermal distribution with a hot resonant “bump” or “tail” will develop. Provided that they are confined, these hot tails will eventually collide with other particles. For example, energetic ion tails in the MeV range are produced by ICRH and ultimately result in bulk electron heating.

The collision term in the Fokker-Planck equation for the equilibrium distribution function must be modified to represent both Coulomb collisional $C(f)$ and wave-particle heating $W(f)$ interactions (i.e. $C \rightarrow C + W$).

12.4.3 Ion Cyclotron Resonance Heating

Ion cyclotron heating in tokamaks is accomplished by launching a fast magnetosonic wave from an antenna in the plasma chamber. The dispersion relation

$$n_{\perp}^2 = (\epsilon_{\perp} + I\epsilon_{xy} - n_{\parallel}^2)(\epsilon_{\perp} - I\epsilon_{xy} - n_{\parallel}^2) / (\epsilon_{\perp} - n_{\parallel}^2) \quad (12.72)$$

describes the propagation of the fast wave (FW) into the resonance region in the center of the plasma where $\omega_{pe}^2/\Omega_e^2 \leq 1$ and $\omega_{pi}^2/\Omega_i^2 \geq 1$. The contribution of the electrons to ϵ_{\perp} is negligible because $\omega \approx \Omega_i$. Charge neutrality can be used in the form $\omega_{pe}^2/\Omega_e = \omega_{pi}^2/\Omega_i$ to evaluate the electron term in ϵ_{xy} , and the resulting expressions can be used in Eq. (12.72) to obtain

$$n_{\perp}^2 = \frac{\left[\sum_j \frac{\omega_{pi}^2}{\Omega_i(\omega + \Omega_i)} - n_{\parallel}^2 \right] \left[\sum_j \frac{\omega_{pi}^2}{\Omega_i(\omega - \Omega_i)} + n_{\parallel}^2 \right]}{\left[\sum_j \frac{\omega_{pi}^2}{(\omega^2 - \Omega_i^2)} + n_{\parallel}^2 \right]} \quad (12.73)$$

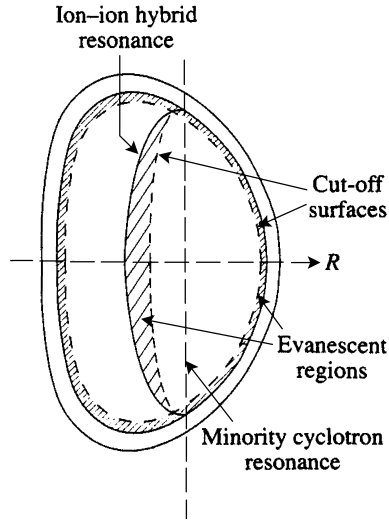


Figure 12.11. Loci of cut off and resonances in the poloidal cross section of a tokamak. The fast wave is evanescent in the hatched regions

Recalling that $n_{\perp}^2 = 0$ corresponds to a cut off, the fast wave cut off condition on n_{\parallel}^2 is obtained by setting the first term in the numerator to zero. For typical tokamak parameters, a fast wave with $\omega \approx 2\Omega_D$ will only propagate for $n_e > 2 \times 10^{18} \text{ m}^{-3}$, which implies that there will be a evanescent region in the edge of the plasma in front of the antenna. Efficient coupling then requires that the antenna be placed within a few cm of the cut off density surface which would expose them directly to the high energy fusion neutron flux in a reactor.

The parallel refractive index is small, $n_{\parallel} \ll \omega_{pi}^2 / (\omega^2 - \Omega_i^2)$, in the interior of a tokamak plasma. In the vicinity of the hybrid resonance in a two-species plasma, the first term in the denominator in Eq. (12.73) vanishes. Therefore, $n_{\perp}^2 \rightarrow \infty$ in the vicinity of the hybrid resonance by virtue of the denominator $\rightarrow 0$ in Eq. (12.73), and the second term in the numerator $\rightarrow 0$ in the same vicinity indicates the presence of a cutoff. A schematic of the cut off and resonance surfaces is shown in Fig. 12.11.

12.4.4 Lower Hybrid Resonance Heating

Propagation in the 1 GHz to 8 GHz LHR frequency range is well described by Eq. (12.54) with

$$\epsilon_{\perp} \approx 1 + \frac{\omega_{pe}^2}{\omega_{ce}^2} - \frac{\omega_{pi}^2}{\omega^2} \quad \epsilon_{\parallel} \approx 1 - \frac{\omega_{pe}^2}{\omega^2} \quad \epsilon_{xy} \approx -\frac{i\omega_{pe}^2}{\omega\omega_{ce}} \quad (12.74)$$

Equation (12.65) can be solved for the resonance plasma density corresponding to a given lower hybrid frequency $f_{w_{LH}}$ (GHz)

$$n_{\text{res}} = \frac{2.3 \times 10^{19} A_i f_{w_{\text{LH}}}^2}{(1 - 2.3 A_i f_{w_{\text{LH}}}^2 / B_0^2)} (m^{-3}) \quad (12.75)$$

where A_i is the ion mass in amu.

Bulk ion heating by lower hybrid waves has not yet proven to be reliable and reproducible. However, lower hybrid waves have proven to be efficient for driving plasma current and interest in them continues for this reason. For current drive (and for electron coupling) it is not necessary for the conditions of Eq. (12.75) to be satisfied in the plasma. The wave must have $n_{\parallel} > 1$ in order to reach the center of the plasma, otherwise complete reflection of the wave energy occurs.

12.4.5 Electron Cyclotron Resonance Heating

Since $\Omega_e \geq \omega_{pe} \gg \omega_{pi}$, only the electrons can respond to waves in the 100 GHz to 200 GHz ECRH frequency range, but ion heating can result from collisional energy transfer from the heated electrons. Propagation is again described by Eq. (12.54), which for propagation perpendicular to the equilibrium magnetic field ($n_{\parallel} = 0$) becomes

$$\begin{aligned} n_{\perp}^2 &= 1 - \frac{\omega_{pe}^2}{\omega^2} && \text{(O-mode)} \\ n_{\perp}^2 &= \frac{\left(1 - \frac{\omega_{pe}^2}{\omega^2} - \frac{\Omega_e}{\omega}\right) \left(1 - \frac{\omega_{pe}^2}{\omega^2} + \frac{\Omega_e}{\omega}\right)}{\left(1 - \frac{\omega_{pe}^2}{\omega^2} - \frac{\Omega_e^2}{\omega^2}\right)} && \text{(X-mode)} \end{aligned} \quad (12.76)$$

for the ordinary (O) and extraordinary (X), respectively, modes. The X-mode corresponds to an elliptically polarized wave with $\mathbf{E} \perp \mathbf{B}$, and the O-mode corresponds to a linearly polarized wave with $\mathbf{E} \parallel \mathbf{B}$. Both modes are able to propagate across the equilibrium magnetic field and, when thermal effects are taken into account, have absorption resonances at integral multiples of Ω_e . Resonance absorption at these frequencies and at the upper hybrid frequency is used in ECRH heating.

When $\omega = m\Omega_e$, the accessibility condition is $\omega_{pe}^2/\Omega_e^2 = m^2$ for the O-mode and $= m(m \pm 1)$ for the X-mode. The various cut offs are illustrated in Fig. 12.12, which is basically a plot of magnetic field squared versus density. The trajectory of the $m = 1$ X-mode launched from the low magnetic field side (dashed line 1) is reflected from the low density cut off surface before reaching any resonance absorption surface. The $m = 2$ X-mode (dashed line 2) is able to penetrate to the second harmonic resonance ($\omega = 2\Omega_e$) absorption surface, but not to the upper hybrid resonance absorption surface when launched from the low field side. When launched from the high field side, the $m = 1$ X-mode (dashed line 3) can propagate to reach both the fundamental ($\omega = \Omega_e$) and upper hybrid resonance absorption surfaces. In contrast to this complicated accessibility for the X-mode, the O-mode trajectory is independent of high field or low field side launching and will penetrate to all resonance absorption surfaces, provided only that the density remains below the cut off.

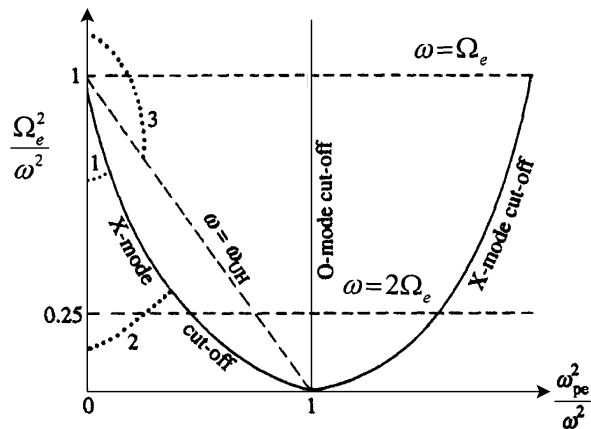


Figure 12.12. CMA diagram (plot of square magnetic field versus density) showing accessibility to X-mode and O-mode resonances ((solid line) cut offs, (dashed line) resonances, (dotted line) X-mode trajectories)

12.4.6 Current Drive

12.4.6.1 Lower Hybrid

In contrast to their limited success in plasma heating, waves in the 1 GHz to 8 GHz lower hybrid frequency range have been very successful in driving plasma current at low plasma densities and high magnetic fields. The waves are launched from a “grilled” waveguide structure located close to the plasma edge. The waves are launched with a well defined phase velocity along the magnetic field chosen to resonate with ≈ 100 kV electrons. This is accomplished by successively advancing the phase (typically 90°) in toroidally adjacent waveguides.

Wave energy absorption by the plasma takes place by Landau damping by plasma electrons that have parallel velocities that are resonant with the phase velocity of the waves. The accelerated electrons not only gain momentum directly from the wave but, more importantly, become less collisional and lose momentum at a reduced rate, thus driving an electron current resulting from the difference between momentum input and collisional momentum loss.

The lower hybrid waves accelerate electrons from a velocity v_{\parallel} parallel to the equilibrium magnetic field to a velocity $v_{\parallel} + \Delta v_{\parallel}$. The number of accelerated electrons per unit volume per second is $\Gamma_e \approx P_d/m_e v_{\parallel} \Delta v_{\parallel}$ for small Δv_{\parallel} , where P_d is the power absorbed per unit volume and the denominator is the change in kinetic energy. Each accelerated electron produces an initial current of $-e\Delta v_{\parallel}$ which subsequently decays due to collisions. A simple steady state momentum balance between the momentum input from the wave and collisional momentum loss (collision frequency ν) is $v_j = -\Gamma_e e v_{\parallel}$. A more detailed calculation of the resulting current requires a calculation of the electron distribution function, taking into account slowing down and pitch angle scattering of the accelerated electrons

and the loss of the pre-accelerated electrons. Such a calculation, but neglecting the loss of pre-accelerated electrons, yields

$$j = -\frac{1}{5 + Z_{\text{eff}}} \frac{\Gamma_e e v_{\parallel}}{v} \quad (12.77)$$

where

$$v = v_0 Z_{\text{eff}} \left(\frac{v_{\text{the}}}{v} \right)^3, \quad v_0 = \frac{n e^4 \ln \Lambda}{4 \pi \epsilon_0^2 m_e^2 v_{\text{the}}^2} \quad (12.78)$$

The loss of pre-accelerated electrons constitutes an effective current in the other direction, but this opposing current is smaller because the pre-accelerated electrons had a larger collision frequency and a smaller velocity. The resulting net electron current is

$$j = -\frac{\Gamma_e}{5 + Z_{\text{eff}}} \Delta v_{\parallel} \frac{d}{dv_{\parallel}} \left(\frac{v_{\parallel}}{v} \right) \quad (12.79)$$

Since $v \sim v_{\parallel}^{-3}$ for $v_{\parallel} \gg v_{\perp}$, this equation becomes

$$j = -\frac{4}{5 + Z_{\text{eff}}} \frac{\Gamma_e}{v} \Delta v_{\parallel} = -\frac{4 P_d e}{m_e v_{\parallel} v} \quad (12.80)$$

Defining normalized currents and power density,

$$j^* = \frac{|j|}{n e v_{\text{the}}} \quad \text{and} \quad P^* = \frac{P_d}{n m_e v_{\text{the}}^2 v_0} \quad (12.81)$$

the current drive efficiency is conventionally defined as

$$\eta \equiv \frac{j^*}{P^*} = \frac{4}{5 + Z_{\text{eff}}} \left(\frac{v_p}{v_{\text{the}}} \right)^2 \quad (12.82)$$

where the resonance condition for Landau damping, $v_{\parallel} = v_p$, the phase velocity of the wave, has been used. The practical efficiency, I/P , of any current drive scheme can be defined in terms of η by

$$\frac{I}{P} (AW^{-1}) = 0.061 \frac{T_e(\text{keV})}{R(n/10^{20}) \ln \Lambda} \eta \quad (12.83)$$

12.4.6.2 Fast Wave ICRH

Fast magnetosonic waves also damp at the Landau resonance, but the force accelerating the electrons includes the interaction of the parallel gradient of the wave's magnetic field with the magnetic moment associated with gyromotion, as well as the wave's electric field. The net wave-particle interaction is much weaker than described above for the lower hybrid waves. The theoretical efficiency is somewhat greater for FW current drive than for LH current drive, under the same plasma conditions, and fast waves have no difficulty in penetrating high density plasmas, unlike other wave current drive mechanisms.

12.4.6.3 Electron Cyclotron

Current can be driven by electron cyclotron waves with a frequency such that the Doppler shift due to electron velocity along the equilibrium magnetic field results in a wave with the electron cyclotron frequency or one of its harmonics, $\omega - \Omega_e = k_{\parallel} v_p$. These heated electrons are less collisional than electrons circulating toroidally in the opposite direction, resulting in a net transfer of momentum from electrons to ions, which causes the ions and electrons to have oppositely directed net flows (i.e. a current).

The wave-particle interaction is an acceleration of resonant electrons in the perpendicular direction. The equivalent of Eq. (12.79) for this situation is

$$j = -\frac{\Gamma e}{5 + Z_{\text{eff}}} \Delta v_{\perp} \frac{d}{dv_{\parallel}} \left(\frac{v_{\parallel}}{v} \right) \quad (12.84)$$

and the normalized efficiency is

$$\eta = \frac{3}{5 + Z_{\text{eff}}} \left(\frac{v_p}{v_{\text{the}}} \right)^2 \quad (12.85)$$

which is 75 % the value for lower hybrid current drive.

From the resonance condition, $\omega - \Omega_e(R) = k_{\parallel} v_{\parallel}$, it follows that the resonant value of the parallel velocity changes signs as the spatially dependent $\Omega_e(R)$ varies with R from $> \omega$ to $< \omega$, for a fixed propagation direction (sign of k_{\parallel}). This possibility for driving oppositely directed currents at nearby radii on opposite sides of a resonance surface provides a means for detailed tailoring of the current profile.

12.4.6.4 Fast Wave Minority Ion

Heating a minority ion species makes it less collisional than the main ion species, creating oppositely directed bulk velocities for the two species, as described above. A net ion current would flow if the two species have different charge to mass ratios. However, the ion-electron collisions cause a compensating electron current.

12.4.6.5 Figure of Merit

A figure of merit for current drive efficiency

$$\gamma = \frac{RI}{P} \frac{\bar{n}_e}{10^{20}} \left(m^{-2} A W^{-1} \right) \quad (12.86)$$

is frequently used. Experimental values are shown in Fig. 12.13 for lower hybrid (LHCD), electron cyclotron (ECCD), fast wave (FWCD) and neutral beam (NBCD) current drive.

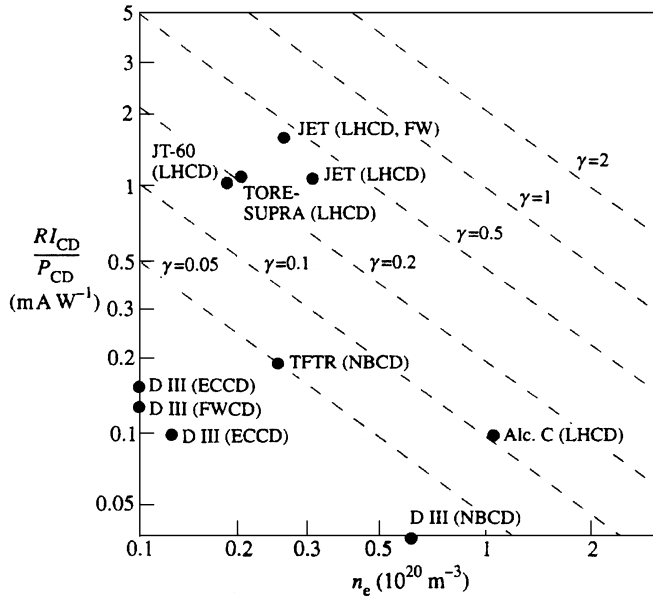


Figure 12.13. Experimentally measured current drive efficiencies for lower hybrid waves, neutral beam injection and fast magnetosonic waves. The dashed lines represent different values of the figure of merit γ

Problems for Chapter 12

1. Calculate the maximum temperature that can be achieved by ohmic heating in a tokamak with $q_0 = 1$, $q_a = 3$, $Z_{\text{eff}} = 2$ as a function of (aB_ϕ/R) . (Use Alcator confinement scaling.)
2. Calculate the characteristic times for fast deuterium ion slowing down by collisions with electrons (τ_{eb}) and ions (τ_{ib}) in a deuterium plasma with $n_e = n_i = 5 \times 10^{19} \text{ m}^{-3}$ and $T_e = T_i = 5 \text{ keV}$.
3. Calculate the “critical” fast ion initial energy for which the fast ion slowing down rates by ions and electrons is equal. What fraction of the initial fast ion energy is given to the electrons in this case?
4. Calculate and plot the fast ion distribution function for the plasma of problem 2.
5. Calculate the ion-ion resonance frequency for a helium minority ion with concentration $n_{\text{He}}/n_D = 0.03$ present in a deuterium plasma with $n_D = 5 \times 10^{19} \text{ m}^{-3}$ and $B = 5 \text{ T}$.
6. Calculate the cut off condition on n_{\parallel} for the fast ICRH wave with $\omega = 2\Omega_D$ in the plasma of problem 5.
7. Calculate and plot the resonance density for lower hybrid resonance heating in a deuterium plasma with $B = 3 \text{ T}$ as a function of $f_{\text{LH}}(\text{GHz})$.
8. Calculate the lower hybrid current drive efficiency [$I(A)/P(W)$] in a deuterium plasma with $n_e = n_i = 5 \times 10^{19} \text{ m}^{-3}$, $T_e = T_i = 5 \text{ keV}$ and $R = 1.7 \text{ m}$.

13 Plasma–Material Interaction

Up to this point we have treated the physics of plasmas as if they were isolated from the rest of the universe, but they are not, and this treatment was only a matter of convenience. In fact, plasmas interact strongly with the immediately surrounding materials that constitute the plasma chamber. Ions, electrons and radiation from the plasma are incident on the surrounding material surfaces, heating them and producing neutral atoms and molecules of plasma and wall materials which return to the plasma to undergo a variety of reactions with plasma ions and electrons, producing further charged and neutral particles incident upon the wall surfaces, etc. These processes both refuel and cool the plasma, and also greatly affect its composition. In this chapter we examine the various physical processes that are involved in plasma–material interactions.

13.1 Sheath

It is perhaps not surprising that the actual interface between two states of matter – plasma and solid – is not a simple one. Consider the situation of plasma ions and electrons flowing along magnetic field lines which are incident on a material surface. If the upstream plasma regime is collisional, then the ions and electrons will have similar temperatures because of collisional equilibration, as a result of which the thermal speed of the much less massive electrons is much greater than that of the ions, $v_{\text{the}} \gg v_{\text{thi}}$. If uncompensated, this situation would result in electrons reaching the surface much faster and building up a large negative charge relative to the plasma. However, an electric field is created which equalizes the two flows by accelerating the ions and decelerating the electrons. This electric field is, for the most part, located in a thin “sheath” of width a few Debye lengths at the surface, although a smaller electric field extends more deeply into a “pre-sheath” region of the plasma. This situation is illustrated in Fig. 13.1.

The electrostatic potential satisfies Poisson’s equation

$$\frac{d^2\phi}{dx^2} = \frac{e}{\epsilon_0} (n_e - n_i) \quad (13.1)$$

We define this “sheath potential” to be zero at the sheath boundary (dashed vertical line). If n_0 is the average value of the electron or ion density at the entrance to the sheath from the pre-sheath region (i.e. the value at the dashed vertical line in Fig. 13.1), then the actual electron distribution is described by the Boltzmann distribution

$$n_e = n_0 \exp \frac{e\phi}{T_e} \quad (13.2)$$

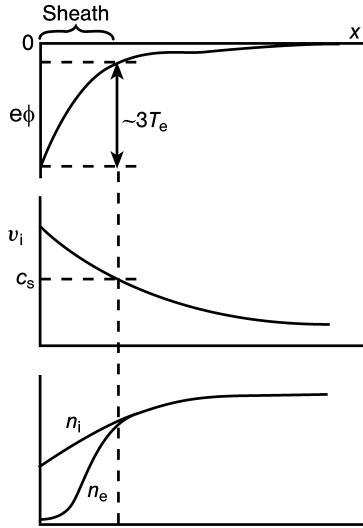


Figure 13.1. Spatial variation of the electrostatic potential, ϕ , the ion speed, v_i , and the ion and electron densities across the sheath from the wall (on the left) to the pre-sheath (on the right)

If v_0 is the speed with which ions enter the sheath from the pre-sheath region, then conservation of energy provides an expression for the ion velocity in the sheath

$$\frac{1}{2}m_i v_i^2 = \frac{1}{2}m_i v_0^2 - e\phi \quad (13.3)$$

Assuming no sources or sinks of ions in the sheath, $n_i v_i$ must be constant across the sheath, which leads to an expression for the ion density in the sheath

$$n_i = n_0 \left(\frac{\frac{1}{2}m_i v_0^2}{\frac{1}{2}m_i v_0^2 - e\phi} \right)^{\frac{1}{2}} \quad (13.4)$$

Combining these equations yields an equation for the electrostatic potential in the sheath region

$$\frac{d^2\phi}{dx^2} = \frac{n_0 e}{\epsilon_0} \left[\exp \frac{e\phi}{T_e} - \left(\frac{\frac{1}{2}m_i v_0^2}{\frac{1}{2}m_i v_0^2 - e\phi} \right)^{\frac{1}{2}} \right] \quad (13.5)$$

The ion velocity at the pre-sheath, v_0 , is determined by requiring that the solution of Eq. (13.5) at the pre-sheath boundary matches the slowly varying and small potential outside the sheath. For small ϕ , Eq. (13.5) becomes

$$\frac{d^2\phi}{dx^2} = \left(1 - \frac{T_e/m_i}{v_0^2} \right) \frac{\phi}{\lambda_D^2} \quad (13.6)$$

where λ_D is the Debye length. A slowly varying solution of Eq. (13.6) requires

$$v_0 \simeq (T_e/m_i)^{\frac{1}{2}} \quad (13.7)$$

Generalizing this development to include ion temperature effects yields

$$v_0 = [(T_e + T_i)/m_i]^{\frac{1}{2}} \simeq c_s \quad (13.8)$$

Thus, we find the important result that the plasma enters the sheath at the speed of sound.

The potential across the sheath, ϕ_0 , is determined by the requirement that the total current to the surface be zero. The ion current density into and across the sheath into the surface is

$$j_i = n_0 e c_s \quad (13.9)$$

The electron flux to the surface is $n_e \bar{c}_e / 4$, where $\bar{c}_e = (8T_e/\pi m_e)^{\frac{1}{2}}$ is the average electron speed for a Maxwellian electron distribution. Using Eq. (13.2), the electron current density into the surface is

$$j_e = -\frac{1}{4} n_0 e \bar{c}_e \exp \frac{e\phi_0}{T_e} \quad (13.10)$$

The requirement $j_i + j_e = 0$ then leads to

$$-\frac{e\phi_0}{T_e} = \frac{1}{2} \ln \left[\frac{m_i/m_e}{2\pi(1+T_i/T_e)} \right] \quad (13.11)$$

For a deuterium plasma with $T_i = T_e$, this yields $-e\phi_0/T_e = 2.8$.

Secondary electrons are produced at the surface by ion and electron bombardment, with emission coefficient δ , and are accelerated out of the sheath into the pre-sheath by the electric field. Including this effect in the above derivation leads to

$$-\frac{e\phi_0}{T_e} = \frac{1}{2} \ln \left[\frac{(1-\delta)^2 m_i/m_e}{2\pi(1+T_i/T_e)} \right] \quad (13.12)$$

Plasma ions enter the sheath with their thermal energy and are accelerated across the sheath into the surface by the electric field. Similarly for the electrons, except that they are decelerated. The distributions can be approximately represented by Maxwellians, but at temperatures that are lower than the pre-sheath temperature for the electrons and higher for the ions. However, only the higher energy pre-sheath electrons actually survive the deceleration and reach the sheath.

The energy transported to the surface in a Maxwellian distribution of ions or electrons is $2T$ per particle. Including the acceleration of ions in the sheath, the power flux to the surface is

$$P = n_e c_s T_e \left[\frac{2T_i}{T_e} + \frac{2}{1-\delta} + \frac{1}{2} \ln \left(\frac{(1-\delta)^2 m_i/m_e}{2\pi(1+T_i/T_e)} \right) \right] \equiv \gamma_s \Gamma T_e \quad (13.13)$$

where Γ is the ion flux and $\gamma_s \approx 7$ to 8 is an effective sheath power transmission coefficient.

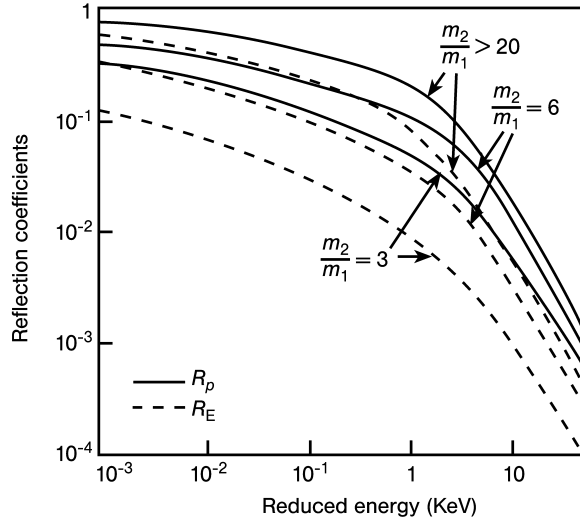


Figure 13.2. Particle and energy reflection coefficients for particles reflected from solid surfaces. (The reduced energy is defined as $\epsilon = 32.5m_w E / ((m_i + m_w)z_i z_w (z_i^{2/3} + z_w^{2/3})^{1/2})$ with E in eV)

13.2 Recycling

A plasma ion or neutral atom incident upon a surface will undergo one or more elastic or inelastic scattering events with the atoms of the surface material. The incident particle may be “reflected” with a significant fraction of its original energy after one or more collisions, or it may lose essentially all of its energy in collisions and come into equilibrium with the atoms of the surface and near-surface material and subsequently diffuse (preferentially) to the incident surface and be “re-emitted” into the plasma with the thermal energy of the surface (usually after molecule formation).

The reflection of incident ions or atoms depends on the energy of the incident particle and on the ratio of masses of the incident particle and the surface atom. Particle reflection is characterized by a particle coefficient $R_p(E)$, defined as the ratio of the particle flux returning to the plasma to the incident particle flux, and an energy reflection coefficient $R_E(E)$, defined as the ratio of the energy flux returning to the plasma to the incident energy flux. The energy and particle reflection coefficients are related by

$$R_E(E_0) = \frac{\bar{E}(E_0)}{E_0} R_p(E_0) \quad (13.14)$$

where E_0 is the energy of the incident particle and \bar{E} is the average energy of the reflected particles. Values of R_p and R_E are given in Fig. 13.2. The reflected particles are primarily neutral atoms and are distributed continuously in energy with mean reflected energy of 30 % to 50 % of the incident energy.

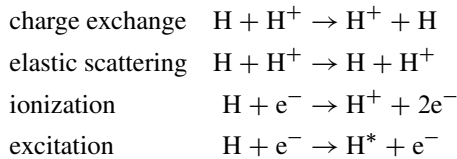
The $(1 - R_p)$ fraction of the incident particles that are not reflected are thermalized within the solid and reside in interstitial sites or defects, such as vacancies, in the metal. For hydrogen isotopes, diffusion readily occurs at room temperature and above in many materials, with the notable exception of carbon, carbides and oxides. Since the penetration of the incident particles has a very short range, the concentration gradient and thus the diffusion is greatest back towards the plasma surface. In those materials for which diffusion occurs, the release of hydrogen isotopes back into the plasma depends on the heat of solution of hydrogen in the material. In the exothermic case, there is, effectively, a potential barrier at the surface that prevents the release of hydrogen back into the plasma, in which case it diffuses back and is distributed over the material volume. In the endothermic case, hydrogen atoms reaching the plasma surface form molecules and are released back into the plasma with an energy distribution similar to that of the atoms in the solid.

A recycling coefficient can be defined as the ratio of the total particle flux returning to the plasma (reflection plus re-emission) to the incident particle flux. The instantaneous recycling coefficients for a given machine will vary considerably with operating history. Operation at low temperature such that diffusion is inhibited or with heavy continuous gas fueling might be expected to lead to particle recycling coefficients less than unity because of gas build up in the walls, and subsequent operation at high temperature or without continuous fueling might have recycling coefficients greater than unity because previously adsorbed particles are being released. However, after prolonged operation, the recycling of particles will reach an equilibrium (for the situation in which hydrogen can be re-emitted) in which the reflected and re-emitted particle fluxes balance the incident particle flux. In a typical situation, about 50 % (30 % for low- Z surface materials) of the incident particles would be reflected with energies $\leq 5T_e$ (taking account of sheath acceleration) and about 50 % (70 % for low- Z surface materials) would be re-emitted as molecules with energies ≈ 0.025 eV.

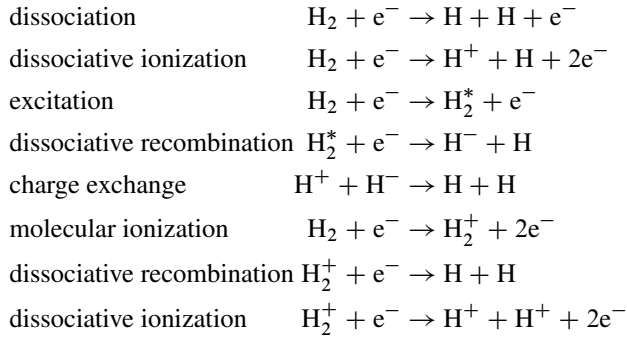
Hydrogen retention in surface materials is a major concern when tritium is present in the plasma. In general, when clean surfaces are exposed to incident hydrogen fluxes all of the incident particles which are not reflected are trapped. After a certain fluence of hydrogen on the surface the trapping saturates and re-emission begins to occur, leading, after a sufficient fluence, to essentially 100 % recycling of all incident hydrogen. Because the trapped inventory of hydrogen may be quite large in carbon, which has excellent thermal properties and otherwise would be a logical candidate as a surface material, this material is unlikely to be used as a surface material in fusion reactors.

13.3 Atomic and Molecular Processes

The recycling atoms and molecules and any gas molecules injected for fueling interact with the plasma near the wall. For the reflected hydrogen (or deuterium or tritium) atoms the important processes are



For the re-emitted and gas injected hydrogen (or deuterium or tritium) molecules the important processes are



The reaction rates for these various processes are functions of plasma temperature and density, as indicated by the rate coefficients shown in Fig. 13.3.

Charge exchange and elastic scattering rate coefficients for a Maxwellian distribution of deuterium atoms at temperature T_a colliding with a Maxwellian distribution of deuterium ions at temperature T_i are given in Table 13.1.

Multi-step processes are important in determining overall ionization and recombination rates at lower temperatures, depending on the plasma density. Atomic ionization and recombination rate coefficients, averaged over Maxwellian distributions, are shown for hydrogen in Fig. 13.4.

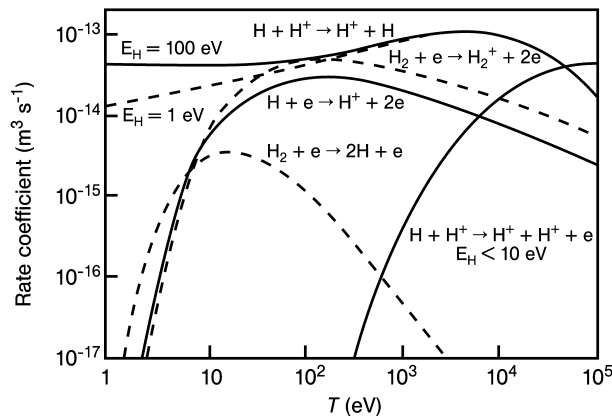


Figure 13.3. Rate coefficients for various common reactions for hydrogen atoms and molecules

Table 13.1. Charge exchange and elastic scattering rate coefficients for deuterium atoms reacting with deuterium ions

Reaction	T_a eV	T_i eV	$\langle \sigma v \rangle$ $10^{-14} \text{ m}^3 \cdot \text{s}^{-1}$
$D^+ + D \rightarrow D + D^+$	1	1	0.8
charge-exchange	1	10	1.2
	1	100	2.8
	10	1	1.2
	10	10	1.5
	10	100	2.9
	100	1	2.8
	100	10	2.9
	100	100	3.7
$D^+ + D \rightarrow D^+ + D$	1	1	2.0
elastic scatter	1	10	3.5
	1	100	6.9
	10	1	3.5
	10	10	5.1
	10	100	6.8
	100	1	6.9
	100	10	6.8
	100	100	12.0

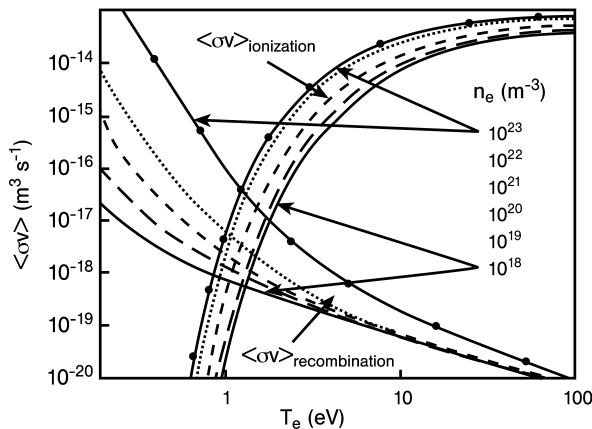


Figure 13.4. Hydrogen ionization and recombination rate coefficients

The various molecular reactions involved in the eventual production of H atoms and H^+ ions from a H_2 molecule in the ground state, as indicated above, constitute a rather

complicated multi-step process. Because of differences in reaction rate coefficients, certain steps in multi-step processes are rate limiting. Some simplification that aid in understanding the resulting effects can be achieved by identifying the rate limiting steps and summing reactions that lead to the same outcome. Table 13.2 summarizes the summed and rate-limiting reaction rate coefficients for a number of molecular reactions involving excited and ground state D₂ molecules. Also shown in the table are the number of atoms (D⁰) and ions (D⁺, D⁻) formed by each dissociation channel.

Table 13.2. Summed and rate-limiting reaction rate coefficients for D₂

Reaction	Reaction rates (m ³ ·s ⁻¹) and products		
	1 eV	10 eV	100 eV
(a) Ground state molecules			
<i>Elastic</i>			
D ₂ + D ⁺ /D	10 × 10 ⁻¹⁵	9 × 10 ⁻¹⁵	9 × 10 ⁻¹⁵
Producing per event			
D ₂ Molecules	1	1	1
<i>Inelastic</i>			
D ₂ + D ⁺ /D	3 × 10 ⁻¹⁷	1 × 10 ⁻¹⁶	2 × 10 ⁻¹⁵
Producing per event			
D atoms	1.77	1.12	2.0
D ⁺ ions	0.23	0.88	0
<i>Inelastic</i>			
D ₂ + e ⁻	1 × 10 ⁻¹⁹	9 × 10 ⁻¹⁵	5 × 10 ⁻¹⁴
Producing per event			
D atoms	1.77	1.44	1.0
D ⁺ ions	0.23	0.56	1.0
(b) Excited (vibrational) molecules			
<i>Excitation of ground state D₂</i>	7.0 × 10 ⁻¹⁸	3.5 × 10 ⁻¹⁷	1.3 × 10 ⁻¹⁷
Producing D ₂ [*]	1	1	1
<i>Electron dissociation of excited D₂[*]</i>	2.0 × 10 ⁻¹⁴	1.0 × 10 ⁻¹⁴	5.0 × 10 ⁻¹⁴
Producing per event			
D ⁰	1	1.37	1
D ⁺	0	0.49	1
D ⁻	1	0.14	0

Ionization and, at very low temperatures, recombination are, respectively, important atomic cooling and heating mechanisms for plasma electrons

$$P_{\text{cool}}^{\text{H}} = P_{\text{cool, iz}}^{\text{H}} + P_{\text{cool, rec}}^{\text{H}} = (P_{\text{rad, iz}}^{\text{H}} + I_{\text{iz}} \langle \sigma v \rangle_{\text{iz, H}}) + (P_{\text{rad, rec}}^{\text{H}} - I_{\text{iz}} \langle \sigma v \rangle_{\text{rec, H}}) \quad (13.15)$$

where $I_{\text{iz}} = 13.6 \text{ eV}$ is the ionization potential of hydrogen, $\langle \sigma v \rangle$ are the Maxwellian averaged rate coefficients for ionization and recombination given in Fig. 13.4, and the P_{rad} are the radiation emission rates for ionization and recombination given in Fig. 13.5 and Fig. 13.6.

When the plasma is large in size and/or the hydrogen ion density is greater than about 10^{19} m^{-3} , the Lyman-alpha photons can be trapped and their energy retained in the plasma.

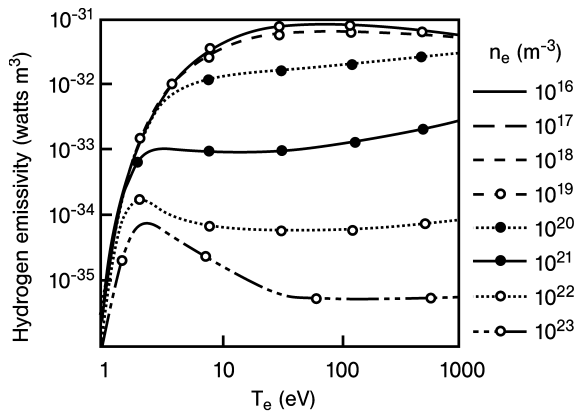


Figure 13.5. Hydrogen radiation emission coefficients due to ionization

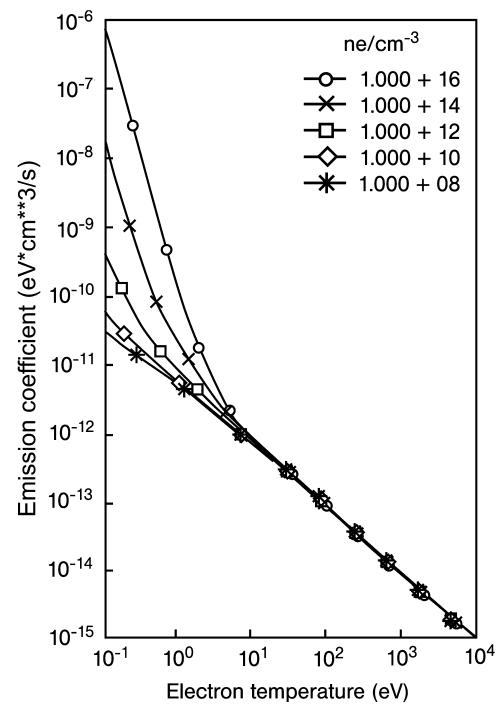


Figure 13.6. Hydrogen radiation emission coefficients due to recombination. (Multiply by 1.6×10^{-25} for $\text{W} \cdot \text{m}^3$ units)

This radiation re-absorption not only reduces the radiative cooling rate but also alters the relative populations of excited states, leading to changes in the effective rate coefficients

for ionization and recombination. Ionization and recombination rate coefficients for deuterium are shown in Table 13.3 with and without suppression of Lyman-alpha radiation. Absorption of Lyman-alpha radiation by the plasma significantly enhances ionization at low temperatures.

Table 13.3. Ionization and recombination rate coefficients for deuterium

Reaction	T eV	n_e m^{-3}	$\langle \sigma v \rangle$ $\text{m}^3 \cdot \text{s}^{-1}$	$\langle \sigma v \rangle$ Lyman suppressed $\text{m}^3 \cdot \text{s}^{-1}$
ionization	1	10^{16}	7.6×10^{-21}	1.8×10^{-18}
	10	10^{16}	5.3×10^{-15}	2.4×10^{-14}
	10	10^{20}	1.2×10^{-14}	2.4×10^{-14}
	10	10^{21}	2.2×10^{-14}	2.4×10^{-14}
	100	10^{16}	3.1×10^{-14}	8.0×10^{-14}
	100	10^{20}	4.0×10^{-14}	8.0×10^{-14}
recombination	100	10^{21}	6.0×10^{-14}	8.0×10^{-14}
	1	10^{16}	4.5×10^{-19}	3.9×10^{-19}
	1	10^{20}	2.0×10^{-18}	4.0×10^{-19}
	1	10^{21}	5.5×10^{-18}	1.3×10^{-18}
	10	all	6.5×10^{-20}	4.0×10^{-20}
	100	all	6.0×10^{-21}	7.0×10^{-21}

13.4 Sputtering

The removal of atoms of wall surface material as a result of the impact of incident ions and neutral atoms is known as sputtering. The mechanism for physical sputtering is the transfer to an atom on the surface sufficient energy to overcome the binding energy, resulting in the atom being ejected from the surface. Since the maximum energy that can be transferred to a stationary wall atom of mass m_w by a collision with an incident ion or neutral of mass m_i is a fraction $\xi = 4m_i m_w / (m_i + m_w)^2$ of the incident energy, there is a lower threshold energy for an incident particle to be able to transfer an amount of energy equal to the binding energy, U_B , given by

$$E_{\text{th}} = \frac{U_B}{\xi} \quad (13.16)$$

For incident particle energy $E > E_{\text{th}}$, the yield, defined as the number of sputtered wall atoms per incident ion or neutral atom, can be represented by

$$Y(E) = Q(m_i, m_w, U_B) s_n(E) g(E_{\text{th}}/E) \quad (13.17)$$

where the nuclear stopping cross section is given by

$$s_n(\epsilon) = \frac{3.441 \sqrt{\epsilon} \ln(\epsilon + 2.718)}{1 + 6.355 \sqrt{\epsilon} + \epsilon(6.882 \sqrt{\epsilon} - 1.708)} \quad (13.18)$$

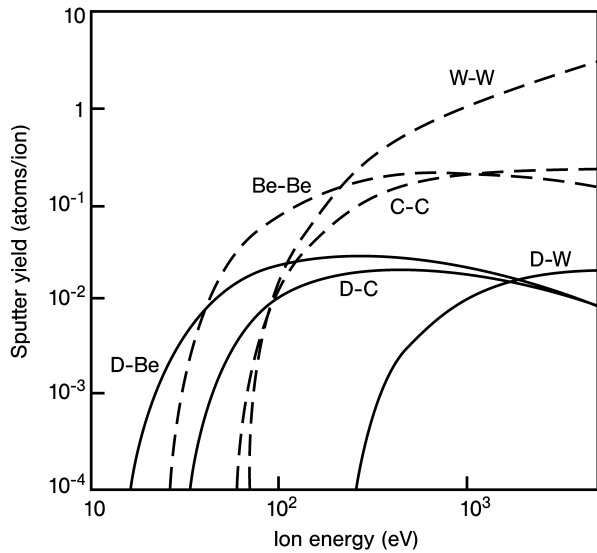


Figure 13.7. Energy dependence of the physical sputtering yield for deuterium- and self-sputtering of surfaces of beryllium, carbon and tungsten

with $\epsilon = E/E_{\text{TF}}$, where E_{TF} is the Thomas–Fermi energy,

$$g(\delta) = (1 - \delta^{\frac{2}{3}})(1 - \delta)^2 \quad (13.19)$$

where $\delta = E_{\text{th}}/E$, accounts for threshold effects, and Q is an empirical yield factor for each material. Normal incidence sputtering yields are given in Fig. 13.7 for deuterium- and self-sputter for several wall materials.

The parameters needed to evaluate Eq. (13.17) for a wider range of incident particles and surface materials are given in Table 13.4.

Table 13.4. Parameters for the physical sputter yield of Eq. (13.17); E_{th} , E_{TF} in eV; Q in atoms per ion

	Beryllium			Graphite			Iron			Molybdenum			Tungsten		
	E_{th}	E_{TF}	Q	E_{th}	E_{TF}	Q	E_{th}	E_{TF}	Q	E_{th}	E_{TF}	Q	E_{th}	E_{TF}	Q
H	20	256	0.1	35	415	0.035	64	2 544	0.042	199	4 718	0.007	443	9 870	0.007
D	9	282	0.3	30	447	0.10	44	2 589	0.13	90	4 767	0.023	220	9 923	0.019
T	21	308	0.24	30	479	0.20	40	2 634	0.21	70	4 816	0.045	140	9 977	0.038
${}^4\text{He}$	30	780	0.59	29	1 087	0.32	33	5 514	0.44	46	9 944	0.12	110	20 373	0.106
C	40	4 152	1.6	42	5 687	1.5	35	20 247	3.2	55	34 183	0.93	80	66 507	0.93
O	70	6 970	1.3		9 298			29 839			48 322		40	91 979	2.2
Self	25	2 208	1.4	42	5 687	1.5	40	174 096	13	64	533 048	18	65	1 998 599	20

The sputtering yield increases as the angle of incidence changes from normal (perpendicular) to oblique incidence.

In chemical sputtering, the chemical potential energy of the incident hydrogen ion or atom is available to break C–C lattice bonds and to make C–H bonds, eventually leading

to the formation of volatile CH₄ which is released from the surface. Chemical sputtering yields are larger than physical sputtering yields for carbon for incident energies ≤ 100 eV and are comparable for $E > 100$ eV.

13.5 Impurity Radiation

Sputtered wall “impurity” atoms, and other nonhydrogenic atoms present, are quickly ionized in plasmas at electron temperatures of a few eV or more. At higher electron temperatures the atoms become successively more highly ionized. The dominant charge state is determined by the electron temperature, as shown in Fig. 13.8 for carbon.

Radiation from partially ionized impurity atoms is an important power loss mechanism in plasmas. For most plasmas of interest for fusion, the important elementary atomic processes are electron collisional excitation followed by radiative decay, electron ionization, and radiative recombination. Collisional de-excitation and three-body recombination can usually be neglected.

On time scales of interest for plasma physics, radiative decay can be assumed to occur instantaneously following collisional excitation of an orbital electron, yielding a photon whose energy is equal to the energy difference of the excited and ground states. The power loss from the plasma by this “line radiation” process is determined by the rate of production of excited states,

$$P_L = n_e \sum_z \sum_l n_z E_{z,l} X_{z,l} \quad (13.20)$$

where n_e and n_z are the electron and z th charge state densities, $E_{z,l}$, is the transition energy between the l th energy level and the ground state of the z th charge state, and $X_{z,l}$, is the

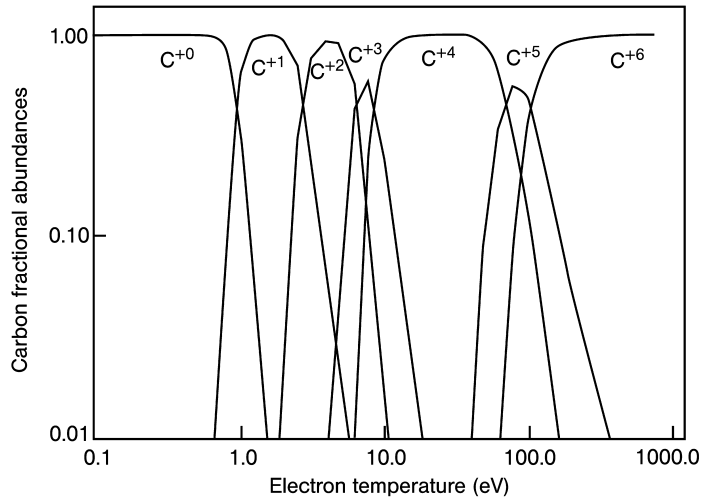


Figure 13.8. Carbon equilibrium ionization state distribution

electron collisional excitation rate for the l th energy level of the z th charge state from the ground level.

Radiative recombination involves the recombination of a free plasma electron with an ion in the $(z + 1)$ th ionic ground state to form an ion in the z th ionic ground state. The power loss from the plasma by this “recombination radiation” process is

$$\begin{aligned} P_R &= n_e \sum_z n_{z+1} \langle (E_{z+1} + E) \sigma_R v \rangle_{z+1} \\ &= n_e \sum_z n_{z+1} (E_{z+1} R_{z+1} + \langle E \sigma_R v \rangle_{z+1}) \end{aligned} \quad (13.21)$$

where E_{z+1} is the ionization potential for the $(z + 1)$ th ionic ground state relative to the z th ionic ground state, R_{z+1} is the recombination rate for the formation of ground state z from ground state $z + 1$, and $\langle E \sigma_u R v \rangle_{z+1}$ is an average over the plasma electron distribution. The quantity E is the energy of the free electron, and $n_e n_{z+1} \sigma_R v$ is the reaction rate for the recombination process. The spectral distribution of the emitted radiation is continuous and characteristic of the plasma electron energy distribution.

The distribution of z th ionic ground levels is governed by a coupled set of rate equations (equal in number to the atomic number of the impurity nucleus plus one)

$$\frac{dn_z}{dt} + \nabla \cdot n_z \mathbf{v}_z = n_e (I_{z-1} n_{z-1} + R_{z+1} n_{z+1} - I_z n_z - R_z n_z) \quad (13.22)$$

where I_z is the ionization rate from ground state z to ground state $z + 1$. The ionization and recombination rates are of the form

$$I_z = s_z (T_e / \chi_z)^{\frac{1}{2}} e^{-\chi_z / T_e} T_e / (1 + T_e / \chi_z) \quad (13.23)$$

and

$$R_z = a_z (\chi_z / T_e)^{\frac{3}{2}} + c_z (\chi_z / T_e) \quad (13.24)$$

where s_z , a_z , and c_z are rate coefficients and the χ_z are the ionization energies.

The procedure for calculating the impurity radiative power loss is to solve Eq. (13.22) for the ground charge state distribution, then evaluate the power losses from Eq. (13.20) and Eq. (13.21). When the time scales for the atomic processes are short compared to the other time scales of interest and when spatial gradients are not significant, the solution of the time-independent form of Eq. (13.22) with the transport term on the left set to 0 provides a good approximation to the ground charge state distribution. This “coronal equilibrium” model has been used to compute the specific power loss from a plasma for different impurity species, assuming a Maxwellian distribution for the plasma electron energy. The results are shown in Fig. 13.9 and Table 13.5.

The impurity radiative power loss is a sensitive function of the electron temperature of the plasma and varies dramatically with the atomic number of the impurity. The radiative power first increases with T_e , as successively higher charge states can become ionized, then decreases with T_e , as the impurity becomes fully ionized, and finally increases with T_e again because of bremsstrahlung (which is also included in Fig. 13.9 and discussed in

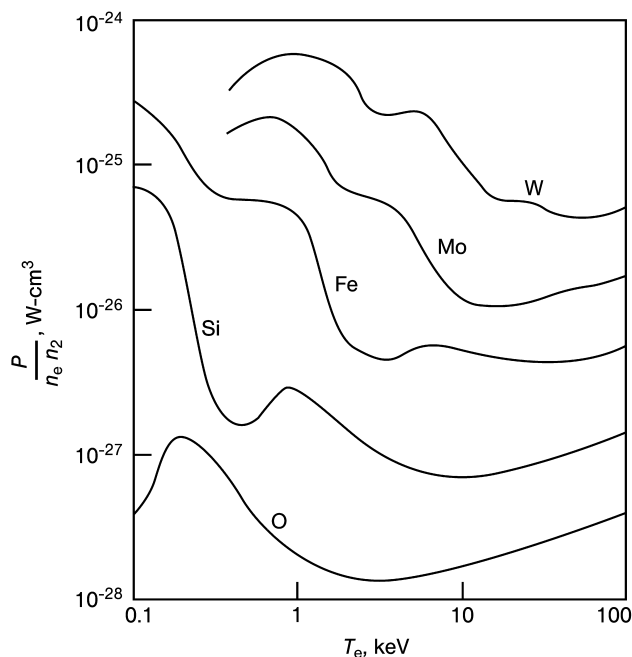


Figure 13.9. Impurity radiative power loss from a plasma

Table 13.5. Impurity radiation characteristics

Impurity atom	Atomic no.	Electron temperature, T_e (eV)	
		Maximum power loss	Fully ionized
He	2	~ 7	~ 10
Be	4	~ 2	~ 70
C	6	~ 6	~ 300
O	8	~ 20	~ 600
Al	13	~ 100	$\sim 3 \times 10^3$
Si	14	~ 120	$\sim 4 \times 10^3$
V	23	~ 100	$\sim 2 \times 10^4$
Fe	26	~ 100	$\sim 3 \times 10^4$
Nb	41	~ 100	$\sim 10^5$
Ta	73	$\sim 10^3$	$> 10^5$
W	74	$\sim 10^3$	$> 10^5$

chapter 17). The irregularities in the curves correspond to ionizing successive shells in the orbital electron structure. The plasma electron temperatures at which the maximum impurity radiation occurs and at which the impurity becomes fully ionized both increase with the atomic number of the impurity.

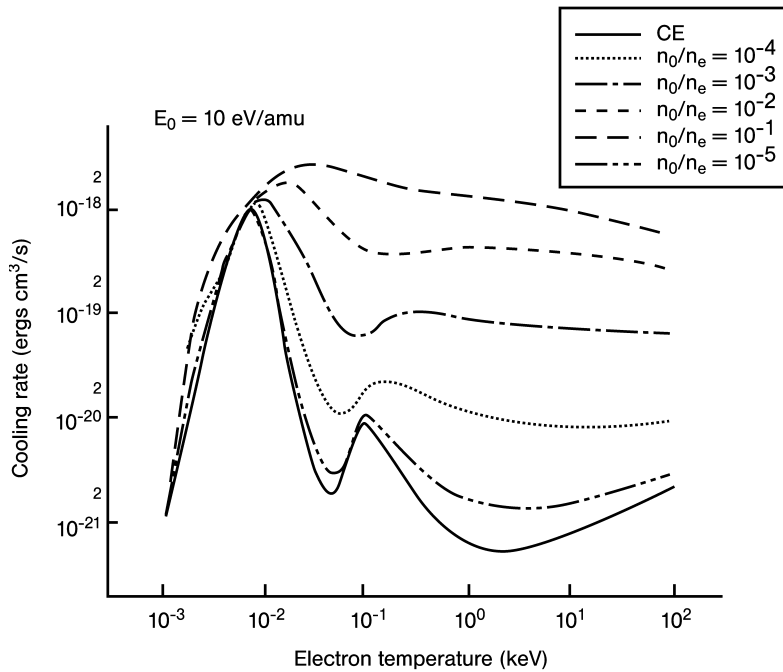


Figure 13.10. Effects of neutral hydrogen atoms on carbon impurity radiation

A simple fit which approximates the features of the detailed radiative power loss calculations reasonably well is

$$P_{\text{imp}}(\text{MW/m}^3) = (1 + 0.3T_e) \times 10^{-43} n_e n_z z^{(3.7 - 0.33 \ln T)} \quad (13.25)$$

where z is the atomic number of the impurity. (T is in keV and other quantities are in MKS units.)

Charge-exchange and recombination processes between partially stripped impurity ions and neutral hydrogen atoms and recombination processes can greatly enhance the impurity cooling rate at higher neutral atom densities, as shown in Fig. 13.10, where the carbon radiation emissivity at coronal equilibrium is plotted as a function of electron temperature.

Problems for Chapter 13

- Calculate the energy (R_E) and particle (R_p) reflection coefficients for 10 eV deuterons incident on a graphite wall.
- Estimate the rate of deuterium atom recycling from the walls of a tokamak plasma with $R = 1.7 \text{ m}$, $a = 0.7 \text{ m}$, $n_D = 5 \times 10^{19} \text{ m}^{-3}$ and a plasma particle confinement time of $\tau_p = 0.1 \text{ s}$.

3. Calculate the elastic scattering, charge exchange and electron impact ionization rates ($\text{m}^3 \cdot \text{s}^{-1}$) for deuterium atoms in a deuterium plasma, both in Maxwellian distributions at $T = 50 \text{ eV}$.
4. Write the balance equations that govern the populations of D^+ , D^0 , D^- , D_2 and D_2^* . Estimate the values of the various rate coefficients at 10 eV for a plasma electron density of $n_e = 5 \times 10^{19} \text{ m}^{-3}$.
5. Calculate the sputtering yield of 100 eV deuterons incident on a graphite wall. Compare your answer with Fig. 13.7.
6. Calculate the radiative power loss ($\text{W} \cdot \text{m}^{-3}$) of a 1 % concentration of O, Fe and W in a plasma with $n_e = 5 \times 10^{19} \text{ m}^{-3}$ and $T_e = 10 \text{ eV}$.
7. Discuss the various atomic physics and surface physics processes involved in the interaction of the recycling plasma with the divertor plate in a tokamak.

14 Divertors

In early tokamak experiments, the plasma aperture was determined by a bar, or “limiter,” protruding from the chamber wall, as depicted in Fig. 14.1. Plasma ions and electrons following field lines around the torus were transported radially outward until they reached a field line which passed within a gyroradius of the limiter, at which point they impacted the limiter and recycled as neutral atoms and molecules. In this manner the region occupied by plasma, or the plasma aperture, was determined, and the region between the tip of the limiter and the chamber wall proper was filled with a neutral gas.

One disadvantage of this arrangement was that the recycling of neutrals and the production of impurities took place adjacent to the plasma, affording little opportunity for controlling the flow of either into the plasma. The original motivation for the “divertor” was to remove this site of recycling and impurity production some distance from the plasma by diverting magnetic field lines to guide particles escaping the main plasma into a separate chamber, thus affording an opportunity to control the flow of recycling neutrals and impurities back into the plasma. Divertor configurations related to the various possible limiter configurations are illustrated in Fig. 14.1.

14.1 Configuration, Nomenclature and Physical Processes

As the name implies, a divertor configuration is produced by locating other coils so as to divert the outermost magnetic field lines out of the main plasma chamber into a separate chamber where they intersect a material divertor target. Because it is easier to divert the small poloidal field due to the plasma current than the larger toroidal field, the poloidal divertor is the usual choice. A poloidal divertor is formed by nearby coil(s) carrying current in the same direction as the plasma current so as to form a null, or X-point, in the net poloidal field of the plasma current plus that of the divertor coil(s), as depicted in Fig. 14.2. The magnetic field lines passing through the X-point create the last closed flux surface (LCFS), known as the “separatrix.” All field lines interior to the separatrix remain within the confinement volume and particles on them are confined, but particles that cross the separatrix are swept along field lines to the divertor target in a separate chamber.

Figure 14.2 establishes some of the divertor nomenclature that will be used. The plasma “core” region is well inside, and the plasma “edge” region is just inside, the “separatrix,” or last closed flux surface (LCFS). Particles crossing the separatrix radially outward into the “scrape-off layer” (SOL) are swept along field lines past the “X-point” into the “divertor region” where they eventually intersect the divertor “target plate.” Here they recycle as neutral atoms and molecules and produce sputtered impurity target plate surface atoms. The SOL and the divertor region have a relatively high plasma density flowing towards the target plate; this density is highest at or near the separatrix and decreases rapidly

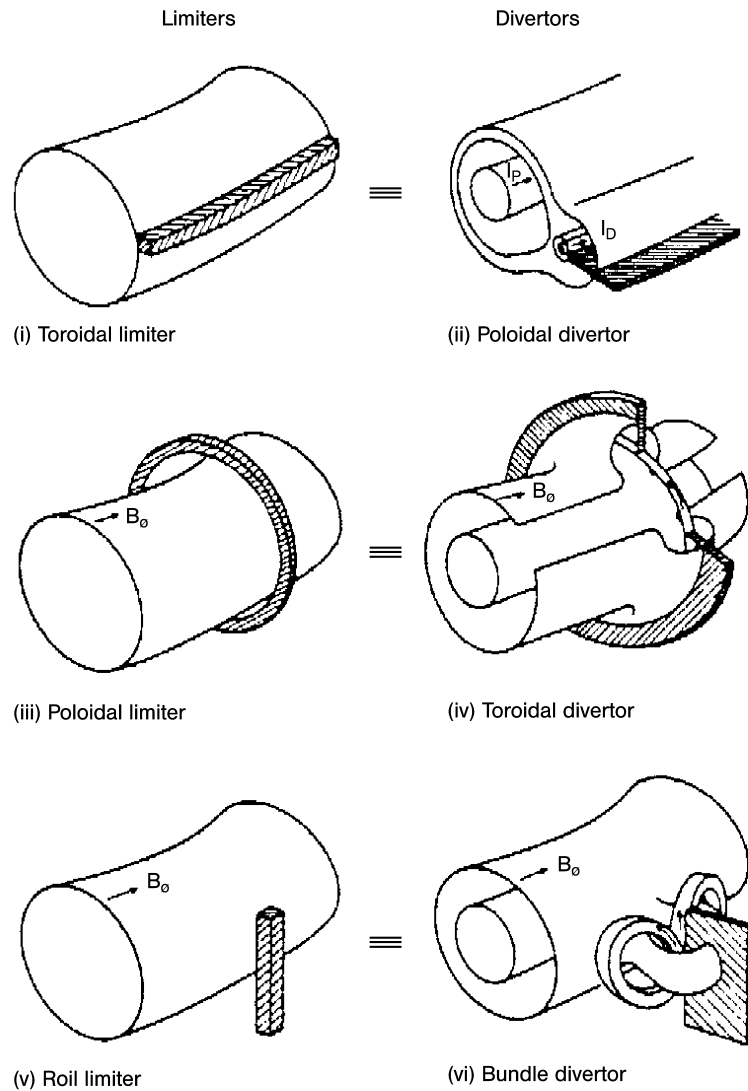


Figure 14.1. Limiter and divertor configurations

towards the chamber wall. The “baffle” structure partially closes the entrance to the divertor region for the purpose of inhibiting the flow of neutral atoms and impurities back into the main plasma chamber. The magnetic field structure in the “private flux” region below the X-point is isolated from the magnetic field structure in both the core plasma and the divertor region. A “lower single-null” (LSN) divertor is shown; “upper single-null” (USN) and “double-null” (DN) (upper and lower) are also common.

The various plasma, atomic and molecular processes that take place in the plasma edge, SOL and divertor are depicted schematically in Fig. 14.3. Most of the recycling

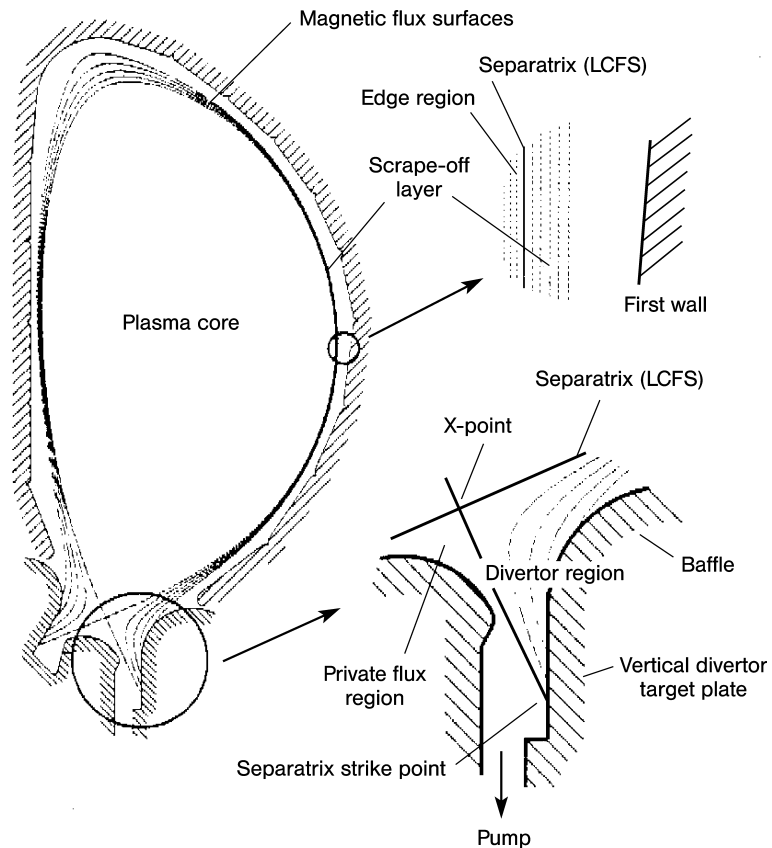


Figure 14.2. A single-null poloidal divertor configuration

neutrals interact with the incident plasma just in front of the divertor target, undergoing charge-exchange and elastic scattering reactions that cool the plasma and dissipate some of its momentum, and ionization reactions that cool the plasma and increase its density. If the plasma in front of the divertor plate becomes sufficiently cool (1 eV to 2 eV), the plasma ions and electrons will recombine to form neutral atoms. Under certain conditions a thin layer of neutral gas will form just in front of the divertor target, “detaching” the plasma in the divertor region from the target. Some neutral atoms and molecules escape the “recycling” region just in front of the target plate and are transported through the low-density private flux region and along the chamber wall back up into the plasma chamber and into the edge plasma region to cool the edge plasma by ionization, charge-exchange and elastic scattering and to refuel the core plasma. Sputtered impurity atoms will mostly be ionized just in front of the target plate and will diffuse against the inflowing plasma back up into the divertor and SOL plasmas and into the edge and core plasmas, radiating in each of these locations.

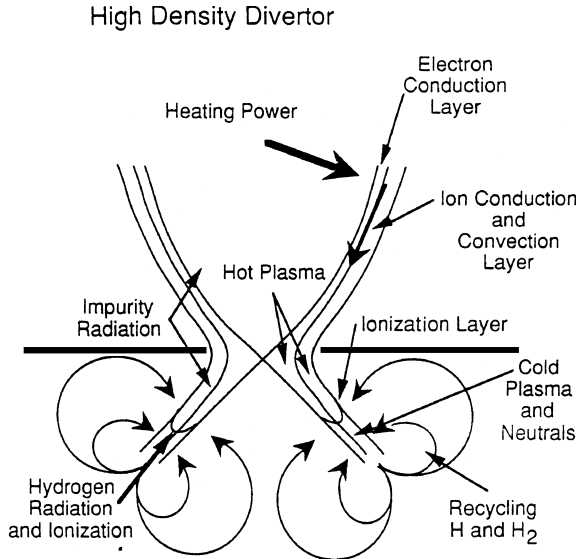


Figure 14.3. Processes taking place in the divertor

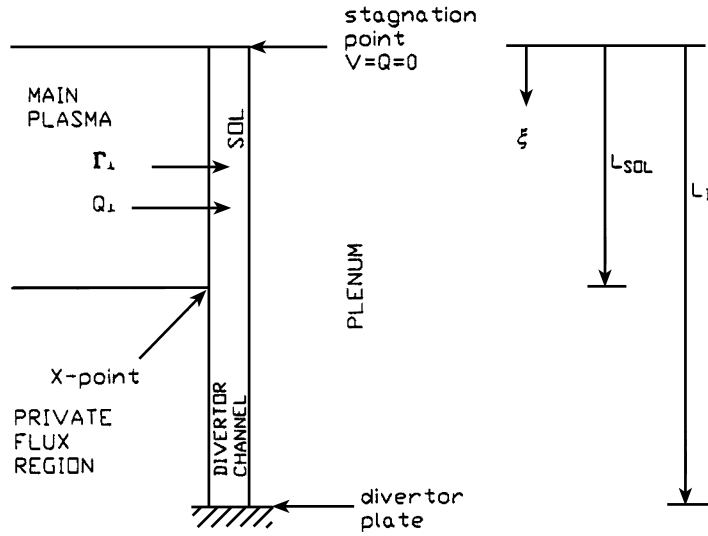
14.2 Simple Divertor Model

14.2.1 Strip Geometry

Although the physics and the geometry of a divertor are both quite complex, useful physical insight can be obtained from a relatively simple model of both that is amenable to analytical treatment. The SOL and divertor are idealized as a one-dimensional strip running along magnetic field lines (i.e. spiraling about the torus in the toroidal direction while gradually spiraling down in the poloidal direction), as shown in Fig. 14.4. Since the sheath conditions at the divertor target plates require plasma flow towards both of the target plates, there must be a flow stagnation point in the SOL somewhere near the top in Fig. 14.2. Defining the distance variable ξ along the field lines from the stagnation point ($\xi = 0$) to the divertor target plate ($\xi = L_D$) identifies the length of the strip model. The sheath boundary conditions on flow speed and heat flux into the sheath pertain at the divertor target, and stagnation (symmetry) boundary conditions are appropriate at the stagnation point, as indicated in the figure. Over the length $0 \leq \xi \leq L_{\text{SOL}}$ between the stagnation point and the X-point, there are heat (Q_\perp) and particle (Γ_\perp) fluxes from the plasma core into the SOL portion of the strip model. Note that the distances (e.g. $L_{\text{SOL}} = q_{95}\pi R$) are along the spiraling field lines.

14.2.2 Radial Transport and Widths

We assume that the density and temperature are exponentially decreasing with radius (x) across the width of the SOL and divertor region; i.e. $n(x) = n_{\text{SOL}} \exp(-x/\Delta_n)$ and $T(x) = T_{\text{SOL}} \exp(-x/\Delta_T)$, where the subscript ‘‘SOL’’ denotes the value at the sep-



$$V = c_{SD} = \sqrt{\frac{2T_D}{m}}$$

$$Q = n_D c_{SD} (\gamma_{SH} T_D)$$

Figure 14.4. “Strip” model for SOL/divertor plasma calculation

ratrix. Invoking continuity of radial particle and heat fluxes across the separatrix allows the Δ 's to be determined in terms of the fluxes from the core into the SOL and the transport coefficients in the SOL. The continuity requirements

$$\Gamma_\perp = -D_\perp \frac{dn}{dx} \Big|_{x=0} = \frac{D_\perp n_{SOL}}{\Delta_n} \quad (14.1)$$

and

$$Q_\perp = -n_{SOL} \chi_\perp \frac{dT}{dx} \Big|_{x=0} - 3T_{SOL} D_\perp \frac{dn}{dx} \Big|_{x=0}$$

$$= \frac{n_{SOL} T_{SOL} \chi_\perp}{\Delta_T} + 3 \frac{n_{SOL} T_{SOL} D_\perp}{\Delta_n} \quad (14.2)$$

can be solved for

$$\Delta_n = \frac{D_\perp}{(\Gamma_\perp / n_{SOL})} \quad (14.3)$$

$$\Delta_T = \frac{\chi_\perp}{(Q_\perp / n_{SOL} T_{SOL}) - 3D_\perp / \Delta_n}$$

Bohm diffusion, $D_\perp \approx \chi_\perp \approx T/16eB$ is frequently used to model the radial transport in the SOL.

Another width of interest is the energy width that governs the decrease with radius of the heat flux along the field lines in the SOL, $Q_{\parallel} \approx -\kappa_0 T^{\frac{5}{2}} dT/d\xi$, which is

$$\Delta_E = \frac{2}{7} \Delta_T \quad (14.4)$$

A different estimate of the energy width can be obtained by balancing the radial heat flux into the SOL from the core, Q_{\perp} , with the parallel heat flux along the SOL, or

$$-\nabla \cdot Q_{\perp} \approx \frac{Q_{\perp}}{\Delta_E} = \nabla \cdot Q_{\parallel} \frac{\approx Q_{\parallel}}{L_D}$$

to obtain

$$\Delta_E = \left[\frac{\chi_{\perp}/\Delta_T + 3D_{\perp}/\Delta_n}{\chi_{\parallel}/L_D} \right] L_D \quad (14.5)$$

As may be seen in Fig. 14.2, the field lines expand when they leave the SOL and enter the divertor region. This may be treated approximately by applying a flux expansion factor ϵ_{div} to the above widths in the divertor region.

14.2.3 Parallel Transport

The appropriate one-dimensional continuity equation can be derived from the two-dimensional (ξ, x) fluid continuity equation for the strip by integrating over x and using the boundary condition of a incident particle flux from the core for $0 \leq \xi \leq L_{\text{SOL}}$,

$$\begin{aligned} \frac{d(nv)}{d\xi} &= n(n_0 \langle \sigma v \rangle_{\text{ion}} - n \langle \sigma v \rangle_{\text{rec}}) + \frac{\Gamma_{\perp} H_{\text{SOL}}}{\Delta_n} \\ n(\xi = 0) &= n_{\text{SOL}} \quad n(\xi = L_D) = n_D \end{aligned} \quad (14.6)$$

where the quantity H_{SOL} is the Heaviside function which is unity for $0 \leq \xi \leq L_{\text{SOL}}$ and zero elsewhere. Similarly, the appropriate one-dimensional momentum equation and boundary (stagnation and sheath) conditions are

$$\begin{aligned} \frac{d(2nT + nmv^2)}{d\xi} &= -mnv n_0^c \langle \sigma v \rangle_{\text{at}} - mn^2 v \langle \sigma v \rangle_{\text{rec}} \\ v(\xi = 0) &= 0 \quad v(\xi = L_D) = c_{SD} \end{aligned} \quad (14.7)$$

and the appropriate one-dimensional energy equation and boundary (stagnation and sheath) conditions are

$$\begin{aligned} \frac{dQ}{d\xi} - \frac{Q_{\perp}(0)}{\Delta_E} H_{\text{SOL}} + n_Z n L_Z + E_{\text{ion}} n n_0 \langle \sigma v \rangle_{\text{ion}} - f I_{\text{ion}} n^2 \langle \sigma v \rangle_{\text{rec}} \\ + \frac{3}{2}(T - T_0^c) n n_0^c \langle \sigma v \rangle_{\text{at}} &= 0 \\ Q(\xi = 0) &= 0 \quad Q(\xi = L_D) = n_D c_{SD} (\gamma_{SH} T_D) \end{aligned} \quad (14.8)$$

Parallel energy transport is assumed to be by electron conduction

$$q = -\kappa_0 T^{\frac{5}{2}} \frac{dT}{d\xi}, T(\xi = 0) = T_{\text{SOL}}, T(\xi = L_D) = T_D \quad (14.9)$$

where $\kappa_0 = 3.07 \times 10^4 / Z_{\text{eff}} \ln \Lambda$ for MKS units and T in keV. The quantities n_0 and n_0^c are the total and “cold” or previously uncollided, respectively, neutral atom densities, T_0^c is the temperature of the “cold” atoms, the quantity f is the fraction of the ionization potential released upon recombination that is absorbed in the plasma, and $\gamma_{\text{sh}} \approx 7-8$ is the sheath heat transmission coefficient.

14.2.4 Solution of Plasma Equations

Implicit solutions to the above equations, which provide physical insight, can be obtained. Eliminating density derivatives between Eqs. (14.6) and (14.7) and integrating, subject to the corresponding boundary conditions and with some simplifying assumptions, yields an expression for the normalized velocity (Mach number) as a function of position

$$M(\xi) = \alpha^{\frac{1}{2}}(\xi) \tan \left[\frac{\alpha(\xi)}{\alpha_D} \right]^{\frac{1}{2}} \tan^{-1} \left(\frac{1}{\alpha_D^{\frac{1}{2}}} \right) - \frac{1}{2} \int_{\xi}^{L_D} \frac{v_{\text{tot}} d\xi'}{c_s(\xi')} \quad (14.10)$$

where

$$M(\xi) \equiv \frac{v(\xi)}{c_s(\xi)} \equiv \frac{v(\xi)}{\sqrt{2T(\xi)/m}} \quad (14.11)$$

with sheath boundary condition $M(L_D) = 1$, and

$$\alpha(\xi) \equiv \frac{n_0 \langle \sigma v \rangle_{\text{ion}} - n \langle \sigma v \rangle_{\text{rec}} + \frac{\Gamma_{\perp} H_{\text{SOL}}}{n \Delta_n}}{n_0 \langle \sigma v \rangle_{\text{ion}} + n_0^c \langle \sigma v \rangle_{\text{at}} + \frac{\Gamma_{\perp} H_{\text{SOL}}}{n \Delta_n}} \quad (14.12)$$

The quantity $v_{\text{tot}} = n_0 \langle \sigma v \rangle_{\text{ion}} + n_0^c \langle \sigma v \rangle_{\text{at}}$.

Equations (14.6) and (14.7) can also be solved for the density as a function of the Mach number

$$n(\xi) = n_D M^2(\xi) e^{A(\xi)} \quad (14.13)$$

where

$$A(\xi) = \frac{1}{2} \left(1 - M^2(\xi) \right) + \int_{\xi}^{L_D} \sqrt{\frac{2m}{T}} M v_{\text{tot}} d\xi' \quad (14.14)$$

Equation (14.9) can be used to evaluate $Q = q$ in Eq. (14.8), allowing the latter to be solved for the temperature distribution

$$T(\xi) = \left[T_D^{\frac{7}{2}} + \frac{7}{2\kappa_0} \left\{ \int_{\xi}^{L_D} d\xi' \int_0^{\xi'} n_z n L_z d\xi'' \right. \right. \\ \left. \left. + \int_{\xi}^{L_D} d\xi' \int_0^{\xi'} n \left(\frac{3}{2} (T - T_0^c) v_{at} + E_{ion} v_{ion} \right) d\xi'' \right. \right. \\ \left. \left. - \int_{\xi}^{L_D} d\xi' \int_0^{\xi'} \frac{Q_{\perp}(0)}{\Delta_E} H_{SOL} d\xi'' \right\} \right]^{\frac{2}{7}} \quad (14.15)$$

14.2.5 Two-Point Model

Integrating the balance equations over the entire SOL-divertor strip $0 \leq \xi \leq L_D$ and making use of the appropriate boundary conditions yields a set of equations that can be solved for the temperature and density at the divertor target plate (denoted by D subscript) and upstream at the stagnation point or plasma mid-plane (now denoted by the SOL subscript). The integral energy balance equation is obtained by integrating Eq. (14.8) to obtain

$$n_D c_{SD} \gamma_{SH} T_D = \frac{\langle Q_{\perp} \rangle L_{SOL}}{\Delta_E} - \Delta Q_{rad} - \Delta Q_{at} \quad (14.16)$$

where

$$\langle Q_{\perp} \rangle \equiv \int_0^{L_{SOL}} Q_{\perp}(0, \xi) d\xi / L_{SOL} \quad (14.17)$$

is the average radial heat flux from the core into the SOL,

$$\Delta Q_{rad} \equiv \int_0^{L_D} n_z n L d\xi \equiv f_z \int_0^{L_D} n^2 L_z d\xi \quad (14.18)$$

is the total impurity radiation in the SOL-divertor divided by the width, and

$$\Delta Q_{at} \equiv \int_0^{L_D} n \left(\frac{3}{2} (T - T_0^c) v_{at} + E_{ion} v_{ion} - f I_{ion} v_{rec} \right) d\xi \quad (14.19)$$

is the net energy loss by atomic physics reactions in the SOL-divertor divided by the width.

The integral particle balance equation is obtained by integrating Eq. (14.6)

$$n_D c_{SD} = \frac{\langle \Gamma_{\perp} \rangle L_{SOL}}{\Delta_n} + \Delta N_{at} \quad (14.20)$$

where

$$\langle \Gamma_{\perp} \rangle \equiv \int_0^{L_{SOL}} \Gamma_{\perp}(0, \xi) d\xi / L_{SOL} \quad (14.21)$$

is the average particle flux into the SOL from the core, and

$$\begin{aligned}\Delta N_{\text{at}} &\equiv \int_0^{L_D} n (n_0 \langle \sigma v \rangle_{\text{ion}} - n \langle \sigma v \rangle_{\text{rec}}) d\xi \\ &= n_D \int_0^{L_D} M^2 e^A (n_0 \langle \sigma v \rangle_{\text{ion}} - n_D M^2 e^A \langle \sigma v \rangle_{\text{rec}}) d\xi\end{aligned}\quad (14.22)$$

is the net ionization minus recombination rate in the SOL-divertor divided by the width. Equation (14.13) has been used in obtaining the second form of Eq. (14.22).

Equations (14.16) and (14.20) can be solved for the plasma temperature just in front of the divertor target plate

$$T_D = \frac{1}{\gamma_{SH}} \frac{\langle Q_\perp \rangle}{\langle \Gamma_\perp \rangle} \frac{\Delta_n}{\Delta_E} \left[\frac{1 - \frac{(\Delta Q_{\text{rad}} + \Delta Q_{\text{at}})}{\langle Q_\perp \rangle L_{\text{SOL}} / \Delta_E}}{1 + \frac{\Delta N_{\text{at}}}{\langle \Gamma_\perp \rangle L_{\text{SOL}} / \Delta_n}} \right] \quad (14.23)$$

The temperature at the core mid-plane separatrix, T_{SOL} , can be found by evaluating Eq. (14.15) at $\xi = 0$ (it is assumed that the temperature does not vary much between the stagnation point and the mid-plane)

$$T_{\text{SOL}} = \left\{ T_D^{\frac{7}{2}} + \frac{7}{2\kappa_0} \left[\langle Q_\perp \rangle L_{\text{SOL}} \left(L_D - \frac{1}{2} L_{\text{SOL}} \right) - (\Delta Q_{\text{rad}} + \Delta Q_{\text{at}}) \frac{1}{2} L_D \right] \right\}^{\frac{2}{7}} \quad (14.24)$$

The integral momentum balance over the plasma is obtained by integrating Eq. (14.7) to obtain

$$n_{\text{SOL}} = n_D \left[\frac{2T_D + \frac{1}{2}(\Delta M_{\text{at}}/n_D)(\Delta_n/\Delta_{nT})}{T_{\text{SOL}}} \right] \equiv n_D K_{D \text{ SOL}} \quad (14.25)$$

where

$$\Delta_{nT} \equiv \frac{\Delta_n}{1 + \Delta_n/\Delta_T} \quad (14.26)$$

and

$$\begin{aligned}\frac{\Delta M_{\text{at}}}{n_D} &\equiv \int_0^{L_D} \frac{n}{n_D} (n_0^c \langle \sigma v \rangle_{\text{at}} + n \langle \sigma v \rangle_{\text{rec}}) m v d\xi \\ &= \int_0^{L_D} M^2 e^{A(\xi)} (n_0^c \langle \sigma v \rangle_{\text{at}} + n \langle \sigma v \rangle_{\text{rec}}) m v d\xi\end{aligned}\quad (14.27)$$

is the momentum loss by the flowing plasma due to charge exchange, elastic scattering and recombination reactions, in which the resulting neutral carries the momentum to the wall.

Finally, these equations can be used to obtain an explicit solution for the plasma density just in front of the divertor target plate

$$n_D = \frac{1}{c_{SD}^{\frac{1}{2}}} \left[\frac{\langle \Gamma_\perp \rangle L_{\text{SOL}}}{\gamma_n K_{D \text{ SOL}}} + \frac{\Delta N_{\text{at}}}{n_D} \right]^{\frac{1}{2}} = \frac{1}{c_{SD}^{\frac{1}{2}}} \left[\frac{\langle \Gamma_\perp \rangle L_{\text{SOL}} + \Delta N_{\text{at}}/\beta}{\Delta_n \epsilon^{\text{DIV}}} \right] \quad (14.28)$$

where $\gamma_n = \Delta_n/n_{\text{SOL}} = D_\perp/\Gamma_\perp$, $\beta = B_\theta/B_\phi$ and ϵ^{DIV} is a flux expansion factor.

The set of nonlinear Eq. (14.23) for T_D , Eq. (14.24) for T_{SOL} , Eqs. (14.3) and (14.4) for the Δ 's, (14.28) for n_D , and Eq. (14.25) for n_{SOL} constitute a self-consistent model for calculating the plasma density and temperature along the separatrix at two points (the mid-plane, or stagnation point, and in front of the divertor target). This model can now be used to gain physical insight about the operation of divertors.

14.3 Divertor Operating Regimes

Divertor plasmas are observed to operate in either: (1) a “sheath-limited,” or “linear,” regime in which the plasma pressure is essentially constant along the field lines and there is little difference in the plasma temperatures at the SOL (stagnation point) mid-plane and just in front of the divertor target; (2) in a “high recycling” regime in which pressure is essentially constant along the field lines but the density increases significantly at the divertor in inverse proportion to the decrease in temperature; or (3) a “detached” regime in which both the density and temperature decrease sharply just in front of the divertor target plate.

In order to more readily understand these observations in terms of the model, we relate some of the model parameters to more familiar experimental parameters. The radial heat flux across the separatrix $\langle Q_{\perp} \rangle = P_{\text{sep}}/A_{\text{sep}}$, where P_{sep} is the total power crossing the separatrix and $A_{\text{sep}} \approx 2\pi R 2\pi a \sqrt{\kappa}$ is the area of the separatrix. The radial particle flux across the separatrix $\langle \Gamma_{\perp} \rangle = n_p V_p / \tau_p A_{\text{sep}}$, where $V_p = 2\pi R \pi a^2 \kappa$ is the plasma volume within the separatrix and τ_p is the particle confinement time within this volume. The parallel distance along the field lines from the stagnation point to the X-point is $L_{\text{SOL}} = \pi q_{95} R$ for a single null divertor.

14.3.1 Sheath-Limited Regime

The condition that the plasma temperature will be almost the same at the mid-plane (stagnation point) and the divertor target requires that the second term in Eq. (14.24) be small compared to $T_D^{7/2}$, which may be written

$$\begin{aligned} & \frac{7}{2\kappa_0} \left(\frac{n_p V_p}{\tau_p} \right)^{7/2} \frac{q_{95}}{4\pi^2 a \sqrt{\kappa} \Delta_E} \\ & \times \left[\left(L_D - \frac{1}{2} L_{\text{SOL}} \right) - \frac{(\Delta Q_{\text{rad}} + \Delta Q_{\text{at}}) \Delta_E 4\pi^2 a \sqrt{\kappa} L_D}{q_{95} P_{\text{sep}}} \right] \\ & \times \left[P_{\text{sep}} \left(\frac{1}{\gamma_{SH}} \frac{\Delta_n}{\Delta_E} \right)^{7/2} \left(\frac{1 - \frac{(\Delta Q_{\text{rad}} + \Delta Q_{\text{at}}) \Delta_E 4\pi^2 a \sqrt{\kappa}}{q_{95} P_{\text{sep}}}}{1 + \frac{\Delta N_{\text{at}} 2 \Delta_n \tau_p}{n_p a \sqrt{\kappa} q_{95} \pi R}} \right)^{7/2} \right]^{-1} \leq 1 \end{aligned} \quad (14.29)$$

This relation illustrates why the sheath-limited regime is associated experimentally with high power crossing the separatrix and low core plasma density, n_p . Atomic physics cooling is more significant in reducing the denominator (enters to $7/2$ power) than in reducing the numerator in Eq. (14.29), so the presence of recycling neutrals and impurities would be expected to shift the boundary between the sheath-limited and high recycling regimes towards higher powers crossing the separatrix and lower core plasma densities. Recycling neutrals further shift this boundary in the same direction by contributing to the build up of the plasma density (the ΔN_{at} term).

14.3.2 Detached Regime

At the other limit, detached plasma operation requires that essentially all of the heat transported across the separatrix into the SOL be radiated or otherwise removed by atomic physics processes, i.e. that

$$\frac{\Delta Q_{\text{rad}} + \Delta Q_{\text{at}}}{\langle Q_{\perp} \rangle L_{\text{SOL}} / \Delta E} \rightarrow 1 \quad (14.30)$$

which may be written in the limit $n_D T_D \rightarrow 0$ in a form

$$\frac{(\Delta Q_{\text{rad}} + \Delta Q_{\text{at}}) \chi_{\perp} \frac{1}{2} \Delta M_{\text{at}}}{(P_{\text{sep}}/A_p)^2 q_{95} \pi R} \left(\frac{1}{1 - 3n_p V_p T_{\text{SOL}} / P_{\text{sep}} \tau_p} \right) \rightarrow 1 \quad (14.31)$$

that illustrates the requirement for momentum exchange of the plasma with the recycling neutrals (the ΔM_{at} term) in order to detach. Equation (14.31) suggests four possible paths to detachment: (1) increase impurity concentration or L_z (impurity species); (2) increase the recycling neutral concentration to increase ΔQ_{at} and ΔM_{at} ; (3) reduce the power flux ($P_{\text{sep}}/A_{\text{sep}}$) transported across the separatrix (e.g. by increased radiation inside the separatrix, by reduced auxiliary heating or by increased plasma surface area); and (4) increase the connection length $L_{\text{SOL}} = q_{95} \pi R$. The fraction of the heat transported across the separatrix into the SOL that is radiated or otherwise removed to the wall by atomic physics processes is

$$f_{\text{ex}} \equiv \left(\frac{\Delta Q_{\text{rad}} + \Delta Q_{\text{at}}}{\langle Q_{\perp} \rangle L_{\text{SOL}} / \Delta E} \right) = 1 - \frac{\frac{2}{7} n_D \left(2T_D + \frac{1}{2} \frac{\Delta N_{\text{at}}}{n_D} \frac{\Delta_n}{\Delta_{nT}} \right) \left(\chi_{\perp} + 3D_{\perp} \frac{\Delta_T}{\Delta_n} \right) (\gamma_{SH} T_D)}{\langle Q_{\perp} \rangle^2 L_{\text{SOL}}} \quad (14.32)$$

This expression makes clear that the fraction of the plasma exhaust power that is “radiated” in the divertor and SOL can approach unity for a detached plasma ($n_D \rightarrow 0$).

14.3.3 High Recycling Regime

Also in the high recycling regime the exhaust fraction, f_{ex} , approaches unity as $T_D \rightarrow 0$. The maximum fraction of the power transported across the separatrix that can be “radiatively” exhausted in the divertor and SOL decreases with increasing core plasma density

and with increasing power across the separatrix, and decreases with recycling neutral concentration when ionization dominates recombination ($\Delta N_{\text{at}} > 0$).

The frictional plasma momentum dissipation due to reactions with recycling neutrals is important for maximizing the fraction of the power radiated by impurities from the divertor and SOL plasma. Note that Eq. (14.32) describes the fraction radiated by impurities and plasma plus the fraction transferred to the wall by neutrals which have gained energy from plasma ions by charge-exchange and elastic scattering. Although impurity radiation is usually dominant, other atomic physics reactions with recycling neutrals can exhaust up to half the power crossing the separatrix in some tokamaks.

In contrast to the situation for the detached regime, where plasma momentum loss to the recycling neutrals increases f_{ex} , in the high recycling regime plasma momentum loss to recycling neutrals decreases f_{ex} , unless recombination dominates ionization ($\Delta N_{\text{at}} < 0$).

14.3.4 Parameter Scaling

Rewriting Eqs. (14.23) and (14.28) leads to expressions that indicate the relationship of the plasma density and temperature just in front of the divertor target plate to the plasma core parameters (e.g. the density).

$$n_D = \frac{1}{\sqrt{c_{SD}}} \left[\frac{(n_p V_p / \tau_p) q_{95} \pi R P_{\text{sep}}}{\left(2T_D + \frac{1}{2} \frac{\Delta M_{\text{at}}}{n_p} \frac{\Delta_n}{\Delta_{nT}} \right) \left(\frac{\Delta_n}{\Delta_T} \right) \left(\chi_{\perp} + 3D_{\perp} \frac{\Delta_T}{\Delta_n} \right)} + \frac{\Delta N_{\text{at}}}{n_D} \right]^{\frac{1}{2}} \quad (14.33)$$

and

$$T_D = \frac{1}{\gamma_{SH}} \left[\frac{P_{\text{sep}}}{(n_p V_p / \tau_p)} \frac{\Delta_n}{\Delta_E} \times \left\{ \frac{1 - (\Delta Q_{\text{rad}} + \Delta Q_{\text{at}}) \Delta_E A_p / P_{\text{sep}} q_{95} \pi R}{1 + \frac{\Delta N_{\text{at}} \Delta_n A_p}{(n_p V_p / \tau_p) q_{95} \pi R}} \right\} \right] \quad (14.34)$$

Note from Eq. (14.22) and Eq. (14.27) that $\Delta N_{\text{at}}/n_D$ and $\Delta M_{\text{at}}/n_D$ are not functions of n_D .

It is interesting to consider the dependence on core plasma density displayed in these two equations. In the sheath-limited regime, the $(\Delta Q_{\text{rad}} + \Delta Q_{\text{at}})$ term is negligible compared to unity, from Eq. (14.24) and the requirement that $T_{\text{SOL}} \approx T_D$, in which case Eq. (14.34) indicates a scaling $T_D \sim n_p^{-1}$ and Eq. (14.33) then indicates the scaling $n_D \sim n_p$. In the high recycling regime, $T_D < T_{\text{SOL}}$, which requires that the $(\Delta Q_{\text{rad}} + \Delta Q_{\text{at}})$ term in Eq. (14.24), which itself scales directly with n_p , be non-negligible also in Eq. (14.34). Thus, the scaling of both n_D and T_D with n_p is predicted to be similar to that in the sheath-limited regime, but somewhat stronger. In the detached regime, the $(1 - \Delta Q_{\text{rad}} - \Delta Q_{\text{at}})/(1 + \Delta N_{\text{at}})$ term becomes important in determining the scaling of

T_D , which tends to small values in this regime. However, an inverse scaling $T_D \sim n_p^{-1}$ still roughly obtains. Setting $T_D = 0$ in Eq. (14.33) leads to

$$\begin{aligned} n_D & \left(1 - \frac{(\Delta N_{\text{at}}/n_D)}{n_D^2 c_{\text{SD}}} \right) \\ & \approx \frac{1}{c_{\text{SD}}} \left[\frac{(n_p V_p / \tau_p) (\Delta Q_{\text{rad}} + \Delta Q_{\text{at}}) A_p^2}{\frac{\Delta_n}{\Delta_{nT}} \frac{\Delta_n}{\Delta_T} \left(1 + \frac{3D_{\perp}}{\chi_{\perp}} \frac{\Delta_T}{\Delta_n} \right) P_{\text{sep}} \left(1 - 3 \left(\frac{n_p V_p}{\tau_p} \right) \right) \frac{T_{\text{SOL}}}{P_{\text{sep}}}} \right] \end{aligned} \quad (14.35)$$

the right side of which scales somewhat more strongly than $\sim n_p^{\frac{3}{2}}$. On the other hand, when the ΔN_{at} term is nonnegligible, the predicted scaling of n_D rolls over to an inverse dependence on n_p . These scalings are qualitatively consistent with experimental scalings found in several tokamaks.

Using the momentum balance on the divertor of Eq. (14.25), it follows that the parameter $f_m = 2n_D T_D / n_{\text{SOL}} T_{\text{SOL}} = 1 - (\Delta M_{\text{at}} (\Delta_n / \Delta_{nT}) / 2n_{\text{SOL}} T_{\text{SOL}})$. Postulating almost any neutral recycling model at the divertor target plate, it can be shown from Eq. (14.27) that $\Delta M_{\text{at}} \sim n_D^2 / \nu_{\text{tot}}$, where ν_{tot} is the ionization plus charge-exchange plus elastic scattering collision frequency. The ionization rate coefficient averaged over electron and neutral atom thermal distributions increases dramatically in the interval 1 eV to 10 eV, which produces a dramatic decrease in ΔM_{at} and increase in f_m over this interval, as has been observed in at least one tokamak.

14.3.5 Experimental Results

The three regimes of divertor operation are illustrated in Fig. 14.5, where the electron density and the ion and electron temperatures measured just in front of the divertor plate for a set of ASDEX discharges with different plasma densities ($n_p = n_e$) are plotted.

14.4 Impurity Retention

One of the original purposes of a divertor was to locate the source of impurities away from the plasma, so as to afford the opportunity for controlling the access of these impurities to the core plasma. This benefit is only realized if the impurities, produced mostly by ion impact sputtering at the divertor target plate, are retained in the divertor.

With reference to Fig. 14.2, the sputtered impurities must be transported out of the divertor and through the complex edge plasma region in order to reach the core plasma. There are several such potential transport pathways. One pathway for the sputtered impurity atoms ejected into the divertor plasma just in front of the divertor target plate, where they will be ionized immediately, is to then diffuse upstream against the inflowing divertor plasma to reach the SOL plasma, then be transported inward across the separatrix to the edge plasma and further inward to the core plasma. Other pathways involve variants of

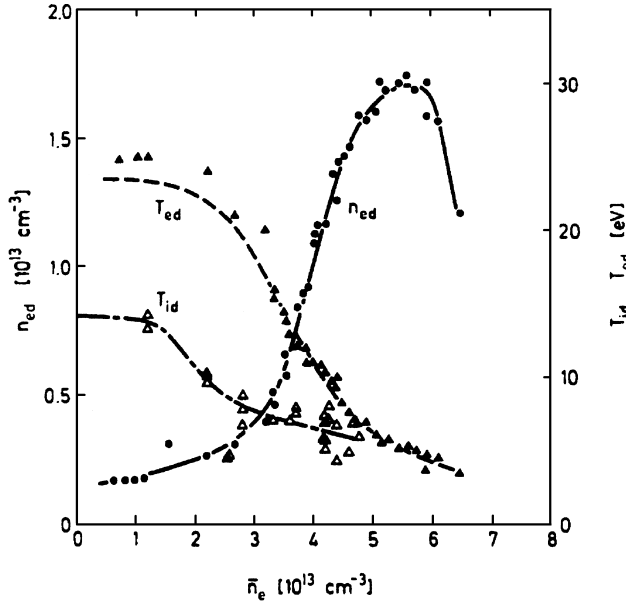


Figure 14.5. Scaling of the electron temperature and density measured by a Langmuir probe, and the ion temperature deduced from Doppler-broadened CIII radiation in the ASDEX divertor plasma. (The decrease in n_{ed} ($= n_D$) at the highest density is attributed to divertor detachment

this first pathway in which the impurity escapes the divertor plasma channel and is transported across the substantially less dense private flux region or regions next to the wall, as a neutral atom or ion for some or all of the distance traversed to reach the edge plasma. We consider only the first pathway in this section.

We model the transport of impurity ions upstream parallel to the magnetic field lines and against the inflowing divertor plasma using the same type of strip model discussed in previous sections and illustrated in Fig. 14.4. Neglecting viscous and inertial terms, the fluid momentum balance on an impurity species (denoted by z) in an ion (i)–electron (e) divertor plasma is

$$\frac{\partial p_z}{\partial \xi} = z e n_z E_{\parallel} + R_{ze} + R_{zi} \quad (14.36)$$

where z is the charge state of the impurity species,

$$R_{ze} = \frac{n_z z^2}{n_i} R_{ie} = \frac{n_z z^2}{n_i} \left[-\eta_{\parallel} \frac{n_i}{z_{\text{eff}}} e j_{\parallel} + C_e^{(2)} \frac{n_i}{z_{\text{eff}}} \frac{\partial T_e}{\partial \xi} \right] \quad (14.37)$$

and

$$R_{zi} = C_i^{(1)} n_i m_i v_{iz} (v_i - v_z) + C_i^{(2)} n_z z^2 \frac{\partial T_i}{\partial \xi} \quad (14.38)$$

are the collisional friction forces acting on the impurities due to interactions with the plasma electrons (R_{ze}) and plasma ions (R_{zi}). The C s are fitted parameters

$$\begin{aligned} C_e^{(2)} &= 1.5 (1 - 0.6934/1.3167 z_{\text{eff}}) \\ C_i^{(1)} &= \frac{(1 + 0.24z_0)(1 + 0.93z_0)}{(1 + 2.65z_0)(1 + 0.285z_0)} \\ C_i^{(2)} &= \frac{1.56 (1 + \sqrt{2}z_0)(1 + 0.52z_0)}{(1 + 2.65z_0)(1 + 0.285z_0)} \frac{1}{\left\{ z_0 + \left[\frac{1}{2} (1 + (m_i/m_z)) \right]^{\frac{1}{2}} \right\}} \end{aligned} \quad (14.39)$$

and

$$\begin{aligned} z_{\text{eff}} &\equiv \sum_j^{\text{ions}} n_j z_j^2 / n_e \\ z_0 &\equiv \sum_z^{\text{imp}} n_z z_z^2 / n_i \end{aligned} \quad (14.40)$$

with the first sum being over all ion charge states (plasma plus impurities) and the second sum being over all impurity ion charge states.

The term $\eta_{\parallel} = (m_e v_{ei}/n_e e^2)[0.457/(1.077 + z_{\text{eff}}) + 0.29z_{\text{eff}}]$ is the parallel viscosity.

The electron momentum balance

$$\frac{\partial p_e}{\partial \xi} = -n_e e E_{\parallel} - R_{ie} - R_{ze} = -n_e e E_{\parallel} - \left(1 + \frac{n_z z^2}{n_i}\right) R_{ie} \quad (14.41)$$

may be used to eliminate E_{\parallel} from Eq. (14.36), and this equation can then be rearranged, under the assumption $T_i = T_e$, to obtain

$$\frac{1}{n_z} \frac{\partial n_z}{\partial \xi} = \beta_1 \left(\frac{1}{T} \frac{\partial T}{\partial \xi} \right) - z \left(\frac{1}{n_e} \frac{\partial n_e}{\partial \xi} \right) + C_i^{(1)} \frac{m_z v_{zi}}{T} (v_{i\parallel} - v_{z\parallel}) - \frac{\beta_2 \eta_{\parallel} e j_{\parallel}}{T z_{\text{eff}}} \quad (14.42)$$

which may be integrated along the separatrix field lines from a stagnation point near the plasma core mid-plane (SOL) to the divertor target (D) to obtain

$$\begin{aligned} \ln \left(\frac{n_{zD}}{n_{zSOL}} \right) &= \beta_1 \ln \left(\frac{T_D}{T_{SOL}} \right) - z \ln \left(\frac{n_D}{n_{SOL}} \right) \\ &+ \int_0^{L_D} C_i^{(1)} \frac{m_i v_{zi}}{T} (v_{i\parallel} - v_{z\parallel}) d\xi - \beta_2 \int_0^{L_D} \frac{\eta_{\parallel} e j_{\parallel}}{T z_{\text{eff}}} d\xi \end{aligned} \quad (14.43)$$

where

$$\begin{aligned} \beta_1 &\equiv z^2 \left(C_i^{(2)} + \frac{C_e^{(2)}}{z_{\text{eff}}} \right) - z \left(1 + \frac{C_e^{(2)}}{z_{\text{eff}}} (1 + \alpha) \frac{n_i}{n_e} \right) - 1 \\ \beta_2 &\equiv z^2 - z (1 + \alpha) \frac{n_i}{n_e} \end{aligned} \quad (14.44)$$

Since the C 's, $\alpha = n_z z^2 / n_i$ and n_i/n_e are all of order unity or smaller, the β s should be positive for most impurities ($z > 1$).

The requirement for good impurity retention is $n_{zD} \gg n_{zSOL}$, or $\ln(n_{zD}/n_{zSOL}) > 0$. Thus, by examining the sign of the terms on the right side of Eq. (14.43), we can determine which effects contribute to (> 0) or inhibit (< 0) impurity retention. The first term, arising primarily from the thermal friction force, detracts from impurity retention ($\ln(T_D/T_{SOL}) < 0$) to a degree depending on how much the plasma is cooled in flowing around the SOL and down the divertor channel to the target plate (small in the sheath-limited regime but substantial in the high recycling regime).

The second term, arising from the electron pressure gradient along the field lines, can contribute to or inhibit impurity retention, depending on the divertor operating regime (i.e. depending on whether the plasma density in front of the divertor target, n_D , is smaller or larger than the plasma density upstream in the SOL, n_{SOL}).

The third term accounts for the collisional entrainment of the impurity ions by the plasma ion flow towards the divertor target plate ($v_{\parallel} > 0$). This term is generally positive and thus contributes to impurity retention.

The fourth term accounts for the effect of any electric current along the field lines on the collisional friction term R_{ie} . When the current flows towards the target plate ($j_{\parallel} > 0$), this term inhibits impurity retention, and conversely when the current flows away from the divertor target.

14.5 Thermal Instability*

Sudden redistribution of the plasma density along the field lines in the divertor and SOL, usually following detachment of the plasma from the divertor target plate and resulting in the formation of a high density/low temperature region of intense radiation in the divertor-SOL plasma near the X-point (“divertor MARFE”), is frequently observed in tokamaks. At low temperatures (1 eV–50 eV) the radiation emissivity function, L_Z , for typical impurities such as carbon and oxygen, hence the radiation cooling rate, is very sensitive to the local electron temperature, and below about 10 eV the ionization and recombination rate coefficients, hence the volumetric particle source and sink, are very sensitive to the local electron temperature. Thus, the possibility for thermal instability in the particle and energy balances in the divertor plasma being responsible for the sudden redistributions that are observed seems plausible.

We will use the same strip model of the divertor-SOL developed in previous sections and depicted in Fig. 14.4 to examine the possibility of a divertor thermal instability. The relevant parallel particle, momentum and energy transport equations are

$$\frac{\partial n}{\partial t} + \frac{\partial (nv)}{\partial \xi} = n(v_{ion} - v_{rec}) + \frac{\Gamma_{\perp} H_{SOL}}{\Delta_n} \quad (14.45)$$

$$\frac{\partial (nmv)}{\partial t} + \frac{\partial}{\partial \xi} (2nT + nmv^2) = -nmv(v_{at} + v_{rec}) \quad (14.46)$$

$$\begin{aligned} \frac{\partial}{\partial t} (3nT + \frac{1}{2}nmv^2) - \frac{\partial}{\partial \xi} \left(\kappa_0 T^{\frac{5}{2}} \frac{\partial T}{\partial \xi} \right) + \frac{\partial}{\partial \xi} \left(\frac{1}{2}nmv^3 + 5nTv \right) \\ = -n^2 f_z L_z - \frac{3}{2}nT v_{at} - nE_{ion} v_{ion} + \frac{Q_{\perp} H_{SOL}}{\Delta_E} \end{aligned} \quad (14.47)$$

with the atomic physics frequencies given by

$$\begin{aligned} v_{\text{ion}} &\equiv n_0 \langle \sigma v \rangle_{\text{ion}} \\ v_{\text{at}} &\equiv n_0^{\text{cold}} (\langle \sigma v \rangle_{cx} + \langle \sigma v \rangle_{el}) \\ v_{\text{rec}} &\equiv n \langle \sigma v \rangle_{\text{rec}} \end{aligned} \quad (14.48)$$

Note that now convective heat transport is also included in Eq. (14.47).

The equilibrium solutions of Eq. (14.45) to Eq. (14.47) satisfy

$$v \left[\left(\frac{1}{v} \frac{\partial v}{\partial \xi} \right) + \frac{1}{n} \frac{\partial n}{\partial \xi} \right] = (v_{\text{ion}} - v_{\text{rec}}) + \frac{\Gamma_{\perp} H_{\text{SOL}}}{n \Delta_n} \quad (14.49)$$

$$v \left[\left(\frac{1}{T} \frac{\partial T}{\partial \xi} \right) + (1 + M^2) \left(\frac{1}{n} \frac{\partial n}{\partial \xi} \right) + 2M^2 \left(\frac{1}{v} \frac{\partial v}{\partial \xi} \right) \right] = -M^2 (v_{\text{at}} + v_{\text{rec}}) \quad (14.50)$$

where $M = v/c_s$ is the Mach number, and

$$\begin{aligned} -\frac{\partial}{\partial \xi} \left(\frac{2}{7} \kappa_0 \frac{\partial T^{\frac{7}{2}}}{\partial \xi} \right) &= -\frac{1}{2} nm v^3 \left[\left(\frac{1}{n} \frac{\partial n}{\partial \xi} \right) + 3 \left(\frac{1}{v} \frac{\partial v}{\partial \xi} \right) \right] \\ &\quad - 5nT v \left[\left(\frac{1}{n} \frac{\partial n}{\partial \xi} \right) + \left(\frac{1}{v} \frac{\partial v}{\partial \xi} \right) + \left(\frac{1}{T} \frac{\partial T}{\partial \xi} \right) \right] \\ &\quad - n^2 f_z L_z - \frac{3}{2} nT v_{\text{at}} - nE_{\text{ion}} v_{\text{ion}} + \frac{Q_{\perp} H_{\text{SOL}}}{\Delta_E} \end{aligned} \quad (14.51)$$

In order to examine the stability of the solution of these equilibrium equations, a normal mode type analysis will be performed on Eq. (14.45) to Eq. (14.47); i.e. the general space- and time-dependent solutions of these equations – $n'(\xi, t)$, $v'(\xi, t)$, $T'(\xi, t)$ – are expanded about the equilibrium solutions satisfying Eq. (14.49)–Eq. (14.51) in the form

$$x'(\xi, t) = x(\xi) + \tilde{x}(\xi)e^{\omega t} \quad x = n, v, T \quad (14.52)$$

the equilibrium equations are used to eliminate terms, and only terms which are linear in the perturbations are retained. This results in a coupled set of differential eigenvalue equations for the perturbed solutions and the eigenvalue, ω . These equations may be reduced to a dispersion relation by expanding the spatial dependence as $\tilde{x}(\xi)/x(\xi) \sim \exp(ik_{\parallel})$. Since we are interested in representing a large scale redistribution phenomenon along the field lines in the divertor and SOL, we take $k_{\parallel} = m/L_D$. The resulting dispersion relation is still quite complex and must be solved numerically.

However, we can gain some physical insight by performing the same analysis for the density equation assuming that only density perturbations occur, for the momentum equation assuming only velocity perturbations occur, and for the energy equation assuming only temperature perturbations occur. The dispersion relation for such a “pure density” instability is

$$\omega_r^n = -\frac{\Gamma_{\perp} L_{\text{SOL}}}{n_s \Delta_n} + \left\langle \frac{n \partial (v_{\text{ion}} - v_{\text{rec}})}{\partial n} \right\rangle \quad (14.53)$$

the dispersion relation for such a “pure flow” instability is

$$\omega_r^v = -\frac{1}{\langle M^2 \rangle} \left\{ 3 \left\langle M^2 (\nu_{\text{ion}} - \nu_{\text{rec}}) \right\rangle + \left\langle M^2 (\nu_{\text{at}} + \nu_{\text{rec}}) \right\rangle + 3 \frac{\Gamma_{\perp} L_{\text{SOL}} M_s^2}{n_s \Delta_n} - 2 \left\langle M^2 v \left(\frac{1}{n} \frac{\partial n}{\partial \xi} \right) \right\rangle \right\} \quad (14.54)$$

and the dispersion relation for such a “pure temperature” instability is

$$\begin{aligned} \omega_r^T = & -\frac{1}{3} \left\{ \left\langle \frac{\kappa_0 T^{\frac{5}{2}}}{n} \right\rangle k_{\parallel}^2 + \frac{7}{2} \frac{Q_{\perp} L_{\text{SOL}}}{n_s T_s \Delta_E} - \left(\frac{33}{2} - \frac{21}{2} M_s^2 \right) \frac{\Gamma_{\perp} L_{\text{SOL}}}{n_s \Delta_n} \right. \\ & - \left\langle \left(\frac{33}{2} - \frac{43}{2} M^2 \right) v \left(\frac{1}{n} \frac{\partial n}{\partial \xi} \right) \right\rangle - \left\langle n f_z \left(\frac{7}{2} \frac{L_z}{T} - \frac{\partial L_z}{\partial T} \right) \right\rangle \\ & - \left\langle \nu_{\text{ion}} \left\{ \left(\frac{33}{2} - \frac{21}{2} M^2 + \frac{7}{2} \frac{E_{\text{ion}}}{T} \right) - \left(3 - M^2 - \frac{7}{2} \frac{E_{\text{ion}}}{T} \right) \frac{T}{\nu_{\text{ion}}} \frac{\partial \nu_{\text{ion}}}{\partial T} \right\} \right\rangle \\ & - \left\langle \nu_{\text{at}} \left\{ \left(\frac{15}{4} - \frac{29}{2} M^2 \right) - \left(\frac{3}{2} - 2M^2 \right) \frac{T}{\nu_{\text{at}}} \frac{\partial \nu_{\text{at}}}{\partial T} \right\} \right\rangle \\ & \left. + \left\langle \nu_{\text{rec}} \left\{ \left(\frac{33}{2} + 4M^2 \right) - (3 + M^2) \frac{T}{\nu_{\text{rec}}} \frac{\partial \nu_{\text{rec}}}{\partial T} \right\} \right\rangle \right\} \quad (14.55) \end{aligned}$$

The symbol $\langle X \rangle$ denotes an integral along the field lines $0 \leq \xi \leq L_D$. This decoupling of density, flow and temperature instabilities is unphysical and is used here only to simplify the formalism so that some physical insight can be obtained.

Since $\omega_r > 0$ indicates an instability, a “pure density” instability would require that the plasma density dependence of the ionization frequency be greater than the plasma density dependence of the recombination frequency, both frequencies being integrated over $0 \leq \xi \leq L_D$. Such a condition is favored by low temperatures (see Fig. 13.4). Otherwise, small particle flows across the separatrix into the SOL and large SOL plasma density (n_s) reduce the first, stabilizing term in (14.53) and hence favor the possibility of a “pure density” instability. The ‘s’ subscript denotes the value at the stagnation point.

The stabilizing and destabilizing phenomena for a “pure temperature” instability are represented by the negative and positive terms, respectively, in Eq. (14.55). Heat conduction along fields lines in the SOL–divertor, heat flow across the separatrix into the SOL and volumetric recombination are all stabilizing. Impurity radiation will be destabilizing, provided that the integral over $0 \leq \xi \leq L_D$ of $(3.5 L_z / T - dL_z / dT) > 0$, which will usually be the case. Cooling of the SOL–divertor plasma by ionization, charge exchange and elastic scattering are generally destabilizing. A large ion flux across the separatrix into the SOL is destabilizing. Comparison of the prediction of Eq. (14.55) with the growth rate calculated numerically for the coupled density–flow–temperature instability indicated good agreement in the vicinity of $\omega_r \approx 0$, indicating that the physics contained in Eq. (14.55) provides useful physical insight. Experimental conditions for which $\omega_r^T \approx 0$ were also found to correspond to conditions for which sudden redistributions of the plasma density and temperature along field lines were observed to take place in a few experiments.

14.6 2D Fluid Plasma Calculation*

The present state-of-the-art in SOL–divertor analysis consists of coupled 2D fluid plasma numerical calculations iterated with 2D neutral particle transport numerical calculations. The toroidal symmetry in tokamaks allows the third, toroidal dimension to be neglected. The calculation model for the 2D fluid plasma calculation is briefly discussed in this section, and neutral transport calculations are described in chapter 16.

The simplest 2D divertor–SOL geometry is a straightforward extension of the “strip” model used in previous sections to a pie-shaped “wedge” which represents the divertor–SOL geometry by (1) the distance, ξ , along field lines from some upper boundary (stagnation point, horizontal midplane, X-point, etc.) to the divertor target plate, and (2) the “radial” distance, r , (measured from the separatrix, the torus centerline, etc.). More detailed geometric representations taking into account the exact field-line geometry are sometimes used, but the equations are greatly complicated thereby, and the simple representation will serve our purpose of indicating the important physics phenomena that must be taken into account. There are transformations for mapping the simplified geometry solutions onto flux surface geometry. Specializing somewhat the plasma fluid equations of chapter 5, the particle balance equation in this simple cylindrical geometry becomes

$$\frac{\partial}{\partial \xi} (nv_{\parallel}) - \frac{1}{r} \frac{\partial}{\partial r} r \left(D_{\perp} \frac{\partial n}{\partial r} + nv_{\text{pinch}} \right) = S_{\text{ion}}(r, \xi) \quad (14.56)$$

with D_{\perp} and v_{pinch} being a diffusion coefficient and a “pinch velocity.” These transport coefficients are generally unknown and are usually chosen to match some aspect of the experimental data. $S_{\text{ion}} = nn_0 \langle \sigma v \rangle_{\text{ion}} - nn \langle \sigma v \rangle_{\text{rec}}$ is the net ionization source rate (ionization minus recombination), the calculation of which requires knowledge of the local neutral density, n_0 .

The momentum balance equation is

$$\begin{aligned} \frac{\partial}{\partial \xi} (p_i + p_e + m_i n v_{\parallel}^2 + \pi_i) &= S_{\text{mom}}(r, \xi) \\ &+ \frac{1}{r} \frac{\partial}{\partial r} r \left[m_i v_{\parallel} \left(D_{\perp} \frac{\partial n}{\partial r} + nv_{\text{pinch}} \right) \right] \\ &+ \frac{1}{r} \frac{\partial}{\partial r} r \left[\eta_{\perp} \frac{\partial v_{\parallel}}{\partial r} \right] \end{aligned} \quad (14.57)$$

where the last term represents the radial diffusion of momentum and the next-to-last term represents the radial convection of momentum. This form for momentum diffusion corresponds to the form for neoclassical “perpendicular” momentum transfer, which is well known to be too small, and η_{\perp} is usually adjusted to match some feature of the experimental data. The larger gyroviscosity from neoclassical theory is of the form of the last term but with radial derivative within the [] replaced by $(1/r)(\partial/\partial\theta)$, indicating that a 3D calculation of the flow velocity is necessary in order to properly model the radial transport of momentum. $S_{\text{mom}} = m_i v_0 S_{\text{ion}} - m_i v_{\parallel} n n_0 (\langle \sigma v \rangle_{cx} + \langle \sigma v \rangle_{el})$ is the net parallel momentum source to the ions due to ionization of neutrals with parallel velocity v_0 less the parallel momentum loss by elastic scattering and charge-exchange reactions with neutral atoms.

We use the standard diffusive plus pinch form of the radial particle flux

$$n v_r \equiv \Gamma_r = -D_{\perp} \frac{\partial n}{\partial r} - n v_{\text{pinch}} \quad (14.58)$$

The ion energy balance equation is

$$\begin{aligned} & \frac{\partial}{\partial \xi} \left[\left(\frac{5}{2} p_i + \frac{1}{2} m_i n v_{\parallel}^2 + \pi_i \right) v_{\parallel} - \kappa_{0i} T_i^{5/2} \frac{\partial T_i}{\partial \xi} \right] \\ & - \frac{1}{r} \frac{\partial}{\partial r} r \left[n \chi_{\perp}^i \frac{\partial (T_i)}{\partial r} - \left(\frac{5}{2} T_i + \frac{1}{2} m_i v_{\parallel}^2 \right) \Gamma_r \right] \\ & = e n v_{\parallel} E_{\parallel} + Q_{eq} + Q_{Ei}(r, \xi) \end{aligned} \quad (14.59)$$

where Q_{eq} is the rate of Coulomb collisional energy transfer from the plasma electrons to ions, Q_{Ei} is any external heating rate of ions (e.g. electromagnetic waves, neutral beams), the last term on the left represents the radial conduction plus convection of ion energy (the transport coefficient χ_{\perp} is usually chosen to match some feature of the experimental data) and E_{\parallel} is the electric field along the field lines governed by Ohm's law

$$E_{\parallel} = -\frac{0.71}{e} \frac{\partial T_e}{\partial \xi} - \frac{1}{en} \frac{\partial p_e}{\partial \xi} + \frac{j_{\parallel}}{\sigma_{\parallel}} \quad (14.60)$$

The electron energy balance is

$$\begin{aligned} & \frac{\partial}{\partial \xi} \left[\frac{5}{2} p_e v_{\parallel} - \kappa_{0e} T_e^{5/2} \frac{\partial T_e}{\partial \xi} \right] - \frac{1}{r} \frac{\partial}{\partial r} r \left[-\frac{5}{2} T_e \Gamma_r + n \chi_{\perp}^e \frac{\partial T_e}{\partial r} \right] \\ & = -env_{\parallel} E_{\parallel} - Q_{eq} + Q_R + Q_{Ee} \end{aligned} \quad (14.61)$$

where Q_R (a negative quantity) represents the radiation cooling of electrons, Q_{Ee} represents any external heating of electrons, and the last term on the left represents the radial conduction plus convection of electron energy.

These equations must be solved numerically (e.g. finite difference in space and time, iterative matrix inversion) for a given neutral particle, n_0 , distribution. Then the plasma n , v_{\parallel} , T_i and T_e distributions (ξ, r) must be determined and used to represent the background plasma in a recalculation of the neutral particle distribution, then the plasma n , v_{\parallel} , T_i and T_e distributions (ξ, r) must be redetermined, etc., and this process must be repeated until the various solutions no longer change significantly when recalculated. If the problem is time dependent, each of the calculations may be taken to represent a time step, but the size of the time step is constrained to be no larger than the time scale of the most rapidly changing phenomenon.

There are now four boundaries of the computational problem. The stagnation and sheath boundary conditions discussed previously are appropriate at $(\xi = 0, r)$ and at $(\xi = L_D, r)$, respectively. The particle and ion and electron heat fluxes across the separatrix into the SOL can be used to construct separatrix boundary conditions (r_{sep}, ξ) for n , T_i and T_e (and a similar zero parallel momentum inflow condition can be used to construct a separatrix condition on v_{\parallel}). The outer, wall-side boundary conditions (r_{at}, ξ) are

usually specified rather arbitrarily by assigning small values of the plasma density and temperatures at these locations.

Many features of the plasma distributions observed in divertors have been reproduced by 2D fluid plasma calculations, with judiciously chosen values of the various transport coefficients.

14.7 Drifts*

14.7.1 Basic Drifts in the SOL and Divertor

The grad- B drift velocity is given by

$$v_{\nabla B} = \pm \frac{v_{\perp}^2 m}{2eB^3} \mathbf{B} \times \nabla B \quad (14.62)$$

where the $+$ / $-$ signs are for ions/electrons. Taking the “normal” direction for \mathbf{B}_ϕ as shown in Fig. 14.6, the normal direction of the grad- B drift is down for ions and up for electrons. These opposite vertical flows of ions and electrons cause a charge separation, which in turn produces (in the configuration of Fig. 14.6) a downward directed electric field.

The curvature drift is given by

$$v_c = \pm \frac{mv_{\parallel}^2}{e} \frac{\mathbf{R}_c \times \mathbf{B}}{R_c B^2} \quad (14.63)$$

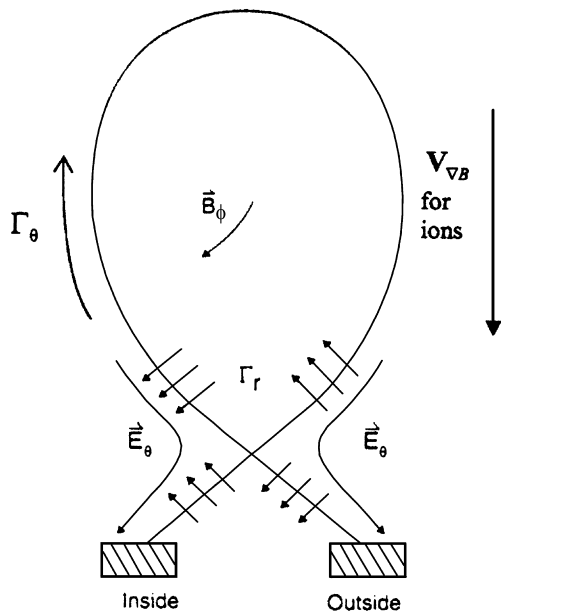


Figure 14.6. Drifts and electric fields

where R_c is the (major) radius of curvature of the field line and the $+/-$ signs are for ions/electrons. The quantitative effects of the curvature drifts are the same as for the grad- B drifts.

The total vertical drift velocity due to grad- B and curvature drifts is $v_{\text{dr}} \approx \pm 2p/enBR$, where $+/-$ refers to ions/electrons, for the normal \mathbf{B}_ϕ direction. The resulting charge separation drives parallel Pfirsch–Schlüter drifts and currents.

The transformer action of the central solenoid coil induces a toroidal electric field, \mathbf{E}_ϕ , which drives a toroidal current, \mathbf{I}_ϕ , as a result of ions and electrons drifting (v_ϕ) in opposite toroidal directions. These currents and drifts are smaller in the SOL, because of the higher plasma resistivity, than in the core, but nevertheless exist. Thus, we can speak of the “ion (ohmic) drift side” and the “electron (ohmic) drift side” of the divertor targets as the sides receiving the respective \mathbf{E}_ϕ drifts. As shown in Fig. 14.7, the ion drift side is on the inside and the electron drift side is on the outside for normal \mathbf{B}_ϕ direction. Conversely, for \mathbf{B}_ϕ in the anti-normal direction, the ion drift side is on the outside and the electron drift side is on the inside, independent of the direction of \mathbf{I}_ϕ and \mathbf{E}_ϕ . Similar, but more complex, results obtain for a double-null divertor.

Radial electric fields (potential gradients) and pressure gradients will inevitably arise in the SOL and divertor plasma. These radial gradients result in $\mathbf{E} \times \mathbf{B}$ drifts

$$v_{\mathbf{E} \times \mathbf{B}} = \frac{\mathbf{E} \times \mathbf{B}}{B^2} \quad (14.64)$$

and diamagnetic drifts

$$v_{\nabla p} = \pm \frac{\mathbf{B} \times \nabla p}{enB^2} \quad (14.65)$$

where the $+/-$ sign refers to ions/electrons.

14.7.2 Poloidal and Radial $\mathbf{E} \times \mathbf{B}$ Drifts

A radial electric field can arise in the SOL and divertor from a number of causes, probably the simplest of which is that the divertor target is usually electrically conducting. Because plasma flow to the target is usually ambipolar, the plasma potential at each radial location is $V_{\text{plasma}}(r) \sim 3T_e(r)/e$. Since $T_e(r)$ usually decreases with radius, $dV_{\text{plasma}}/dr < 0$, and the radial electric field is

$$E_r \equiv -\partial V/\partial r \approx \frac{3T_e}{e\lambda_{Te}} \quad (14.66)$$

This field points radially outward in the SOL surrounding the plasma above the X-point, but is radially inward in the private flux region below the X-point (single-null). The resulting $\mathbf{E} \times \mathbf{B}$ drift in the SOL above the X-point is in the poloidal direction, from the inside divertor target counter-clockwise around the plasma towards the outside divertor target, as indicated in Fig. 14.7, for the normal B_ϕ direction

$$F_\theta^{\text{dr}} \approx \frac{3T_e n}{e\lambda_{Te} B} \quad (14.67)$$

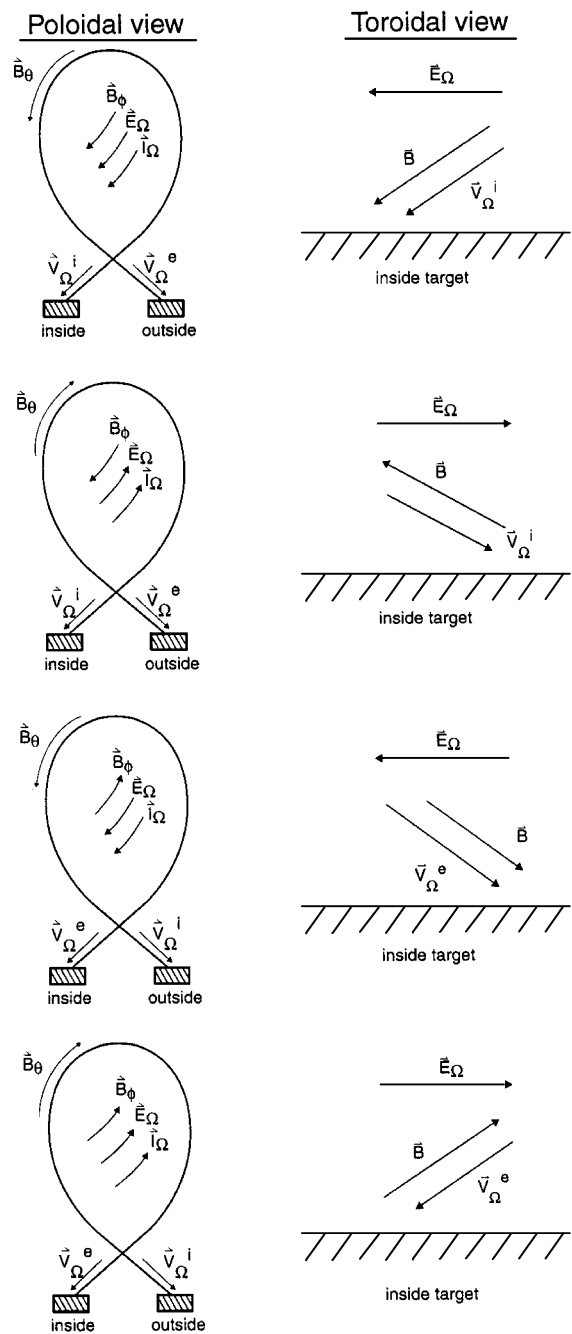


Figure 14.7. “Ohmic” drifts. (For toroidal \mathbf{B}_ϕ in the “normal direction” the ion (ohmic) drift side is always toward the inner target, with the electron (ohmic) drift side toward the outside target, regardless of the direction of the toroidal plasma current I_ϕ . The “ Ω ” subscripts on E and I correspond to “ ϕ ” and on the V correspond to “ θ ”)

Parallel electric fields exist in the SOL, governed by Ohm's law

$$E_{\parallel} = \frac{j_{\parallel}}{\sigma_{\parallel}} - \frac{0.71}{e} \frac{\partial T_e}{\partial \xi} - \frac{1}{en} \frac{\partial p_e}{\partial \xi} \quad (14.68)$$

As an example, in the sheath-limited regime, $dT_e/d\xi \approx 0$ and p drops by a factor of 1/2 from $\xi = 0$ to $\xi = L_D$. Taking $j_{\parallel} \approx 0$ then leads to $E_{\parallel} \approx -T_e/2eL_D$, the poloidal projection of which is $E_{\theta} \approx -(B/B_{\theta})E_{\parallel}$, directed towards each divertor target, as shown in Fig. 14.7. The resulting radial $\mathbf{E} \times \mathbf{B}$ drift

$$\Gamma_r^{\text{dr}} \approx (B/B_{\theta}) n T_e / 2e L_D B \quad (14.69)$$

is directed from the outer SOL into the main plasma but from the main plasma into the inner SOL, as indicated in Fig. 14.5.

For the high-recycling regime this radial $\mathbf{E} \times \mathbf{B}$ drift is in the same direction but stronger, since the thermoelectric term in Eq. (14.68) can be large. Using $E_{\parallel} \approx -T_{eu}/eL_D$ and $E_{\theta} \approx -(B/B_{\theta})E_{\parallel}$, where T_{eu} is the upstream temperature ($T_{eu} \simeq T_{\text{SOL}}$), results in

$$\Gamma_r^{\text{dr}} \approx (B/B_{\theta}) n T_{eu} / e L_D B \quad (14.70)$$

The poloidal $\mathbf{E} \times \mathbf{B}$ drift, $\Gamma_{\theta}^{\text{dr}}$, is in the same direction as the normal parallel flows (i.e. the flows resulting from the ionization of incident neutrals) in the SOL. This drift enhances the flow in the SOL towards the outer target, while reducing the flow towards the inner target, for normal B_{ϕ} . Thus, the plasma density and pressure are increased at the outer target relative to the inner target.

On the other hand, the radial $\mathbf{E} \times \mathbf{B}$ drift, Γ_r^{dr} , forms a closed flow loop. Assuming that the neutrals recycling from each target are ionized in the vicinity of that target and form a plasma flow back to that target (e.g. a high recycling divertor), the flow pattern produced by Γ_r^{dr} would be a flow from the outer SOL inwards across the separatrix into the core plasma, an inward flow across the bottom of the core plasma, and then an outward flow across the separatrix into the inner SOL. There is also a Γ_r^{dr} drift across the private flux region under the X-point from the outer divertor plasma to the inner divertor plasma. The flow loop is completed by the $\Gamma_{\theta}^{\text{dr}}$ drift along field lines from the inner SOL over the top of the plasma to the outer SOL, as indicated in Fig. 14.7. Clearly, the possibility for much more complex flow patterns exists if other phenomena (e.g. the spatial distribution of ionization, relaxation of the local recycling assumption, intermingling of the different flows) are taken into account.

14.8 Thermoelectric Currents*

14.8.1 Simple Current Model

With the complex mix of phenomena involved in the SOL and divertor, there are many possibilities for electrical currents in this region. We will examine thermoelectric currents, as an example, in this section.

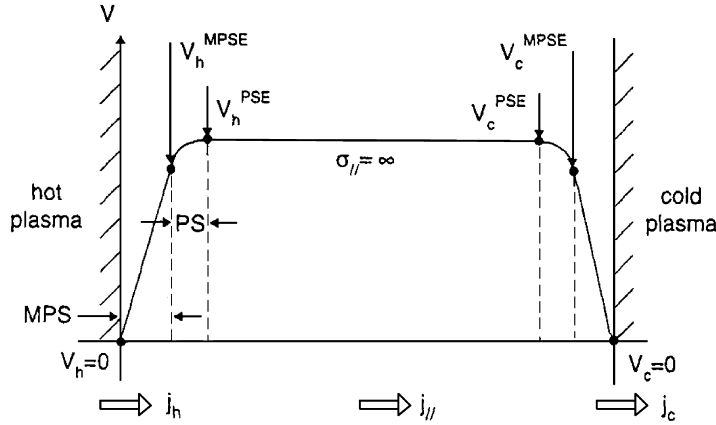


Figure 14.8. Electrothermal currents in the SOL and divertor

Consider the schematic representation of a lower single null (LSN) divertor shown in Fig. 14.8.

Here we consider the possibility that the plasma at one divertor target is hotter than the plasma at the other divertor target and adopt the convention that the positive sense of the current is from left to right. We assume that $T_i(\xi) = T_e(\xi)$ is sufficiently large that σ_{\parallel} is very large, that the pressure is uniform along the field lines connecting the two divertor targets (sheath-limited divertor), that the radial plasma conductivity vanishes ($\sigma_{\perp} \rightarrow 0$), and that both divertor targets are grounded and that there is no applied voltage. The sheath and presheath (PS) regions at both the hot and cold divertor targets are indicated in Fig. 14.8.

Because of the large σ_{\parallel} there is no voltage drop along the field line between the entrances to the hot and cold presheaths. The total current at the hot target is

$$j_h = e (\Gamma_h^i - \Gamma_h^e) \quad (14.71)$$

where the ion and electron particle fluxes at the hot target are

$$\Gamma_h^i = -n_h c_{sh} \quad (14.72)$$

$$\Gamma_h^e = -\frac{1}{4} n_h \bar{c}_e h \exp(-e V_h^{\text{MPSE}} / T_h) \quad (14.73)$$

with n_h being the density at the magnetic presheath entrance (MPSE) at the hot target.

Similarly, at the cold target

$$j_c = e (\Gamma_c^i - \Gamma_c^e) \quad (14.74)$$

$$\Gamma_c^i = n_c c_{sc} \quad (14.75)$$

$$\Gamma_c^e = \frac{1}{4} n_c \bar{c}_e c \exp(-e V_c^{\text{MPSE}} / T_c) \quad (14.76)$$

with n_c being the density at the magnetic presheath entrance (MPSE) at the cold target. The quantity \bar{c}_e is the average speed of electrons in a Maxwellian distribution.

We further assume that a potential drop $T \ln 2$ occurs across the presheath region in front of each target, where ionization of recycling neutral atoms and the acceleration of plasma ions to the sound speed also occurs

$$eV^{\text{MPSE}} + T \ln 2 = eV^{\text{PSE}} \quad (14.77)$$

where PSE indicates the presheath entrance.

Current continuity requires

$$j_h = j_{\parallel} = j_c \quad (14.78)$$

Defining the temperature ratio

$$r_T \equiv T_h/T_c \quad (14.79)$$

and the parameters

$$\eta_h \equiv eV_h^{\text{MPSE}}/T_h \quad (14.80)$$

$$\alpha \equiv \frac{1}{2} (m_i/\pi m_e)^{\frac{1}{2}} \quad (14.81)$$

and using the parallel pressure balance $n_c T_c = n_h T_h$, we can obtain an equation for $V_h = V_h^{\text{PSE}}$, the floating potential at the hot target

$$-1 + \alpha e^{-\eta_h} = r_T^{\frac{1}{2}} \left(1 - 2^{r_T-1} \alpha e^{-r_T \eta_h} \right) \quad (14.82)$$

In terms of these parameters the normalized parallel current density can be written

$$\hat{j}_{\parallel} \equiv \frac{j_{\parallel}}{en_h c_s h} = -1 + \alpha e^{-\eta_h} \quad (14.83)$$

The normalized floating potential at the hot target, η_h , of Eq. (14.80) and the normalized parallel current of Eq. (14.83) are plotted as a function of the ratio $r_T = T_h/T_c$ in Fig. 14.9, for D⁺ ions. As can be seen, for a divertor with no in-out temperature asymmetry ($T_h = T_c$) there is no parallel thermoelectric current flow. A positive value of $r_T = T_h/T_c$ drives a positive j_{\parallel} (i.e. the net electron flow in the SOL plasma is towards the hot end). As r_T becomes large, the floating potential saturates.

14.8.2 Relaxation of Simplifying Assumptions

We consider a more realistic model in which the parallel electrical conductivity is finite, allow an externally imposed bias $V_0 = V_c - V_h$ between the hot and cold targets, allow for a parallel pressure gradient in Ohm's law

$$ej_{\parallel}/\sigma_{\parallel} = -e \frac{dV}{d\xi} + 0.71 \frac{dT_e}{d\xi} + \frac{1}{n} \frac{dp_e}{d\xi} \quad (14.84)$$

allow for the temperature dependence of the parallel electrical conductivity

$$\sigma_{\parallel} \approx 3.6 \times 10^7 T_e^{\frac{3}{2}} \quad (14.85)$$

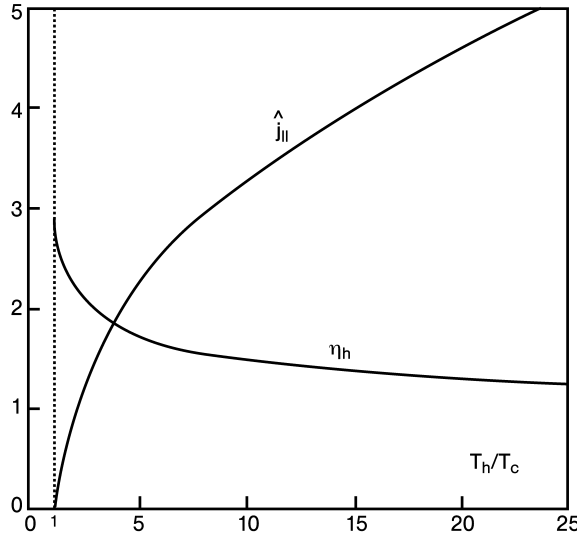


Figure 14.9. Normalized hot end floating potential and thermoelectric current density. (Net electron flow is from cold to hot target, resulting in a parallel current from the hot to cold target.)

where the units are $\sigma[\Omega^{-1} \cdot m^{-1}]$ and $T[\text{keV}]$, and define an average conductivity

$$\bar{\sigma}_{\parallel} \equiv \left(\frac{1}{L} \int_h^c \frac{d\xi}{\sigma_{\parallel}} \right)^{-1} \quad (14.86)$$

where the integral is from the hot to the cold target. The voltage distribution along the field lines in the SOL now will look more like Fig. 14.10.

Ohm's law, Eq. (14.84), can be integrated to obtain

$$\hat{j}_{\parallel} = -\gamma \left[\frac{eV_c^{\text{PSE}}}{T_h} - \frac{eV_h^{\text{PSE}}}{T_h} - 0.71 \left(\frac{T_c}{T_h} - 1 \right) - \frac{1}{T_h} \int_h^c \frac{1}{n} \frac{dP_e}{d\xi} d\xi \right] \quad (14.87)$$

where

$$\gamma \equiv \frac{\bar{\sigma}_{\parallel} T_h}{e^2 L n_h c_{sh}} \quad (14.88)$$

Equation (14.77) still holds at both targets and Eq. (14.83) still defines the normalized current at the hot target, but now the normalized current at the cold target is

$$\hat{j}_c = r_n^{-1} r_T^{-\frac{1}{2}} \left(1 - \alpha e^{-(V_c^{\text{MPSE}} - V_0) T_c} \right) \quad (14.89)$$

where $r_n = n_h/n_c$. Continuity of current still requires

$$\hat{j}_c = \hat{j}_{\parallel} = \hat{j}_h \quad (14.90)$$

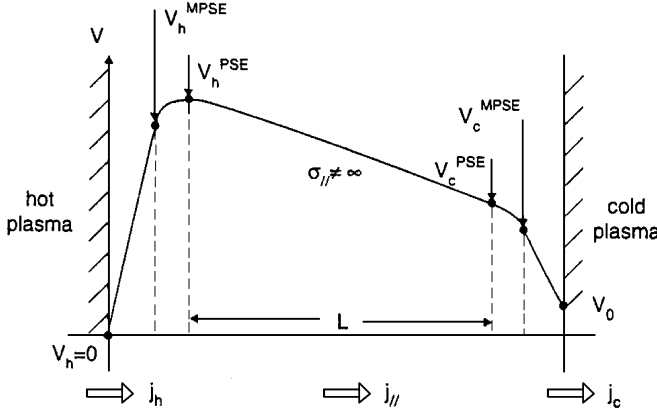


Figure 14.10. Voltage distribution along field lines between target plates with finite electrical conductivity and externally applied bias V_0 .

Combining Eq. (14.87) to Eq. (14.90) leads to a more general expression for the normalized parallel current

$$\hat{j}_{\parallel} = -\gamma \left\{ \frac{eV_0}{T_h} + \left(\frac{1}{r_T} - 1 \right) (\ln 2 - 0.71 + \ln \alpha) + \ln \left[\frac{1 + \hat{j}_{\parallel}}{\left(1 - r_n r_T^{\frac{1}{2}} \hat{j}_{\parallel} \right)^{\frac{1}{r_T}}} \right] - \frac{1}{T_h} \int_h^c \frac{1}{n} \frac{dp_e}{d\xi} d\xi \right\} \quad (14.91)$$

14.9 Detachment

As discussed in earlier sections of this chapter, under certain conditions a thin layer of neutral gas can form in front of the divertor plate, effectively “detaching” the plasma from contact with the plate. When such a condition occurs only over part of the divertor plate, the more usual case, we speak of “partial detachment.” We now consider in somewhat more detail the conditions affecting detachment.

One experimental indication of detachment is a sharp drop of the ion current ($j_+ = e\Gamma$) to the divertor target plate (as measured by probes). The ion flux must satisfy the continuity equation

$$\frac{d(nv)}{d\xi} \equiv \frac{d\Gamma}{d\xi} = n (n_0 \langle \sigma v \rangle_{\text{ion}} - n \langle \sigma v \rangle_{\text{rec}}) = n (v_{\text{ion}} - v_{\text{rec}}) \quad (14.92)$$

Following the convention of this chapter of ξ being the variable along the field lines with positive direction towards the divertor plate, this equation suggests that $d\Gamma/d\xi < 0$, which must occur in the region slightly upstream from the divertor plate in a detached plasma, can be produced if the recombination rate exceeds the ionization rate. With reference to Fig. 13.4, this can occur when the plasma temperature is a few eV or less. However, we need also to examine if this detachment is allowed by momentum balance.

The parallel plasma momentum and energy balance equations that must be satisfied along the field lines upstream from the divertor plates are

$$\frac{d}{d\xi} (2nT + nmv^2) = -nmvv_{at} - nmvv_{rec} \quad (14.93)$$

and

$$\frac{dQ}{d\xi} = -n_z n L_z - E_{ion} n v_{ion} + f I_{ion} n v_{rec} - \frac{3}{2} (T - T_0^c) n v_{at} \quad (14.94)$$

Ionization requires an energy $E_{ion}(\text{eV}) = 17.5 + (5.0 + 35.5/T(\text{eV})) \log_{10}(10^{21}/n)$, which is the ionization potential energy plus the excitation line radiation, from the plasma electrons and is a plasma cooling mechanism, while recombination releases the ionization potential energy $I_{ion} = 13.6 \text{ eV}$, a fraction f of which is absorbed by the plasma, so that recombination is a plasma heating mechanism.

Equations (14.92) and (14.93) can be combined to obtain an equation for the Mach number $M \equiv v/c_s$

$$\frac{dM}{d\xi} = \frac{M^2 (v_{at} + v_{ion}) - (v_{rec} - v_{ion})}{c_s (1 - M^2)} + \frac{1}{2} \frac{M (1 + M^2)}{(1 - M^2)} \left(\frac{1}{T} \frac{dT}{d\xi} \right) \quad (14.95)$$

and an equation for the plasma density

$$\frac{1}{n} \frac{dn}{d\xi} = -\frac{M}{(1 - M^2)} \left[\frac{v_{at} - v_{rec} + 2v_{ion}}{c_s} + 2 \left(\frac{1}{T} \frac{dT}{d\xi} \right) \right] \quad (14.96)$$

along the field lines upstream from the divertor plate. One or both of these quantities must vanish at the divertor plate in order for the ion flux to vanish, which requires a negative derivative over the region immediately upstream from the divertor plate.

We know that just prior to detachment $M_D = 1$ at the divertor plate, so that the reduction of the plasma density towards zero while M_D remains at about unity seems the more reasonable path to detachment. If the flow upstream of the divertor plate is subsonic ($M < 1$) and we neglect the temperature derivative terms, a negative derivative of the plasma density requires that the frequency v_{at} for the charge-exchange and elastic scattering of previously uncollided neutrals recycling from the divertor plate plus about two times the frequency v_{ion} for the ionization of all recycling neutral exceed the recombination frequency v_{rec} . This same condition is sufficient for an increasing M along the field lines towards the divertor plate. The recombination frequency becomes large for large plasma density and for temperatures of a few eV or less, while v_{at} and v_{ion} become large in the presence of a large recycling neutral concentration.

Now consider the temperature gradient terms. Well upstream of the divertor plate the plasma cooling due to impurity radiation and ionization, charge-exchange and elastic scattering reactions with recycling neutrals far exceed the recombination heating at temperatures above a few eV, so that $dT/d\xi < 0$. However, when T drops to the 1 eV – 2 eV range just in front of the divertor plate, the ionization and charge-exchange/scattering cooling becomes negligible and the recombination heating can become significant at high plasma density, so that $dT/d\xi > 0$, further contributing to $dn/d\xi < 0$, hence to detachment, and to $dM/d\xi > 0$.

If, on the other hand, the plasma is supersonic upstream from the divertor plate, the situation is quite different. The condition $v_{at} + 2v_{ion} > v_{rec}$ (which was required for detachment in the subsonic case above) now leads to $dn/d\xi > 0$ and $dM/d\xi < 0$; i.e. to stagnation of flow towards the divertor plate and density build up. This does not seem to be consistent with experimental observations and it certainly can not lead to an equilibrium. Thus, it seems that $v_{at} + 2v_{ion} < v_{rec}$ is the condition for detachment when the flow upstream of the divertor is supersonic.

Problems for Chapter 14

1. Using Bohm diffusion, $D_\perp = T/16eB$, calculate the scrapeoff layer thickness when the density at the separatrix is $n_{SOL} = 2 \times 10^{19} \text{ m}^{-3}$ and the outward ion flux across the separatrix is $\Gamma_\perp = 10^{21} \text{ m}^{-2} \cdot \text{s}^{-1}$.
2. Calculate the parallel heat conduction in the SOL when $T = 100 \text{ eV}$ and the temperature gradient scale length along the SOL is $L_T = 1 \text{ m}$.
3. Calculate the temperature at the divertor plate in a tokamak with power and heat fluxes across the separatrix into the SOL of $Q_\perp = 0.75 \times 10^5 \text{ W} \cdot \text{m}^{-2}$ and $\Gamma_\perp = 10^{20} \text{ m}^{-2} \cdot \text{s}^{-1}$ for a distance $L_{SOL} = 22.5 \text{ m}$, with 30 % of the power into the SOL being radiated or charge exchanged to the divertor wall ($\Delta Q_{rad} + \Delta Q_{at} = 0.3(Q_\perp)L_{SOL}$), and with the divertor ion source due to recycling being 20 % of that from the core ($\Delta N_{at} = 0.2(\Gamma_\perp)L_{SOL}$). Use Bohm diffusion, $D_\perp = \chi_\perp = T/16eB$ to calculate the scrapeoff layer thicknesses.
4. Calculate the temperature at the separatrix midplane (T_{SOL}) for the divertor of problem 3 with a divertor length along fields lines of 3.2 m leading to $L_D = 25.7 \text{ m}$.
5. Calculate the densities at the separatrix midplane (n_{SOL}) and at the divertor plate (n_D), neglecting the momentum loss in the divertor ΔM_{at} .
6. Calculate the radial $\mathbf{E} \times \mathbf{B}$ drift in the divertor of problems 3 and 4 when $B = 4 \text{ T}$, $B_\theta/B = 0.17$ and $n = 2 \times 10^{19} \text{ m}^{-3}$.
7. Derive Eqs. (14.95) and (14.96) for the parallel gradients of the Mach number and plasma density along the fields lines in the divertor.
8. Graph the detachment condition $v_{at} + 2v_{ion} > v_{rec}$ as a contour on a $n_D - T_D$ plot for different values of the recycling neutral density at the divertor plate, for a deuterium plasma.
9. Discuss the conditions under which “detachment” could take place.

15 Plasma Edge

The plasma edge, a region extending inward from the last closed flux surface (LCFS) for a few centimeters, has only recently become an area of intensive theoretical and experimental investigation. There are many experimental indications that phenomena taking place in this relatively thin region at the outer edge of the confined plasma play a major role in determining the overall performance characteristics of the confined plasma. These phenomena involve an interplay of the transport and MHD stability phenomena that are dominant in the core plasma and the atomic physics and radiation phenomena that are dominant in the divertor. In a mathematical sense, the edge plasma conditions determine the boundary conditions for the core plasma solutions, and in a physical sense the particles and energy that are transported out of the confined plasma region must pass through the plasma edge before they enter the unconfined scrape-off layer and divertor region.

15.1 H-Mode Edge Transport Barrier

Certainly one of the most interesting and important phenomena associated with the edge plasma is the formation of steep edge density and temperature gradients when the nonradiative power flux through the LCFS in a tokamak exceeds a certain empirical threshold value

$$P_{\text{LH}}^{(\text{MW})} = (2.84/A_i)\bar{n}_{20}^{0.58} B^{0.82} Ra^{0.81} \quad (15.1)$$

where $R(\text{m})$ and $a(\text{m})$ are the major and minor radii, $A_i(\text{amu})$ is the plasma ion mass, $\bar{n}_{20}(10^{20} \text{ m}^{-3})$ is the plasma line-average electron density, and $B(\text{T})$ is the toroidal magnetic field. The formation of these steep edge gradients, referred to as an edge transport barrier or edge pedestal, is accompanied by a significant ($\approx \times 2$) increase in energy confinement time for the confined plasma. The plasma is said to transition from a low confinement (L) mode prior to the formation of the steep gradients to a high confinement (H) mode after their formation. The sharp edge gradients are sometimes observed subsequently to deteriorate, invariably with an accompanying reduction in energy confinement, and if the nonradiative power crossing the LCFS drops below about $1/2 P_{\text{LH}}$ the sharp edge gradients disappear and the energy confinement returns to the L-mode value.

Figure 15.1 shows the edge pressure, temperature and density distributions in two similar discharges, one in L-mode and one in H-mode. The steep gradients occur over a region of 1 cm to 2 cm inside the LCFS. The location at which the steep edge gradient changes abruptly to a more gradual gradient that extends inward into the core plasma is referred to as the “pedestal” location. As can be seen in this figure, the temperature and density pedestals may be at different locations.

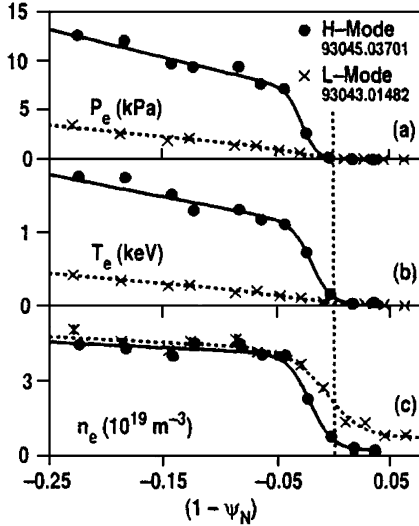


Figure 15.1. Edge pressure, temperature and density distributions in otherwise similar L-mode and H-mode discharges. (Data are plotted vs. a normalized poloidal flux function which is > 0 for values outside the LCFS and < 0 for values inside the LCFS. Location of the LCFS is indicated by the vertical dashed line)

Since its initial discovery in the asymmetric divertor experiment (ASDEX), the H-mode has now been observed in all tokamaks that have operated with auxiliary heating (needed to satisfy Eq. (15.1)) since 1982. While it is a ubiquitous phenomenon in tokamaks and has been investigated for two decades, the H-mode edge transport barrier is not yet fully understood. In the remainder of this section, we summarize the fundamental phenomena that are believed to occur in the edge pedestal, and in the sections 15.2 and 15.3 we summarize the present understanding of the edge transport barrier formation.

15.1.1 Relation of Edge Transport and Gradients

The ion flux passing through the edge plasma (inside the LCFS) increases as a function of radial position because of the ionization of incoming neutral atoms

$$\frac{d\Gamma_{\perp}}{dr} = nn_0 \langle \sigma v \rangle_{\text{ion}} \equiv n v_{\text{ion}} \quad (15.2)$$

Integrating this equation from the pedestal location (ped) outward to the LCFS, or separatrix (sep), and using average values of the plasma density (n_{TB}) and ionization frequency ($v_{\text{ion}}^{\text{TB}}$) in this edge transport barrier region of width $\Delta_{\text{TB}} \equiv r_{\text{sep}} - r_{\text{ped}}$ yields a relation between the net outward ion fluxes crossing the pedestal location ($\Gamma_{\perp}^{\text{ped}}$) and crossing the separatrix ($\Gamma_{\perp}^{\text{sep}}$)

$$\Gamma_{\perp}^{\text{sep}} - \Gamma_{\perp}^{\text{ped}} = \int_{\Delta_{\text{TB}}} n v_{\text{ion}} dr \equiv n_{\text{TB}} v_{\text{ion}}^{\text{TB}} \Delta_{\text{TB}} \quad (15.3)$$

We define an average (over the transport barrier) value of the net outward ion flux

$$\Gamma_{\perp}^{\text{av}} \equiv \frac{1}{2}(\Gamma_{\perp}^{\text{sep}} + \Gamma_{\perp}^{\text{ped}}) \quad (15.4)$$

and relate this quantity to the general diffusive/pinch form for the ion transport flux

$$\Gamma_{\perp}^{\text{av}} = -D \frac{dn}{dr} + n_{\text{TB}} v_p = n_{\text{TB}}(DL_n^{-1} + v_p) \quad (15.5)$$

and solve these equations for the average (over the transport barrier) value of the density gradient scale length ($L_n = -n(dn/dr)^{-1}$)

$$\begin{aligned} L_n &= \frac{D}{\Gamma_{\perp}^{\text{sep}}/n_{\text{TB}} - \frac{1}{2}v_{\text{ion}}^{\text{TB}}\Delta_{\text{TB}} - v_p} \\ &= \frac{D}{\Gamma_{\perp}^{\text{ped}}/n_{\text{TB}} + \frac{1}{2}v_{\text{ion}}^{\text{TB}}\Delta_{\text{TB}} - v_p} = -\left(\frac{1}{n} \frac{dn}{dr}\right)^{-1} \end{aligned} \quad (15.6)$$

The second form of this equation shows that any increase in particle flux leaving the core, the ionization of neutrals and any inward pinch ($v_p < 0$), as well as any decrease in the diffusion coefficient, will reduce the average density gradient scale length (steeperen the average density gradient) in the transport barrier.

The same type of relations obtain for the average (over the transport barrier) ion and electron temperature gradient scale lengths. Assuming for simplicity that ions and electrons cross the thin transport barrier in a time short compared to the ion-electron equilibration time, we can neglect ion-electron equilibration and write the change across the transport barrier in the electron heat flux due to ionization and radiation cooling as

$$\frac{dQ_{\perp e}}{dr} = -n_{\text{TB}}n_0\langle\sigma v\rangle_{\text{ion}}E_{\text{ion}} - n_{\text{TB}}n_zL_z \equiv -n_{\text{TB}}v_{\text{ion}}E_{\text{ion}} - n_{\text{TB}}n_zL_z \quad (15.7)$$

and the change across the transport barrier in the ion heat flux due to charge exchange and elastic scattering with previously uncollided “cold” neutral atoms (n_0^c) as

$$\frac{dQ_{\perp i}}{dr} = -n_{\text{TB}}n_0^c\langle\sigma v\rangle_{\text{at}}\frac{3}{2}T_i \equiv -n_{\text{TB}}v_{\text{at}}^c\frac{3}{2}T_i \quad (15.8)$$

Integrating these equations across the transport barrier and defining average values of the various reaction rates involved yields

$$\begin{aligned} Q_{\perp e}^{\text{sep}} - Q_{\perp e}^{\text{ped}} &= - \int_{\Delta_{\text{TB}}} n v_{\text{ion}} E_{\text{ion}} dr - \int_{\Delta_{\text{TB}}} n n_z L_z dr \\ &\equiv -n_{\text{TB}}v_{\text{ion}}^{\text{TB}}E_{\text{ion}}\Delta_{\text{TB}} - n_{\text{TB}}(n_z L_z)_{\text{TB}}\Delta_{\text{TB}} \end{aligned} \quad (15.9)$$

and

$$Q_{\perp i}^{\text{sep}} - Q_{\perp i}^{\text{ped}} = - \int_{\Delta_{\text{TB}}} n v_{\text{at}}^c \frac{3}{2}T_i dr \equiv -n_{\text{TB}}v_{\text{at}}^{c,\text{TB}}\frac{3}{2}T_i^{\text{TB}}\Delta_{\text{TB}} \quad (15.10)$$

Proceeding as above, defining average electron and ion heat fluxes in the transport barrier and equating these to the standard form for the average conductive plus convective heat

fluxes

$$Q_{\perp}^{\text{av}} \equiv \frac{1}{2}(Q_{\perp}^{\text{sep}} + Q_{\perp}^{\text{ped}}) = -\chi n \frac{dT}{dr} + \frac{5}{2} T \Gamma_{\perp} = \chi n T L_T^{-1} + \frac{5}{2} T \Gamma_{\perp} \quad (15.11)$$

leads to expressions for the average electron and ion temperature gradient scale lengths ($L_T = -T(dT/dr)^{-1}$)

$$\begin{aligned} L_{Te} &= \frac{\chi_e^{\text{TB}}}{\left\{ \left(\frac{Q_{\perp e}^{\text{sep}}}{n_{\text{TB}} T_e^{\text{TB}}} - \frac{5}{2} \frac{\Gamma_{\perp}^{\text{sep}}}{n_{\text{TB}}} \right) + \frac{1}{2} \Delta_{\text{TB}} \left[\frac{(n_z L_z)_{\text{TB}}}{T_e^{\text{TB}}} + v_{\text{ion}}^{\text{TB}} \left(\frac{E_{\text{ion}}}{T_e^{\text{TB}}} + \frac{5}{2} \right) \right] \right\}} \\ &= \frac{\chi_e^{\text{TB}}}{\left\{ \left(\frac{Q_{\perp e}^{\text{ped}}}{n_{\text{TB}} T_e^{\text{TB}}} - \frac{5}{2} \frac{\Gamma_{\perp}^{\text{ped}}}{n_{\text{TB}}} \right) - \frac{1}{2} \Delta_{\text{TB}} \left[\frac{(n_z L_z)_{\text{TB}}}{T_e^{\text{TB}}} + v_{\text{ion}}^{\text{TB}} \left(\frac{E_{\text{ion}}}{T_e^{\text{TB}}} + \frac{5}{2} \right) \right] \right\}} \end{aligned} \quad (15.12)$$

and

$$\begin{aligned} L_{Ti} &= \frac{\chi_i^{\text{TB}}}{\left[\left(\frac{Q_{\perp i}^{\text{sep}}}{n_{\text{TB}} T_i^{\text{TB}}} - \frac{5}{2} \frac{\Gamma_{\perp}^{\text{sep}}}{n_{\text{TB}}} \right) + \frac{1}{2} \Delta_{\text{TB}} \left(\frac{3}{2} v_{\text{at}}^{c,\text{TB}} + \frac{5}{2} v_{\text{ion}}^{\text{TB}} \right) \right]} \\ &= \frac{\chi_i^{\text{TB}}}{\left[\left(\frac{Q_{\perp i}^{\text{ped}}}{n_{\text{TB}} T_i^{\text{TB}}} - \frac{5}{2} \frac{\Gamma_{\perp}^{\text{ped}}}{n_{\text{TB}}} \right) - \frac{1}{2} \Delta_{\text{TB}} \left(\frac{3}{2} v_{\text{at}}^{c,\text{TB}} + \frac{5}{2} v_{\text{ion}}^{\text{TB}} \right) \right]} \end{aligned} \quad (15.13)$$

As the above expressions make clear, the gradient scale lengths in the transport barrier depend on the local transport coefficients, local density and temperatures, local atomic physics reaction rates and on the particle and conductive heat fluxes flowing across the edge transport barrier from the core into the SOL.

15.1.2 MHD Stability Constraints on Pedestal Gradients

The steep edge pressure gradients associated with H-modes often result in intermittent bursts of edge-localized mode MHD instabilities (ELMs). Each ELM burst produces a significant pulsed flow of particles and energy across the separatrix into the SOL and ultimately onto the divertor targets, diminishing the edge pressure gradients in the process. Following an ELM the edge pedestal builds up again until the next burst.

ELMs have been categorized into three types:

1. Giant ELMs. When the heating power is well ($\geq 20\%$) above the L–H threshold power of Eq. (15.1), relatively isolated, large amplitude ELMs which can eject up to 10 % of the confined plasma energy ($\Delta E/E \leq 10\%$) occur at a relatively low frequency (1 Hz to 100 Hz) that itself increases linearly with heating power. The ejected power goes preferentially to the inside target in a single-null divertor configuration, for reasons that are not yet understood. The energy loss per ELM burst seems to be approximately constant, independent of heating power; thus, the time-averaged power loss due to giant

ELMs increases with ELM frequency, hence linearly with heating power, remaining a constant fraction of the heating power. The degradation in time-averaged energy confinement due to giant ELMs is modest, 10 % to 20 %.

2. Grassy ELMs. These ELMs with very small fractional energy loss ($\Delta E/E \ll 1\%$) are sometimes observed in highly shaped plasmas, but are relatively rare.
3. Common ELMs. When the heating power is just ($\leq 20\%$) above the L–H threshold, small amplitude ($\Delta E/E \approx 1\%$), high-frequency (0.1 kHz to 1 kHz) ELMs are observed. The burst frequency decreases with increasing heating power, an opposite trend to that for type 1 giant ELMs.

Because a magnetic perturbation signal is observed with ELMs, they are analyzed as MHD instabilities. The large pressure gradients in H-mode edge plasmas lead to the prediction of high toroidal mode number (n) ballooning instabilities, but these instabilities are at least partially stabilized by the reduction in magnetic shear in the plasma edge due to the large bootstrap current associated with the steep edge pressure gradient. On the other hand, the large edge bootstrap current can drive high- n kink, or “peeling” modes, which in turn are at least in part stabilized by the large edge pressure gradient. This interaction of the edge pressure gradient and edge bootstrap current leads to an extremely complex situation that can only be analyzed numerically. Such analyses are performed by considering the δW stability of perturbations corresponding to thin strips of various toroidal mode number, n , as discussed in chapter 8.

The local stability to ideal MHD ballooning modes depends on both the current density and the discharge shape. In the infinite- n limit the ballooning stability boundaries are a function of the magnetic shear, $s = (r/q)(dq/dr)$, and the normalized pressure gradient, $\alpha = -(q^2 R/(B^2/2\mu_0))(dp/dr)$, at the location of each flux surface (i.e. a contour in $s-\alpha$ space).

In the first stability regime, at relatively large values of s and small values of α , the pressure gradient cannot be increased indefinitely without destabilizing the ballooning mode, as indicated in Fig. 15.2(a). However, with certain discharge shapes there is a region at low values of s with access to a second stability regime, as indicated in Fig. 15.2(b), in which the pressure gradient can be increased indefinitely without destabilizing the ballooning mode.

Larger values of the edge pressure gradient produce larger values of the bootstrap current, of course, which will constitute the majority of the current in the edge plasma. An increase in the edge current density decreases the local shear and increases the stability boundary to higher s values. This introduces the possibility that as the edge pressure gradient increases, the trajectory in $s-\alpha$ space will never intersect the stability boundary, and the equilibrium will evolve to the region of relatively low shear for which the second stability regime is accessible.

The access to the second stability regime has been found to depend on the shape of the discharge. For example, Fig. 15.2 displays a strong dependence on the “squareness,” δ_2 , of the discharge. In the higher-squareness discharge of Fig. 15.2(a) the peak value of the edge

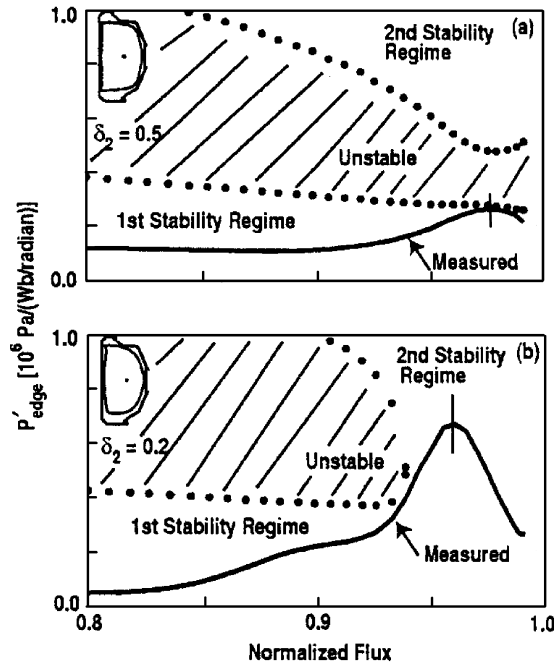


Figure 15.2. Measured edge pressure gradients and the marginal stability boundaries for the ideal infinite- n ballooning mode in DIII-D. (a) During small amplitude ELMs in a high squareness discharge, and (b) during type 1 giant ELMs in a medium squareness discharge

pressure gradient is at the calculated first stability regime ballooning mode limit, and second stability access is not predicted. In the lower squareness discharge of Fig. 15.2(b) the outermost region of the plasma is predicted to have access to the second stability regime, and the measured pressure gradient in that region exceeds the first stability regime limit by a factor of 2. There is a large increase in ELM frequency and a somewhat smaller decrease in ELM amplitude with increasing squareness in these discharges.

In the high squareness discharges such as shown in Fig. 15.2(a), in which the pressure gradient was limited by the ballooning mode first stability regime boundary, the highest toroidal mode number (n) modes are predicted to be stabilized when finite Larmor radius (FLR) effects are taken into account in the analysis. Moreover, including finite- n corrections in the ballooning mode equations of chapter 8 causes the predicted pressure gradient threshold for ballooning instability to decrease with n , as shown in Fig. 15.3. This leads to the expectation that any observed ELMs would correspond to the highest n -mode that is not stabilized by FLR effects. For the edge parameters of the discharges shown in these figures, modes with $n > 40$ are FLR stabilized. Figure 15.3 shows that the predicted first stability regime pressure gradient threshold for $n = 40$ is about 20 % larger than the predicted infinite- n pressure gradient threshold and is about equal to the largest observed edge pressure gradient in any of the discharges exhibiting common (high frequency) ELMs.

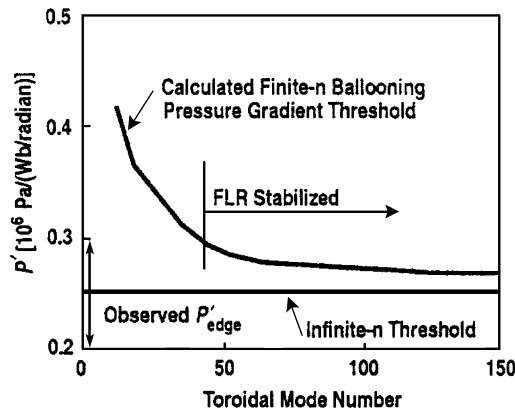


Figure 15.3. Finite- n ballooning mode first stability regime pressure gradient threshold as a function of toroidal mode number, n

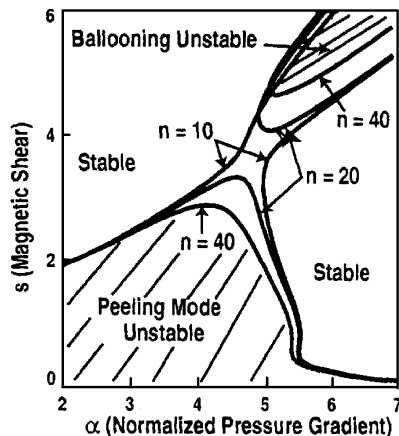


Figure 15.4. Stability boundaries for coupled ballooning and peeling modes for $n = 10, 20$ and 40

However, bootstrap current-driven kink modes (not included in the analysis) can become destabilized for $n < 40$. When these “peeling” modes are taken into account the $s-\alpha$ stability boundary for combined ballooning and peeling modes becomes quite complex, as shown in Fig. 15.4, where the stable region to the left is the first stability regime and the stable region to the right is the second stability regime. An important issue is whether access to the second stability regime exists between the ballooning mode and peeling mode stability boundaries for ballooning stable modes with $n < 40$. In this calculation, there is a gap for second stability access for modes with $n = 20$ and 40 , but not for modes with $n = 10$; thus, modes with $15 < n < 40$ are predicted to have second stability access for these particular DIII-D edge parameters.

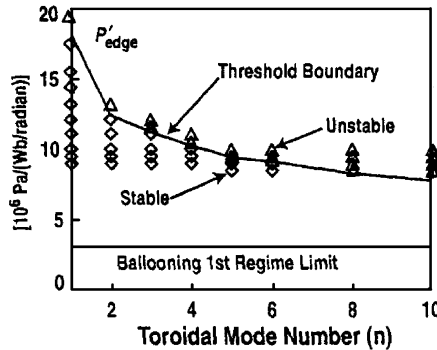


Figure 15.5. Pressure gradient threshold for low- n ballooning mode instability. (Symbols indicate data points; lines are calculations)

Both theory and experiment indicate that for DIII-D discharges with low to medium squareness ($\delta_2 \approx 0.05\text{--}0.2$) the higher- n ballooning modes should be stable because of second stability regime access. Predictions of the ballooning mode pressure gradient threshold for lower- n modes have been calculated for $\delta_2 \approx 0.05$ and are shown in Fig. 15.5. Since the threshold pressure gradient decreases with toroidal mode number, n , the most unstable mode will have n approximately at the threshold for second stability regime access (e.g. Fig. 15.4).

15.1.3 Representation of MHD Pressure Gradient Constraint

The gradient scale lengths determined from the transport considerations of section 15.1.1 are constrained by the MHD stability requirements on the maximum pressure gradient, or equivalently on the minimum pressure gradient scale length, discussed in section 15.1.2. This constraint is conventionally written in the form

$$-\left(\frac{dp}{dr}\right)_{\text{crit}} = \frac{\alpha_c (B^2/2\mu_0)}{q_{95}^2 R} \quad (15.14)$$

where B is the toroidal field, R is the major radius, q_{95} is the safety factor at the 95 % flux surface, and α_c is in general a function of magnetic shear and plasma geometry. The nominal ideal ballooning mode value of α_c discussed in chapter 8 is of order unity in the absence of second stability access, shear reduction by bootstrap currents, and other factors discussed in the previous section.

Access to second stability for high toroidal mode number (n) modes increases α_c to the point at which lower toroidal mode number modes, which do not have access to second stability, become unstable. The presence of steep pressure gradients in the plasma edge will drive a bootstrap current, which will reduce the shear, which in turn will reduce the maximum stable edge pressure gradient. These effects, which were discussed in detail in

the previous section, may be represented by writing

$$\left(-\frac{dp}{dr}\right)_{\text{crit}} = \frac{B^2/2\mu_0}{q_{95}^2 R} C_s A_s(s) \left[s_0 - 2 \frac{j_{\text{bs}}}{\langle j \rangle} \right] \equiv \alpha_c(s) \frac{(B^2/2\mu_0)}{q_{95}^2 R} \quad (15.15)$$

where $\langle j \rangle = I/\pi a^2 \kappa$ is the average current density over the entire plasma cross section (minor radius "a" and elongation κ) and j_{bs} is the bootstrap current density in the edge. C_s is a quantity of order unity depending on the shear in the magnetic field, and $A_s(s)$ is intended to contain the physics of the $s - \alpha$ diagram for ballooning modes and peeling modes (e.g. Fig. 15.4). The general effect of this physics is to increase A_s above unity because of FLR stabilization of high- n ballooning modes, stabilization of all ballooning modes by ion diamagnetic drift effects, access to the second stable regime, etc.

The requirement for stability against ballooning and peeling modes

$$\left(-\frac{dp}{dr}\right) \leq \left(-\frac{dp}{dr}\right)_{\text{crit}} \quad (15.16)$$

can be written as a MHD constraint on the allowable values of the gradient scale lengths

$$L_p^{-1} \equiv \left(L_n^{-1} + \frac{T_e}{T_e + T_i} L_{T_e}^{-1} + \frac{T_i}{T_e + T_i} L_{T_i}^{-1} \right) \leq L_{\text{MHD}}^{-1} \equiv \frac{1}{p} \left(-\frac{dp}{dr}\right)_{\text{crit}} \quad (15.17)$$

15.1.4 Pedestal Widths

The steep edge gradients in temperature and density extend only a few cm inside the separatrix or LCFS. Identification of the mechanisms that determine these pedestal widths remains an active research area, but there are two phenomena which are likely to be involved.

15.1.4.1 MHD Pressure Constraint

The MHD stability constraint discussed in section 15.1.2 could probably be characterized as a threshold pedestal pressure constraint, instead of a threshold pressure gradient constraint. While the nominal ideal ballooning stability is phenomenologically constrained by a threshold pressure gradient, the actual situation is more complex, as discussed in section 15.1.2. The numerical results are typically given as a maximum stable pressure for a given assumed pressure width, which could certainly be interpreted as a maximum pressure constraint.

Let us suppose that the MHD stability limit can be characterized as a maximum threshold pressure, p_{crit} . Such a pressure limit can be combined with the transport constraints on edge gradients discussed in section 15.1.1 to determine a pressure width Δ_p . For example, stability of the edge pedestal against MHD ideal pressure-driven surface modes imposes a maximum allowable value on the pedestal pressure

$$p_{\text{crit}} = \frac{8}{3} \frac{B^2/2\mu_0}{q_{95}^2} \left(\frac{T_i}{2(T_i + T_e)} \right)^{\frac{1}{3}} \left(\frac{\rho_i}{R} \right)^{\frac{2}{3}} \quad (15.18)$$

where ρ_i is the ion gyroradius.

For a given edge pressure gradient scale length, L_p , and a given pressure at the separatrix (p_{sep} determined by divertor physics), the limit on the maximum allowable pedestal pressure, p_{crit} , results in the constraint

$$p_{\text{crit}} = n^{\text{TB}}(T_i^{\text{TB}} + T_e^{\text{TB}}) \quad (15.19)$$

when p_{crit} is understood to pertain to the average pressure over the pedestal region.

We set $\Delta_p = \Delta_n = \Delta_{Ti} = \Delta_{Te} = \Delta_{\text{TB}}$, $p_{\text{TB}} = (p_{\text{ped}} + p_{\text{sep}})/2 = p_{\text{crit}}$ and solve $L_p^{-1} = -(dp/dr)/p$ to obtain

$$\Delta_{\text{TB}} = L_p(\Delta_{\text{TB}}) \ln \left(2 \frac{p_{\text{crit}}}{p_{\text{sep}}} - 1 \right) \equiv L_p(\Delta_{\text{TB}})G \quad (15.20)$$

where the constraint of Eq. (15.18) has been used. This “common pedestal width” approximation is made for analytical convenience. Combining the above equations results in a quadratic equation in Δ_{TB} , which has the solution

$$\Delta_{\text{TB}} = \frac{b}{2a} \left[\sqrt{1 + \frac{4aG}{b^2}} - 1 \right] \approx \frac{G}{b} \left[1 - \left(\frac{aG}{b^2} \right) + \left(\frac{aG}{b^2} \right)^2 - \dots \right] \quad (15.21)$$

The second form of this result is valid when atomic physics effects are not dominant; i.e. when $|aG/b^2| < 1$. The constants in Eq. (15.21) are

$$a \equiv \frac{1}{2} \left\{ -\frac{v_{\text{ion}}}{D} + \gamma_i \frac{\left(\frac{3}{2} v_{\text{at}}^c + \frac{5}{2} v_{\text{ion}} \right)}{\chi_i} + \gamma_e \frac{\left[n_z L_z / T_e + v_{\text{ion}} \left(E_{\text{ion}} / T_e + \frac{5}{2} \right) \right]}{\chi_e} \right\} \quad (15.22a)$$

$$b \equiv \left\{ \frac{(\Gamma_{\perp}^{\text{sep}} / n - v_p)}{D} + \gamma_i \frac{\left(Q_{\perp i}^{\text{sep}} / n T_i - \frac{5}{2} (\Gamma_{\perp}^{\text{sep}} / n) \right)}{\chi_i} + \gamma_e \left[\frac{\left(Q_{\perp e}^{\text{sep}} / n T_e - \frac{5}{2} \frac{\Gamma_{\perp}^{\text{sep}}}{n} \right)}{\chi_e} \right] \right\} \quad (15.22b)$$

and

$$\gamma_i \equiv \frac{T_i}{T_e + T_i}, \quad \gamma_e \equiv \frac{T_e}{T_e + T_i} \quad (15.22c)$$

When atomic physics effects are not dominant, the leading order term for the pedestal width

$$\Delta_{\text{TB}}^{(0)} \equiv \frac{G}{b} = \frac{\ln \left[\frac{16}{3} \frac{1}{2} \left(\frac{4\pi}{5 \times 10^6 \mu_0} \right)^2 \left(\frac{B_\theta^2 / 2\mu_0}{p_{\text{sep}}} \right) \frac{(1+\kappa^2)}{\epsilon^2 g^2} \left(\frac{1}{2} \gamma_i \right)^{\frac{1}{3}} \left(\frac{\rho_i}{R} \right)^{\frac{2}{3}} - 1 \right]}{\left[\left(\frac{\Gamma_{\perp}^{\text{sep}} / n - v_p}{D} \right) + \gamma_i \left(\frac{\frac{Q_{\perp i}^{\text{sep}}}{n T_i} - \frac{5}{2} \frac{\Gamma_{\perp}^{\text{sep}}}{n}}{\chi_i} \right) + \gamma_e \left(\frac{\frac{Q_{\perp e}^{\text{sep}}}{n T_e} - \frac{5}{2} \frac{\Gamma_{\perp}^{\text{sep}}}{n}}{\chi_e} \right) \right]} \quad (15.23)$$

is determined by the MHD pressure constraint and the edge transport physics. In this case, the atomic physics effects enter to higher order through the term (aG/b^2) in Eq. (15.21). The quantity $g \equiv [1 + \kappa^2(1 + 2\delta^2 - 1.2\delta^3)](1.17 - 0.65\epsilon)/(1 - \epsilon^2)^2$ is a geometric factor arising from the definition $q_{95} = \left(\frac{5}{2}\right)(a^2/R)(B/I)g$.

15.1.4.2 Neutral Penetration Constraint

The build up in plasma density from the separatrix inward to the top of the density pedestal is due, at least in part, to the ionization of recycling and fueling neutrals that are diffusing inward across the separatrix, which implies that the limit of penetration of these neutrals into the plasma will play an important role in determining the extent of the steep density gradient region, or the density pedestal width, Δ_n . Using a simple diffusion theory model (chapter 16)

$$-\frac{d}{dr} \left(\frac{1}{3n_{TB}\sigma_{tr}} \frac{d\phi}{dr} \right) + n_{TB}\sigma_{ion} = 0 \quad (15.24)$$

for inward neutral atom transport and replacing the varying plasma density in the pedestal with an average value, n_{TB} , it can be shown that the neutral atom flux ($\phi = n_0 v_0$) attenuates exponentially into the plasma with a mean free path $\lambda_0 = [n_{TB}(3\sigma_{tr}\sigma_{ion})^{\frac{1}{2}}]^{-1}$, i.e. that

$$\phi(r) = \phi(r = 0) \exp(-r/\lambda_0) \quad (15.25)$$

where r is measured inward from the separatrix, σ_{ion} is the ionization cross section, $\sigma_{tr} = \sigma_{ion} + \sigma_{cx}(1 - \mu_{cx}) + \sigma_{el}(1 - \mu_{el})$ is the “transport” cross section, σ_{cx} and σ_{el} are the charge-exchange and elastic scattering cross sections, and μ_{cx} and μ_{el} are the average cosine of the neutral atom “scattering” angle in charge-exchange and elastic scattering collisions with plasma ions. Since the direction of the neutral atom emerging from a charge-exchange collision with a plasma ion is equally likely to be in any direction, $\mu_{cx} = 0$. For the elastic scattering of a neutral atom from an ion, $\mu_{el} \approx 2/3A$, where A = ion mass/neutral mass.

A plausible approximation for the density width of the pedestal is the mean-free-path for neutral particle attenuation

$$\Delta_n = \lambda_0 = \left[n_{TB}(3\sigma_{tr}\sigma_{ion})^{\frac{1}{2}} \right]^{-1} \quad (15.26)$$

15.2 $E \times B$ Shear Stabilization of Turbulence

A large number of phenomena have been suggested as the cause of the formation of the steep gradient region in the plasma edge and the coincident improvement in plasma confinement that is associated with the transition from the low (L) mode to the high (H) mode of confinement in tokamaks. Although the subject is still under active experimental and theoretical investigation, the $E \times B$ shear stabilization of turbulent edge transport has emerged as the reigning paradigm.

15.2.1 $E \times B$ Shear Stabilization Physics

The fundamental physics involved in edge transport reduction is believed to be the effect of $E \times B$ velocity shear in the edge on the growth and radial extent of turbulent eddies in the edge plasma. Both nonlinear decorrelation and linear stabilization effects have been considered in the analysis. The basic nonlinear effect predicted is the reduction in radial transport due to a decrease in the radial correlation length and the change in phase among density, temperature and electrostatic potential fluctuations. There are a multitude of linear effects specific to various modes; however, one general feature of the linear stabilization is the coupling of unstable modes to more stable modes caused by the $E \times B$ velocity shear.

The radial momentum balance equation

$$E_r = (Z_i e n_i)^{-1} \nabla p_i - v_{\theta i} B_\phi + v_{\phi i} B_\theta \quad (15.27)$$

indicates that the radial electric field may be changed by altering the radial pressure gradient or the toroidal or poloidal flow velocity. We have seen that changes in the edge pressure distribution are a characteristic of the L-H transition, and changes in the radial distribution of v_θ are also routinely observed. Resulting changes in the radial distribution of E_r (i.e. the shear in E_r) produce changes in the radial distribution (i.e. shear) of $v_{E \times B} \sim E \times B$.

There are two important concepts relating to the effect of $E \times B$ shear on turbulence. The first concept is nonlinear decorrelation of turbulence, leading to a reduction in turbulent transport even if the underlying turbulence is not completely suppressed. The second concept is linear stabilization of modes leading to elimination of any transport originally associated with the de-stabilized modes.

Figures 15.6 and 15.7 illustrate the first concept of turbulence decorrelation, treating the plasma density as a passive scalar that is affected by the velocity field of turbulent eddies. Figures 15.6(a), 15.7(a) and 15.7(b) depict the situation in which there is no shear in average velocity, while 15.6(b), 15.7(c) and 15.7(d) depict the situation in which there is a gradient, or shear, in $v_{E \times B} \sim E \times B$. Without velocity shear, the eddies couple with a linear background density to produce hills and valleys in the density spatial distribution. As shown in Figs. 15.7(a) and 15.7(b), the correlation between density and velocity perturbations then leads to radial transport.

A shear in $v_{E \times B} \sim E \times B$ distorts the flow eddies, as depicted in Fig. 15.6(b), and reduces radial transport, as depicted in Figs. 15.7(c) and 15.7(d). This reduction in radial transport is due both to the changes in phase between the velocity and density perturbations and to decreases in the amplitudes of these perturbations.

In general, the linear stabilization effects are mode-specific, but the stabilizing $E \times B$ shear effect of coupling otherwise unstable modes to nearby stable modes often leads to enhanced Landau damping.

The $E \times B$ shearing rate for flute-like modes in tokamak flux surface geometry is

$$\omega_{E \times B} = \frac{\Delta\psi_0}{\Delta\phi} \left(\frac{\partial}{\partial\psi} \right) \frac{E_r}{RB_\theta} \quad (15.28)$$

where $L_r = \Delta\psi_0/RB_\theta$ is the radial correlation length and $R\Delta\phi$ is the toroidal correlation length for the ambient turbulence. For flute-like modes, the poloidal correlation

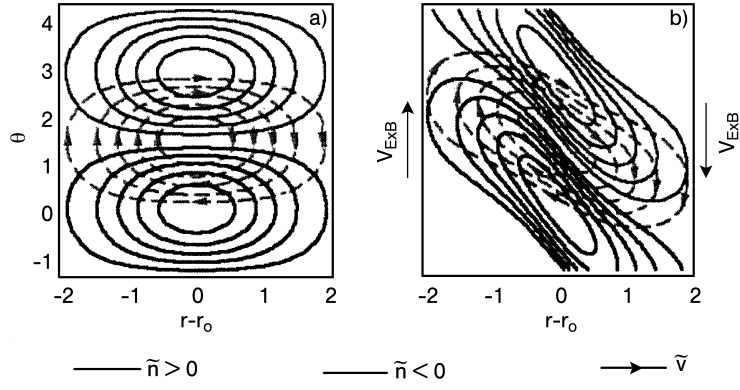


Figure 15.6. A simple model of turbulence which treats density as a passive scalar convected by an eddy velocity field. (a) No velocity shear, and (b) with velocity shear

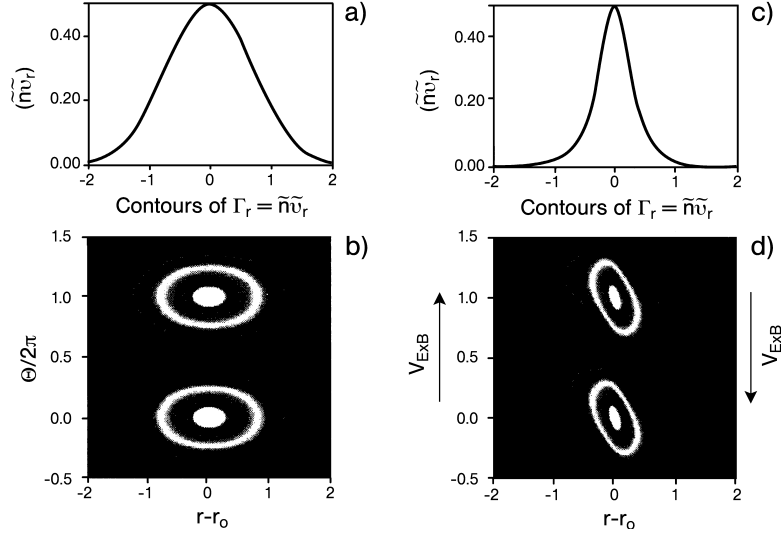


Figure 15.7. The radial particle flux for the model depicted in Fig. 15.6 (a) and (b) o velocity shear, and (c) and (d) with velocity shear

length is $L_\theta = RB_\theta \Delta\phi / B_\phi$ and the corresponding perpendicular correlation length is $L_\perp = RB_\theta \Delta\phi / B$. Numerical calculations and experimental observations show $L_\perp \approx L_r$, which can be used to reduce Eq. (15.28) to

$$\omega_{\mathbf{E} \times \mathbf{B}} = \frac{(RB_\theta)^2}{B} \frac{\partial}{\partial \psi} \left(\frac{E_r}{RB_\theta} \right) \quad (15.29)$$

Since this shearing rate enters the various stabilization theories quadratically, the sign is unimportant. The quantity E_r/RB_θ , which is constant over the flux surface, is the toroidal angular rotation due to E_r in standard neoclassical theory, which suggests that the basic shearing is in the toroidal direction for flute-like modes in toroidal geometry.

In order for $\mathbf{E} \times \mathbf{B}$ shear to decorrelate turbulence, $\omega_{\mathbf{E} \times \mathbf{B}}$ must be at least comparable to $\Delta\omega_D$, the nonlinear turbulence decorrelation rate in the absence of $\mathbf{E} \times \mathbf{B}$ shear. Although $\Delta\omega_D$ can be calculated for some modes, it is not generally known for the many possible modes of turbulence in tokamaks. However, nonlinear gyro-Landau fluid calculations have shown complete turbulence suppression when $\omega_{\mathbf{E} \times \mathbf{B}}$ is comparable to γ_{\max} , the maximum linear growth rate of all the unstable modes in the plasma. Thus, $\omega_{\mathbf{E} \times \mathbf{B}} \geq \gamma_{\max}$ is generally used as a prediction of $\mathbf{E} \times \mathbf{B}$ turbulence suppression.

15.2.2 Comparison with Experiment

There is a common set of phenomena observed in all tokamaks (and other devices) that transition to H-mode confinement. The formation of the edge transport barrier with steep density and temperature gradients was discussed. Coincident with this transport barrier formation is a sharp reduction in the D_α radiation everywhere around the plasma, indicating a sharp reduction in the particle outflux, which is confirmed by Langmuir probe measurements. The density fluctuation amplitude is observed to decrease in the same edge region in which the transport barrier, or pedestal, is formed. Coincident with the transport barrier formation, a steep gradient in E_r develops in the edge plasma.

Clearly, the prediction of reduced radial particle transport due to the nonlinear decorrelation of turbulence by $\mathbf{E} \times \mathbf{B}$ shear that was discussed in the previous section is qualitatively consistent with the observed decrease in D_α and Langmuir probe signals.

The calculated $\omega_{\mathbf{E} \times \mathbf{B}}$ values have been compared with measured turbulence decorrelation rates in several devices. The calculated $\omega_{\mathbf{E} \times \mathbf{B}}$ values increased significantly when the plasma transitioned from L-mode to H-mode confinement, and $\omega_{\mathbf{E} \times \mathbf{B}}$ significantly exceeded $\Delta\omega_D$, the measured nonlinear turbulence decorrelation rate in the absence of $\mathbf{E} \times \mathbf{B}$ shear. An example is shown in Fig. 15.8, where $\omega_{\mathbf{E} \times \mathbf{B}}$ is comparable to $\Delta\omega_D$ in L-mode, but is significantly larger in H-mode.

These observations are consistent with the $\mathbf{E} \times \mathbf{B}$ shear stabilization of turbulence explanation of the L–H transition given in the previous section, but they do not demonstrate that $\mathbf{E} \times \mathbf{B}$ shear actually causes the reduction in turbulence and transport. However, the $\mathbf{E} \times \mathbf{B}$ shear has been observed to change before changes in turbulence and transport were observed during a series of L–H transitions on DIII-D, which is suggestive of the causal role of $\mathbf{E} \times \mathbf{B}$ shear in the L–H transition. Further evidence is provided for the causal role of $\mathbf{E} \times \mathbf{B}$ shear by several experiments in which L–H mode transitions are produced by biasing the plasma to control the edge E_r profile.

15.2.3 Possible “Trigger” Mechanism for the L–H Transition

A variety of mechanisms have been suggested that could generate sheared $\mathbf{E} \times \mathbf{B}$ flow. The basic mechanisms for the generation of this flow and an associated radial electric field

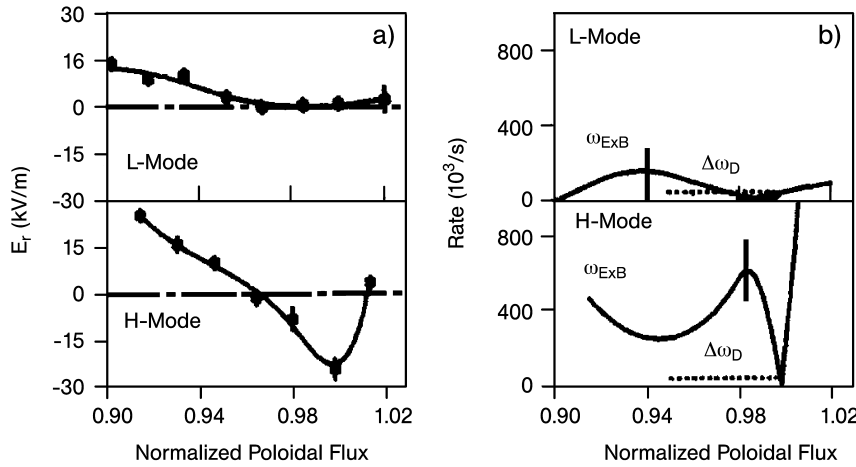


Figure 15.8. Comparison of E_r and $\omega_{E \times B}$ just before and after a L–H mode transition

require either toroidal effects (e.g. ion-orbit loss or poloidally asymmetric transport driven by Stringer spin-up) or the generalized Reynold's stress of the turbulent waves responsible for the “anomalous” L-mode transport, which waves become unstable to the generation of the sheared flow. However, at present there is no direct experimental confirmation that “zonal” flow driven by plasma turbulence is the mechanism causing the observed L–H transition.

At the most sophisticated level, fully three-dimensional fluid simulation codes which provide first principle modeling of the edge turbulence and anomalous transport and their interplay with self-generated or imposed shear flows have been developed. 3D transport simulations in a poloidally and radially localized edge region flux-tube that wound around the torus showed that the level of turbulent transport could be related to two parameters – a normalized pressure gradient “ballooning” parameter $\alpha = -Rq^2(d\beta/dr)$ and a diamagnetic parameter, $\alpha_d = [\rho_s c_s (RL_n/2)^{1/2}]/[(1 + T_{i0}/T_{e0})L_n L_0]$, where L_n is the density gradient scale length, $L_0 = (2\pi q_a R)[(C^2 \eta_{||})/4\pi v_A^2 (Rq^2/2)]^{1/2}$, C is a geometric function, v_A is the Alfvén speed, ρ_s is the gyroradius, $\eta_{||}$ is the parallel viscosity, and c_s is the ion sound speed. For small α_d the calculated turbulence resulted mainly from the nonlinear development of resistive ballooning modes and at very small α_d the calculated ion radial energy flux became very large (inferred transport coefficients $\approx 60 \text{ m}^2/\text{s}$), a result that is consistent with an effective density limit above which stable operation is impossible and with the observed confinement deterioration as the density limit is approached. For $\alpha_d \approx 1$ the turbulent transport was predicted to be primarily due to nonlinear electron drift waves, with small increases in pressure gradients (α) leading to a strong suppression of transport, which would further increase the pressure gradient and lead to the spontaneous formation of a transport barrier (i.e. the L–H transition) above a certain threshold value of α .

15.3 Thermal Instabilities

A significant level of density fluctuations is observed in the edge of L-mode plasmas, and these are observed to be reduced significantly after a transition to H-mode. We examine in this section short wavelength radial instabilities that can be supported in the plasma edge by imbalances in the local plasma power, momentum and particle balances.

15.3.1 Temperature Perturbations in the Plasma Edge

The essential physics of short wavelength radial thermal instabilities in the edge transport barrier may be elucidated by considering the stability of the energy balance equation with respect to radial temperature perturbations. Since coupled perturbations in the density and radial flow would also be expected, this assumption of pure temperature perturbations is a mathematical simplification which brings out the essential physics without unnecessary complications. A more complete treatment is presented in the next section.

Using a slab approximation for the thin plasma edge, the energy balance equation summed over plasma ions, electrons and impurities can be written

$$3 \frac{\partial(nT)}{\partial t} - \frac{\partial}{\partial r} \left(n\chi_{\perp} \frac{\partial T}{\partial r} \right) = H - nn_z L_z - \frac{3}{2}nT\nu_{\text{at}} - nE_{\text{ion}}\nu_{\text{ion}} \quad (15.30)$$

where T is the common temperature (strong temperature equilibration assumption), m is the ion mass, n is the ion density, n_z and L_z are the impurity density and radiation emissivity function, χ_{\perp} is the radial thermal diffusivity, H is any “external” heating or cooling (e.g. true external heating or neglected terms such as viscous heating or convective cooling), ν_{at} is the frequency for atomic “scattering” collisions (elastic scattering, charge exchange), and $\nu_{\text{ion}} = 17.5 + (5 + 37.5/T_e(\text{eV})) \log(10^{21}/n_e)$ are the ionization frequency and energy.

The equilibrium solution to Eq. (15.30) satisfies

$$\begin{aligned} -\bar{n}\bar{\chi}_{\perp}\bar{T} & \left[\frac{1}{T} \frac{\partial^2 \bar{T}}{\partial r^2} + \nu \left(\frac{1}{T} \frac{\partial \bar{T}}{\partial r} \right)^2 + \left(\frac{1}{T} \frac{\partial \bar{T}}{\partial r} \right) \left(\frac{1}{n} \frac{\partial \bar{n}}{\partial r} \right) \right] \\ & = \bar{H} - \bar{n}\bar{n}_z\bar{L}_z - \frac{3}{2}\bar{n}\bar{T}\bar{\nu}_{\text{at}} - \bar{n}E_{\text{ion}}\bar{\nu}_{\text{ion}} \end{aligned} \quad (15.31)$$

describing the balance between edge heating by conduction and any “external” source H and cooling by atomic processes (including radiation). The thermal diffusivity has been assumed to be temperature dependent, $\chi_{\perp} = CT^{\nu}$; various anomalous transport theories suggest $3/2 < \nu < 7/2$. Equation (15.31) specifies a consistency requirement for the temperature profile in order for the existence of an equilibrium solution.

With an edge localized radial temperature fluctuation \tilde{T} , temperature may be written

$$T'(r, t) = \bar{T}(r) + \tilde{T}(r)e^{\omega t} \quad (15.32)$$

where \tilde{T} is the solution to the equilibrium Eq. (15.31). Using this form in Eq. (15.30) and linearizing results in

$$\begin{aligned} & -\bar{n}\bar{\chi}_{\perp}\frac{\partial^2\tilde{T}}{\partial r^2}+\bar{n}\bar{\chi}_{\perp}(L_n^{-1}+2\nu L_T^{-1})\frac{\partial\tilde{T}}{\partial r} \\ & +\left[3\bar{n}\omega+\bar{n}\bar{\chi}_{\perp}\nu L_T^{-2}-\bar{n}\bar{n}_z\left(\nu\frac{\bar{L}_z}{T}-\frac{\partial L_z}{\partial T}\right)-\frac{3}{n}\bar{n}\bar{v}_{\text{at}}\left(\nu-1-\frac{T}{\nu_{\text{at}}}\frac{\partial v_{\text{at}}}{\partial T}\right)\right. \\ & \left.-\bar{n}\bar{v}_{\text{ion}}\frac{E_{\text{ion}}}{T}\left(\nu-\frac{T}{\nu_{\text{ion}}}\frac{\partial v_{\text{ion}}}{\partial T}\right)+\left(\nu\frac{\bar{H}}{T}-\frac{\partial H}{\partial T}\right)\right]\tilde{T}=0 \quad (15.33) \end{aligned}$$

The equilibrium energy balance of Eq. (15.31) has been used to self-consistently determine the value of $\frac{1}{T}(\partial^2\tilde{T}/\partial r^2)$ which characterizes the particular equilibrium in terms of the other edge parameters, allowing Eq. (15.33) to be written in a form that incorporates the equilibrium energy balance constraint on the temperature distribution.

Since we are interested in instabilities localized in a transport barrier of thickness Δ_{TB} inside the separatrix, we adopt a coordinate system with $r = 0$ at the pedestal a distance Δ_{TB} inside the separatrix and with $r = \Delta_{\text{TB}}$ at the separatrix, and then expand the perturbed solution

$$\tilde{T}(r)=\sum_{m=1}^M a_m \sin\left(\frac{m\pi r}{\Delta_{\text{TB}}}\right) \quad (15.34)$$

Note that $\tilde{T}(r)$ vanishes at the separatrix and at the pedestal a distance Δ_{TB} inside the separatrix.

Using Eq. (15.34) in Eq. (15.33), multiplying by $\sin\left(\frac{p\pi r}{\Delta_{\text{TB}}}\right)$ and integrating over $0 \leq r \leq \Delta_{\text{TB}}$ results in the set of M equations that constitute a dispersion relation

$$\begin{aligned} & \left\{3\omega+\bar{\chi}_{\perp}\left[\nu L_T^{-2}+\left(\frac{p\pi}{\Delta_{\text{TB}}}\right)^2\right]-\bar{n}_z\left(\nu\frac{\bar{L}_z}{T}-\frac{\partial L_z}{\partial T}\right)\right. \\ & -\frac{3}{2}\bar{v}_{\text{at}}\left(\nu-1-\frac{\bar{T}}{\nu_{\text{at}}}\frac{\partial v_{\text{at}}}{\partial T}\right)-\bar{v}_{\text{ion}}\frac{E_{\text{ion}}}{T}\left(\nu-\frac{\bar{T}}{\nu_{\text{ion}}}\frac{\partial v_{\text{ion}}}{\partial T}\right) \\ & \left.+\frac{1}{n}\left(\nu\frac{\bar{H}}{T}-\frac{\partial H}{\partial T}\right)\right\}a_p \\ & +\sum_{m \neq p}^M\left(\frac{m\pi}{\Delta_{\text{TB}}}\right)A_{pm}\bar{\chi}_{\perp}(L_n^{-1}+2\nu L_T^{-1})a_m=0 \quad p=1,\dots,M \quad (15.35) \end{aligned}$$

where

$$A_{pm}=\left(\frac{2}{\pi}\right)\int_0^\pi \sin p\xi \cos m\xi d\xi \quad (15.36)$$

Equation (15.35) are coupled through the $\partial\tilde{T}/\partial r$ perturbation to the heat conduction in Eq. (15.33).

The simplest case results from terminating the sum in Eq. (15.34) at $M = 1$ with a single term, which leads to an expression for the growth rate

$$\begin{aligned} \gamma_1 = & -\frac{1}{3} \left\{ \bar{\chi}_{\perp} \left[\nu L_T^{-2} + \left(\frac{\pi}{\Delta_{\text{TB}}} \right)^2 \right] - \bar{n}_z \left(\nu \frac{\bar{L}_z}{T} - \frac{\partial L_z}{\partial T} \right) \right. \\ & - \frac{3}{2} \bar{v}_{\text{at}} \left(\nu - 1 - \frac{\bar{T}}{\nu_{\text{at}}} \frac{\partial \nu_{\text{at}}}{\partial T} \right) - \bar{v}_{\text{ion}} \frac{E_{\text{ion}}}{T} \left(\nu - \frac{T}{\nu_{\text{ion}}} \frac{\partial \nu_{\text{ion}}}{\partial T} \right) \\ & \left. + \frac{1}{n} \left(\nu \frac{\bar{H}}{T} - \frac{\partial H}{\partial T} \right) \right\} \equiv -\frac{1}{3} C_1 \quad (15.37) \end{aligned}$$

Retaining the first two terms in Eq. (15.34) leads to an expression for the growth rate

$$\gamma_2^{\pm} = -\frac{(C_1 + C_2)}{6} \left[1 \pm \sqrt{1 - \frac{4(C_1 C_2 - B_1 A_{12} B_2 A_{21})}{(C_1 + C_2)^2}} \right] \quad (15.38)$$

where

$$\begin{aligned} C_p = & \left\{ \bar{\chi}_{\perp} \left[\nu L_T^{-2} + \left(\frac{p\pi}{\Delta_{\text{TB}}} \right)^2 \right] - \bar{n}_z \left(\nu \frac{\bar{L}_z}{T} - \frac{\partial L_z}{\partial T} \right) \right. \\ & - \frac{3}{2} \bar{v}_{\text{at}} \left(\nu - 1 - \frac{\bar{T}}{\nu_{\text{at}}} \frac{\partial \nu_{\text{at}}}{\partial T} \right) - \bar{v}_{\text{ion}} \frac{E_{\text{ion}}}{T} \left(\nu - \frac{\bar{T}}{\nu_{\text{ion}}} \frac{\partial \nu_{\text{ion}}}{\partial T} \right) \\ & \left. + \frac{1}{n} \left(\nu \frac{\bar{H}}{T} - \frac{\partial H}{\partial T} \right) \right\} \quad (15.39) \end{aligned}$$

$$B_p = \bar{\chi}_{\perp} (L_n^{-1} + 2\nu L_T^{-1}) \left(\frac{p\pi}{\Delta_{\text{TB}}} \right) \quad p = 1, 2, \dots M$$

The physical phenomena which are capable of driving radial temperature instabilities are represented by the terms in Eq. (15.37) or Eq. (15.38) which can be positive. The additional conductive cooling $-\bar{\chi}_{\perp}(p\pi/\Delta_{\text{TB}})^2$ associated with the temperature perturbation is stabilizing (negative). A negative temperature dependence ν_{ion} of L_z or ν_{at} is destabilizing because an increase in edge temperature would decrease the edge cooling rate. A positive temperature dependence of $\bar{\chi}_{\perp}(\nu > 0)$ would couple with the atomic physics terms (through their effect on the equilibrium power balance) to contribute a destabilizing term $\nu \left[\frac{3}{2} \bar{v}_{\text{at}} + \bar{v}_{\text{ion}} E_{\text{ion}}/T + \bar{n}_z \bar{L}_z/T \right]$ and would contribute a stabilizing conductive plus external heating term $-\nu \left(\bar{\chi}_{\perp} ((1/T)(\partial \bar{T}/\partial r))^2 + \bar{H}/nT \right)$. A positive temperature dependence $(\partial H/\partial T > 0)$ of any external heating mechanism would increase the edge heating (in response to a positive temperature perturbation) and thus be destabilizing, and conversely a negative temperature dependence would be stabilizing.

The heating term in Eq. (15.37) or Eq. (15.38) is stabilizing for collisional heating, for which the collision frequency $\nu \simeq T^{-3/2}$. For example, $H = \eta_{\parallel} j_{\parallel}^2$ for ohmic heating and

$H = \dot{N}_{\text{NBI}} E_{\text{NBI}} v_b$ for neutral beam heating, leading in both cases to

$$-\frac{1}{n} \left(v \frac{H}{T} - \frac{\partial H}{\partial T} \right) = -\left(v + \frac{3}{2} \right) \frac{H}{nT} \quad (15.40)$$

Thus, radial thermal instabilities in the plasma edge can potentially be driven by the presence of neutral atoms (the \bar{v}_{ion} and \bar{v}_{at} terms) and by the presence of impurities (the \bar{L}_z term). A positive temperature dependence of $\chi_{\perp}(v > 0)$ provides the mechanism by which neutral atoms and impurities can drive such pure temperature instabilities, in the absence of flow and density perturbations.

Because the stabilizing $\bar{\chi}_{\perp} (p\pi/\Delta_{\text{TB}})^2$ term increases with p , γ_2^{\pm} will be less positive (more negative) than γ_1 , and growth rates for higher order expansions ($m > 2$) would be expected intuitively to be even less positive (more negative). Thus, γ_1 provides a conservative estimate of the linear stability growth rate. This is an example of the general phenomenon of stabilization of the least stable mode via coupling to other more stable modes.

It is clear from Eq. (15.37) that the larger the temperature gradient, $L_T^{-1} \equiv -(1/T) \times (\partial \bar{T} / \partial r)$, characterizing the equilibrium solution, the more stable is that solution. In fact, when

$$L_T^{-1} \geq (L_T^{-1})_{\min} \equiv \left[\frac{\bar{n}_z \left(v \frac{\bar{L}_z}{T} - \frac{\partial L_z}{\partial T} \right) + \frac{3}{2} \bar{v}_{\text{at}} \left(v - 1 - \frac{\bar{T}}{v_{\text{at}}} \frac{\partial v_{\text{at}}}{\partial T} \right)}{v \chi_{\perp}} + \frac{\bar{v}_{\text{ion}} \left(\frac{E_{\text{ion}}}{T} \right) \left(v - \frac{\bar{T}}{v_{\text{ion}}} \frac{\partial v_{\text{ion}}}{\partial T} \right) - \left(\frac{\pi}{\Delta_{\text{TB}}} \right)^2 \bar{\chi}_{\perp} - \frac{1}{n} \left(v \frac{\bar{H}}{T} - \frac{\partial H}{\partial T} \right)}{v \chi_{\perp}} \right]^{\frac{1}{2}} \quad (15.41)$$

the growth rate $\gamma \leq 0$, and the mode is stable. Since no undamped ($\gamma = 0$) or growing ($\gamma > 0$) perturbation can exist for $L_T^{-1} > (L_T^{-1})_{\min}$, Eq. (15.41) defines a minimum threshold edge temperature gradient for the stabilization of edge localized thermal fluctuations. Using Eq. (15.41), Eq. (15.37) can be rewritten in a form which emphasizes this point

$$\gamma_1 = \frac{1}{3} v \bar{\chi}_{\perp} \left[(L_T^{-1})_{\min}^2 - (L_T^{-1})^2 \right] \quad (15.42)$$

15.3.2 Coupled Two-Dimensional Density–Velocity–Temperature Perturbations

In the previous section, purely radial perturbations were considered. This can be justified in part by the fact that the large value of the thermal diffusivity along the field lines will act to stabilize any perturbation along with field lines. However, there is no such inhibition for perturbations in the direction perpendicular to both the field lines and the radial direction.

We now extend the analysis to consider two-dimensional perturbations in the plane (r , \perp) perpendicular to the magnetic field and to consider the effect of coupled v_{\perp} , v_r and

density perturbations on the temperature perturbations. We also generalize the formalism to include convective as well as conductive heat transport. The governing equations are the ion particle balance equation

$$\frac{\partial n}{\partial t} + \frac{\partial}{\partial r}(n v_{ir}) + \frac{\partial}{\partial l_{\perp}}(n v_{i\perp}) = n v_{ion} \quad (15.43)$$

and a similar equation for the electrons; the ion radial momentum balance equation

$$m_i \frac{\partial(n v_{ir})}{\partial t} + \frac{\partial(n T_i)}{\partial r} - ne E_r - ne v_{i\perp} B = nm_i v_{ie}(v_{er} - v_{ir}) - nm_i v_{ir} v_{at} \quad (15.44)$$

where v_{ie} is the ion-electron collision frequency, and a similar equation for the electrons, but with $a(-e)$ in the third term and no v_{at} term; the ion perpendicular momentum equation

$$m_i \frac{\partial(n v_{i\perp})}{\partial t} + \frac{\partial(n T)}{\partial l_{\perp}} - ne E_{\perp} + ne v_{ir} B = nm_i v_{ie}(v_{e\perp} - v_{i\perp}) - nm_i v_{at} v_{i\perp} \quad (15.45)$$

and a similar equation for the electrons, but with $a(-e)$ in the third term and no v_{at} term; and the energy balance equation. For the case of strong temperature equilibration, we use the energy balance equations summed over ions and electrons

$$\begin{aligned} & 3 \frac{\partial(n T)}{\partial t} - \frac{\partial}{\partial r} \left[n(\chi_{ri} + \chi_{re}) \frac{\partial T}{\partial r} \right] - \frac{\partial}{\partial l_{\perp}} \left[n(\chi_{\perp} + \chi_{\perp e}) \frac{\partial T}{\partial l_{\perp}} \right] \\ & + \frac{5}{2} \frac{\partial(n T v_{ir})}{\partial r} + \frac{5}{2} \frac{\partial(n T v_{er})}{\partial r} + \frac{5}{2} \frac{\partial(n T v_{i\perp})}{\partial l_{\perp}} + \frac{5}{2} \frac{\partial(n T v_{e\perp})}{\partial l_{\perp}} \\ & = H - nn_z L_z - \frac{3}{2} n T v_{at} - n E_{ion} v_{ion} \end{aligned} \quad (15.46)$$

For the case of weak temperature equilibration, we use the separate ion and electron energy balance equations, with the equilibration term set to zero

$$\begin{aligned} & \frac{3}{2} \frac{\partial(n T_i)}{\partial t} - \frac{\partial}{\partial r} \left(n \chi_{ri} \frac{\partial T_i}{\partial r} \right) - \frac{\partial}{\partial l_{\perp}} \left(n \chi_{\perp i} \frac{\partial T_i}{\partial l_{\perp}} \right) + \frac{5}{2} \frac{\partial(n T_i v_{ir})}{\partial r} \\ & + \frac{5}{2} \frac{\partial(n T_i v_{i\perp})}{\partial l_{\perp}} = H_i - \frac{3}{2} n T_i v_{at} \end{aligned} \quad (15.47)$$

and

$$\begin{aligned} & \frac{3}{2} \frac{\partial(n T_e)}{\partial t} - \frac{\partial}{\partial r} \left(n \chi_{re} \frac{\partial T_e}{\partial r} \right) - \frac{\partial}{\partial l_{\perp}} \left(n \chi_{\perp e} \frac{\partial T_e}{\partial l_{\perp}} \right) + \frac{5}{2} \frac{\partial(n T_e v_{re})}{\partial r} \\ & + \frac{5}{2} \frac{\partial(n T_e v_{e\perp})}{\partial l_{\perp}} = H_e - nn_z L_z - n E_{ion} v_{ion} \end{aligned} \quad (15.48)$$

Note that with respect to the previous derivations, we have changed notation so that the subscript “ r ” refers to radial and the subscript “ \perp ” now refers to the direction perpendicular to B in the flux surface.

The equilibrium solution to Eq. (15.43) yields an equilibrium relationship among the radial density and velocity gradients and the ionization frequency

$$L_v^{-1} = - \left(L_n^{-1} + \frac{v_{\text{ion}}}{v_r} \right) - \left(\Delta_n^{-1} + \Delta_v^{-1} \right) \frac{v_{i\perp}}{v_{ir}} \simeq - \left(L_n^{-1} + \frac{v_{\text{ion}}}{v_r} \right) \quad (15.49)$$

where we have assumed in the last step that perpendicular gradients, $\Delta_n^{-1} \equiv -(1/n) \times (\partial n / \partial l_\perp)$, etc., are small compared to radial gradients in the plasma edge. We note that Eq. (15.49) sets the radial velocity profile to be consistent with the ionization source of ions and electrons.

The equilibrium solution to Eq. (15.44) and the similar equation for electrons yields expressions for the equilibrium perpendicular velocities

$$\begin{aligned} \bar{v}_{e\perp} &= \frac{-eE_r + T_e(L_n^{-1} + L_{T_e}^{-1})}{eB} \\ \bar{v}_{i\perp} &= \frac{-eE_r - T_i(L_n^{-1} + L_{T_i}^{-1})}{eB} \end{aligned} \quad (15.50)$$

The equilibrium solutions of Eq. (15.45) for ions and electrons can be added to obtain

$$(2\Delta_n^{-1} + \Delta_{T_i}^{-1} + \Delta_{T_e}^{-1}) = -\frac{v_{at}}{\Omega_i}(L_n^{-1} + L_{T_i}^{-1}) + \frac{e}{T_i}E_r \quad (15.51)$$

and subtracted to obtain

$$\begin{aligned} E_\perp &= v_r B - \frac{T_e}{e(T_e + T_i)} \left(\frac{v_{at}}{\Omega_i} \left(eE_r + T_i \left(L_n^{-1} + L_{T_i}^{-1} \right) \right) + \frac{v_{ie}}{\Omega_i} \left(1 + \frac{v_{ei}}{v_{ie}} \frac{c_{si}^2}{c_{se}^2} \right) \right. \\ &\quad \left. \times \left(L_n^{-1} (T_e + T_i) + T_e L_{T_e}^{-1} + T_i L_{T_i}^{-1} \right) \right) \end{aligned} \quad (15.52)$$

where $\Omega_i \equiv eB/m_i$ is the ion gyrofrequency.

For the strong temperature equilibration case, the equilibrium solution to Eq. (15.46) yields an equilibrium constraint on the temperature profile.

$$\begin{aligned} &- \bar{\chi}_r \left[\left(\frac{1}{T} \frac{\partial^2 T}{\partial r^2} \right) + L_T^{-1} (L_n^{-1} + v L_T^{-1}) \right] - \bar{\chi}_\perp \left[\frac{1}{T} \frac{\partial^2 T}{\partial l_\perp^2} + \Delta_T^{-1} (\Delta_n^{-1} + v \Delta_T^{-1}) \right] \\ &= 5\bar{v}_r (L_n^{-1} + L_T^{-1} + L_v^{-1}) + \frac{5}{2}\bar{v}_{i\perp} (\Delta_n^{-1} + \Delta_T^{-1} + \Delta_{vi}^{-1}) + \frac{5}{2}\bar{v}_{e\perp} (\Delta_n^{-1} + \Delta_T^{-1} + \Delta_{ve}^{-1}) \\ &\quad + \frac{\bar{H}}{nT} - \bar{n}_z \frac{\bar{L}_z}{T} - \bar{v}_{at} - \frac{E_{\text{ion}}}{T} \bar{v}_{\text{ion}} \end{aligned} \quad (15.53)$$

where $\chi_r \equiv \chi_{ri} + \chi_{re}$ and $\chi_\perp \equiv \chi_{\perp i} + \chi_{\perp e}$.

For the weak temperature equilibration case, the equilibrium solutions to Eqs. (15.47) and (15.48) provide a constraint on the equilibrium ion temperature profile

$$\begin{aligned} -\bar{\chi}_{ir} \left[\left(\frac{1}{T} \frac{\partial^2 T_i}{\partial r^2} \right) + L_{Ti}^{-1} (L_n^{-1} + v L_{Ti}^{-1}) \right] - \bar{\chi}_{i\perp} \left[\frac{1}{T_i} \frac{\partial^2 T_i}{\partial l_\perp^2} + \Delta_{Ti}^{-1} (\Delta_n^{-1} + v \Delta_{Ti}^{-1}) \right] \\ = \frac{5}{2} \bar{v}_{ir} (L_n^{-1} + L_{Ti}^{-1} + L_{vi}^{-1}) + \frac{5}{2} \bar{v}_{i\perp} (\Delta_n^{-1} + \Delta_{Ti}^{-1} + \Delta_{vi}^{-1}) + \frac{\bar{H}_i}{n T_i} - \frac{3}{2} \bar{v}_{at} \end{aligned} \quad (15.54)$$

and a similar constraint on the equilibrium electron temperature profile but with the last two terms on the right side replaced by $\left(\frac{\bar{H}_e}{n T_e} - \bar{n}_z \frac{\bar{L}_z}{T_e} - \frac{E_{ion}}{T_e} \bar{v}_{ion} \right)$.

Certain other physical constraints will be imposed on the equilibrium solution. Charge neutrality requires that the equilibrium solutions satisfies $n_i = n_e \equiv n$, which in turn requires $L_{ni}^{-1} = L_{ne}^{-1} \equiv L_n^{-1}$. Ambipolarity requires $v_{ir} = v_{er} \equiv v_r$, which in turn requires $L_{vi}^{-1} = L_{ve}^{-1} \equiv L_v^{-1}$. The current must satisfy

$$0 = \nabla \cdot \mathbf{j} = \frac{\partial}{\partial r} (n_i v_{ir} - n_e v_{er}) + \frac{\partial}{\partial l_\perp} (n_i v_{i\perp} - n_e v_{e\perp}) \quad (15.55)$$

which leads to the requirement $v_{i\perp} (\Delta_{ni}^{-1} + \Delta_{vi}^{-1}) = -v_{e\perp} (\Delta_{ne}^{-1} + \Delta_{ve}^{-1})$, when charge neutrality and ambipolarity are used. Since $v_{i\perp} \neq -v_{e\perp}$ in general, $(\Delta_{ni}^{-1} + \Delta_{vi}^{-1}) = (\Delta_{ne}^{-1} + \Delta_{ve}^{-1}) = 0$ is required in order to satisfy Eq. (15.55).

Now we consider a two-dimensional (r, \perp) perturbation about the equilibrium solutions of the form

$$x'(r, l_\perp, t) = x(r, l_\perp) + \tilde{x} \sin \left(\frac{\pi r}{\Delta_{TB}} \right) \sin \left(\frac{\pi l_\perp}{L_\perp} \right) e^{\omega t} \quad (15.56)$$

where the overbar previously used to denote the equilibrium solution is now omitted.

Here we have generalized Eq. (15.34) to include an expansion in separable functions, one of which vanishes at the separatrix and at a distance Δ_{TB} inside the separatrix, and the other of which vanishes at $l_\perp = 0$ and $l_\perp = L_\perp \simeq$ the poloidal circumference of the plasma. We have here retained only the leading term in a more general expansion. By analogy with the result of the previous section, this approximation includes only the least stable mode without the stabilizing effect of coupling to more stable modes. Thus, we expect to derive a conservative estimate of the growth rate.

Using these expansions in Eq. (15.43) for ions and electrons leads, upon linearizing, to

$$\frac{\tilde{n}_i}{n} \left(\hat{\omega} - L_v^{-1} \hat{v}_r - \Delta_{vi}^{-1} \hat{v}_{i\perp} \right) + (-\hat{v}_{ion}) \frac{\tilde{n}_e}{n} + \frac{\tilde{v}_{ir}}{c_{si}} \left(-L_n^{-1} \right) + \frac{\tilde{v}_{i\perp}}{c_{si}} \left(-\Delta_n^{-1} \right) = 0 \quad (15.57)$$

and a similar equation for electrons, except that the \hat{v}_{ion} term is included with the terms in the first () and there is no \tilde{n}_i/n_i term. The carat () indicates that the quantity is divided by $c_s \equiv \sqrt{2T/m}$ for the species.

Using the expansions of Eq. (15.56) in Eq. (15.55), linearizing, and then using the results in Eq. (15.57) and in the equivalent equation for electrons leads to

$$\frac{\tilde{n}_i}{n_i} = \frac{\tilde{n}_e}{n_e} \equiv \frac{\tilde{n}}{n} \quad (15.58)$$

i.e. the ion and electron densities are constrained by $\nabla \cdot \mathbf{j} = 0$ to fluctuate together.

Next, we use the expansion of Eq. (15.56) in Eqs. (15.44) and (15.45) and the equivalent equations for the electrons, linearize, note that $v_{ei}/\Omega_e \ll 1$, $v_{ie}/\Omega_i \ll 1$, $v_{at}/\Omega_i \ll 1$ and restrict attention to low frequency perturbations such that $\omega/\Omega_e \ll \omega/\Omega_i \ll 1$, and make use of Eqs. (15.50) to obtain

$$\begin{aligned} \frac{\tilde{v}_{er}}{c_{se}} &\simeq \frac{\tilde{n}}{n} \left(-\Delta_n^{-1} \rho_e \right) + \frac{\tilde{T}_e}{T_e} \left(-\Delta_n^{-1} \rho_e \right) \\ \frac{\tilde{v}_{ir}}{c_{si}} &\simeq \frac{\tilde{n}}{n} \left(\Delta_n^{-1} \rho_i \right) + \frac{\tilde{T}_i}{T_i} \left(\Delta_n^{-1} \rho_i \right) \\ \frac{\tilde{v}_{e\perp}}{c_{se}} &\simeq \frac{\tilde{n}}{n} \left(-L_n^{-1} \rho_e \right) + \frac{\tilde{T}_e}{T_e} \left(L_n^{-1} \rho_e \right) \\ \frac{\tilde{v}_{i\perp}}{c_{si}} &\simeq \frac{\tilde{n}}{n} \left(L_n^{-1} \rho_i \right) + \frac{\tilde{T}_i}{T_i} \left(-L_n^{-1} \rho_i \right) \end{aligned} \quad (15.59)$$

where $\rho = mc_s/eB$ is the gyroradius.

Using the expansions of Eq. (15.56) in Eq. (15.46), using the previous equilibrium constraints and using Eqs. (15.57) to (15.59) leads to an expression for the growth rate in the case of strong temperature equilibration in the transport barrier

$$\begin{aligned} \gamma_{NVT} = -\frac{1}{3} \left\{ \chi_r \left[\left(\frac{\pi}{\Delta_{AB}} \right)^2 + v L_T^{-2} \right] + \chi_\perp \left[\left(\frac{\pi}{L_\perp} \right)^2 + v \Delta_T^{-2} \right] + 5v_r v L_T^{-1} \right. \\ + \frac{5}{2} v \Delta_T^{-1} (v_{i\perp} + v_{e\perp}) - n_z \left(v \frac{L_z}{T} - \frac{\partial L_z}{\partial T} \right) - v_{ion} \left[\left(5(v-1) - 3 \frac{T}{v_{ion}} \frac{\partial v_{ion}}{\partial T} \right) \right] \\ - v_{ion} \frac{E_{ion}}{T} \left(v - \frac{T}{v_{ion}} \frac{\partial v_{ion}}{\partial T} \right) - \frac{3}{2} v_{at} \left[v - \left(1 + \frac{T}{v_{at}} \frac{\partial v_{at}}{\partial T} \right) \right] \\ \left. + \frac{1}{n} \left(v \frac{H}{T} - \frac{\partial H}{\partial T} \right) \right\} \quad (15.60) \end{aligned}$$

where $\chi_r = (\chi_{ri} + \chi_{re})$ and $\chi_\perp = (\chi_{i\perp} + \chi_{e\perp})$.

Comparison of Eqs. (15.60) and (15.37) shows the effect of two-dimensional (r, l_\perp) perturbations in density, velocity and temperature instead of one-dimensional (r) perturbations in temperature and the effect of representing heat convection. Note that the radial convection (v_r) term would also have been obtained in Eq. (15.37) if convection had been taken into account. Taking the second, perpendicular dimension into account results in additional heat conduction (χ_\perp) and convection (v_\perp) terms, which are probably stabilizing on the whole but are small compared to the equivalent radial (χ_\perp, v_r) terms, in general. The inclusion of density and velocity perturbations introduces the potentially important

sixth (v_{ion}) term in Eq. (15.60), which arises from the dependence of the density profile on the ionization rate via Eq. (15.49) and is generally destabilizing.

Simple estimates indicate that the ion–electron equilibration time in the transport barrier is long compared to the time required for a particle to diffuse across the transport barrier of width $\Delta_{\text{TB}} \simeq 1 \text{ cm}$ to $2 \text{ cm} (\Delta^2/D_{\perp} \simeq (1-2)^2/10^3 \sim 10^{-3} \text{ s})$.

Thus, the weak temperature equilibration case is more realistic. Using Eq. (15.56) to expand the ion density, velocities and temperature in Eq. (15.47), linearizing, and using the previous equilibrium constraints on the ion distributions leads to a solution for the growth rate of the thermal instability mode associated with ion temperature perturbations, in the weak equilibration limit

$$\begin{aligned} \gamma_{NVT_i} = & -\frac{1}{3} \left\{ 2\chi_{ir} \left[\left(\frac{\pi}{\Delta_{\text{TB}}} \right)^2 + v L_{T_i}^{-2} \right] + 2\chi_{i\perp} \left[\left(\frac{\pi}{L_{\perp}} \right)^2 + v \Delta_{T_i}^{-2} \right] \right. \\ & + 5v_r v L_{T_i}^{-1} + 5v_{i\perp} v \Delta_{T_i}^{-1} - 5(v-1)v_{\text{ion}} \\ & - 3v_{\text{at}} \left[v - \left(1 + \frac{T_i}{v_{\text{at}}} \frac{\partial v_{\text{at}}}{\partial T_i} \right) \right] - 5\rho_i c_{si} (L_n^{-1} \Delta_{T_i}^{-1} - L_{T_i}^{-1} \Delta_n^{-1}) \\ & \left. + \frac{2}{n} \left(v \frac{H_i}{T_i} - \frac{\partial H_i}{\partial T_i} \right) \right\} \quad (15.61) \end{aligned}$$

Making use of Eq. (15.56) to expand the electron density, velocities and temperature in Eq. (15.48), linearizing, and using the previous equilibrium constraints on the electron distribution leads to a solution for the growth rate of the thermal instability mode associated with electron temperature perturbations, in the weak equilibration limit

$$\begin{aligned} \gamma_{NVT_e} = & -\frac{1}{3} \left\{ 2\chi_{er} \left[\left(\frac{\pi}{\Delta_{\text{TB}}} \right)^2 + v L_e^{-2} \right] + 2\chi_{e\perp} \left[\left(\frac{\pi}{L_{\perp}} \right)^2 + v \Delta_{T_e}^{-2} \right] \right. \\ & + 5v v_r L_{T_e}^{-1} + 5v_{e\perp} v \Delta_{T_e}^{-1} - 2n_z \left(v \frac{L_z}{T_e} - \frac{\partial L_z}{\partial T_e} \right) \\ & - v_{\text{ion}} \left[5(v-1) - 3 \frac{T_e}{v_{\text{ion}}} \frac{\partial v_{\text{ion}}}{\partial T_e} \right] - 2v_{\text{ion}} \frac{E_{\text{ion}}}{T_e} \left(v - \frac{T_e}{v_{\text{ion}}} \frac{\partial v_{\text{ion}}}{\partial T_e} \right) \\ & \left. + 5\rho_e c_{se} (L_{T_e}^{-1} \Delta_n^{-1} - \Delta_{T_e}^{-1} L_n^{-1}) + \frac{2}{n} \left(v \frac{H_e}{T_e} - \frac{\partial H_e}{\partial T_e} \right) \right\} \quad (15.62) \end{aligned}$$

15.3.3 Spontaneous Edge Transport Barrier Formation

In this section, the models previously discussed for the calculation of edge temperature gradients and of the growth rates of edge thermal instabilities are combined with a model for the enhancement of edge transport coefficients due to thermal instability growth rates. The composite model predicts the existence of threshold values of the edge power flux at which the edge transport coefficients sharply decrease and the edge temperature gradients sharply increase; i.e. an edge transport barrier forms. Predicted consequences of this transport barrier formation mechanism are shown to be consistent with phenomena observed experimentally in conjunction with the L–H transition.

Subject to the assumption of weak ion-electron equilibration within the thin edge region, the growth rates, γ , of the thermal instabilities associated with both the ion and the electron power balances that were discussed in the previous section may be written in the form

$$\gamma = -\frac{2}{3} \left(\chi(vL_T^{-2} + k_r^2) + \frac{5}{2}v \frac{\Gamma_\perp}{n} L_T^{-1} - \alpha \right) \quad (15.63)$$

where the first two terms represent the stabilizing effect of heat conduction and convection, respectively, and the α -terms arise from the destabilizing atomic physics (including impurity radiation) cooling terms and the stabilizing effect of any heating that may be present in the plasma edge, and are given to leading order for ions (i) and electrons (e) by

$$\alpha_i = \frac{5}{2}(v-1)v_{ion} + \frac{3}{2}v_{at}^c \left[v - \left(1 + \frac{T_i}{v_{at}^c} \frac{\partial v_{at}^c}{\partial T_i} \right) \right] - \frac{1}{n} \left(v \frac{H_i}{T_i} - \frac{\partial H_i}{\partial T} \right) \quad (15.64a)$$

and

$$\begin{aligned} \alpha_e = n_z \left(\frac{vL_z}{T_e} - \frac{\partial L_z}{\partial T_e} \right) + v_{ion} \left[\frac{5}{2}(v-1) + v \frac{E_{ion}}{T_e} - \left(\frac{3}{2} + \frac{E_{ion}}{T_e} \right) \frac{T_e}{v_{ion}} \frac{\partial v_{ion}}{\partial T_e} \right. \\ \left. - \frac{1}{n} \left(v \frac{H_e}{T_e} - \frac{\partial H_e}{\partial T_e} \right) \right] \end{aligned} \quad (15.64b)$$

The driving functions, α , the thermal diffusivities, χ , the particle fluxes, Γ_\perp , the non-radiative power fluxes, Q_\perp , and the temperatures, T , are in general different in the plasma edge for the ions and the electrons. Hence, the growth rates of thermal instabilities are in general different for ions and electrons. However, since the general form of the relevant equations is identical for ions and electrons, we will suppress subscripts in the following development, which applies for both species.

A simple and frequently used estimate of the incremental transport associated with instabilities with linear growth rate γ and de-correlation length δ is the mixing length estimate (chapter 10) $\Delta\chi \approx \gamma\delta^2$. Since we are considering instabilities with a radial wavelength k_r^{-1} , we take $\delta \approx k_r^{-1}$. Thus, we write the thermal diffusivity for ions and electrons in the edge as the sum of a ‘‘background’’ transport term, χ^0 , and a thermal instability term $C_\chi\gamma k_r^{-2}$

$$\chi = \chi^0 + C_\chi\gamma k_r^{-2}H(\gamma > 0) \quad (15.65)$$

where C_χ is an order unity constant and H is now the Heaviside function, which vanishes when $\gamma \leq 0$ and is unity when $\gamma > 0$.

The standard form for thermal conduction can be used to relate the average ion and electron temperature gradients in the edge to the corresponding heat diffusivities and average total power flux, Q_\perp , and convective particle flux, Γ_\perp , through the edge

$$G_\perp \equiv \left(\frac{Q_\perp}{nT} - \frac{5}{2} \frac{\Gamma_\perp}{n} \right) = \chi L_T^{-1} \quad (15.66)$$

The average values of Q_\perp and Γ_\perp in an edge region extending a distance Δ (here we drop the ‘‘TB’’ on Δ_{TB} used previously) inward from the separatrix, or last closed flux

surface, differ from the values of these quantities crossing the separatrix because of atomic physics cooling and ionization particle sources

$$\Gamma_{\perp} = \Gamma_{\perp}^{\text{sep}} - \frac{1}{2} n v_{\text{ion}} \Delta \quad (15.67\text{a})$$

$$Q_{\perp e} = Q_{\perp e}^{\text{sep}} + \frac{1}{2} n T_e \left(\frac{n_z L_z}{T_e} + \frac{3}{2} v_{\text{ion}} \right) \Delta \quad (15.67\text{b})$$

$$Q_{\perp i} = Q_{\perp i}^{\text{sep}} + \frac{1}{2} n T_i \frac{3}{2} v_{\text{at}}^c \Delta \quad (15.67\text{c})$$

Equation (15.63) can be solved for the threshold value of the average temperature gradient in the edge, above which thermal instabilities are suppressed, by setting $\gamma = 0$

$$(L_T^{-1})_{\text{thresh}} = \frac{((5/4)(\Gamma_{\perp}/n))}{\chi^0} \left[\sqrt{1 + \frac{(\chi^0(\alpha - \chi^0 k_r^2)/v)}{((5/4)(\Gamma_{\perp}/n))^2}} - 1 \right] \quad (15.68)$$

Equations (15.66) and (15.68) can be combined to obtain the threshold value of the average non-radiative power flux through the edge, above which thermal instabilities are suppressed

$$\left(\frac{Q_{\perp}}{n T} \right)_{\text{thresh}} = \left(\frac{5}{4} \frac{\Gamma_{\perp}}{n} \right) \left[\sqrt{1 + \frac{(\chi^0(\alpha - \chi^0 k_r^2)/v)}{((5/4)(\Gamma_{\perp}/n))^2}} + 1 \right] \quad (15.69)$$

These threshold values are different for ions and electrons, in general. For values of the ion or electron power flux greater than the respective threshold value, the respective thermal diffusivity is reduced to the background value, χ^0 , and the respective temperature gradient is decreased to $L_T^{-1} = G_{\perp}/\chi^0$.

However, for values of the ion or electron heat flux less than the threshold value, Eqs. (15.63), (15.65) and (15.66) can be reduced to quadratic equations in L_T^{-1} or χ that can be satisfied by two different values of the temperature gradient or thermal diffusivity

$$L_T^{-1} = \frac{\frac{1}{2} \left(1 + \frac{2}{3} C_{\chi} + \xi \right)}{\left(\frac{\xi v}{\alpha - \chi^0 k_r^2} \right) \left(\frac{Q_{\perp}}{n T} \right)} \times \left[1 \pm \sqrt{1 - \frac{4 \left(\frac{\xi}{\chi} \right) \left(1 + \frac{2}{3} C_{\chi} \right) \left(\frac{Q_{\perp}}{n T} \right) \left(\frac{Q_{\perp}}{n T} - \frac{5}{2} \frac{\Gamma_{\perp}}{n} \right)}{\left(1 + \frac{2}{3} C_{\chi} + \xi \right)^2}} \right] \quad (15.70)$$

and

$$\chi = \frac{\chi^0 \left(1 + \frac{2}{3} C_{\chi} + \xi \right)}{\left(1 + \frac{2}{3} C_{\chi} \right)} \times \left\{ 1 - \frac{1}{2} \left[1 \pm \sqrt{1 - \frac{4 \left(\frac{\xi}{\chi} \right) \left(1 + \frac{2}{3} C_{\chi} \right) \left(\frac{Q_{\perp}}{n T} \right) \left(\frac{Q_{\perp}}{n T} - \frac{5}{2} \frac{\Gamma_{\perp}}{n} \right)}{\left(1 + \frac{2}{3} C_{\chi} + \xi \right)^2}} \right] \right\} \quad (15.71)$$

where the two composite parameters

$$\xi \equiv \frac{\frac{2}{3}C_\chi k_r^{-2}(\alpha - \chi^0 k_r^2)}{\chi^0}, \quad \zeta \equiv \frac{\chi^0(\alpha - \chi^0 k_r^2)}{\nu} \quad (15.72)$$

together with Q_\perp/nT and Γ_\perp/n , determine the nature of the above solutions.

In the limit that $(Q_\perp/nT) \rightarrow (Q_\perp/nT)_{\text{thresh}}$ from below, the two roots for the heat diffusivity and temperature gradient given by Eqs. (15.70) and (15.71) approach

$$\chi_+^{\text{thresh}} = y\chi^0 \quad y = \begin{cases} 1 & \xi < 1 + \frac{2}{3} \\ \left(\frac{\xi}{1 + \frac{2}{3}C_\chi} \right) & \xi > 1 + \frac{2}{3}C_\chi \end{cases} \quad (15.73a)$$

$$\chi_-^{\text{thresh}} = z\chi^0 \quad z = \begin{cases} \left(\frac{\xi}{1 + \frac{2}{3}C_\chi} \right) & \xi < 1 + \frac{2}{3}C_\chi \\ 1 & \xi > 1 + \frac{2}{3}C_\chi \end{cases} \quad (15.73b)$$

and

$$(L_T^{-1})_+^{\text{thresh}} = \frac{\left(\frac{5}{4} \frac{\Gamma_\perp}{n} \right)}{\chi^0} \left[\sqrt{1 + \frac{y\xi}{\left(\frac{5}{4} \frac{\Gamma_\perp}{n} \right)^2}} - 1 \right] \quad y = \begin{cases} 1 & \xi < 1 + \frac{2}{3}C_\chi \\ \frac{1 + \frac{2}{3}C_\chi}{\xi} & \xi > 1 + \frac{2}{3}C_\chi \end{cases} \quad (15.74a)$$

$$(L_T^{-1})_-^{\text{thresh}} = \frac{\left(\frac{5}{4} \frac{\Gamma_\perp}{n} \right)}{\chi^0} \left[\sqrt{1 + \frac{z\xi}{\left(\frac{5}{4} \frac{\Gamma_\perp}{n} \right)^2}} - 1 \right] \quad z = \begin{cases} \frac{1 + \frac{2}{3}C_\chi}{\xi} & \xi < 1 + \frac{2}{3}C_\chi \\ 1 & \xi > 1 + \frac{2}{3}C_\chi \end{cases} \quad (15.74b)$$

When $\xi > 1 + 2C_\chi/3$, the $(-)$ roots of Eq. (15.73b) and Eq. (15.74b) continue across the threshold to become the single values obtained from Eq. (15.65) and Eq. (15.66) when $(Q_\perp/nT) \rightarrow (Q_\perp/nT)_{\text{thresh}}$ from above. However, the root $(L_T^{-1})_+$ increases discontinuously and the root χ_+ decreases discontinuously as (Q_\perp/nT) increases from below to above $(Q_\perp/nT)_{\text{thresh}}$, spontaneously forming an edge transport barrier region with reduced transport coefficients and steep gradient. This behavior is illustrated in Fig. 15.9 for typical edge parameters. We have plotted the more familiar temperature gradient scale length (L_T), which is just the inverse of (L_T^{-1}) . The root χ_+ will decrease and the root $(L_T^{-1})_+$ will increase as the power flux increases from below to above the power threshold for all combinations of parameters for which $\xi > 1 + 2C_\chi/3$.

If $\xi < 1 + \frac{2}{3}C_\chi$, it is the $(-)$ roots that undergo sharp changes at the threshold while the $(+)$ roots are continuous. The effect is the same, however, the formation of a transport

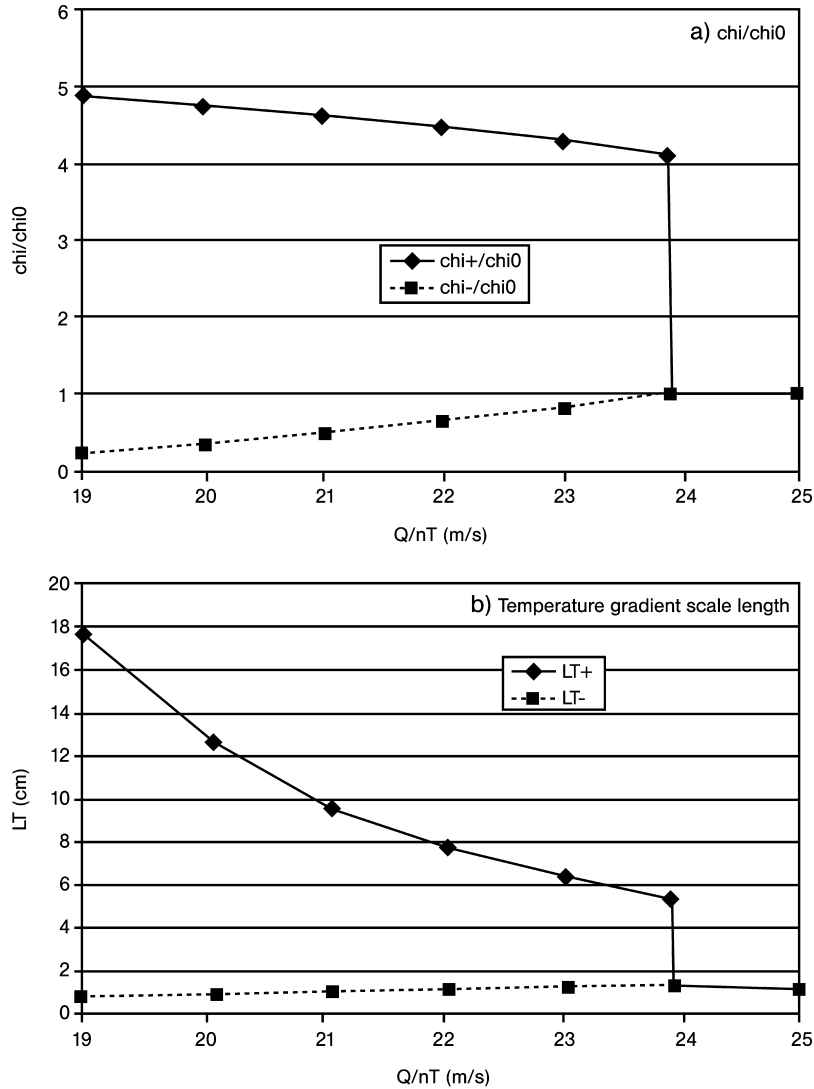


Figure 15.9. Behavior of temperature gradient scale length and thermal conductivity as power crossing separatrix passes through threshold value

barrier as the threshold given by Eq. (15.69) is exceeded by the average nonradiative power flux through the edge.

It is convenient for comparison with the empirical L-H power threshold of Eq. (15.1) to convert the nonradiative power flux threshold of Eq. (15.69) to a power threshold for the respective ion or electron thermal instability

$$P_{\text{thresh}} = \frac{5}{4} \Gamma_{\perp} T A_{\text{sep}} \left[\sqrt{1 + \frac{(\chi^0(\alpha - \chi^0 k_r^2)/\nu)}{\left(\frac{5}{4} \frac{\Gamma_{\perp}}{n}\right)^2}} + 1 \right] \quad (15.75)$$

where A_{sep} is the area of the plasma surface at the separatrix. We note that Eq. (15.75) defines a separate power threshold for ion and electron thermal instabilities, while the empirical fit of Eq. (15.1) is a threshold for the total nonradiative power across the LCFS.

15.3.4 Consistency with Observed L–H Phenomena

The general transport barrier formation behavior illustrated in Fig. 15.9, a sharp increase in temperature gradient and a sharp decrease in transport coefficient when the power flux crossing the separatrix exceeds a threshold value, is suggestive of the L–H transition. In this section we examine the qualitative consistency of other L–H transition phenomena observed experimentally in DIII-D with the predicted further consequences of a transport barrier formation, as required by momentum conservation. We also qualitatively compare certain general trends in the threshold power for the L–H transition observed in many tokamaks with the predictions of the thermal instability power threshold model of Eqs. (15.69) and (15.75).

15.3.4.1 L–H Transition Phenomena in DIII-D

The radial electric field in the DIII-D plasma edge region extending a few cm inside the separatrix was observed to become strongly negative and the local poloidal rotation, v_{θ} , was observed to become strongly positive at the time of a L–H transition. The sharp increase in edge temperature gradient which is predicted by the thermal instability suppression model when the power flux increases above the threshold value would produce a sharp increase in the (negative) edge pressure gradient, and radial momentum balance ($E_r \approx [(dp/dr)/ne - v_{\theta} B_{\phi} + v_{\phi} B_{\theta}]$) would require a compensating sharp negative change in the radial electric field. (If the particle transport coefficient was similarly related to thermal instability growth rates in the edge, one would also expect a sharp increase in density gradient when the threshold power flux is exceeded, which would further enhance this sharp increase in negative pressure gradient.) Hence, the sharp increase in negative edge pressure gradient predicted by the above model is consistent with the observed strongly negative radial electric field.

However, there is further experimental evidence from DIII-D that the change in pressure gradient is not sufficient to cause the measured change in radial electric field, from which it was concluded that it was instead a strong positive change in v_{\perp} or v_{θ} that was responsible for producing the strong negative E_r at the L–H transition. Such a positive change in v_{θ} can be reconciled with the prediction of the above model if it is assumed that the sharp decrease in transport predicted for the heat flux also obtains for the particle flux, which is supported by the experimental observation of a sharp reduction in the D_{α} signal at the L–H transition and by Langmuir probe measurements. It was shown in chapter 10 from poloidal momentum balance that the poloidal rotation for species "j" is driven by the

toroidal rotation, by the radial particle flux, by the frictional coupling to the rotation of the other species, and by viscous and inertial terms which include the pressure gradient (P'_j)

$$\begin{aligned} & \left[v_{jk}^* + v_{\text{ion},j}^* - q^2 \left(\frac{n_j^s}{\epsilon} + \frac{\Phi^s}{\epsilon} \right) - q^2 f_j \left(1 + \frac{A^{s/c}}{\epsilon} \right) \right] \hat{v}_{\theta j} \\ &= v_{jk} \hat{v}_{\theta k} - q^2 \hat{v}_{\phi j} \left[(\hat{v}_{\phi j} + \hat{P}'_j) \frac{\Phi^s}{\epsilon} \right] \\ & \quad - \frac{e_j B_\phi}{m_j} \frac{\Gamma_{\perp j}}{n_j} - q^2 f_j \left[(\hat{v}_{\phi j} + \hat{P}'_j) \frac{1}{2} \left\{ \frac{n_j^s}{\epsilon} \frac{\Phi^s}{\epsilon} + \left(3 + \frac{n_j^c}{\epsilon} \right) \frac{\Phi^c}{\epsilon} \right\} \right] \quad (15.76) \end{aligned}$$

where v_{jk} is the interspecies collision frequency, v_{at}^c and v_{ion} are the atomic physics reaction frequencies defined previously, f contains the collisionality dependence of the parallel viscosity, $\epsilon = r/R$, q is the safety factor, $\Phi^{s/c}$ and $n^{s/c}$ are the sine/cosine components of the poloidal variation in potential and density, and \tilde{A} is a function of sine and cosine components of the density and potential poloidal variations.

The [] term on the left in Eq. (15.76) is generally positive in the plasma edge of present experiments. Thus, with reference to Eq. (15.76), a reduction in Γ_{\perp} at the L–H transition would produce a positive v_θ , as seen experimentally, and this positive v_θ would produce a negative E_r via the radial momentum balance. Furthermore, the increase in negative pressure gradient at the L–H transition contributes to a change in v_θ through the viscous and inertial terms; in the few calculations made to date this contribution has been positive. For example, using edge parameters representative of DIII-D, it has been calculated that doubling the steepness of the edge gradients (from $L = 10$ cm to $L = 5$ cm) causes an order of magnitude increase in positive v_θ . Thus, the thermal instability suppression model is qualitatively consistent with the production of negative E_r and a positive v_θ just inside the separatrix at the L–H transition. (Note that the signs depend on the direction of the magnetic fields.)

The measured fluctuation level in the density and magnetic field in the plasma edge are observed to decrease sharply at the L–H transition. This observation is widely attributed to $v_{E \times B}$ shear (arising from the sheared, negative E_r) stabilization of turbulence. Since the thermal instability suppression model predicts a sheared negative E_r driven by v_θ , it is qualitatively consistent with this explanation for turbulence suppression, and in fact provides a trigger mechanism for the negative E_r .

While sharp increases in the edge temperature and pressure gradients are observed immediately in a L–H transition, the subsequent increases in edge pedestal density and temperature are observed to follow a short time later. The thermal instability suppression model predicts a sharp increase in the edge temperature gradient and a sharp decrease in the edge thermal diffusivity when the power flux through the edge increases from just below to just above the threshold value, but there is no prediction of sharp changes in density and temperature. One might then expect the pedestal density and temperature to build up on a slower transport time scale once this edge transport barrier is formed, which is qualitatively consistent with experimental observation.

Measured edge temperature gradients are observed to increase in the L-mode phase before the transition. This is qualitatively consistent with the predicted behavior of $(L_T^{-1})_+$ (see the plot of $(L_T)_+$ in Fig. 15.9(b)).

We note that the reigning paradigm for the L–H transition is that a sheared negative E_r produces a sheared $v_E \times B$ stabilization of edge turbulence that reduces edge transport, and the edge gradients increase as necessary to remove the power. The thermal instability suppression model provides a possible cause for this E_r trigger mechanism – a sharp increase of the negative edge pressure gradient and a sharp increase of the positive poloidal rotation due to a reduction in radial particle transport associated with the suppression of edge thermal instabilities and due to the increase in the magnitude of the negative pressure gradient.

We further note that other mechanisms (e.g. orbit loss and “Stringer spin-up” of v_θ) have also been suggested as a trigger mechanism for the production of the negative E_r . These models also qualitatively predict certain phenomena observed in conjunction with the L–H transition, and a detailed quantitative comparison of the predictions of the various models with experiment is needed. However, no general consensus has yet evolved on the trigger mechanism.

Although we have discussed phenomena that would result from the suppression of a single mode, there are probably a number of edge modes that could be present. In the first place, there may be multiple harmonics with wavelengths $k_{rm}^{-1} = \Delta_{\text{edge}}/m$, $m = 1, 2, 3, \dots$. Thus, as the power flux through the edge increases, one might expect from Eq. (15.69) that first the $m = 1$ mode with $k_{r1} = 1/\Delta_{\text{edge}}$ and then successively higher $m = 2, 3$, etc. modes with $k_{rm} = m/\Delta_{\text{edge}}$ would be stabilized. If the reduction in confinement associated with the stabilization of the mode is proportional to $k_{rm}^{-2} = (\Delta_{\text{edge}}/m)^2$, as assumed here, then it hence is largest for the $m = 1$ mode and decreases with increasing m . The L–H transition may correspond to (Q_\perp/nT) increasing above $(Q_\perp/nT)_{\text{thresh } m=1}$, and then as (Q_\perp/nT) further increases above the threshold of higher m -modes a further increase in confinement and steepening of the temperature gradients would be expected. Conversely, as the edge radiation or atomic physics cooling increased in an H-mode plasma such that (Q_\perp/nT) decreased below the threshold for successively lower m -modes, one would expect the edge transport to decrease and the temperature gradient to relax.

These qualitative predictions are consistent with experimental observation. The increase in calculated edge thermal instability growth rates in several gas fueled DIII-D H-mode shots have been found to correlate in time with measured confinement deterioration, and the deterioration of the pedestal gradient is a common observation in gas fueled DIII-D H-mode shots.

15.3.4.2 H-Mode Power Threshold Database

While the power threshold of Eq. (15.75) compared well with the experimental power threshold in several DIII-D shots, broader comparison remains to be made. However, a database on the parameter dependence of the L–H mode power threshold for ten tokamaks has been compiled and analyzed. The best regression fit of the threshold power to all of the data scales as $P \sim n^{0.58} B^{0.82}$, as given by Eq. (15.1), where n is the line averaged density. It is not possible to compare this with Eq. (15.69) or Eq. (15.75) without knowing

how the parameters that enter these equations depend on n and B . However, there are several qualitative trends in the database that can be compared with the thermal instability suppression model.

The measured threshold power for the L–H transition is observed to be much higher when the ion ∇B drift is away from the X-point than when it is towards the X-point, in single-null divertor discharges. Theoretically, when the ion ∇B drift is away from the X-point there is an outward component of the neoclassical particle flux, and conversely when the ion ∇B drift is towards the X-point there is an inward component of the neoclassical particle flux. Thus, other things being equal, one would expect a larger outward Γ_{\perp} when the ion ∇B drift is away from the X-point than when it is towards the X-point. Thus, with reference to Eq. (15.75), a larger power threshold would be predicted when the ion ∇B drift is away from the X-point than when it is towards the X-point, as observed experimentally.

A “hysteresis” effect is often observed for the power threshold; i.e. once the threshold for the L–H transition is exceeded and the plasma is in H-mode, the power through the edge can drop below this transition threshold value by as much as a factor of two before the plasma makes a back transition to L-mode. One might expect the particle flux Γ_{\perp} from the core to be reduced in H-mode relative to L-mode because of the better confinement, and this would seem to be supported by the much lower D_{α} signal for H-mode than for L-mode. One might also expect the neutral concentration (hence α of Eq. (15.64)) in the steeper H-mode edge pedestal to be reduced relative to L-mode because of the increased neutral attenuation due to the higher edge density. With reference to Eq. (15.75), both of these effects would reduce the power across the separatrix that is needed to stay in H-mode relative to the power needed to make the L–H transition, consistent with experimental observation.

Wall conditioning to reduce recycling has been observed generally to reduce the L–H power threshold. Since a reduction in recycling would reduce the neutral concentration in the plasma edge, hence α of Eq. (15.64), Eq. (15.75) would predict that wall conditioning would reduce the L–H power threshold, consistent with experimental observation.

15.4 MARFES

Under most conditions, tokamaks operate with a more or less poloidally and toroidally uniform band of radiation from the lower temperature plasma edge region. However, under certain conditions this uniform radiating band will evolve quickly into a highly poloidally nonuniform, but still toroidally uniform, radiating edge configuration known as a multi-faceted asymmetric radiation from the edge (MARFE). In divertor tokamaks the highly radiating region is usually near the X-point location, and in limited tokamaks it is usually on the inboard midplane.

MARFE formation can be understood as the onset of a radiative condensation type of thermal instability in the plasma edge that is driven primarily by the increase in impurity radiation with a decrease in plasma temperature over certain edge temperature ranges specific to different impurities. Once poloidally localized cooling starts, the increase in

local impurity radiation with decreasing temperature enhances the local cooling. In order to maintain constant pressure on the flux surface, plasma flows along the field lines into the cooled, highly radiative region, further enhancing the local radiative cooling.

The direct effect of MARFEs is to radiatively cool the edge, which is not, per se, detrimental to plasma performance. However, a universal consequence of MARFEs in H-mode plasmas is a back transition to inferior L-mode confinement, probably because the local nonradiative power flux across the LCFS is reduced below a threshold value (e.g. Eq. (15.69)) due to excessive local radiation from the MARFE.

Since the MARFE perturbation is observed to be localized in a thin band in the edge plasma and to be toroidally symmetric, we can analyze the thermal stability of essentially parallel (l_{\parallel}) perturbations localized (r) in a thin band in the edge of the plasma in a slab approximation and make use of toroidal symmetry to write $d/dl_{\perp} = \beta(d/dl_{\parallel})$, where $\beta = B_{\phi}/B_{\theta}$. Neglecting radial convection, parallel current and parallel electric field in the edge plasma just inside the LCFS, and assuming the impurity ions to be collisionally entrained to flow with the main plasma ions, the 3D fluid particle, parallel momentum and energy balance equations, summed over species, in the edge plasma are

$$\frac{\partial n}{\partial t} + \frac{\partial}{\partial l_{\parallel}} [n(v_{\parallel} + v_{\perp}\beta)] = n(v_{\text{ion}} - v_{\text{rec}}) \equiv nv_n \quad (15.77)$$

$$\begin{aligned} m \frac{\partial(nv_{\parallel})}{\partial t} - \frac{\partial}{\partial r} \left(\beta\eta_{\Omega} \frac{\partial v_{\parallel}}{\partial l_{\parallel}} \right) \\ + \frac{\partial}{\partial l_{\parallel}} \left[nm \left(v_{\parallel}^2 + v_{\parallel}\beta v_{\perp} \right) + nT - \frac{2}{3}\eta_0 \left(2 \frac{\partial v_{\parallel}}{\partial l_{\parallel}} - \beta \frac{\partial v_{\perp}}{\partial l_{\parallel}} \right) + \beta\eta_{\Omega} \frac{\partial v_{\parallel}}{\partial r} \right] \\ = nM_{\parallel} - nmv_{\parallel}(v_{\text{cx}} + v_{\text{el}}) + \left(C_e^{(2)} - \alpha C_i^{(2)} \right) n \frac{\partial T}{\partial l_{\parallel}} \end{aligned} \quad (15.78)$$

and

$$\begin{aligned} \frac{\partial}{\partial t} \left(3nT + \frac{1}{2}nmv_{\parallel}^2 \right) - \frac{\partial}{\partial l_{\parallel}} \left(n\chi_{\parallel} \frac{\partial T}{\partial l_{\parallel}} \right) - \frac{\partial}{\partial r} \left(n\chi_{\perp} \frac{\partial T}{\partial r} \right) \\ + \frac{\partial}{\partial l_{\parallel}} \left[\left(\frac{1}{2}nmv_{\parallel}^2 + 5nT \right) (v_{\parallel} + \beta v_{\perp}) - \frac{2}{3}\eta_0 \left(2 \frac{\partial v_{\parallel}}{\partial l_{\parallel}} - \beta \frac{\partial v_{\perp}}{\partial l_{\parallel}} \right) (v_{\parallel} - \beta v_{\perp}) \right] \\ = -nn_z L_z(T) - \frac{3}{2}nT(v_{\text{cx}} + v_{\text{el}}) - nE_{\text{ion}}v_{\text{ion}} \end{aligned} \quad (15.79)$$

where $\eta_0 = nmv_{\text{th}}qRf(v^*)$ and $\eta_{\Omega} = nT\tau/\Omega\tau$ are the parallel viscosity and gyroviscosity (chapter 10), v_{\parallel} and v_{\perp} are the ion velocities along the field lines and perpendicular to the field lines in the flux surface, nM_{\parallel} is the parallel momentum input to the plasma ions, the $C^{(2)}$ are thermal friction constants defined in chapter 14, and the other terms have their usual meaning.

We expand about the equilibrium solutions of Eq. (15.77) to (15.79)

$$n(r, l_{\parallel}, t) = \bar{n}(r) + \tilde{n} \exp[\omega t + i(k_{\parallel}l_{\parallel} + k_r r)] \quad (15.80)$$

and similarly for the parallel velocity and temperature, then substitute into Eq. (15.77) to Eq. (15.79) and take account of the equations satisfied by the equilibrium solutions to

eliminate terms, and linearize to obtain a dispersion relationship among the frequency ω and the wave propagation functions k_r and k_\parallel .

The requirement for thermal stability, $\text{Re}(\omega) \equiv \gamma \leq 0$, leads to a constraint on the maximum impurity density allowed for thermal stability of a mode with $k_r \approx k/\Delta_{\text{TB}}$ and $k_\parallel \approx (m + nqB_\theta/B)/qR$, with k, m and n integers. We have associated the radial extent of the perturbation with the transport barrier width and the parallel extent with the poloidal and toroidal connection lengths. The equilibrium solution has a uniform edge ($n, m = 0$).

The $k_\parallel = 0$ ($n = m = 0$) perturbation, corresponding to a uniform cooling or heating of the edge region, is stable at any impurity density if $dL_z/dT \geq vL_z/T$ (where $\chi_\perp \sim T^\nu$), but if this condition is not satisfied then there is a maximum impurity density consistent with thermal stability ($\text{Re}(\omega) = \gamma \leq 0$)

$$\begin{aligned} n_z \left(v \frac{L_z}{T} - \frac{\partial L_z}{\partial T} \right) &\leq (k_r^2 + vL_T^{-2})\chi_\perp + \frac{3}{2}\nu_{\text{at}} \left(\frac{T}{\nu_{\text{at}}} \frac{\partial \nu_{\text{at}}}{\partial T} + 1 - v \right) \\ &\quad + \frac{E_{\text{ion}}}{T} \nu_{\text{ion}} \left(\frac{T}{\nu_{\text{ion}}} \frac{\partial \nu_{\text{ion}}}{\partial T} - v \right) + 3T \frac{\partial \nu_n}{\partial T} \end{aligned} \quad (15.81)$$

where $L_T \equiv -T/(dT/dr)$ is the temperature radial gradient scale length. The $k_\parallel = 0$ ($n = m = 0$) instability is stabilized by a positive temperature dependence of χ_\perp ($v > 0$) and is de-stabilized by atomic physics and radiation cooling.

The situation with the ($n \neq 0$ and/or $m \neq 0$) modes is more complex. The stabilizing effect of parallel conductivity along field lines and the destabilizing condensation effect both come into play, the thermal friction force and the parallel viscosity enter through the parallel flow fluctuation coupling, and the temperature dependences of the atomic collision frequencies enter directly through the temperature fluctuations and indirectly through the coupled parallel flow and density fluctuations.

The ($n \neq 0$ and/or $m \neq 0$) modes are unconditionally stable when $dL_z/dT > (v + K_1)L_z/T$, where

$$K_1 = 1 - \left[\frac{4}{3}\tau_{ii} + \nu_{\text{at}} \left(\frac{qR}{mc_s} \right)^2 \right] T \frac{\partial \nu_n}{\partial T} \quad (15.82)$$

except possibly at very low temperatures where the ionization and recombination frequencies vary rapidly with T . On the other hand, if $dL_z/dT < (v + K_1)L_z/T$, there is a maximum impurity density for which the mode is stable, given by

$$\begin{aligned} n_z \left[(v + K_1) \frac{L_z}{T} - \frac{\partial L_z}{\partial T} \right] &\leq \left[k_r^2 + L_T^{-1} \left(vL_T^{-1} - K_1 L_n^{-1} \right) \right] \chi_\perp \\ &\quad + \frac{3}{2}\nu_{\text{at}} \left(\frac{T}{\nu_{\text{at}}} \frac{\partial \nu_{\text{at}}}{\partial T} + 1 - \nu_{\text{at}} \right) + \frac{E_{\text{ion}}}{T} \nu_{\text{ion}} \left(\frac{T}{\nu_{\text{ion}}} \frac{\partial \nu_{\text{ion}}}{\partial T} - v \right) + 5T \frac{\partial \nu_n}{\partial T} + k_\parallel^2 \chi_\parallel \end{aligned} \quad (15.83)$$

A number of interesting points are brought out by comparison of Eq. (15.81) for $k_\parallel = 0$ ($n = m = 0$) and Eq. (15.83) for ($n \neq 0$ and/or $m \neq 0$). Using the equilibrium heat balance constraint, $-d/dr(n\chi_\perp dT/dr) = -\chi_\perp L_T^{-1}[L_n^{-1} + (v + 1)L_T^{-1}] =$

$-nn_z L_z - 3/2nT(\nu_{\text{cx}} + \nu_{\text{el}}) - nE_{\text{ion}}$, it can be seen that a positive temperature dependence of $\chi_{\perp}(\nu > 0)$ contributes a term to the growth rate of both the $k_{\parallel} = 0$ ($n = m = 0$) and the ($n \neq 0$ and/or $m \neq 0$) modes

$$\Delta\gamma = \nu \left(-\chi_{\perp} L_T^{-2} + \frac{n_z L_z}{T} + \frac{3}{2} \nu_{\text{at}} + \frac{E_{\text{ion}}}{T} \nu_{\text{ion}} \right) \quad (15.84)$$

The first, radial conduction term is stabilizing ($\Delta\gamma < 0$), but the other terms are destabilizing.

The major differences in stability of the ($n \neq 0$ and/or $m \neq 0$) and the ($n = m = 0$) modes are due to the parallel conduction and condensation effects which are present for the ($n \neq 0$ and/or $m \neq 0$) modes. Because χ_{\parallel} is very large, parallel heat conduction is large in proportion to the parallel temperature gradient of the mode, contributing a stabilizing term to the growth rate for the $k_{\parallel} \neq 0$ modes

$$\Delta\gamma = -k_{\parallel}^2 \chi_{\parallel} = - \left[\frac{(m + nqB_{\theta}/B)}{qR} \right]^2 \chi_{\parallel} \quad (15.85)$$

which make successively higher k_{\parallel} modes successively more stable.

The existence of parallel fluctuations in the parallel flow for the ($n \neq 0$ and/or $m \neq 0$) modes allows a local density change of opposite sign from the temperature change, the condensation effect, which destabilizes these modes

$$\begin{aligned} \Delta\gamma &= \frac{2n_z L_z}{T} - (1 + \nu) L_T^{-2} \chi_{\perp} + \frac{3}{2} \nu_{\text{at}} + \frac{E_{\text{ion}}}{T} \nu_{\text{ion}} \\ &= \frac{n_z L_z}{T} + L_n^{-1} L_T^{-1} \chi_{\perp} \end{aligned} \quad (15.86)$$

The temperature dependence of the net ionization source $n\nu_{\text{n}} \equiv n(\nu_{\text{ion}} - \nu_{\text{rec}})$ modifies the condensation effect to further enhance the instability of ($n \neq 0$ and/or $m \neq 0$) modes

$$\Delta\gamma = \frac{T}{k_{\parallel}^2} \frac{\partial \nu_{\text{n}}}{\partial T} \left(k_{\parallel}^2 \frac{4}{3} \tau_{ii} c_s + \nu_{\text{at}} \right) \left(\frac{n_z L_z}{T} + \Delta_n^{-1} \Delta_T^{-1} \chi_{\perp} \right) \quad (15.87)$$

The radiative condensation effect is represented by the K_1 terms in Eq. (15.83).

Clearly, the least stable mode will be a ($n \neq 0$ and/or $m \neq 0$) mode, in which the destabilizing condensation effect is present, but with $k_{\parallel} \approx 0$ so that the stabilizing parallel conduction effect is not significant. This mode represents an almost uniform cooling (or heating) of the edge plasma. Numerical multimode calculations indicate that such a $k_{\parallel} \approx 0$ mode is the first to go unstable, but that it quickly couples to other $k_{\parallel} \neq 0$ modes which evolve into a highly poloidally asymmetric plasma edge characteristic of the MARFE observations. These multimode calculations also showed that the calculated growth rate is independent of how many (m, n) modes are included in the calculation, provided only that the $k_{\parallel} \approx 0$ mode is included, indicating that an analysis of a single $k_{\parallel} \approx 0$ mode will lead to a good estimate of the initial linear growth rate and hence to a prediction of the onset of a MARFE.

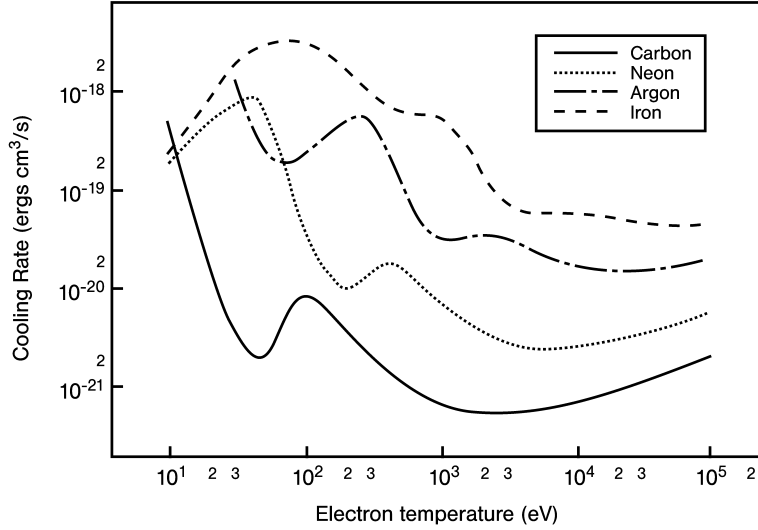


Figure 15.10. Radiation cooling rate as a function of local electron temperature for coronal equilibrium

Thus, we develop a conservative estimate for the threshold edge density for MARFE onset by using Eq. (15.83) for a ($n \neq 0$ and/or $m \neq 0$) mode (thus including the destabilizing condensation effect) but take the $k_{\parallel} \rightarrow 0$ limit to remove the stabilizing effect of parallel heat conduction along the field lines. Since the presence of neutral atoms can play a major role, both directly through the atomic physics reaction rates indicated in this equation and indirectly through the enhancement of the impurity radiation emissivity (chapter 13), we define $f_z \equiv n_z/n$ and $f_0 \equiv n_0/n$ and rewrite Eq. (15.83) as a threshold on the plasma density in the edge region for MARFE onset

$$\begin{aligned}
 n_{\text{MARFE}}^2 \equiv & \left\{ f_{\text{cond}} Q_{\perp} \left[v L_T^{-2} + (C^{(2)} - 1) L_n^{-1} \right] \right\} \\
 & \times \left(T \left\{ f_z \left[\left(v + 1 - C^{(2)} \right) \frac{L_z}{T} - \frac{\partial L_z}{\partial T} \right] \right. \right. \\
 & \quad \left. \left. + f_0 \left[\frac{E_{\text{ion}} \langle \sigma v \rangle_{\text{ion}}}{T} \left(v - \frac{T}{\langle \sigma v \rangle_{\text{ion}}} \frac{\partial \langle \sigma v \rangle_{\text{ion}}}{\partial T} \right) \right] \right. \right. \\
 & \quad \left. \left. + f_0^{\text{cold}} \left[\frac{3}{2} (\langle \sigma v \rangle_{\text{ex}} + \langle \sigma v \rangle_{\text{el}}) \left(v - 1 - T \frac{\partial (\langle \sigma v \rangle_{\text{ex}} + \langle \sigma v \rangle_{\text{el}}) / \partial T}{(\langle \sigma v \rangle_{\text{ex}} + \langle \sigma v \rangle_{\text{el}})} \right) \right] \right\} \right)^{-1} \quad (15.88)
 \end{aligned}$$

where f_{cond} is the conductive fraction of the nonradiative heat flux, the transport relation $f_{\text{cond}} Q_{\perp} = n T \chi_{\perp} L_T^{-1}$ has been used, f_0^{cold} refers to the concentration of “cold” neutral atoms which have just entered the plasma edge from the SOL and have not yet had a collision, the volumetric recombination terms have been suppressed and $K_1 \approx 1$ has been used.

The threshold edge density for MARFE onset given by Eq. (15.88) increases with the nonradiative heat flux across the LCFS (Q_{\perp}) and the steepness of the edge temperature gradient (L_T^{-1}) and decreases with impurity (f_z) and neutral atom (f_0 , f_0^{cold}) concentrations in the edge plasma. The dependence on edge temperature is rather more complex than the explicit $\sim 1/T$ dependence displayed in the above equation. The temperature dependence of the impurity emissivity, shown in Fig. 15.10 for several impurities, plays a major role in determining the temperature dependence of n_{MARFE} , and the less dramatic temperature dependencies of the atomic physics reaction rates may also be important in the lower range of edge temperatures.

15.5 Radiative Mantle

In future tokamak reactors, in which hundreds of MW of power would be exhausted across the LCFS, the heat load on the divertor targets would be excessive if this power were concentrated on the narrow (order of cm) toroidal strip that is the divertor target strike zone. As a remedy, it has been suggested to inject impurities specifically chosen to be only partially ionized at the edge plasma temperature, which would result in copious radiation from the plasma edge to the surrounding wall. In effect the power would be conducted outward from the center of the plasma to the edge, where it would be mostly radiated uniformly to the large first wall area, rather than concentrated on the small area of the divertor target strike zone.

Injection of impurities seems paradoxical at first glance, given the amount of effort that has been devoted to preventing intrinsic impurities from entering the plasma and degrading the plasma performance. The key to the practicality of the radiative mantle is the temperature dependence of the impurity cooling emissivity shown in Fig. 15.10. L_z increases with T at low temperature as the outermost few electrons are being ionized, passes through a peak range corresponding to +3 or +4 ionization, then decreases with increasing ionization until fully stripped, and finally increases as $\sim T^{\frac{1}{2}}$ due to bremsstrahlung. If the edge plasma temperature corresponds to the peak radiative temperature range for the injected impurity, then the impurity will radiate copiously as it passes inward through the edge plasma, but the radiation will decrease sharply as the impurity diffuses further inward into the higher temperature plasma core and becomes fully ionized.

As can be seen in Fig. 15.10, the peak radiative cooling temperature range generally increases with the atomic number of the impurity species. For example, the peak range is < 10 eV for carbon, 20 eV to 50 eV for neon, and 200 eV to 400 eV for Kr.

The total radiative power fraction, γ_{tot} , and the local radiative power fractions from the SOL/divertor, γ_{SOL} , from the radiating mantle in the plasma edge, γ_m , and from the plasma core inside the mantle, γ_{core} , are shown in Fig. 15.11 for a simulation of the future ITER plasma (chapter 19). These simulations were constrained to have minimal deleterious effect on the overall plasma power balance (i.e. < 5 % reduction in fusion alpha heating, small reduction only in Q_p).

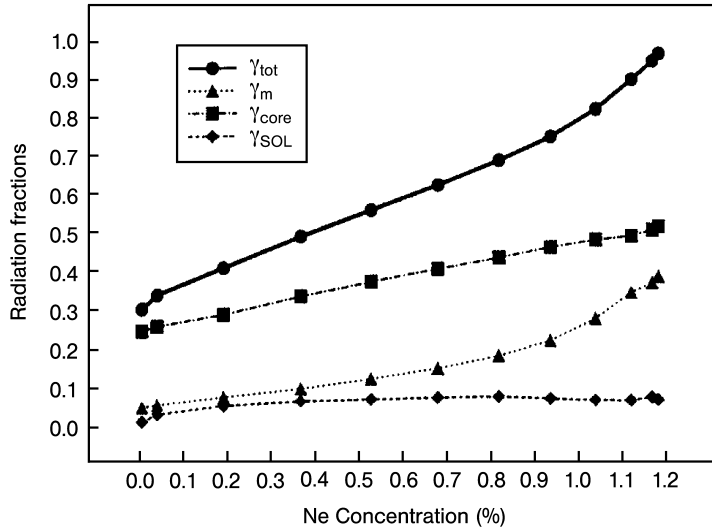


Figure 15.11. Radiation fractions from different plasma regions in a simulation of neon injection to form a radiative mantle in the future ITER plasma

15.6 Edge Operation Boundaries

As the discussion of this chapter makes clear, there are a number of limiting phenomena that create practical operational boundaries in the edge parameter space of tokamaks. If the pressure or pressure gradient is too large, MHD instabilities will be a problem. Access to H-mode requires stabilization of edge instabilities that otherwise would enhance transport. MARFE formation limits the allowable edge plasma density, by an amount that depends on the edge temperature, heating power, and impurity and neutral atom concentrations. The effect of these various limiting phenomena is reflected in the experimentally determined edge operational space for tokamaks, as given for ASDEX upgrade in Fig. 15.12.

15.7 Ion Particle Transport in the Edge*

The importance of the edge pedestal region in establishing and maintaining high confinement mode (H-mode) plasmas is now well established. The temperature and density gradient scale lengths ($L_x \equiv -x/(dx/dr)$) in the edge pedestal are determined by transport constraints, at least between or in the absence of ELMs. Expressions for calculating (L_{T_e} , L_{T_i} , L_n) in terms of local particle and heat fluxes from the core, local transport coefficients, atomic physics effects associated with recycling neutral atoms and impurities were presented in section 15.1. These expressions were based on the conventional heat conduction closure relation $q = nT\chi L_T^{-1}$ and the pinch-diffusion particle flux relation $\Gamma = nDL_n^{-1} + v_p$. The heat conduction relation is theoretically well founded, but the pinch-diffusion relation is heuristic. The purpose of this section is (1) to present a theoretically well founded pinch-diffusion model for particle fluxes in the edge pedestal and

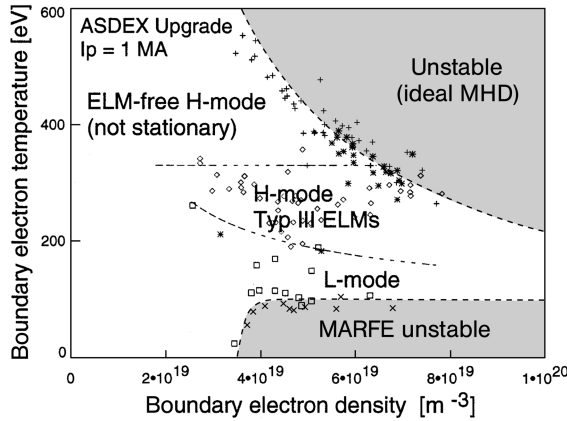


Figure 15.12. Edge operational boundaries for ASDEX upgrade

(2) to employ this model to develop an expression for the first-principles calculation of density gradient scale lengths in the edge pedestal.

15.7.1 Generalized ‘‘Pinch-Diffusion’’ Particle Flux Relations

The particle continuity equation for ion species ‘‘ j ’’ is

$$\nabla \cdot n_j \mathbf{v}_j = S_j \quad (15.89)$$

where $S_j(r, \theta) = n_e(r, \theta)n_{j0}(r, \theta)\langle\sigma v\rangle_{\text{ion}} \equiv n_e(r, \theta)v_{\text{ion}}(r, \theta)$ is the ionization source rate of ion species ‘‘ j ’’ and n_{j0} is the local concentration of neutrals of species ‘‘ j ’’. Taking the flux surface average of this equation yields $\langle(\nabla \cdot n_j \mathbf{v}_j)_r\rangle = \langle S_j \rangle$ because $\langle(\nabla \cdot n_j \mathbf{v}_j)_\theta\rangle = 0$ identically and $\langle(\nabla \cdot n_j \mathbf{v}_j)_\phi\rangle = 0$ by axisymmetry, which allows Eq. (15.89) to be written

$$\langle(\nabla \cdot n_j \mathbf{v}_j)\rangle_\theta = S_j - \langle S_j \rangle \equiv \tilde{S}_j \quad (15.90)$$

Integration of this equation, in toroidal (r, θ, ϕ) coordinates, yields

$$n_j v_{\theta j} = \frac{K_j \bar{B}_\theta + r \bar{B}_\theta \int_0^\theta (1 + \epsilon \cos \theta) \tilde{S}_j d\theta}{1 + \epsilon \cos \theta} \equiv [K_j(r) + I_j(r, \theta)] B_\theta(r) \quad (15.91)$$

where $K_j = \langle n_j v_{\theta j} \rangle / \bar{B}_\theta \approx \bar{n}_j \bar{v}_{\theta j} / \bar{B}_\theta$ and the overbar denotes the average value over the flux surface.

Subtracting $m_j \mathbf{v}_j$ times Eq. (15.89) from the momentum balance equation (5.7) for ion species ‘‘ j ’’ and noting that $(\nabla \cdot n_j \mathbf{v}_j)_r \ll (\nabla \cdot n_j \mathbf{v}_j)_\theta$ leads to

$$\begin{aligned} n_j m_j (\mathbf{v}_j \cdot \nabla) \mathbf{v}_j + \nabla p_j + \nabla \cdot \boldsymbol{\pi}_j &= n_j e_j (\mathbf{v}_j \times \mathbf{B}) + n_j e_j \mathbf{E} + \mathbf{F}_j + \mathbf{M}_j \\ &\quad - n_j m_j v_{\text{at}}^j \mathbf{v}_j - m_j \tilde{S}_j \mathbf{v}_j \end{aligned} \quad (15.92)$$

where \mathbf{F}_j represents the interspecies collisional friction, \mathbf{M}_j represents the external momentum input rate, and the last two terms represent the momentum loss rate due to elastic

scattering and charge exchange with neutrals of all ion species “k” [$v_{atj} = \Sigma_k n_{k0}^c (\langle \sigma v \rangle_{el} + \langle \sigma v \rangle_{cx})_{jk}$] and due to the introduction of ions with no net momentum via ionization of a neutral of species ”j”. Only the “cold” neutrals that have not already suffered an elastic scattering or charge exchange collision in the pedestal are included in v_{atj} .

Taking the cross product $\mathbf{B} \times$ Eq. (15.92) yields a “radial” (\mathbf{n}_r) component equation

$$\begin{aligned} n_j e_j v_{rj} B^2 &= B_\theta \left\{ n_j m_j [(\mathbf{v}_j \cdot \nabla) \mathbf{v}_j]_\phi + [\nabla \cdot \pi]_\phi - M_{j\phi} - F_{j\phi} \right. \\ &\quad - n_j e_j E_\phi + m_j (n_j v_{atj} + \tilde{S}_j) v_{\phi j} \Big\} \\ &\quad - B_\phi \left\{ n_j m_j [(\mathbf{v}_j \cdot \nabla) \mathbf{v}_j]_\theta + [\nabla \cdot \pi]_\theta + \frac{\partial p_j}{\partial l_\theta} - M_{j\theta} - F_{j\theta} \right. \\ &\quad \left. - n_j e_j E_\theta + m_j (n_j v_{atj} + \tilde{S}_j) v_{\theta j} \right\} \quad (15.93) \end{aligned}$$

and a “perpendicular” ($B_\phi \mathbf{n}_\theta - B_\theta \mathbf{n}_\phi$) component equation

$$n_j m_j [(\mathbf{v}_j \cdot \nabla) \mathbf{v}_j]_r + [\nabla \cdot \pi_j]_r + \frac{\partial p_j}{\partial r} = n_j e_j (v_{\theta j} B_\phi - v_{\phi j} B_\theta + E_r) \quad (15.94)$$

and taking the scalar product $\mathbf{B} \cdot$ Eq. (15.92) yields a third, independent parallel momentum balance equation

$$\begin{aligned} B_\phi \left\{ n_j m_j [(\mathbf{v}_j \cdot \nabla) \mathbf{v}_j]_\phi + [\nabla \cdot \pi]_\phi - M_{j\phi} - F_{j\phi} \right. \\ &\quad - n_j e_j E_\phi + m_j (n_j v_{atj} + \tilde{S}_j) v_{\phi j} \Big\} \\ &= -B_\theta \left\{ n_j m_j [(\mathbf{v}_j \cdot \nabla) \mathbf{v}_j]_\theta + [\nabla \cdot \pi]_\theta + \frac{\partial p_j}{\partial l_\theta} - M_{j\theta} - F_{j\theta} \right. \\ &\quad \left. - n_j e_j E_\theta + m_j (n_j v_{atj} + \tilde{S}_j) v_{\theta j} \right\} \quad (15.95) \end{aligned}$$

The quantity E_ϕ^A is the induced toroidal field due to transformer action.

Using Eq. (15.95) in Eq. (15.93), multiplying the result by R and taking the flux surface average leads to an expression for the flux surface average radial particle flux

$$\begin{aligned} \bar{R} \bar{B}_\theta e_j \langle n_j v_{rj} \rangle &\simeq R B_\theta e_j \bar{n}_j \bar{v}_{rj} = \left\langle R^2 \nabla \phi \cdot n_j m_j (\mathbf{v}_j \cdot \nabla) \mathbf{v}_j \right\rangle + \left\langle R^2 \nabla \phi \cdot \nabla \cdot \pi_j \right\rangle \\ &\quad - \langle R M_{j\phi} \rangle - \langle R F_{j\phi} \rangle - \left\langle R n_j e_j E_\phi^A \right\rangle + \left\langle R m_j \langle n_j v_{atj} + \tilde{S}_j \rangle v_{\phi j} \right\rangle \quad (15.96) \end{aligned}$$

The first (inertial) term on the right vanishes identically. The remaining terms on the right represent the transport fluxes in response to the toroidal viscous force, the (beam) momentum input, the interspecies collisional momentum exchange, the inductive toroidal electric field, and the momentum loss due to interactions with neutral particles, respectively.

Neglecting the viscous and inertial terms in Eq. (15.94), using Eq. (15.91), and assuming that the radial electric field is electrostatic leads to an expression for the flow velocity

of ion species "j" in the flux surface

$$n_j \mathbf{v}_j = (K_j + I_j) \mathbf{B} - \frac{1}{e_j B_\theta} \left(\frac{\partial p_j}{\partial r} + n_j e_j \frac{\partial \phi}{\partial r} \right) \mathbf{n}_\phi \quad (15.97)$$

Flux surface averaging this equation yields an expression for the average toroidal rotation over the flux surface in terms of the average poloidal rotation and radial gradients of the pressure and electrostatic potential

$$\bar{v}_{\phi j} = f_p^{-1} \bar{v}_{\theta j} - (\bar{P}'_j + \bar{\Phi}') \quad (15.98)$$

where

$$f_p \equiv B_\theta / B_\phi, \quad \bar{P}'_j \equiv \frac{1}{\bar{n}_j e_j \bar{B}_\theta} \frac{\partial \bar{p}_j}{\partial r}, \quad \bar{\Phi}' \equiv \frac{1}{\bar{B}_\theta} \frac{\partial \phi}{\partial r} = -\frac{\bar{E}_r}{\bar{B}_\theta} \quad (15.99)$$

The particle fluxes within and across the flux surface are determined by Eqs. (15.97) and (15.96), respectively. In order to evaluate these fluxes it is necessary to specify the models for the viscosity and collisional friction, to know the constant K_j (equivalently the average value of the poloidal velocity), and to know the radial electric field.

Using the Lorentz approximation for the collisional friction

$$\mathbf{F}_j = -n_j m_j \sum_{k \neq j} v_{jk} (\mathbf{v}_j - \mathbf{v}_k) \quad (15.100)$$

Equation (15.96) may be reduced to

$$\begin{aligned} \Gamma_{rj} \equiv \bar{n}_j \bar{v}_{rj} &= \frac{1}{e_j \bar{B}_\theta} \left[- \left(\bar{M}_{\phi j} + \bar{n}_j e_j \bar{E}_\phi^A \right) + \bar{n}_j m_j \sum_{k \neq j} \bar{v}_{jk} (\bar{v}_{\phi j} - \bar{v}_{\phi k}) \right. \\ &\quad \left. + \bar{n}_j m_j \bar{v}_{dj}^* \bar{v}_{\phi j} \right] \end{aligned} \quad (15.101)$$

where the total 'drag' frequency v_{dj}^* is given by

$$\bar{v}_{dj}^* \equiv \bar{v}_{dj} + \bar{v}_{atj} + \bar{v}_{ionj} \xi_j \quad (15.102)$$

which consists of a cross-field viscous momentum transport frequency formally given by

$$\bar{v}_{dj} \equiv \langle R^2 \nabla \phi \cdot \nabla \cdot \pi_j \rangle / \bar{R} \bar{n}_j m_j \bar{v}_{\phi j} \quad (15.103)$$

and of the two atomic physics momentum loss terms discussed previously, with the neutral ionization source asymmetry characterized by

$$\xi_j \equiv \langle R^2 \nabla \phi \cdot m_j \tilde{S}_j v_{\phi j} \rangle / \bar{R} m_j \bar{S}_j \bar{v}_{\phi j} \quad (15.104)$$

Writing

$$\bar{P}'_j = -\frac{T_j}{e_j B_\theta} \left(L_{nj}^{-1} + L_{Tj}^{-1} \right) \quad (15.105)$$

the “perpendicular” component of the momentum balance given by Eq. (15.92) can be used to eliminate the toroidal velocity in the ‘radial’ component given by Eq. (15.101) to obtain a generalized pinch-diffusion equation for each ion species present

$$\Gamma_j = n_j D_{jj} \left(L_{nj}^{-1} + L_{Tj}^{-1} \right) - n_j D_{jk} \left(L_{nk}^{-1} + L_{Tk}^{-1} \right) + n_j v_{pj} \quad (15.106)$$

where the diffusion coefficients are given by

$$D_{jj} \equiv \frac{m_j T_j \left(v_{dj}^* + v_{jj} \right)}{\left(e_j B_\theta \right)^2}, \quad D_{jk} \equiv \frac{m_j T_k v_{jk}}{e_j e_k B_\theta^2} \quad (15.107)$$

the pinch velocity is given by

$$n_j v_{pj} \equiv -\frac{\bar{M}_{\phi j}}{e_j B_\theta} - \frac{n_j \bar{E}_\phi^A}{B_\theta} + \frac{n_j m_j v_{dj}^*}{e_j B_\theta} \left(\frac{E_r}{B_\theta} \right) + \frac{n_j m_j f_p^{-1}}{e_j B_\theta} \left[\left(v_{jk} + v_{dj}^* \right) \bar{v}_{\theta j} - v_{jk} \bar{v}_{\theta k} \right] \quad (15.108)$$

and where a sum over the “ k ” terms is understood when more than two ion species are present. Note that the “self-diffusion” coefficient D_{jj} involves the atomic physics and viscous momentum transfer rates as well as the interspecies collisional momentum exchange frequency. The v_θ can be obtained by solving the poloidal momentum balance equations numerically, as discussed in chapter 10 and later in this chapter.

15.7.2 Density Gradient Scale Length

Since the temperature gradient scale lengths for each ion species in principle can be determined from the heat conduction relations $q_j = n_j T_j \chi_j L_{Tj}^{-1}$, the set of Eq. (15.106) can be recast as a coupled set of inhomogeneous equations that can be solved for density gradient scale lengths in terms of these temperature gradient scale lengths, the local particle fluxes, Γ_j , the terms appearing in the generalized pinch velocities given by Eq. (15.108) and the diffusion coefficients given by Eq. (15.107)

$$D_{jj} L_{nj}^{-1} - D_{jk} L_{nk}^{-1} = \frac{\Gamma_j}{n_j} - v_{pj} - D_{jj} L_{Tj}^{-1} + D_{jk} L_{Tk}^{-1} \equiv \alpha_j \quad (15.109)$$

There are as many coupled Eqs. (15.109) as there are ion species present, and again the “ k ” terms are understood to represent sums over species $k \neq j$.

For a two-species (ion – i , impurity – I) model these equations can be solved explicitly for the ion density gradient scale length

$$L_{ni}^{-1} = \frac{\left(\frac{m_i T_i v_{II}}{(e_I B_\theta)^2} \right) \left(1 + \frac{v_{dI}^*}{v_{II}} \right) \alpha_i + \left(\frac{m_i T_i v_{iI}}{e_i e_I B_\theta^2} \right) \alpha_I}{\left(\frac{m_I T_I v_{II}}{(e_I B_\theta)^2} \right) \left(\frac{m_i T_i v_{iI}}{(e_i B_\theta)^2} \right) \left[\left(1 + \frac{v_{dI}^*}{v_{II}} \right) \left(1 + \frac{v_{di}^*}{v_{iI}} \right) - 1 \right]} \quad (15.110)$$

and a similar expression for the impurity density gradient scale length with the “*i*” and “*I*” interchanged.

In order to more clearly display the physics involved, we use Eqs. (15.105) and (15.98) to eliminate the toroidal velocity only in the last term in Eq. (15.101), leading to an expression for the density gradient scale length of ion species “*j*”

$$L_{nj}^{-1} = \frac{e_j B_\theta}{n_j m_j v_{dj}^* T_j} \left[e_j B_\theta \Gamma_j + M_{\phi j} + n_j e_j E_\phi^A - n_j m_j v_{jk} (v_{\phi j} - v_{\phi k}) - n_j m_j v_{dj}^* \left(f_p^{-1} v_{\theta j} + \frac{E_r}{B_\theta} \right) \right] - L_{Tj}^{-1} \quad (15.111)$$

The coupling among species has not disappeared; it is present in the friction term, which may be small, and in the poloidal rotation velocity and radial electric field dependence on all species. The density gradient scale length not only depends on the particle flux, as would be intuitively expected, but also on the poloidal rotation velocity and the radial electric field, which latter in turn depends on the toroidal and poloidal rotation velocities because of toroidal momentum balance.

15.7.3 Edge Density, Temperature, Electric Field and Rotation Profiles

15.7.3.1 Pressure Gradient Scale Length

When it is assumed that (1) the plasma contains a main ion species “*i*” and a single effective impurity species “*z*” the concentration of which is a constant fraction $f_z = n_z/n_i$ of the main ion concentration, and that (2) both ion species have the same temperature T_i , Eq. (15.109) reduce to a flux-gradient-pinch relationship for the main ions

$$-\frac{1}{p_i} \frac{dp_i}{dr} \equiv L_{pi}^{-1} = \frac{\Gamma_i/n_i - v_{pi}}{\hat{D}_i} \equiv \frac{v_{ri} - v_{pi}}{\hat{D}_i} \quad (15.112)$$

where Γ_i is the radial ion flux. The effective diffusion coefficient is

$$\hat{D}_i \equiv D_{ii} - D_{iz} = \frac{m_i T_i v_{iz}}{(e_i B_\theta)^2} \left(1 + \frac{v_{di}^*}{v_{iz}} - \frac{1}{\langle Z \rangle} \right) \quad (15.113)$$

where v_{iz} is the interspecies collision frequency, v_{di}^* is the viscous plus atomic physics (charge-exchange, elastic scattering, ionization) frequency for the radial transfer of toroidal momentum given by Eq. (15.102), and $\langle Z \rangle$ is the average local charge state of the impurity species. The remaining collection of quantities entering this relationship is identified as the ‘pinch’ velocity given by Eq. (15.108).

An expression for calculating the radial electric field can be derived by summing the toroidal component of the momentum balance equation for all species and using the radial component of the momentum balance Eq. (15.98), $v_{\phi j} = f_p^{-1} v_{\theta j} + E_r/B_\theta - (dp_j/dr)/(n_j e_j B_\theta)$, to obtain

$$\frac{E_r}{B_\theta} = \frac{\sum_{\text{ions}} \left\{ M_{\phi j} - n_j m_j v_{dj}^* [f_p^{-1} v_{\theta j} - (dp_j/dr)/(n_j e_j B_\theta)] \right\}}{\sum_{\text{ions}} n_j m_j v_{dj}^*} \quad (15.114)$$

15.7.3.2 Local Temperature and Density Gradient Scale Lengths

The local heat conduction relation $q_j = -n_j \chi_j dT_j / dr$, $j = i, e$, can be used to express the local ion and electron temperature gradient scale lengths, $L_{Tj}^{-1} \equiv -T_j / (dT_j / dr)$, in terms of the respective local total heat fluxes, Q_j , and convective heat fluxes, $5/2 T_j \Gamma_j$

$$L_{Tj}^{-1} = \frac{1}{\chi_j} \left(\frac{Q_j}{n_j T_j} - \frac{5}{2} \frac{\Gamma_j}{n_j} \right) \quad j = i, e \quad (15.115)$$

The inverse ion density gradient scale length may then be determined by subtracting the inverse ion temperature gradient scale length of Eq. (15.115) from the inverse ion pressure gradient scale length given by Eq. (15.112)

$$L_{ni}^{-1} = L_{pi}^{-1} - L_{T_i}^{-1} \quad (15.116)$$

15.7.3.3 Local Particle and Heat Fluxes

With reference to the discussion following Eq. (15.89), the local flux surface averaged particle balance equation for the main ion particle flux in the edge region can be written

$$\frac{d\Gamma_i}{dr} = n_e v_{ioni} + n_i v_{ionb} \quad \Gamma_i(r_{sep}) = \Gamma_i^{sep} \quad (15.117)$$

where v_{ioni} and v_{ionb} are the frequencies for the ionization by electron-impact of recycling neutral atoms of the main ion species and for ionization of neutral beam injected particles, respectively. In order to solve this equation it is necessary to specify a boundary condition either at the separatrix or at some radius interior to the pedestal location. Because we are interested in calculating profiles from the separatrix inward and because we can determine the particle flux crossing the separatrix from a particle balance on the region inside the separatrix, we choose to specify the (net outward) ion particle flux crossing the separatrix, $\Gamma_{sep,i}$, as the boundary condition and to numerically integrate this equation inward from the separatrix to determine the local particle flux within the edge region of interest.

The ion and electron heat fluxes in the edge region satisfy the energy balance equations

$$\frac{dQ_i}{dr} = -\frac{3}{2} T_i n_e v_{ati} - \dot{Q}_{ie} + \dot{Q}_{nbi}, \quad Q_i(r_{sep}) = Q_i^{sep} \quad (15.118)$$

and

$$\frac{dQ_e}{dr} = -E_{ion} n_e v_{ioni} - n_e n_z L_z + \dot{Q}_{ie} + \dot{Q}_{nbe}, \quad Q_e(r_{sep}) = Q_e^{sep} \quad (15.119)$$

where \dot{Q}_{ie} is the rate of collisional energy transfer from ions to electrons, $\dot{Q}_{nbi,e}$ is the rate of energy deposition in the ions or electrons by injected neutral beams (or any other form of heating), v_{ati} is the frequency of charge-exchange plus elastic scattering of cool recycling neutral atoms which have not previously suffered a collision in the scrape-off layer or edge region, E_{ion} is the ionization energy, and L_z is the radiation emissivity of the impurity ions (which should be calculated taking into account the enhancement due

to charge-exchange and recombination with the recycling neutrals). For reasons similar to those discussed above for the ion particle flux, we specify the values of the ion and electron heat fluxes at the separatrix as boundary conditions and numerically integrate Eqs. (15.118) and (15.119) inward from the separatrix into the edge region. The total heat flux at the separatrix, $Q^{\text{sep}} = Q_i^{\text{sep}} + Q_e^{\text{sep}}$, can be determined from a power balance on the region inside the separatrix, but the split between ion and electron heat flux is generally unknown experimentally.

15.7.3.4 Density and Temperature Profiles in the Plasma Edge

The ion density profile and the ion and electron temperature profiles in the plasma edge are calculated by numerically integrating the defining relations for the respective inverse gradient scale lengths inward from the separatrix

$$-\frac{1}{n_i} \frac{dn_i}{dr} = L_{ni}^{-1} = L_{pi}^{-1} - L_{Ti}^{-1} = \frac{v_{ri} - v_{pi}}{\hat{D}_i} - L_{Ti}^{-1} \quad n_i(r_{\text{sep}}) = n_i^{\text{sep}} \quad (15.120)$$

$$-\frac{1}{T_i} \frac{dT_i}{dr} = L_{Ti}^{-1} = \frac{1}{\chi_i} \left[\frac{Q_i}{n_i T_i} - \frac{5}{2} \frac{\Gamma_i}{n_i} \right] \quad T_i(r_{\text{sep}}) = T_i^{\text{sep}} \quad (15.121)$$

and

$$-\frac{1}{T_e} \frac{dT_e}{dr} = L_{Te}^{-1} = \frac{1}{\chi_e} \left[\frac{Q_e}{n_e T_e} - \frac{5}{2} \frac{\Gamma_e}{n_e} \right] \quad T_e(r_{\text{sep}}) = T_e^{\text{sep}} \quad (15.122)$$

subject to separatrix boundary conditions.

15.7.3.5 Boundary Conditions for Edge Plasma Profile Calculations

In order to solve Eqs. (15.117) to (15.122) for the profiles in the edge plasma it is necessary to specify the indicated separatrix boundary conditions on density, temperature and particle and heat fluxes and the SOL inward recycling neutral flux boundary condition. For this purpose the above edge plasma calculation may be embedded within a larger calculation which: (1) performs core plasma particle and power balance calculations (including radiative cooling and recycling neutral influx) to determine outward plasma particle and heat fluxes across the separatrix into the SOL which; (2) are input to a divertor model (including radiative and atomic physics cooling, particle sources, and momentum sinks) to calculate plasma density and temperature in the SOL and divertor and to calculate the plasma flux to the divertor plate which; (3) creates the recycling source of neutral molecules and atoms for a 2D neutral transport recycling calculation throughout the divertor and plasma chamber that provides the neutral influx for the core particle balance calculation. Thus, such a larger code would calculate all of the boundary conditions needed for the edge plasma calculation. Experimental values of n_e^{sep} , T_e^{sep} and T_i^{sep} can also be used as input, if available.

15.7.3.6 Viscous Cross-Field Momentum Transport

In order to actually evaluate the above equations it is necessary to specify the toroidal viscous force, $\langle R^2 \nabla \phi \cdot \nabla \cdot \boldsymbol{\pi} \rangle$, which determines the viscous momentum transport frequency,

v_{dj} , given by Eq. (15.103). As discussed in 10, there are three neoclassical viscosity components – parallel, perpendicular and gyroviscous. The “parallel” component of the neoclassical viscosity vanishes identically in the viscous force term, and the “perpendicular” component is several orders of magnitude smaller than the “gyroviscous” component

$$\langle R^2 \nabla \phi \cdot \nabla \cdot \pi_j \rangle = \frac{1}{2} \tilde{\theta}_j G_j \frac{n_j m_j T_j}{e_j B_\phi} \frac{v_{\phi j}}{\bar{R}} \equiv R n_j m_j v_{dj} v_{\phi j} \quad (15.123)$$

where

$$\begin{aligned} \tilde{\theta}_j \equiv (4 + \tilde{n}_j^c) \tilde{v}_{\phi j}^s + \tilde{n}_j^s (1 - \tilde{v}_{\phi j}^c) &= (4 + \tilde{n}_j^c) \left[-\frac{\hat{v}_{\theta j}}{\hat{v}_{\phi j}} (\tilde{\Phi}^s + \tilde{n}_j^s) + \tilde{\Phi}^s \right] \\ &\quad + \tilde{n}_j^s \left[\frac{\hat{v}_{\theta j}}{\hat{v}_{\phi j}} (2 + \tilde{\Phi}^c + \tilde{n}_j^c) - \tilde{\Phi}^c \right] \end{aligned} \quad (15.124)$$

represents poloidal asymmetries and

$$G_j \equiv -\frac{r}{\eta_{4j} v_{\phi j}} \frac{\partial(\eta_{4j} v_{\phi j})}{\partial r} = r(L_{pj}^{-1} + L_{v\phi j}^{-1}) \quad (15.125)$$

with the gyroviscosity coefficient $\eta_{4j} \approx n_j m_j T_j / e_j B$ and $L_x^{-1} = -(dx/dr)/x$.

15.7.3.7 Poloidal Velocities and Density Asymmetries

In order to evaluate Eq. (15.125) it is first necessary to calculate the sine and cosine components of the density and toroidal velocity poloidal variations over the flux surface. This calculation is similar to the calculation described in 10, but also includes the effects of the influx of neutral atoms into the plasma edge, the density of which is denote n_{0j} . Using a low-order Fourier expansion of the poloidal dependence of the densities and rotation velocities over the flux surface in the poloidal component of the momentum balance equation and taking the flux surface average with 1, $\sin \theta$ and $\cos \theta$ weighting yields a coupled set of three nonlinear moments equations per species that can be solved numerically for the flux surface average poloidal velocities and the sine and cosine components of the density variations over the flux surface, for the various ion species present.

$$\begin{aligned}
& \hat{v}_{\theta j} \left(-q\hat{v}_{\phi j}\epsilon(\tilde{n}_j^s + \tilde{\Phi}^s) - q^2 f_j f_p (1 + \tilde{\Phi}^c + \frac{2}{3}\tilde{n}_j^c) + f_p \sum_{k \neq j} v_{jk}^* + \frac{q}{\epsilon} v_{atj}^* f_p \right. \\
& + \frac{1}{2} f_p \epsilon v_{ionj}^* \left\{ (1 + \tilde{n}_j^c) \left[\frac{\bar{n}_e}{\bar{n}_j} (\tilde{n}_e^c + \tilde{n}_{0j}^c) - (\tilde{n}_j^c + \tilde{n}_{0j}^c) \right] \right. \\
& \quad \left. \left. + \tilde{n}_j^s \left[\frac{\bar{n}_e}{\bar{n}_j} (\tilde{n}_e^s + \tilde{n}_{0j}^s) - (\tilde{n}_j^s + \tilde{n}_{0j}^s) \right] \right\} \right) \\
& - \sum_{k \neq j} v_{k\theta} \left[f_p v_{jk} \sqrt{\frac{m_j}{m_k}} \right] \\
& = -\hat{v}_{rj} - q\epsilon \frac{1}{4} \tilde{n}_j^s - q\epsilon \hat{\Phi}_j \left[\frac{1}{4} (\tilde{\Phi}^s + \tilde{n}_j^c \tilde{\Phi}^s - \tilde{n}_j^s \tilde{\Phi}^c) \right] \\
& \quad - q^2 f_j f_p (\hat{v}_{\phi j} + \hat{P}'_j) \tilde{\Phi}^c \\
& \quad - q\epsilon \hat{v}_{\phi j} \left[(\hat{v}_{\phi j} + \hat{P}'_j) \tilde{\Phi}^s + \frac{1}{2} \hat{v}_{\phi j} \tilde{n}_j^s \right] \\
& \quad - \frac{\bar{n}_e}{\bar{n}_j} v_{ionj}^* q \left[\hat{v}_{\phi j} \epsilon (\tilde{n}_e^c + \tilde{n}_{0j}^c) - \frac{2}{3} q f_j (\tilde{n}_e^s + \tilde{n}_{0j}^s) \right] \quad (15.126)
\end{aligned}$$

$$\begin{aligned}
& \tilde{n}_j^s \left(\frac{1}{3} \frac{q^2}{\epsilon} f_j f_p \hat{v}_{\theta j} + \frac{1}{2} \epsilon \hat{v}_{rj} - \frac{1}{2} \epsilon f_p \sum_{k \neq j} v_{jk}^* \hat{v}_{\theta k} \sqrt{\frac{m_j}{m_k}} + \frac{1}{2} q v_{ion}^* f_p \hat{v}_{\theta j} \right) \\
& + \tilde{n}_j^c \left(\frac{1}{2} q f_p^2 \hat{v}_{\theta j}^2 - \frac{1}{4} q + \frac{1}{2} q v_{atj}^* v_{ionj}^* \right) \\
& = -\frac{1}{2} \epsilon f_p \sum_{k \neq j} v_{jk}^* \hat{v}_{\theta j} \tilde{n}_k^s - \frac{1}{4} q \hat{\Phi}_j [-\tilde{\Phi}^c] \\
& \quad - \frac{q^2}{\epsilon} f_j f_p [\frac{1}{2} (\hat{v}_{\theta j} - \hat{v}_{\phi j} - \hat{P}'_j) \tilde{\Phi}^s - \frac{1}{2} q f_p^2 \hat{v}_{\theta j}^2 - \frac{1}{2} q \hat{v}_{\phi j}^2] \\
& \quad - \frac{1}{2} q v_{atj}^* [f_p \hat{v}_{\theta j} \tilde{n}_{0j}^s + v_{ionj}^* \tilde{n}_{0j}^c] \\
& \quad - q v_{ionj}^* f_p \left\{ \frac{1}{2} \hat{v}_{\theta j} \left[\tilde{n}_{0j}^s \left(1 + \frac{\bar{n}_e}{\bar{n}_j} \right) + \frac{\bar{n}_e}{\bar{n}_j} \tilde{n}_e^s \right] + \frac{1}{3} \frac{q}{\epsilon} f_j \frac{\bar{n}_e}{\bar{n}_j} (\tilde{n}_e^c + \tilde{n}_{0j}^c) \right\} \quad (15.127)
\end{aligned}$$

and

$$\begin{aligned}
& \tilde{n}_j^c \left(\frac{1}{3} \frac{q^2}{\epsilon} f_j f_p \hat{v}_{\theta j} + \frac{1}{2} \epsilon \hat{v}_{rj} - \frac{1}{2} \epsilon f_p \sum_{k \neq j} v_{jk}^* \hat{v}_{\theta k} \sqrt{\frac{m_j}{m_k}} + \frac{1}{2} q v_{ionj}^* f_p \hat{v}_{\theta j} \right) \\
& + \tilde{n}_j^s \left(-\frac{1}{2} q f_p \hat{v}_{\theta j}^2 + \frac{1}{4} q - \frac{1}{2} q v_{atj}^* v_{ionj}^* \right) \\
& = - \sum_{k \neq j} \tilde{n}_k^c \left(\frac{1}{2} \epsilon f_p v_{jk}^* \hat{v}_{\theta j} \right) - \frac{1}{4} q \tilde{\Phi}_j [\tilde{\Phi}^s] \\
& - \frac{q^2}{\epsilon} f_j f_p \left\{ \frac{1}{2} \left[(1 + \tilde{\Phi}^c) \hat{v}_{\theta j} - (\hat{v}_{\phi j} - \hat{P}'_j) \tilde{\Phi}^c \right] \right\} \\
& - q \hat{v}_{\phi j}^2 \left\{ \frac{1}{4} \epsilon \left[\tilde{v}_{\phi j}^s \tilde{v}_{\phi j}^c + \tilde{n}_j^c \tilde{v}_{\phi j}^s + \tilde{n}_j^s \tilde{v}_{\phi j}^c \right] \right\} - \frac{1}{2} q v_{atj}^* (f_p \hat{v}_{\theta j} \tilde{n}_{0j}^c - v_{ionj}^* \tilde{n}_{0j}^s) \\
& - q f_p v_{ionj}^* \left\{ \frac{1}{2} \hat{v}_{\theta j} \left[\tilde{n}_{0j}^c \left(1 + \frac{\bar{n}_e}{\bar{n}_j} \right) + \frac{\bar{n}_e}{\bar{n}_j} \tilde{n}_e^c \right] + \frac{1}{3} \frac{q}{\epsilon} f_j \frac{\bar{n}_e}{\bar{n}_j} (\tilde{n}_e^s + \tilde{n}_{0j}^s) \right\}
\end{aligned} \tag{15.128}$$

where

$$\begin{aligned}
\hat{v}_{\theta j} &\equiv \frac{\bar{v}_{\theta j}}{|f_p| v_{thj}} & \hat{v}_{\phi j} &\equiv \frac{\bar{v}_{\phi j}}{v_{thj}} & \tilde{v}_{\theta j}^s &= \frac{\tilde{I}_j^s B_\theta^0}{v_{\theta j}^0 n_j^0} - \tilde{n}_j^s \\
\hat{v}_{rj} &\equiv \frac{\bar{v}_{rj}}{\frac{m_j v_{thj}}{e_j B_\theta^0} |f_p| \frac{v_{thj}}{qR}} & f_p &\equiv \frac{B_\theta}{B_\phi} & \tilde{v}_{\theta j}^c &= \frac{\tilde{I}_j^c B_\theta^0}{v_{\theta j}^0 n_j^0} - (I + \tilde{n}_j^c) \\
\tilde{n}_j^{\frac{c}{s}} &\equiv \frac{n_j^{\frac{c}{s}}}{\epsilon} & \tilde{\Phi}^{\frac{c}{s}} &\equiv \frac{\Phi^{\frac{c}{s}}}{\epsilon} & \tilde{n}_{0j}^{\frac{c}{s}} &\equiv \frac{n_{0j}^{\frac{c}{s}}}{\epsilon} \\
v_{jk}^* &\equiv \frac{v_{jk}}{\frac{v_{thj}}{qR}} & v_{ionj}^* &\equiv \frac{\bar{v}_{ionj} r}{v_{thj}} & v_{atj}^* &\equiv \frac{\bar{v}_{atj} r}{v_{thj}} \\
\tilde{\Phi}_j &\equiv \frac{e_j \tilde{\Phi}}{T_j} & \hat{P}'_j &\equiv \frac{1}{B_\theta^0 \tilde{n}_j e_j v_{thj}} \frac{\partial p_j}{\partial r} & \tilde{I}_j &= \frac{R_0 B_\theta^0 \int_0^\theta (I + \epsilon \cos \theta') \tilde{S}_j(\theta') d\theta'}{I + \epsilon \cos \theta'}
\end{aligned} \tag{15.129}$$

In order to solve the poloidal moments of the momentum equation given above, we can use the neoclassical parallel viscosity tensor obtained by extending the classical rate-of-strain tensor formalism to toroidal geometry, as discussed in chapter 10, leading to the poloidal component of the divergence of the parallel viscosity tensor

$$\mathbf{n}_\theta \cdot \nabla \cdot \boldsymbol{\pi} = \eta_{0j} \left(\frac{1}{2} A_{0j} \right) \left[\frac{1}{r} \frac{\partial \ln(\eta_{0j} A_{0j})}{\partial \theta} \right] \tag{15.130}$$

where

$$\frac{1}{2} A_{0j} = -\frac{1}{3} \frac{1}{r} \frac{\partial v_{\theta j}}{\partial \theta} + v_{\theta j} \left(\frac{1}{R} \frac{1}{r} \frac{\partial R}{\partial \theta} + \frac{1}{3} \frac{1}{B_\theta} \frac{1}{r} \frac{\partial B_\theta}{\partial \theta} \right) + \frac{B_\theta}{B_\phi} \frac{R}{r} \frac{\partial (v_{\phi j}/R)}{\partial \theta} \tag{15.131}$$

and by replacing the classical parallel viscosity coefficient with a neoclassical form

$$\eta_{0j} = \frac{n_j m_j v_{\text{th},j} q R \epsilon^{-\frac{3}{2}} v_{jj}^*}{(1 + \epsilon^{-\frac{3}{2}} v_{jj}^*)(1 + v_{jj}^*)} \equiv n_j m_j v_{\text{th},j} q R f(v_{jj}^*) \quad (15.132)$$

that takes banana–plateau collisionality effects into account.

15.7.3.8 Penetration of Recycling Neutrals

Penetration of the inward flux of recycling neutrals, $J^+(r)$, into the edge region can be calculated using an Interface Current Balance method discussed in chapter 16, using as a boundary condition the recycling neutral current $J^+(r_{\text{SOL}}) = J_{\text{SOL}}^+$, passing inward across the outer boundary of the scrape-off layer. The inward (+) and outward (−) partial currents at successive interfaces r_n and r_{n+1} are related by

$$\begin{aligned} J_+(r_{n+1}) &= T_n J_+(r_n) + R_n J_-(r_{n+1}) \\ J_-(r_n) &= T_n J_-(r_{n+1}) + R_n J_+(r_n) \quad n = 1, 2, \dots, N \end{aligned} \quad (15.133)$$

where T_n is the probability that a neutral atom is transmitted through the interval $\Delta_n = r_{n+1} - r_n$ without a collision and $2R_n$ is the probability that a neutral atom (or its neutral progeny via charge exchange) that does have one or more collisions in the interval Δ_n ultimately escapes from the interval across the interface at r_n or r_{n+1} .

Two groups of neutrals are treated: (1) ‘cold’ neutrals which have recycled from the wall and penetrate across the SOL and into the separatrix with a temperature characteristic of the wall recycling atoms; and (2) neutrals that have undergone one or more charge-exchange or scattering collisions in the SOL or pedestal regions and take on the local ion temperature as a result. The first group of neutrals is used to compute the ‘cold’ neutral density that is used to evaluate v_{ati} , while both groups contribute to v_{ioni} .

Defining the albedo as the ratio of inward to outward partial currents, $\alpha_n \equiv J_n^+ / J_n^-$, a recursive relation relates the albedos at successive interfaces $n = 1, 2, \dots, N$ numbered successively from the outer boundary of the SOL ($n = 1$) inward to the innermost interface ($n = N$).

$$\alpha_n = \frac{\alpha_{n-1}(T_{n-1}^2 - R_{n-1}^2) + R_{n-1}}{1 - \alpha_{n-1} R_{n-1}} \quad n = 2, 3, \dots, N \quad (15.134)$$

Once the albedos are calculated by sweeping inward from $n = 2$ to $n = N$, the ratio of outward partial currents at successive interfaces can be calculated by sweeping outward from $n = N - 1$ to $n = 1$ using the recursive relation

$$\frac{J_n^-}{J_{n+1}^-} = R_n T_n^{-1} \alpha_{n+1} + (T_n - R_n^2 T_n^{-1}) \quad n = N - 1, N - 2, \dots, 1 \quad (15.135)$$

The appropriate boundary conditions are $J_1^+ = J_{\text{SOL}}^+$ and $\alpha_N = \alpha_{\text{plasma}}$. The quantity α_{plasma} is the albedo of a semi-infinite plasma medium, but the actual value is not important if the location of interface N is sufficiently far (several mean free paths) inside the separatrix that the neutral influx is highly attenuated.

The quantities R_n and T_n are the reflection and transmission coefficients for the region of thickness $\Delta_n = x_{n+1} - x_n$ with total (ionization + charge exchange + elastic scattering) mean free path λ_n calculated for the local ion and electron temperatures and densities

$$R_n = \frac{\frac{1}{2}C \frac{\lambda_n}{\Delta_n} \left[\frac{1}{2} - E_3\left(\frac{\Delta_n}{\lambda_n}\right) \right] \left[1 - E_2\left(\frac{\Delta_n}{\lambda_n}\right) \right]}{1 - C \left[1 - \frac{\lambda_n}{\Delta_n} \left(\frac{1}{2} - E_3\left(\frac{\Delta_n}{\lambda_n}\right) \right) \right]} \quad T_n = E_2\left(\frac{\Delta_n}{\lambda_n}\right) + R_n \quad (15.136)$$

where “C” is the ratio of the charge-exchange plus elastic scattering cross sections to the total cross section, and $E_m(y)$ is the exponential integral function of m th order and of argument “ y .” The neutral density in each mesh interval is determined by equating the divergence of the neutral current to the ionization rate.

The transmission of uncollided “cold” neutrals into the edge plasma is calculated from $J_{n+1}^c = E_2(\Delta_n/\lambda_n^c) J_n^c$, where the mean free path λ^c is calculated for the temperature of neutrals entering the scrape-off layer from the plenum region.

15.7.3.9 Thermal Diffusivity Models

Several models that have been used to represent the thermal conductivity in the plasma edge are collected below for convenience. However, it is to be emphasized that the mechanisms determining heat transport in the plasma edge are not yet understood.

Neoclassical The basic neoclassical expression for ion heat diffusivity for a two-species (ion-impurity) plasma is

$$\chi_i = \epsilon^{\frac{1}{2}} \rho_{i\theta}^2 v_{iI} \quad (15.137)$$

where $\epsilon = r/R$ is the ratio of minor and major radii, $\rho_{i\theta}$ is the ion poloidal gyro-radius, and v_{iI} is the ion–impurity collision frequency. A more complete expression is given by the Chang–Hinton formula

$$\chi_i = \epsilon^{\frac{1}{2}} \rho_{i\theta}^2 v_{ii} [a_1 g_1 + a_2 (g_1 - g_2)] \quad (15.138)$$

where the a s account for impurity, collisionality and finite inverse aspect ratio effects and the g s account for the effect of the Shafranov shift, as given in section 9.7.

In the presence of a strong shear in the radial electric field, E_r , the particle banana orbits are “squeezed,” resulting in a reduction in the ion thermal diffusivity by a factor of $S^{-\frac{3}{2}}$, where

$$S = \left| 1 - \rho_{i\theta} \frac{d \ln E_r}{dr} \frac{E_r}{v_{thi} B_\theta} \right| \quad (15.139)$$

v_{thi} is the ion thermal speed, and B_θ is the poloidal magnetic field.

Ion Temperature Gradient Mode For a sufficiently large temperature gradient ($L_{T_i} < L_{T_i}^{\text{crit}} \approx 0.1R$) the toroidal ion temperature gradient (ITG) mode becomes unstable. An estimate of the ion thermal diffusivity due to ITG modes is given by

$$\chi_i = \frac{5}{2} \left(\frac{1}{RL_{T_i}} \right)^{\frac{1}{2}} \frac{T_e}{m_i e_i B} \frac{1}{2} \rho_i \quad (15.140)$$

where $k_{\perp} \rho_i = 2$ has been used, with ρ_i being the ion gyro-radius in the toroidal field.

Electron Drift Waves The principal electron drift wave instabilities with $k_{\perp} c_s \leq \Omega_i$ arise from trapped particle effects when $v_e^* = v_e/(v_{\text{the}}/qR)\epsilon^{\frac{3}{2}} < 1$. In more collisional plasmas the mode becomes a collisional drift wave destabilized by passing particles. An expression for the electron thermal diffusivity that encompasses both the dissipative trapped electron mode (TEM) and the transition to the collisionless mode as $v_e^* \rightarrow 0$ is given by

$$\chi_e = \frac{5 \epsilon^{\frac{3}{2}}}{2 v_e} \frac{c_s^2 \rho_s^2}{L_n L_{T_e}} \left(\frac{1}{1 + 0.1/v_e^*} \right) \quad (15.141)$$

where c_s is the speed of sound and $\rho_s = c_s/\Omega_i$, with Ω_i being the ion cyclotron frequency.

Electron Temperature Gradient Modes The electron temperature gradient (ETG) mode (an electron drift wave with $k_{\perp} c_s \leq \omega_{pe}$) is unstable for $\eta_e = L_n/L_{T_e} \geq 1$. An expression for the electron thermal diffusivity associated with the ETG mode is given by

$$\chi_e = 0.13 \left(\frac{c_s}{\omega_{pe}} \right)^2 \frac{v_{\text{the}} S_m}{qR} \eta_e (1 + \eta_e) \quad (15.142)$$

where ω_{pe} is the electron plasma frequency and $S_m = (r/q)(dq/dr)$ is the magnetic shear.

Problems for Chapter 15

- Measured heat and particle fluxes across the separatrix in one tokamak experiment were $Q_{\perp} = 10^5 \text{ W} \cdot \text{m}^{-2}$ and $\Gamma_{\perp} = 1.9 \times 10^{20} \text{ m}^{-2} \cdot \text{s}^{-1}$. In the same experiment the measured ion and electron temperature pedestal widths were 3.5 cm, the measured average density and temperatures in the transport barrier were $n_{TB} = 4.3 \times 10^{19} \text{ m}^{-3}$, $T_i = 369 \text{ eV}$ and $T_e = 290 \text{ eV}$, and the calculated ionization and charge-exchange plus scattering frequencies were $\nu_{\text{ion}} = 93.2 \text{ s}^{-1}$ and $\nu_{\text{at}} = 3.9 \text{ s}$. What values of the ion and electron thermal diffusivities would you infer from Eq. (15.12) and Eq. (15.13) if the total heat flux across the separatrix is assumed to be equally distributed between ions and electrons and the measured temperature gradient scale lengths are $L_{T_e} = 2.6 \text{ cm}$ and $L_{T_i} = 6.2 \text{ cm}$?

2. Assuming that ideal MHD pressure-driven surface modes limit the maximum allowable average pedestal pressure and using the data and results of problem 1, calculate the predicted pressure width of the transport barrier. Is this result consistent with the measured widths $\Delta_n = 3.5 \text{ cm}$ and $\Delta_{T_e} = 5.0 \text{ cm}$?
3. Calculate the ion and electron threshold power fluxes $(Q_\perp/nT)_{\text{thresh}}$ for the plasma of problem 1 with a 2% carbon impurity. Use $\chi_0 = 0.10 \text{ m}^2\text{s}^{-1}$ and $v = 2.5$. Compare these results with the measured fluxes given in problem 1 for this H-mode plasma.
4. Calculate the MARFE density limit for the plasma of problem 1 and problem 3. Note that $v_{\text{ion}} = n_0 \langle \sigma v \rangle_{\text{ion}}$, $v_{\text{at}} = n_0^{\text{cold}} \langle \sigma v \rangle_{\text{at}}$, $f_0 = n_0/n$, $f_0^{\text{cold}} = n_0^{\text{cold}}/n$ and use $n_0 = 3.8 \times 10^{15} \text{ m}^{-3}$ and $n_0^{\text{cold}} = 3.1 \times 10^{13} \text{ m}^{-3}$. Compare this with the measured density and make a prediction about MARFE stability for this experiment.
5. A deuterium fueled tokamak plasma with major radius $R = 4.5 \text{ m}$, aspect ratio $A = 4$, and toroidal field $B = 5 \text{ T}$ needs to operate in H-mode with a line-average electron density $\bar{n} = 2e20 \text{ m}^{-3}$ and an average temperature $T = 15 \text{ keV}$. If 30% of the auxiliary input power is radiated, what input power is necessary to insure that the plasma operates in H-mode?

16 Neutral Particle Transport*

It is clear from the previous chapters that atomic physics processes involving recycling and fueling atoms are important in a number of plasma phenomena, particularly in the divertor and plasma edge region. Thus, the transport of neutral atoms and molecules in the complex divertor geometry and in the edge plasma is an important topic in plasma physics. Fortunately, the field of neutral particle transport is rather highly developed from neutron transport applications in nuclear engineering, and several methods are available for the calculation of neutral particle transport in plasmas.

We describe in this chapter four classes of essentially kinetic neutral particle transport methods that have been carried over into plasma physics from neutron transport theory: (1) the spherical harmonics or P_N methods, of which diffusion theory is the most familiar; (2) the integral transport, or collision probability, methods; (3) the interface current balance methods; and (4) Monte Carlo methods. In all of these methods, the neutral transport calculation must be carried out on a fixed plasma background, which is usually determined by a plasma fluid calculation of the type described in chapter 14, which in turn is affected by the atomic physics processes arising from the presence of neutrals. Thus, the neutral-fluid plasma calculation must proceed iteratively.

It is also possible to treat the neutrals as another fluid species and represent them with the Navier–Stokes equations of conventional fluid dynamics. In this instance, the coupled ion and neutral fluid equations can be solved simultaneously. We also describe the Navier–Stokes representation of neutral transport.

16.1 Fundamentals

We will formulate and solve the neutral atom/molecule (henceforth, “atom” or “particle” will be used for “atom/molecule” in the discussion of the transport model) transport equation in one spatial dimension, which suffices to illustrate the various concepts that are being introduced without unnecessary complication. Multidimensional effects, which are important in modeling tokamak divertors, will be introduced in later sections.

16.1.1 1D Boltzmann Transport Equation

The transport of neutral particles is governed by the Boltzmann transport equation,

$$\begin{aligned} \mu \frac{\partial \psi(x, \mu, E)}{\partial x} \Sigma_t(x, E) \psi(x, \mu, E) \\ = S(x, \mu, E) + \int_0^\infty dE' \int_{-1}^1 d\mu' \Sigma_s(x, \mu' \rightarrow \mu, E' \rightarrow E) \psi(x, \mu', E') \end{aligned} \quad (16.1)$$

where the neutral particle flux $\psi = n\nu$ is the neutral particle density per $dx d\mu dE$ multi-

plied by the speed; μ is the cosine of the angle made by the neutral particle velocity vector and the positive x -axis; Σ_t represents the cross section for all interactions with plasma ions and electrons (and with other neutral particles) that remove a neutral atom from $dx d\mu dE$ either by elimination (e.g., ionization) or by altering μ or E (e.g., charge-exchange, elastic scattering); S is the source of neutral atoms into $dx d\mu dE$ from external regions or due to creation processes (e.g., recombination); and $\Sigma_s(\mu' \rightarrow \mu, E' \rightarrow E)$ represents the cross section for processes (e.g., charge-exchange, scattering) which change the direction and energy of the neutral atom.

The boundary conditions associated with Eq. (16.1) depend on the physical situation. Considering a boundary at the left surface $x = x_b$ of a slab, such that exiting particles have $\mu < 0$ and entering particles have $\mu > 0$: vacuum for $x \leq x_b$:

$$\psi(x_b, \mu, E) = 0, \quad 0 \leq \mu \leq 1 \quad (16.2a)$$

reflection at $x = x_b$:

$$\psi(x_b, \mu, E) = \int_0^\infty dE \int_{-1}^0 d\mu' R(\mu' \rightarrow \mu, E' \rightarrow E) \psi(x, \mu', E') \quad 0 \leq \mu \leq 1 \quad (16.2b)$$

incident flux at $x \leq x_b$:

$$\psi(x_b, E, \mu) = \Gamma_{in}(x_b, \mu, E) \quad 0 \leq \mu \leq 1 \quad (16.2c)$$

where $R(\mu' \rightarrow \mu, E' \rightarrow E)$ is an energy-angle reflection function or generalized albedo.

16.1.2 Legendre Polynomials

It is convenient to represent the angular (μ) dependence in terms of Legendre polynomials, the properties of which are summarized in this section. The first few Legendre polynomials are

$$\begin{aligned} P_0(\mu) &= 1 & P_2(\mu) &= \frac{1}{2}(3\mu^2 - 1) \\ P_1(\mu) &= \mu & P_3(\mu) &= \frac{1}{2}(5\mu^3 - 3\mu) \end{aligned} \quad (16.3)$$

and higher-order polynomials can be generated from the recursion relation

$$(2n + 1)\mu P_n(\mu) = (n + 1)P_{n+1}(\mu) + nP_{n-1}(\mu) \quad (16.4)$$

The Legendre polynomials satisfy the orthogonality relation

$$\int_{-1}^1 d\mu P_m(\mu) P_n(\mu) = \frac{2\delta_{mn}}{2n + 1} \quad (16.5)$$

With reference to Fig. 16.1.2, the Legendre polynomials of $\mu_0 = \cos \theta_0$, the cosine of the angle between μ' and μ , can be expressed in terms of the Legendre polynomials of μ' and μ by the addition theorem

$$P_n(\mu_0) = P_n(\mu) P_n(\mu') + 2 \sum_{m=1}^n \frac{(n-m)!}{(n+m)!} P_n^m(\mu') P_n^m(\mu) \cos m(\phi - \phi') \quad (16.6)$$

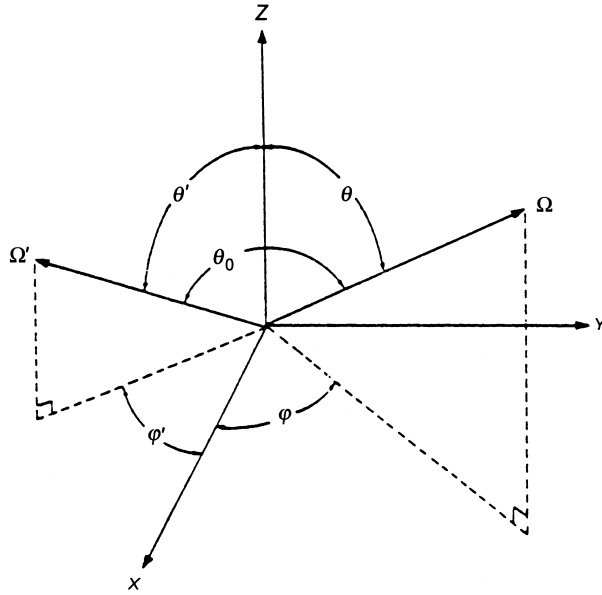


Figure 16.1. Scattering from Ω' to Ω

where the associated Legendre functions are

$$P_n^m(\mu) = (1 - \mu^2)^{\frac{m}{2}} \frac{d^m P_n(\mu)}{d\mu^m} \quad (16.7)$$

16.1.3 Charge Exchange Model

We choose an x -axis parallel to the magnetic field lines, with the origin at the divertor plate (for example). The plasma ions move along the field lines, either toward (negative $v_{||}$) or away from (positive $v_{||}$) the divertor plate, and spiral about the field lines. Upon charge-exchange, these ions become neutral particles but retain the original ion speed and direction.

We will represent the charge-exchange event by an expansion in Legendre polynomials of the cosine (μ_L) of the angle made by the final direction with the positive x -axis,

$$\Sigma_{\text{cx}}(\mu'_L \rightarrow \mu_L, E' \rightarrow E) = N f_i(E) \sum_{l=0}^{2l+1} \frac{2l+1}{2} \sigma_{\text{cx}}^l(E') P_l(\mu_L) \quad (16.8)$$

where $N f_i(E)$ is the ion density at energy E . The first moment, σ_{cx}^0 , can be determined by requiring that Eq. (16.8) yield the total charge-exchange cross section, σ_{cx} , when integrated over $-1 \leq \mu_L \leq 1$. The second moment, σ_{cx}^1 , can be determined by requiring that the net current of charge-exchanged neutrals is the same as the net current of incident ions prior

to the charge-exchange,

$$J_{\text{cx}} \equiv \int_{-1}^1 \mu_L \Sigma_{\text{cx}}(\mu'_L \rightarrow \mu_L) d\mu_L \equiv N \langle v_{\parallel} \rangle \equiv -N v_{\text{th}} M \quad (16.9)$$

where $\langle v_{\parallel} \rangle$ is the average ion flow velocity and $M \equiv -\langle v_{\parallel} \rangle/v_{\text{th}}$ is the Mach number. The result is

$$\begin{aligned} \sigma_{\text{cx}}^1(E') &= \sigma_{\text{cx}}(E') h_l \\ h_0 &= 1, \quad h_1 = -M \end{aligned} \quad (16.10)$$

The ratio $\sigma_{\text{cx}}^1/\sigma_{\text{cx}}^0 = -M$ is a measure of the anisotropy of the charge-exchange event in the laboratory system. In the absence of flow, both the neutral and the ion engaging in a charge-exchange event are equally likely to be traveling in any given direction, and the charge-exchanged neutral emerging from the event is consequently equally likely to be traveling in any given direction. Thus, the cosine of the angle in the laboratory between the incident and emergent neutral particles is equally likely to be any value in the range $-1 \leq \Delta\mu \leq 1$; i.e., the charge-exchange event is isotropic when formulated in terms of the incident neutral and the emergent charge-exchanged neutral. With ion flow in the negative μ -direction, the likelihood of a neutral emerging from a charge-exchange event in the negative μ -direction is greater than for emerging in the positive μ -direction.

16.1.4 Elastic Scattering Model

The kinematics of the elastic scattering event between a neutral particle and an ion depends upon the velocities of both. If the ion velocity distribution is known, then it would be possible to calculate the kinematics at each ion energy and form an appropriate average. In general, the ion distribution will not be available, or will be approximated, so that this is not a practical procedure. The quantities that are likely to be known are the ion density, mean energy, or temperature, and average flow velocity. Thus, we formulate a model for elastic scattering that correctly incorporates these quantities into the elastic scattering representation. The actual ion distribution function must be anisotropic in order for the average flow velocity to be nonzero, but should reduce to a near-Maxwellian when the average flow velocity is small. We model this as

$$Nf_i = N(1 - M)f_{\max} + NMf_B \quad (16.11)$$

where f_{\max} is a Maxwellian distribution and f_B represents a beam (in the negative x -direction toward the divertor plate) of particles with speed $-M v_{\text{th}}$. Such a model preserves both the total number of ions and the average ion flow toward the divertor.

16.1.4.1 Scattering from a Maxwellian Ion Population

The representation of the elastic scattering cross section for a neutral particle interacting with a Maxwellian gas has been developed in neutron thermalization theory. The incoherent approximation yields an expression for $\sigma(E' \rightarrow E, \Delta\mu_L)$ in terms of $\epsilon = E' - E$

and K the momentum transfer of the neutral. The latter may be related to the initial (E') and final (E) energies and to the difference between final and initial directional cosines, $\Delta\mu_L \equiv \mu_L - \mu'_L$. Defining

$$K^2 \equiv (E' + E - 2\sqrt{EE'}\Delta\mu_L) \quad (16.12)$$

the incoherent scattering approximation is

$$\hat{\sigma}_{\text{el}}(E' \rightarrow E, \Delta\mu_L) = \frac{\sigma_{\text{f}}(E')}{4E'} \left(\frac{A}{\pi T}\right)^{\frac{1}{2}} \frac{E^{\frac{1}{2}} e^{-(A/4T)(E'-E-A^{-1}K^2)^2/K^2}}{K} \quad (16.13)$$

where σ_{f} is the free atom scattering cross section, A is the ion mass/neutral mass ratio, and T is the temperature of the ion Maxwellian distribution.

Equation (16.13) may be integrated over final energies to obtain the cross section for scattering through $\Delta\mu_L$,

$$\hat{\sigma}_{\text{el}}(E', \Delta\mu_L) = \frac{\sigma_{\text{f}}(E')}{4E'} \left(\frac{A}{\pi T}\right)^{\frac{1}{2}} D(E', \Delta\mu_L) \quad (16.14)$$

where

$$D(E', \Delta\mu_L) \equiv \int_0^\infty dE \frac{E^{\frac{1}{2}} \exp\left\{\frac{(A/4T)\left[E' - E - A^{-1}(E' + E - \sqrt{EE'}\Delta\mu_L)\right]^2}{(E' + E - \sqrt{EE'}\Delta\mu_L)}\right\}}{\left(E' + E - \sqrt{EE'}\Delta\mu_L\right)^{\frac{1}{2}}} \quad (16.15)$$

The angular dependence of Eq. (16.14) may be expanded in Legendre polynomials.

$$\hat{\sigma}_{\text{el}}(E', \Delta\mu_L) = \sum_{l=0}^{\infty} \left(\frac{2l+1}{2}\right) \hat{\sigma}_{\text{el}}^l(E') P_l(\Delta\mu_L) \quad (16.16)$$

where

$$\hat{\sigma}_{\text{el}}^l(E') = \int_{-1}^1 d(\Delta\mu_L) P_l(\Delta\mu_L) \hat{\sigma}_{\text{el}}(E', \Delta\mu_L) \quad (16.17)$$

The quantity $\mu_0 \equiv \sigma_{\text{el}}^1/\sigma_{\text{el}}^0$ is a measure of the intrinsic anisotropy of the elastic scattering event. For a test particle incident on a stationary target particle, classical collision kinematics yields $\bar{\mu}_0 = 2/(3A)$. Averaging over a Maxwellian distribution of incident and target particles reduces the intrinsic anisotropy of the elastic scattering event.

Equation (16.13) may also be integrated over $\Delta\mu_L$ to obtain the total cross section for neutral energy change $E' \rightarrow E$,

$$\hat{\sigma}_{\text{el}}(E' \rightarrow E) = \frac{\sigma_{\text{f}}(E')\theta^2}{2E'} x(\epsilon, \epsilon', A) \quad (16.18)$$

where

$$\theta \equiv \frac{(A+1)}{2\sqrt{A}}, \quad \xi \equiv \frac{(A-1)}{2\sqrt{A}}, \quad \epsilon \equiv \frac{E}{T} \quad (16.19)$$

and

$$\begin{aligned} x &= e^{-(\epsilon-\epsilon')} \left[\operatorname{erf}(\theta\sqrt{\epsilon'} - \xi\sqrt{\epsilon}) + \operatorname{erf}(\theta\sqrt{\epsilon'} + \xi\sqrt{\epsilon}) \right] \\ &\quad + \operatorname{erf}(\theta\sqrt{\epsilon} - \xi\sqrt{\epsilon'}) - \operatorname{erf}(\theta\sqrt{\epsilon} + \xi\sqrt{\epsilon'}) \quad \epsilon' < \epsilon \\ &= e^{-(\epsilon-\epsilon')} \left[\operatorname{erf}(\theta\sqrt{\epsilon'} - \xi\sqrt{\epsilon}) - \operatorname{erf}(\theta\sqrt{\epsilon'} + \xi\sqrt{\epsilon}) \right] \\ &\quad + \operatorname{erf}(\theta\sqrt{\epsilon} - \xi\sqrt{\epsilon'}) - \operatorname{erf}(\theta\sqrt{\epsilon} + \xi\sqrt{\epsilon'}) \quad \epsilon' > \epsilon \end{aligned} \quad (16.20)$$

In our approximate representation of the flowing ion distribution, the neutrals also scatter from a beam of ions directed along the negative x -axis toward the divertor plate. The scattering term in Eq. (16.1) leads to quantities

$$\sigma_{\text{el}}^{nm} \equiv \left(\frac{2m+1}{2} \right) \int_{-1}^1 P_m(\mu'_L) d\mu'_L \int_{-1}^1 P_n(\mu_L) \sigma_L(\mu'_L \rightarrow \mu_L) d\mu_L \quad (16.21)$$

Since elastic scattering is essentially isotropic in the center-of-mass (CM) system, it is convenient to transform the integral over final direction cosines (μ'_L), using the identity

$$\sigma_L(\mu'_L \rightarrow \mu_L) d\mu_L \equiv \sigma_{\text{CM}}(\mu_c' \rightarrow \mu_c) d\mu_c = \frac{1}{2} \sigma_{\text{el}}^0 d\mu_c \quad (16.22)$$

to obtain

$$\sigma_{\text{el}}^{nm} \equiv \frac{2m+1}{4} \sigma_{\text{el}}^0 \int_{-1}^1 P_m(\mu'_L) d\mu'_L \int_{-1}^1 P_n[\mu_c(\mu'_L, \mu_L)] d\mu_c \quad (16.23)$$

where the final direction cosine in the laboratory system (LAB) (μ_L) is now a dependent function of the initial direction cosine in the LAB (μ'_L) and the final direction cosine in the CM (μ_c). The quantity σ_{el}^0 is the total elastic scattering cross section. Applying conservation of kinetic energy and momentum,

$$\mu_L \equiv \frac{v_{nx}}{\sqrt{v_{nx}^2 + v_{ny}^2}} \quad (16.24)$$

where

$$v_{nx} = \frac{A\mu_c v_n K + v_n' \mu'_L - A v_i'}{A+1} \quad (16.25)$$

and

$$v_{ny} = \frac{A v_n' K \sqrt{1 - (\mu_c)^2} + v_n' \sqrt{1 - (\mu'_L)^2}}{A+1} \quad (16.26)$$

are the components along and perpendicular to the x -axis, respectively, following the elastic collision of a neutral particle with initial speed v'_n and direction cosine μ'_L with an ion

directed along the negative x -axis with initial speed v'_i . The quantity $A = m_i/m_n$, the ion to neutral mass ratio, and

$$K \equiv \sqrt{1 + \left(\frac{v'_i}{v'_n}\right)^2 + 2\left(\frac{v'_i}{v'_n}\right)\mu'_L} \quad (16.27)$$

If the neutral density becomes sufficiently large (comparable to the ion density), then elastic scattering from other neutrals becomes competitive with elastic scattering from ions. The scattering kinematics and cross section are the same for neutral-neutral as for neutral-ion elastic scattering in the energy range of interest, 1 eV to 100 eV.

The neutral-neutral scattering reaction rate, $N_n\sigma_{el}(N_n v_n)$, introduces a nonlinear term into an otherwise linear transport equation. This term can be handled iteratively within the framework of the linear transport theory, which is developed in subsequent sections.

16.1.5 Recombination Model

At sufficiently low ion and electron temperatures ($1 \leq 2$ eV–3 eV), volumetric recombination becomes an important neutral atom source. The angular distribution of the recombined neutral atoms is that of the ions prior to recombination. Using the same arguments as for the charge-exchange representation, the source of recombined neutral atoms may be expressed as

$$S_{rec}(x, \mu, E) = \sum_{l=0}^{\infty} \left(\frac{2l+1}{2} \right) S_{rec}^l(x, E) P_l(\mu_L) \quad (16.28)$$

where

$$S_{rec}^l(x, E) \equiv \int_{-1}^1 P_l(\mu_L) S_{rec}(x, \mu_L, E) d\mu_L = N_e N_i \langle \sigma v \rangle_{rec}^{ei} h_l f_i(E) \quad (16.29)$$

where $\langle \sigma v \rangle_{rec}^{ei}$ is the ion-electron recombination rate, N_e is the electron density, N_i is the ion density, f_i is the ion distribution function, and the first two h_l are given in Eq. (16.10).

16.1.6 First Collision Source

The neutrals recycling from the divertor plate are highly anisotropic (distributed over $0 \leq \mu \leq 1$ and zero over $-1 \leq \mu \leq 0$ in our representation). To include these neutrals directly would require a transport approximation capable of representing an extremely high order of anisotropy. Instead, we calculate the first collision distribution of these neutrals analytically, and then use it as a “first collision” source for the neutral particle transport calculation. Thus, we distinguish between “uncollided” and “collided” neutral populations, the former providing a source for the latter, via collisions, and the latter providing a source for the former via recycling from the wall. This strategy allows the first step in the transport process to be calculated exactly, while ameliorating the degree of anisotropy that must be represented in the subsequent calculation.

Consider a plane source of neutral atoms at $x = 0$ with angular distribution $Q_s(\mu)$. Elementary transport considerations lead to an expression for the collided angular neutral flux at a distance x in front of the plate

$$\psi_s(x, E, \mu) = Q_s(E, \mu) \frac{e^{-\int_0^x \Sigma_t dx / \mu}}{\mu}, \quad \mu > 0, \quad x > 0 \quad (16.30)$$

These neutral atoms undergo charge-exchange and elastic scattering events with the plasma ions to form a distributed “first collision” source to the collided neutral population (we suppress the L subscript on μ),

$$\begin{aligned} S(x, E, \mu) &= \int_0^\infty dE' \int_0^1 d\mu' \left[\Sigma_{\text{cx}}(x, E' \rightarrow E, \mu' \rightarrow \mu) \right. \\ &\quad \left. + \Sigma_{\text{el}}(x, E' \rightarrow E, \mu' \rightarrow \mu) \right] \\ &\quad \times Q_s(E', \mu') \frac{e^{-\int_0^x \Sigma_t dx / \mu'}}{\mu'} \equiv S_{\text{cx}}(x, E, \mu) + S_{\text{el}}(x, E, \mu) \end{aligned} \quad (16.31)$$

Anticipating the subsequent development, we expand the angular dependence of the plane source in half-range Legendre polynomials,

$$Q_s(E', \mu') = \sum_{n=0}^{\infty} (2n+1) p_n^+(\mu') q_{sn}(E'), \quad 0 \leq \mu' \leq 1 \quad (16.32)$$

where the properties of the half-range polynomials follow from those of the full-range polynomials

$$\begin{aligned} p_l^+(\mu) &\equiv P_l(2\mu - 1), \quad 0 \leq \mu \leq 1 \\ p_l^-(\mu) &\equiv P_l(2\mu + 1), \quad -1 \leq \mu \leq 0 \end{aligned} \quad (16.33)$$

with recursion relations

$$\begin{aligned} (l+1)p_{l+1}^+(\mu) + (2l+1)p_l^+(\mu) + lp_{l-1}^+(\mu) &= 2(2l+1)\mu p_l^+(\mu) \\ (l+1)p_{l+1}^-(\mu) - (2l+1)p_l^-(\mu) + lp_{l-1}^-(\mu) &= 2(2l+1)\mu p_l^-(\mu) \end{aligned} \quad (16.34)$$

and orthogonality relations

$$\int_0^1 p_l^+(\mu) p_m^+(\mu) d\mu = \int_{-1}^0 p_l^-(\mu) p_m^-(\mu) d\mu = \frac{\delta_{lm}}{2l+1} \quad (16.35)$$

and where

$$q_{sn}(E') = \int_0^1 d\mu' p_n^+(\mu') Q_s(x, E, \mu') \quad (16.36)$$

We further define the Legendre moments of the first collision sources,

$$\begin{aligned} S_{\text{cx}}^1(x, E) &\equiv \int_{-1}^1 d\mu P_l(\mu) S_{\text{cx}}(x, E, \mu) \\ &= N f_i(E) \sigma_{\text{cx}}(E) h_l \sum_{n=0}^{\infty} (2n+1) q_{sn}(E') K_{0n}^+(\Sigma_l x) \end{aligned} \quad (16.37)$$

and

$$\begin{aligned} S_{\text{el}}^l(x, E) &\equiv \int_{-1}^1 d\mu P_l(\mu) S_{\text{el}}(x, E, \mu) \\ &= N \sum_{n=0} (2n+1) q_{sn} \left(M \sum_{k=0} \sigma_{\text{el}}^{lk}(E) K_{kn}^+ + (1-M) \hat{\sigma}_{\text{el}}^{lk}(E) K_{kn}^+ \right) \\ &\equiv N \sum_{n=0} (2n+1) q_{sn} \sum_{k=0} \bar{\sigma}_{\text{el}}^{lk}(E) K_{kn}^+(\Sigma_t x) \quad (16.38) \end{aligned}$$

where the functions

$$K_{ln}^+(x \Sigma_t) \equiv \int_x^\infty dR \frac{e^{-\frac{R}{\lambda}}}{R} P_l\left(\frac{x}{R}\right) p_n^+\left(\frac{x}{R}\right) \quad (16.39)$$

are related to the exponential integrals

$$E_n(z) \equiv \int_1^\infty e^{-tz} \frac{dt}{t^n} \quad (16.40)$$

and where $\lambda^{-1} \equiv \int_0^R \Sigma_t dR' / R'$. Expressions for evaluating the K_{ln}^+ functions are

$$\begin{aligned} K_{00}^+(z) &= E_1(z) \\ K_{10}^+(z) &= E_2(z) \\ K_{20}^+(z) &= \frac{3}{2} E_3(z) - \frac{1}{2} E_1(z) \\ K_{30}^+(z) &= \frac{5}{2} E_4(z) - \frac{3}{2} E_2(z) \\ K_{40}^+(z) &= \frac{1}{8} [35E_5(z) - 30E_3(z) + 3E_1(z)] \\ K_{50}^+(z) &= \frac{1}{8} [63E_6(z) - 70E_4(z) + 15E_2(z)] \\ &\vdots \\ K_{01}^+(z) &= 2E_2(z) - K_{00}^+(z) \\ K_{11}^+(z) &= 2E_3(z) - K_{10}^+(z) \\ K_{21}^+(z) &= 3E_4(z) - E_2(z) - K_0^+(z) \end{aligned} \quad (16.41)$$

16.2 P_N Transport and Diffusion Theory

16.2.1 P_N Equations

The P_N transport approximation is developed by expanding

$$\psi(x, E, \mu_L) = \sum_{m=0}^N \left(\frac{2n+1}{2} \right) P_m(\mu_L) \phi_m(x, E) \quad (16.42)$$

The orthogonality properties of the Legendre polynomials lead immediately to

$$\phi_m(x, E) \equiv \int_{-1}^1 P_m(\mu_L) \psi(x, E, \mu_L) d\mu_L \quad (16.43)$$

16.2.1.1 Uncollided Neutral Flux

The uncollided flux of neutral atoms from the wall is given by Eq. (16.30). Making use of Eq. (16.32) and Eq. (16.39), the Legendre moments of the uncollided flux are

$$\phi_n^{\text{un}}(x, E) = \sum_{m=0} (2m+1) q_{sm} K_{nm}^+(x \Sigma_t) \quad (16.44)$$

16.2.1.2 Collided Neutral Flux

Equations satisfied by the Legendre moments of the collided neutral flux are obtained by substituting an expansion of the form of Eq. (16.42) for the collided neutral flux into Eq. (16.1), multiplying through by $P_n(\mu_L)$, and integrating over $-1 \leq \mu_L \leq 1$ for $n = 0, 1, \dots, N$. The resulting equations are

$$\begin{aligned} \frac{d\phi_1}{dx} + (\Sigma_t - \Sigma_{00})\phi_0 &= S^0 + \sum_{k \neq 0} \Sigma_{0k}\phi_k \\ \frac{l+1}{2l+1} \frac{d\phi_{l+1}}{dx} + \frac{l}{2l+1} \frac{d\phi_{l-1}}{dx} + (\Sigma_t - \Sigma_{ll})\phi_l &= S^l + \sum_{k \neq l}^N \Sigma_{lk}\phi_k \end{aligned} \quad (16.45)$$

$l = 1, \dots, N$

where

$$\Sigma_{lk} = N(x) \left[\sigma_{\text{cx}}^l(E) \delta_{k0} + (1-M) \hat{\sigma}_{\text{el}}^l(E) \delta_{lk} + M \sigma_{\text{el}}^{lk}(E) \right] \quad (16.46)$$

and

$$\Sigma_t(x, E) = \Sigma_{00}(x, E) + N_e(x) \sigma_{\text{ion}}(E) \quad (16.47)$$

$$S^l = S_{\text{cx}}^l + S_{\text{el}}^l + S_{\text{rec}}^l + S_{\text{ex}}^l \quad (16.48)$$

where S_{ex}^l is the l th Legendre moment of any injected neutral atom source. The quantity σ_{ion} is the electron-impact ionization cross section.

Equations (16.45) lack closure in that the $(l+1)$ moment appears in the l -equation. The usual procedure is to neglect this term in the final equation. It is common to use odd-order P_N equations in order to avoid certain difficulties associated with interface conditions, and we will follow this practice. Thus, the three lowest-order P_N approximations that we consider are the P_1 approximation,

$$\begin{aligned} \frac{d\phi_1}{dx} + (\Sigma_t - \Sigma_{00})\phi_0 &= S^0 + \Sigma_{10}\phi_1 \\ \frac{1}{3} \frac{d\phi_0}{dx} + (\Sigma_t - \Sigma_{11})\phi_1 &= S^1 + \Sigma_{10}\phi_0 \end{aligned} \quad (16.49)$$

the P_3 approximation,

$$\begin{aligned} \frac{d\phi_1}{dx} + (\Sigma_t - \Sigma_{00})\phi_0 &= S^0 + \sum_{k \neq 0}^3 \Sigma_{0k}\phi_k \\ \frac{2}{3} \frac{d\phi_2}{dx} + \frac{1}{3} \frac{d\phi_0}{dx} + (\Sigma_t - \Sigma_{11})\phi_1 &= S^1 + \sum_{k \neq 1}^3 \Sigma_{1k}\phi_k \\ \frac{3}{5} \frac{d\phi_3}{dx} + \frac{2}{5} \frac{d\phi_1}{dx} + (\Sigma_t - \Sigma_{22})\phi_2 &= S^2 + \sum_{k \neq 2}^3 \Sigma_{2k}\phi_k \\ \frac{3}{7} \frac{d\phi_2}{dx} + (\Sigma_t - \Sigma_{33})\phi_3 &= S^3 + \sum_{k \neq 3}^3 \Sigma_{3k}\phi_k \end{aligned} \quad (16.50)$$

and the P_5 approximation, which consists of the first three of Eqs. (16.50), with an additional $\frac{4}{7}(d\phi_4/dx)$ term in the last one and with the sum extended to 5, plus

$$\begin{aligned} &\vdots \\ \frac{4}{7} \frac{d\phi_4}{dx} + \frac{3}{7} \frac{d\phi_2}{dx} + (\Sigma_t - \Sigma_{33})\phi_3 &= S^3 + \sum_{k \neq 3}^5 \Sigma_{3k}\phi_k \\ \frac{5}{9} \frac{d\phi_5}{dx} + \frac{4}{9} \frac{d\phi_3}{dx} + (\Sigma_t - \Sigma_{44})\phi_4 &= S^4 + \sum_{k \neq 4}^5 \Sigma_{4k}\phi_k \\ \frac{5}{11} \frac{d\phi_4}{dx} + (\Sigma_t - \Sigma_{55})\phi_5 &= S^5 + \sum_{k \neq 5}^5 \Sigma_{5k}\phi_k \end{aligned} \quad (16.51)$$

The last summation term in Eqs. (16.45), (16.49), 16.50), or (16.51) represents a scattering coupling among the Legendre moments of the flux, which is introduced by the directionality of the ion flow in the elastic scattering event. This term vanishes when the ion flow vanishes, and the P_N equations reduce to their more familiar form, in which the coupling among Legendre moments of the flux is only via the transport (derivative) term.

The boundary conditions of Eq. (16.2) cannot, of course, be imposed exactly. Marshak-type boundary conditions corresponding to the three conditions of Eq. (16.2) are vacuum for $x \leq x_b$:

$$\sum_{n=0}^N \left(\frac{2n+1}{2} \right) \phi_n(x_b, E) \int_0^1 P_m(\mu) P_n(\mu) d\mu = 0 , \quad m = 1, 3, \dots, N \quad (16.52a)$$

reflection at $x = x_b$:

$$\begin{aligned}
& \sum_{n=0}^N \left(\frac{2n+1}{2} \right) \phi_n(x_b, E) \int_0^1 P_m(\mu) P_n(\mu) d\mu \\
&= \sum_{n=0}^N \left(\frac{2n+1}{2} \right) \int_0^1 d\mu P_m(\mu) \int_{-1}^0 d\mu' P_n(\mu') \\
&\quad \times \int_0^\infty dE' R(\mu' \rightarrow \mu, E' \rightarrow E) \phi_n(x_b, E') \\
&\qquad\qquad\qquad m = 1, 3, \dots, N
\end{aligned} \tag{16.52b}$$

incident flux at $x = x_b$:

$$\begin{aligned}
& \sum_{n=0}^N \left(\frac{2n+1}{2} \right) \phi_n(x_b, E) \int_0^1 P_m(\mu) P_n(\mu) d\mu \\
&= \int_0^1 P_m(\mu) \Gamma_{in}(x_b, \mu, E) d\mu , \\
&\qquad\qquad\qquad m = 1, 3, \dots, N
\end{aligned} \tag{16.52c}$$

These $N/2$ conditions and the $N/2$ similar conditions at the other boundary constitute N boundary conditions on the N unknown ϕ_n . The appropriate wall boundary condition for the collided flux is given by Eq. (16.52a), since the flux from the wall is treated as a separate, uncollided flux and is included in the collided flux equations via the first collision sources.

16.2.2 Extended Diffusion Theories

We now show that the odd- NP_N equations can be cast in the form of $(N + 1)/2$ coupled diffusion equations to derive extended diffusion theories that can incorporate the anisotropic effects found in tokamak divertors.

Ordinary diffusion theory is usually derived from the P_1 equations (Eq. 16.49) without the anisotropic source (S^1) and scattering (Σ_{01}, Σ_{10}) terms. The simplest extension of diffusion theory is thus to retain all terms in Eqs. (16.49) in the derivation. Solving the second of Eqs. (16.49) for ϕ_1 ,

$$\phi_1 = -\hat{D}_0 \frac{d\phi_0}{dx} + \frac{S^1 + \Sigma_{10}\phi_0}{\Sigma_t - \Sigma_{11}} \tag{16.53}$$

and using the result to eliminate ϕ_1 from the first of Eqs. (16.49) leads to

$$-\frac{d}{dx} \hat{D}_0 \frac{d\phi_0}{dx} + \hat{\Sigma}_0 \phi_0 = \hat{S}^0 \tag{16.54}$$

where

$$\begin{aligned}
\hat{D}_0 &\equiv -\frac{1}{3(\Sigma_t - \Sigma_{11})}, \quad \hat{\Sigma}_0 \equiv (\Sigma_t - \Sigma_{00}) \\
\hat{S}^0 &\equiv S^0 + \Sigma_{01}\phi_1 - \frac{d}{dx} \left(\frac{S^1 + \Sigma_{10}\phi_0}{\Sigma_t - \Sigma_{11}} \right)
\end{aligned} \tag{16.55}$$

Equations (16.53) and (16.54) differ from “standard” neutral diffusion theory by the presence of the last two terms in the definition of \hat{S}^0 in Eq. (16.55). The directionality of the plasma flow enters Eq. (16.54) through the anisotropic source term, S^1 , and through the anisotropic “scattering” terms, Σ_{10} , Σ_{01} , and Σ_{11} . With the exception of retaining Σ_{11} in the definition of \hat{D}_0 , these terms are usually neglected.

The Marshak vacuum boundary condition of Eq. (16.52a) becomes, for a vacuum region for $x < 0$,

$$\frac{1}{2}\phi_0(0) = -\phi_1(0) = \left. \frac{\hat{D}_0}{dx} \frac{d\phi_0}{dx} \right|_0 \quad (16.56)$$

This condition can be interpreted geometrically as ϕ_0 extrapolating to zero at distance λ_{extrap} to the left of $x = 0$ where

$$\lambda_{\text{extrap}}^{-1} = \frac{2}{3\Sigma_{\text{tr}}^{(0)}} \quad (16.57)$$

Similar conditions obtain at the other boundary.

Higher-order, coupled, diffusion-like equations can be developed from higher-order, odd- $N P_N$ approximations by using the odd- N equations to eliminate the odd- N moments of the flux. The next higher-order diffusion approximation is obtained from the P_3 approximation of Eqs. (16.50). Changing variables to

$$\begin{aligned} F_0 &\equiv \phi_0 + 2\phi_2 \\ F_1 &\equiv \phi_2 \end{aligned} \quad (16.58)$$

the P_3 equations yield two coupled diffusion equations,

$$\begin{aligned} -\frac{d}{dx}(\hat{D}_0 \frac{dF_0}{dx}) + \hat{\Sigma}_0 F_0 &= 2\hat{\Sigma}_0 F_1 + \hat{S}^0 \\ -\frac{d}{dx}(\hat{D}_0 \frac{dF_1}{dx}) + \hat{\Sigma}_1 F_1 &= \frac{2}{3}\hat{\Sigma}_0 F_1 + \hat{S}^1 \end{aligned} \quad (16.59)$$

where

$$\begin{aligned} \hat{D}_1 &\equiv \frac{3}{7(\Sigma_t - \Sigma_{33})} \\ \hat{\Sigma}_1 &\equiv \frac{5}{3}(\Sigma_t - \Sigma_{22}) + \frac{4}{3}\hat{\Sigma}_0 \\ \hat{\Sigma}_1 &\equiv \frac{1}{3} \left[5 \left(S^2 + \sum_{k \neq 2}^3 \Sigma_{2k} \phi_k \right) - 2 \left(S^0 + \sum_{k \neq 0}^3 \Sigma_{0k} \phi_k \right) \right] \\ &\quad - \frac{d}{dx} \left(\frac{S^3 + \sum_{k \neq 3}^3 \Sigma_{3k} \phi_k}{\Sigma_t - \Sigma_{33}} \right) \end{aligned} \quad (16.60)$$

and now

$$\hat{S}_0 \equiv S_0 + \sum_{k \neq 0}^3 \Sigma_{0k} \phi_k - \frac{d}{dx} \left(\frac{S^1 + \sum_{k \neq 1}^3 \Sigma_{1k} \phi_k}{\Sigma_t - \Sigma_{11}} \right) \quad (16.61)$$

The odd moments of the flux in this approximation are

$$\begin{aligned}\phi_1 &= \frac{S^1 + \sum_{k \neq 1}^3 \Sigma_{1k} \phi_k}{\Sigma_t - \Sigma_{11}} - \hat{D}_0 \frac{d(2\phi_2 + \phi_0)}{dx} \\ \phi_3 &= \frac{S^3 + \sum_{k \neq 3}^3 \Sigma_{3k} \phi_k}{\Sigma_t - \Sigma_{33}} - \hat{D}_1 \frac{d\phi_2}{dx}\end{aligned}\quad (16.62)$$

The Marshak vacuum boundary conditions of Eq. (16.52a) become, for a vacuum region for $x < 0$,

$$\begin{aligned}\frac{1}{2} F_0(0) - \frac{3}{8} F_1(0) &= -\phi_1(0) = \hat{D}_0 \frac{dF_0}{dx} \Big|_0 \\ -\frac{1}{8} F_0(0) + \frac{7}{8} F_1(0) &= -\phi_3(0) = \hat{D}_1 \frac{dF_1}{dx} \Big|_0\end{aligned}\quad (16.63)$$

Equations (16.59) formally look like a coupled set of diffusion equations, similar in structure to the multigroup diffusion equations of neutron transport theory, hence amenable to the highly developed solution techniques that have evolved for the latter. In fact, there are derivatives of flux moments appearing in the “source” terms \hat{S}^0 and \hat{S}^1 , and Eq. (16.59) are not, strictly speaking, diffusion equations. However, we anticipate that these flux moment derivative terms in \hat{S}^0 and \hat{S}^1 are not dominant terms in the equations, and thus can be treated as source terms in an iterative solution procedure. Similar comments apply with regard to Eq. (16.54).

Following a similar procedure, the P_5 equations of Eq. (16.51) can be reduced to a coupled set of diffusion equations,

$$\begin{aligned}-\frac{d}{dx} \left(\hat{D}^0 \frac{dF_0}{dx} \right) + \hat{\Sigma}_0 F_0 &= S^0 + \sum_{k \neq 0}^5 \Sigma_{0k} \phi_k + 2\hat{\Sigma}_0 F_1 - \frac{8}{3} \hat{\Sigma}_0 F_2 - \frac{d}{dx} \left(\frac{S^1 + \sum_{k \neq 1}^5 \Sigma_{1k} \phi_k}{\Sigma_t - \Sigma_{11}} \right) \\ -\frac{d}{dx} \left(\hat{D}_1 \frac{dF_1}{dx} \right) + \hat{\Sigma}_1 F_1 &= \frac{2}{3} \hat{\Sigma}_0 F_0 + \frac{4}{3} \hat{\Sigma}_1 F_2 + \frac{5}{3} \left(S^2 + \sum_{k \neq 3}^5 \Sigma_{2k} \phi_k \right) \Sigma_t - \Sigma_{33} \\ -\frac{2}{3} \left(S^0 + \sum_{k \neq 0}^5 \Sigma_{0k} \phi_k \right) - \frac{d}{dx} \left(\frac{S^3 + \sum_{k \neq 3}^5 \Sigma_{3k} \phi_k}{\Sigma_t - \Sigma_{33}} \right) &= -\frac{d}{dx} \left(\hat{D}_2 \frac{dF_2}{dx} \right) + \hat{\Sigma}_2 F_2 = \frac{9}{5} \left(S^4 + \sum_{k \neq 4}^5 \Sigma_{4k} \phi_k \right) - \frac{4}{3} \left(S^2 + \sum_{k \neq 2}^5 \Sigma_{2k} \phi_k \right) \\ + \frac{8}{15} \left(S^0 + \sum_{k \neq 0}^5 \Sigma_{0k} \phi_k \right) - \frac{8}{15} \hat{\Sigma}_0 F_0 + \frac{4}{5} \hat{\Sigma}_1 F_1 - \frac{d}{dx} \left(\frac{S^5 + \sum_{k \neq 5}^5 \Sigma_{5k} \phi_k}{\Sigma_t - \Sigma_{55}} \right) &\end{aligned}\quad (16.64)$$

where now

$$F_0 \equiv 2\phi_2 + \phi_0 \quad (16.65)$$

$$F_1 \equiv \frac{4}{3}\phi_4 + \phi_2$$

$$F_2 \equiv \phi_4$$

$$\hat{D}_2 \equiv \frac{5}{11(\Sigma_t - \Sigma_{55})}, \quad \hat{\Sigma}_2 \equiv \frac{9}{5}(\Sigma_t - \Sigma_{44}) + \frac{16}{15}\hat{\Sigma}_1 \quad (16.66)$$

and

$$\begin{aligned} \phi_1 &= \frac{S^1 + \sum_{k \neq 1}^5 \Sigma_{1k}\phi_k}{\Sigma_t - \Sigma_{11}} - \frac{1}{3(\Sigma_t - \Sigma_{11})} \frac{d}{dx}(2\phi_2 + \phi_0) \\ \phi_3 &= \frac{S^3 + \sum_{k \neq 3}^5 \Sigma_{3k}\phi_k}{\Sigma_t - \Sigma_{33}} - \frac{3}{7(\Sigma_t - \Sigma_{33})} \frac{d}{dx} \left(\frac{4}{3}\phi_4 + \phi_2 \right) \\ \phi_5 &= \frac{S^5 + \sum_{k \neq 5}^5 \Sigma_{5k}\phi_k}{\Sigma_t - \Sigma_{55}} - \frac{5}{11(\Sigma_t - \Sigma_{55})} \frac{d\phi_4}{dx} \end{aligned} \quad (16.67)$$

The Marshak vacuum boundary conditions of Eq. (16.52a) become, for a vacuum region for $x < 0$,

$$\begin{aligned} \frac{1}{2}F_0(0) - \frac{3}{8}F_1(0) + \frac{5}{16}F_2(0) &= -\phi_1(0) = \hat{D}_0 \frac{dF_0}{dx} \Big|_0 \\ -\frac{1}{8}F_0(0) + \frac{7}{8}F_1(0) - \frac{205}{384}F_2(0) &= -\phi_3(0) = \hat{D}_1 \frac{dF_0}{dx} \Big|_0 \\ -\frac{1}{16}F_0(0) - \frac{41}{128}F_1(0) + \frac{407}{384}F_2(0) &= -\phi_5(0) = \hat{D}_2 \frac{dF_2}{dx} \Big|_0 \end{aligned} \quad (16.68)$$

There will be a current of collided neutrals into a material surface boundary that will be recycled as “uncollided” neutrals, ending up as a first collision source to the equations for the collided neutrals. The partial current of neutrals into a material surface at $x \leq 0$ is

$$\begin{aligned} - \int_{-1}^0 P_1(\mu)\psi(x=0, \mu) d\mu &= \frac{1}{4}\phi_0 - \frac{1}{2}\phi_1, \quad P_1 \text{ approx.} \\ = \frac{1}{4}\phi_0 - \frac{1}{2}\phi_1 + \frac{5}{16}\phi_2, & \quad P_3 \text{ approx.} \\ = \frac{1}{4}\phi_0 - \frac{1}{2}\phi_1 + \frac{5}{16}\phi_2 - \frac{3}{32}\phi_4, & \quad P_5 \text{ approx.} \end{aligned} \quad (16.69)$$

The diffusion equation of Eq. (16.54) contains all the information of the P_1 equations of Eqs. (16.49), and the coupled diffusion equations of Eqs. (16.59) contain all the information of the P_3 equations of Eqs. (16.50), etc. Thus, the choice between the diffusion and P_N forms must be based on the ease of solution and the extendability to multidimensional geometry. The P_N equations and associated boundary conditions constitute (in one dimension) a two-point boundary value problem that must be solved by relaxation

or shooting methods, whereas the diffusion equations can be solved by simpler forward elimination-backward substitution methods.

The extended diffusion equations can readily be extended to multidimensional geometries by letting

$$-\frac{d}{dx} \left(\hat{D} \frac{dF}{dx} \right) \rightarrow -\nabla \cdot (\hat{D} \nabla F) \quad (16.70)$$

This extension to multidimensions is only well founded theoretically for diffusion theory. A rigorous development of the higher order P_N theory in multidimensional geometries would involve expansions in multidimensional spherical harmonics and lead to results quite different than would be obtained by making the simple extension indicated by equation (16.70). It may be possible to define anisotropic diffusion coefficients to take this into account but this remains an area of active research.

Methods for solving coupled diffusion equations (e.g., the multigroup equations of neutron diffusion theory) are highly developed, and there are many existing multidimensional diffusion codes that could be adapted to solve the equations of the extended diffusion theories.

16.3 Multidimensional Neutral Transport

We now turn to a more general development of neutral particle transport theory.

16.3.1 Formulation of Transport Equation

The distribution of neutrals in space and angle is defined by the particle distribution function $N(\mathbf{r}, \Omega, t)$, such that $N(\mathbf{r}, \Omega, t) d\mathbf{r} d\Omega$ is the number of neutrals in volume element $d\mathbf{r}$ at position \mathbf{R} moving in the cone of directions $d\Omega$ about direction Ω , as depicted in Fig. 16.2. An equation for $N(\mathbf{r}, \Omega, t)$ can be derived by considering a balance on the differential cylindrical volume element of length $dl = v dt$, where v is the neutral speed, and cross section area dA surrounding the direction of neutral motion, as shown in Fig. 16.3. The rate of change of $N(\mathbf{r}, \Omega, t)$ within this differential volume is equal to the rate at which neutrals with direction Ω are flowing into the volume element (e.g. across the left face in Fig. 16.3) less the rate at which they are flowing out of the volume element (e.g. across the right face), plus the rate at which neutrals traveling in direction Ω are being introduced into the volume element by scattering or charge-exchange of neutrals within the volume element from different directions Ω' , plus the rate at which neutrals are being introduced into the volume element by an external source S_{ex} , minus the rate at which neutrals within the volume element traveling in direction Ω are being ionized or being

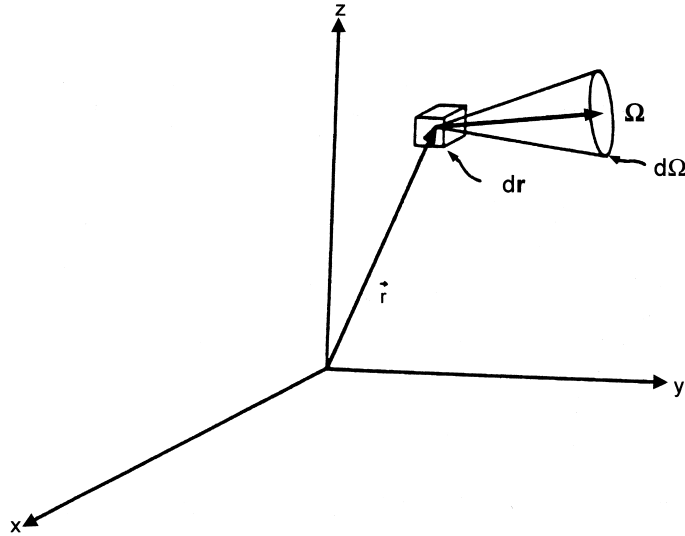


Figure 16.2. Particles in $d\mathbf{r}$ at location \mathbf{r} moving in the cone $d\Omega$ about the direction $\boldsymbol{\Omega}$

scattered or charge-exchanged into a different direction $\boldsymbol{\Omega}'$

$$\begin{aligned} \frac{dN}{dt}(\mathbf{r}, \boldsymbol{\Omega}, t) d\mathbf{r} d\boldsymbol{\Omega} &= v [N(\mathbf{r}, \boldsymbol{\Omega}, t) - N(\mathbf{r} + \boldsymbol{\Omega} dl, \boldsymbol{\Omega}, t)] dA d\boldsymbol{\Omega} \\ &+ \int_0^{4\pi} d\boldsymbol{\Omega}' \Sigma_s(\mathbf{r}, \boldsymbol{\Omega}' \rightarrow \boldsymbol{\Omega}) v N(\mathbf{r}, \boldsymbol{\Omega}', t) d\mathbf{r} d\boldsymbol{\Omega}' \\ &+ S_{\text{ex}}(\mathbf{r}, \boldsymbol{\Omega}) d\mathbf{r} d\boldsymbol{\Omega} - (\Sigma_{\text{ion}}(\mathbf{r}) + \Sigma_s(\mathbf{r})) v N(\mathbf{r}, \boldsymbol{\Omega}, t) d\mathbf{r} d\boldsymbol{\Omega} \quad (16.71) \end{aligned}$$

In the following development we will use “scattering” to mean “elastic scattering plus charge-exchange.”

Making a Taylor’s series expansion

$$\begin{aligned} N(\mathbf{r} + \boldsymbol{\Omega} dl, \boldsymbol{\Omega}, t) &= N(\mathbf{r}, \boldsymbol{\Omega}, t) + \frac{\partial N(\mathbf{r}, \boldsymbol{\Omega}, t)}{\partial l} dl + \dots \\ &= N(\mathbf{r}, \boldsymbol{\Omega}, t) + \boldsymbol{\Omega} \cdot \nabla N(\mathbf{r}, \boldsymbol{\Omega}, t) + \dots \quad (16.72) \end{aligned}$$

to evaluate the streaming term, defining the directional flux distribution

$$\psi(\mathbf{r}, \boldsymbol{\Omega}, t) \equiv v N(\mathbf{r}, \boldsymbol{\Omega}, t) \quad (16.73)$$

and taking note of the fact that the scattering from $\boldsymbol{\Omega}'$ to $\boldsymbol{\Omega}$ depends only on $\boldsymbol{\Omega}' \cdot \boldsymbol{\Omega} \equiv \mu_0$, so that

$$\Sigma_s(\mathbf{r}, \boldsymbol{\Omega}' \rightarrow \boldsymbol{\Omega}) = \frac{1}{2\pi} \Sigma_s(\mathbf{r}, \boldsymbol{\Omega} \cdot \boldsymbol{\Omega}') \equiv \frac{1}{2\pi} \Sigma_s(\mathbf{r}, \mu_0) \quad (16.74)$$

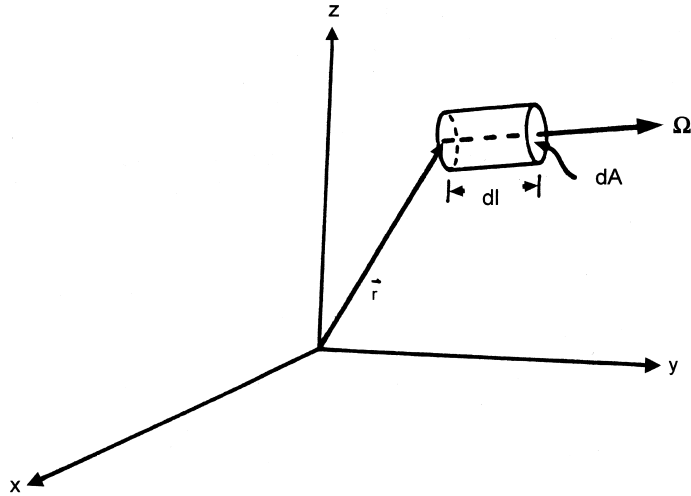


Figure 16.3. Incremental volume element for particles at location \mathbf{r} moving in the direction Ω

and writing $\Sigma_t = \Sigma_{\text{ion}} + \Sigma_s$, leads to the neutral transport equation

$$\begin{aligned} \frac{1}{v} \frac{\partial \psi}{\partial t}(\mathbf{r}, \Omega, t) + \Omega \cdot \nabla \psi(\mathbf{r}, \Omega, t) + \Sigma_t(\mathbf{r})\psi(\mathbf{r}, \Omega, t) \\ = \int_{-1}^1 d\mu_0 \Sigma_s(\mathbf{r}, \mu_0)\psi(\mathbf{r}, \Omega, t) + S_{\text{ex}}(\mathbf{r}, \pi, t) \quad (16.75) \end{aligned}$$

The representation of the neutron streaming operator, $\Omega \cdot \nabla \psi$, in the common geometries is given in Table 16.1, and the respective coordinate systems are defined in Figs. 16.4 to 16.6.

16.3.2 Boundary Conditions

Boundary conditions for Eq. (16.75) are generally specified by the physical situation. For a left boundary at \mathbf{r}_L with inward normal vector \mathbf{n} , such that $\mathbf{n} \cdot \Omega > 0$ indicates inward, one of the following boundary conditions is usually appropriate

$$\begin{aligned} \psi(\mathbf{r}_L, \Omega) = 0, \quad \Omega \cdot \mathbf{n} > 0 & \text{ vacuum} \\ \psi(\mathbf{r}_L, \Omega) = \psi_{\text{in}}(\mathbf{r}_L, \Omega), \quad \Omega \cdot \mathbf{n} > 0 & \text{ incident flux known} \\ \psi(\mathbf{r}_L, \Omega) = \alpha \psi(\mathbf{r}_L, \Omega'), \quad \Omega \cdot \mathbf{n} > 0 & \text{ reflection} \end{aligned} \quad (16.76)$$

where α is a reflection coefficient or albedo.

16.3.3 Scalar Flux and Current

The scalar flux is the product of the total number of neutrals in a differential volume, which is the integral over direction of the number of neutrals with direction within $d\Omega$ about Ω ,

Table 16.1. Neutral streaming operator in conservative form

Spatial variables	Angular variables	$\Omega \cdot \nabla \psi$
Streaming operator in rectangular coordinates		
x (one dimension)	μ	$\mu \frac{\partial \psi}{\partial x}$
x, y (two dimensions)	μ, η	$\mu \frac{\partial \psi}{\partial x} + \eta \frac{\partial \psi}{\partial y}$
x, y, z (three dimensions)	μ, η, ξ	$\mu \frac{\partial \psi}{\partial x} + \eta \frac{\partial \psi}{\partial y} + \xi \frac{\partial \psi}{\partial z}$
Streaming operator in cylindrical coordinates in conservation form		
ρ (one dimension)	ω, ξ	$\frac{\mu}{\rho} \frac{\partial}{\partial \rho}(\rho \psi) - \frac{1}{\rho} \frac{\partial}{\partial \omega}(\eta \psi)$
ρ, θ (two dimensions)	ω, ξ	$\frac{\mu}{\rho} \frac{\partial}{\partial \rho}(\rho \psi) - \frac{\eta}{\rho} \frac{\partial \psi}{\partial \theta} - \frac{1}{\rho} \frac{\partial}{\partial \omega}(\eta \psi)$
ρ, z (three dimension)	ω, ξ	$\frac{\mu}{\rho} \frac{\partial}{\partial \rho}(\rho \psi) + \xi \frac{\partial \psi}{\partial z} - \frac{1}{\rho} \frac{\partial}{\partial \omega}(\eta \psi)$
ρ, θ, z	ω, ξ	$\frac{\mu}{\rho} \frac{\partial}{\partial \rho}(\rho \psi) - \frac{\eta}{\rho} \frac{\partial \psi}{\partial \theta} + \xi \frac{\partial \psi}{\partial z} - \frac{1}{\rho} \frac{\partial}{\partial \omega}(\eta \psi)$
		$\mu = (1 - \xi^2)^{\frac{1}{2}} \cos \omega \quad \eta = (1 - \xi^2)^{\frac{1}{2}} \sin \omega$
Streaming operator in spherical coordinates in conservation form		
ρ	μ	$\frac{\mu}{\rho^2} \frac{\partial}{\partial \rho}(\rho^2 \psi) + \frac{1}{\rho} \frac{\partial}{\partial \mu}[(1 - \mu^2)\psi]$
ρ, θ	μ, ω	$\frac{\mu}{\rho^2} \frac{\partial}{\partial \rho}(\rho^2 \psi) + \frac{\eta}{\rho \sin \theta} \frac{\partial}{\partial \theta}(\sin \theta \psi)$ $+ \frac{1}{\rho} \frac{\partial}{\partial \mu}[(1 - \mu^2)\psi] - \frac{\cot \theta}{\rho} \frac{\partial}{\partial \omega}(\xi \psi)$
ρ, θ, ϕ	μ, ω	$\frac{\mu}{\rho^2} \frac{\partial}{\partial \rho}(\rho^2 \psi) + \frac{\eta}{\rho \sin \theta} \frac{\partial}{\partial \theta}(\sin \theta \psi)$ $+ \frac{\xi}{\rho \sin \theta} \frac{\partial \psi}{\partial \phi} + \frac{1}{\rho} \frac{\partial}{\partial \mu}[(1 - \mu^2)\psi] - \frac{\cot \theta}{\rho} \frac{\partial}{\partial \omega}(\xi \psi)$
		$\eta = (1 - \mu^2)^{\frac{1}{2}} \cos \omega; \quad \xi = (1 - \mu^2)^{\frac{1}{2}} \sin \omega$

times the speed

$$\phi(r) \equiv \int_0^4 \pi d\Omega \psi(r, \Omega) \quad (16.77)$$

and the current with respect to the ξ -coordinate is the net flow of neutrals in the positive ξ -direction

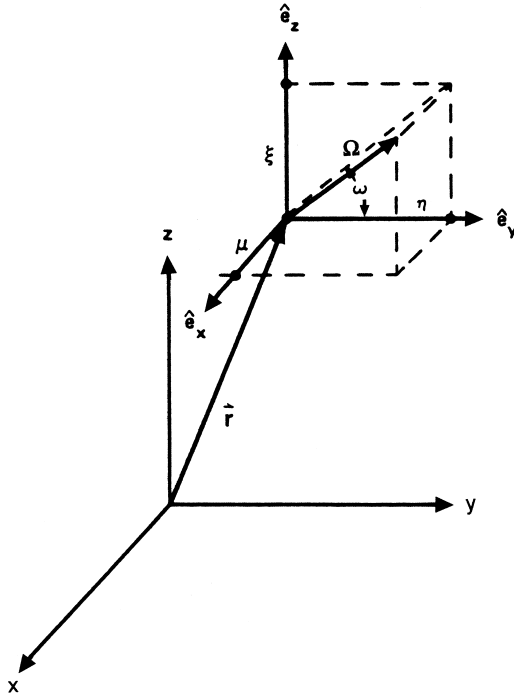


Figure 16.4. Cartesian space-angle coordinate system

$$J_\xi(\mathbf{r}) \equiv \mathbf{n}_\xi \int_0^{4\pi} d\Omega (\mathbf{n}_\xi \cdot \Omega) \psi(\mathbf{r}, \Omega) \quad (16.78)$$

16.3.4 Partial Currents

The positive and negative partial currents, with respect to the ξ -direction, are the total neutral flows in the positive and negative ξ -directions, respectively

$$\begin{aligned} J_\xi^+(\mathbf{r}) &\equiv \mathbf{n}_\xi \int_0^{2\pi} d\phi \int_0^1 d\mu (\mathbf{n}_\xi \cdot \Omega) \psi(\mathbf{r}, \Omega) \\ J_\xi^-(\mathbf{r}) &\equiv n_\xi \int_0^{2\pi} d\phi \int_{-1}^0 d\mu (\mathbf{n}_\xi \cdot \Omega) \psi(\mathbf{r}, \Omega) \end{aligned} \quad (16.79)$$

16.4 Integral Transport Theory

The multidimensional version of Eq. (16.1) may be written

$$\frac{d}{dR} \psi(\mathbf{r}, \Omega) dR d\Omega + \Sigma_t(\mathbf{r}) \psi(\mathbf{r}, \Omega) d\mathbf{r} d\Omega = S(\mathbf{r}, \Omega) d\mathbf{r} d\Omega \quad (16.80)$$

where the scattering source and the external source have been combined into S and where dR is the differential length along the direction Ω (i.e., $\Omega \cdot \nabla = d/dR$). This equation

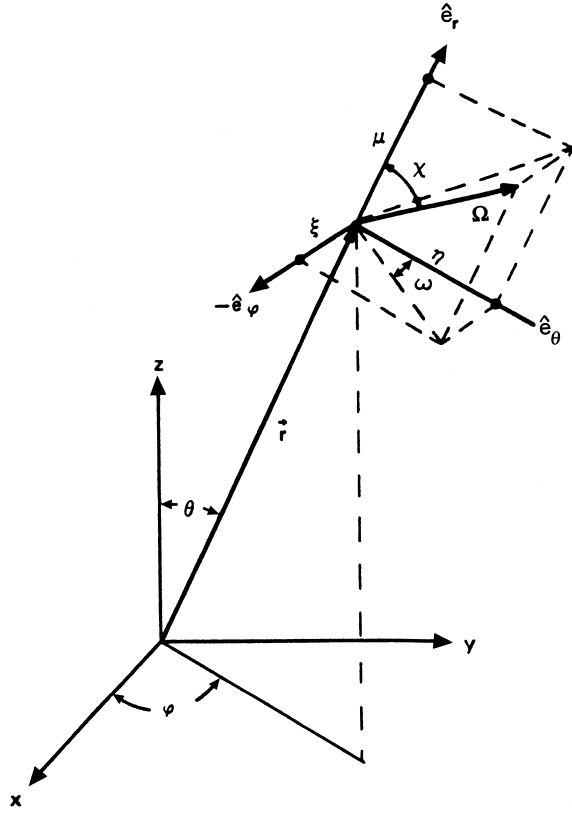


Figure 16.5. Spherical space-angle coordinate system

maybe integrated along the direction Ω from r_0 to r , to obtain

$$\psi(r, \Omega) dr = e^{-\alpha(r_0, r)} \psi(r_0, \Omega) dr_0 + \int_{r_0}^r dR' e^{-\alpha(r', r)} S(r', \Omega) dr' \quad (16.81)$$

where $\alpha(r', r)$ is the “optical” path length along the direction Ω between r' and r

$$\alpha(r', r) \equiv \left| \int_{r'}^r \Sigma_t(R) dR \right| \quad (16.82)$$

16.4.1 Isotropic Point Source

For an isotropic point source of strength $S_0(n/s)$ located at r_0 , the directional flux outward through the cone $d\Omega$ about the Ω -direction is $S_0(d\Omega/4\pi)$. The volume element dr subtended by this cone at distance $R = |r - r'|$ is $4\pi d\Omega R^2 dR$, as depicted in Fig. 16.7. From Eq. (16.2), the directional flux at r of uncollided neutrons from an isotropic point

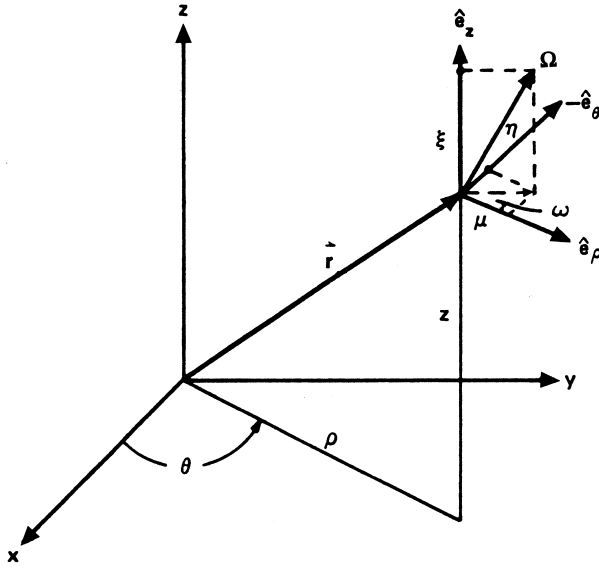


Figure 16.6. Cylindrical space-angle coordinate system

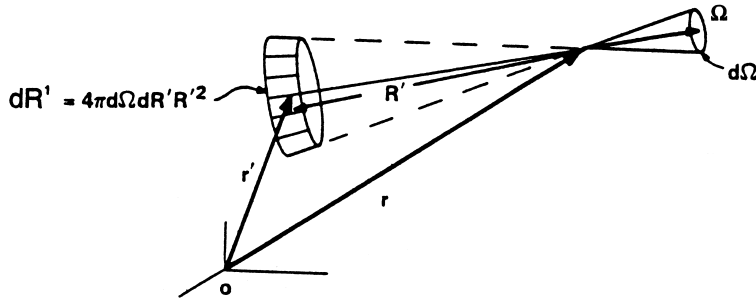


Figure 16.7. Incremental volume subtended by cone $d\Omega$ at distance $R = |\mathbf{r} - \mathbf{r}'|$ from point \mathbf{r}

source at \mathbf{r}' (such that the direction from \mathbf{r}' to \mathbf{r} is Ω) is given by

$$\psi_{pt}(R) = \psi(|(\mathbf{r} - \mathbf{r}')|, \Omega) = \frac{S_0 e^{-\alpha(\mathbf{r}, \mathbf{r}')}}{4\pi |\mathbf{r} - \mathbf{r}'|^2} = \frac{S_0 e^{-\alpha(R, 0)}}{4\pi R^2} \quad (16.83)$$

16.4.2 Isotropic Plane Source

The scalar flux of uncollided neutrals at a distance x from a uniform planar isotropic source can be constructed by treating each point in the plane as an isotropic point source

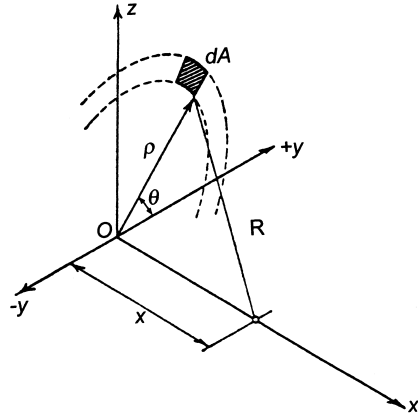


Figure 16.8. Coordinate system for plane isotropic source calculation

and integrating over the plane, as indicated in Fig. 16.8, to obtain

$$\begin{aligned}\phi_{\text{pl}}(x, 0) &= \int_0^\infty 2\pi\rho\psi_{\text{pt}}(R) d\rho = \int_x^\infty 2\pi R\psi_{\text{pt}}(R) dR \\ &= \frac{S_0}{2} \int_x^\infty e^{-\alpha(R, 0)} \frac{dR}{R} = \frac{1}{2} S_0 E_1(\alpha(x, 0))\end{aligned}\quad (16.84)$$

where the exponential integral function is defined as

$$E_n(y) \equiv \int_1^\infty du e^{-yu} u^{-n} = \int_0^1 d\mu e^{-y/\mu} \mu^{n-2} \quad (16.85)$$

The x -direction current of uncollided neutrons at a distance x from a uniform planar isotropic source can also be constructed in a similar manner by noting that for a neutron originating on the plane with direction Ω the quantity $\mu = \Omega \cdot n_x = x/R$:

$$\begin{aligned}J_{\text{pl},x}(x, 0) &= \int_0^\infty 2\pi\rho \left(\frac{x}{R}\right) \psi_{\text{pt}}(R) d\rho = x \int_x^\infty 2\pi R\psi_{\text{pt}}(R) \frac{dR}{R} \\ &= \frac{S_0}{2} \int_x^\infty e^{-\alpha(R, 0)} \frac{dR}{R^2} = \frac{1}{2} S_0 E_2(\alpha(x, 0))\end{aligned}\quad (16.86)$$

A one-dimensional isotropic source distribution $S_0(x)$ in a slab of thickness a can be considered as a distribution of isotropic planar sources, and the uncollided scalar flux distribution can be constructed by integrating over the contributions from each planar source:

$$\phi(x) = \int_0^a S_0(x') \phi_{\text{pl}}(x, x') dx' = \frac{1}{2} \int_0^a S_0(x') E_1(\alpha(x, x')) dx' \quad (16.87)$$

16.4.3 Anisotropic Plane Source

Using the relations $\mu = \cos\theta = x/R$ and $R^2 = x^2 + \rho^2$ and noting that all source neutrals in the annular region $2\pi\rho d\rho$ on the source plane will pass through a point at

a distance x above the center of the annular region within $d\mu$ about the same value of μ , the directional flux of uncollided neutrals which results from an anisotropic planar source $S(\mu)$ can be constructed:

$$\psi(x, \mu) d\mu = \psi_{pt}(R(\rho)) 2\pi\rho d\rho = \frac{S(\mu)e^{-\alpha(x,0)/\mu}}{\mu} d\mu \quad (16.88)$$

The scalar flux and current of uncollided neutrons at distance x from an uniform anisotropic planar source $S(\mu)$ are

$$\phi(x) \equiv \int_{-1}^1 \psi(x, \mu) d\mu = \int_0^1 S(\mu)e^{-\alpha(x,0)/\mu} \frac{d\mu}{\mu} \quad (16.89)$$

and

$$J_x(x) \equiv \int_{-1}^1 \mu \psi(x, \mu) d\mu = \int_0^1 S(\mu)e^{-\alpha(x,0)/\mu} d\mu \quad (16.90)$$

It is convenient to expand the directional dependence of the source

$$S(\mu) = \sum_{n=0}^{\infty} (2n+1)p_n^+(\mu)S_n \quad (16.91)$$

in half-range Legendre polynomials. With the orthogonality properties, it follows immediately that

$$S_n = \int_0^1 p_n^+(\mu)S(\mu) d\mu \quad (16.92)$$

Using this expansion in Eq. (16.89), the flux of uncollided neutrals at a distance x from an uniform anisotropic planar source is

$$\phi(x) = \sum_{n=0}^{\infty} (2n+1)S_n B_n^+(\alpha(x,0)) \quad (16.93)$$

where

$$\begin{aligned} B_n^+(\alpha(x,0)) &\equiv \int_x^{\infty} p_n^+(\mu)e^{-\alpha(x,0)/\mu} \frac{d\mu}{\mu} \\ B_0^+(\alpha(x,0)) &= E_1(\alpha(x,0)) \\ B_1^+(\alpha(x,0)) &= 2E_2(\alpha(x,0)) - E_1(\alpha(x,0)), \quad \text{etc.} \end{aligned} \quad (16.94)$$

Similarly, the x -directed current of uncollided neutrals at a distance x from an uniform anisotropic planar source is

$$J_x(x) = \sum_{n=0}^{\infty} (2n+1)S_n L_n^+(\alpha(x,0)) \quad (16.95)$$

where

$$\begin{aligned} L_n^+(\alpha(x,0)) &= \int_x^{\infty} p_n^+(\mu)e^{-\alpha(x,0)/\mu} d\mu \\ L_0^+(\alpha(x,0)) &= E_2(\alpha(x,0)) \\ L_1^+(\alpha(x,0)) &= 2E_3(\alpha(x,0)) - E_2(\alpha(x,0)), \quad \text{etc.} \end{aligned} \quad (16.96)$$

16.4.4 Transmission and Probabilities

As an example of an application of the above formalism, consider a purely ionizing slab of thickness “ a ” with an isotropic plane source of neutrals on one surface (e.g. the recycling of neutrals from the wall, if scattering is small compared to ionization). The transmission probability for the slab is just the ratio of the exiting current on the opposite surface to the incident partial current on the other surface

$$T = \frac{J(a)}{J_{\text{in}}(0)} = \frac{S_0 L_0^+(\alpha(a, 0))}{S_0} = E_2(\alpha(a, 0)) \quad (16.97)$$

and the ionization probability is $I = 1 - T = 1 - E_2(\alpha(a, 0))$.

16.4.5 Escape Probability

As another example, consider a uniform, purely ionizing slab of thickness “ a ” with an isotropic neutral source S_0 (e.g. volume recombination) distributed uniformly throughout. Representing the source of neutrals at x within the slab as a plane isotropic source of $S_0/2$ to the right and $S_0/2$ to the left, the current of neutrals produced by the source at $x = x'$ which exit through the surface at $x = a$ is

$$J_{\text{out}}(a : x') = \frac{1}{2} S_0 L_0^+(\alpha(a, x')) = \frac{1}{2} S_0 E_2(\alpha(a, x')) \quad (16.98)$$

The total current of neutrals out through the surface at $x = a$ is found by integrating this expression over the slab:

$$J_{\text{out}}(a) = \int_0^a dx' J_{\text{out}}(a : x') = \frac{1}{2} S_0 \int_0^a dx' E_2(\alpha(a, x')) \quad (16.99)$$

Using the differentiation property of the exponential integral function

$$\frac{dE_n}{dy} = -E_{n-1}(y), \quad n = 1, 2, 3 \dots \quad (16.100)$$

Equation (16.99) may be evaluated

$$\begin{aligned} J_{\text{out}}(a) &= -\frac{1}{2} S_0 \int_0^a \frac{dE_3(\alpha)}{d\alpha} dx' = -\frac{1}{2} \frac{S_0}{\Sigma_t} \int_0^{a(a, 0)} \frac{dE_3}{d\alpha} d\alpha \\ &= \frac{1}{2} \frac{S_0}{\Sigma_t} [E_3(0) - E_3(\alpha(a, 0))] = \frac{1}{2} \frac{S_0}{\Sigma_t} \left[\frac{1}{2} - E_3(\alpha(a, 0)) \right] \end{aligned} \quad (16.101)$$

By symmetry, the current out through the surface at $x = 0$ must be the same.

The escape probability from the slab is the ratio of the total current out of the slab through both surfaces to the total neutral source rate aS_0 in the slab

$$P_0 = \frac{J_{\text{out}}(a) + J_{\text{out}}(0)}{aS_0} = \frac{1}{a\Sigma_t} \left[\frac{1}{2} - E_3(a\Sigma_t) \right] \quad (16.102)$$

16.4.6 Inclusion of Isotropic Scattering and Charge Exchange

Consider again the slab with a distributed isotropic source of neutrals, but now with isotropic elastic scattering and charge-exchange, as well as ionization, represented explicitly. The flux of uncollided source neutrals is

$$\phi_0(x) = \int_0^a S_0(x') E_1(\alpha(x, x')) dx' \quad (16.103)$$

If the first collision rate at $x = x'$ is considered as a plane isotropic source of once-collided neutrals at x' , then the flux of once-collided neutrals due to the once-collided source at x' is

$$\phi_1(x : x') = \frac{1}{2} (\Sigma_s(x') + \nu) \phi_0(x') E_1(\alpha(x, x')) \quad (16.104)$$

and the total flux of once-collided neutrals at x is found by integrating over the distribution of first-collision sources:

$$\phi_1(x) = \int_0^a \phi_1(x : x') dx' = \int_0^a \left[\frac{1}{2} (\Sigma_s(x') + \Sigma_{cx}(x')) \right] E_1(\alpha(x, x')) dx' \quad (16.105)$$

Continuing in this vein, the flux of n -collided neutrals is given by

$$\phi_n(x) = \int_0^a \left[\frac{1}{2} (\Sigma_s(x') + \Sigma_{cx}(x')) \phi_{n-1}(x') \right] \cdot E_1(\alpha(x, x')) dx' \quad n = 1, 2, 3, \dots, \infty \quad (16.106)$$

The total neutral flux is the sum of the uncollided, once-collided, twice-collided, etc. fluxes:

$$\begin{aligned} \phi(x) &\equiv \phi_0(x) + \sum_{n=1}^{\infty} \phi_n(x) = \int_0^a \frac{1}{2} [\Sigma_s(x') + \Sigma_{cx}(x')] \\ &\times \sum_{n=1}^{\infty} \phi_{n-1}(x') E_1(\alpha(x, x')) dx' + \frac{1}{2} \int_0^a [S_0(x') E_1(\alpha(x, x'))] dx' \\ &= \int_0^a \frac{1}{2} (\Sigma_s(x') + \Sigma_{cx}(x')) \phi(x') E_1(\alpha(x, x')) dx' \\ &\quad + \frac{1}{2} \int_0^a S_0(x') E_1(\alpha(x, x')) dx' \quad (16.107) \end{aligned}$$

Thus, we have found an integral equation for the neutral flux in a slab with isotropic scattering and charge-exchange, with a kernel $(1/2)[\Sigma_s(x') + \Sigma_{cx}(x')]E_1(\alpha(x, x'))$ and a first collision source $S_0 E_1(\alpha(x, 0))$. Recall that Σ_s represents elastic scattering plus charge-exchange.

16.4.7 Distributed Volumetric Sources in Arbitrary Geometry

The scalar flux of uncollided neutrals resulting from an arbitrary neutral source distribution (e.g. volumetric recombination in the divertor) can be constructed by treating each spatial location as a point source with strength given by the source distribution for that location. The uncollided directional flux at \mathbf{r} arising from a point source at \mathbf{r}' is given by Eq. (16.83). The total uncollided directional flux at \mathbf{r} is obtained by integrating over all source points \mathbf{r}' , and the total uncollided scalar flux is then calculated by integrating over Ω

$$\phi_{\text{un}}(\mathbf{r}) = \int d\Omega \int d\mathbf{r}' \frac{S_0(\mathbf{r}') e^{-\alpha(\mathbf{r}, \mathbf{r}')}}{4\pi |\mathbf{r}' - \mathbf{r}|^2} \quad (16.108)$$

Following the same development as that leading to Eq. (16.107), an integral equation for the total neutral flux can be developed for the case of isotropic scattering

$$\begin{aligned} \phi(\mathbf{r}) &= \int d\mathbf{r}' \frac{(\Sigma_s(\mathbf{r}') + \Sigma_{\text{cx}}(\mathbf{r}')) \phi(\mathbf{r}') e^{-\alpha(\mathbf{r}, \mathbf{r}')}}{4\pi |\mathbf{r}' - \mathbf{r}|^2} + \phi_{\text{un}}(\mathbf{r}') \\ &= \int d\mathbf{r}' [(\Sigma_s(\mathbf{r}') + \Sigma_{\text{cx}}(\mathbf{r}')) \phi(\mathbf{r}') + S_0(\mathbf{r}')] \frac{e^{-\alpha(\mathbf{r}, \mathbf{r}')}}{4\pi |\mathbf{r}' - \mathbf{r}|^2} \end{aligned} \quad (16.109)$$

where $e^{-\alpha(\mathbf{r}, \mathbf{r}')}/4\pi |\mathbf{r} - \mathbf{r}'|^2$ is the isotropic point source kernel and ϕ_{un} given by Eq. (16.108) is the uncollided flux contribution.

The derivations leading to Eqs. (16.107) and (16.109) did not explicitly take boundary conditions into account. Since scattering source rates integrated over volume were used to derive successive n -collided fluxes, the implicit assumption was that neutrals which escaped from the volume did not return. Thus, these equations are valid with vacuum boundary conditions, but not with reflective boundary conditions.

16.4.8 Flux from a Line Isotropic Source

Consider the situation illustrated in Fig. 16.9 of a line isotropic source of neutrals of strength $S_0(\text{cm} \cdot \text{s})$. The point source kernel can be used to construct the differential scalar flux at a point P located a distance t from the line source due to the differential element dz of the line source located at z :

$$d\phi(t) = \frac{S_0 dz e^{-\alpha(t, z)}}{4\pi R^2} \quad (16.110)$$

Noting that $R = t/\cos\theta$ and $dz = R d\theta/\cos\theta = t d\theta/\cos^2\theta$, the total flux at a point at a distance t can be found by integrating the differential flux contribution from all such differential elements dz

$$\phi(t) = \int_{-\infty}^{\infty} \frac{S_0 dz e^{-\alpha(t, z)}}{4\pi R^2} = S_0 \int_0^{\infty} \frac{dz e^{-\alpha(t, 0)/\cos\theta}}{(2\pi t^2/\cos^2\theta)} \equiv \frac{Ki_1[\alpha(t, 0)]}{2\pi R} S_0 \quad (16.111)$$

where $Ki_1(x)$ is the Bickley function of order one.

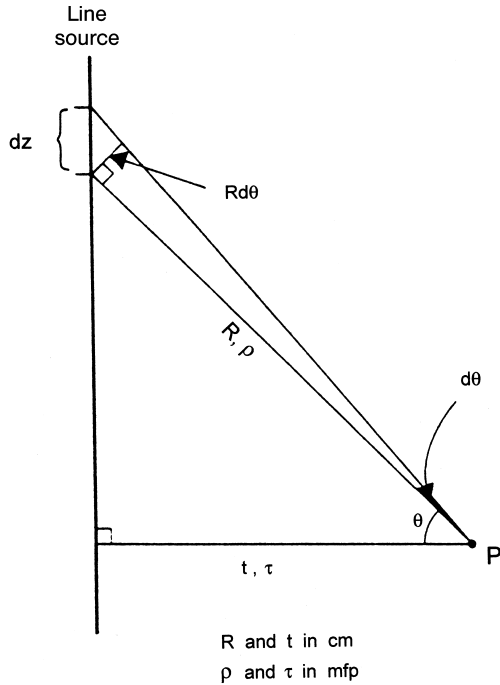


Figure 16.9. Geometry for calculating flux at P from a line isotropic neutral source ($t = x$, $t = \alpha Z(x, 0)$)

16.4.9 Bickley Functions

The general Bickley function is defined

$$Ki_n(x) \equiv \int_0^{\pi/2} \cos^{n-1}\theta e^{-x/\cos\theta} d\theta = \int_0^\infty \frac{e^{-x \cosh(u)}}{\cosh^n(u)} du \quad (16.112)$$

These functions satisfy the following differential and integral laws

$$\frac{dKi_n(x)}{dx} = -Ki_{n-1}(x) \quad (16.113)$$

and

$$Ki_n(x) = Ki_n(0) - \int_0^x Ki_{n-1}(x') dx' = \int_x^\infty Ki_{n-1}(x') dx' \quad (16.114)$$

and the recurrence relation

$$nKi_{n+1}(x) = (n-1)Ki_{n-1}(x) + x(Ki_{n-2}(x) - Ki_n(x)) \quad (16.115)$$

The Bickley functions must be evaluated numerically.

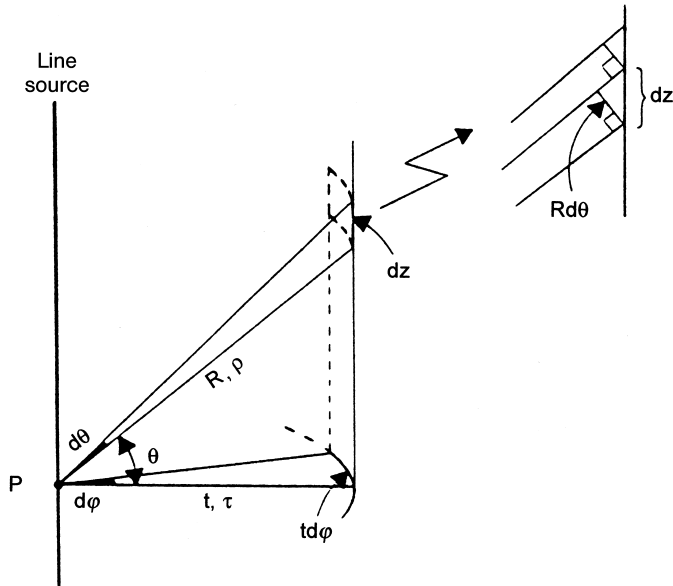


Figure 16.10. Geometry for calculating probability that a neutral from an isotropic line source does not have a collision within a perpendicular distance t from the line source ($t = x, t = a(x, 0)$)

16.4.10 Probability of Traveling a Distance t from a Line, Isotropic Source without a Collision

With reference to Fig. 16.10, the probability P that a neutral emitted isotropically from point P on the line source is able to travel a perpendicular distance t away from the line source without having a collision depends on the direction in which the neutral is traveling relative to the perpendicular to the line source. The uncollided differential neutral current arising from a point on the line source and passing through a differential surface area $dA = R d\theta t d\phi = t^2 d\theta d\phi / \cos \theta$ normal to the R -direction at a perpendicular distance t from the line source is

$$dJ(t, \theta) = \frac{e^{-\alpha(t, z)}}{4\pi R^2} dA = \frac{e^{-\alpha(t, 0)/\cos \theta}}{4\pi(t/\cos \theta)^2} \frac{t^2 d\theta d\phi}{(\cos \theta)} \quad (16.116)$$

where the optical thickness $\alpha(t, z)$ is taken along the path length R . Integrating over all possible values of the angles, the probability of a neutral emitted isotropically from a line source crossing the cylindrical surface at a distance t from the line source is

$$P(t) = \int_0^{2\pi} d\phi \int_{-\pi/2}^{\pi/2} d\theta \frac{e^{-\alpha(t, 0)/\cos \theta} (t^2 / \cos \theta)}{4\pi(t/\cos \theta)^2} = Ki_2(\alpha(t, 0)) \quad (16.117)$$

where now $a(t, 0)$ is the optical pathlength perpendicular to the line source out to the cylindrical surface at distance t .

The Bickley and exponential integral functions arise because of the assumption of spatial symmetry. They take into account that the neutral flight path is always in three spatial dimensions, even though symmetry otherwise allows reduction in the dimensionality of the problem.

16.5 Collision Probability Methods

If the domain of the problem of interest is partitioned into discrete volumes, V_i , within each of which uniform average cross sections and a flat flux are assumed, Eq. (16.109) can be integrated over V_i , and the resulting equation can be divided by V_i to obtain

$$\phi_i = \sum_j T^{j \rightarrow i} [(\Sigma_{sj} + \Sigma_{cxj}) \phi_j + S_{0j}] \quad (16.118)$$

which relates the fluxes in the various volumes by the “first-flight transmission probabilities” $T^{j \rightarrow i}$

$$T^{j \rightarrow i} \equiv \frac{1}{V_i} \int_{V_i} d\mathbf{r}_i \int_{V_j} d\mathbf{r}_j \frac{e^{-\alpha(\mathbf{r}_i, \mathbf{r}_j)}}{4\pi |\mathbf{r}_i - \mathbf{r}_j|^2} \quad (16.119)$$

16.5.1 Reciprocity among Transmission and Collision Probabilities

Since $\alpha(\mathbf{r}_i, \mathbf{r}_j) = \alpha(\mathbf{r}_j, \mathbf{r}_i)$, i.e. the optical path is the same no matter which way the neutral traverses the straightline distance between \mathbf{r}_i and \mathbf{r}_j , there is a reciprocity relation between the transmission probabilities

$$V_i T^{j \rightarrow i} = V_j T^{i \rightarrow j} \quad (16.120)$$

Upon multiplication by $\Sigma_{ti} V_i$, where the total cross section Σ_{ti} represents ionization, elastic scattering and charge-exchange, Eq. (16.118) can be written

$$\Sigma_{ti} V_i \phi_i = \sum_j P^{ji} \frac{[(\Sigma_{sj} + \Sigma_{cxj}) \phi_j + S_{0j}]}{\Sigma_{tj}} \quad (16.121)$$

where the collision rate in cell i is related to the neutrals introduced by scattering, charge-exchange and an external source in all cells by the “collision probabilities”

$$P^{ji} \equiv \Sigma_{tj} \Sigma_{ti} V_i T^{j \rightarrow i} = \Sigma_{tj} \Sigma_{ti} \int_{V_i} d\mathbf{r}_i \int_{V_j} d\mathbf{r}_j \frac{e^{-\alpha(\mathbf{r}_i, \mathbf{r}_j)}}{4\pi |\mathbf{r}_i - \mathbf{r}_j|^2} \quad (16.122)$$

Because $\alpha(\mathbf{r}_i, \mathbf{r}_j) = \alpha(\mathbf{r}_j, \mathbf{r}_i)$, there is reciprocity between the collision probabilities; i.e.

$$P^{ij} = P^{ji} \quad (16.123)$$

16.5.2 Collision Probabilities for Slab Geometry

For a slab lattice the volumes, V_i , become the widths $\Delta_i \equiv x_{i+\frac{1}{2}} - x_{i-\frac{1}{2}}$ of the slab regions centered at x_i and the slab kernel $E_1(\alpha(x_i, x_j))/2$ replaces the point source kernel in Eq. (16.122), which becomes

$$P^{ji} = \Sigma_{ti} \Sigma_{tj} \int_{\Delta_i} dx_i \int_{\Delta_j} dx_j \frac{1}{2} E_1(\alpha(x_i, x_j)) \quad (16.124)$$

For $j = i$, the probability that a neutral introduced in cell i has its next collision in cell i is

$$P^{ii} = \Sigma_{ti} \Delta_i \left[1 - \frac{1}{2 \Sigma_{ti} \Delta_i} (1 - 2E_3(\Sigma_{ti} \Delta_i)) \right] \quad (16.125)$$

and for $j \neq i$, the probability that a neutral introduced in cell j has its next collision in cell i is

$$\begin{aligned} P^{ji} = \frac{1}{2} & \left[E_3(\alpha_{i+\frac{1}{2}, j+\frac{1}{2}}) - E_3(\alpha_{i-\frac{1}{2}, j+\frac{1}{2}}) \right. \\ & \left. - E_3(\alpha_{i+\frac{1}{2}, j-\frac{1}{2}}) + E_3(\alpha_{i-\frac{1}{2}, j-\frac{1}{2}}) \right] \end{aligned} \quad (16.126)$$

where $\alpha_{ij} \equiv \alpha(x_i, x_j)$.

16.5.3 Collision Probabilities in Two-Dimensional Geometry

Consider the two-dimensional cross section shown in Fig. 16.11, in which the volumes V_i and V_j extend indefinitely in the direction perpendicular to the page. With respect to Fig. 16.10, a neutral emitted at point t defined by the angle ϕ and coordinate y in volume V_i in Fig. 16.11 and traveling in the direction defined by the angle ϕ which passes through volume V_j may be traveling at any angle $-\pi/2 \leq \theta \leq \pi/2$ with respect to the horizontal cross section shown in Fig. 16.11.

The probability that a neutral emitted at point t will reach some point on the line perpendicular to the page which passes through the page at point t' in volume V_j is, from Eq. (16.117), given by $Ki_2(\alpha(t', t))$, where $\alpha(t', t)$ is the optical path length in the horizontal plane of Fig. 16.11. With respect to Fig. 16.11, identify t_i and t_j as the points along the horizontal line between t and t' at which the line passes through the surfaces of volumes V_i and V_j , respectively. Thus, $Ki_2(\Sigma_{ti}(t_i - t) + \alpha(t_j, t_i))$ is the probability that a neutral emitted from point t in volume V_i in direction ϕ reaches volume V_j , and $Ki_2(\Sigma_{ti}(t_i - t) + \alpha(t_j, t_i) + \alpha(t_j + \Delta t_j, t_j))$, with Δt_j being the distance in the horizontal plane across volume V_j , is the probability that the neutral not only reaches volume V_j but continues through volume V_j and emerges from the opposite side without a collision, both probabilities being averaged over an isotropic distribution of neutral directions with respect to the horizontal, as measured by the angle φ . The probability that neutrals emitted from point t in volume V_i with direction ϕ have their first collision

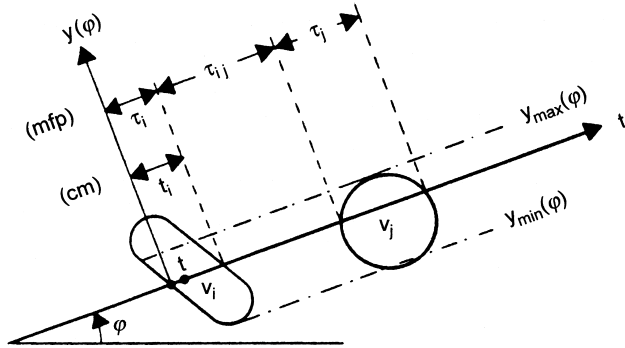


Figure 16.11. Geometry for calculating collision probabilities in two-dimensional geometry (τ is the optical path length α over the indicated path)

in volume V_j is then $p_{ij}(t, \varphi, y) = -Ki_2(\Sigma_{ti}(t_i - t) + \alpha(t_j, t_i) + \alpha(t_j + \Delta t_j, t_j)) + Ki_2(\Sigma_{ti}(t_i - t) + \alpha(t_j, t_i))$. Averaging this probability over all source points along the line defined by angle φ within volume V_i and using the differential property of the Bickley functions given by Eq. (16.113) leads to

$$\begin{aligned} p_{ij}(\phi, y) &= \frac{1}{t_i} \int_0^i p_{ij}(t, \phi, y) dt \\ &= \frac{1}{\Sigma_{ti} t_i} \left\{ Ki_3(\alpha(t_j, t_i)) - Ki_3[\alpha(t_j, t_i) + \alpha(t_j + \Delta t_j, t_j)] \right. \\ &\quad - Ki_3[\alpha(t_j, t_i) + \alpha(t_i, 0)] \\ &\quad \left. + Ki_3[\alpha(t_j, t_i) + \alpha(t_j + \Delta t_j, t_i) + \alpha(t_i, 0)] \right\} \end{aligned} \quad (16.127)$$

To obtain the average probability P^{ij} that a neutral introduced by an isotropic source uniformly distributed over volume V_i will have its first collision in volume V_j , this expression must be multiplied by the probability that an isotropically emitted neutral source will emit a neutral in the differential direction $d\varphi$ about φ , which is $d\varphi/2\pi$, and the probability that for a uniform source within V_i the neutral will be emitted from along the chord of length $t_i(y)$ at coordinate y , which is $t_i(y) dy/V_i$, and integrated over all relevant values of φ and y . Note that the “volumes” V_i and V_j are actually the respective areas within the planar cross section of Fig. 16.11. The result for the collision probability is

$$\begin{aligned} P^{ij} &= \frac{1}{2\pi} \int_{\varphi_{\min}}^{\varphi_{\max}} d\varphi \int_{y_{\min}(\varphi)}^{y_{\max}(\varphi)} dy \left\{ Ki_3(\alpha(t_j, t_i)) \right. \\ &\quad - Ki_3[\alpha(t_j, t_i) + \alpha(t_j + \Delta t_j, t_j)] - Ki_3[\alpha(t_j, t_i) + \alpha(t_i, 0)] \\ &\quad \left. + Ki_3[\alpha(t_j, t_i) + \alpha(t_j + \Delta t_j, t_j) + \alpha(t_i, 0)] \right\} \end{aligned} \quad (16.128)$$

A similar development leads to an expression for the probability that the next collision for a neutral introduced in volume V_i is within that same volume V_i

$$P^{ii} = \Sigma_{ti} V_i - \frac{1}{2\pi} \int_{\varphi_{\min}}^{\varphi_{\max}} d\varphi \int_{y_{\min}(\varphi)}^{y_{\max}(\varphi)} dy [K_{i3}(0) - K_{i3}(\alpha(t_i, 0))] \quad (16.129)$$

16.6 Interface Current Balance Methods

16.6.1 Formulation

The interface current method is essentially a reformulation of the collision probabilities method in such a way that the coupling among regions is via the partial currents flowing between adjacent regions. Consider the 2D configuration in Fig. 16.12. The current from region k into region i is denoted J_{ki} ($\Gamma_{k \rightarrow i}$ in the figure), the probability that the current entering region i from region k is transmitted across region i without collision to contribute to the current from region i into region j is denoted T_{0i}^{kj} , and the probability that a collided or source neutral escaping from region i escapes into region j is denoted Λ_{ij} . The total partial current flowing from region i into region j may be written

$$J_{ij} = \sum_k^i T_{0i}^{kj} J_{ki} + \sum_k^i (1 - \sum_l^i T_{0i}^{kl}) J_{ki} c_i P_i \Lambda_{ij} + \Lambda_{ij}^s s_i P_i \quad (16.130)$$

where the summation \sum_k^i is over all regions k that are contiguous to region i . The three terms in Eq. (16.130) correspond physically to: (1) the sum of the currents incident into region i from all contiguous regions times the probability that each is transmitted across region i without collision to exit into region j (note that the possibility of concave surfaces is allowed by including uncollided transmission from region j across region i back into region j); (2) the sum of the currents incident into region i from all contiguous regions times the probability $(1 - \sum_l^i T_{0i}^{kl})$ that each is *not* transmitted without collision across region i to any of the contiguous regions, times the probability c_i that the first collision is a “scattering” (elastic scattering or charge-exchange) event, times the probability $P_i \Lambda_{ij}$ that the “scattered” neutral eventually escapes from region i into region j ; and (3) the source of neutrals (injected or volumetric recombination) in region i times the probability $P_i \Lambda_{ij}^s$ that a source neutral in region i eventually escapes into region j .

16.6.2 Transmission and Escape Probabilities

The general form for the evaluation of transmission and escape probabilities can be developed using the point kernel discussed previously. We will treat the case of incident fluxes which are isotropically distributed in the incident hemisphere of directions, as shown in Fig. 16.13, and volumetric neutral sources (injected, recombination) which are uniformly distributed over volume and emitted isotropically in direction. These results can be extended to anisotropic incident fluxes and nonuniform and anisotropic volumetric source distributions by extending the procedures indicated below.

The probability that a neutral introduced isotropically at location \mathbf{r}_i within volume V_i escapes without collision across the surface S_{ki} which defines the interface between volume V_i and contiguous volume V_k is the probability $d\Omega/4\pi|\mathbf{r}_{S_{ki}} - \mathbf{r}_i|^2$ that the neutral

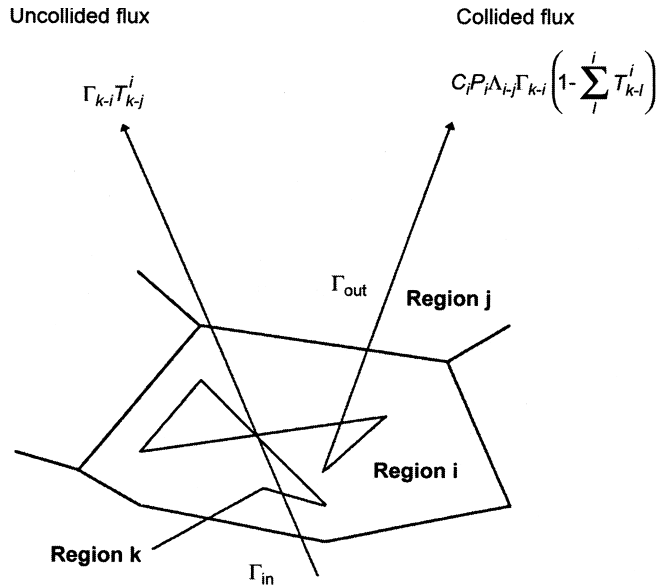


Figure 16.12. Planar projection of geometry for multidimensional interface current methods

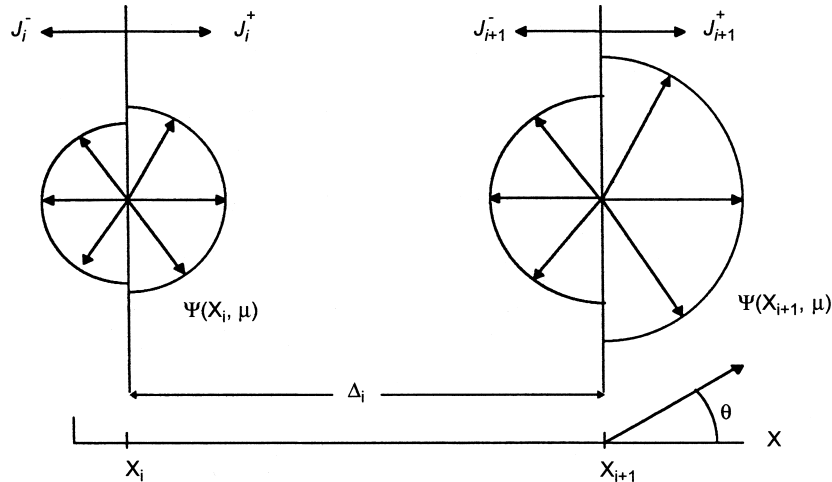


Figure 16.13. Interface distribution of neutrals is isotropic in each half space

is traveling within a cone of directions $d\Omega$ which intersects that surface, times the probability $\exp(-\alpha(\mathbf{r}_{S_{ki}}, \mathbf{r}_i))$ that the neutral reaches the surface at location $\mathbf{r}_{S_{ki}}$ along the direction Ω from \mathbf{r}_i without a collision, integrated over all Ω that intersect the surface S_{ki} from point \mathbf{r}_i . This probability is then averaged over all points \mathbf{r}_i within volume V_i to obtain

$$P_{oi} \Lambda_k = \frac{1}{4\pi V_i} \int_{V_i} d\mathbf{r}_i \int_{S_{ki}} dS \frac{e^{-\alpha(\mathbf{r}_{S_{ki}}, \mathbf{r}_i)}}{|\mathbf{r}_{S_{ki}} - \mathbf{r}_i|^2} \quad (16.131)$$

The probability that an incident unit neutral flux which is isotropically distributed over the inward hemisphere of directions entering volume V_i from volume V_k across surface S_{ki} is transmitted without collision across volume V_i to the surface S_{ji} which forms the interface with contiguous volume V_j is the product of the probability $\mathbf{n}_{S_{ki}} \cdot d\Omega / 2\pi |\mathbf{r}_{S_{ki}} - \mathbf{r}_{S_{ji}}|^2 = (\mathbf{n}_{S_{ki}} \cdot \boldsymbol{\Omega}) d\Omega / 2\pi |\mathbf{r}_{S_{ki}} - \mathbf{r}_{S_{ji}}|^2$ that a neutral incident across S_{ki} is traveling within a cone of directions $d\Omega$ which intersects the surface S_{ji} , times the probability $\exp(-\alpha(\mathbf{r}_{S_{ji}}, \mathbf{r}_{S_{ki}}))$ that the neutral reaches the surface at location $\mathbf{r}_{S_{ji}}$ along the direction $\boldsymbol{\Omega}$ from $\mathbf{r}_{S_{ki}}$ without a collision, integrated over all Ω that intersect the surface S_{ji} from point $\mathbf{r}_{S_{ki}}$. The quantity $\mathbf{n}_{S_{ki}}$ is the unit vector normal to the surface S_{ki} in the direction from volume V_k into volume V_i . This probability is then averaged over all points $\mathbf{r}_{S_{ki}}$ on S_{ki} to obtain

$$T_{oi}^{kj} = \frac{\int_{S_{ki}} dS \int_{S_{ji}} dS \frac{e^{-\alpha(\mathbf{r}_{S_{ji}}, \mathbf{r}_{S_{ki}})} (\mathbf{n}_{S_{ki}} \cdot \boldsymbol{\Omega})}{|\mathbf{r}_{S_{ji}} - \mathbf{r}_{S_{ki}}|^2}}{\int_{\mathbf{n}_{S_{ki}} \cdot \boldsymbol{\Omega} > 0} d\Omega \int_{S_{ki}} dS} \quad (16.132)$$

16.6.3 2D Transmission/Escape Probabilities (TEP) Method

In order to develop computational algorithms, we consider geometries with symmetry in one direction, which are conventionally known as 2D geometries. It is important to keep in mind, however, that neutral flight paths take place in three dimensions.

16.6.3.1 Transmission Probabilities

Consider a volume V_i which is symmetric in the axial direction and bounded by flat vertical surfaces, so that a horizontal ($x-y$) planar slice is as shown in Fig. 16.14, with the vertical dimension normal to the page. We want to calculate the transmission coefficient from volume 1 through the volume i into volume 3. A three-dimensional projection and a vertical projection are shown in Fig. 16.15. The “point” ξ_1 in Fig. 16.14 is the projection onto the horizontal plane of the vertical axis shown in Fig. 16.15. The differential solid angle in this coordinate system is

$$d\Omega = \frac{1}{4\pi} \sin \theta' d\theta' d\phi = -\frac{1}{4\pi} \cos \theta d\theta d\phi \quad (16.133)$$

The incident directional flux from volume 1 at “point” ξ_1 , $\psi(\mathbf{r} - R\boldsymbol{\Omega}, \boldsymbol{\Omega})$ is attenuated when it traverses the distance R to reach the “point” ξ_3 and enter volume 3

$$\psi(\mathbf{r}, \boldsymbol{\Omega}) = \psi(\mathbf{r} - R\boldsymbol{\Omega}, \boldsymbol{\Omega}) e^{-\Sigma R} \quad (16.134)$$

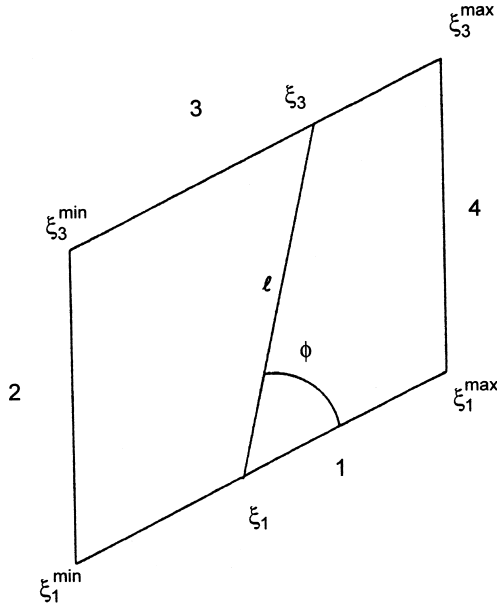


Figure 16.14. Planar projection of geometry for transmission probability calculation in 2D

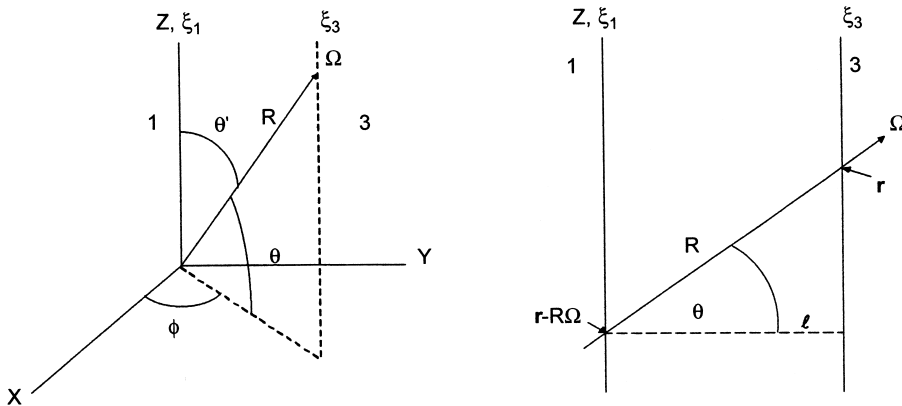


Figure 16.15. 3D and axial projection of geometry for transmission probability calculation in 2D

The incident partial current density (cm^2/s) from volume 1 at point ξ_1 is

$$\begin{aligned} j_{\text{in}}(\xi_1) &= \int_{\mathbf{n}_{\text{in}}, \Omega > 0} d\Omega (\mathbf{n}_{\text{in}} \cdot \Omega) \psi(\mathbf{r} - R\Omega, \Omega) d\Omega \\ &= -\frac{1}{4\pi} \int_0^\pi d\phi \int_{-\pi/2}^{\pi/2} d\theta \cos^2 \theta \sin \phi \psi(\mathbf{r} - R\Omega, \Omega) \end{aligned} \quad (16.135)$$

where $\mathbf{n}_{\text{in}} \cdot \boldsymbol{\Omega} = \cos \theta \sin \phi$ has been used. When the incident flux is isotropic in the incident hemisphere (double- P_0 approximation), this becomes

$$j_{\text{in}}^{\text{iso}}(\xi_1) = \frac{1}{4}\psi(\mathbf{r} - R\boldsymbol{\Omega}) \quad (16.136)$$

The incident partial current (#/s) is obtained by multiplying by the (arbitrary) axial dimension H and integrating over $\xi_1^{\min} \leq \xi_1 \leq \xi_1^{\max}$

$$J_{\text{in}} = H \int_{\xi_1^{\min}}^{\xi_1^{\max}} d\xi_1 j_{\text{in}}(\xi_1) \quad (16.137)$$

The incident neutrals from volume 1 which enter volume V_i at ξ_1 within the solid angle subtended by volume 3 and traverse volume i without collision to enter volume 3 constitute an uncollided neutral flux out of volume V_i into volume 3, and hence a contribution to the incident current into volume 3 from volume i . For the moment we write this contribution to the current into volume 3 as

$$\begin{aligned} J_{\text{out}} &= H \int_{\xi_1^{\min}}^{\xi_1^{\max}} d\xi_1 \int_{\substack{(\boldsymbol{\Omega} \cdot \hat{\mathbf{n}}_{\text{out}}) > 0 \\ \phi(\xi_1) \ni 3}} d\boldsymbol{\Omega} (\boldsymbol{\Omega} \cdot \mathbf{n}_{\text{out}}) \psi(\mathbf{r} - R\boldsymbol{\Omega}, \boldsymbol{\Omega}) e^{-\Sigma R} \\ &= H \int_{\xi_1^{\min}}^{\xi_1^{\max}} d\xi_1 \int_{\phi_{\min}(\xi_1)}^{\phi_{\max}(\xi_1)} d\phi \int_{-\pi/2}^{\pi/2} d\theta \cos^2 \theta \sin \phi e^{-\frac{\Sigma l(\phi(\xi_1))}{\cos \theta}} \psi(\mathbf{r} - R\boldsymbol{\Omega}, \boldsymbol{\Omega}) \end{aligned} \quad (16.138)$$

where $\mathbf{n}_{\text{out}} \cdot \boldsymbol{\Omega} = \cos \theta \sin \phi_{\text{out}}$ may differ from $\mathbf{n}_{\text{in}} \cdot \boldsymbol{\Omega} = \cos \theta \sin \phi$ if the interfaces with volumes 1 and 3 are not parallel, and $\phi(\xi_1) \ni 3$ indicates angles ϕ from a point ξ_1 which intersect the interface with region 3. When the incident flux from volume 1 is isotropic in the incident directional hemisphere, this becomes

$$J_{\text{out}}^{\text{iso}} = \frac{H}{2\pi} \int_{\xi_1^{\min}}^{\xi_1^{\max}} d\xi_1 \int_{\phi_{\min}(\xi_1)}^{\phi_{\max}(\xi_1)} d\phi \sin \phi_{\text{out}} K_{i3}(\Sigma l(\phi(\xi_1))) \psi(\mathbf{r} - R\boldsymbol{\Omega}) \quad (16.139)$$

The transmission probability, for an isotropic incident flux distribution from volume 1 that is uniform over $\xi_1^{\min} \leq \xi_1 \leq \xi_1^{\max}$ can be written in a form that couples the contribution to the incident current into volume 3 with the incident current into volume i

$$T_{oi}^{13} \equiv \frac{J_{\text{out}}^{\text{iso}}}{J_{\text{in}}^{\text{iso}}} = \frac{2}{\pi} \frac{\int_{\xi_1^{\min}}^{\xi_1^{\max}} d\xi_1 \int_{\phi_{\min}(\xi_1)}^{\phi_{\max}(\xi_1)} d\phi \sin \phi_{\text{out}} K_{i3}(\Sigma l(\phi(\xi_1)))}{(\xi_1^{\max} - \xi_1^{\min})} \quad (16.140)$$

When the incident and exiting surfaces (the interfaces of volumes 1 and i and of volumes 3 and i in this example) are not parallel, there is a subtlety about the direction to take for \mathbf{n}_{out} in the above equations. The incident current into volume i from volume 1 was calculated on the basis of a DP-0 angular flux approximation with respect to the orientation of the incident surface. The transport of the uncollided incident DP-0 angular flux across region i is properly calculated, and by using $\mathbf{n}_{\text{out}} = \mathbf{n}_{\text{in}}$ the exiting uncollided partial current in the direction normal to the incident surface is properly calculated. So, the neutral

flow into volume 3 is properly calculated, although the direction of this current exiting volume i is not normal to the exit surface. In constructing the incident current for region 3 from region i , this uncollided contribution from region 1 is added to the uncollided contribution from regions 2 and 4 and to the collided contribution, and the combination is assumed to have a DP-0 incident angular distribution into volume 3 with respect to the orientation of this incident interface of volume 3 (the exiting interface of volume i). Thus, in the above equations $\mathbf{n}_{\text{out}} = \mathbf{n}_{\text{in}}$ should be used.

16.6.3.2 Escape Probabilities

The neutral flux per unit surface area, dA , normal to the direction of neutral flight at a distance R away from an isotropic point source is $\exp(-\Sigma R)/4\pi R^2$, and, with reference to Fig. 16.15, the surface area normal to the direction Ω of neutron travel is $dA = R d\theta d\phi = l^2 d\theta d\phi / \cos \theta$. Thus, with reference to Fig. 16.16, an isotropic neutral source of unit strength per axial length located at \mathbf{r}_i within volume V_i produces an outward current of uncollided neutrals over the surface labeled ξ_2 into volume 3 that is described by

$$\begin{aligned} J_{\text{out}}^3(\mathbf{r}_i) &= \int_{A \supset S_3} (\mathbf{n}_{\text{out}} \cdot \Omega) \frac{e^{-\Sigma R} dA}{4\pi R^2} \\ &= \int_{\phi \supset S_3} d\phi \int_{-\pi/2}^{\pi/2} d\theta (\cos \theta \sin \phi_{\text{out}}) \frac{e^{-\frac{\Sigma l(\phi)}{\cos \theta}} \left(\frac{l^2}{\cos \theta} \right)}{4\pi \left(\frac{l}{\cos \theta} \right)^2} \\ &= \int_{\phi \supset S_3} d\phi \sin \phi_{\text{out}} \frac{1}{2\pi} \int_0^{\pi/2} d\theta \cos^2 \theta e^{-\frac{\Sigma l(\phi)}{\cos \theta}} \\ &= \int_{\phi \supset S_3} d\phi \sin \phi_{\text{out}} \frac{Ki_3(\Sigma l(\phi))}{2\pi} \end{aligned} \quad (16.141)$$

where $\phi \supset S_3$ indicates the range of $\phi_{\min} < \phi < \phi_{\max}$ subtended by side S_3 at location \mathbf{r}_i within volume V_i .

The average value of $J_{\text{out}}^3(x, y)$ over the planar 2D area A_i of volume V_i is just the probability that an isotropic, uniform neutral source s_i will produce an uncollided current $s_i A_{i3}^s P_{0i}$ from volume V_i into volume V_3

$$\begin{aligned} A_{i3} P_{0i} &= \frac{1}{A_i} \int_{A_i} dx dy J_{\text{out}}^3(x, y) \\ &= \frac{1}{A_i} \int_{A_i} dx dy \int_{\phi \supset S_3} d\phi \sin \phi_{\text{out}} \frac{Ki_3(\Sigma l(\phi))}{2\pi} \end{aligned} \quad (16.142)$$

The proper value of \mathbf{n}_{out} is the outward normal to the surface in question, and ϕ_{out} is measured with respect to the orientation of that surface, whereas ϕ may be measured with respect to a fixed coordinate system, so that in general $\phi_{\text{out}} \neq \phi$, although it is convenient to orient the coordinate system so that $\phi_{\text{out}} = \phi$.

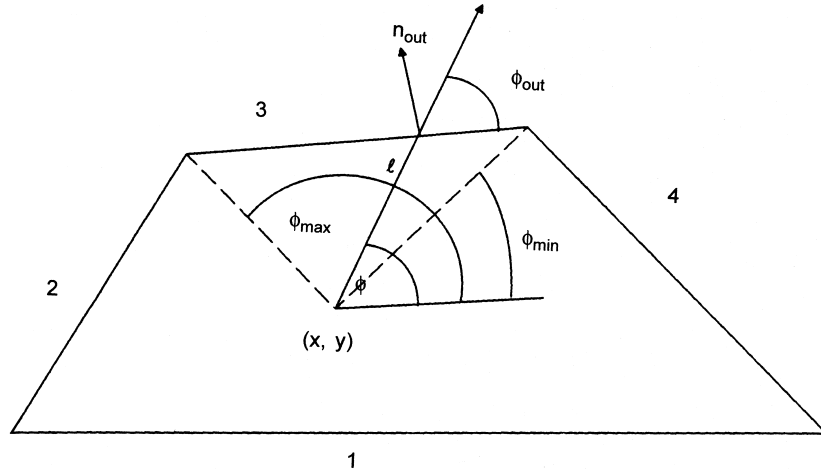


Figure 16.16. Planar projection of geometry for escape probability calculation in 2D

The total uncollided escape probability is obtained by summing Eq. (16.142) over all volumes V_k that are contiguous to volume V_i

$$P_{oi} = \sum_k \Lambda_{ik} P_{oi} \quad (16.143)$$

and the directional escape fractions are calculated from

$$\Lambda_{ij} = \frac{\Lambda_{ij} P_{oi}}{P_{oi}} = \frac{\Lambda_{ij} P_{oi}}{\sum_k \Lambda_{ik} P_{oi}} \quad (16.144)$$

The total escape probability including escape after zero, one, two, ... etc. collisions can be calculated from

$$P_i \equiv P_{oi} \sum_{n=0}^{\infty} [c_i(1 - P_{oi})]^n = \frac{P_{oi}}{1 - c_i(1 - P_{oi})} \quad (16.145)$$

where $c_i = (\Sigma_{si} + \Sigma_{xi})/\Sigma_{ti}$ is the number of secondary neutrals emerging from a collision.

16.6.3.3 Simple Approximations for the Escape Probability

Physical considerations lead to a simple approximation for the first-flight escape probability. In the limit that the average neutral path length $\langle l \rangle$ in a volume V is much less than the mean free path λ for a collision, the escape probability tends to unity. In the limit when $\langle l \rangle \gg \lambda$, a simple approximation for the first-flight escape probability is $1 - \exp(-\lambda/\langle l \rangle) \approx \lambda/\langle l \rangle$. If we associate the average neutral path length in the volume with the mean chord length $4V/S$, where S is the surface area of the volume V , then

a simple “rational” approximation for the escape probability, first proposed by Wigner and with which his name is associated, is

$$P_o = \frac{1}{1 + \frac{\langle l \rangle}{\lambda}} = \frac{1}{1 + \frac{4V}{S\lambda}} = \frac{1}{(4V/S\lambda)} \left(1 - \frac{1}{1 + (4V/S\lambda)} \right) \quad (16.146)$$

This Wigner rational approximation is known to underpredict the first-flight escape probability. However, extensive Monte Carlo calculations have confirmed that the first-flight escape probability depends only on the parameter $4V/S\lambda$, and improved rational approximations of the form

$$P_o = \frac{1}{(4V/S\lambda)} \left(1 - \frac{1}{\left(1 + \frac{(4V/S\lambda)}{c} \right)^c} \right) \quad (16.147)$$

have been proposed. The Sauer approximation, developed from theoretical considerations for cylindrical geometry, corresponds to $c = 4.58$. The best fit to Monte Carlo calculations of first-flight escape probabilities for a uniform neutral source distribution in volumes with a wide range of geometries and values of the parameter $4V/S\lambda$ was found by using $c = 2.09$.

16.6.4 1D Slab Method

The one-dimensional formulation of the interface current method for a multilayer slab is convenient for the calculation of neutral penetration into the plasma from the surrounding plenum. With respect to Fig. 16.13, the currents exiting a slab layer i to the right (+) and left (−) may be written

$$\begin{aligned} J_{i+1}^+ &= T_i J_i^+ + R_i J_{i+1}^- + \frac{1}{2} s_i P_i + (s_i^+ - \frac{1}{2} s_i) P_{oi} \\ J_i^- &= T_i J_i^- + R_i J_i^+ + \frac{1}{2} s_i P_i + (s_i^- - \frac{1}{2} s_i) P_{oi} \end{aligned} \quad (16.148)$$

where the total reflection probability

$$R_i \equiv \frac{\frac{1}{2} c_i P_{oi} (1 - 2E_3(\Delta_i \Sigma_{ti}))}{1 - c_i (1 - P_{oi})} = \frac{1}{2} c_i P_i (1 - T_{oi}) \quad (16.149)$$

and the total transmission probability

$$T_i = T_{oi} + R_i = T_{oi} + \frac{1}{2} c_i P_i (1 - T_{oi}) \quad (16.150)$$

and the total escape probability after multiple collisions

$$P_i \equiv P_{oi} \sum_{n=0}^{\infty} [c_i (1 - P_{oi})]^n = \frac{P_{oi}}{1 - c_i (1 - P_{oi})} \quad (16.151)$$

are given in terms of the first-flight transmission (T_0) and escape (P_0) probabilities in slab geometry given by Eqs. (16.97) and (16.102).

16.7 Discrete Ordinates Methods

The discrete ordinate methods are based on a conceptually straightforward evaluation of the transport equation at a few discrete angular directions, or ordinates, and the use of quadrature relationships to replace scattering neutral source integrals over angle with summations over ordinates. The essence of the methods are the choice of ordinates, quadrature weights, differencing schemes and iterative solution procedures. In one dimension, the ordinates can be chosen such that the discrete ordinates methods are completely equivalent to the P_L methods discussed previously, and in fact the use of discrete ordinates is probably the most effective way to solve the P_L equations in one dimension. This equivalence does not carry over into multidimensional geometries.

Making use of the spherical harmonics expansion of the differential scattering cross section of Eq. (16.8) and the addition theorem for Legendre polynomials of Eq. (16.6), the one dimensional neutral transport equation (16.1) in slab geometry becomes

$$\begin{aligned} \mu \frac{d\psi}{dx}(x, \mu) + \Sigma_t(x)\psi(x, \mu) = \\ \sum_{l'=0}^{\infty} \left(\frac{2l'+1}{2} \right) \Sigma_{sl'}(x) P_{l'}(\mu) \int_{-1}^1 d\mu' P_{l'}(\mu') \psi(x, \mu') + S(x, \mu) \end{aligned} \quad (16.152)$$

where the source term includes an injected source and volumetric recombination.

Defining N ordinate directions, μ_n , and corresponding quadrature weights, w_n , the integral over angle in Eq. (16.152) can be replaced by

$$\phi_l(x) \equiv \int_{-1}^1 d\mu P_l(\mu) \psi(x, \mu) \simeq \sum_n w_n P_l(\mu_n) \psi_n(x) \quad (16.153)$$

where $\psi_n = \psi(\mu_n)$. The quadrature weights are normalized by

$$\sum_{n=1}^N w_n = 2 \quad (16.154)$$

It is convenient to choose ordinates and quadrature weights symmetric about $\mu = 0$, hence providing equal detail in the description of forward and backward neutral fluxes. This can be accomplished by choosing

$$\begin{aligned} \mu_{N+1-n} &= -\mu_n, & \mu_n > 0, & n = 1, 2, \dots, N/2 \\ w_{N+1-n} &= w_n, & w_n > 0, & n = 1, 2, \dots, N/2 \end{aligned} \quad (16.155)$$

With such even ordinates, reflective boundary conditions are simply prescribed

$$\psi_n = \psi_{N+1-n}, \quad n = 1, 2, \dots, N/2 \quad (16.156)$$

Known incident flux, $\psi_{in}(\mu)$, boundary conditions are,

$$\psi_n = \psi_{in}(\mu_n), \quad n = 1, 2, \dots, N/2 \quad (16.157)$$

including vacuum conditions when $\psi_{in}(\mu) = 0$. Normally, an even number of ordinates is used ($N = \text{even}$), because this results in the correct number of boundary conditions and

avoids certain other problems encountered with $N = \text{odd}$. Even with these restrictions, there remains considerable freedom in the choice of ordinates and weights.

16.7.1 P_L and $D-P_L$ Ordinates

If the ordinates are chosen to be the N roots of the Legendre polynomial of order N

$$P_N(\mu_i) = 0 \quad (16.158)$$

and the weights are chosen to correctly integrate all Legendre polynomials up to P_{N-1}

$$\int_{-1}^1 P_l(\mu) d\mu \simeq \sum_{n=1}^N w_n P_l(\mu_n) = 2\delta_{l0}, \quad n = 0, 1, \dots, N-1 \quad (16.159)$$

then the discrete ordinates equations with N ordinates are equivalent to the P_{N-1} equations. To establish this, we multiply Eq. (16.152) by $w_n P_l(\mu_n)$ for $0 \leq l \leq N-1$, in turn, and use the recursion relation of Eq. (16.4) to obtain

$$\begin{aligned} & w_n \left[\left(\frac{l+1}{2l+1} \right) P_{l+1}(\mu_n) + \left(\frac{l}{2l+1} \right) P_{l-1}(\mu_n) \right] \frac{d\psi_n}{dx} + w_n \Sigma_t \psi_n \\ &= \sum_{l'=0}^{N-1} \left(\frac{2l'+1}{2} \right) \Sigma_{sl'} w_n P_{l'}(\mu_n) P_l(\mu_n) \phi_{l'} + w_n P_l(\mu_n) S(\mu_n) \\ & \quad l = 0, \dots, N-1 \end{aligned} \quad (16.160)$$

Summing these equations over $1 \leq n \leq N$ yields

$$\begin{aligned} & \left(\frac{l+1}{2l+1} \right) \frac{d\phi_{l+1}}{dx} + \left(\frac{l}{2l+1} \right) \frac{d\phi_{l-1}}{dx} + \Sigma_t \phi_l \\ &= \sum_{l'=0}^{N-1} \left(\frac{2l'+1}{2} \right) \Sigma_{sl'} \phi_{l'} \left[\sum_{n=0}^N w_n P_{l'}(\mu_n) P_l(\mu_n) \right] + \sum_{n=1}^N w_n P_l(\mu_n) S(\mu_n) \\ & \quad l = 0, \dots, N-1 \end{aligned} \quad (16.161)$$

Weights chosen to satisfy Eq. (16.159) obviously correctly integrate all polynomials through order N (any polynomial of order n can be written as a sum of Legendre polynomials through order n), but fortuitously they also integrate correctly all polynomials through order less than $2N$. Thus, the term in the scattering integral becomes

$$\sum_{n=1}^N w_n P_{l'}(\mu_n) P_l(\mu_n) = \int_{-1}^1 P_{l'}(\mu) P_l(\mu) d\mu = \frac{2\delta_{ll'}}{2l+1} \quad (16.162)$$

and assuming that the angular dependence of the scattering term can be represented by a polynomial of order $< 2N$

$$\sum_{n=1}^N w_n P_l(\mu_n) S(\mu_n) = \int_{-1}^1 P_l(\mu) S(\mu) d\mu = \frac{2S_l}{2l+1} \quad (16.163)$$

where S_l is the Legendre moment of the scattering source.

Using Eq. (16.162) and Eq. (16.163), Eq. (16.161) becomes

$$\begin{aligned} \left(\frac{l+1}{2l+1} \right) \frac{d\phi_{l+1}}{dx} + \left(\frac{l}{2l+1} \right) \frac{d\phi_{l-1}}{dx} + (\Sigma_t - \Sigma_{sl})\phi_l &= S_l \quad l = 0, \dots, N-2 \\ \frac{N-1}{2(N-1)+1} \frac{d\phi_{(N-1)-1}}{dx} + (\Sigma_t - \Sigma_{s,N-1})\phi_{N-1} &= S_{N-1} \quad l = N-1 \end{aligned} \quad (16.164)$$

which, when ϕ_{-1} is set to zero, are identical to the P_L equations (16.45) for $L = N-1$. These P_L ordinates and weights are given in Table 16.2.

Table 16.2. P_{N-1} ordinates and weight

	$\pm\mu_n$	w_n		$\pm\mu_n$	w_n
$N = 2$	0.57735	1.00000	$N = 10$	0.14887	0.29552
$N = 4$	0.33998	0.65215		0.43340	0.26927
	0.86114	0.34785		0.67941	0.21909
$N = 6$	0.23862	0.46791		0.86506	0.14945
	0.66121	0.36076		0.97391	0.06667
	0.93247	0.17132	$N = 12$	0.12523	0.24915
$N = 8$	0.18343	0.36268		0.36783	0.23349
	0.52553	0.31371		0.58732	0.20317
	0.79667	0.22238		0.76990	0.16008
	0.96029	0.10123		0.90412	0.10694
				0.98156	0.04718

The $D-P_L$ ordinates are the roots of the half-angle Legendre polynomials for $L = N/2 - 1$

$$\begin{aligned} P_{(N-2)/2}(2\mu_n + 1) &= 0 \quad n = 1, 2, \dots, N/2 \\ P_{(N-2)/2}(2\mu_n - 1) &= 0 \quad n = \frac{N}{2} + 1, \dots, N \end{aligned} \quad (16.165)$$

and the corresponding weights are determined from

$$\begin{aligned} \sum_{n=1}^{N/2} w_n P_l(2\mu_n + 1) &= \delta_{l0}, \quad l = 0, \dots, (N-2)/2 \\ \sum_{n=(N+2)/2}^{N/2} w_n P_l(2\mu_n - 1) &= \delta_{l0}, \quad l = 0, \dots, (N-2)/2 \end{aligned} \quad (16.166)$$

These ordinates and weights may be evaluated from the data in Table 16.2.

The P_L ordinates and weights are preferable to the $D - P_L$ ordinates and weights for deep penetration problems in heterogeneous media and for problems in which anisotropic scattering is important, for both of which the correct calculation of a large number of Legendre moments of the flux are required. Conversely, for the calculation of highly

anisotropic neutral fluxes near boundaries, the $D - P_L$ ordinates and weights are preferable. With either set of ordinates and weights, the discrete ordinates method in one dimension is essentially a numerical method for solving the P_L or $D - P_L$ equations. Other choices of weights and ordinates can be made to specialize the discrete ordinates method to the problem to be solved; e.g. bunching ordinates to emphasize an accurate calculation of the neutral flux in a certain direction. However, care must be exercised when choosing ordinates and weights that do not correctly integrate the low order angular polynomials, because surprising results sometimes turn up.

16.8 Monte Carlo Methods

At a fundamental level, neutral transport through matter is formulated as an essentially stochastic process. The total cross section is a probability (per unit path length and unit atom density), but not a certainty, that a neutral will have a collision while traversing a certain spatial interval. If the neutral does have a collision, the cross sections for the various processes are probabilities, but not certainties, that the collision will be an elastic scattering, charge-exchange or ionization event. The neutral flux that we have discussed in the previous sections of this chapter is actually the mean, or expectation, value of the neutral distribution function. The Monte Carlo method directly simulates neutral transport as a stochastic process.

16.8.1 Probability Distribution Functions

Let us postulate that variable x may take on various values over the interval $a \leq x \leq b$ and that there exists a probability distribution function (pdf), $f(x)$, such that $f(x) dx$ is the probability that a variable takes on a value within dx about x . The normalization is chosen such that

$$\int_a^b f(x) dx = 1 \quad (16.167)$$

A more useful quantity is the cumulative probability distribution function (cdf), $F(x)$, defined as the probability that the variable x' takes on a value less than or equal to x

$$F(x) = \int_a^x f(x') dx' \quad (16.168)$$

which is a monotonically increasing function of x . Thus, the probability of a neutral having a value of x' between x and $x + dx$ is $F(x + dx) - F(x) = f(x) dx$. If κ is a random number distributed between 0 and 1, then the values of x determined from $F(x) = \kappa$ will be distributed as $f(x)$. In some cases, it is possible to solve directly for $x = F^{-1}(\kappa)$. In other cases, the cumulative distribution function may be known as a large table of $F(x_i)$ and the value of x is determined by interpolation, e.g. if $F(x_j) < \kappa < F(x_{j-1})$ linear interpolation yields

$$x = x_j - \left(\frac{F(x_j) - \kappa}{F(x_j) - F(x_{j-1})} \right) (x_j - x_{j-1}) \quad (16.169)$$

There are also methods of selection from the pdf, but it is generally preferable to select from the cdf.

16.8.2 Analog Simulation of Neutral Particle Transport

By tracing the path of an individual neutral atom or molecule as it traverses the plasma edge and considering the various processes that may determine its history, we can understand how a Monte Carlo calculation simulates the stochastic nature of neutral transport in a plasma. We begin with the sources of neutrals in a plasma, which include injected sources in the plenum, recycling sources at the divertor target plates and volumetric recombination source near the target plates. The neutral source thus has a distribution in space near the divertor target, a distribution in energy, as discussed in chapter 13, and a distribution in direction that is directed away from the target. There may also be a gas fueling source with different spatial and energy distributions that is isotropic in direction. Each of these distributions may be characterized by a pdf and a cdf. Generating a random number and selecting from the cdf for the spatial source distribution defines a location in space for the source particle. Generating another random number and selecting from the cdf for the source energy spectrum determines the energy of the source particle. Generating third and fourth random numbers and selecting from the cdfs for the two independent angular variables (say $\mu = \cos \theta$ and ϕ) defines the direction of the source neutral.

Once “launched,” the source neutral will travel in a straight line until it has a collision. The probability that a neutral has a collision at a distance s along the flight path is

$$T(s) = \Sigma_t(s) \exp\left(-\int_0^s \Sigma_t(s') ds'\right) \quad (16.170)$$

which is the pdf for the collision distance s . Generating a random number λ and selecting s from the cdf

$$-\ln \lambda = \int_0^s \Sigma_t(s') ds' \quad (16.171)$$

locates the position of the first collision, in principle. In fact, the process is considerably complicated by the nonuniform geometry. It is necessary to know the plasma density, temperature and composition at the point of the first collision. We treat the medium as piecewise homogeneous and define the lengths of each uniform segment of the straightline flight path as s_j . If

$$\sum_{j=1}^{n-1} \Sigma_{tj} s_j \leq -\ln \lambda < \sum_{j=1}^n \Sigma_{tj} s_j \quad (16.172)$$

the collision occurs in the n th region at a distance

$$s'_n = \frac{1}{\Sigma_{tn}} \left(-\ln \lambda - \sum_{j=1}^{n-1} \Sigma_{tj} s_j \right) \quad (16.173)$$

beyond the entrance of the flight path into region n . The actual procedures for treating flight paths in complex geometries are quite involved but highly developed. Modern Monte Carlo codes can essentially model any geometry exactly, which a great strength of the method.

Having determined that a collision occurred at a distance s_n into region n on the original flight path, it is now necessary to determine what type of target particle and what type of reaction are involved. The probability for a reaction of type x with a particle of species i is

$$p_{ix} = \frac{N_i \sigma_{ix}}{\sum_{i,x} N_i \sigma_{ix}} \quad (16.174)$$

where N_i is the number density of species i in region n , σ_{ix} is the microscopic cross section for reaction x for species i at the energy of the neutral. Constructing a pdf and a cdf, generating a random number η and selecting the particle and reaction type by equating η and the cdf (probably involving table interpolation per Eq. (16.169)), the particle and reaction type can be determined.

If the reaction type is ionization, the neutral history is terminated, the energy and location of the absorbed neutral are recorded, and another history is started.

If the reaction type is elastic scattering, another random number is generated and equated to the cdf for the cosine of the scattering angle in the center of mass to obtain μ_{CM} (it is convenient to work in the CM because the scattering is almost isotropic and the pdf and cdf are simple) and by transformation to obtain the scattering angle in the lab. When the neutral energy is much greater than the target ion energy, the energy of the scattered neutral is uniquely correlated to μ_{CM} from the scattering kinematics, e.g. if the target particle is at very low temperature or very heavy relative to the neutral

$$E' = \frac{E(A^2 + 2A\mu_{CM} + 1)}{(A + 1)^2} \quad (16.175)$$

The actual expression for E' is usually more complicated. Knowing E' , the cosine of the scattering angle in the lab can be determined from

$$\mu = \cos \theta = \frac{1}{2}(A + 1)\sqrt{\frac{E}{E'}} + \frac{1}{2}(A - 1)\sqrt{\frac{E'}{E}} \quad (16.176)$$

Elastic scattering from energetic ions is more complex, but similar relationships can be developed from the material discussed at the beginning of the chapter. Generating another random number and equating it to the cdf for the azimuthal angle ϕ , the direction of the scattered neutral can be determined.

Charge exchange is treated similarly to elastic scattering. The energy of the emergent neutral is selected from the ion energy distribution, and the direction is selected from an isotropic distribution or from a distribution representing the ion directionality.

16.8.3 Statistical Estimation

The mean, or expectation, value of a function $h(x)$ of x is defined in terms of the pdf for x by

$$\langle h \rangle = \int_a^b dx h(x) f(x) \quad (16.177)$$

and the standard deviation, σ , and the variance, V , are defined

$$\sigma(h) = \sqrt{V(h)} = \left\{ \int_a^b dx [h(x) - \langle h \rangle]^2 f(x) \right\}^{\frac{1}{2}} = [\langle h^2 \rangle - \langle h \rangle^2]^{\frac{1}{2}} \quad (16.178)$$

If N random values of the variable x are chosen from the cdf, as discussed above, then a statistical estimate of the mean value $\langle h \rangle$ is

$$\bar{h} = \frac{1}{N} \sum_{n=1}^N h(x_n) \quad (16.179)$$

A bound for the error in an estimate of this type is given by the *Central Limit Theorem*, which states that if many estimates \bar{h} of $\langle h \rangle$ are obtained, each estimate involving N trials, then the variable \bar{h} is normally distributed about $\langle h \rangle$ to terms of accuracy $O(1/N^{\frac{1}{2}})$. In the limit $N \rightarrow \infty$, this theorem takes the form

$$\text{Prob} \left\{ \langle h \rangle - \frac{M\sigma(h)}{\sqrt{N}} \leq \bar{h} \leq \langle h \rangle + \frac{M\sigma(h)}{\sqrt{N}} \right\} = \begin{cases} 0.6826 & M = 1 \\ 0.954 & M = 2 \\ 0.997 & M = 3 \end{cases} \quad (16.180)$$

i.e. the probability that the statistical estimate of the mean value of Eq. (16.179) is within $\pm M\sigma/\sqrt{N}$ of the exact value $\langle h \rangle$ is 68.3% for $M = 1$, 95.4% for $M = 2$, 99.7% for $M = 3$, etc.

In general, the first and second moments of $h(x)$ are unknown. The statistical data can be used to construct approximations to these moments. The expectation value of \bar{h} is

$$\begin{aligned} \langle \bar{h} \rangle &= \frac{1}{N} \sum_{n=1}^N \langle h(x_n) \rangle = \frac{1}{N} \sum_{n=1}^N \int_a^b dx_n f(x_n) h(x_n) \\ &= \frac{1}{N} \sum_{n=1}^N \int_a^b dx f(x) h(x) = \frac{1}{N} \sum_{n=1}^N \langle h \rangle = \langle h \rangle \end{aligned} \quad (16.181)$$

i.e. the statistical estimate \bar{h} is an unbiased estimate of $\langle h \rangle$ since $\langle \bar{h} \rangle = \langle h \rangle$. The expected value of \bar{h}^2 is

$$\begin{aligned}\langle \bar{h}^2 \rangle &= \frac{1}{N^2} \left\langle \sum_{n=1}^N h(x_n) \sum_{m=1}^N h(x_m) \right\rangle = \frac{1}{N^2} \left\langle \sum_{n=1}^N h^2(x_n) + \sum_{n=1}^N h(x_n) \sum_{m \neq n}^N h(x_m) \right\rangle \\ &= \frac{1}{N^2} \left[N \langle h^2 \rangle + N(N-1) \langle h \rangle^2 \right] = \frac{\langle h^2 \rangle}{N} - \frac{N-1}{N} \langle h \rangle^2 \quad (16.182)\end{aligned}$$

i.e. the statistical estimate \bar{h}^2 is a biased estimate of $\langle h^2 \rangle$ since $\langle \bar{h}^2 \rangle \neq \langle h^2 \rangle$.

Since $\langle \bar{h}^2 \rangle = \langle h^2 \rangle$, the variance in the statistical estimate of \bar{h} , can be approximated

$$V(\bar{h}) = \frac{1}{N} \left[\langle h^2 \rangle - \langle h \rangle^2 \right] = \frac{V(h)}{N} \simeq \frac{1}{N-1} \left[\bar{h}^2 - \langle h \rangle^2 \right] \quad (16.183)$$

and the mean square fractional error associated with the statistical estimate of \bar{h} , is

$$\epsilon^2 = \frac{1}{N} \left[\frac{\langle h^2 \rangle}{\langle h \rangle^2} - 1 \right] \simeq \frac{1}{N-1} \left[\frac{\bar{h}^2}{\langle h \rangle^2} - 1 \right] \quad (16.184)$$

It is clearly important to reduce the mean square error in order to increase confidence in the Monte Carlo calculation of the mean value of a quantity $h(x)$ based on a random sampling of the variable x . From Eq. (16.184), this can be accomplished by just running more histories, but that involves longer computational times. There are other methods of reducing the mean square error, or the related variance, which are known as variance reduction methods.

16.9 Navier–Stokes Fluid Model

The neutral atoms and molecules present in the divertor and plasma edge can be treated as one or more additional plasma species in a fluid model of the plasma. This extended Navier–Stokes representation of each neutral species includes a continuity equation

$$\frac{\partial n_0}{\partial t} + \frac{\partial n_0 u_0}{\partial x} + \frac{\partial n_0 v_0}{\partial y} = nm \langle \sigma v \rangle_{\text{rec}} - nn_0 \langle \sigma v \rangle_{\text{ie}} \quad (16.185)$$

and three components of the momentum balance equation

- Neutral poloidal momentum (u_0 = neutral poloidal velocity)

$$\begin{aligned}\frac{\partial m n_0 u_0}{\partial t} + \frac{\partial}{\partial x} \left(m n_0 u_0^2 - \eta^n \frac{\partial u_0}{\partial x} \right) + \frac{\partial}{\partial y} \left(m n_0 u_0 v_0 - \eta^n \frac{\partial u_0}{\partial y} \right) \\ = - \frac{\partial p_0}{\partial x} + m n^2 \langle \sigma v \rangle_{\text{rec}} \frac{B_x}{B} u_{\parallel} \\ - m n_0 n \langle \sigma v \rangle_{\text{ion}} u_0 - m n_0 n \langle \sigma v \rangle_{\text{at}} - \left(u_0 - \frac{B_x}{B} u_{\parallel} \right) \quad (16.186)\end{aligned}$$

2. Neutral radial momentum (v_0 = neutral radial velocity)

$$\begin{aligned} \frac{\partial mn_0 v_0}{\partial t} + \frac{\partial}{\partial x} \left(mn_0 u_0 v_0 - \eta^n \frac{\partial v_0}{\partial x} \right) + \frac{\partial}{\partial y} \left(mn_0 v_0^2 - \eta^n \frac{\partial v_0}{\partial y} \right) \\ = -\frac{\partial p_0}{\partial y} - mn_0 n \langle \sigma v \rangle_{\text{ion}} v_0 - mn_0 n \langle \sigma v \rangle_{\text{at}} (v_0 - v) \quad (16.187) \end{aligned}$$

3. Neutral toroidal momentum (w_0 = neutral toroidal velocity)

$$\begin{aligned} \frac{\partial mn_0 w_0}{\partial t} + \frac{\partial}{\partial x} \left(mn_0 u_0 w_0 - \eta^n \frac{\partial w_0}{\partial x} \right) + \frac{\partial}{\partial y} \left(mn_0 v_0 w_0 - \eta^n \frac{\partial w_0}{\partial y} \right) \\ = -mn_0 n \langle \sigma v \rangle_{\text{ion}} w_0 - mn_0 n \langle \sigma v \rangle_{\text{at}} \left(w_0 - \frac{B_z}{B} u_{\parallel} \right) \\ + mn^2 \langle \sigma v \rangle_{\text{rec}} \frac{B_z}{B} u_{\parallel} \quad (16.188) \end{aligned}$$

Here, u_{\parallel} and v are the plasma parallel and radial velocities and (x, y, z) -coordinates correspond to (r, θ, ϕ) -coordinates in a tokamak.

A separate neutral energy equation may be written, or the neutral energy balance may be included with the ion energy balance under the assumption $T_n = T_i$, which yields the combined ion-neutral energy balance equation

$$\begin{aligned} \frac{\partial}{\partial t} \left[\frac{3}{2} (n + n_0) T_i \right] + \frac{\partial}{\partial x} \left(\frac{3}{2} n u T_i - \kappa_x^i \frac{\partial T_i}{\partial x} \right) \\ + \frac{\partial}{\partial y} \left(\frac{3}{2} n v T_i - \kappa_y^i \frac{\partial T_i}{\partial y} \right) + \frac{\partial}{\partial x} \left(\frac{3}{2} n_0 u_0 T_i - \kappa^n \frac{\partial T_i}{\partial x} \right) \\ + \frac{\partial}{\partial y} \left(\frac{3}{2} n_0 v_0 T_i - \kappa^n \frac{\partial T_i}{\partial y} \right) \\ = -p_i \left(\frac{\partial u}{\partial x} \right) - p_0 \left(\frac{\partial u_0}{\partial x} + \frac{\partial v_0}{\partial y} \right) + \kappa_{\text{eq}} (T_e - T_i) \quad (16.189) \end{aligned}$$

In the above equations the subscripts “ion,” “at” and “rec” refer to ionization, elastic scattering plus charge-exchange and recombination; κ^i and κ^n are ion and neutral heat conductivities, and κ_{eq} is the ion–electron equilibration coefficient; and η^n is the neutral viscosity.

The neutral transport coefficients may be formulated to include both neutral–ion and neutral–neutral collisions

$$\frac{1}{\eta_n} = \frac{1}{\eta_{n-u}} + \frac{1}{\eta_{n-i}} \quad (16.190)$$

and

$$\frac{1}{\kappa_n} = \frac{1}{\kappa_{n-n}} + \frac{1}{\kappa_{n-i}} \quad (16.191)$$

Using simple transport arguments of the type discussed at the beginning of chapter 9 leads to approximations for the neutral transport coefficients

$$\eta_{n-n} \simeq \frac{1}{2} n_0 m_0 v_{\text{th}0} \lambda_{n-n}, \quad \eta_{n-i} = \frac{1}{2} n_0 m_0 v_{\text{th}0} \lambda_{n-i} \quad (16.192)$$

and

$$\kappa_{n-n} \simeq \frac{3}{4} n_0 v_{\text{th}0} \lambda_{n-n}, \quad \kappa_{n-i} \simeq \frac{3}{4} n_0 v_{\text{th}0} \lambda_{n-i} \quad (16.193)$$

where λ_{n-n} and λ_{n-i} are the mean free paths for neutral-neutral and neutral-ion 90° deflection collisions.

Problems for Chapter 16

1. Derive the P_n equations of Eq. (16.45) by expanding the angular dependence of the neutral flux in Legendre polynomials.
2. Derive the diffusion theory Eq. (16.54) from the P_1 equations.
3. Solve the diffusion equation to obtain an exponential attenuation $e^{-x/\lambda}$ of the neutral flux with distance into a plasma. What is the penetration mean free path, λ ?
4. Calculate the probability that neutral deuterium atoms incident on a plasma slab of thickness $a = 1 \text{ cm}$, density $n = 3 \times 10^{19} \text{ m}^{-3}$ and temperature $T = 50 \text{ eV}$ are transmitted across the slab without a collision.
5. Calculate the probability that neutral atoms created by volumetric recombination uniformly throughout a plasma slab of thickness $a = 1 \text{ cm}$, density $n = 3 \times 10^{19} \text{ m}^{-3}$ and temperature $T = 2 \text{ eV}$ escape from the slab without a collision.
6. Evaluate the transmission probability of Eq. (16.140) for transmission from one side to the opposite side of a square plasma cylinder of infinite length. Each side is 5 cm in length and the plasma density and temperature are $n = 3 \times 10^{19} \text{ m}^{-3}$ and $T = 50 \text{ eV}$.
7. Evaluate the first flight escape probability for neutral deuterium atoms created uniformly throughout the plasma of problem 6 to escape the plasma without a collision.
8. Derive the discrete ordinates Eq. (16.160).
9. Construct a pdf and a cdf for the microscopic cross sections for the different reactions that deuterium atoms in a Maxwellian distribution with $T_a = 10 \text{ eV}$ could have in a collision in a deuterium plasma also in a Maxwellian distribution at $T = 10 \text{ eV}$.

17 Power Balance

In order for any plasma to maintain thermonuclear temperatures, once heated, there must be a balance between heat sources and power losses. This balance may be written

$$P_\Omega + P_\alpha + P_{\text{aux}} = P_{\text{TR}} + P_{\text{R}} \quad (17.1)$$

Here, P_Ω is the ohmic heating by currents flowing in the plasma, P_α is the 3.5 MeV per D-T fusion event that is released in the form of α -particle kinetic energy and hence remains in the plasma because the charged alpha particle is confined, and P_{aux} is auxiliary power input to the plasma by neutral beams, electromagnetic waves, etc. The power losses are by transport, P_{TR} , and by radiation, P_{R} . The radiation loss includes impurity line and recombination radiation, bremsstrahlung and cyclotron radiation.

Neglecting P_Ω , which becomes negligible at high temperatures, Eq. (17.1) may be written

$$\frac{1}{4}n^2 \langle \sigma v \rangle_f U_\alpha \left(1 + Q_p^{-1} \right) = \frac{3nT}{\tau_E} + n^2 L_{\text{R}} \quad (17.2)$$

for the purpose of discussion. We have assumed $n_D = n_T = \frac{1}{2}n$, used L_{R} to represent the total radiation emissivity by all processes, used $U_\alpha = 3.5 \text{ MeV}$, and defined the plasma energy amplification factor.

$$Q_p \equiv P_\alpha / P_{\text{aux}} \quad (17.3)$$

All quantities in Eq. (17.2) are appropriate averages over the volume of the plasma, as will be discussed in this chapter.

17.1 Energy Confinement Time

17.1.1 Definition

The balance of the total (rotational-kinetic plus thermal) energy in a plasma is

$$\dot{W}_{\text{rot}} + \dot{W}_{\text{th}} + H_Q = P_{\text{HEAT}} - P_{\text{R}} \quad (17.4)$$

where

$$W_{\text{rot}} \equiv \int_{\psi_o}^{\psi_a} \left\langle \frac{1}{2}nmv^2 \right\rangle V'(\psi) d\psi \quad (17.5)$$

is the rotational energy,

$$W_{\text{th}} \equiv \int_{\psi_o}^{\psi_a} \left\langle \frac{3}{2} p + E_f \right\rangle V'(\psi) d\psi \quad (17.6)$$

is the thermal energy, including both “thermal” ions and electrons ($\frac{3}{2} p$ each) and “fast” ions in the process of thermalizing (E_f), $P_{\text{HEAT}} = P_{\text{aux}} + P_{\Omega}$ is the total heating power integrated over the plasma volume, and

$$H_Q \equiv \int_{\psi_o}^{\psi_a} \langle \nabla \cdot Q \rangle V'(\psi) d\psi \quad (17.7)$$

is the total energy flowing out of the plasma. The integrals are from the center of the plasma (ψ_o) to the LCFS (ψ_a), and $\langle \rangle$ indicates a flux surface average.

The total energy flux

$$Q = \left\{ \left(\frac{1}{2} nm v^2 + \frac{5}{2} p \right) v \right\} + \{q\} + \{v \cdot \pi\} \equiv Q_{\text{conv}} + Q_{\text{cond}} + Q_{\text{vis}} \quad (17.8)$$

consists of convective, conductive and viscous components. There are corresponding components of the energy loss defined by Eq. (17.7).

The energy confinement time is intended to represent the mean time energy is confined, so it must be defined in terms of the ratio of the plasma energy content to the plasma energy loss rate. However, there are many possible definitions. The plasma energy content may be considered to be just the energy content of the “thermalized” ions and electrons (W_{th} without the E_f term), the thermal energy content of the thermalized and fast particles (W_{th}), or the thermal plus rotational energy ($W_{\text{th}} + W_{\text{rot}}$). Similarly, the plasma energy loss rate may be due to convection, conduction, viscosity and radiation or to any one or combination of these processes.

For our purposes here, we will define “thermal” energy confinement times by using W_{th} to represent the plasma “thermal” energy content. We may define separate energy confinement times for the separate energy loss mechanisms indicated in Eq. (17.8)

$$\tau_E^{\text{conv}} \equiv \frac{W_{\text{th}}}{H_Q^{\text{conv}}} , \quad \tau_E^{\text{cond}} \equiv \frac{W_{\text{th}}}{H_Q^{\text{cond}}} , \quad \tau_E^{\text{vis}} \equiv \frac{W_{\text{th}}}{H_Q^{\text{vis}}} \quad (17.9)$$

Radiation is usually excluded from the definition of energy confinement time. Thus, a total “thermal” energy confinement time is

$$\frac{1}{\tau_E} = \frac{H_Q^{\text{conv}} + H_Q^{\text{cond}} + H_Q^{\text{vis}}}{W_{\text{th}}} = \frac{1}{\tau_E^{\text{conv}}} + \frac{1}{\tau_E^{\text{cond}}} + \frac{1}{\tau_E^{\text{vis}}} \quad (17.10)$$

17.1.2 Experimental Energy Confinement Times

If we use Eq. (17.4) to replace H_Q in Eq. (17.10), we can express the thermal energy confinement time in terms of experimentally measured or otherwise known quantities

$$\frac{1}{\tau_E^{\text{exp}}} = \frac{P_{\text{HEAT}} - P_R - \dot{W}_{\text{th}} - \dot{W}_{\text{rot}}}{W_{\text{th}}} \quad (17.11)$$

In practice, \dot{W}_{rot} is usually ignored, but this can introduce error for strongly rotating plasmas. E_f is sometimes omitted from measured W_{th} , in which case a “thermalized” thermal energy confinement time with no fast particle contribution is obtained.

One of the purposes of measuring energy confinement times is to check theoretical transport models, which can be used to evaluate the H_Q^x that are used in Eq. (17.10) to obtain a theoretical thermal energy confinement time. Most commonly, the theoretical transport model is for the thermal conductivity, χ , which enters the conductive ($\mathbf{q} = -n\chi\nabla T$) energy confinement time. Equating Eq. (17.10) to the measured energy confinement time and solving for

$$\frac{1}{\tau_E^{\text{cond}}} = \frac{1}{\tau_E^{\text{exp}}} - \frac{1}{\tau_E^{\text{conv}}} - \frac{1}{\tau_E^{\text{vis}}} \quad (17.12)$$

provides a correction to the measured energy confinement time that is needed for such comparisons.

17.1.3 Empirical Correlations

When experimental and theoretical energy confinement times are compared (albeit usually without the corrections indicated above), it is usually found that neoclassical transport theory overpredicts the confinement time by an order of magnitude or more. This has led to correlation of measured energy confinement times in order to obtain expressions that could be used in predicting the power balance in future tokamaks.

The confinement behavior can be conveniently put into four categories. The first covers ohmically heated plasmas and the other three relate to plasmas with additional heating. The two basic modes of auxiliary heated plasma confinement are the so-called L (for low) and H (for high) confinement regimes. The fourth category covers a variety of plasmas for which operational procedures have been found which produce enhanced confinement.

17.1.3.1 Ohmically Heated Plasmas

At low density it was found that the energy confinement time scaled as

$$\tau_E(s) = 0.07 \left(n/10^{20} \right) aR^2 q \quad (17.13)$$

where n is the average electron density, a and R the minor and major plasma radii, and q is the cylindrical equivalent edge safety factor. (Unless otherwise indicated, MKS units are used in this chapter.) The improved confinement with increased density is in conflict with the decrease in confinement predicted by neoclassical theory.

As the density is increased the linear improvement of τ_E with n is lost and τ_E saturates at a density

$$n_{\text{sat}}(m^{-3}) = 0.06 \times 10^{20} I RM^{0.5} \kappa^{-1} a^{-2.5} \quad (17.14)$$

where I is the plasma current, M is the atomic mass of the ions in amu and κ is the plasma elongation, b/a .

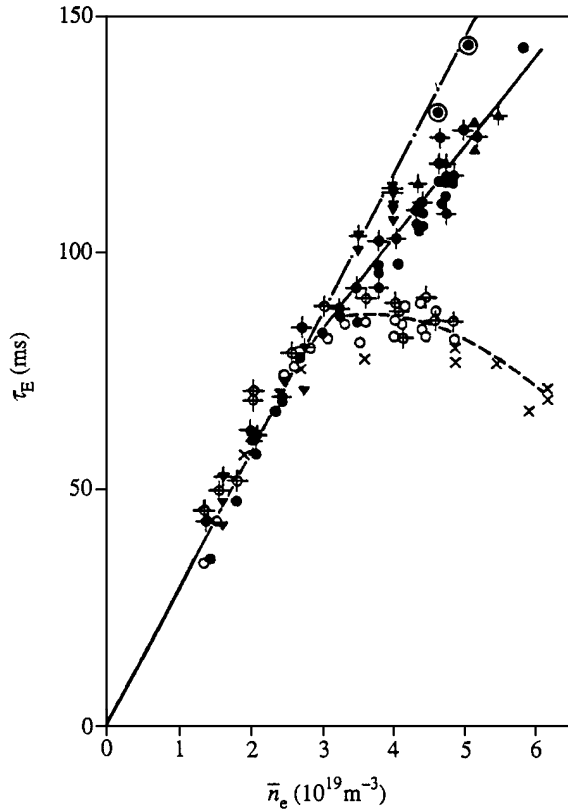


Figure 17.1. Improved ohmic confinement mode in ASDEX. The broken curve, with the open circles and crosses, corresponds to the saturation mode; the upper lines are for two different scans in IOC modes

By controlling the density in such a way as to maintain a peaked density profile it has proved possible to extend the linear scaling into the so-called Improved Ohmic Confinement (IOC) regime. Results from the ASDEX tokamak are given in Fig. 17.1.

17.1.3.2 L-Mode Confinement

In order to increase the plasma energy content above that achieved with ohmic heating alone, additional heating was applied using beams of energetic neutral particles or RF waves. The results were initially disappointing in that, for given operational conditions, the confinement was found to degrade with increasing power. By analyzing the results from several tokamaks Goldston obtained the confinement scaling law that bears his name

$$\tau_G(s) = 0.037 \frac{IR^{1.75} \kappa^{0.5}}{P^{0.5} a^{0.37}} \quad (17.15)$$

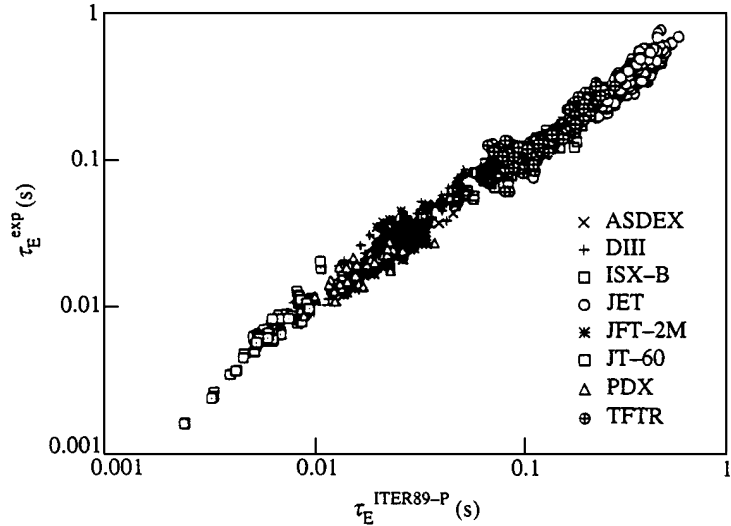


Figure 17.2. Comparison of the experimental values of confinement time from a number of tokamaks with the L -mode scaling $\tau_E^{\text{ITER89-P}}$

(I in MA, P in MW), where P is the applied power. The degradation is apparent through the factor $P^{0.5}$ in the denominator.

Although the scaling was obtained before the large tokamaks such as JET were operational, it was also found to describe the results on these machines. In order to improve the predictive capability for the proposed tokamak reactor ITER, an extended data base, including the larger tokamaks, was used to generate a more precise form of Goldston's scaling. The resulting confinement time, which was given the name ITER89-P, is given by

$$\tau_E^{\text{ITER89-P}}(s) = 0.048 \frac{I^{0.85} R^{1.2} a^{0.3} \kappa^{0.5} (n/10^{20})^{0.1} B^{0.2} M^{0.5}}{P^{0.5}} \quad (17.16)$$

(I in MA, P in MW) where B is the toroidal magnetic field. A comparison between this formula and data from a number of tokamaks is shown in Fig. 17.2.

17.1.3.3 H-Mode Confinement

It was found that when sufficient power was applied to an L -mode discharge the discharge made an abrupt transition in which the edge transport was apparently reduced, leading to edge pedestals in the temperature and density, as discussed in chapter 15. The effect of this was to produce roughly a doubling of the confinement time.

This behavior was subsequently obtained in many tokamaks, and analogues of the ITER89-P L -mode scaling law have been derived for H -mode discharges. The results are represented by

$$\tau_E^{\text{ITERH93-P}}(s) = 0.053 \frac{I^{1.06} R^{1.9} a^{-0.11} \kappa^{0.66} (n/10^{20})^{0.17} B^{0.32} M^{0.41}}{P^{0.67}} \quad (17.17)$$

(I in MA, P in MW). It is seen that the dependences are generally similar to those of the L -mode.

A more recent H -mode correlation is

$$\tau_E^{\text{IPB98}(y,2)}(s) = \frac{0.144 I^{0.93} B^{0.15} (n/10^{20})^{0.41} M^{-0.58} R^{1.97} \kappa^{0.78}}{P^{0.69}} \quad (17.18)$$

where P (MW) is the heating power, I (MA) is the plasma current, and κ is the elongation.

17.2 Radiation

Radiation is a major power loss mechanism in plasmas, as well as being a useful diagnostic tool. Acceleration of plasma particles due to their mutual interactions and due to their interaction with the electric and magnetic fields results in the emission of electromagnetic radiation. We will develop a general formalism for radiation fields resulting from the acceleration of charged particles and will apply this formalism to two important radiation processes – bremsstrahlung and cyclotron emission – in this section. The third, and most important, radiation process in plasmas arises from orbital electron transitions in partially ionized impurity atoms that are present in the plasma and were discussed in chapter 13.

17.2.1 Radiation Fields

First, we consider the radiation field from a charged particle moving with velocity \mathbf{v} . In Fig. 17.3 we denote by A the location of the particle at time t when it is accelerated and radiation is emitted. Let C be the point at which the radiation is “observed,” or computed, at a later time $t + |\mathbf{r}|/c$, and let D denote the actual location of the accelerated particle at this time. Let B denote the “virtual” location of the particle at $t + |\mathbf{r}|/c$ if it had not been accelerated. In computing the scalar and vector potentials observed at C at time $t + |\mathbf{r}|/c$, the position and motion of the particle at time t must be used. These delayed, Lienard–Wiechart potentials are

$$\phi(r) = \frac{1}{4\pi\epsilon_0} \frac{e}{|\mathbf{r}| - (\mathbf{r} \cdot \mathbf{v})/c} \quad (17.19)$$

and

$$\mathbf{A}(r) = \frac{\frac{1}{4\pi}\mu_0 e \mathbf{v}}{|\mathbf{r}| - (\mathbf{r} \cdot \mathbf{v})/c} \quad (17.20)$$

The magnetic and electric fields at C due to the charged particle can be computed from these potentials,

$$\mathbf{B} = \nabla \times \mathbf{A} \quad (17.21)$$

and

$$\mathbf{E} = -\nabla\phi - \frac{\partial \mathbf{A}}{\partial t} \quad (17.22)$$

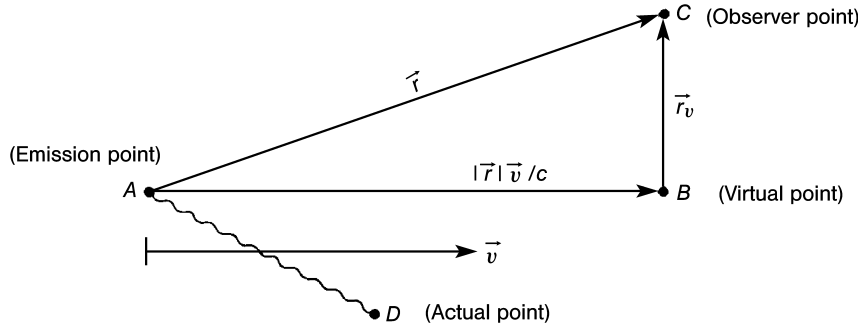


Figure 17.3. Radiation field nomenclature

Using these equations, and identifying the $1/r$ -component of the resulting fields with the radiation field, we obtain

$$\mathbf{E}_{\text{rad}} \simeq \frac{e}{4\pi\epsilon_0 c^2 r^3} \mathbf{r} \times (\mathbf{r} \times \dot{\mathbf{v}}) \quad (17.23)$$

and

$$\mathbf{B}_{\text{rad}} \simeq \frac{\mu_0 e}{4\pi c r^2} (\dot{\mathbf{v}} \times \mathbf{r}) = \mu_0 \mathbf{H}_{\text{rad}} \quad (17.24)$$

where the nonrelativistic limit, $|\mathbf{v}|/c \ll 1$, has been assumed. The acceleration of the charged particle is $\dot{\mathbf{v}}$. The Poynting vector for the radiation field is

$$\mathbf{P}_{\text{rad}} \equiv \mathbf{E}_{\text{rad}} \times \mathbf{H}_{\text{rad}} = \frac{e^2}{(4\pi)^2 \epsilon_0 c^3 r^5} [\mathbf{r} \times (\mathbf{r} \times \dot{\mathbf{v}})] \times (\dot{\mathbf{v}} \times \mathbf{r}) \quad (17.25)$$

The outward radiation flux per unit solid angle ($d\Omega = \sin \theta d\theta d\phi$ in spherical coordinates) is found by computing the power flux through an incremental surface area, $dA = r^2 d\Omega$, on a sphere of radius r centered on A :

$$\frac{dW_{\text{rad}}}{d\Omega} = r^2 (\mathbf{E}_{\text{rad}} \times \mathbf{H}_{\text{rad}}) \cdot \hat{\mathbf{n}}_r = \frac{e^2 |\dot{\mathbf{v}}|^2 \sin^2 \theta}{(4\pi)^2 \epsilon_0 c^3} \quad (17.26)$$

where $\hat{\mathbf{n}}_r$ is the unit vector along \mathbf{r} in Fig. 17.3, and θ is the angle between \mathbf{r} and $\dot{\mathbf{v}}$. The total power radiated by the accelerated charge is

$$W_{\text{rad}} = \int_0^{2\pi} d\phi \int_0^\pi \frac{dW_{\text{rad}}}{d\Omega} \sin \theta d\theta = \frac{1}{6\pi} \frac{e^2 |\dot{\mathbf{v}}|^2}{\epsilon_0 c^3} \quad (17.27)$$

A generalization of this development to remove the nonrelativistic approximation ($\frac{|\mathbf{v}|}{c} \ll 1$) leads to

$$\frac{dW_{\text{rad}}}{d\Omega} = \frac{e^2 |\dot{\mathbf{v}}|^2 \sin^2 \theta}{(4\pi)^2 \epsilon_0 c^3} \left(1 - \frac{v}{c} \cos \theta\right)^{-6} \quad (17.28)$$

instead of Eq. (17.26).

The rate at which radiated power originating at point A at time t passes through an incremental surface area at point C at time $t + |\mathbf{r}|/c \equiv t'$ is

$$\left(\frac{d^2 W_{\text{rad}}}{dt d\Omega} \right) d\Omega = |\mathbf{E}_{\text{rad}} \times \mathbf{H}_{\text{rad}}| \left(\frac{dt'}{dt} \right) r^2 d\Omega \quad (17.29)$$

Using Eq. (17.28) and

$$\frac{dt'}{dt} = 1 - \frac{\mathbf{r} \cdot \dot{\mathbf{v}}}{|\mathbf{r}|c} = 1 - \frac{\mathbf{v}}{c} \cos \theta \quad (17.30)$$

we can write Eq. (17.29)

$$\left(\frac{d^2 W_{\text{rad}}}{dt d\Omega} \right) d\Omega = \frac{e^2 |\dot{\mathbf{v}}|}{(4\pi)^2 \epsilon_0 c^3} \sin^2 \theta \left(1 - \frac{\mathbf{v}}{c} \cos \theta \right)^{-5} d\Omega \quad (17.31)$$

The general Poynting vector, which is valid for relativistic as well as nonrelativistic particles, can be constructed by the same procedure used to obtain Eq. (17.25), but without making the nonrelativistic approximation. The result is

$$|\mathbf{P}_{\text{rad}}| \equiv |\mathbf{E}_{\text{rad}} \times \mathbf{H}_{\text{rad}}| = \frac{e^2 |\mathbf{r} \times (\mathbf{r}_v \times \dot{\mathbf{v}})|^2}{(4\pi)^2 \mu_0 \epsilon_0^2 c^5 |\mathbf{r}|^6 \left(1 - \frac{\mathbf{v}}{c} \cos \theta \right)^6} \quad (17.32)$$

where

$$\mathbf{r}_v \equiv \mathbf{r} - \frac{|\mathbf{r}| \mathbf{v}}{c} \quad (17.33)$$

(refer to Fig. 17.3). Finally, the general expression for the outward radiation power flux per unit solid angle is

$$\left(\frac{d^2 W_{\text{rad}}}{d\Omega dt} \right) = \frac{e^2}{(4\pi)^2 \epsilon_0 c^3 s^5} |\mathbf{r} \times (\mathbf{r}_v \times \dot{\mathbf{v}})|^2 |\mathbf{r}| \quad (17.34)$$

where

$$s = \left(1 - \frac{\mathbf{r} \cdot \mathbf{v}}{|\mathbf{r}|c} \right) |\mathbf{r}| \quad (17.35)$$

This formalism is generally applicable to the radiation produced by the acceleration of a charged particle. Specific types of radiation fields are obtained for specific acceleration mechanisms in the following sections.

17.2.2 Bremsstrahlung

Bremsstrahlung – the German term for “braking radiation” – results from the collisional deceleration of charged particles. A photon is produced with energy equal to the energy loss in the collision process. Bremsstrahlung arises from any two-body collision between charged particles. However, in the nonrelativistic limit ($|\mathbf{v}|/c \ll 1$), the radiation fields

produced by the two particles in a like-particle collision exactly cancel, so that it is only the electron–ion collisions that produce bremsstrahlung.

Quantum mechanics must be used to treat electron bremsstrahlung correctly. However, the classical theory of the previous section provides a reasonable approximate result and some insight into the physics of the process.

The Coulomb scattering law gives

$$|\dot{\mathbf{v}}| \simeq \frac{ze^2}{4\pi\epsilon_0 m_e x^2} \quad (17.36)$$

For the transverse acceleration of an electron incident upon an ion, with impact parameter x . Using this expression for acceleration in Eq. (17.27) leads to an expression for the rate of energy loss in a single electron–ion collision

$$W_{\text{rad}} = \frac{z^2 e^6}{96\pi^3 \epsilon_0^3 c^3 m_e^2 x^4} \quad (17.37)$$

This energy loss lasts for a time of about $x/|\mathbf{v}_e|$, and the number of such collisions experienced per unit time by an electron in passing through a plasma with ion density n_i is $n_i \mathbf{v}_e$. Thus the total bremsstrahlung power radiated by n_e electrons is

$$P_{\text{brem}} = n_i n_e |\mathbf{v}_e| \int_{x_{\min}}^{x_{\max}} W_{\text{rad}} \left(\frac{x}{|\mathbf{v}_e|} \right) 2\pi x \, dx \quad (17.38)$$

The result obtained from Eq. (17.38) differs only by an order unity numerical factor from the correct result, which is (T in keV, other in mks)

$$P_{\text{brem}} = 1.7 \times 10^{-38} z^2 n_i n_e T_e^{1/2} \left(W/m^3 \right) \quad (17.39)$$

When more than one ion species is present, z^2 in Eq. (17.39) is replaced by

$$z_{\text{eff}} \equiv \sum_{j \neq e} \frac{n_j z_j^2}{n_e} \quad (17.40)$$

A small impurity concentration significantly enhances the bremsstrahlung power radiated.

17.2.3 Cyclotron Radiation

Charged particles in a magnetically confined plasma spiral about the field lines with gyrofrequency

$$\Omega = -\frac{eB}{m} \quad (17.41)$$

and gyroradius

$$r_L = \frac{v_\perp}{|\Omega|} \quad (17.42)$$

The centrifugal acceleration of these charged particles is a significant radiation process in sufficiently hot plasmas.

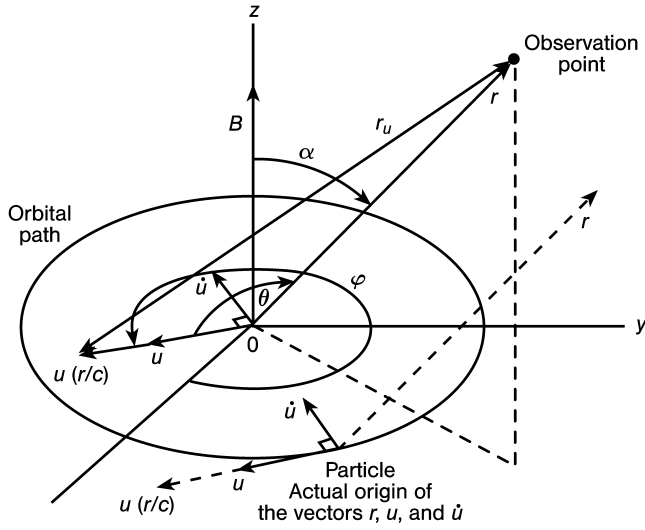


Figure 17.4. Cyclotron radiation nomenclature

Using the nomenclature of Fig. 17.4, the magnitudes of the particle velocity and acceleration are

$$|\mathbf{v}| = r_L \Omega \quad (17.43)$$

and

$$|\dot{\mathbf{v}}| = r_L \Omega^2 \quad (17.44)$$

The direction of $\dot{\mathbf{v}}$ is always radially inward, and the direction of \mathbf{v} is always tangential to the gyro-orbit (motion along the field line is ignored). For a fixed observation point, the angle α between the axis of rotation (field line) and the direction to the observation point is approximately constant. We use the relations

$$\begin{aligned} \mathbf{v} \cdot \mathbf{r} &= |\mathbf{v}| |\mathbf{r}| \cos \theta \\ \dot{\mathbf{v}} \cdot \mathbf{r} &= |\dot{\mathbf{v}}| |\mathbf{r}| \cos \theta \tan \phi \\ \mathbf{r}_v &= \mathbf{r} - \frac{\mathbf{v} |\mathbf{r}|}{c} \end{aligned} \quad (17.45)$$

to evaluate the term

$$[\mathbf{r} \times (\mathbf{r}_v \times \dot{\mathbf{v}})]^2 = |\dot{\mathbf{v}}|^2 r^4 \left[\left(1 - \frac{v}{c} \cos \theta \right)^2 - \left(1 - \frac{v^2}{c^2} \right) \tan^2 \phi \cos^2 \theta \right] \quad (17.46)$$

that appears in the general radiation formula, Eq. (17.34), allowing that expression to be written

$$\left(\frac{d^2 W_{\text{rad}}}{dt d\Omega} \right) = \frac{e^2 |\dot{\mathbf{v}}|^2}{(4\pi)^2 \epsilon_0 c^3} \frac{\left[\left(1 - \frac{v}{c} \cos \theta \right)^2 - \left(1 - \frac{v^2}{c^2} \right) \tan^2 \phi \cos^2 \theta \right]}{\left(1 - \frac{v}{c} \cos \theta \right)^5} \quad (17.47)$$

Making use of the trigonometric relation, $\cos \theta = \sin \alpha \cos \phi$, and writing the unit solid angle as $d\Omega = \sin \alpha d\alpha d\phi$, we can integrate Eq. (17.47) over a solid angle to obtain the rate of energy loss from a single particle because of the acceleration associated with its gyromotion,

$$\left(\frac{dW_{\text{rad}}}{dt} \right) = \frac{e^2}{6\pi\epsilon_0 c^3} \frac{r_L^2 \Omega^4}{\left[1 - \left(\frac{r_L \Omega}{c} \right)^2 \right]^2} \quad (17.48)$$

where we have made use of Eqs. (17.43) and (17.44). Because $(r_L \Omega^2)_e \gg (r_L \Omega^2)_i$, the cyclotron radiation is generally much larger for electrons than for ions.

The computation of the total power emitted from a plasma by cyclotron radiation of electrons is quite complex, involving as it does relativistic electron distribution functions, the correlation of radiation from different electrons, the absorption and reemission of the cyclotron radiation by the plasma, and the reflection of the radiated power by the surrounding wall. An approximate formula for the total cyclotron radiation power density emitted from a plasma with electrons in a Maxwellian distribution is (T_e in keV, otherwise mks)

$$P_{\text{cyl}} = 6.2 \times 10^{-17} B^2 n_e T_e (1 + T_e/204 + \dots) \left(\text{w/m}^3 \right) \quad (17.49)$$

17.3 Impurities

Ideally, D-T fusion would involve the presence of only hydrogenic species in the plasma. However, plasma impurities are unavoidable. At a minimum, He ash from the D-T fusion reactions will be present. Plasma-surface interactions are also inevitable, resulting in the release into the plasma of atoms and molecules from the solid structural components by evaporation, sputtering, etc.

Plasma impurities have both harmful and helpful consequences. The principal harmful consequence is cooling of the main plasma. The radiation power function varies greatly among elements, (see Fig. 17.5). That fractional impurity level which results in radiation power equal to 50 % of the alpha-heating power is shown in Fig. 17.6. Clearly, it is much more deleterious to have high- Z elements present in the core than low- Z ones. Figure 17.5 brings out a second critical difference between low- Z and high- Z impurities, as regards their radiative properties.

Low- Z elements become completely stripped of their orbital electrons at relatively low temperatures, $T_e \ll 1 \text{ keV}$. This results in a sharp decrease in the radiation power function to the low residual level given by bremsstrahlung radiation. The high- Z elements, however, retain some orbital electrons, even at the high temperatures of the core plasma, and their line radiation continues to make them efficient radiators. Fortunately, the intrinsic impurity helium can be tolerated more than other impurities. Nevertheless, a maximum level of about 10 % is acceptable for a reactor-like device.

A fit for impurity radiation from a plasma is

$$P_{\text{imp}} \left(M \text{w/m}^3 \right) = (1 + 0.3T_e) \times 10^{-43} n_e n_z z^{(3.7 - 0.33 \ln T)} \quad (17.50)$$

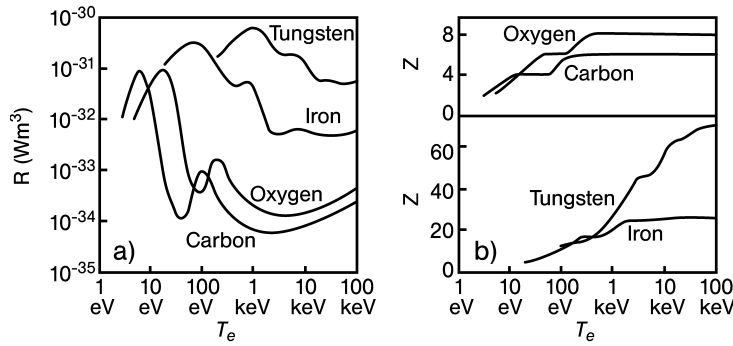


Figure 17.5. (a) The radiation loss or power function R (defined as L_z elsewhere) and (b) the mean charge \bar{Z} as functions of T_e for C, O, Fe and W

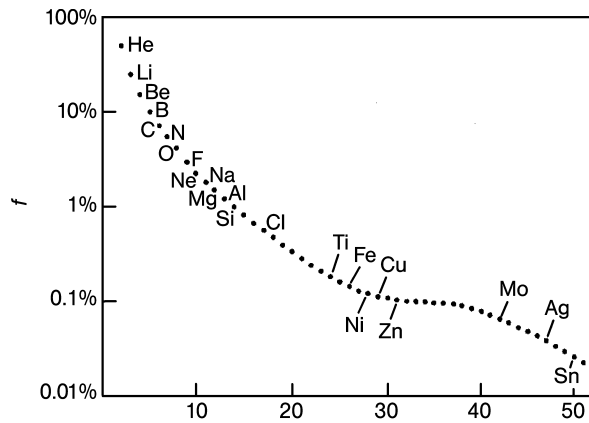


Figure 17.6. Fractional impurity level which produces a radiation power equal to half of the alpha-heating power

where T is in keV, z is the atomic number of the impurity ions, and the other quantities are in mks units.

Impurities present in the fusion core of the plasma are also harmful because of fuel dilution. The total plasma pressure, for a given field strength, B , is limited by MHD instabilities. The plasma β ($\equiv \sum_i n_i T_i / (B^2/2\mu_0)$) summed over electrons and all ion species cannot exceed the MHD beta limit. The electrons released by the impurities can “use up” a lot of this permitted maximum plasma pressure, even for impurity fractions which are rather low, thus diluting the beta-fraction of fuel ions.

Low- Z impurities radiate near the edge of the main plasma, where T_e is low enough that the ions are not fully stripped. This is potentially very advantageous, as was discussed in chapter 15 regarding the radiative mantle. It is also potentially harmful. Sufficiently

strong radiation in the periphery of the confined plasma can reduce the electrical conductivity so much that the tokamak current profile contracts, leading to an increased destabilizing current gradient inside the $q = 2$ surface. This then results in a disruption of the plasma, as will be discussed in chapter 18.

Unless impurity levels are kept below a critical level, there is the risk of a sputtering run-away catastrophe. While the normal incidence ion yields of hydrogenic species on all substrates are less than unity, self-sputtering yields often exceed unity. Since most sputtered neutrals become ionized within the plasma they can return to the solid surfaces as multiple charged ions and be accelerated by the sheath potential drop to very large impact energies.

Plasma impurity effects are not all deleterious, and we consider also their beneficial effects. As already discussed, the greatest benefit of impurities is volumetric power loss, so long as it occurs either in the SOL or near the periphery of the main plasma, and does not compromise the energy confinement. Such disposal of the exhaust power is greatly preferable to the intense, highly localized power deposition by particle impact on the very small divertor target areas, $\sim 1 \text{ m}^2$, that characterize magnetically confined devices. The photons can distribute the exhaust power over most of the large wall area – hundreds of square meters for a reactor-like device. Furthermore, photons do not cause sputtering. It is almost certainly essential that reactor-like devices dispose of a substantial portion of the exhaust power through radiation.

17.4 Burning Plasma Dynamics

A set of global equations may be written to describe the power and particle balances in a D-T plasma operating under fusion “burning” plasma conditions.

$$\frac{dn_i}{dt} = S_i - \frac{1}{2} n_i^2 \langle \sigma v \rangle_f - \frac{n_i}{\tau_i} \quad (17.51)$$

$$\frac{dn_\alpha}{dt} = S_\alpha + \frac{1}{4} n_i^2 \langle \sigma v \rangle_f - \frac{n_\alpha}{\tau_\alpha} \quad (17.52)$$

$$\frac{dn_z}{dt} = S_z - \frac{n_z}{\tau_z} \quad (17.53)$$

$$\frac{3}{2} \frac{d}{dt} (n_e T_e) = P_\Omega + P_{\text{aux}}^e + \frac{1}{4} n_i^2 \langle \sigma v \rangle_f U_{\alpha e} - Q_{ie} - P_R - \frac{3}{2} \frac{n_e T_e}{\tau_E^e} \quad (17.54)$$

and

$$\frac{3}{2} \frac{d}{dt} (n_i T_i) = P_{\text{aux}}^i + Q_{ie} + \frac{1}{4} n_i^2 \langle \sigma v \rangle_f U_{\alpha i} - \frac{3}{2} \frac{n_i T_i}{\tau_E^i} \quad (17.55)$$

The subscripts i , α , z and e refer to ions, alpha particles, impurity ions and electrons, respectively. The quantities in Eq. (17.51) to Eq. (17.55) are appropriate spatial averages of the previously defined quantities with the same symbol. The particle confinement times, τ , are defined in a similar manner as the energy confinement times, τ_E , but from the particle balance.

The sources (S_i , S_α , and S_z) depend on the particle and heat fluxes leaving the core and upon the specifics of the boundary region, plasma chamber wall and any impurity control mechanism present. Any external fuel source also contributes to S_i . A simple, order-of-magnitude estimate of these sources can be made when there is no impurity removal mechanism and the boundary region is sufficiently tenuous that charge exchange is unimportant,

$$S_i = R_i^W \frac{n_i}{\tau_i} \quad (17.56)$$

$$S_\alpha = R_\alpha^W \frac{n_\alpha}{\tau_\alpha} \quad (17.57)$$

and

$$S_z = (R_z^W + Y_z^W) \frac{n_z}{\tau_z} + Y_i^W \frac{n_i}{\tau_i} + Y_\alpha^W \frac{n_\alpha}{\tau_\alpha} \quad (17.58)$$

where R^W and Y^W are the recycling coefficient and sputtering yield, respectively.

We now examine some of the problems that will be encountered in maintaining a steady state power balance in a thermonuclear plasma and consider some control mechanisms that can be used to achieve this objective. The problems fall into two categories, composition changes and dynamic instabilities. We can use an overall power balance on the plasma to examine the problems,

$$\frac{dU}{dt} = (P_\alpha + P_{\text{aux}}) - (P_R + P_{\text{TR}}) \quad (17.59)$$

where $U = 3nT$ is the plasma internal energy, the terms in the first bracket on the right side are the alpha and supplemental power sources, and the terms in the second bracket are the radiation and transport power losses. A power balance is achieved when the RHS of Eq. (17.59) vanishes.

Assume that a power balance has been achieved at the beginning of a burn cycle, and consider the effects of the accumulation of wall eroded and fusion alpha impurities upon the power balance. The most obvious effect is the increase in P_R , which is usually the principal effect. The accumulation of impurities may also change $P_{\text{TR}} \sim (\tau_E)^{-1}$. If the maximum value of β is limited by MHD stability requirements, then the accumulation of impurity ions must be compensated by a reduction in the principal plasma ion concentration, so that $\bar{\beta} \propto (n_i + n_\alpha + n_z + n_e)T$ remains constant. This reduces $P_\alpha = n_i^2 \langle \sigma v \rangle_f U_\alpha$. The net effect of impurity accumulation is usually to decrease the plasma temperature.

Again, assume that a power balance has been achieved, and now consider the effect of a small temperature perturbation. A linear expansion of Eq. (17.59) about the power balance condition yields,

$$\frac{dU}{dt} = \left[\left(\frac{\partial P_\alpha}{\partial T} \right) \Delta T + \left(\frac{\partial P_{\text{aux}}}{\partial T} \right) \Delta T \right] - \left[\left(\frac{\partial P_R}{\partial T} \right) \Delta T + \left(\frac{\partial P_{\text{TR}}}{\partial T} \right) \Delta T \right] \quad (17.60)$$

If the RHS of Eq. (17.60) is positive the response to the perturbation is such as to increase the temperature perturbation. Thus the power balance is unstable if

$$\left[\left(\frac{\partial P_\alpha}{\partial T} \right) + \left(\frac{\partial P_{\text{aux}}}{\partial T} \right) \right] - \left[\left(\frac{\partial P_R}{\partial T} \right) + \left(\frac{\partial P_{\text{TR}}}{\partial T} \right) \right] > 0 \quad (17.61)$$

Because the fusion cross section increases sharply with the temperature (up to about $T = 80$ keV for D-T fusion), the alpha heating term is destabilizing. The sign of $\partial P_{\text{aux}}/\partial T$ depends on the type of auxiliary heating. The radiative loss term is generally negative, thus destabilizing, for impurities which are partially ionized (see Fig. 13.9). The transport loss term can be stabilizing or destabilizing depending on whether τ_E varies inversely (e.g. most “anomalous” transport theories) or directly (e.g., neoclassical with $\tau_E \sim T^{1/2}$) with temperature.

This power balance instability can be analyzed quantitatively by using Eq. (17.51) to Eq. (17.55), which are of the generic form

$$\frac{dx_i}{dt} = f_i(x_1, \dots, x_5), \quad i = 1, \dots, 5 \quad (17.62)$$

The equilibrium solutions that obtain when the power balance is achieved satisfy

$$f_i(x_{10}, \dots, x_{50}) = 0, \quad i = 1, \dots, 5 \quad (17.63)$$

To examine the stability of the power balance condition to perturbations in density and temperature, expansions about the equilibrium solutions,

$$x_i(t) = x_{i0} + \Delta x_i(t), \quad i = 1, \dots, 5 \quad (17.64)$$

are substituted into Eq. (17.62) and the resulting equations are Laplace-transformed and linearized to obtain

$$\sum_{j=1}^5 \left[\left(\frac{\partial f_i}{\partial x_j} \right)_0 - s \delta_{ij} \right] \Delta x_j = 0, \quad i = 1, \dots, 5 \quad (17.65)$$

Eq. (17.65) can be solved for the frequency, s . When $R_e(s) < 0$, the equilibrium is stable.

A qualitative picture of the thermal stability properties of a fusion reactor can be obtained from the contours of constant auxiliary power in the $\langle n_e \rangle - \langle T \rangle$ space, commonly referred to as POPCONs. The POPCON plots are calculated here from the energy balance equations for the electrons and ions, obtained from the equilibrium versions of Eq. (17.54) and Eq. (17.55).

For each point in the $\langle n_e \rangle - \langle T \rangle$ space, we fix n_e and the electron (or ion) temperature and we solve the resulting nonlinear algebraic system of power balance equations for the ion (or electron) temperature and the required auxiliary power P_{aux} .

The thermal stability properties of a point are determined by the slope of the resulting P_{aux} curve. Points are unstable to temperature excursions if $\partial P_{\text{aux}}/\partial T < 0$, since, if the temperature increases from its equilibrium value due to a positive temperature perturbation, the plasma moves to a region where the required auxiliary power for equilibrium is lower. Therefore, a net energy gain heats the plasma and removes it further from the original equilibrium point. This temperature excursion lasts until a stable operating point is found in the $\langle n_e \rangle - \langle T \rangle$ space (in reality the beta limit will likely be exceeded and a disruption would terminate the discharge).

The shape of a POPCON, and hence the stability properties of the plasma, depends on the energy confinement scaling, but even for the same confinement scaling it is sensitive to several parameters such as the Z_{eff} , the thermal alpha-particle concentration, and the

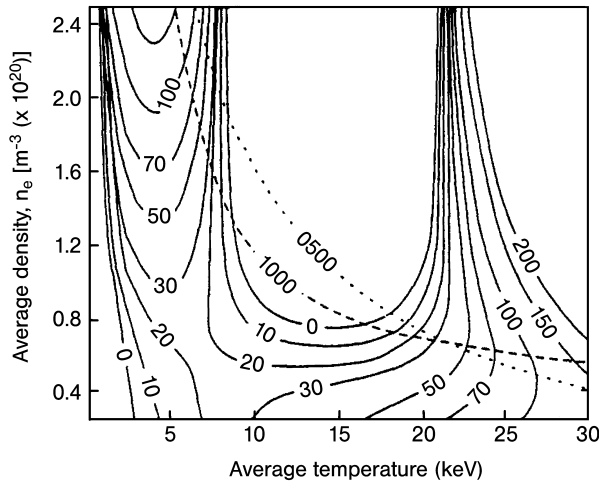


Figure 17.7. POPCON for ITER, assuming Goldston scaling with enhancement factor $H = 2.0$ and alpha-particle concentration of 5 %

L -mode enhancement factor H . In Fig. 17.7, the POPCON for Goldston scaling, assuming thermal alpha-particle concentration $n_\alpha/n_e = 5\%$ and $H = 2$, is shown. Also shown on the same plot are curves of constant fusion power of 500 MW and 1000 MW. There are two possible ignited operating points at each of these power levels, one unstable in the low $\langle T \rangle$, high $\langle n \rangle$ region, and one stable in the high $\langle T \rangle$, low $\langle n \rangle$ region.

Problems for Chapter 17

- Calculate the experimental energy confinement time of a plasma of volume 24 m^3 that is maintained at a constant density $n = 3 \times 10^{19} \text{ m}^{-3}$ and temperature $T = 5 \text{ keV}$ by neutral beam injection power of $P_{\text{nb}} = 5.5 \text{ MW}$. The measured radiation from the plasma core is 1.5 MW.
- Calculate the predicted energy confinement times of an H-mode deuterium plasma with $I = 3 \text{ MA}$, $R = 1.7 \text{ m}$, $a = 0.6 \text{ m}$, $\kappa = 1.75$, $n = 3 \times 10^{19} \text{ m}^{-3}$ and $B = 3T$ using the ITER93-P and the IPB98(y,2) empirical scaling laws.
- Calculate the bremsstrahlung and cyclotron radiation power from the plasma of problem 2 operating at 5 keV. Calculate the impurity radiation that would result from a 5 % carbon concentration and from a 1 % iron concentration.
- Solve Eq. (17.51) to Eq. (17.53) and Eq. (17.56) to Eq. (17.58) for the equilibrium density levels for deuterium–tritium plasma ions, alpha particles and carbon impurities for a 10 keV plasma.
- Derive an explicit power balance stability criterion by substituting explicit expressions for the various power terms in Eq. (17.61).

18 Operational Limits

There are limits on the allowable values of the plasma operational parameters. The maximum plasma density is constrained by a number of phenomena, the most dramatic of which in a tokamak is the “disruption,” a sudden and complete loss of confinement due to large-scale MHD activity and accompanied by the generation of large electromagnetic and pressure forces in the surrounding structure. There are also less dramatic density limits, due to thermal instabilities and confinement degradation, beyond which the plasma density cannot be further increased by continued fueling. In addition, there are plasma pressure, or beta, limits beyond which the plasma pressure cannot be further increased without the onset of large-scale MHD activity with deleterious consequences for plasma performance.

18.1 Disruptions

The disruption in a tokamak is a dramatic event. The plasma confinement is suddenly destroyed and some, if not all, of the plasma current is transferred to the surrounding conducting paths in the tokamak structure. Disruptions limit the operational density and current, and their existence poses a major problem for future tokamak reactors with larger currents because of the intense heat load and large mechanical forces that will be produced.

18.1.1 Physics of Disruptions

While the physics involved in a disruption is not yet fully understood, a general sequence of events can be described:

1. The evolution of the current profile leading to the instability of a tearing mode, in particular the $m = 2$ mode, is a common initiating feature. This is frequently caused by an inward radiative collapse of the radial temperature profile, which reduces the temperature and increases the plasma resistivity in the outer plasma regions, producing a central peaking of the current profile.
2. The tearing mode grows nonlinearly.
3. There is a sudden flattening of the current profile and a dramatic loss of confinement, with a collapse of the plasma temperature profile.
4. The plasma current decays on a time scale faster than can be accounted for by the plasma resistivity.
5. Under certain conditions, a current of runaway electrons is produced which lasts after the plasma current decay.

6. Large currents are induced in the vacuum vessel (or other nearby conducting material) by both the decay of the plasma current and the loss of plasma energy, producing large electromagnetic forces.

The tearing mode, in particular with $m = 2$, is a common precursor to a disruption. The tearing mode is destabilized by a negative current gradient inside the resonant surface and in particular by negative current gradients close to the resonant surface. The constraint on $q(0)$ imposed by sawtooth oscillations causes a flattening of the central current gradient and an increase in the current gradient in the outer regions. Increasing total current, thus lowering $q(a)$, leads increasingly to an outward movement of the $q = 2$ surface and increased negative current gradient, if $q(0) > 1$ is constrained by sawtooth oscillations. Increased radiation in the outer region can cause a reduction of the current in the outer regions and a steepening of the negative current gradient in the vicinity of the $q = 2$ surface.

The tearing mode instability first appears as a low level magnetic oscillation, the oscillatory form resulting from the motion of the helical instability around the torus with a velocity that is the sum of mass velocity of the plasma and the propagation velocity of the tearing mode instability. The oscillation growth is a sporadic series of bursts, each of which is a minor disruption, followed by a disappearance of the oscillation due to mode locking when the amplitude becomes large enough to allow the instability to interact with external conductors in such a way as to dampen the mode propagation.

Following the onset of mode locking, the perturbed B_r grows continuously, implying the growth of a magnetic island in the plasma. These magnetic islands produce rapid radial transport via parallel transport around the magnetic islands. The temperature is constant on each flux surface forming the magnetic island because of the high thermal conduction along the field lines, which results in the electron temperature being almost constant across a magnetic island, except for a narrow layer close to the separatrix of the island.

The calculated (and observed) $m = 2$ island grows to a width typically 20 % of the plasma radius. There is a flattening of the current profile, which suggests a break up of the magnetic surfaces and multiple magnetic reconnections. There is also evidence of a large $m = 1$ structure to the soft X-ray data at the time of the sudden loss of energy confinement. The relationship among these phenomena is not well understood.

Following the rapid loss of energy confinement, the plasma current decays to zero. The current decay rate is faster than can be explained on the basis of the plasma resistance, implying that an additional impedance (e.g. due to persisting MHD turbulence) or enhanced resistivity is present. An influx of impurities into the central plasma, resulting in eV level plasma temperatures and greatly enhanced resistivity, is believed to account for the rapid current decay.

Disruptions cause large $\mathbf{j} \times \mathbf{B}$ forces in the vacuum vessel (or other nearby conductor). The currents are induced by transient electric fields. The loss of plasma pressure leads to an increase in the toroidal magnetic field pressure inside the plasma, $\delta(B_\phi^2/2\mu_0) \approx \delta p$, which initially balances the poloidal magnetic pressure (i.e. $\delta p \simeq B_\theta^2/2\mu_0$) and lowers the toroidal magnetic field between the plasma and the vacuum vessel to conserve magnetic flux. The resulting difference in magnetic field across the vacuum vessel induces a poloidal

current, which produces an inward force $\approx \delta p$. The subsequent current decay also transfers the toroidal magnetic field pressure to the vacuum vessel. Finally, there is a toroidal current

$$I_v = \left(\frac{L_v}{R_v} \right) I_p \quad (18.1)$$

induced in the vacuum vessel, where L_v and R_v are the inductance and resistance of the vacuum vessel and I_p is the plasma current. This current produces a pressure

$$p_v \sim \frac{B_{\theta a}^2}{\mu_0} \frac{\tau_{\text{vessel}}}{\tau_{\text{decay}}} \quad (18.2)$$

on the vacuum vessel, where $\tau_{\text{vessel}} = L_v/R_v$, and $\tau_{\text{decay}} > \tau_{\text{vessel}}$ is the decay time. All forces result in pressures on the vacuum vessel of about $10^5 \text{ N} \cdot \text{m}^{-2}$, or several hundred tonnes, when parameters typical of present large tokamaks are used. These forces will be an order of magnitude larger for future tokamak reactors.

18.1.2 Causes of Disruptions

Several operational causes for disruptions have been identified, most of which involve unstable current profiles that result in tearing modes. Vertical instabilities and magnetic field errors have also been associated with disruptions. However, most disruptions can be associated with either operation at too small a value of $q(a)$ – steep negative current gradients – or too large a value of the density, leading to a radiative collapse of the temperature profile and to steep negative current gradients. The stable operating space with respect to disruptions can be characterized for most tokamaks by a plot of the type shown in Fig. 18.1, which is known as a Hugill diagram. As shown, the stable operational regime is generally increased by auxiliary heating.

The cause of low- q disruptions seems to be the $q = 2$ surface moving outward into the region of sharp, negative current density gradients. If $q(0) \gtrsim 1$ is constrained by sawtooth $m = 1$ instabilities, then increasing the current moves the $q = 2$ surface outward into the edge region and steepens the negative current density gradient that destabilizes the $m = 2$ tearing mode. As shown in Fig. 18.2, the calculated nonlinear amplitudes of the tearing modes (\sim island width) and of the surface kink modes increase as $q(a) \rightarrow 2$. The low $q(a)$ disruption limit is essentially a current limit on tokamak operation.

At higher $q(a)$, the radial collapse of the current channel moves the sharp, negative current density gradient in towards the location of the $q = 2$ surface. Low- z edge radiation increases in the edge as the plasma density increases, causing a decrease in edge temperature and an increase in resistivity, which contracts the current channel. When the sharp, negative current density gradient moves inward to the $q = 2$ surface, the $m = 2$ tearing mode is destabilized.

18.2 Disruption Density Limit

Since density limit disruptions are preceded by an inward radiative collapse of the radial temperature profile, a prediction of the conditions for which the radial temperature profile

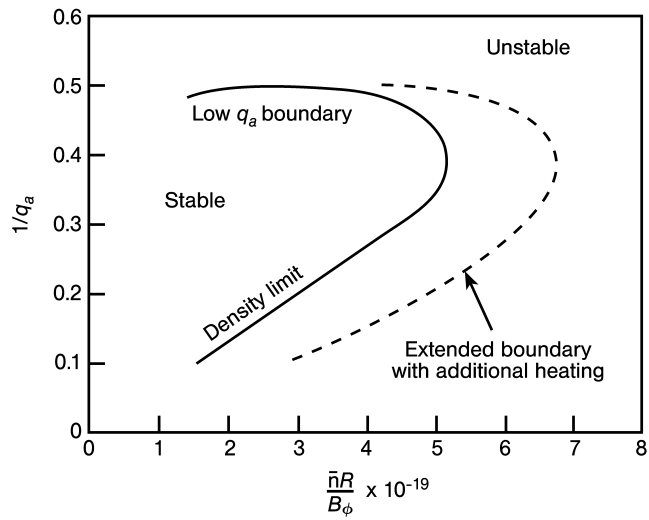


Figure 18.1. Typical Hugill diagram of the disruption operational boundary in a tokamak

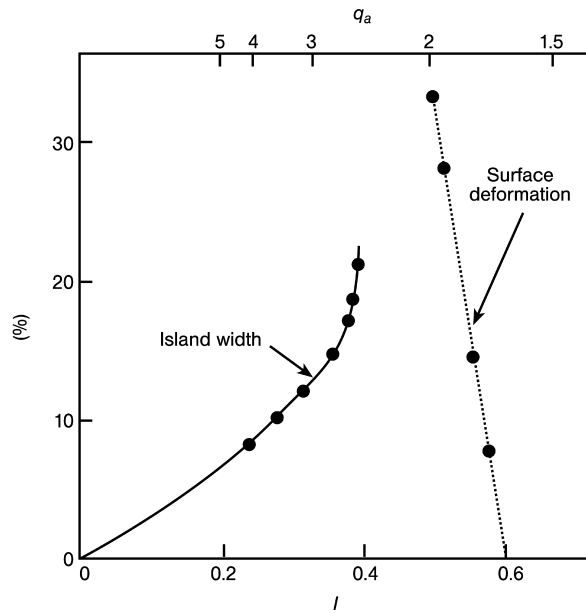


Figure 18.2. Instability amplitudes of $m = 2$ helical perturbation (island width of tearing mode for $q(a) > 2$; surface deformation of kink mode for $q(a) < 2$)

becomes unstable to a perturbation that represents an inward collapse of the temperature profile may be used as a surrogate for a prediction of the subsequent disruption. To this end, we examine thermal instabilities in the radial power and particle balance equations driven by impurity radiation in the outer plasma regions.

18.2.1 Radial Temperature Instabilities

We first consider the possibility of radial instabilities in the temperature profile that might lead to a thermal collapse of the temperature profile. The thermal balance equation summed over ions and electrons (neglecting poloidal transport effects) may be written in the cylindrical approximation as

$$3 \frac{\partial(nT)}{\partial t} - \frac{1}{r} \frac{\partial}{\partial r} \left(r \kappa_{\perp} \frac{\partial T}{\partial r} \right) = H - L \quad (18.3)$$

where

$$H \equiv \hat{H} + \frac{1}{4} n^2 (\sigma v) U_{\alpha} \quad (18.4)$$

$$L \equiv f_z n^2 L_z(T) \quad (18.5)$$

with H representing the heating due to auxiliary sources, due to Ohmic heating, and due to fusion alpha particles, and L representing the cooling due to impurity radiation. In these equations, n is the ion or electron density, T is the common temperature, κ_{\perp} is the thermal conductivity, (σv) is the fusion reactivity, U_{α} is the fusion energy release, $f_z = n_z/n$ is the impurity fraction, and L_z is the impurity radiation function. To simplify the derivation, we assume that the density and thermal conductivity are uniform and fixed and that κ is independent of T , these assumptions will be removed in a subsequent section.

The time-dependent temperature is represented as

$$T(r, t) = \bar{T}(r) + \tilde{T}(r) e^{\omega t} \quad (18.6)$$

where \bar{T} is the equilibrium solution of Eq. (18.3). Substituting Eq. (18.6) into Eq. (18.3) and linearizing leads to the equation satisfied by the temperature perturbation \tilde{T} ,

$$3n\omega \tilde{T} - \frac{1}{r} \frac{\partial}{\partial r} \left(r \kappa_{\perp} \frac{\partial \tilde{T}}{\partial r} \right) = \frac{\partial(H-L)}{\partial T} \tilde{T} \quad (18.7)$$

This equation may be multiplied through by r^2 and rearranged to obtain the equivalent form

$$r^2 \frac{\partial^2 \tilde{T}}{\partial r^2} + r \frac{\partial \tilde{T}}{\partial r} + \frac{r^2}{\kappa_{\perp}} \left(\frac{\partial(H-L)}{\partial T} - 3n\omega \right) \tilde{T} = 0 \quad (18.8)$$

If the spatially dependent term in () could be replaced by a constant, Eq. (18.8) would be the equation for the Bessel functions J_0 and I_0 , depending on the sign of the constant.

We assume that $\partial(H-L)/\partial T$ can be replaced by an average value (this assumption will be removed in a subsequent section) and write

$$\begin{aligned}\kappa_{\perp}\mu^2 &\equiv \left(\frac{\partial(H-L)}{\partial T} - 3n\omega \right) \\ &= \left\{ \frac{\partial\hat{H}}{\partial T} + n^2 \left[\frac{1}{4}U_{\alpha}\frac{\partial(\sigma v)}{\partial T} + f_z \left(-\frac{\partial L_z}{\partial T} \right) \right] - 3n\omega \right\} \quad (18.9)\end{aligned}$$

where \hat{H} represents ohmic plus auxiliary heating.

If $\mu^2 > 0$, the solution of Eq. (18.9) is $\tilde{T}(r) \sim J_0(\mu r)$, and if $\mu^2 < 0$, the solution of Eq. (18.8) is $\tilde{T}(r) \sim I_0(\mu r)$. The J_0 function with $\mu a \approx 5.5$ corresponding to the second zero crossing of the function, where a is the plasma radius, would represent a perturbation that diminished the temperature in the outer region ($2.4 < \mu a < 5.5$) and increased it in the central region ($\mu a < 2.4$). Such a perturbation has the form of a collapsing temperature profile.

The quantity $\partial(\sigma v)/\partial T > 0$ for $T \lesssim 100$ keV, for deuterium-tritium (D-T) fusion. The quantity $\partial L_z/\partial T$ generally is positive at lower T and negative at higher T (chapter 13); the transition temperature generally increases with the impurity atomic number, Z , varying from a few electronvolts for low- Z species through a few tens of electronvolts for intermediate- Z impurities to hundreds of electronvolts for high- Z impurities.

Ohmic heating goes as $H_{\Omega} = \eta j^2$. From Ohm's law, $j = E/\eta$, which implies $H_{\Omega} \sim 1/\eta \sim T_e^{3/2}$. Thus, $\partial H_{\Omega}/\partial T = \frac{3}{2}(H_{\Omega}/T)$. If the auxiliary heating is collisional (e.g., neutral beam), the temperature dependence will be $H_{\text{aux}} \sim v \sim T_e^{-3/2}$, and $\partial H_{\text{aux}}/\partial T = -\frac{3}{2}(H_{\text{aux}}/T)$. Since $\hat{H} \rightarrow H_{\text{aux}} > H_{\Omega}$ in general, $\partial\hat{H}/\partial T < 0$ for auxiliary-heated plasmas.

The generally positive $n^2()$ term in Eq. (18.9) could thus drive instabilities ($\omega > 0$) for which $\mu^2 > 0$ and $\tilde{T}(r) \sim J_0(\mu r)$; i.e., Eq. (18.9) admits a growing perturbation with the $J_0(\mu r)$ distribution. Equation (18.9) may be solved for the instability growth rate, ω ,

$$\begin{aligned}\omega = \frac{1}{3n} \left\{ -\left(-\frac{\partial\hat{H}}{\partial T} \right) + n^2 \left[\frac{1}{4}U_{\alpha}\frac{\partial(\sigma v)}{\partial T} + f_z \left(-\frac{\partial L_z}{\partial T} \right) \right] \right. \\ \left. - \kappa_{\perp} \left(\frac{5.5}{a} \right)^2 \right\} \quad (18.10)\end{aligned}$$

If we require that $\tilde{T}(a) = J_0(\mu a) = 0$ and select the second zero crossing of J_0 so that $J_0(\mu a)$ corresponds to a collapsing temperature profile, then $\mu a = 5.5$. The condition for stability against a collapsing temperature profile, $\omega < 0$, can then be used with Eq. (18.10) to define a density limit,

$$n^2 \leq \frac{\kappa_{\perp}(5.5/a)^2 + (-\partial\hat{H}/\partial T)}{\frac{1}{4}U_{\alpha}[\partial(\sigma v)/\partial T] + f_z(-\partial L_z/\partial T)} \quad (18.11)$$

If we take into account the possibility that $\kappa_{\perp} = n\chi_{\perp}$, then the density limit is of the form

$$n \leq \chi_{\perp}(5.5/a)^2 \times \frac{1 \pm \sqrt{1 + 4 \left[\frac{1}{4} U_{\alpha} [\partial(\sigma v)/\partial T] + f_z(-\partial L_z/\partial T) \right] (-\partial \hat{H}/\partial T)/\chi_{\perp}^2(5.5/a)^4}}{2 \left[\frac{1}{4} U_{\alpha} [\partial(\sigma v)/\partial T] + f_z(-\partial L_z/\partial T) \right]} \quad (18.12)$$

When $\partial \hat{H}/\partial T = 0$, the density limit given by the (+) root of (18.12) is identical to the density limit of (18.11) and the (−) root vanishes. When $\partial \hat{H}/\partial T < 0$ (e.g., for neutral beam heating) and $f_z(\partial L_z/\partial T) < \frac{1}{4} U_{\alpha} [\partial(\sigma v)/\partial T]$ (the usual situation), the (−) root leads to a negative density limit. Thus, we are led by physical considerations to associate the (+) root in Eq. (18.12) with the physical situation and to ignore the (−) root as being introduced by the mathematics.

If we take into account the further possibility of a density dependence of the heating term $\hat{H} = n\hat{h}$, the density limit is

$$n \leq \frac{\chi_{\perp}(5.5/a)^2 - \partial \hat{h}/\partial T}{\frac{1}{4} U_{\alpha} [\partial(\sigma v)/\partial T] + f_z(-\partial L_z/\partial T)} \quad (18.13)$$

which is identical to Eq. (18.11).

We can use these expressions to make an order of magnitude estimate of the predicted density limit for present experiments, in which the fusion term is absent. Estimating $\tau_E \simeq a^2/\chi_{\perp} \simeq 1$ s, $f_z = 5 \times 10^{-2}$ for carbon impurity, and $T_{av} = 5$ keV, Eq. (18.10)b predicts $n \lesssim 10^{20} \cdot m^{-3}$. (We have set $\partial H/\partial T = 0$.) This prediction is the right order of magnitude. We will develop better quantitative algorithms in a later section.

An interesting prediction emerges from Eq. (18.4) and Eq. (18.12). Since generally we expect $\partial \hat{H}/\partial T < 0$ for collisional auxiliary heating and for the magnitude of the $|\partial H/\partial T|$ to increase with the heating power, the density limit for auxiliary-heated plasmas is predicted to be larger than the density limit for ohmic plasmas. This agrees with the experimental results shown in the Hugill diagram of Fig. 18.1.

18.2.2 Spatial Averaging

Since the major effects of the ohmic heating, the auxiliary heating, the fusion alpha heating, and the impurity cooling generally will occur at different radial locations, we need theoretical guidance in order to choose appropriate average values to evaluate the above equations. Appropriate averages can be developed by repeating the above derivation, but now integrating Eq. (18.7) and defining the quantity μ^2 from

$$\begin{aligned} & \int_0^a r \left[-\frac{1}{r} \frac{\partial}{\partial r} \left(r \kappa_{\perp} \frac{\partial \tilde{T}}{\partial r} \right) \right] dr \\ & \equiv \kappa_{\perp} \mu^2 \int_0^a r \tilde{T}(r) dr = \int_0^a r \left(\frac{\partial(H - L)}{\partial T} - 3n\omega \right) \tilde{T}(r) dr \end{aligned} \quad (18.14)$$

Using Eq. (18.3) and Eq. (18.4), Eq. (18.14) can be solved for the instability growth rate,

$$\begin{aligned} \omega &= \frac{1}{3n} \\ &\times \left(\frac{\int_0^a r \left\{ -(-\partial \hat{H}/\partial T) + n^2 \left[\frac{1}{4} U_\alpha \partial(\sigma v)/\partial T + f_z(-\partial L_z/\partial T) \right] \right\} \tilde{T}(r) dr}{\int_0^a r \tilde{T}(r) dr} - \kappa_\perp \mu^2 \right) \end{aligned} \quad (18.15)$$

The stability condition, $\omega \leq 0$, then leads to a density limit,

$$n^2 \leq \frac{\kappa_\perp \mu^2 \int_0^a r \tilde{T}(r) dr + \int_0^a r (-\partial \hat{H}/\partial T) \tilde{T}(r) dr}{\int_0^a r \left\{ \frac{1}{4} U_\alpha [\partial(\sigma v)/\partial T] + f_z(-\partial L_z/\partial T) \right\} \tilde{T}(r) dr} \quad (18.16)$$

If we now specialize to the temperature profile collapse mode $\tilde{T}(r) \sim J_0(\mu r)$ and require $\tilde{T}(a) = 0$ at the second zero crossing of J_0 , so that $\mu a = 5.5$; Eq. (18.16) becomes

$$n^2 \leq \frac{\kappa_\perp (5.5/a)^2 + \langle -\partial \hat{H}/\partial T \rangle}{\left\langle \frac{1}{4} U_\alpha [\partial(\sigma v)/\partial T] + f_z(-\partial L_z/\partial T) \right\rangle} \quad (18.17)$$

This equation is of the same form as Eqs. (18.11) and (18.13), but now the appropriate spatial average for a quantity X is defined as

$$\langle X \rangle \equiv \frac{\int_0^a r X(r) J_0(5.5r/a) dr}{\int_0^a r J_0(5.5r/a) dr} \quad (18.18)$$

The $J_0(5.5r/a)$ weighting is negative in the regions, where the temperature is lower and $\partial L_z/\partial T$ may be positive, and is positive in the higher temperature inner regions, where $\partial L_z/\partial T$ is smaller and probably negative. This weighting also emphasizes the central peaking of the fusion heating term. Thus, this weighting emphasizes the destabilizing nature of the radiation cooling and fusion alpha heating terms – the denominator of Eq. (18.17).

As before, if we take note of the possibility that $\kappa_\perp = n\chi_\perp$, the derivation now leads to a density limit,

$$\begin{aligned} n &\leq \chi_\perp (5.5/a)^2 \\ &\times \frac{\left(1 \pm \sqrt{1 + 4 \langle -\partial \hat{H}/\partial T \rangle \left\langle \frac{1}{4} U_\alpha [\partial(\sigma v)/\partial T] + f_z(-\partial L_z/\partial T) / \chi_\perp (5.5/a)^2 \right\rangle} \right)}{2 \left\langle \frac{1}{4} U_\alpha [\partial(\sigma v)/\partial T] + f_z(-\partial L_z/\partial T) \right\rangle} \end{aligned} \quad (18.19)$$

Equations (18.17) and (18.19) have the same physical content and form as Eq. (18.11) and (18.12), but now the appropriate spatial weighting is explicit in the $\langle \rangle$ averages.

For ohmic-heated tokamaks, the experimental data is well represented by the empirical Murakami/Hugill limit.

$$\bar{n} \leq c_1 (B/Rq_0) \quad (18.20)$$

where c_1 is a constant of order unity, $B(T)$ is the magnetic field strength, $R(m)$ is the major radius, q_0 is the safety factor at the center, and \bar{n} (10^{20} m^{-3}) is the line-averaged density. More recently, Greenwald et al. proposed.

$$\bar{n} \leq \frac{I}{\pi a^2} \quad (18.21)$$

where I is the plasma current (in MA) and a is the minor radius (in m).

Writing

$$q_0 = \left(\frac{q_0}{q} \right) q = \left(\frac{q_0}{q} \right) \frac{2\pi a^2 B}{\mu_0 RI} (1 + \kappa^2) \quad (18.22)$$

it is seen that these two empirical limits are equivalent when Eq. (18.22) is an appropriate representation for q . The Greenwald limit seems to fit ohmic and also many auxiliary-heated discharges, although plasmas with auxiliary heating and/or pellet injection frequently exceed the Greenwald limit (section 18.4). Here κ is the elongation of the plasma.

In order to compare with these empirical representations of the experimental density limit we specialize Eqs. (18.4), (18.12), (18.17), or (18.19) to the case of an ohmically heated plasma by suppressing the auxiliary and fusion alpha heating terms, and imposing the power balance for an ohmic heated plasma,

$$\frac{nT}{\tau_E} = \eta j^2 \quad (18.23)$$

where η is the plasma resistivity and τ_E is the energy confinement time, and use the relation

$$\chi_{\perp} \simeq \frac{a^2}{2\tau_E} \quad (18.24)$$

to reduce the predicted density limit to the form

$$n \leq j \left(\frac{\eta}{2f_z (-\partial L_z / \partial T)} \right)^{1/2} (5.5 \times 10^6) \quad (18.25)$$

for j in $\text{MA}\cdot\text{m}^{-2}$. Thus, the predicted disruption density limit of this section has the current scaling of the Greenwald limit for ohmic heated plasmas.

18.2.3 Coupled Radial Temperature–Density Instabilities

We now extend the previous analysis to allow simultaneous contractive perturbations in the temperature and density distributions.

The ion density satisfies

$$\frac{\partial n}{\partial t} - \frac{1}{r} \frac{\partial}{\partial r} \left[r \left(D_{\perp} \frac{\partial n}{\partial r} + n v_p \right) \right] = S \quad (18.26)$$

where $S = nn_0(\sigma\nu)_{\text{ion}}$ is the ionization particle source, with n_0 being the neutral density and $(\sigma\nu)_{\text{ion}}$ being the ionization reactivity; and D_{\perp} and v_p are the diffusion coefficient and pinch velocity, respectively. We will expand the ion density about the equilibrium solution of Eq. (18.26)

$$n(r, t) = \bar{n}(r) + \tilde{n}(r)e^{\omega t} \quad (18.27)$$

We allow the transport coefficients (D_{\perp} , χ_{\perp} and v_p) to be temperature dependent. Substituting the expansions of Eq. (18.6) and Eq. (18.27) into Eq. (18.3) and Eq. (18.26), and linearizing leads to

$$\begin{aligned} 3(\bar{n}\tilde{T} + \tilde{n}\bar{T})\omega - \frac{1}{r} \frac{\partial}{\partial r} & \left[r \left(\bar{n}\tilde{\chi}_{\perp} \frac{\partial \tilde{T}}{\partial r} + \tilde{n}\tilde{\chi}_{\perp} \frac{\partial \bar{T}}{\partial r} + \bar{n} \frac{\partial \bar{T}}{\partial r} \tilde{\chi}_{\perp} \right) \right] \\ &= \frac{\partial H}{\partial T} \tilde{T} + \frac{\partial H}{\partial T} \tilde{n} - 2f_z \bar{n} \bar{L}_z \tilde{n} - f_z \bar{n}^2 \frac{\partial L_z}{\partial T} \tilde{T} \end{aligned} \quad (18.28)$$

and

$$\tilde{n}\omega - \frac{1}{r} \frac{\partial}{\partial r} \left[r \left(D_{\perp} \frac{\partial \tilde{n}}{\partial r} + \tilde{D}_{\perp} \frac{\partial \bar{n}}{\partial r} + \tilde{n}\bar{v}_p + \bar{n}\tilde{v}_p \right) \right] = \frac{\partial S}{\partial T} \tilde{T} + \frac{\partial S}{\partial n} \tilde{n} \quad (18.29)$$

where

$$\tilde{\chi}_{\perp} = \frac{\partial \chi_{\perp}}{\partial T} \tilde{T} \quad \tilde{D}_{\perp} = \frac{\partial D_{\perp}}{\partial T} \tilde{T} \quad \tilde{v}_p = \frac{\partial v_p}{\partial T} \tilde{T} + \frac{\partial v_p}{\partial n} \tilde{n} \quad (18.30)$$

We are guided by the results of the previous section to integrate Eq. (18.28) and Eq. (18.29), to make the replacements.

$$-\int_0^a r \left[\frac{1}{r} \frac{\partial}{\partial r} \left(r \bar{n} \tilde{\chi}_{\perp} \frac{\partial \tilde{T}}{\partial r} \right) \right] dr \equiv \mu^2 \int_0^a r \bar{n} \tilde{\chi}_{\perp} \tilde{T} dr \equiv \mu^2 \hat{\chi}_{\perp} \int_0^a r \bar{n} \tilde{T} dr \quad (18.31)$$

$$-\int_0^a r \left[\frac{1}{r} \frac{\partial}{\partial r} \left(r \tilde{D}_{\perp} \frac{\partial \tilde{n}}{\partial r} \right) \right] dr \equiv \mu^2 \int_0^a r D_{\perp} \tilde{n} dr \equiv \mu^2 \hat{D}_{\perp} \int_0^a r \tilde{n} dr \quad (18.32)$$

and to approximate the perturbed temperature and density distributions with $\tilde{T}(r) = \tilde{T}_0 J_0(\mu r)$ and $\tilde{n}(r) = \tilde{n}_0 J_0(\mu r)$, where $\mu a = 5.5$. Using these, forms, the effective transport coefficients are defined as

$$\hat{\chi} = \langle \bar{n} \tilde{\chi}_{\perp} \rangle / \langle \bar{n} \rangle, \hat{D}_{\perp} \equiv \langle \tilde{D}_{\perp} \rangle \quad (18.33)$$

Defining

$$y \equiv \tilde{n}_0 / \tilde{T}_0 \quad (18.34)$$

and integrating Eq. (18.28) and (18.29) leads to the solution

$$y = -\frac{b(1 \pm \sqrt{1 - 4ac/b})}{2a} \quad (18.35)$$

where

$$\begin{aligned} a &\equiv 3 \langle \bar{T} \rangle \left(\left\langle \frac{\partial S}{\partial n} \right\rangle - \mu^2 \hat{D}_\perp \right) - \left\langle \frac{\partial \hat{H}}{\partial n} + 2\bar{n} \left(\frac{1}{4} U_\alpha (\sigma v) - f_z L_z \right) \right\rangle \\ b &\equiv 3 \langle \bar{n} \rangle \left(\left\langle \frac{\partial S}{\partial n} \right\rangle - \mu^2 \hat{D}_\perp \right) \\ &+ 3 \langle T \rangle \left\langle \frac{\partial S}{\partial T} \right\rangle - \left\langle \frac{\partial \hat{H}}{\partial n} + \bar{n}^2 \left[\frac{1}{4} U_\alpha \frac{\partial (\sigma v)}{\partial T} + f_z \left(-\frac{\partial L_z}{\partial T} \right) \right] \right\rangle \\ c &\equiv 3 \langle \bar{n} \rangle \left\langle \frac{\partial S}{\partial T} \right\rangle \end{aligned} \quad (18.36)$$

The requirements $\tilde{T}(a) = \tilde{n}(a) = 0$ used in deriving Eqs. (18.35) and (18.36) eliminate all terms associated with the temperature dependence of the transport coefficients and with the pinch.

Next, Eq. (18.29) – after integration and the substitutions described above – is solved for the growth rate,

$$\omega = \left\langle n_0 \left(\bar{n} \frac{\partial (\sigma v)_{\text{ion}}}{\partial T} y^{-1} + (\sigma v)_{\text{ion}} \right) \right\rangle - \mu^2 \hat{D}_\perp \quad (18.37)$$

The stability requirement $\omega \leq 0$ then leads to a fueling neutral density limit,

$$\left\langle n_0 \left(\bar{n} \frac{\partial (\sigma v)_{\text{ion}}}{\partial T} y^{-1} + (\sigma v)_{\text{ion}} \right) \right\rangle \leq \hat{D}_\perp \left(\frac{5.5}{a} \right)^2 \quad (18.38)$$

Finally, Eq. (18.28) – after integration and the substitutions described above – is solved for the growth rate,

$$\begin{aligned} \omega &= \frac{1}{3} \left(\frac{-\mu^2 \hat{\chi}_\perp \langle \bar{n} \rangle + \langle \partial \hat{H} / \partial T \rangle}{\langle \bar{n} \rangle + y \langle \bar{T} \rangle} \right. \\ &+ \left. \frac{\langle \bar{n}^2 \left\{ \frac{1}{4} U_\alpha [\partial(\sigma v)/\partial T] + f_z (-\partial L_z/\partial T) \right\} \rangle + \langle y \partial \hat{H} / \partial n + 2\bar{n} \left[\frac{1}{4} U_\alpha (\sigma v) - f_z \bar{L}_z \right] \rangle}{\langle \bar{n} \rangle + y \langle \bar{T} \rangle} \right) \end{aligned} \quad (18.39)$$

The stability requirement $\omega \leq 0$ then leads to a limit on the average plasma density,

$$n_{av} \leq f^{-1} \frac{\left\{ \hat{\chi}_{\perp}(5.5/a)^2 \langle g \rangle + 2y \left[f_z \langle g L_z \rangle - \left\langle \frac{1}{4} U_{\alpha} g(\sigma v) \right\rangle \right] \right\}}{2 \left\{ \left\langle \frac{1}{4} U_{\alpha} [\partial(\sigma v)/\partial T] + f_z (-\partial L_z/\partial T) \right\rangle g^2 \right\}} \times \begin{pmatrix} 1 \pm \\ \sqrt{1 + \frac{4 \left(\langle -\partial \hat{H}/\partial T \rangle - y \langle \partial \hat{H}/\partial n \rangle \right) \left\{ \left\langle \frac{1}{4} U_{\alpha} [\partial(\sigma v)/\partial T] + f_z (-\partial L_z/\partial T) \right\rangle g^2 \right\}}{\left\{ \hat{\chi}_{\perp}(5.5/a)^2 \langle g \rangle + 2y \left[f_z \langle g L_z \rangle - \left\langle \frac{1}{4} U_{\alpha} g(\sigma v) \right\rangle \right] \right\}^2}} \end{pmatrix} \quad (18.40)$$

where the equilibrium density distribution has been written as $\bar{n}(r) = n(0)g(r)$, and $f = n(0)/n_{av}$ is the peak-to-average factor for the equilibrium density distribution. Eq. (18.40) generalizes the density limit of Eq. (18.19) to take into account a nonuniform equilibrium density profile and a density perturbation as well as a temperature perturbation; the y terms introduce the effect of coupled density instabilities on the density limit for collapse of the temperature profile. This equation has successfully predicted the densities at which disruptions occurred in several DIII-D discharges.

18.3 Nondisruptive Density Limits

Although disruptions are the most dramatic density limits in tokamaks, the most common density limits arise as simply an inability to further increase density by continued fueling.

18.3.1 MARFEs

As discussed in chapter 15, under certain conditions a radiative condensation instability along field lines in the edge plasma can produce a high density, radiative, poloidally localized, region in the edge plasma (known as a MARFE) of H-mode tokamaks. Immediately following the formation of the stable MARFE configuration, the plasma makes a back transition into inferior L-mode confinement. Thus, MARFE formation constitutes an effective density limit for H-mode plasmas, although the plasma can continue to operate stably in L-mode after MARFE formation. As developed in chapter 15, the threshold edge density for MARFE onset is

$$\begin{aligned} n^2 \leq n_{\text{MARFE}}^2 &= \left\{ \frac{Q_{\perp}^{\text{edge}}}{T} f_{\text{cond}} \left[v L_T^{-1} - \left(1 - C^{(2)} \right) \right] L_n^{-1} \right\} \\ &\div \left\{ f_z \left[\left(v + 1 - C^{(2)} \right) \frac{L_z}{T} - \frac{\partial L_z}{\partial T} \right] \right. \\ &\quad + f_0 \left[\frac{E_{\text{ion}}}{T} \langle \sigma v \rangle_{\text{ion}} \left(v - \frac{T}{\langle \sigma v \rangle_{\text{ion}}} \frac{\partial \langle \sigma v \rangle_{\text{ion}}}{\partial T} \right) \right] \\ &\quad \left. + f_0^c \left[\frac{3}{2} (\langle \sigma v \rangle_{cx} + \langle \sigma v \rangle_{el}) \left(v - 1 - T \frac{\partial (\langle \sigma v \rangle_{cx} + \langle \sigma v \rangle_{el}) / \partial T}{(\langle \sigma v \rangle_{cx} + \langle \sigma v \rangle_{el})} \right) \right] \right\} \quad (18.41) \end{aligned}$$

where $f_{\text{cond}} Q_{\perp}$ is the conductive heat flux across the last closed flux surface, L_n and L_T are the density and temperature gradient scale lengths, f_z and f_0 are the impurity and neutral atom concentrations, $\chi_{\perp} \sim T^{\nu}$, and the various other terms were defined in chapter 15. Eq. (18.41) has successfully predicted the edge density limit for MARFE onset in a couple of dozen discharges in DIII-D and TEXTOR.

18.3.2 Confinement Degradation

An even more benign density limit phenomenon is sometimes seen in tokamak discharges with continuous gas fueling; the measured density is observed to increase up to a point, then saturate or actually decrease with further fueling. The measured energy confinement time is usually observed to decrease with continued fueling over the time at which the density build up saturates, but usually without a back H-L mode transition occurring. Confinement deterioration is frequently observed prior to the onset of other density limiting phenomena. While this degradation in confinement could be due to enhanced transport resulting from increased levels of electromagnetic and thermal turbulence throughout the confined plasma, a correlation between the reduced energy confinement time and a deterioration of the edge temperature gradient has been observed in several tokamaks, suggesting that it is a deterioration of the edge transport barrier (e.g. enhancement of edge transport) that is responsible for this confinement degradation.

18.3.2.1 Electromagnetic Instabilities

Many electromagnetic instabilities which could enhance plasma transport (chapter 11) are predicted to be present in the core and edge of tokamak plasmas, and enhanced turbulence levels are generally observed as density limits are approached.

Modeling of turbulence in the plasma edge must take into account the parallel electron dynamics, electromagnetic and diamagnetic effects, resulting in turbulence that is a combination of drift, Alfvén, and ballooning modes. Three-dimensional, nonlinear gyrofluid simulations including these phenomena have found a regime of high edge transport which may characterize density limited discharges, as depicted schematically in Fig. 18.3. The axes are the normalized pressure gradient, $\alpha = -Rq^2(d\beta/dr)$, and the diamagnetic parameter, $\alpha_d = \rho_s c_s t_0 / L_n L_0$, where $c_s = [(T_e + T_i)/m_i]^{1/2}$, $t_0 = (RL_n/2)^{1/2}$, $\rho_s = c_s/\Omega_i$, $L_0 = 2\pi q(v_{ei} R \rho_s / 2\Omega_e)^{1/2}$ and L_n is the density gradient scale length. Simulations just inside the region labeled “density limit” in Fig. 18.3 had very high levels of turbulence and transport, and simulations deeper in this region did not converge. The turbulence at low values of α_d resulted primarily from resistive ballooning modes, and transport at higher α was due primarily to the dependence of the turbulence saturation levels of magnetic perturbations. Using the definitions of α and α_d , this “density limit” region of phase space is consistent with high density, low temperature regimes, which are typical near the density limit.

Figure 18.4 shows ASDEX Upgrade data plotted in the same $\alpha-\alpha_d$ plane. Using typical ASDEX Upgrade parameters, the simulated diffusion coefficient was $D \approx 60 \text{ m}^2 \cdot \text{s}^{-1}$ for

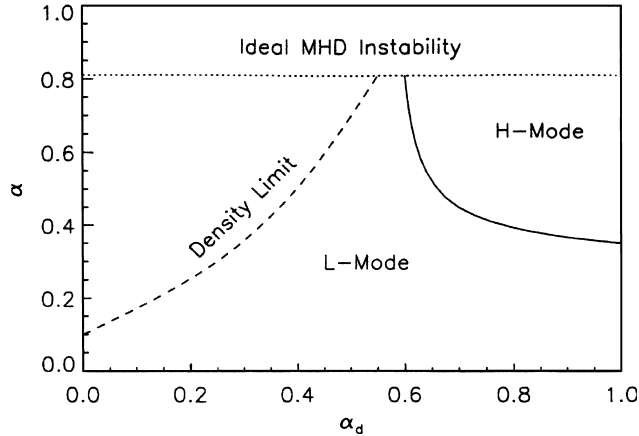


Figure 18.3. Depiction of the result of nonlinear gyro-fluid simulations of turbulent transport

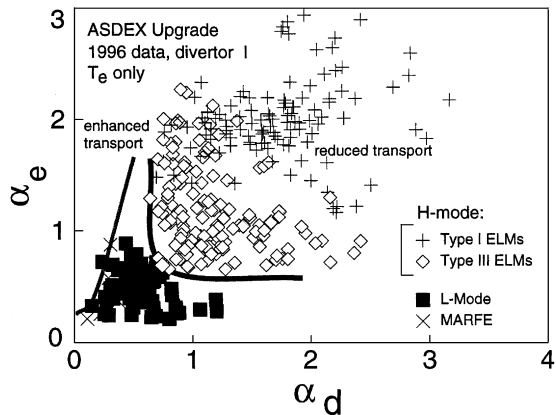


Figure 18.4. ASDEX Upgrade data plotted on the same $\alpha - \alpha_d$ plane used in Fig. 18.3. (Discharges near the density limit, indicated by x, roughly correspond to the theoretical boundary of Fig. 18.3)

the “density limit” regime indicated in Fig. 18.3. Transport at this level would certainly lead to a collapse of the edge plasma.

18.3.2.2 Thermal Instabilities

Edge thermal instabilities provide another possible explanation for the observed confinement degradation with continued gas fueling. Turbulence arising from thermal instabilities in the edge transport barrier was modeled in chapter 15 based on a linear analysis of the stability of the power, particle and momentum balances in the plasma edge against two-dimensional ($r - \perp$) density–velocity–temperature instabilities with radial wavelength

on the order of the edge transport barrier width, Δ_{TB} . This analysis lead to an estimate of linear growth rates of such instabilities associated with the ion and electron temperatures

$$\begin{aligned} \omega_i = -\frac{1}{3} \left\{ & 2\chi_{ir} \left[\left(\frac{\pi}{\Delta_{TB}} \right)^2 + v L_{T_i}^{-2} \right] + 2\chi_{i\perp} \left[\left(\frac{\pi}{L_\perp} \right)^2 + v \Delta_{T_i}^{-2} \right] \right. \\ & + 5v_r v L_{T_i}^{-1} + 5v_{i\perp} v \Delta_{T_i}^{-1} - 5(v-1)v_{ion} \\ & - 3v_{at} \left[v - \left(1 + \frac{T_i}{v_{at}} \frac{\partial v_{at}}{\partial T_i} \right) \right] \\ & \left. - 5\rho_i c_{si} \left(L_n^{-1} \Delta_{T_i}^{-1} - L_{T_i}^{-1} \Delta_n^{-1} \right) + \frac{2}{n} \left(v \frac{H_i}{T_i} - \frac{\partial H_i}{\partial T_i} \right) \right\} \end{aligned} \quad (18.42)$$

and

$$\begin{aligned} \omega_e = -\frac{1}{3} \left\{ & 2\chi_{er} \left[\left(\frac{\pi}{\Delta_{TB}} \right)^2 + v L_{T_e}^{-2} \right] + 2\chi_{e\perp} \left[\left(\frac{\pi}{L_\perp} \right)^2 + v \Delta_{T_e}^{-2} \right] \right. \\ & + 5v v_r L_{T_e}^{-1} + 5v_{e\perp} v \Delta_{T_e}^{-1} - 2n_z \left(v \frac{L_z}{T_e} - \frac{\partial L_z}{\partial T_e} \right) \\ & - v_{ion} \left[5(v-1) - 3 \frac{T_e}{v_{ion}} \frac{\partial v_{ion}}{\partial T_e} \right] \\ & - 2v_{ion} \frac{E_{ion}}{T_e} \left(v - \frac{T_e}{v_{ion}} \frac{\partial v_{ion}}{\partial T_e} \right) \\ & \left. + 5\rho_e c_{se} \left(L_{T_e}^{-1} \Delta_n^{-1} - \Delta_{T_e}^{-1} L_n^{-1} \right) + \frac{2}{n} \left(v \frac{H_e}{T_e} - \frac{\partial H_e}{\partial T_e} \right) \right\} \end{aligned} \quad (18.43)$$

Here the χ 's are average thermal diffusivities for ions and electrons in the transport barrier, $v_{at} = f_0^{\text{cold}} n (\langle \sigma v \rangle_{cx} + \langle \sigma v \rangle_{cl})$, $v_{ion} = f_0 n \langle \sigma v \rangle_{ion}$, $\Delta_{n,T}$ are perpendicular gradient scale lengths which are set equal to the poloidal pathlength, $L_\theta = 2\pi a$, the $\rho_{e,i}$ are gyroradii, the c_s are sound speeds, the $H_{e,i}$ are any external electron/ion heating rates in the edge transport barrier, L_n and L_T are radial gradient scale lengths, and the other parameters were defined previously.

The edge parameter dependence of these growth rates is complicated, but some general remarks can be made. The ion temperature instability growth rate of Eq. (18.42) becomes more positive (or less negative) as the neutral density (the v_{at} and v_{ion} terms) and the ion temperature gradient scale length (L_T) increase and as the edge density and temperature increase; and this growth rate becomes less positive (or more negative) when the conductive ion heat flux ($Q_{\text{cond}} = n T \chi L_T^{-1}$) through the edge increases. The electron temperature instability becomes more positive (or less negative) when the edge neutral and impurity densities and emissivities and the electron temperature gradient scale length increase, and becomes more negative (or less positive) when the conductive electron heat flux through

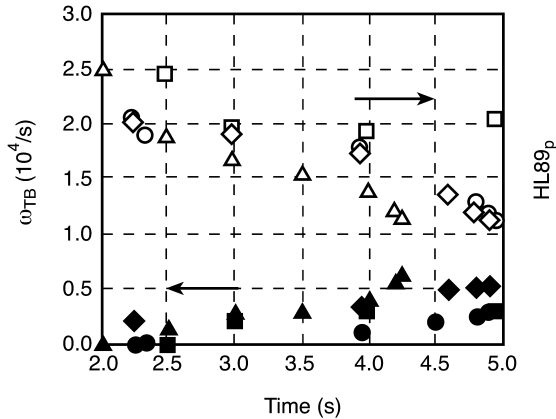


Figure 18.5. Experimental energy confinement time degradation and increasing calculated ion temperature thermal instability linear growth rate in DIII-D discharges with continuous gas fueling. (solid symbol $\omega_{TB} = \omega_i$ of Eq. (18.42); open symbol $HL89P = \tau_E^{\exp}/\tau_{89P}$)

the edge increases. Both growth rates become more positive or less negative with increasing edge density or temperature of the respective species.

A “connection length” estimate (chapter 11) of the incremental transport associated with thermal instabilities with growth rate ω and decorrelation length δ is given by

$$\Delta\chi \approx \omega\delta^2 \quad (18.44)$$

Since $\Delta\chi \approx 10^3 \text{ cm}^2 \cdot \text{s}^{-1}$ or more is necessary to impact edge transport and $\delta \approx \Delta_{TB} \approx O(cm)$ for the type of instabilities under consideration, the growth rate must be greater than $\approx 10^3 \text{ s}^{-1}$ in order for these instabilities to influence transport in the plasma edge.

The calculated linear growth rate of the ion temperature thermal instability in the transport barrier ($\omega_i = \omega_{TB}$) and the measured energy confinement time ($HL89P = \tau_E^{\exp}/\tau_{89P}$, where τ_{89P} is the ITER89-P empirical correlation; see chapter 17) are plotted in Fig. 18.5 as a function of time for several DIII-D discharges in which the edge neutral density increased with time as a result of continued gas fueling. There is a clear correlation between an increase in linear growth rate due to the increasing neutral density in the plasma edge (due to the v_{at} and v_{ion} terms in Eq. (18.42)) and the measured degradation in energy confinement. We also see that the calculated linear growth rates are large enough to cause a significant enhancement of the $O(10^3 \text{ cm}^2 \cdot \text{s}^{-1})$ background (in the absence of turbulence) edge transport.

18.3.3 Thermal Collapse of Divertor Plasma

It can be demonstrated from the “2-point” divertor equations of chapter 14 that there is an upper bound on the scrape-off layer (SOL) density above which a thermal collapse of the divertor plasma occurs. Physically, the upper SOL layer density for which a solution

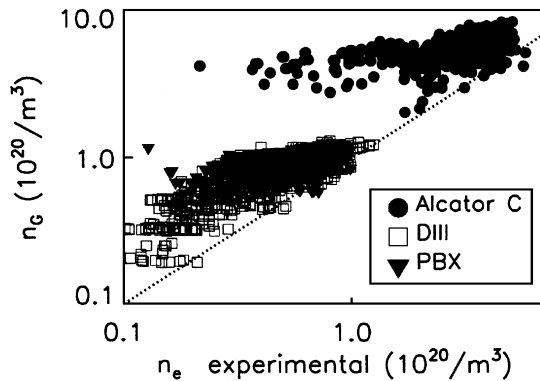


Figure 18.6. Comparison of Greenwald and experimental densities

to the “2-point” divertor equations, with a standard sheath boundary condition at the strike point, would seem to correspond to a detachment density limit, since it corresponds to the density above which the divertor equations with a sheath boundary condition no longer have a solution. A disruption or some other density limiting mechanism may be triggered by a sequence of events beginning with detachment, but this would not seem to always be the case, since many detached discharges have operated stably. Nevertheless, this “divertor collapse” disruption model has been shown to correlate ASDEX disruption data.

18.4 Empirical Density Limit

More than a decade ago, a simple fit (now known as the Greenwald density)

$$n_G = I/\pi a^2 \quad (18.45)$$

was found to bound the densities of stable operating points in three ohmic heated tokamaks, as shown in Fig. 18.6.

Over the years, this simple empirical fit has been found to provide a reasonable bound (to within a factor of about 2) on the density limit for a variety of tokamaks with shaping, auxiliary heating, etc. However, stable discharges have been achieved with densities up to approximately a factor of 2 greater than the empirical Greenwald limit.

The plasma confinement is usually observed to deteriorate significantly as the Greenwald limit is approached, as shown for the JET tokamak data in Fig. 18.7. $H_{97} = \tau_E^{\text{exp}}/\tau_{97}$, where τ_{97} is an empirical H-mode confinement scaling relation (chapter 17).

18.5 MHD Instability Limits

18.5.1 β -Limits

There are many MHD instabilities that are driven by the pressure gradient or the pressure, so it is plausible that there are pressure limits, usually expressed as β -limits. Since MHD

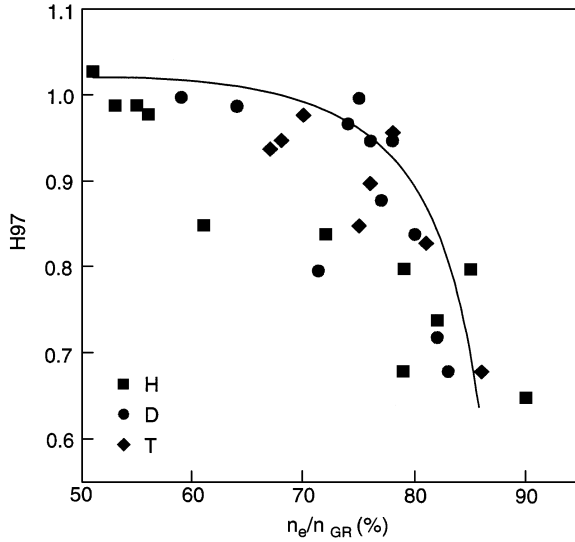


Figure 18.7. H-mode confinement degradation in JET as the Greenwald density limit is approached.
 $(H_{97} = \tau_E^{\text{exp}} / \tau_{97})$

stability depends on profiles and which modes are considered in the analysis, and the consequences of the instability of various modes differs in severity, the concept of a β -limit is not an exact one. However, there is an intrinsic usefulness in an analytical β -limit that overcomes the imprecision in its definition.

The most useful case to consider to this end is the limit imposed by ballooning modes. The definition of β (in cylindrical geometry) is

$$\beta = \frac{2\pi \int_0^a p r dr}{\pi a^2 B_\phi^2 / 2\mu_0} \quad (18.46)$$

Integrating by parts yields

$$\beta = \frac{2\mu_0}{a^2 B_\phi^2} \int_0^a -\frac{dp}{dr} r^2 dr \quad (18.47)$$

It was seen in chapter 8 that the stability limit for ballooning modes could be represented by a straight line $s \approx 1.67\alpha$ (s = shear, α = normalized pressure gradient) except for the low- s –low- α region. This can be represented by

$$-\frac{dp}{dr} = 0.30 \frac{B_\phi^2}{\mu_0 R} \frac{r}{q^3} \frac{dq}{dr} \quad (18.48)$$

which, when used in Eq. (18.47), leads to

$$\beta = -0.30 \frac{1}{Ra^2} \int_0^a \frac{d}{dr} \left(\frac{1}{q^2} \right) r^3 dr \quad (18.49)$$

Taking $q(0)$ to be constrained to unity or greater, this expression is maximized with respect to $q(r)$ by a current density distribution which is constant within a central region and zero outside this central region. The central region produces a zero contribution to the integral in Eq. (18.49) for this idealized current distribution, and the entire contribution comes from the outer region, $r/a > (q(0)/q(a))^{1/2}$. Setting $q(0) = 1$ leads to

$$\beta_m = 1.2 \frac{\epsilon}{q_a^2} \left(q_a^{\frac{1}{2}} - 1 \right) \quad (18.50)$$

This expression is quite well represented by

$$\beta_m(\%) = 28 \frac{\epsilon}{q_a} = 5.6 \frac{I}{a B_\phi} \quad (18.51)$$

with I in MA, B in T and a in m.

This result is unrealistic because of the unrealistic current distribution, which is singular and would be unstable to tearing modes. A more reasonable β -limit can be obtained by retaining the scaling of Eq. (18.51) in the form

$$\beta_m(\%) = c \frac{\epsilon}{q_a} \quad (18.52)$$

but assuming a parabolic current profile and $q(0) = 1$ to obtain the q profile

$$q = \frac{1}{\left(1 - \frac{1}{2} r^2 / a^2 \right)} \quad (18.53)$$

which, when used to evaluate Eq. (18.49), yields $\beta = 0.077\epsilon$. Noting that $q(a) = 2$ for this profile, the constant c can be evaluated to obtain

$$\beta_m(\%) = 15 \frac{\epsilon}{q_a} = 3 \frac{I}{a B_\phi} \quad (q_a \lesssim 2) \quad I \text{ in MA} \quad (18.54)$$

Computer simulations have shown this general form to have wider applicability, including also elongated and D-shaped plasmas, leading to the Troyon β limit

$$\beta_m(\%) = g \frac{I}{a B_\phi} \quad (18.55)$$

The quantity

$$\beta_N = \frac{\beta(\%)}{I/a B_\phi} \quad (18.56)$$

is known as the normalized β .

The present tokamak operating experience is characterized by Eq. (18.55) with $g \approx 2.5$ to 3.0, except when there is access to the second stability regime, which allows higher values of g . The experimental current profiles have not, in general, been optimized to

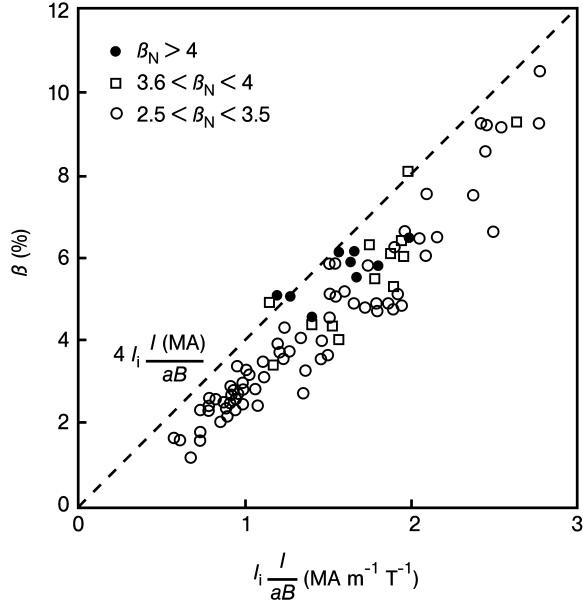


Figure 18.8. Experimental values of β plotted against $l_i I / aB$ for DIII-D

date. The optimization process would concentrate the current towards the center, which is equivalent to increasing the internal inductance, l_i . In fact, the experimental results shown in Fig. 18.8 display a linear dependence on l_i given by (I in MA, B in T, a in m)

$$\beta_m(\%) = 4l_i \frac{I}{aB_\phi} \quad (18.57)$$

When there is access to the second stability regime over part of the plasma, the above considerations are not strictly appropriate. Furthermore, a $s(\alpha)$ stability boundary is more difficult to define for realistic configurations. The first and second stability regimes are joined in the low shear region, which allows access to substantially higher β -values than indicated by the above first stability regime considerations.

18.5.2 Kink Mode Limits on $q(a)/q(0)$

We found in chapter 8 that surface kink modes imposed a constraint $q(a)/q(0) \geq 2$ to 3.5 and that internal kink, or interchange, modes imposed a constraint $q(0) \geq 1$, as summarized in Fig. 8.8 for parabola-to-a-power current profiles. The most straightforward procedure for combining these kink mode constraints with the previously discussed β -limit is to map the profile parameter v of Fig. 8.8 into a value of the internal inductance, using $l_i = \ln[1.65 + 0.89(q_{\text{edge}} - 1)]$. The resulting (l_i, q_{edge}) MHD stability diagram is shown in Fig. 18.9, where $q_{\text{edge}} = q(a)$ for circular plasmas and $q_{\text{edge}} = q_{95}$ for noncircular plasmas.

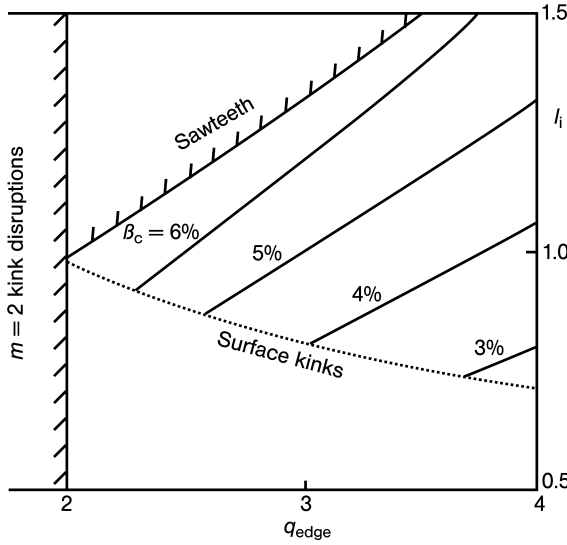


Figure 18.9. MHD stability operational boundaries in tokamaks

The region of MHD stability is bounded to the left by the $m = 2$ instability, which results in a disruption as $q_{\text{edge}} \rightarrow 2$ from above, corresponding to the $q = 2$ resonant surface approaching the plasma boundary from inside the plasma, at which point the $m = 2$ tearing mode is transformed into an $m = 2$ surface kink mode. The $m = 2$ tearing mode becomes important either when $q_{\text{edge}} \rightarrow 2$ or when the current profile is narrow with high l_i , producing $q \approx 2$ at the edge of the effective current channel.

The central value of $q(0)$ is limited by sawtooth oscillations. The actual limiting value is about $q(0) \approx 0.7$, rather than the 1.0 that the simplified arguments of chapter 8 suggest. This sawtooth constraint limits the allowable values of l_i and is most stringent at low q_{edge} .

Both the stability and consequences of the surface kink modes depend on the edge current profile and are harder to characterize. The surface kink limit is shown as a dashed line in Fig. 18.9 to indicate this.

Using the form of the β -limit given by Eq. (18.57) and using the empirical relation

$$q_{95} = \frac{5a^2 B}{2RI} (1 + \kappa^2) \left[1 + \frac{2}{3} \left(\frac{a}{R} \right)^2 \right] \quad (18.58)$$

the critical β for representative tokamak parameters ($R/a = 3$, $\kappa = b/a = 5/3$) is

$$\beta_c(\%) = 15 \frac{l_i}{q_{95}} \quad (18.59)$$

The resulting lines of constant β_c are shown in Fig. 18.9. Again, access to the second stability regime will allow substantially higher values of β to be achieved.

Problems for Chapter 18

1. Estimate from Eq. (18.13) the density limit for radiative collapse for a tokamak deuterium plasma with $T = 5 \text{ keV}$, $B = 3 \text{ T}$, $a = 0.6 \text{ m}$, $R = 1.7 \text{ m}$, $\kappa = 1.75$, $I = 2 \text{ MA}$, $P_{\text{heat}} = 3 \text{ MW}$ and carbon concentration $f_z = 0.08$. Make the estimate for both the ITER93-P and the IPB98($\gamma, 2$) scaling laws for energy confinement. Compare this with the Greenwald limit for this plasma. (Hint: iterate between the predicted density limit and the density needed to evaluate the scaling laws.)
2. Estimate the enhancement of the electron and ion thermal conductivities due to thermal instabilities in the edge of a tokamak plasma with $n_D = 4 \times 10^{19} \text{ m}^{-3}$, $n_{\text{carbon}} = 3 \times 10^{18} \text{ m}^{-3}$, $T_e = T_i = 500 \text{ eV}$, $L_{T_i} = 10 \text{ cm}$, $L_{T_e} = 5 \text{ cm}$, $L_n = 5 \text{ cm}$, $v_{\text{ion}} = 10^3 \text{ s}^{-1}$, $v_{\text{at}} = 95 \text{ s}^{-1}$. Use $\chi_{er} = \chi_{ir} = 0.1 \text{ m}^2 \text{s}^{-1}$, $\nu = 2.5$ and $\nu_r = 5 \text{ ms}^{-1}$; and neglect poloidal fluctuation effects (the Δ and L_\perp in Eq. (18.42) and Eq. 18.43), the temperature dependence of v_{ion} and v_{at} and the heating terms.
3. Calculate the MARFE density limit for the plasma edge of problem 2 when the edge heat flux $Q_{\perp}^{\text{edge}} = 0.2 \times 10^5 \text{ W} \cdot \text{m}^2$ is 70 % conductive.
4. Calculate the ballooning mode β -limit for a tokamak with $I = 3 \text{ MA}$ distributed radially as $j(r) = j_0[1 - (r/a)^2]$, major radius $R = 1.7 \text{ m}$, minor radius $a = 0.8 \text{ m}$, elongation $\kappa = 1.75$ and toroidal magnetic field $B_\phi = 3 \text{ T}$.
5. Calculate and plot the critical β_c for the tokamak parameters of problem 4 but with current distributions $j(r) = j_0[1 - (r/a)^2]^\nu$ for $\nu = 0, 1, 2$ and 3 (i.e. reproduce Fig. 18.9 for these tokamak parameters).
6. Discuss the observation and causes of density limits in tokamaks.

19 Fusion Reactors and Neutron Sources

Plasma physics research is undertaken to obtain a fundamental understanding of plasma physics, of course, but also ultimately to produce a source of energy or neutrons that can be used for the benefit of mankind. The physical characteristics of future fusion reactors will be constrained, and therefore determined, by limits on the underlying plasma physics and fusion technology. In this chapter we first discuss these plasma physics and fusion technology limits and then review the projected physical characteristics of future fusion reactors and neutron sources that are determined by these limits. Since the understanding of plasma physics is sufficiently well developed to make such an exercise meaningful only for the tokamak confinement concept, we will limit these considerations to the tokamak.

19.1 Plasma Physics and Engineering Constraints

We have discussed a number of limits – on confinement, on pressure, on density, etc. – that are imposed by various plasma phenomena. Some of these limits (e.g. MHD instabilities) are reasonably well understood at a fundamental level, while others (e.g. energy confinement) exist more as empirical limits of broad generality. We will use the nomenclature of Fig. 19.1 to discuss the effect of the various limits on the dimensions of a tokamak.

19.1.1 Confinement

The requirement to achieve a given level of energy confinement time, as needed to satisfy the plasma power balance, imposes a constraint on the set of physics and engineering parameters that determine energy confinement. At present, this set of parameters and the form of the constraint is best represented by an empirical confinement scaling law. Using the ITER IPB98($y, 2$) scaling (see chapter 17)

$$\tau_E = H_H \tau_E^{\text{IPB98}(y,2)} \quad (19.1)$$

where

$$\tau_E^{\text{IPB98}(y,2)} = 0.144 I^{0.93} B^{0.15} P^{-0.69} \bar{n}_{e20}^{0.41} M^{0.19} R^{1.97} A^{-0.58} \kappa^{0.78} \quad (19.2)$$

imposes a constraint among the plasma current I_p (MA), magnetic field B (T), heating power P (MW), line-average electron density $\bar{n}_e(10^{20} \text{ m}^{-3})$, plasma ion mass M (AMU), major radius R (m), minor radius a (m) via $A = R/a$, and plasma elongation κ . H_H is the confinement enhancement factor relative to the H-mode. The objective of current confinement research, in addition to understanding the phenomena determining confinement, is to increase H_H above unity. It is encouraging that $H_H > 1$ has been obtained under various conditions on several tokamaks.

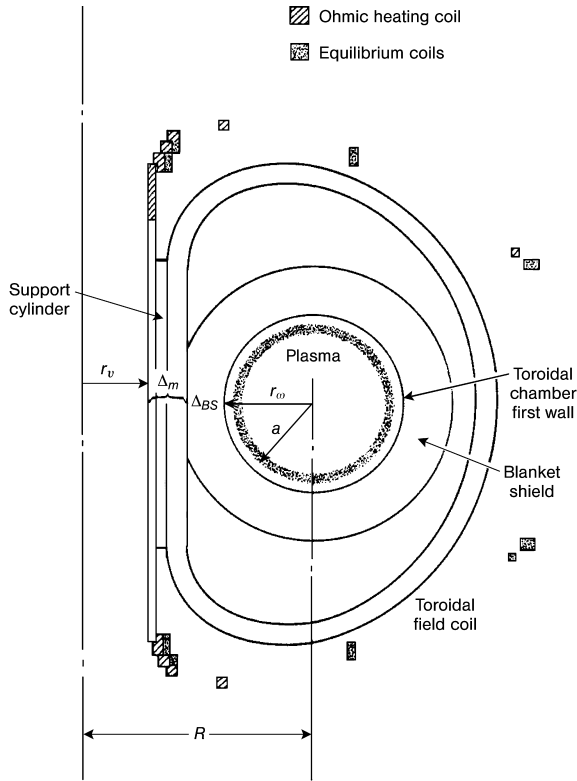


Figure 19.1. Nomenclature of tokamak configuration

Equation (19.2) indicates that the major factors determining energy confinement are the plasma current and the size of the plasma.

There is a threshold power crossing the LCFS that is required for access to H-mode confinement. While there are some theoretical models for this power (e.g. section 15.3.4), this threshold power must at present be taken from the empirical correlation

$$P_{LH}(\text{MW}) = (2.84/M) B^{0.82} \bar{n}_{e20}^{0.58} Ra^{0.81} \quad (19.3)$$

which defines a further constraint on magnetic field and plasma size. Providing a theoretical understanding of this power threshold is an active area of plasma physics research.

19.1.2 Density Limit

The fusion power in a 50–50 D-T plasma is

$$P_{DT} = \frac{1}{4} n^2 \langle \sigma v \rangle U (2\pi R \pi a^2 \kappa) \quad (19.4)$$

where $U = 3.5 \text{ MeV}$ for the alpha heating of the plasma and $U = 17.6 \text{ MeV}$ for the total fusion power. Clearly, achieving high power density requires achieving high particle density.

The empirical Greenwald density limit

$$\bar{n}_{e20} \leq \frac{I_p(\text{MA})}{\pi a^2} \quad (19.5)$$

provides a reasonable bound on a large amount of experimental data, although there are many discharges that exceed this limit by up to a factor of 2, and there are many discharges that are limited to densities that are only a fraction of the Greenwald limit. The simple expression of Eq. (19.5), which is good to within roughly a factor of 2, indicates that high current density is important for achieving high plasma density, thus defining a further constraint among plasma current, plasma size and fusion power (via Eq. (19.4)).

Phenomenological models for specific density limiting phenomena provide better constraints, to the extent that these models have been confirmed by comparison with experiment. For example, the disruption and MARFE density limits of Eqs. (18.40) and (18.41), respectively, indicate a strong dependence of the limiting densities on impurity concentration, the radial heat transport coefficient and, in the case of the MARFE density limit, the edge neutral density. The “softer” density limits associated with confinement degradation (section 18.3), once more fully understood, will undoubtedly indicate further dependences.

19.1.3 Beta Limit

The MHD stability limit on the plasma pressure

$$\beta_t \equiv \frac{\langle n_e T_e + n_i T_i + p_\alpha \rangle}{B^2} \leq \beta_N \frac{I(\text{MA})}{aB} = \text{const} \times l_i \frac{I}{aB} \quad (19.6)$$

where the internal inductance is given by

$$l_i = \ln[1.65 + 0.89(q_{95} - 1)] \quad (19.7)$$

bounds a wide range of discharges from several tokamaks. Here, as elsewhere in the text, q_{95} refers to the safety factor evaluated on the flux surface that encloses 95 % of the plasma volume.

In a beta-limited tokamak, Eq. (19.6) can be solved for $nT \sim \beta_t B^2$ and this result can be used to write Eq. (19.4) as

$$\begin{aligned} P_{DT} &\sim \beta_t^2 B^4 \frac{\langle \sigma v \rangle}{T^2} (2\pi R \pi a^2 \kappa) \\ &\sim \beta_N^2 I^2 B^2 \frac{\langle \sigma v \rangle}{T^2} (2\pi R \pi \kappa) \end{aligned} \quad (19.8)$$

The quantity $\langle \sigma v \rangle \sim T^2$ at the lower temperatures of the thermonuclear regime that are of the greatest practical interest, so that $\langle \sigma v \rangle / T^2$ has a broad peak in the temperature range $10 < T < 20 \text{ keV}$, as shown in Fig. 19.2.

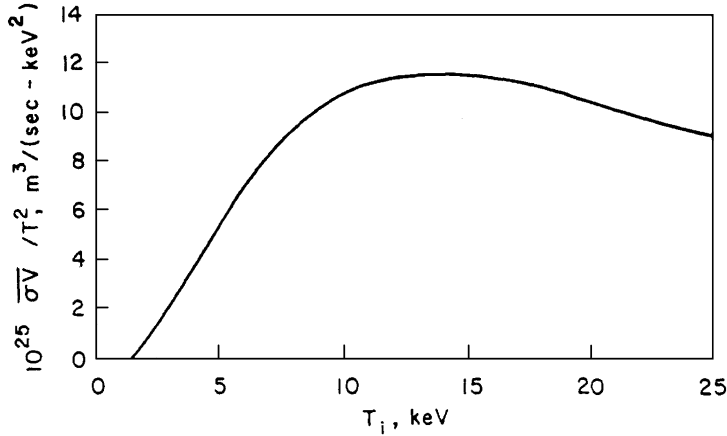


Figure 19.2. Fusion reaction parameter $\langle \sigma v \rangle / T^2$

Relation (19.8) highlights the importance of achieving high values of β_N , I and B in order to achieve high plasma power density and also defines a constraint among these variables and plasma size for a given fusion power level. The achievement of high values of β_N is a major focus of plasma physics research.

If the alpha particle “ash” is not exhausted from the plasma but allowed to build up, the alpha pressure build-up, p_α , will reduce the fraction of β_t that can be used to confine the D-T ions, and P_{DT} will be correspondingly reduced. Thus, alpha exhaust is an important research issue.

19.1.4 Kink Stability Limit

The kink stability limit depicted in Fig. 8.8 can be roughly characterized by the requirement

$$q_{95} = \frac{5a^2 B}{RI} \left[\frac{1 + \kappa^2(1 + 2\delta^2 - 1.2\delta^3)}{2} \right] \frac{\left(1.17 - \frac{0.65}{A}\right)}{\left(1 - \frac{1}{A^2}\right)^2} \geq 3 \quad (19.9)$$

where δ is the plasma triangularity. This limit imposes a constraint on the allowable combination of B , I , R and a .

19.1.5 Start-Up Inductive Volt-Seconds

The present practice is to provide enough inductive volt-seconds through transformer action of the poloidal coil system to start up and maintain the plasma current for the entire discharge. While maintenance of the discharge largely by noninductive current drive is envisioned for future tokamaks, it will always be prudent to have a capability at least for

inductive start up. The start-up volt-second requirement consists of a component to induce the plasma current in the absence of resistive losses

$$(\Delta\Phi)_{\text{ind}} = IL_p \quad (19.10)$$

plus a component to overcome resistive losses during startup

$$(\Delta\Phi)_{\text{res}} = C_{\text{Ejima}}\mu_0 RI \quad (19.11)$$

where the Ejima coefficient is about 0.4 and the plasma inductance is given by

$$L_p = \mu_0 R \left[\ln \left(\frac{8R}{a\sqrt{\kappa}} \right) + \frac{l_i}{2} - 2 \right] \quad (19.12)$$

With reference to Fig. 19.1, all of the poloidal coils – the central solenoid (CS) and other “ohmic heating” coils and the equilibrium field (EF) coils – can, depending on the design, provide a flux linkage with the plasma and thus contribute to providing volt-seconds. Normally, the majority of the volt-seconds are provided by the CS.

The total required inductive volt-seconds to maintain the plasma discharge after start-up will be determined by a trade-off involving the required length of the burn pulse (availability requirement and fatigue limits), the practically achievable bootstrap current, the amount of power required for noninductive current drive, and the overall design of the coil systems. These volt-seconds plus the start-up volt-seconds discussed above must be supplied by the poloidal coil system, and some part of this, $\Delta\Phi_{\text{CS}}$, must be provided by the central solenoid.

Providing $\Delta\Phi_{\text{CS}}$ volt-seconds requires

$$(\Delta\Phi)_{\text{CS}} = \pi B_{\text{OH}} r_v^2 \left[1 + \frac{\Delta_{\text{OH}}}{r_v} + \frac{1}{3} \left(\frac{\Delta_{\text{OH}}}{r_v} \right)^2 \right] \quad (19.13)$$

where B_{OH} is the maximum field in the CS, r_v is the flux core radius shown in Fig. 19.1, and Δ_{OH} is the thickness of CS (which contributes to the “magnet” thickness Δ_m indicated in Fig. 19.1). The CS thickness Δ_{OH} must be sufficient so that the tensile stress in the CS

$$\sigma_{\text{CS}} = \frac{B_{\text{OH}}^2}{2\mu_0} \left(\frac{r_v}{\Delta_{\text{OH}}} + \frac{1}{3} \right) \leq S_m \quad (19.14)$$

satisfies the American Society of Mechanical Engineers (ASME) Code; i.e. $S_m \min(1/3$ ultimate stress, $2/3$ yield stress).

19.1.6 Noninductive Current Drive

The plasma current during the discharge in present tokamaks is maintained inductively against resistive losses. However, because of implications for fatigue limits and availability, this is not an attractive option for future tokamak reactors. So, current maintenance during the discharge by a combination of noninductive current drive and bootstrap current is envisioned for future tokamak reactors.

The current drive efficiency, $\eta_{CD} \equiv I_{CD}(\text{MA})/P_{CD}(\text{MW})$, achieved to date on a number of tokamaks is given in Fig. 12.13. Neutral beam (section 12.3) and electromagnetic wave (section 12.4) current drive favor high electron temperature and low density to achieve high efficiencies. For fast wave current drive, a useful formula is

$$\gamma_{FW} \equiv R n_{e20} \eta_{CD} = 0.062 T_e(\text{keV})^{0.56} \quad (19.15)$$

The present current drive efficiencies are rather low, implying the need for both improvement in the efficiency of noninductive current drive and the achievement of a high bootstrap current fraction – both items are being actively investigated.

19.1.7 Bootstrap Current

The bootstrap current fraction of the total current is given by

$$f_{bs} = C_{BS} (\sqrt{\epsilon} \beta_p)^{1.3} \quad (19.16)$$

where

$$C_{BS} = 1.32 - 0.235 q_{95} + 0.0185 q_{95}^2 \quad (19.17)$$

and

$$\beta_p = \beta_t (B/B_p)^2, \quad B_p = \frac{I_p(\text{MA})}{5a \sqrt{\frac{1+\kappa^2}{2}}} \quad (19.18)$$

Achievement of a high bootstrap current fraction clearly depends on achieving a high plasma pressure.

19.1.8 Toroidal Field Magnets

Achievement of a large magnetic field, B , in the plasma was shown above to be of value in achieving favorable values of several plasma parameters. However, electromagnetic forces in the toroidal field (TF) coils scale like $F \sim I_{TF} \times B_{TF} \sim B_{TF}^2$, so high magnetic fields require a lot of structure in the coils to remain within stress limits, which increases the magnet thickness Δ_m in Fig. 19.1.

The “centering” force (directed radially inward towards the center of the tokamak) of the TF coil system is

$$F_R = \frac{\mu_0 N I_{TF}^2}{2} \left[1 - \frac{1}{\sqrt{(1 - \epsilon_{TF}^2)}} \right] \quad (19.19)$$

where N is the number of TF coils, I_{TF} is the current flowing in each TF coil, and $\epsilon_{TF} = R_{\text{bore}}/R$ (where R_{bore} is the bore radius of the TF coil and R is the major radius from

the central axis of the tokamak to the center of the TF coil). This centering force must be reacted either by a support cylinder (see Fig. 19.1) or by wedging the TF coils (like a stone arch).

The tensile force in the TF coil is

$$F_{\text{TF}} = \frac{1}{2} \frac{\mu_0 N I_{\text{TF}}^2}{4\pi} \ln \left(\frac{1 + \epsilon_{\text{TF}}}{1 - \epsilon_{\text{TF}}} \right) \quad (19.20)$$

and the corresponding tensile (hoop) stress is

$$\sigma_t = F_{\text{TF}} / A_{\text{TF}} \quad (19.21)$$

where A_{TF} is the cross-sectional area of the TF coil (excluding coolant and insulator). There is a bending stress due to the interaction among adjacent TF coils (for off-normal conditions) that is also $\sim B_{\text{TF}}^2$. The ASME code requires

$$\sigma_t + \sigma_{\text{bend}} \leq 1.5 S_m \quad (19.22)$$

Since

$$B_{\text{TF}} = \frac{\mu_0 N I_f}{2\pi R} = \frac{\mu_0 N I_f}{2\pi(r_v + \Delta_m)} \quad (19.23)$$

the centering, tensile and bending forces cause the contribution of the TF coils to the magnet thickness Δ_m to scale $\sim B_{\text{TF}}^2$.

The toroidal field in the plasma, B , is related to the peak toroidal field in the TF coil, B_{TF} , which is located at $(r_v + \Delta_m)$, by

$$B = B_{\text{TF}} \left(1 - \frac{r_w + \Delta_{\text{BS}}}{R} \right) = B_{\text{TF}} \frac{(r_v + \Delta_m)}{R} \quad (19.24)$$

which follows from the $B \sim 1/R$ scaling dictated by Ampère's law taken around a toroidal loop at major radius R .

19.1.9 Blanket and Shield

The thickness of the blanket plus shield, Δ_{BS} , must be sufficient to: (1) include a lithium-containing region for producing tritium by neutron capture in order to replace the tritium consumed in the fusion reactions; (2) transform 95+% of the fusion energy which is in the form of fast neutrons into heat energy by neutron scattering reactions and remove it for conversion to electricity; and (3) shield the sensitive superconducting magnets from neutron irradiation damage and heating by neutrons and capture gammas. Studies indicate that $\sim 1.0 < \Delta_{\text{BS}} < 1.5$ m is required to accomplish these objectives.

19.1.10 Plasma Facing Component Heat Fluxes

There are limits on the allowable peak heat flux to the plasma facing components surface arising from several different phenomena. The most limiting of these constraints places a lower limit on the required surface area needed to handle a given amount of plasma exhaust power, hence a given fusion alpha power plus auxiliary heating power level.

19.1.10.1 Heat Fluxes

The peak heat flux to the “first wall” of the surrounding plasma chamber is

$$q''_{\text{FW}} = \frac{(0.2P_{\text{fus}} + P_{\text{aux}})(1 - f_{\text{div}})\hat{f}_{\text{FW}}}{(2\pi R) \left[2\pi a \sqrt{\frac{1}{2}(1 + \kappa^2)} \right] (1 - \epsilon_{\text{div}})} \quad (19.25)$$

where f_{div} is the fraction of the plasma power that goes to the divertor, as opposed to the first wall ($f_{\text{div}} \geq 0.5$ is a representative range), and \hat{f}_{fw} is the first wall heat flux peaking factor ($\hat{f}_{\text{fw}} \leq 2$ is representative), and ϵ_{div} is the fraction of the area around the plasma that is occupied by the divertor.

The divertor is represented here as a fraction ϵ_{div} of the first wall surface area. The divertor target plate is represented as a toroidal strip of thickness Δ_{div} circling the torus at the major radius, R . The peak heat flux of the divertor target plate can be written

$$q''_{\text{DP}} = \frac{(0.2P_{\text{fus}} + P_{\text{aux}})f_{\text{div}}f_{\text{dp}}\hat{f}_{\text{dp}}}{\Delta_{\text{div}}2\pi R} \quad (19.26)$$

where f_{dp} is the fraction of the exhaust power going to the divertor that ends up on the divertor plate, as opposed to being radiated to the divertor channel walls ($f_{\text{dp}} \approx 0.3$ to 0.9 is representative), and \hat{f}_{dp} is the divertor target plate heat flux peaking factor ($\hat{f}_{\text{dp}} \approx 10$ to 20 is representative).

19.1.10.2 Stress Limits

Using a tube bank model of the plasma facing components, as indicated in Fig. 19.3, the primary stress in the coolant tubes is given by

$$\sigma_p = \frac{(p_c + p_{\text{dis}})r_c}{t_c} \leq S_m \quad (19.27)$$

where p_c is the coolant pressure, r_c is the coolant tube radius, t_c is the coolant tube thickness, and $p_{\text{dis}} \approx B_\theta/2\mu_0$ is the disruption pressure.

The thermal bending stress due to a temperature gradient across the coolant tube wall is

$$\sigma_{\text{th}} = \frac{\alpha E \left(f_{\text{pfc}} q'' t_c + \frac{1}{2} q''' t_c^2 \right)}{2\kappa(1 - \nu)} \quad (19.28)$$

where f_{pfc} is an adjustable parameter normalized to more detailed modeling ($f_{\text{pfc}} \approx 4/3$ is a representative value), q'' is the surface heat flux from the plasma, q''' is the volumetric heat source due to neutrons, α is the coefficient of expansion, E is Young's modulus, κ is the thermal conductivity, and ν is Poisson's ratio.

The ASME Code specifies a maximum combination of primary plus bending stress

$$\sigma_{\text{th}} + \sigma_p \leq 3S_m \quad (19.29)$$

Since both σ_{th} and σ_p depend on q'' , this equation specifies a stress limit on the maximum allowable heat flux to the plasma facing component, q''_{stress} .

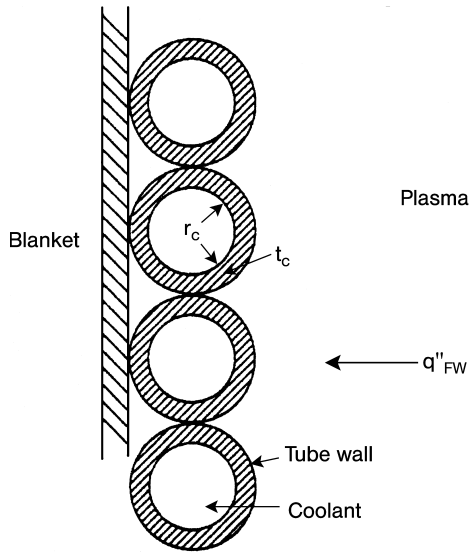


Figure 19.3. Tube bank model of plasma facing components

19.1.10.3 Temperature Limit

The maximum surface temperature of the plasma facing component is usually constrained to remain below some maximum value, T_s^{\max} , usually the melting temperature. The surface temperature constraint can be written

$$T_s = T_c + f_{\text{pfc}} q''_T \left(\frac{t_c}{\kappa} + \frac{1}{h} \right) + \frac{q''' t_c^2}{2\kappa} \leq T_s^{\max} \quad (19.30)$$

where T_c is the coolant temperature and h is the surface heat transfer ‘film’ coefficient. This relation defines a maximum allowable heat flux, q''_T .

19.1.10.4 Fatigue Limit

When the plasma facing components are subjected to a cyclic loading (e.g. variation in thermal stress due to a repetitively pulsed mode of tokamak operation) they will fail after a mean number of cycles, $N_D(\epsilon)$, which depends on the material and the cyclic strain, ϵ , produced by the cyclic loading (e.g. thermal stress). Using Eq. (19.28) for the thermal stress, which is related to the thermal strain, the maximum allowable heat flux can be written

$$q''_{\text{fat}} = \frac{2\kappa(1-\nu)}{f_{\text{pfc}}\alpha} \frac{\epsilon_{\max}(N_D)}{t_c} - \frac{1}{2} q''' t_c \quad (19.31)$$

where ϵ_{\max} is the maximum allowable strain for N_D cycles (from fatigue curves).

We only discuss fatigue here, but the phenomenon of growth of microscopic defects under cyclic loading also takes place and constitutes a similar limit on the surface heat flux.

19.1.10.5 Heat Flux Limit

The heat flux limit on the plasma facing components is just the most limiting of the above three maximum allowable heat fluxes

$$q''_{\max} = \max \{q''_{\text{th}}, q''_T, q''_{\text{fat}}\} \quad (19.32)$$

Although present tokamaks are not limited by the surface heat flux to plasma facing components, this will be an issue for future tokamaks with more auxiliary heating power and fusion alpha power to exhaust. The ability to take advantage of anticipated advances in plasma confinement and β -limits to achieve compact, high power density tokamaks may be thwarted by heat flux limits unless advanced materials that can handle higher surface heat loads are also developed.

19.1.11 Radiation Damage to Plasma Facing Components

The first wall average 14 MeV neutron power flux is

$$\Gamma_n = \frac{0.8 P_{\text{fus}}}{\left(2\pi R 2\pi a \sqrt{\frac{1}{2}(1 + \kappa^2)}\right)} \quad (19.33)$$

and the first wall peak 14 MeV neutron power flux is

$$\hat{\Gamma}_n = \Gamma_n \hat{f}_n \sqrt{\frac{1}{2}(1 + \kappa^2)} \quad (19.34)$$

where \hat{f}_n is the neutron poloidal peaking factor (typically 1.1 to 1.3).

The 14 MeV fusion neutrons incident on the plasma facing components displace from the lattice and transmute atoms of the wall material. These microscopic changes manifest themselves as swelling, loss of ductility, reduction of the number of cycles to fatigue failure for a given strain or in the allowable strain for a given number of cycles, and other macroscopic changes in materials properties that lead to failure of the plasma facing components to perform their intended function. This radiation damage does not directly limit the size or other parameters of a tokamak, but it does determine the radiation damage lifetime of the plasma facing components. If this lifetime is too short and it is necessary to replace the component too frequently, then the design is impractical. One direct effect on the design of a tokamak is the reduction in the allowable strain to achieve a given number of cycles before fatigue failure, which requires an increase in the coolant tube thickness that in turn causes a reduction in the stress limited allowable surface heat flux.

Radiation damage limits are conveniently expressed in terms of the energy fluence of 14 MeV neutrons, in units of $\text{MW}\cdot\text{yr}\cdot\text{m}^{-2}$. The average neutron flux is $\Gamma_n(\text{MW} \cdot \text{m}^{-2}) =$

$0.8 P_{\text{fus}}(\text{MW})/A_{\text{wall}}(\text{m}^2)$, and the fluence is $\Phi(\text{MW} \cdot \text{yr} \cdot \text{m}^{-2}) = \Gamma_n(\text{MW} \cdot \text{m}^{-2} \times \Delta t(\text{yr}))$. A neutron flux of $1 \text{ MW} \cdot \text{m}^{-2}$ corresponds to 4.48×10^{17} (14 MeV neutrons) $\text{m}^{-2} \cdot \text{s}^{-1}$. The only structural material that is presently suitable for building a tokamak reactor is austenitic stainless steel, which has a radiation damage lifetime of about $4 \text{ MW} \cdot \text{yr} \cdot \text{m}^{-2}$, which would be less than one effective full power year for the type of tokamak reactors presently envisioned (see section 19.3). Ferritic steels and vanadium alloys which promise to have much greater radiation damage lifetimes are under development. Unless the development of an advanced material with a radiation damage lifetime greater than ≈ 10 to $20 \text{ MW} \cdot \text{yr} \cdot \text{m}^{-2}$ is developed, it may prove impossible to take advantage of the anticipated advances in plasma confinement and beta limits to achieve a practical compact, high power density fusion reactor.

19.2 International Tokamak Program

The international tokamak program began with T-3 at the Kurchatov Institute in Moscow in 1962. When the then surprisingly high temperatures found in T-3 were reported at an international meeting and subsequently confirmed by a British team, the world fusion community put other confinement concepts aside and turned its attention to the tokamak. In the intervening 40 years about 60 experiments (see Table 19.1) in the USSR, the USA, Europe, Japan and other countries have developed our present understanding of tokamak physics and advanced the fusion parameter $nT\tau$ by about 5 orders of magnitude. While numerous other magnetic confinement concepts have also been investigated over this period, most of them fell by the wayside relative to the tokamak, and of those remaining none are nearly as developed as the tokamak.

Table 19.1. Tokamaks

Year	Device	<i>R</i> (m)	<i>a</i> (m)	<i>B</i> (T)	<i>I</i> (MA)	Divertor	NBI <i>P</i> (MW)	ICR <i>P</i> (MW)	LHR <i>P</i> (MW)	ECR <i>P</i> (MW)
1962	T-3	1.0	0.12	2.5	0.06					
1963	TM-3	0.4	0.08	4.0	0.11					
1968	LT-1	0.4	0.10	1.0	0.04					
1970	ST	1.09	0.14	4.4	0.13					
	T-4	1.0	0.17	5.0	0.24					
1971	Ormak	0.8	0.23	1.8	0.20		0.34			
	T6	0.7	0.25	1.5	0.22					
	TumanII	0.4	0.08	2.0	0.05					
1972	ATC	0.88–0.35	0.17–0.11	2.0–5.0	0.11–0.28		0.1	0.16		0.2
	Cleo	0.9	0.18	2.0	0.12		0.4			0.4
	JFT-2	0.9	0.25	1.8	0.23		1.5	1.0	0.3	0.2
	T-12	0.36	0.08	1.0	0.03					
	TO-1	0.6	0.13	1.5	0.07					
1973	AlcatorA	0.54	0.1	10.0	0.31			0.1	0.1	
	Pulsator	0.7	0.12	2.7	0.09					
	TFR400	0.98	0.20	6.0	0.41		0.7			
1974	DIVA	0.6	0.10	2.0	0.06	x			0.5	
	Petula	0.72	0.16	2.7	0.16					
	Tosca	0.3	0.09	0.5	0.02				0.2	

Table 19.1. (continued)

Year	Device	<i>R</i> (m)	<i>a</i> (m)	<i>B</i> (T)	<i>I</i> (MA)	Divertor	NBI <i>P</i> (MW)	ICR <i>P</i> (MW)	LHR <i>P</i> (MW)	ECR <i>P</i> (MW)
1975	DITE	1.17	0.26	2.7	0.26	x	2.4			
	FT	0.83	0.20	10.0	0.80				1.0	
	PLT	1.3	0.40	3.5	0.72		3.0	5.0	1.0	
	T-10	1.5	0.37	4.5	0.68					1.0
	T-11	0.7	0.22	1.5	0.17		0.7			
1976	JIPPT2	0.91	0.17	3.0	0.16		0.1		0.2	
	Microtor	0.3	0.10	2.5	0.14		0.5			
	TNT-A	0.4	0.10	0.44	0.02					
1977	ISX-A	0.92	0.26	1.8	0.22					
	Macrator	0.9	0.40	0.4	0.12			0.5		
1978	ISX-B	0.93	0.27	1.8	0.24		2.5			0.2
	TFR600	0.98	0.20	6.0	0.41			1.5		0.6
	TUMANIII	0.55	0.15	3.0	0.20					
	Versator	0.4	0.13	1.5	0.11				0.1	0.1
1979	AlcatorC	0.64	0.17	12.0	0.90				4.0	
	PDX	1.4	0.45	2.5	0.60	x	7.0			
	ASDEX	1.54	0.40	3.0	0.52	x	4.5	3.0	2.0	
1980	DIII	1.45	0.45	2.6	0.61	x	7.0			2.0
	LT-4	0.5	0.10	3.0	0.10					
	TEXT	1.0	0.27	2.8	0.34	x				0.6
1981	T-7	1.22	0.31	3.0	0.39				0.25	
	TFTR	2.4	0.80	5.0	2.2		40.0	11.0		
1982	HT-6B	0.45	0.12	0.75	0.04				0.1	0.1
	JET	3.0	1.25	3.5	7.0	x	20.0	20.0	7.0	
	TEXTOR	1.75	0.46	3.0	0.6		4.0	4.0		
1985	HT-6M	0.65	0.2	1.5	0.15			1.0	0.15	0.2
	JT60	3.0	0.95	4.5	2.3	x	20.0	2.5	7.5	
1986	DIII-D	1.67	0.67	2.1		x	20.0	4.4		2.0
	Tore Supra	2.37	0.80	4.5	2.0	ergodic	1.7	12.0	8.0	
1989	COMPASS	0.56	0.21	2.1	0.28	x			0.6	2.0
	RTP ^b	0.72	0.16	2.5	0.16					0.9
1990	FT-U	0.93	0.30	8.0	1.3			2.0	4.0	1.0
	ASDEX-U	1.65	0.50	3.9	1.4	x	10.0	6.0		0.5
1991	JT60-U	3.4	1.1	4.2	5.0	x	40.0	7.0	8.0	
	START	0.2–0.3	0.15–0.24	0.6	0.12	x				0.2
1993	AlcatorCM	0.67	0.22	9.0	1.1	x		4.0		
	KSTAR									
2015	ITER	6.2	2.00	5.3	15.0	x				

^a Formerly T-7, ^b formerly Petula

In 1979, the USA, USSR, Europe (EC) and Japan came together, under the auspices of the International Atomic Energy Agency in a series of International Tokamak Reactor (INTOR) Workshops that spanned the following decade, to assess the readiness of the tokamak to move forward to a “burning plasma,” or experimental reactor, phase, to identify the physical characteristics and required R&D for such a device, and to perform supporting feasibility and conceptual design analyses. Based on the positive outcome of this work, Secretary Gorbachev proposed to President Reagan the collaborative design, construction and operation of such a device, which subsequently led to the formation of the Interna-

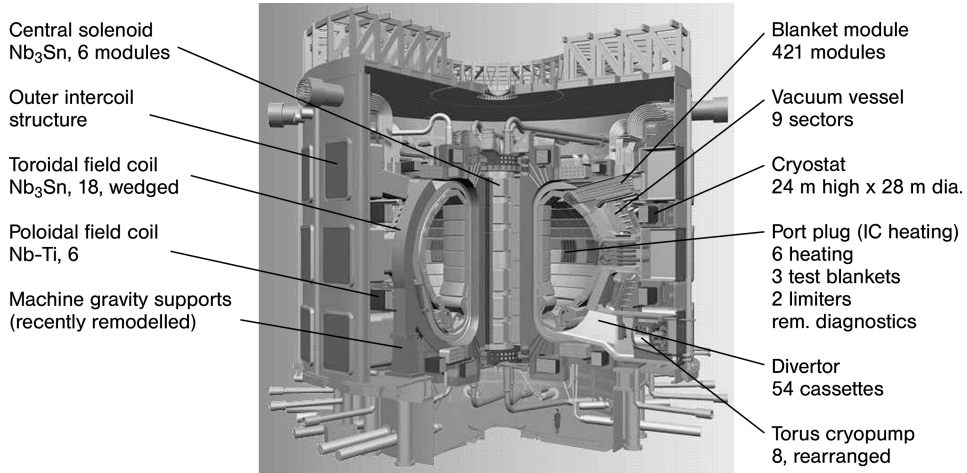


Figure 19.4. ITER design – main features

tional Thermonuclear Experimental Reactor (ITER) project involving the same Parties.

As of 2003, the design of ITER has been developed and reviewed by numerous international bodies, the supporting R&D has been completed, and siting negotiations are nearing completion. Construction should start within a year, with operation following within a decade.

The ITER device is illustrated in Fig. 19.4, and the major parameters are given in Table 19.2. The purpose of ITER is to establish the scientific and technological feasibility of fusion. To this end, ITER is intended to: (1) investigate moderate- Q_p burning plasma conditions, with an ultimate goal of achieving steady-state plasma operation; (2) to integrate into a single fusion system reactor-relevant nuclear and plasma support technologies and a reactor-relevant fusion plasma; (3) to test high heat flux and fusion nuclear components; and (4) to demonstrate the safety and environmental acceptability of fusion. In order to achieve these objectives, ITER is designed to achieve $Q_p \geq 10$, an inductive burn pulse of ≥ 300 s, an average first wall neutron flux $\geq 0.5 \text{ MW} \cdot \text{m}^{-2}$ and a lifetime fluence $\geq 0.3 \text{ MW} \cdot \text{yr} \cdot \text{m}^{-2}$, with the ultimate objective of steady-state operation at $Q_p \geq 5$.

Table 19.2. ITER Parameters

P_{fus} (MW _{th})	410	τ_E (s)	3.7
P_{aux} (MW)	40	β_N	1.8
$Q_p = P_{\text{fus}}/P_{\text{aux}}$	10	q_{95}	3.0
P_{LCFS}/P_{L-H}	1.6	κ	1.8
R (m)	6.2	δ	0.4
B (T)	5.3	$n/n_{\text{greenwald}}$	0.85
I (MA)	15.0	$q_{\text{FW}}(\text{MW} \cdot \text{m}^{-2})$	0.15
H_H	1.0	$\Gamma_n(\text{MW} \cdot \text{m}^{-2})$	0.5

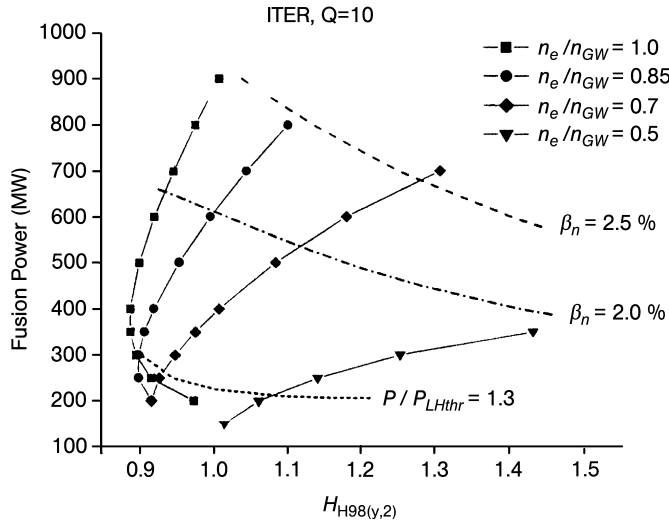


Figure 19.5. Range of operating conditions for which ITER can achieve $Q_p = 10$

As an example of but one of the thousands of extensive analyses that have been carried out in support and evaluation of the ITER design, Fig. 19.5 depicts the range of operating conditions for which ITER can achieve the $Q_p \geq 10$ design objective. Perhaps the most important uncertainties that could affect the ITER performance are the achievable energy confinement and plasma density. The solid lines in Fig. 19.5 indicate the value of the energy confinement enhancement factor, relative to the empirical fit of H-mode tokamak experimental confinement times, that would be required to achieve $Q_p = 10$, for various values of the plasma density as a fraction of the Greenwald density limit (chapter 18). The upper dashed lines indicate the contours of the normalized β_N , which are generally below the limiting values for currently operating tokamaks. The lower dotted line indicates the contour for which the nonradiative power crossing the separatrix is 30 % greater than the threshold value for access to H-mode. It is clear that ITER is conservatively designed to achieve the $Q_p \geq 10$ design objective.

19.2.1 Advanced Tokamak

The H-mode confinement scaling, the beta limit, the current drive efficiencies, etc. which can be routinely achieved today and which are described in section 19.1 are known as the “conventional” tokamak database, which forms the basis for the ITER design. Much of the emphasis in the tokamak R&D programs is on extending this performance capability to create an “advanced” tokamak (AT) database for the design of future tokamak reactors.

Although there are no sharp boundaries between the conventional and advanced tokamak parameters, Table 19.3 provides representative values for certain parameters that are important for performance.

Table 19.3. Conventional and advanced tokamak parameters

Parameter	“Conventional”	“Advanced”
H_H (confinement enhancement)	1.0	1.5–2.0
β_N	≤ 2.5	3.0–6.0
κ (elongation)	1.6–1.8	2.0–2.2
δ (triangularity)	0.1–0.5	0.5–0.9
f_{bs} (bootstrap I fraction)	< 0.5	> 0.5
q_{95}	3	4

Following the operation of ITER, it is anticipated that a generation of Demonstration Reactors would be built for the purpose of demonstrating reactor-level performance (e.g. availability $> 50\%$) and the potential for economic competitiveness. Assuming that advanced tokamak physics is developed in parallel with ITER and tested to a limited extent on ITER, and assuming that an advanced structural material capable of handling high surface heat loads and high neutron fluxes is developed in parallel with ITER, one possible set of parameters for an AT-DEMO is shown in Table 19.4.

A conceptual design for a third or fourth generation commercial reactor, ARIES-AT, has been carried out by projecting the ultimate evolution of the AT physics database. The parameters of this conceptual design are also shown in Table 19.4.

Table 19.4. Possible parameters of future advanced tokamak reactors

Parameter	AT-DEMO	ARIES-AT
P (MW _e)	400	1000
R (m)	5.4	5.2
B (T)	6.0	5.8
I (MA)	9.4	12.8
H_H	2.0	
β_N	4.2	5.4
q_{95}	4.0	
f_{bs}	0.7	0.9
κ	2.0	2.2
δ	0.8	0.8
Γ_n (MW·m ⁻²)	2.0 (average)	4.8 (max.)

19.3 Neutron Sources

While the development of magnetic fusion has been primarily motivated by the promise of a limitless and environmentally benign source of electrical power, there are other potential “nonelectrical” applications of fusion as a source of neutrons, some of which may be possible to undertake at an earlier stage in the development of fusion science and technology. The use of fusion neutron sources to produce hydrogen for a hydrogen economy, or tritium

for national security purposes, or radioisotopes for medical and industrial applications, or neutrons for materials and fundamental research have all been suggested.

It has also been suggested that a fusion neutron source could be used with a subcritical nuclear reactor to “breed” fissionable nuclei (^{239}Pu or ^{233}U) from nonfissionable (for all practical purposes) nuclei (^{238}U or ^{232}Th), to “dispose” of surplus weapons-grade plutonium by transmuting enough of the ^{239}Pu into ^{240}Pu to make the mixture unsuitable for weapons, or to transmute (fission) the plutonium and higher actinides remaining in spent nuclear fuel instead of storing that material for millions of years in high level waste repositories. All of these “nuclear” missions have in common that most of the neutrons are provided by the fission reactor and that the purpose of the fusion neutrons is to maintain the neutron chain reaction in the subcritical reactors, thus the performance requirements (for high beta, high density, high confinement, etc.) for the fusion device are much less demanding than for electrical power production by fusion.

Studies of such fusion spent nuclear fuel transmutation reactors indicate that the existing “conventional” tokamak physics database, on which ITER is designed, and the fusion technology that has been developed for ITER could be used to design the fusion neutron source for a transmutation reactor. The parameters for such tokamak fusion neutron sources using superconducting and normal copper magnets are given in Table 19.5. The operation of ITER will provide the prototype experience needed to achieve the higher availability needed for the transmutation mission.

Table 19.5. “Conventional” tokamak neutron sources for fusion transmutation of waste reactors

Parameter	Superconducting magnets	Normal magnets
R (m)	5.0	3.1
I (MA)	6.0	7.0
κ	1.8	1.7
δ	0.4	0.4
B (T)	7.5	6.1
H_H	1.0	1.1
P_{fus} (MW)	225	150
Γ_n (MW·m $^{-2}$)	0.8	0.8
q_{FW} (MW·m $^{-2}$)	0.29	0.27
f_{BS}	0.24	0.38
$n(10^{20} \text{ m}^{-3})$	1.9	2.0
Neutron source (# s $^{-1}$)	8.00×10^{19}	5.32×10^{19}
β_N	2.5	2.5
$n/n_{\text{greenwald}}$	0.80	0.75
q_{95}	3.1	3.0
$Q_p(P_{\text{fus}}/P_{\text{aux}})$	2.0	2.0
$Q_e(P_e^{\text{out}}/P_e^{\text{in}})$	5.0	1.0

Problems for Chapter 19

1. Calculate the D-T fusion power produced by a tokamak reactor with $R = 5.0\text{ m}$, $a = 1.8\text{ m}$, $\kappa = 1.8$, $I = 10\text{ MA}$, $B_\phi = 5\text{ T}$ operating at the β -limit.
2. Calculate the start up volt-second requirement for the reactor of problem 1.
3. Calculate the bootstrap current fraction for the reactor of problem 1.
4. Calculate the flux core radius, r_v , and the thickness, Δ_{OH} , of a central solenoid that could provide the start up volt-seconds of problem 2 with a maximum field of $B_{\text{OH}} = 12\text{ T}$ while satisfying the ASME Code requirements for $S_m = 200\text{ MPa}$.
5. Calculate the field at the TF coil that is required to produce $B_\phi = 5\text{ T}$ at the plasma centerline ($R = 5\text{ m}$). Assume that the radius to the wall of the plasma chamber $r_m = 1.1a$ and that the inboard blanket plus shield thickness $\Delta_{\text{BS}} = 1.1\text{ m}$.
6. Calculate the peak heat flux to the first wall and to the divertor plate if the fraction of the plasma exhaust power going to the divertor is $f_{\text{div}} = 0.5$, the fraction of this power entering the divertor that reaches the plate is $f_{\text{dp}} = 0.5$, the divertor plate and first wall peaking factors are $f_{\text{dp}}^* = 10$ and $f_{\text{FW}}^* = 1.3$, the fraction of the area surrounding the plasma that is subtended by the divertor is $\epsilon_{\text{div}} = 0.1$, the width of the divertor plate is $\Delta_{\text{div}} = 10\text{ cm}$ and the auxiliary heating power is 50 MW.
7. Calculate the thickness range of the first wall tube that can satisfy the ASME stress limits of Eq. (19.27) and Eq. (19.29) on a “tube bank” first wall for the peak heat flux of problem 6. Consider two cases: (a) stainless steel ($S_m = 110\text{ MPa}$, $M = \alpha E/\kappa(1 - \nu) = 0.22\text{ MPa} \cdot \text{m} \cdot \text{W}^{-1}$) first wall tubes of radius $r_c = 2.5\text{ cm}$ and water coolant at 10 MPa pressure; and (b) vanadium alloy ($S_m = 146\text{ MPa}$, $M = \alpha E/\kappa(1 - \nu) = 0.055\text{ MPa} \cdot \text{m} \cdot \text{W}^{-1}$) first wall tubes of radius $r_c = 2.5\text{ cm}$ with lithium coolant at 1 MPa pressure. (Neglect the volumetric neutron heating q''').
8. Calculate the power flux of 14 MeV D-T fusion neutrons incident on the first wall of the reactor of problem 1.
9. Discuss the physics and engineering constraints that govern the choice of design parameters for a tokamak experimental reactor like ITER.

Appendices

Appendix A

Frequently Used Physical Constants

c	Speed of light in vacuum	$2.99793 \times 10^8 \text{ m} \cdot \text{s}^{-1}$
ϵ_0	Permittivity of vacuum	$8.854 \times 10^{-12} \text{ F} \cdot \text{m}^{-1}$
μ_0	Permeability of vacuum	$1.257 \times 10^{-6} \text{ H} \cdot \text{m}^{-1}$
a	Stefan–Boltzmann constant	$5.67 \times 10^{-8} \text{ J} \cdot \text{m}^{-2} \cdot \text{s}^{-1} \cdot \text{K}^{-4}$
h	Planck constant	$6.625 \times 10^{-34} \text{ J} \cdot \text{s}$
k	Boltzmann constant	$1.3804 \times 10^{-23} \text{ J} \cdot \text{K}^{-1}$
A	Avogadro constant	$6.025 \times 10^{23} \text{ mol}^{-1}$
e	Charge of proton	$1.6021 \times 10^{-19} \text{ C}$
1 eV	Electron volt	$1.6021 \times 10^{-19} \text{ J}$
e/k		$11\,600 \text{ K} \cdot \text{V}^{-1}$

Particle	Mass ($\text{kg} \times 10^{-27}$)	Rest energy (MeV)
e	9.108×10^{-4}	0.511
n	1.674	939.512
${}^1\text{H}$ atom	1.673	938.730
${}^2\text{H}$ atom	3.343	1 876.017
${}^3\text{H}$ atom	5.006	2 809.272
${}^3\text{He}$ atom	5.006	2 809.250
${}^4\text{He}$ atom	6.643	3 728.189
${}^6\text{Li}$ atom	9.984	5 602.735
${}^7\text{Li}$ atom	11.64	6 534.995

Appendix B

Dimensions and Units

To get the value of a quantity in Gaussian units, multiply the value expressed in mks units by the conversion factor.

Physical quantity	Symbol	Dimensions		Rationalized Conversion factor	Gaussian
		MKS units	Gaussian units		
Capacitance	C	$\frac{t^2 q^2}{ml^2}$	l	F	9×10^{11} cm
Charge	q	q	$\frac{m^{\frac{1}{2}} l^{\frac{3}{2}}}{t}$	C	3×10^9 statcoulomb
Charge density	ρ	$\frac{\rho}{l^3}$	$\frac{m^{\frac{1}{2}}}{l^{\frac{3}{2}} t}$	$C \cdot m^{-3}$	3×10^3 statcoulomb $\cdot cm^{-3}$
Conductance		$\frac{tq^2}{ml^2}$	$\frac{l}{t}$	S	9×10^{11} $cm \cdot s^{-1}$
Conductivity	σ	$\frac{tq^2}{ml^3}$	$\frac{l}{t}$	$S \cdot m^{-1}$	9×10^9 s $^{-1}$
Current	I	$\frac{q}{t}$	$\frac{m^{\frac{1}{2}} t^{\frac{3}{2}}}{t^2}$	A	3×10^9 statampere
Current density	J	$\frac{q}{l^2 t}$	$\frac{m^{\frac{1}{2}}}{l^{\frac{1}{2}} t^2}$	$A \cdot m^{-2}$	3×10^5 statampere $\cdot cm^{-2}$
Density	ρ	$\frac{m}{l^3}$	$\frac{m}{l^3}$	$kg \cdot m^{-3}$	10^{-3} g $\cdot cm^{-3}$
Displacement	D	$\frac{q}{l^2}$	$\frac{m^{\frac{1}{2}}}{l^{\frac{1}{2}} t}$	$C \cdot m^{-2}$	$12\pi \times 10^5$ statcoloumb $\cdot cm^{-2}$
Electric field	E	$\frac{ml}{t^2 q}$	$\frac{m^{\frac{1}{2}}}{tl^{\frac{1}{2}}}$	$V \cdot m^{-1}$	$\frac{1}{3} \times 10^{-4}$ statvolt $\cdot cm^{-1}$
Electromotance	ϵ , Emf	$\frac{ml^2}{t^2 q}$	$\frac{m^{\frac{1}{2}} l^{\frac{1}{2}}}{t}$	V	$\frac{1}{3} \times 10^{-2}$ statvolt
Energy	U, W	$\frac{ml^2}{t^2}$	$\frac{ml^2}{t^2}$	J	10^7 erg

Physical quantity	Symbol	Dimensions		Rationalized mks	Conversion factor	Gaussian
		MKS units	Gaussian units			
Energy density		$\frac{m}{lt^2}$	$\frac{m}{lt^2}$	$J \cdot m^{-3}$	10	$erg \cdot cm^{-3}$
Force	F	$\frac{ml}{t^2}$	$\frac{ml}{t^2}$	N	10^5	dyne
Frequency	f, v, ω	$\frac{l}{t}$	$\frac{l}{t}$	Hz	1	Hz
Impedance	Z	$\frac{ml^2}{tq^2}$	$\frac{t}{l}$	Ω	$\frac{1}{9} \times 10^{-11}$	$s \cdot cm^{-1}$
Inductance	L	$\frac{ml^2}{q^2}$	$\frac{t^2}{l}$	H	$\frac{1}{9} \times 10^{-11}$	$s^2 \cdot cm^{-1}$
Length	l	l	l	m	10^2	cm
Magnetic intensity	H	$\frac{q}{lt}$	$\frac{m^{\frac{1}{2}}}{l^{\frac{1}{2}}t}$	ampere-turn $\cdot m^{-1}$	$4\pi \times 10^{-3}$	Oe
Magnetic flux	Φ	$\frac{ml^2}{tq}$	$\frac{m^{\frac{1}{2}}l^{\frac{3}{2}}}{t}$	Wb	10^8	Mx
Magnetic induction	B	$\frac{m}{tq}$	$\frac{m^{\frac{1}{2}}}{l^{\frac{1}{2}}t}$	T	10^4	G
Magnetization	M	$\frac{q}{lt}$	$\frac{m^{\frac{1}{2}}}{l^{\frac{1}{2}}t}$	ampere-turn $\cdot m^{-1}$	10^{-3}	Oe
Magnetomotance	MMf, \mathfrak{M}	$\frac{q}{t}$	$\frac{m^{\frac{1}{2}}l^{\frac{1}{2}}}{t}$	ampere-turn	$\frac{4\pi}{10}$	gilbert
Mass	m, M	m	m	kg	10^3	g
Momentum	p, P	$\frac{ml}{t}$	$\frac{ml}{t}$	$kg \cdot m \cdot s^{-1}$	10^5	$g \cdot cm \cdot s^{-1}$
Momentum density		$\frac{m}{l^2 t}$	$\frac{m}{l^2 t}$	$kg \cdot m^{-2} \cdot s^{-1}$	10^{-1}	$g \cdot cm^{-2} \cdot s^{-1}$
Permeability	μ	$\frac{ml}{q^2}$	l	$H \cdot m^{-1}$	$\frac{1}{4\pi} \times 10^7$	(dimensionless)
Permittivity	ϵ	$\frac{t^2 q^2}{ml^3}$	l	$F \cdot m^{-1}$	$36\pi \times 10^9$	(dimensionless)
Polarization	P	$\frac{q}{l^2}$	$\frac{m^{\frac{1}{2}}}{l^{\frac{1}{2}}t}$	$C \cdot m^{-2}$	3×10^5	$statcoloumb \cdot cm^{-2}$
Potential	V, ϕ	$\frac{ml^2}{t^2 q}$	$\frac{m^{\frac{1}{2}}l^{\frac{1}{2}}}{t}$	V	$\frac{1}{3} \times 10^{-2}$	statvolt

Physical quantity	Symbol	Dimensions		Rationalized mks	Conversion factor	Gaussian
		MKS units	Gaussian units			
Power	P	$\frac{ml^2}{t^3}$	$\frac{ml^2}{t^3}$	W	10^7	$\text{erg} \cdot \text{s}^{-1}$
Power density		$\frac{m}{lt^3}$	$\frac{m}{lt^3}$	$\text{W} \cdot \text{m}^{-3}$	10	$\text{erg} \cdot \text{cm}^{-3} \cdot \text{s}^{-1}$
Pressure	p	$\frac{m}{lt^2}$	$\frac{m}{lt^2}$	Pa	10	$\text{dyne} \cdot \text{cm}^{-2}$
Reluctance	\mathfrak{R}	$\frac{q^2}{ml^2}$	$\frac{1}{l}$	$\text{amperer-turn} \cdot \text{Wb}^{-1}$	$4\pi \times 10^{-9}$	cm^{-1}
Resistance	R	$\frac{ml^2}{tq^2}$	$\frac{t}{l}$	Ω	$\frac{1}{9} \times 10^{-11}$	$\text{s} \cdot \text{cm}^{-1}$
Resistivity	η, ρ	$\frac{ml^3}{tq^2}$	t	$\Omega \cdot \text{m}$	$\frac{1}{9} \times 10^{-9}$	s
Thermal conductivity	κ	$\frac{ml}{t^3}$	$\frac{ml}{t^3}$	$\text{W} \cdot \text{m}^{-1} \cdot \text{K}^{-1}$	10^5	$\text{erg} \cdot \text{cm}^{-1} \cdot \text{s}^{-1} \cdot \text{K}^{-1}$
Time	t	t	t	s	1	s
Vector potential	A	$\frac{ml}{tq}$	$\frac{m^{\frac{1}{2}} l^{\frac{1}{2}}}{t}$	$\text{Wb} \cdot \text{m}^{-1}$	10^6	$\text{G} \cdot \text{cm}$
Velocity	v	$\frac{l}{t}$	$\frac{l}{t}$	$\text{m} \cdot \text{s}^{-1}$	10^2	$\text{cm} \cdot \text{s}^{-1}$
Viscosity	η, μ	$\frac{m}{lt}$	$\frac{m}{lt}$	$\text{kg} \cdot \text{m}^{-1} \cdot \text{s}^{-1}$	10	P
Vorticity	ζ	$\frac{l}{t}$	$\frac{l}{t}$	s^{-1}	1	s^{-1}
Work	W	$\frac{ml^2}{t^2}$	$\frac{ml^2}{t^2}$	J	10^7	erg

Appendix C

Vector Calculus

Notation: f , g , and so on, are scalars; \mathbf{A} , \mathbf{B} , and so on, are vectors; \mathbf{T} is a tensor

$$\begin{aligned} \mathbf{A} \cdot \mathbf{B} \times \mathbf{C} &= \mathbf{A} \times \mathbf{B} \cdot \mathbf{C} = \mathbf{B} \cdot \mathbf{C} \times \mathbf{A} = \mathbf{B} \times \mathbf{C} \cdot \mathbf{A} = \mathbf{C} \cdot \mathbf{A} \times \mathbf{B} \\ &= \mathbf{C} \times \mathbf{A} \cdot \mathbf{B} \end{aligned} \quad (\text{C.1})$$

$$\mathbf{A} \times (\mathbf{B} \times \mathbf{C}) = (\mathbf{A} \cdot \mathbf{C})\mathbf{B} - (\mathbf{A} \cdot \mathbf{B})\mathbf{C} \quad (\text{C.2})$$

$$\mathbf{A} \times (\mathbf{B} \times \mathbf{C}) + \mathbf{B} \times (\mathbf{C} \times \mathbf{A}) + \mathbf{C} \times (\mathbf{A} \times \mathbf{B}) = 0 \quad (\text{C.3})$$

$$(\mathbf{A} \times \mathbf{B}) \cdot (\mathbf{C} \times \mathbf{D}) = (\mathbf{A} \cdot \mathbf{C})(\mathbf{B} \cdot \mathbf{D}) - (\mathbf{A} \cdot \mathbf{D})(\mathbf{B} \cdot \mathbf{C}) \quad (\text{C.4})$$

$$(\mathbf{A} \times \mathbf{B}) \times (\mathbf{C} \times \mathbf{D}) = (\mathbf{A} \times \mathbf{B} \cdot \mathbf{D})\mathbf{C} - (\mathbf{A} \times \mathbf{B} \cdot \mathbf{C})\mathbf{D} \quad (\text{C.5})$$

$$\nabla(fg) = \nabla(gf) = f\nabla g + g\nabla f \quad (\text{C.6})$$

$$\nabla \cdot (f\mathbf{A}) = f\nabla \cdot \mathbf{A} + \mathbf{A} \cdot \nabla f \quad (\text{C.7})$$

$$\nabla \times (f\mathbf{A}) = f\nabla \times \mathbf{A} + \nabla f \times \mathbf{A} \quad (\text{C.8})$$

$$\nabla \cdot (\mathbf{A} \times \mathbf{B}) = \mathbf{B} \cdot \nabla \times \mathbf{A} - \mathbf{A} \cdot \nabla \times \mathbf{B} \quad (\text{C.9})$$

$$\nabla \times (\mathbf{A} \times \mathbf{B}) = \mathbf{A}(\nabla \cdot \mathbf{B}) - \mathbf{B}(\nabla \cdot \mathbf{A}) + (\mathbf{B} \cdot \nabla)\mathbf{A} - (\mathbf{A} \cdot \nabla)\mathbf{B} \quad (\text{C.10})$$

$$\nabla(\mathbf{A} \cdot \mathbf{B}) = \mathbf{A} \times (\nabla \times \mathbf{B}) + \mathbf{B} \times (\nabla \times \mathbf{A}) + (\mathbf{B} \cdot \nabla)\mathbf{A} + (\mathbf{A} \cdot \nabla)\mathbf{B} \quad (\text{C.11})$$

$$\nabla^2 f = \nabla \cdot \nabla f \quad (\text{C.12})$$

$$\nabla^2 \mathbf{A} = \nabla(\nabla \cdot \mathbf{A}) - \nabla \times \nabla \times \mathbf{A} \quad (\text{C.13})$$

$$\nabla \times \nabla f = 0 \quad (\text{C.14})$$

$$\nabla \cdot \nabla \times \mathbf{A} = 0 \quad (\text{C.15})$$

If $\hat{\mathbf{n}}_1, \hat{\mathbf{n}}_2, \hat{\mathbf{n}}_3$ are orthonormal unit vectors, a second-order tensor \mathbf{T} can be written in the dyadic form

$$\mathbf{T} = \sum_{i,j} T_{ij} \hat{\mathbf{n}}_i \hat{\mathbf{n}}_j \quad (\text{C.16})$$

In cartesian coordinates the divergence of a tensor is a vector with components given by

$$(\nabla \cdot \mathbf{T})_i = \sum_j (\partial T_{ji} / \partial x_j) \quad (\text{C.17})$$

In general

$$\nabla \cdot (\mathbf{AB}) = (\nabla \cdot \mathbf{A})\mathbf{B} + (\mathbf{A} \cdot \nabla)\mathbf{B} \nabla \cdot (f\mathbf{T}) = \nabla f \cdot \mathbf{T} + f \nabla \cdot \mathbf{T} \quad (\text{C.18})$$

Let $\mathbf{r} = \hat{i}x + \hat{j}y + \hat{k}z$ be the radius vector of magnitude r , from the origin to the point x, y, z . Then

$$\nabla \cdot \mathbf{r} = 3 \quad (\text{C.19})$$

$$\nabla \times \mathbf{r} = 0 \quad (\text{C.20})$$

$$\nabla r = \mathbf{r}/r \quad (\text{C.21})$$

$$\nabla(1/r) = -\mathbf{r}/r^3 \quad (\text{C.22})$$

$$\nabla \cdot (\mathbf{r}/r^3) = 4\pi\delta(\mathbf{r}) \quad (\text{C.23})$$

If V is a volume enclosed by a surface S and $d\mathbf{S} = \hat{\mathbf{n}} dS$ where $\hat{\mathbf{n}}$ is the unit normal outward from V ,

$$\int_V dV \nabla f = \int_S d\mathbf{S} f \quad (\text{C.24})$$

$$\int_V dV \nabla \cdot \mathbf{A} = \int_S d\mathbf{S} \cdot \mathbf{A} \quad (\text{C.25})$$

$$\int_V dV \nabla \cdot \mathbf{T} = \int_S d\mathbf{S} \cdot \mathbf{T} \quad (\text{C.26})$$

$$\int_V dV \nabla \times \mathbf{A} = \int_S d\mathbf{S} \times \mathbf{A} \quad (\text{C.27})$$

$$\int_V dV (f \nabla^2 g - g \nabla^2 f) = \int_S d\mathbf{S} \cdot (f \nabla g - g \nabla f) \quad (\text{C.28})$$

$$\int_V dV (\mathbf{A} \cdot \nabla \times \nabla \times \mathbf{B} \cdot \nabla \times \nabla \times \mathbf{A}) = \int_S d\mathbf{S} \cdot (\mathbf{B} \times \nabla \times \mathbf{A} - \mathbf{A} \times \nabla \times \mathbf{B}) \quad (\text{C.29})$$

If S is an open surface bounded by the contour C of which the line element is $d\mathbf{l}$,

$$\int_S d\mathbf{S} \times \nabla f = \oint_C d\mathbf{l} f \quad (\text{C.30})$$

$$\int_S d\mathbf{S} \cdot \nabla \times \mathbf{A} = \oint_C d\mathbf{l} \cdot \mathbf{A} \quad (\text{C.31})$$

$$\int_S (d\mathbf{S} \times \nabla) \times \mathbf{A} = \oint_C d\mathbf{l} \times \mathbf{A} \quad (\text{C.32})$$

$$\int_S d\mathbf{S} \cdot (\nabla f \times \nabla g) = \oint_C f dg = - \oint_C g df \quad (\text{C.33})$$

From D. L. Book, Naval Research Laboratory Report 3332, *Revised and Enlarged Collection of Plasma Physics Formulas and Data*, 1977.

Appendix D

Curvilinear Coordinates

General Curvilinear Coordinates

In any orthogonal curvilinear coordinate system, all of the operations involving ∇ can be defined in terms of the scale factors h_i . These are related to the differential arc length dl by

$$\begin{aligned} dl^2 &= dx^2 + dy^2 + dz^2 \\ &= h_1^2 d\xi_1^2 + h_2^2 d\xi_2^2 + h_3^2 d\xi_3^2 \end{aligned} \quad (\text{D.1})$$

where $\{\xi_1, \xi_2, \xi_3\}$ designate the curvilinear coordinates. For example, the scale factors associated with the spherical coordinates $\{r, \theta, \phi\}$ are l , r , and $r \sin \theta$, respectively.

In orthogonal curvilinear coordinate systems a vector \mathbf{A} can be written as

$$\mathbf{A} = \hat{n}_1 A_1 + \hat{n}_2 A_2 + \hat{n}_3 A_3 \quad (\text{D.2})$$

where the $\{\hat{n}_i\}$ form a right-handed set of unit vectors normal to the surfaces of constant ξ_i . Then the divergence of \mathbf{A} is

$$\nabla \cdot \mathbf{A} = \frac{1}{H} \sum_i \frac{\delta}{\delta \xi_i} \left(\frac{H A_i}{h_i} \right) \quad (\text{D.3})$$

where $H = h_1 h_2 h_3$. The gradient of a scalar f is given by

$$(\nabla f)_i = \frac{1}{h_i} \frac{\delta f}{\delta \xi_i} \quad (\text{D.4})$$

From Eq. (D.3) and Eq. (D.4), it follows that the Laplacian of f is

$$\nabla^2 f = \frac{1}{H} \sum_i \frac{\delta}{\delta \xi_i} \left(\frac{H}{h_i^2} \frac{\delta f}{\delta \xi_i} \right) \quad (\text{D.5})$$

The curl of \mathbf{A} is

$$(\nabla \times \mathbf{A})_i = \sum_{j,k} \epsilon_{ijk} \frac{1}{h_j h_k} \frac{\delta}{\delta \epsilon_j} (h_k A_k) \quad (\text{D.6})$$

where ϵ_{ijk} equals $+1$ if $\{ijk\}$ is even (i.e., an even permutation of $\{123\}$), equals -1 if $\{ijk\}$ is odd, and vanishes if i , j and k are not all distinct.

To obtain expressions for the remaining operations, it is useful to introduce the Christoffel symbols Γ_{jk}^i , defined by

$$\Gamma_{jk}^i = \frac{1}{h_j h_k} \left(\frac{\delta h_j}{\delta \xi_k} \delta_j^i - \frac{\delta h_k}{\delta \xi_j} \delta_k^i \right) \quad (\text{D.7})$$

where δ_j^i equals 1 if $i = j$ and vanishes otherwise. Γ_{jk}^i vanishes if j and k both differ from i or if $j = k$. In addition,

$$\Gamma_{jk}^i + \Gamma_{kj}^i = 0 \quad (\text{D.8})$$

$$\Gamma_{jk}^i + \Gamma_{ki}^j + \Gamma_{ij}^k = 0 \quad (\text{D.9})$$

and

$$\sum_i \Gamma_{ik}^i = \frac{1}{H} \frac{\delta}{\delta \xi_k} \left(\frac{H}{h_k} \right) \quad (\text{D.10})$$

There are at most six independent nonzero components Γ_{jk}^i , and less in most coordinate systems of physical interest. The curvature tensor,

$$\begin{aligned} R_{ijkl} &= \frac{1}{h_j} \frac{\delta \Gamma_{kl}^i}{\delta \xi_j} - \frac{1}{h_i} \frac{\delta \Gamma_{kl}^j}{\delta \xi_i} \\ &\quad + \sum_n \left\{ \Gamma_{ij}^n \Gamma_{kl}^n - \Gamma_{nk}^j \Gamma_{nl}^i + \Gamma_{kn}^i \Gamma_{ln}^j \right\} \end{aligned} \quad (\text{D.11})$$

always vanishes in a flat space, that is, one which can be described by Cartesian coordinates. (This is the only kind of space we usually deal with in plasma physics.)

In terms of the Γ 's, the gradient of a vector \mathbf{A} is a tensor \mathbf{T} given by

$$T_{ji} = (\nabla \mathbf{A})_{ji} = \frac{\delta A_i}{h_j \delta \xi_j} + \sum_l \Gamma_{il}^j A_l \quad (\text{D.12})$$

Contracting this expression (i.e., multiplying by δ_j^i and summing over i and j) recovers Eq. (D.3). The directional derivative is

$$\begin{aligned} [(\mathbf{A} \cdot \nabla) \mathbf{B}]_i &= \sum_j A_j (\nabla \mathbf{B})_{ji} \\ &= \sum_j \left(\frac{A_j}{h_j} \frac{\delta B_i}{\delta \xi_j} + \frac{A_i B_j}{h_i h_j} \frac{\delta h_i}{\delta \xi_j} - \frac{A_j B_j}{h_i h_j} \frac{\delta h_i}{\delta \xi_i} \right) \end{aligned} \quad (\text{D.13})$$

The gradient of a (second-order) tensor is a third-order tensor given by

$$(\nabla \mathbf{T})_{kji} = \frac{\delta T_{ji}}{h_k \delta \xi_k} + \sum_l \left(\Gamma_{il}^k T_{jl} + \Gamma_{jl}^k T_{li} \right) \quad (\text{D.14})$$

The divergence of the tensor \mathbf{T} is obtained by contracting Eq. (D.14) with respect to the first two indices:

$$\begin{aligned} (\nabla \cdot \mathbf{T})_i &= \sum_j \left[\frac{\delta T_{ji}}{h_j \delta \xi_j} + \sum_l (\Gamma_{il}^j T_{jl} + \Gamma_{jl}^i T_{li}) \right] \\ &= \sum_j \left[\frac{1}{H} \frac{\delta}{\delta \xi_j} \left(\frac{HT_{ji}}{h_j} \right) + \sum_l \Gamma_{il}^j T_{jl} \right] \end{aligned} \quad (\text{D.15})$$

If \mathbf{T} is defined according to Eq. (D.12), $\nabla \cdot \mathbf{T}$ is the Laplacian of the vector \mathbf{A} :

$$\begin{aligned} (\nabla^2 \mathbf{A})_i &= \sum_j (\nabla \nabla \mathbf{A})_{jji} = \sum_j \left\{ \frac{1}{H} \frac{\delta}{\delta \xi_j} \left(\frac{H}{h_j^2} \frac{\delta A_i}{\delta \xi_j} \right) \right. \\ &\quad + \frac{h_i A_i}{H} \frac{\delta}{\delta \xi_j} \left(\frac{H}{h_i^2 h_j^2} \frac{\delta h_i}{\delta \xi_j} \right) + \frac{2}{h_i^2 h_j^2} \frac{\delta h_i}{\delta \xi_j} \frac{\delta}{\delta \xi_i} (h_j A_j) \\ &\quad \left. - \frac{2}{h_i h_j^3} \frac{\delta h_j}{\delta \xi_i} \frac{\delta}{\delta \xi_j} (h_j A_j) + \frac{h_j A_j}{h_i} \frac{\delta}{\delta \xi_i} \left[\frac{1}{H} \frac{\delta}{\delta \xi_j} \left(\frac{H}{h_j^2} \right) \right] \right\} \end{aligned} \quad (\text{D.16})$$

Evidently the first term on the RHS is $\nabla^2 A_i$, the scalar Laplacian applied to A_i (Eq. (D.5)). Fortunately, Eq. (D.16) simplifies considerably for most coordinate systems of interest.

In the following sections, the results of Eqs. (D.1) to (D.16) are applied to coordinate systems occasionally encountered in plasma physics problems.

Toroidal Coordinates

An arbitrary point in 3-space can be uniquely identified by the coordinates $\{\rho, \phi, \psi\}$, where ρ is the distance between the given point and the origin, ϕ is the angle between the radius vector to the point and a fixed toroidal angle (i.e., the one sweeping around the major circumference), and ψ is the poloidal angle. (Note that this system differs from the flux surface coordinates commonly used in connection with toroidal devices.) The values assumed by these coordinates are restricted according to $0 \leq \rho < \infty$, $0 \leq \phi < 2\pi$, and $0 \leq \psi < 2\pi$. If r, ϕ, z are the cylindrical coordinates of the point in question, where z is normal to the plane of the torus, then ϕ is the same in both systems and

$$\begin{aligned} R + \rho \cos \psi &= r \\ \rho \sin \psi &= z \end{aligned}$$

Hence the square of the differential arc length is

$$\begin{aligned} dl^2 &= dr^2 + r^2 d\phi^2 + dz^2 \\ &= d\rho^2 + (R + \rho \cos \psi)^2 d\phi^2 + \rho^2 d\psi^2 \end{aligned}$$

Consequently the scale factors are 1, $R + \rho \cos \psi$, and ρ , respectively. From Eq. (D.3), the divergence of \mathbf{A} is

$$\begin{aligned}\nabla \cdot \mathbf{A} = & \frac{1}{R + \rho \cos \psi} \left\{ \frac{1}{\rho} \frac{\delta}{\delta \rho} [\rho(R + \rho \cos \psi) A_\rho] \right. \\ & \left. + \frac{\delta A_\phi}{\delta \phi} + \frac{1}{\rho} \frac{\delta}{\delta \psi} [(R + \rho \cos \psi) A_\psi] \right\}\end{aligned}$$

From Eq. (D.4), the gradient of f has components

$$\begin{aligned}(\nabla f)_\rho &= \frac{\delta f}{\delta \rho} \\ (\nabla f)_\phi &= \frac{1}{R + \rho \cos \psi} \frac{\delta f}{\delta \phi} \\ (\nabla f)_\psi &= \frac{1}{\rho} \frac{\delta f}{\delta \psi}\end{aligned}$$

From Eq. (D.5), the Laplacian of f is

$$\begin{aligned}\nabla^2 f = & \frac{1}{R + \rho \cos \psi} \left\{ \frac{1}{\rho} \frac{\delta}{\delta \rho} \left[\rho(R + \rho \cos \psi) \frac{\delta f}{\delta \rho} \right] \right. \\ & \left. + \frac{1}{R + \rho \cos \psi} \frac{\delta^2 f}{\delta \phi^2} + \frac{1}{\rho^2} \frac{\delta}{\delta \psi} \left[(R + \rho \cos \psi) \frac{\delta f}{\delta \psi} \right] \right\}\end{aligned}$$

From Eq. (D.6), the curl of \mathbf{A} is given by

$$\begin{aligned}(\nabla \times \mathbf{A})_\rho &= \frac{1}{R + \rho \cos \psi} \left\{ \frac{\delta A_\psi}{\delta \phi} - \frac{1}{\rho} \frac{\delta}{\delta \psi} [(R + \rho \cos \psi) A_\phi] \right\} \\ (\nabla \times \mathbf{A})_\phi &= \frac{1}{\rho} \left\{ \frac{\delta A_\rho}{\delta \psi} - \frac{\delta}{\delta \rho} (\rho A_\psi) \right\} \\ (\nabla \times \mathbf{A})_\psi &= \frac{1}{R + \rho \cos \psi} \left\{ \frac{\delta}{\delta \rho} \left[(R + \rho \cos \psi) A_\phi - \frac{\delta A_\rho}{\delta \phi} \right] \right\}\end{aligned}$$

The only nonvanishing Christoffel symbols are

$$\begin{aligned}\Gamma_{21}^2 &= -\Gamma_{12}^2 = \frac{\cos \psi}{R + \rho \cos \psi} \\ \Gamma_{23}^2 &= -\Gamma_{32}^2 = \frac{-\sin \psi}{R + \rho \cos \psi} \\ \Gamma_{31}^3 &= -\Gamma_{13}^3 = \frac{1}{\rho}\end{aligned}$$

Then from Eq. (D.13),

$$\begin{aligned}
 [(\mathbf{A} \cdot \nabla) \mathbf{B}]_\rho &= A_\rho \frac{\delta B_\rho}{\delta \rho} + \frac{A_\phi}{R + \rho \cos \psi} \frac{\delta B_\rho}{\delta \phi} \\
 &\quad + \frac{A_\psi}{\rho} \frac{\delta B_\rho}{\delta \psi} - \frac{A_\phi B_\phi \cos \psi}{R + \rho \cos \psi} - \frac{A_\psi B_\psi}{\rho} \\
 [(\mathbf{A} \cdot \nabla) \mathbf{B}]_\phi &= A_\rho \frac{\delta B_\phi}{\delta \rho} + \frac{A_\phi}{R + \rho \cos \psi} \frac{\delta B_\phi}{\delta \phi} \\
 &\quad + \frac{A_\psi}{\rho} \frac{\delta B_\phi}{\delta \psi} + \frac{A_\phi B_\rho \cos \psi}{R + \rho \cos \psi} - \frac{A_\phi B_\psi \sin \psi}{R + \rho \cos \psi} \\
 [(\mathbf{A} \cdot \nabla) \mathbf{B}]_\psi &= A_\rho \frac{\delta B_\psi}{\delta \rho} + \frac{A_\phi}{R + \rho \cos \psi} \frac{\delta B_\psi}{\delta \phi} \\
 &\quad + \frac{A_\psi}{\rho} \frac{\delta B_\psi}{\delta \psi} + \frac{A_\psi B_\rho}{\rho} + \frac{A_\phi B_\phi \sin \psi}{R + \rho \cos \psi}
 \end{aligned}$$

From Eq. (D.15),

$$\begin{aligned}
 (\nabla \cdot \mathbf{T})_\rho &= \frac{1}{R + \rho \cos \psi} \left\{ \frac{1}{\rho} \frac{\delta}{\delta \rho} [\rho(R + \rho \cos \psi) T_{\rho\rho}] \right. \\
 &\quad + \frac{\delta T_{\phi\rho}}{\delta \phi} + \frac{1}{\rho} \frac{\delta}{\delta \psi} [(R + \rho \cos \psi) T_{\psi\rho}] \\
 &\quad \left. - \cos \psi T_{\phi\phi} \right\} - \frac{1}{\rho} T_{\psi\psi} \\
 (\nabla \cdot \mathbf{T})_\phi &= \frac{1}{R + \rho \cos \psi} \left\{ \frac{1}{\rho} \frac{\delta}{\delta \rho} [\rho(R + \rho \cos \psi) T_{\rho\phi}] \right. \\
 &\quad + \frac{\delta T_{\phi\phi}}{\delta \phi} + \frac{1}{\rho} \frac{\delta}{\delta \psi} [(R + \rho \cos \psi) T_{\psi\phi}] \\
 &\quad \left. + \cos \psi T_{\phi\rho} - \sin \psi T_{\phi\psi} \right\} \\
 (\nabla \cdot \mathbf{T})_\psi &= \frac{1}{R + \rho \cos \psi} \left\{ \frac{1}{\rho} \frac{\delta}{\delta \rho} [\rho(R + \rho \cos \psi) T_{\rho\psi}] \right. \\
 &\quad + \frac{\delta T_{\phi\psi}}{\delta \phi} + \frac{1}{\rho} \frac{\delta}{\delta \psi} [(R + \rho \cos \psi) T_{\psi\psi}] \\
 &\quad \left. + \sin \psi T_{\phi\phi} \right\} + \frac{1}{\rho} T_{\psi\rho}
 \end{aligned}$$

Finally, from Eq. (D.16),

$$\begin{aligned}
 (\nabla^2 \mathbf{A})_\rho &= \nabla^2 A_\rho - A_\rho \left[\frac{1}{\rho^2} + \frac{\cos^2 \psi}{(R + \rho \cos \psi)^2} \right] \\
 &\quad - \frac{2 \cos \psi}{(R + \rho \cos \psi)^2} \frac{\delta A_\phi}{\delta \phi} - \frac{2}{\rho^2} \frac{\delta A_\psi}{\delta \psi} \\
 &\quad + \frac{\sin \psi A_\psi}{R + \rho \cos \psi} \left(\frac{1}{\rho} + \frac{\cos \psi}{R + \rho \cos \psi} \right) \\
 (\nabla^2 \mathbf{A})_\phi &= \nabla^2 A_\phi - \frac{1}{(R + \rho \cos \psi)^2} A_\phi \\
 &\quad + \frac{2}{(R + \rho \cos \psi)^2} \left(\cos \psi \frac{\delta A_\rho}{\delta \phi} - \sin \psi \frac{\delta A_\psi}{\delta \phi} \right) \\
 (\nabla^2 \mathbf{A})_\psi &= \nabla^2 A_\psi - A_\psi \left[\frac{1}{\rho^2} + \frac{\sin^2 \psi}{(R + \rho \cos \psi)^2} \right] \\
 &\quad + \frac{2}{\rho^2} \frac{\delta A_\rho}{\delta \psi} + \frac{\sin \psi}{(R + \rho \cos \psi)^2} \left(2 \frac{\delta A_\phi}{\delta \phi} - \frac{RA_\rho}{\rho} \right)
 \end{aligned}$$

Cylindrical Coordinates

Divergence:

$$\nabla \cdot \mathbf{A} = \frac{1}{r} \frac{\delta}{\delta r} (r A_r) + \frac{1}{r} \frac{\delta A_\theta}{\delta \theta} + \frac{\delta A_z}{\delta z}$$

Gradient:

$$(\nabla f)_r = \frac{\delta f}{\delta r}, \quad (\nabla f)_\theta = \frac{1}{r} \frac{\delta f}{\delta \theta}, \quad (\nabla f)_z = \frac{\delta f}{\delta z}$$

Curl:

$$\begin{aligned}
 (\nabla \times \mathbf{A})_r &= \frac{1}{r} \frac{\delta A_z}{\delta \theta} - \frac{\delta A_\theta}{\delta z} \\
 (\nabla \times \mathbf{A})_\theta &= \frac{\delta A_r}{\delta z} - \frac{\delta A_z}{\delta r} \\
 (\nabla \times \mathbf{A})_z &= \frac{1}{r} \frac{\delta}{\delta r} (r A_\theta) - \frac{1}{r} \frac{\delta A_r}{\delta \theta}
 \end{aligned}$$

Laplacian:

$$\nabla^2 f = \frac{1}{r} \frac{\delta}{\delta r} \left(r \frac{\delta f}{\delta r} \right) + \frac{1}{r^2} \frac{\delta^2 f}{\delta \theta^2} + \frac{\delta^2 f}{\delta z^2}$$

Laplacian of a vector:

$$\begin{aligned}(\nabla^2 \mathbf{A})_r &= \nabla^2 A_r - \frac{2}{r^2} \frac{\delta A_\theta}{\delta \theta} - \frac{A_r}{r^2} \\(\nabla^2 \mathbf{A})_\theta &= \nabla^2 A_\theta + \frac{2}{r^2} \frac{\delta A_r}{\delta \theta} - \frac{A_\theta}{r^2} \\(\nabla^2 \mathbf{A})_z &= \nabla^2 A_z\end{aligned}$$

Components of $(\mathbf{A} \cdot \nabla) \mathbf{B}$:

$$\begin{aligned}(\mathbf{A} \cdot \nabla \mathbf{B})_r &= A_r \frac{\delta B_r}{\delta r} + \frac{A_\theta}{r} \frac{\delta B_r}{\delta \theta} + A_z \frac{\delta B_r}{\delta z} - \frac{A_\theta B_\theta}{r} \\(\mathbf{A} \cdot \nabla \mathbf{B})_\theta &= A_r \frac{\delta B_\theta}{\delta r} + \frac{A_\theta}{r} \frac{\delta B_\theta}{\delta \theta} + A_z \frac{\delta B_\theta}{\delta z} + \frac{A_\theta B_r}{r} \\(\mathbf{A} \cdot \nabla \mathbf{B})_z &= A_r \frac{\delta B_z}{\delta r} + \frac{A_\theta}{r} \frac{\delta B_z}{\delta \theta} + A_z \frac{\delta B_z}{\delta z}\end{aligned}$$

Divergence of a tensor:

$$\begin{aligned}(\nabla \cdot \mathbf{T})_r &= \frac{1}{r} \frac{\delta}{\delta r} (r T_{rr}) + \frac{1}{r} \frac{\delta T_{\theta r}}{\delta \theta} + \frac{\delta T_{zr}}{\delta z} - \frac{1}{r} T_{\theta \theta} \\(\nabla \cdot \mathbf{T})_\theta &= \frac{1}{r} \frac{\delta}{\delta r} (r T_{r\theta}) + \frac{1}{r} \frac{\delta T_{\theta \theta}}{\delta \theta} + \frac{\delta T_{z\theta}}{\delta z} + \frac{1}{r} T_{\theta r} \\(\nabla \cdot \mathbf{T})_z &= \frac{1}{r} \frac{\delta}{\delta r} (r T_{rz}) + \frac{1}{r} \frac{\delta T_{\theta z}}{\delta \theta} + \frac{\delta T_{zz}}{\delta z}\end{aligned}$$

Spherical Coordinates

Divergence:

$$\nabla \cdot \mathbf{A} = \frac{1}{r^2} \frac{\delta}{\delta r} (r^2 A_r) + \frac{1}{r \sin \theta} \frac{\delta}{\delta \theta} (A_\theta \sin \theta) + \frac{1}{r \sin \theta} \frac{\delta A_\phi}{\delta \phi}$$

Gradient:

$$(\nabla f)_r = \frac{\delta f}{\delta r}, \quad (\nabla f)_\theta = \frac{1}{r} \frac{\delta f}{\delta \theta}, \quad (\nabla f)_\phi = \frac{1}{r \sin \theta} \frac{\delta f}{\delta \phi}$$

Curl:

$$\begin{aligned}(\nabla \times \mathbf{A})_r &= \frac{1}{r \sin \theta} \frac{\delta}{\delta \theta} (A_\phi \sin \theta) - \frac{1}{r \sin \theta} \frac{\delta A_\theta}{\delta \phi} \\(\nabla \times \mathbf{A})_\theta &= \frac{1}{r \sin \theta} \frac{\delta A_r}{\delta \phi} - \frac{1}{r} \frac{\delta}{\delta r} (r A_\phi) \\(\nabla \times \mathbf{A})_\phi &= \frac{1}{r} \frac{\delta}{\delta r} (r A_\theta) - \frac{1}{r} \frac{\delta A_r}{\delta \theta}\end{aligned}$$

Laplacian:

$$\nabla^2 f = \frac{1}{r^2} \frac{\delta}{\delta r} \left(r^2 \frac{\delta f}{\delta r} \right) + \frac{1}{r^2 \sin \theta} \frac{\delta}{\delta \theta} \left(\sin \theta \frac{\delta f}{\delta \theta} \right) + \frac{1}{r^2 \sin^2 \theta} \frac{\delta^2 f}{\delta \phi^2}$$

Laplacian of a vector:

$$\begin{aligned}(\nabla^2 \mathbf{A})_r &= \nabla^2 A_r - \frac{2A_r}{r^2} - \frac{2}{r^2} \frac{\delta A_\theta}{\delta \theta} - \frac{2A_\theta \cot \theta}{r^2} - \frac{2}{r^2 \sin \theta} \frac{\delta A_\phi}{\delta \phi} \\(\nabla^2 \mathbf{A})_\theta &= \nabla^2 A_\theta + \frac{2}{r^2} \frac{\delta A_r}{\delta \theta} - \frac{A_\theta}{r^2 \sin^2 \theta} - \frac{2 \cos \theta}{r^2 \sin^2 \theta} \frac{\delta A_\phi}{\delta \phi} \\(\nabla^2 \mathbf{A})_\phi &= \nabla^2 A_\phi - \frac{A_\phi}{r^2 \sin^2 \theta} + \frac{2}{r^2 \sin \theta} \frac{\delta A_r}{\delta \phi} + \frac{2 \cos \theta}{r^2 \sin^2 \theta} \frac{\delta A_\theta}{\delta \phi}\end{aligned}$$

Components of $(\mathbf{A} \cdot \nabla) \mathbf{B}$:

$$\begin{aligned}(\mathbf{A} \cdot \nabla \mathbf{B})_r &= A_r \frac{\delta B_r}{\delta r} + \frac{A_\theta}{r} \frac{\delta B_r}{\delta \theta} + \frac{A_\phi}{r \sin \theta} \frac{\delta B_r}{\delta \phi} - \frac{A_\theta B_\theta + A_\phi B_\phi}{r} \\(\mathbf{A} \cdot \nabla \mathbf{B})_\theta &= A_r \frac{\delta B_\theta}{\delta r} + \frac{A_\theta}{r} \frac{\delta B_\theta}{\delta \theta} + \frac{A_\phi}{r \sin \theta} \frac{\delta B_\theta}{\delta \phi} + \frac{A_\theta B_r}{r} - \frac{A_\phi B_\phi \cot \theta}{r} \\(\mathbf{A} \cdot \nabla \mathbf{B})_\phi &= A_r \frac{\delta B_\phi}{\delta r} + \frac{A_\theta}{r} \frac{\delta B_\phi}{\delta \theta} + \frac{A_\phi}{r \sin \theta} \frac{\delta B_\phi}{\delta \phi} + \frac{A_\phi B_r}{r} + \frac{A_\phi B_\theta \cot \theta}{r}\end{aligned}$$

Divergence of a tensor:

$$\begin{aligned}(\nabla \cdot \mathbf{T})_r &= \frac{1}{r^2} \frac{\delta}{\delta r} (r^2 T_{rr}) + \frac{1}{r \sin \theta} \frac{\delta}{\delta \theta} (T_{\theta r} \sin \theta) \\&\quad + \frac{1}{r \sin \theta} \frac{\delta T_{\phi r}}{\delta \phi} - \frac{T_{\theta \theta} + T_{\phi \phi}}{r} \\(\nabla \cdot \mathbf{T})_\theta &= \frac{1}{r^2} \frac{\delta}{\delta r} (r^2 T_{r\theta}) + \frac{1}{r \sin \theta} \frac{\delta}{\delta \theta} (T_{\theta \theta} \sin \theta) \\&\quad + \frac{1}{r \sin \theta} \frac{\delta T_{\phi \theta}}{\delta \phi} + \frac{T_{\theta r}}{r} - \frac{\cot \theta}{r} T_{\phi \phi} \\(\nabla \cdot \mathbf{T})_\phi &= \frac{1}{r^2} \frac{\delta}{\delta r} (r^2 T_{r\phi}) + \frac{1}{r \sin \theta} \frac{\delta}{\delta \theta} (T_{\theta \phi} \sin \theta) + \frac{1}{r \sin \theta} \frac{\delta T_{\phi \phi}}{\delta \phi} + \frac{T_{\phi r}}{r} \\&\quad + \frac{\cot \theta}{r} T_{\phi \theta}\end{aligned}$$

Appendix E

Plasma Formulas¹

Frequencies

Electron gyrofrequency

$$\Omega_e \equiv \frac{eB}{m_e} = 1.76 \times 10^{11} B \left(\text{s}^{-1} \right)$$

Ion gyrofrequency

$$\Omega_i \equiv \frac{eB}{m_i} = 0.96 \times 10^8 \frac{zB}{(m_i/m_p)} \left(\text{s}^{-1} \right)$$

Electron plasma frequency

$$\omega_{Pe} \equiv \left(\frac{n_e e^2}{\epsilon_0 m_e} \right)^{\frac{1}{2}} = 5.64 \times 10^1 \sqrt{n_e} \left(\text{s}^{-1} \right)$$

Ion plasma frequency

$$\omega_{Pi} \equiv \left(\frac{n_i z^2 e^2}{\epsilon_0 m_i} \right)^{\frac{1}{2}} = 1.32 \frac{z \sqrt{n_i}}{(m_i/m_p)^{\frac{1}{2}}} \left(\text{s}^{-1} \right)$$

Lengths

Debye lenght

$$\lambda_D \equiv \left(\frac{\epsilon_0 T}{n e^2} \right)^{\frac{1}{2}} = 7.43 \times 10^3 \sqrt{\frac{T}{n}} (\text{m})$$

Electron gyroradius

$$r_{Le} = \frac{v_{e,\text{th}} m_e}{eB} = 3.37 \times 10^{-6} \sqrt{\frac{T_e}{B^2}} (\text{m})$$

Ion gyroradius

$$r_{Li} = \frac{v_{i,\text{th}} m_i}{eB} = 1.44 \times 10^{-4} \sqrt{\frac{(m_i/m_p) T_i}{z B^2}} (\text{m})$$

¹ MKS units, except T in eV; z is the charge of the ion, and m_p/m_i is the ratio of ion to proton masses.

Velocities

Electron thermal velocity

$$v_{e,\text{th}} = \left(\frac{2T_e}{m_e} \right)^{\frac{1}{2}} = 5.92 \times 10^5 \sqrt{T_e} \text{ (m} \cdot \text{s}^{-1}\text{)}$$

Ion thermal velocity

$$v_{i,\text{th}} = \left(\frac{2T_i}{m_i} \right)^{\frac{1}{2}} = 1.38 \times 10^4 \sqrt{\frac{T_i}{(m_i/m_p)}} \text{ (m/s)}$$

Ion sound velocity

$$c_s = \left(\frac{T_e}{m_i} \right)^{\frac{1}{2}} = 9.79 \times 10^3 \sqrt{\frac{T_e}{(m_i/m_p)}} \text{ (m/s)}$$

Collision Times

Electron-ion

$$\tau_{ei} = \frac{3.5 \times 10^{10} T_e^{\frac{3}{2}}}{\left(\frac{\ln A_e}{10} \right)} z_i n_i \text{ (s)}$$

Ion-ion

$$\tau_{ii} = \frac{3.0 \times 10^{12}}{\left(\frac{\ln A_i}{10} \right)} \left(\frac{m_i}{2m_p} \right)^{\frac{1}{2}} \frac{T_i}{z^3 n_i} \text{ (s)}$$

Appendix F

Further Reading

Introductory Textbooks

F. F. Chen, *Introduction to Plasma Physics*, 2nd Ed., Plenum, London (1984). *For many years a standard undergraduate introduction to plasma physics.*

W. M. Stacey, *FUSION: An Introduction to the Physics and Technology of Magnetic Confinement Fusion*, Wiley-Interscience, New York (1984). *A broad introduction to the plasma physics and technology of future fusion reactors.*

Textbooks

T. J. M. Boyd, J. J. Sanderson, *The Physics of Plasmas*, Cambridge University Press, Cambridge (2003). *A recent treatment of the standard plasma physics topics – particle motion, fluid theory, kinetic theory, equilibria, waves and instabilities, radiation, etc.*

R. J. Goldston, P. H. Rutherford, *Introduction to Plasma Physics*, Institute of Physics, Bristol (1995). *Good treatment of the standard plasma physics topics, with an emphasis on plasma heating and waves and instabilities.*

K. Miyamoto, *Plasma Physics for Nuclear Fusion*, Rev. Ed., MIT Press, Cambridge (1989). *The most recent edition of a long-used text on the standard topics of plasma physics.*

W. M. Stacey, *Fusion Plasma Analysis*, Wiley-Interscience, New York (1981). *A good treatment of standard plasma physics topics plus introductory material on plasma-materials interactions and fusion reactors.*

References

S. I. Braginskii, Transport Processes in a Plasma, in *Reviews of Plasma Physics, Vol. 1*, Ed. M. A. Leontovich, Consultants Bureau, New York (1965). *The seminal paper on the subject.*

J. P. Freidberg, *Ideal Magnetohydrodynamics*, Plenum Press, New York (1987). *A detailed mathematical treatment of MHD equilibria and stability.*

R. D. Hazeltine, J. D. Meiss, *Plasma Confinement*, Addison-Wesley, Redwood City, CA (1992). *Advanced mathematical development of the foundations of plasma confinement, with good treatments of coordinate systems, kinetic theory and neoclassical transport.*

- P. Helander, D. J. Sigmar, *Collisional Transport in Magnetized Plasmas*, Cambridge University Press, Cambridge (2002). *A modern treatment of neoclassical transport theory for adiabatic plasmas.*
- I. H. Hutchinson, *Principles of Plasma Diagnostics*, Cambridge University Press, Cambridge (1988). *Treatment of the experimental aspects of laboratory plasma physics.*
- K. Itoh, S-I Itoh, A. Fukyama, *Transport and Structural Formation in Plasmas*, Institute of Physics, Bristol (1999). *A modern treatment of turbulence in plasmas.*
- B. B. Kadomtsev, *Tokamak Plasma: A Complex Physical System*, Institute of Physics, Bristol (1992). *An insightful treatment by one of the giants of the field.*
- P. C. Stangeby, *The Plasma Boundary of Magnetic Fusion Devices*, Institute of Physics, Bristol (2000). *A comprehensive compendium of plasma edge phenomena from the experimental point of view.*
- T. H. Stix, *Waves in Plasmas*, American Institute of Physics, New York (1992). *A reprint of the classic text on the subject.*
- J. A. Wesson, *Tokamaks*, 2nd Ed., Clarendon Press, Oxford (1997). *An excellent compilation of tokamak experimental phenomena and theoretical explanations.*

Research Journals

- Contributions to Plasma Physics (plasma physics)
- Fusion Engineering & Design (fusion technology, design)
- Fusion Science & Technology (plasma physics, fusion technology)
- IEEE Transactions of Plasma Science (plasma physics)
- Journal of Computational Physics (plasma codes)
- Journal of Plasma Physics (plasma physics)
- Journal of Nuclear Materials (plasma edge physics, materials interactions)
- Nuclear Fusion (plasma physics)
- Physica Scripta (physics)
- Physical Review Letters (physics)
- Physics of Plasmas (plasma physics)
- Plasma Physics and Controlled Fusion (plasma physics)
- Review of Scientific Instruments (plasma diagnostics)
- Soviet Journal of Plasma Physics (plasma physics)

Conferences/Proceedings

- Controlled Fusion & Plasma Physics, European Physical Society Conference
- Fusion Energy, IAEA International Conference
- Fusion Nuclear Technology, International Symposium
- Fusion Reactor Materials, Internationl Conference
- Fusion Technology, Symposium
- Fusion Theory, Sherwood Conference
- High-Temperature Diagnostics, Topical Conference
- Plasma Edge Theory in Fusion Devices, International Workshop
- Plasma Physics, American Physical Society Plasma Physics Division Meeting
- Plasma Physics, International Congress
- Plasma Science, IEEE International Conference
- Plasma Science & Technology, Asia Pacific Conference
- Plasma-Surface Engineering, International Conference
- Plasma-Surface Interactions in Controlled Fusion Devices, International Conference
- Technology of Fusion Energy, American Nuclear Society Topical Meeting

Appendix G

Attributions

The lecture notes on which this book is based evolved over more than a decade as material was assembled from various sources, edited, integrated, organized, supplemented with original derivations as necessary to fill in the gaps and selectively rewritten a time or two to improve coherence. While it is impossible to credit all the sources, a few major ones stand out. A set of Princeton Plasma Physics Lab lecture notes on plasma physics by Harold Furth, Paul Rutherford, Marshall Rosenbluth and Rip Perkins was of great use in preparing some of the basic material in the first half of this book and in my previous text on the subject (*Fusion Plasma Analysis*, Wiley-Interscience, New York, 1981). The textbook by Goldston and Rutherford (*Introduction to Plasma Physics*, IOP Press, London, 1995) and the research compendia on tokamaks by John Wesson et al. (*Tokamaks*, Oxford University Press, Oxford, 1997), on the plasma boundary by Peter Stangeby (*Plasma Boundary*, IOP Press, London, 2000) and on neoclassical theory by Per Helander and Dieter Sigmar (*Collisional Transport in Magnetized Plasmas*, Cambridge University Press, Cambridge, 2002) proved to be valuable sources of information in selected areas, as of course was the original literature of the field (in particular *Physics of Plasmas*, *Plasma Physics and Controlled Fusion*, and *Nuclear Fusion*). The cover photograph of a DIII-D plasma was provided by General Atomics, and numerous figures were used with permission as indicated below.

Figure Credits

Chapter 1

- | | | |
|----------|---|------------|
| Fig. 1.1 | Stacey, Nuclear Reactor Physics, Wiley, New York (2001) | Fig. 1.2 |
| Fig. 1.2 | Wesson, Tokamaks, Oxford Univ. Press, Oxford (1997) | Fig. 1.3.3 |
| Fig. 1.4 | Stacey, Fusion Plasma Analysis, Wiley, New York (1981) | Fig. 1.3 |
| Fig. 1.5 | Stacey, Fusion Plasma Analysis, Wiley, New York (1981) | Fig. 1.4 |
| Fig. 1.6 | Stacey, Fusion Plasma Analysis, Wiley, New York (1981) | Fig. 1.5 |
| Fig. 1.7 | Stacey, Fusion Plasma Analysis, Wiley, New York (1981) | Fig. 1.6 |

Chapter 2

- | | | |
|----------|--|-----------|
| Fig. 2.1 | Stacey, Fusion Plasma Analysis, Wiley, New York (1981) | Fig. 2.1 |
| Fig. 2.2 | Stacey, Fusion Plasma Analysis, Wiley, New York (1981) | Fig. 2.2 |
| Fig. 2.3 | Stacey, Fusion Plasma Analysis, Wiley, New York (1981) | Fig. 2.3 |
| Fig. 2.4 | Stacey, Fusion Plasma Analysis, Wiley, New York (1981) | Fig. 2.12 |

Chapter 3

Fig. 3.1	Stacey, Fusion, Wiley, New York (1984)	Fig. 4.1.1
Fig. 3.2	Stacey, Fusion, Wiley, New York (1984)	Fig. 4.1.2
Fig. 3.3	Stacey, Fusion, Wiley, New York (1984)	Fig. 4.1.3
Fig. 3.4	Stacey, Fusion, Wiley, New York (1984)	Fig. 4.1.4
Fig. 3.5	Stacey, Fusion, Wiley, New York (1984)	Fig. 4.1.5
Fig. 3.6	Stacey, Fusion, Wiley, New York (1984)	Fig. 4.1.6
Fig. 3.7	Stacey, Fusion, Wiley, New York (1984)	Fig. 4.1.7
Fig. 3.8	Stacey, Fusion, Wiley, New York (1984)	Fig. 1.2.1
Fig. 3.9	Stacey, Fusion, Wiley, New York (1984)	Fig. 1.2.2
Fig. 3.10	Stacey, Fusion, Wiley, New York (1984)	Fig. 1.2.3
Fig. 3.11	Stacey, Fusion Plasma Analysis, Wiley, New York (1981)	Fig. 2.7
Fig. 3.12	Stacey, Fusion Plasma Analysis, Wiley, New York (1981)	Fig. 2.8
Fig. 3.13	Stacey, Fusion Plasma Analysis, Wiley, New York (1981)	Fig. 2.9
Fig. 3.14	Stacey, Fusion Plasma Analysis, Wiley, New York (1981)	Fig. 2.10
Fig. 3.15	Stacey, Fusion Plasma Analysis, Wiley, New York (1981)	Fig. 2.11

Chapter 4

Fig. 4.1	Stacey, Fusion Plasma Analysis, Wiley, New York (1981)	Fig. 3.1
Fig. 4.2	Stacey, Fusion Plasma Analysis, Wiley, New York (1981)	Fig. 3.2
Fig. 4.3	Stacey, Fusion Plasma Analysis, Wiley, New York (1981)	Fig. 3.3
Fig. 4.4	Stacey, Fusion Plasma Analysis, Wiley, New York (1981)	Fig. 3.4

Chapter 6

Fig. 6.1	Stacey, Fusion Plasma Analysis, Wiley, New York (1981)	Fig. 5.1
Fig. 6.2	Wesson, Tokamaks, Oxford Univ. Press, Oxford (1997)	Fig. 3.3.1
Fig. 6.3	Stacey, Fusion Plasma Analysis, Wiley, New York (1981)	Fig. 5.2
Fig. 6.4	Stacey, Fusion Plasma Analysis, Wiley, New York (1981)	Fig. 5.3
Fig. 6.5	Stacey, Fusion Plasma Analysis, Wiley, New York (1981)	Fig. 5.4
Fig. 6.6	Stacey, Fusion Plasma Analysis, Wiley, New York (1981)	Fig. 5.5
Fig. 6.7	Wesson, Tokamaks, Oxford Univ. Press, Oxford (1997)	Fig. 3.4.2
Fig. 6.8	Wesson, Tokamaks, Oxford Univ. Press, Oxford (1997)	Fig. 3.6.1
Fig. 6.9	Wesson, Tokamaks, Oxford Univ. Press, Oxford (1997)	Fig. 3.7.1
Fig. 6.10	Wesson, Tokamaks, Oxford Univ. Press, Oxford (1997)	Fig. 3.5.1
Fig. 6.11	Stacey, Fusion Plasma Analysis, Wiley, New York (1981)	Fig. 5.6

Chapter 7

Fig. 7.1	Stacey, Fusion Plasma Analysis, Wiley, New York (1981)	Fig. 7.1
----------	--	----------

Chapter 8

- | | | |
|-----------|--|------------------|
| Fig. 8.1 | Stacey, Fusion Plasma Analysis, Wiley, New York (1981) | Fig. 8.1 |
| Fig. 8.2 | Stacey, Fusion Plasma Analysis, Wiley, New York (1981) | Fig. 8.2 |
| Fig. 8.3 | Stacey, Fusion Plasma Analysis, Wiley, New York (1981) | Fig. 8.3 |
| Fig. 8.4 | Stacey, Fusion Plasma Analysis, Wiley, New York (1981) | Fig. 8.4 |
| Fig. 8.5 | Stacey, Fusion Plasma Analysis, Wiley, New York (1981) | Fig. 8.5 |
| Fig. 8.6 | Stacey, Fusion Plasma Analysis, Wiley, New York (1981) | Fig. 8.6 |
| Fig. 8.7 | Stacey, Fusion Plasma Analysis, Wiley, New York (1981) | Fig. 8.7 |
| Fig. 8.8 | Wesson, Tokamaks, Oxford, Oxford (1997) | Fig. 6.10.4 |
| Fig. 8.9 | Stacey, Fusion Plasma Analysis, Wiley, New York (1981) | Fig. 8.9 |
| Fig. 8.10 | Stacey, Fusion Plasma Analysis, Wiley, New York (1981) | Fig. 8.10 |
| Fig. 8.11 | Stacey, Fusion Plasma Analysis, Wiley, New York (1981) | Fig. 8.11 |
| Fig. 8.12 | Miyamoto, Fund. Plasma Phys, Iwanami, Tokyo (1997) | Fig. 8.11 |
| Fig. 8.13 | Miyamoto, Fund. Plasma Phys, Iwanami, Tokyo (1997) | Fig. 8.12 |
| Fig. 8.14 | Goldston & Rutherford, Plasma Physics, IOP,
London (1995) | Figs. 20.1, 20.2 |
| Fig. 8.15 | Goldston & Rutherford, Plasma Physics, IOP,
London (1995) | Fig. 20.5 |
| Fig. 8.16 | Goldston & Rutherford, Plasma Physics, IOP,
London (1995) | Fig. 20.6 |
| Fig. 8.17 | Stacey, Fusion Plasma Analysis, Wiley, New York (1981) | Fig. 8.13 |
| Fig. 8.18 | Stacey, Fusion Plasma Analysis, Wiley, New York (1981) | Fig. 8.14 |
| Fig. 8.19 | Wesson, Tokamaks, Oxford, Oxford (1997) | Fig. 7.6.2 |
| Fig. 8.20 | Wesson, Tokamaks, Oxford, Oxford (1997) | Fig. 7.6.3 |
| Fig. 8.21 | Sykes & Wesson, Phys. Rev. Lett., 37, 140 (1976) | Fig. 7.6.4 |
| Fig. 8.22 | Wesson, Tokamaks, Oxford, Oxford (1997) | Fig. 7.6.5 |

Chapter 9

- | | | |
|----------|--|------------|
| Fig. 9.1 | Braginski, Reviews of Plasma Phys., 1, 205–311, New
York (1965) | Fig. 4 |
| Fig. 9.2 | Braginski, Reviews of Plasma Phys., 1, 205–311, New
York (1965) | Fig. 5 |
| Fig. 9.3 | Braginski, Reviews of Plasma Phys., 1, 205–311, New
York (1965) | Fig. 2 |
| Fig. 9.4 | Stacey, Fusion, Wiley, New York (1984) | Fig. 3.1.1 |
| Fig. 9.5 | Stacey, Fusion Plasma Analysis, Wiley, New York (1981) | Fig. 6.1 |
| Fig. 9.6 | Wesson, Tokamaks, Oxford Univ. Press, Oxford (1997) | Fig. 4.8.1 |
| Fig. 9.7 | Helander and Sigmar, Collisional Transport, Cambridge,
Cambridge (2002) | Fig. 7.8 |

Chapter 11

- | | | |
|-----------|---|----------|
| Fig. 11.1 | Itoh, Itoh & Fukuyama, Transport and Structure in Plasmas, IOP, London (1999) | Fig. 4.1 |
| Fig. 11.2 | Itoh, Itoh & Fukuyama, Transport and Structure in Plasmas, IOP, London (1999) | Fig. 4.2 |
| Fig. 11.3 | W. Horton, Rev. Mod. Phys. 71, 735 (1999) | Fig. 13 |

Chapter 12

- | | | |
|------------|---|-------------|
| Fig. 12.1 | Stacey, Fusion, Wiley, New York (1984) | Fig. 7.4.1 |
| Fig. 12.2 | Stacey, Fusion, Wiley, New York (1984) | Fig. 7.4.2 |
| Fig. 12.3 | Wesson, Tokamaks, Oxford Univ. Press, Oxford (1997) | Fig. 5.2.1 |
| Fig. 12.4 | Stacey, Fusion Plasma Analysis, Wiley, New York (1981) | Fig. 9.1 |
| Fig. 12.5 | Stacey, Fusion Plasma Analysis, Wiley, New York (1981) | Fig. 9.2 |
| Fig. 12.6 | Wesson, Tokamaks, Oxford Univ. Press, Oxford (1997) | Fig. 5.3.2 |
| Fig. 12.7 | Wesson, Tokamaks, Oxford Univ. Press, Oxford (1997) | Fig. 7.15.2 |
| Fig. 12.8 | Wesson, Tokamaks, Oxford Univ. Press, Oxford (1997) | Fig. 5.7.1 |
| Fig. 12.9 | Goldston & Rutherford, Plasma Physics, IOP, London (1995) | Fig. 15.1 |
| Fig. 12.10 | Wesson, Tokamaks, Oxford Univ. Press, Oxford (1997) | Fig. 5.8.1 |
| Fig. 12.11 | Wesson, Tokamaks, Oxford Univ. Press, Oxford (1997) | Fig. 5.10.1 |
| Fig. 12.12 | Gormezano, Plasma Phys. Control. Fusion, 35, A, A239 (1993) | Fig. 3.13.1 |

Chapter 13

- | | | |
|-----------|--|------------|
| Fig. 13.1 | Wesson, Tokamaks, Oxford Univ. Press, Oxford (1997) | Fig. 9.2.1 |
| Fig. 13.2 | Janev, et al., Elementary Processes in Plasmas, Springer-Verlag, Berlin (1987) | Fig. 9.5.1 |
| Fig. 13.3 | Post, J. Nucl. Mater., 220–222, 143 (1995) | Fig. 3.23 |
| Fig. 13.4 | Stangeby, Plasma Boundary, IOP, London (2000) | Fig. 3.25 |
| Fig. 13.5 | Post, J. Nucl. Mater., 220–222, 143 (1995) | Fig. 3.26 |
| Fig. 13.6 | Eckstein, Sputtering Data, Max Planck Inst. rpt IPP9/82, Garching (1993) | Fig. 9.7.1 |
| Fig. 13.7 | Stangeby, Plasma Boundary, IOP, London (2000) | Fig. 3.16 |
| Fig. 13.8 | Stacey, Fusion Plasma Analysis, Wiley, New York (1981) | Fig. 10.3 |
| Fig. 13.9 | Original | |

Chapter 14

- | | | |
|------------|---|-----------|
| Fig. 14.1 | McCracken & Stott, Nucl. Fusion, 19, 889 (1979) | Fig. 11.7 |
| Fig. 14.4 | Stacey, Phys. Plasmas, 5, 1015 (1998) | Fig. 1 |
| Fig. 14.5 | Stangeby, Plasma Boundary, IOP, London (2000) | Fig. 16.4 |
| Fig. 14.6 | Stangeby, Plasma Boundary, IOP, London (2000) | Fig. 18.7 |
| Fig. 14.7 | Stangeby, Plasma Boundary, IOP, London (2000) | Fig. 18.4 |
| Fig. 14.8 | Stangeby, Plasma Boundary, IOP, London (2000) | Fig. 17.7 |
| Fig. 14.9 | Stangeby, Plasma Boundary, IOP, London (2000) | Fig. 17.8 |
| Fig. 14.10 | Stangeby, Plasma Boundary, IOP, London (2000) | Fig. 17.9 |

Chapter 15

- | | | |
|------------|--|---------|
| Fig. 15.1 | Groebner et al., Phys. Plasmas, 9, 2134 (2001) | Fig. 4 |
| Fig. 15.2 | Ferron et al., Phys. Plasmas, 7, 1976 (2000) | Fig. 2 |
| Fig. 15.3 | Ferron et al., Phys. Plasmas, 7, 1976 (2000) | Fig. 3 |
| Fig. 15.4 | Ferron et al., Phys. Plasmas, 7, 1976 (2000) | Fig. 4 |
| Fig. 15.5 | Ferron et al., Phys. Plasmas, 7, 1976 (2000) | Fig. 5 |
| Fig. 15.6 | Burrell, Phys. Plasmas, 4, 1499 (1997) | Fig. 1 |
| Fig. 15.7 | Burrell, Phys. Plasmas, 4, 1499 (1997) | Fig. 2 |
| Fig. 15.8 | Burrell, Phys. Plasmas, 4, 1499 (1997) | Fig. 5 |
| Fig. 15.9 | Stacey, Phys. Plasmas, 9, 3082 (2002) | Fig. 1 |
| Fig. 15.10 | Stacey, Phys. Plasmas, 4, 1069 (1997) | Fig. 2 |
| Fig. 15.11 | Mandrekas, Nucl. Fusion, 37, 1015 (1997) | Fig. 3 |
| Fig. 15.12 | Greenwald, Plasma Phys. Control. Fusion | Fig. 10 |

Chapter 16

- | | | |
|------------|---|-----------|
| Fig. 16.1 | Stacey, Nuclear Reactor Physics, Wiley, New York (2001) | Fig. 9.17 |
| Fig. 16.2 | Stacey, Nuclear Reactor Physics, Wiley, New York (2001) | Fig. 9.1 |
| Fig. 16.3 | Stacey, Nuclear Reactor Physics, Wiley, New York (2001) | Fig. 9.2 |
| Fig. 16.4 | Stacey, Nuclear Reactor Physics, Wiley, New York (2001) | Fig. 9.3 |
| Fig. 16.5 | Stacey, Nuclear Reactor Physics, Wiley, New York (2001) | Fig. 9.4 |
| Fig. 16.6 | Stacey, Nuclear Reactor Physics, Wiley, New York (2001) | Fig. 9.5 |
| Fig. 16.7 | Stacey, Nuclear Reactor Physics, Wiley, New York (2001) | Fig. 9.6 |
| Fig. 16.8 | Stacey, Nuclear Reactor Physics, Wiley, New York (2001) | Fig. 9.7 |
| Fig. 16.9 | Stacey, Nuclear Reactor Physics, Wiley, New York (2001) | Fig. 9.8 |
| Fig. 16.10 | Stacey, Nuclear Reactor Physics, Wiley, New York (2001) | Fig. 9.9 |
| Fig. 16.11 | Stacey, Nuclear Reactor Physics, Wiley, New York (2001) | Fig. 9.10 |
| Fig. 16.12 | Stacey, Nuclear Reactor Physics, Wiley, New York (2001) | Fig. 9.13 |
| Fig. 16.13 | Stacey, Nuclear Reactor Physics, Wiley, New York (2001) | Fig. 9.12 |
| Fig. 16.14 | Stacey, Nuclear Reactor Physics, Wiley, New York (2001) | Fig. 9.14 |
| Fig. 16.15 | Stacey, Nuclear Reactor Physics, Wiley, New York (2001) | Fig. 9.15 |
| Fig. 16.16 | Stacey, Nuclear Reactor Physics, Wiley, New York (2001) | Fig. 9.16 |

Chapter 17

- | | | |
|-----------|---|-------------|
| Fig. 17.1 | Aratari et al., Annual Report, Max Planck Inst, Garching (1988) | Fig. 4.12.1 |
| Fig. 17.2 | Yushmanov et al., Nucl. Fusion, 30, 1999 (1990) | Fig. 4.12.2 |
| Fig. 17.3 | Stacey, Fusion Plasma Analysis, Wiley, New York (1981) | Fig. 10.1 |
| Fig. 17.4 | Stacey, Fusion Plasma Analysis, Wiley, New York (1981) | Fig. 10.2 |
| Fig. 17.5 | Strangeby, Plasma Boundary, IOP, London (2000) | Fig. 6.1 |
| Fig. 17.6 | Strangeby, Plasma Boundary, IOP, London (2000) | Fig. 6.2 |
| Fig. 17.7 | Mandrekas, Fusion Techn., 19, 57 (1991) | Fig. 1 |

Chapter 18

- | | | |
|-----------|---|-------------|
| Fig. 18.1 | Wesson, Tokamaks, Oxford Univ. Press, Oxford (1997) | Fig. 7.8.1 |
| Fig. 18.2 | Wesson, Tokamaks, Oxford Univ. Press, Oxford (1997) | Fig. 7.8.2 |
| Fig. 18.3 | Greenwald, PPCF, IOP, London | Fig. 28 |
| Fig. 18.4 | Greenwald, PPCF, IOP, London | Fig. 29 |
| Fig. 18.5 | Stacey, PoP, 9, 2692 | Fig. 3 |
| Fig. 18.6 | Greenwald, PPCF, IOP, London | Fig. 3 |
| Fig. 18.7 | Greenwald, PPCF, IOP, London | Fig. 7 |
| Fig. 18.8 | Taylor et al., Proc. 13th IAEA, Vol. I, p. 177, Vienna (1991) | Fig. 6.16.4 |
| Fig. 18.9 | Wesson, Tokamaks, Oxford, Oxford (1997) | Fig. 7.18.1 |

Chapter 19

- | | | |
|-----------|--|-------------|
| Fig. 19.1 | Stacey, Fusion Plasma Analysis, Wiley, New York (1981) | Fig. 13.6 |
| Fig. 19.2 | Stacey, Fusion Plasma Analysis, Wiley, New York (1981) | Fig. 13.5 |
| Fig. 19.3 | Stacey, Fusion, Wiley, New York (1984) | Fig. 10.4.1 |
| Fig. 19.4 | ITER web site | |

Subject Index

a

- action integral 31
- adiabatic compression heating 288
- adiabatic compression scaling 290
- adiabatic gas law 93, 94, 288
- adiabatic invariant 31
- advanced tokamak 514
- Alfven
 - shear Alfven wave 137
 - speed 138
 - toroidal Alfven (TAE) instabilities 299
 - transit time 95
 - wave 160, 164
- alpha particles
 - distribution 298
 - energy transfer 293
 - toroidal Alfven instabilities 299
- Ampere's law 17
- anisotropic pressure tensor model 96
- anomalous transport 267
- anomalous transport coefficients *see* turbulent transport coefficients
- atomic physics processes 319

b

- ballooning mode transformation 281
- ballooning modes 179, 496
- banana orbit 58
- banana regime 61
- β , beta 23, 104, 123
- β_p , beta poloidal 110, 122, 124
- beta limit 495
- beta normal 497
- Bickley function 440
- binding energy 1
- Boltzmann equation 66, 85
- Boltzmann neutral atom transport equation 413
- Boltzmann or Maxwell–Boltzmann distribution 6, 133, 315
- bootstrap current 242

bounce time or frequency for trapped particles

- 57, 61
- bremsstrahlung 470
- burning plasma dynamics 475

c

- canonical angular momentum 34
- characteristics, method of 143
- charge-exchange neutral “scattering” model 415
- Chew–Goldberger–Low theory 160
- Christoffel symbols 251
- classical transport
 - ambipolarity 214
 - central impurity peaking 215
 - fluid theory 212
 - friction force 210, 213
 - heat conductivities 229
 - heat fluxes and transport coefficients 207
 - momentum fluxes and transport coefficients 208
 - particle fluxes and transport coefficients 205
 - rate-of-strain tensor 226, 230
 - thermal conductivity 237
 - thermal force 210
 - transport parameters 228
 - viscosity coefficients 230
- collision regime 61
- collisional friction models
 - Ignitkhanov 344
 - Lorentz 213, 260
 - Rutherford 217
- compound nucleus 1
- conductivity tensor 137
- confinement scaling *see* energy confinement scaling, particle confinement
- conservation of angular momentum
 - constraint on particle motion 35
- constants of the motion 31, 34

- constraints on fusion reactor design
 - beta limit 503
 - blanket and shield 507
 - bootstrap current 506
 - confinement 502
 - density limit 503
 - fatigue limit 509
 - heat flux limits 507
 - inductive current drive 504
 - kink stability limit 504
 - noninductive current drive 505
 - radiation damage limits 510
 - stress limits 508
- Coulomb potential 6, 12
- Coulomb scattering
 - 90° deflection cross section 15
 - 90° deflection characteristic time 12
 - 90° deflection cross section 12
 - collisional friction 260
 - energy transfer characteristic time 14, 79, 80, 294
 - impact parameter 70
 - Krook scattering operators 82
 - Rutherford scattering cross section 11
- current density 14
- current drive
 - electron cyclotron 307
 - fast wave 306, 307
 - inductive 285
 - lower hybrid 305
 - neutral beam 292
- current induction in a tokamak 285
- curvature drift 28
- curvilinear coordinates 529
- cyclotron radiation 471

- d**
- Debye length 6
- Debye sphere 6
- density asymmetries 260
- density limits
 - confinement deterioration-electromagnetic instabilities 491
 - confinement deterioration-thermal instabilities 492
 - disruption 481, 485, 489
 - divertor collapse or detachment 495
 - empirical Greenwald limit 495
 - empirical Murakami/Hugill limit 487
 - Hugill diagram 482
 - MARFE 490
- diamagnetic current 38
- diamagnetic field 37
- diamagnetism 36, 109
- dielectric tensor 301
- diffusion coefficient
 - Kadomtsev mixing length 273
 - magnetic fluctuation 275
 - weak turbulence 273
- diffusion coefficients
 - Bohm 272, 335
 - classical 62
 - edge 402
 - electrostatic drift waves 272
 - gyro-Bohm 272
 - neoclassical 60
 - Pfirsch-Schlüter 61
- dispersion relation
 - Chew-Goldberger-Low theory 161
 - cold plasma 302
 - collisionless drift waves 195
 - dielectric tensor form 297
 - divertor MARFE thermal instability 347
 - drift-cone waves 200
 - electromagnetic waves 136
 - electrostatic drift waves 185
 - electrostatic waves 149, 193
 - guiding center hydrodynamic 164
 - ion acoustic wave 153, 269
 - ion cyclotron waves 151
 - ion temperature gradient 197, 270
 - kinetic instabilities 193
 - Langmuir waves 140
 - loss-cone waves 200
 - lower hybrid wave 150, 152
 - MARFE thermal instability 394
 - MHD hydrodynamic 160
 - mixed longitudinal and transverse 136
 - radiative collapse thermal instability 484
 - shear Alfvén waves 138
 - thermal instability with short k_r^{-1} 377
 - upper hybrid wave 150
 - Vlasov theory 146

- disruption
 - causes 481
 - current decay 480
 - current in vacuum vessel 481
 - current limit 481
 - density limit 481, 485, 489
 - forces in vacuum vessel 480
 - magnetic island 480
 - magnetic reconnection 480
 - mode locking 480
 - neutral density limit 489
 - physics 479
 - pressure on vacuum vessel 481
 - radiative collapse 481
 - radiative collapse thermal instability 483, 487
 - tearing mode 480
- distribution function
 - guiding center 67, 231
 - joint statistical 65
 - single-particle 65
- divertor
 - bundle 332
 - currents and drifts 351
 - detached regime 341, 358
 - divertor MARFE 346
 - double null 33
 - high recycling regime 341
 - impurity retention 343
 - parameter scaling 342
 - poloidal 332
 - private flux region 332
 - separatrix 331
 - sheath-limit regime 340
 - single null 332
 - target plate 331
 - toroidal 332
 - two-point model 338
 - X-point 331
- double-adiabatic model 98
- Dreicer velocity 14
- drift kinetic equation 66, 68, 69
- drift velocities
 - $E \times B$ 24, 199, 268
 - curvature 28, 32
 - diamagnetic 91, 184
 - divertor 351
- electron diamagnetic 194
- electron drift 269
- grad- B 25, 32, 38
- ion diamagnetic 92, 197
- polarization 27, 199, 268
- poloidal 69
- radial 69
- drift waves 185, 267, 276, 280

- e**
- $E \times B$ drift 24
- $E \times B$ shear stabilization of turbulence
 - comparison with experiment 374, 389
 - criterion for turbulence suppression 374
 - linear stabilization 372
 - nonlinear turbulence decorrelation 372, 374
 - physics 372
 - radial electric field shear 372
 - shearing rate for flute-like modes 372
- edge operation boundary 398
- edge pedestal or transport barrier
 - $s\alpha$ stability boundary 367
 - ballooning modes 365
 - ELMs 364
 - gradients 362
 - neutral penetration constraint on width 371
 - peeling modes 365
 - pressure constraint on width 369
 - pressure gradient constraint 368
 - short k_r^{-1} thermal instabilities 376
 - spontaneous edge transport barrier formation 384
 - spontaneous formation 376
 - threshold edge temperature gradient 379
- edge physics 331, 361
- elastic scattering (neutral) from Maxwellian ions 416
- elastic scattering (neutral) model 416
- electric field
 - radial 262, 403
 - toroidal 264
- electromagnetic energy density 18

- electromagnetic instabilities
 - axisymmetric, rigid body displacement 115
 - bad curvature 178
 - ballooning 179, 496
 - collisionless drift waves 193
 - drift cone 197
 - drift waves 183
 - electron temperature gradient 195
 - energy principle 165, 169
 - firehose 162, 164
 - flute interchange modes 44, 173
 - free energy sources & constraints 155
 - growth rates *see* growth rates, instabilities
 - interchange mode stability condition 175, 177
 - internal kink modes 173, 179, 498
 - ion temperature gradient 196
 - Kruskal–Shafranov surface kink criterion 173
 - loss cone 45, 157, 197
 - Mercier interchange mode stability condition 179
 - MHD instabilities *see* MHD instabilities
 - microinstabilities *see* microinstabilities
 - mirror 164
 - peeling modes 365
 - pinch 169
 - resistive tearing 186
 - sawtooth oscillations 201
 - surface kink modes 498
 - Suydam interchange mode stability condition 179
 - tearing mode 480
 - toroidal Alfvén eigenmode (TAE) 300
 - vertical displacement 114
- electromagnetic stress 18, 19
- electromagnetic theory 15
- electromagnetic wave heating and current drive
 - dispersion relation *see* dispersion relation
 - electron cyclotron resonance heating 310
 - evanescent region 302
 - fast wave electron cyclotron resonance current drive 313
 - fast wave ion cyclotron resonance current drive 312
 - ion cyclotron resonance heating 308
 - lower hybrid current drive 311
 - lower hybrid resonance heating 309
 - physics 304
 - refractive index 301
 - resonance frequencies 305
- energy confinement scaling
 - Alcator 287
 - definitions 463
 - Goldston 466
 - IOC ASDEX 466
 - ITER89-P 467
 - ITERH93-P 467
 - ITERPB93(ym2) 468
 - Ohmic 465
- energy principle 165
- energy transfer characteristic time 79, 80, 294
- equilibria
 - anisotropic pressure 128
 - axisymmetric toroidal plasma 105
 - cylindrical plasma 104
 - force balance 103
 - tokamak large aspect ratio plasma 111
- equipartition of energy 87
- evanescent region 302
- exponential integral function 421
- f*
 - Faraday's law 16
 - finite gyroradius corrections 91
- fluid theory
 - anisotropic pressure tensor model 96
 - anisotropic shear 87
 - charge continuity equation 89
 - charge density 89
 - collisional friction 86, 260
 - continuity or particle balance equation 86
 - current density 89
 - double-adiabatic model 98
 - energy balance equation 86, 88
 - energy flow 86, 88
 - energy flux equation 86

- energy flux tensor 86
- equilibrium condition 100
- external source moment 86
- finite gyroradius corrections 91
- force balance 91
- heat conduction 88
- isotropic pressure 87
- mass continuity equation 89
- mass density 89
- mass source 89
- mass velocity 89
- MHD model 93
- moments equations 85
- momentum balance equation 86, 89, 103
- momentum stress tensor 86
- Ohm's law 91
- one-fluid model 89
- plasma resistivity 90
- pressure tensor 87, 96
- rate-of-strain tensor 251
- strong field, transport ordering 98
- temperature 88
- flux surface
 - average over 107
 - definition 35, 53, 105
 - evolution 125
 - Grad–Shafranov equation 108
- Fokker–Planck
 - equation 69, 72
 - Lorentz model 73, 77
 - Rosenbluth potentials 72
 - theory of collisions 69
 - velocity-space diffusion 74
- force-free current 103
- free energy sources 155
- further reading 539
- fusion
 - break-even condition 4
 - cross section 15
 - energy release 3
 - process 1
 - reaction rates 3
 - reactions 4
- g**
 - Gauss' law 15
 - Grad–Shafranov equation 108, 120
 - grad– \mathbf{B} drift 25
 - growth/damping rates, instabilities
 - collisionless drift waves 195
 - divertor MARFE 348
 - drift waves 185
 - guiding center 22
 - ion temperature gradient 196
 - MARFE 394
 - radiative collapse 484, 486, 489
 - resistive tearing modes 190
 - thermal instabilities with short 383, 385
 - thermal instabilities with short k_r^{-1} 378
 - gyrofluid model 282
 - gyrokinetic model 282, 283
 - gyromotion 21
 - finite gyroradius corrections or effects 90
 - guiding center 55
 - gyrofrequency 22
 - gyroperiod average 30
 - gyroradius or Larmor radius 22
- h**
 - hydromagnetic instabilities
 - Alfvén wave 160
 - Chew–Goldberger–Low theory 160
 - firehose 162
 - guiding center theory 162
 - ion sound waves 133
 - magnetosonic wave 161
 - MHD theory 159
 - mirror 164
- i**
 - ignorable coordinate 31, 34
 - impact parameter 10
 - impurity production 324
 - impurity radiation 326, 473
 - incompressibility 94
 - index of refraction 138
 - inertial confinement 4
 - instabilities
 - electromagnetic *see* electromagnetic instabilities
 - free energy sources 155

- hydromagnetic 158
- inhibiting constraints 155
- thermal 376
- international tokamak program 511
- isobaric surface 91, 103, 105
- ITER 513

k

- kinetic instabilities 192
- kink modes 170, 173, 498

l

- L–H mode transition
 - comparison with experiment 374, 389
 - power threshold 361, 388, 391
 - trigger mechanisms 374
- Landau damping of waves 139
- last closed flux surface LCFS 331
- Legendre polynomials 414, 420
- limiter 332
- Liouville’s equation 65
- lithium resources 5
- Lorentz force 65
- loss cone 43

m

- magnetic
 - diffusion time 95
 - field diffusion 95, 125
 - field index 114
 - flux conservation 126
 - flux requirements 285
 - flux, poloidal 105
 - flux, toroidal 110
 - island 190, 480
 - moment 23, 25, 31, 67
 - pressure 20
 - reconnection 201, 480
 - Reynolds number 95
 - viscosity 95
 - well 41, 44, 56
- magnetic confinement
 - closed field lines 49
 - goals 4
 - open field lines 41
 - principles 41
 - progress and status 5
- magnetization 38

- magnetization current 36
- magnetohydrodynamic (MHD) theory 93, 159, 165

MARFEs

- edge density limit 394, 396
- linear stability analysis 392
- radiative condensation 395

MHD ordering

- mass defect 1
- Maxwell’s equations 93, 103, 131

- Maxwellian distribution 3, 141, 142, 148, 163, 258, 289

minimum-*B* stabilization

- mirror confinement

- central solenoid of tandem mirror 48
- confinement time 44
- loss cone 43
- loss cone instabilities 45
- loss fraction 43
- minimum-*B* 45
- mirror ratio 43
- simple mirror 41
- tandem 46

mode locking

- molecular processes 319

- momentum confinement time 264

n

neoclassical transport

- banana-plateau 237
- bootstrap current 242
- Chang–Hinton thermal conductivity 237
- closure 224
- drift-kinetic derivation 231
- extended neoclassical theory 238
- multifluid formalism 221
- orbit distortion 244
- orbit squeezing 246
- parallel collisional friction 217
- parallel viscous force 257
- Pfirsch–Schlüter 215, 217, 219
- poloidal rotation 260
- potato orbits 245
- radial electric field 262
- rate-of-strain tensor 251

- toroidal rotation 262
- toroidal viscous force 253, 405
- viscosity 251
- viscosity coefficients 258
- ware pinch 244
- neutral beam heating and current drive
 - critical fast ion energy 296
 - cross sections 291
 - current drive 298
 - deposition in the plasma 290
 - energy transfer to plasma 293
 - fast ion distribution 296
 - fast ion energy loss 293
 - neutralization efficiency 293
 - penetration 293
 - production of neutral beams 292
- neutral particle streaming operators 430
- neutral particle transport methods
 - collision probability 442
 - discrete ordinates 453
 - extended diffusion theory 424
 - integral transport 432
 - interface current balance 445
 - Monte Carlo 456
 - Navier–Stokes 460
 - spherical harmonics P_N 421
- neutral particle transport modeling
 - charge-exchange 415
 - collision probabilities 442
 - elastic scattering 416
 - escape probability 437, 445, 450
 - first collision source 419
 - Marshak boundary conditions 425, 426
 - rational approximation for escape probability 451
 - reciprocity 442
 - recombination 419
 - transmission probability 437, 442, 445, 447
- neutral particle transport theory 428
- neutron source 515

- o***
- Ohm's law 15, 91, 350
- ohmic heating of the plasma 287
- orbit turning point 56

- p***
- paramagnetism 109
- particle confinement times
- simple mirror 44
- tandem mirror 48
- tokamak neoclassical 62
- particle transport in edge pedestal
 - density gradient scale length 402
 - diffusion coefficient 402
 - pinch velocity 402
 - pinch-diffusion relation 402
 - pressure gradient scale length 403
- physical constants 521
- pitch angle 42, 56
- plasma
 - definitions 1, 6
 - formulas 537
 - frequency 8, 132, 148
 - inductance 285
 - internal inductance 113, 122, 498
 - resistance 285
 - resistivity 14, 78, 90
- Poisson's equation 6, 17, 140, 149, 152, 315
- polarization drift 27
- polarization of waves 135, 305
- poloidal magnetic flux 105
- poloidal rotation 260, 406
- Poynting vector 19
- pressure 87
- pressure gradient, normalized parameter α 182
- pressure tensor 87, 96
- private flux region 332

- q***
- quasilinear transport analysis 270
- quasineutrality 90, 151, 268

- r***
- radiation
 - bremsstrahlung 470
 - cyclotron 471
 - impurity 326, 473
 - radiative mantle 397
 - radius of field line curvature 29

rate-of-strain tensor 251
 recycling
 – coefficient 319
 – energy reflection coefficient 318
 – hydrogen retention 319
 – particle reflection coefficient 318
 – re-emission 319
 resonance absorption wave heating
 – electron cyclotron 305
 resonance absorption wave heating
 – ion cyclotron 303
 – lower hybrid 303
 rotation
 – poloidal 260
 – toroidal 262
 rotational transform of magnetic field 52
 runaway electrons 14, 479

s

safety factor 110, 116
 sawtooth oscillations 201
 scrape-off layer SOL
 – definition 331
 – length 334
 – width 334
 second adiabatic invariant 32
 second stability regime 365, 498, 499
 separatrix 331
 Shafranov shift 120
 shear of the magnetic field 53
 shear parameter S 182
 sheath
 – potential 315
 – power transmission coefficient 317, 337
 solenoidal law 16
 Sonine polynomials 226
 sputtering 324
 stagnation (flow) point 334
 stellarator 50
 strong field, transport ordering 98

t

temperature 74
 thermal diffusivity
 – chaotic magnetic island overlap 277
 – dissipative trapped electron mode 276

– electron temperature gradient mode 277
 – ion temperature gradient mode 276
 – resistive ballooning mode 277
 – trapped ion mode 276
 thermal instabilities
 – confinement deterioration 491
 – divertor MARFE 346
 – MARFE 392
 – power threshold for L–H transition 388
 – radiative collapse 483
 – short radial wavelength 376
 – spontaneous edge transport barrier formation 384
 thermonuclear temperature 3
 tokamak 50
 toroidal coordinates 531
 toroidal magnetic flux 110
 toroidal rotation 240, 262
 transmutation of spent nuclear fuel 516
 transport in partially ionized gas 247
 transport ordering 98
 trapped particle bounce time 57
 trapped particles 42, 56
 Troyon beta limit 497
 turbulent transport coefficients
 – chaotic magnetic island overlap 277
 – electron temperature gradient modes 277
 – ion temperature gradient modes 276
 – resistive ballooning modes 277
 – trapped electron modes 276
 – trapped ion modes 276

u

units 523

v

vector calculus 527
 vector potential 16, 17
 viscosity
 – gyroviscosity 253
 – neoclassical viscosity 258, 260
 – parallel viscosity 253, 257
 – perpendicular viscosity 253
 – toroidal viscous force 253
 – viscous stress tensor 252
 Vlasov equation 66, 139

w

- Ware pinch 59
- waves in plasmas
 - Bernstein 301
 - circularly polarized 135
 - current drive *see above*
 - cut-off 302, 307, 309, 310
 - dielectric tensor 301
 - direct interaction approximation 279
 - drift waves *see* drift waves
 - electromagnetic 131, 134, 295
 - electron cyclotron 305
 - electrostatic 136, 148
 - evanescence region 302
 - group velocity of wave packet 303
 - Hasegawa–Mima equation 280
 - index of refraction 138, 295
 - ion acoustic 133, 162, 268
 - ion cyclotron 150, 305
 - Landau damping 139
 - Langmuir 139
 - lower hybrid 137, 150, 305

– mode coupling 278

- ordinary (O) and extraordinary (X) 307**
- penetration condition, parallel waves 136**
- phase velocity 138**
- polarization 135, 305**
- propagation 302, 306**
- ray tracing 303**
- reflection 302**
- resonance absorption wave heating *see* above**
- resonance frequencies *see* electromagnetic wave heating**
- shear Alfvén 137, 188**
- upper hybrid 137, 150, 305**
- Vlasov theory of 142, 155**
- wave packets 303**
- wave-particle collisionless dissipation 307**

x

- X-point 331